Where Three Oceans Meet:
The Agulhas Retroflection Region

by

Sara Louise Bennett

B.S. Colorado State University, Fort Collins, Colorado
1977

SUBMITTED IN PARTIAL FULFILLMENT
OF THE REQUIREMENTS FOR THE DEGREE OF
DOCTOR OF PHILOSOPHY

at the

Woods Hole Oceanographic Institution

and

Massachusetts Institute of Technology

September 1988

Signature of author _____
Joint Program in Oceanography, Massachusetts Institute of Technology/Woods Hole Oceanographic Institution

Certified by _____
Thesis Supervisor

Accepted by _____
Chairman, Committee for Physical Oceanography, Massachusetts Institute of Technology/Woods Hole Oceanographic Institution

DEDICATION

to

my grandmother, Josepha Lott Parker,

my oldest friend, Antonie Dehn,

and

all the women of southern Africa

who struggle against *apartheid*

ABSTRACT

The highly energetic Agulhas Retroflection region south of the African continent lies at the junction of the South Indian, South Atlantic, and Circumpolar Oceans. A new survey of the Agulhas Retroflection taken in March 1985, plus historical hydrographic data, allow its dynamical and water-mass characteristics, and its role in exchanging mass, tracers, and vorticity between the three oceans, to be extensively characterized. The 1985 survey is composed of three independent, synoptic elements: a grid of closely-spaced, full-water-depth hydrographic stations (the first entirely full-water-column survey in this area), including several transects of the Agulhas and Agulhas Return Currents; a continuous survey of the path of the currents (the first such survey in the Agulhas); and a contemporaneous and relatively cloud-free sea surface temperature image derived from satellite infrared measurements.

Mass transport balances within the closed grid boxes of the 1985 hydrographic survey provide information about current transport, recirculation (transport in excess of estimated returning interior ocean transport), and the overall Retroflection transport pattern. The current transport values exceed by as much as a factor of 1.5 the maximum interior transport computed from observed wind-stress curl and linear theory. Agulhas Current transports ranged from 56 to 95×10^6 m s^{-1} at four 1985 transects crossing the current. Agulhas Return Current transports at the two 1985 transects were 54 and 65×10^6 m s^{-1}. These transports are computed relative to 2400 dbar, which lies below the deep oxygen minimum emanating from the South Indian Ocean, and above the North Atlantic Deep Water salinity maximum.

The current retroflected in two distinct branches in 1985, with a cold ring and a partially isolated warm recirculation cell found between the two branches. The satellite-derived sea surface temperature (SST) image, in agreement with the *in situ* measurements, showed that the cold ring lacked a cold SST anomaly; that the subsurface current path, as represented by a survey of the 15 C isotherm and 200 dbar surface intersection, was closely followed by a sharp front in sea surface temperature; and that most of the Agulhas's surface warm core retroflected upstream of the second retroflection branch.

Anticyclonic curvature vorticity at sharp turns in the subsurface current path was found to exceed the maximum allowed by gradient wind balance, indicating that at these locations time-dependence and cross-frontal flow are important. The current's density field is found to meet necessary conditions for baroclinic and barotropic instability. These instability mechanisms may play a role in ring formation and current meandering.

Top-to-bottom cross-stream spatial and isopycnal water-mass layering in the Agulhas Current, Agulhas Return Current, and associated rings are presented in two sets of sections, one contoured with pressure and the other with potential density as vertical coordinate. Temperature, salinity, oxygen, potential density and velocity sections are shown contoured versus pressure; and pressure, salinity, oxygen, and planetary potential vorticity are shown contoured versus potential density. These sections clearly illustrate water-mass structure both in space and relative to isopycnal surfaces. Strong salt, oxygen, and potential vorticity fronts on isopycnals in the upper ~300 m across the Agulhas and Agulhas Return Current are observed, as are deep western boundary filaments of *(i)* salty, low oxygen water at intermediate depths traceable to Red Sea Water influences, and *(ii)* salty North Atlantic Deep Water close round the tip of Africa.

The 1985 cold-core ring is the first cold-cored isolated feature to be observed within the Retroflection itself. Its transport was 64×10^6 m s^{-1}, its integrated kinetic and available potential energy anomalies were 8.3 and 61×10^{15} J respectively, and its integrated planetary potential vorticity anomaly was 2.8×10^{-12} m^{-1} s^{-1}. The potential vorticity flux associated with the exchange of 25 warm ring/cold ring pairs per year between the South Indian and Southern Oceans would balance the potential vorticity input by the wind to the entire South Indian Ocean.

Interbasin flow of warm thermocline water (warmer than 8 C) from the South Indian to the South Atlantic Ocean is reconsidered in light of the 1985 hydrographic data. Thermocline water flow from the South Indian Ocean into the South Atlantic in the 1985 and historical observations is found to range from 2.8 to $<9.6 \times 10^6$ m s^{-1}. These values are less than the $\leq 10 \times 10^6$ m s^{-1} needed to balance the Atlantic Ocean export of deep water, and implies that the deep water export is balanced in part by water colder than 8 C.

TABLE OF CONTENTS

FOREWORD

One might consider that if one is born an explorer
he will never find existence dull.
— Ansel Adams: An Autobiography

Roald Amundsen claimed the last great prize of discovery in his dash to the South Pole in 1911. My generation - those who are now young adults - is thus about the last to have direct living ties, through our grandparents and oldest friends, to a world with a frontier. Those who first dreamt of journeying beyond the horizon - painters of caves, builders of earthen mounds, and arrangers of stones - created the frontier millennia ago. We are the last of many generations to experience even indirectly an open, ever-expanding world.

And my generation is the first to grow up with the understanding that our planet is fragile and small compared to the impact of human habitation and technology. Images of Earth rising over the Moon's horizon (taken by the Apollo astronauts in 1969) symbolize this new awareness. As children we read Rachel Carson's Silent Spring (1962) and, as teenagers, the Club of Rome's Limits to Growth (1974). We know that critical natural habitats are threatened by pollution and deforestation; that anthropogenic changes in atmospheric chemistry will cause sea level to rise, with potentially disastrous consequences; that nuclear weapons sufficient to kill most of the inhabitants, human and otherwise, of at least the northern hemisphere are already in place. Nuclear winter captures our imagination because it links environmental collapse and nuclear war in a single image.

Our and our children's futures may yet be found in a crystal ball full of ashes. But we who are scientists, artists, photographers, thinkers, and poets, are again explorers. We seek to understand our world as a single interconnected system, to learn how to minimize our damage to our planet. Our generation is pioneering new ways of thinking, appropriate to our closed fragile world, that will gradually supplant the twin traditions of frontier and war. The expansion, exploitation, confrontation, and conflict that have both glorified and scarred human history will never disappear, but they may become increasingly irrelevant to most of the inhabitants as we learn how to live in harmony with nature and with each other. We know that exploration, broadly defined, has always been a prime source of social innovation, whether benign or brutal. Our discoveries hold forth the promise of a more just and peaceful society.

The remainder of this Foreword summarizes my thesis for my non-oceanographer friends and family.

The Agulhas Current is a warm, swift current found flowing along the eastern coast of southern Africa. It leaves the African coast near the tip of the continent and then curves around in a large loop south of Africa called the Agulhas Retroflection. The Agulhas is the South Indian Ocean counterpart of the Gulf Stream and Brazil Currents in the North and South Atlantic, and of the Kuroshio and the East Australia Currents in the North and South Pacific. These currents are all found in the Earth's temperate, subtropical zone, and they each flow poleward.

As natural features of the Earth's surface, these currents are impressive in scale. Only in 1970 was it possible to see the Gulf Stream system clearly as a whole entity, in the first very-high-resolution satellite infrared image of the North Atlantic, and then only in two dimensions at the ocean's surface. These currents are sometimes called 'rivers in the ocean' even though they do not flow 'through' the ocean but are inseparable from it. Each transports about two thousand times as much water as the Mississippi, about 100 million cubic meters of water per second.

Velocities in the currents' core are 1 - 2 meters per second, or 2 - 4 knots. This is the speed of an easy jog, slow compared to modern means of transportation. But in 1770, mail packets often took two weeks longer than merchant ships to make the passage from England to New England, until the Postmaster General for the American colonies, Benjamin Franklin, had a chart of the Gulf Stream engraved and distributed.[1]

In the ocean interior, away from the boundary currents, water flows equatorward on average at subtropical latitudes. This slow equatorward interior flow depends upon spatial variations in the wind field[2] and the sphericity of the Earth. It is an

---

[1]B. Franklin, 1786: A letter . . . containing sundry maritime observations. Trans. Amer. Philos. Soc., Philadelphia, 2:294 - 329. From H. Stommel, 1958: The Gulf Stream.

[2] Plus a small contribution due to atmospheric heating, cooling, evaporation, and precipitation.

expression of the physical principle of angular momentum conservation.[3] The Agulhas and other western boundary currents exist to return the equatorward interior flow back toward the poles. Without this return flow, the polar oceans would quickly run dry.

The western boundary currents are found along western rather than eastern boundaries of the ocean again because of the principle of angular momentum conservation. The western boundary supplies to a water column moving poleward torques of the right sign to balance increases in angular momentum with latitude on the spherical Earth. Eastern boundary currents do indeed occur when winds blow alongshore near an eastern boundary. The California Current along the California coast in the North Pacific and the Peru Current along the Peruvian coast in the South Pacific are examples. But no net transport of water across latitude lines occurs in these currents - the near-surface flow is balanced by equal and opposite deep flow - so no net torque from the boundary is needed to sustain them.

The western boundary currents make a significant contribution to the global heat balance since they bring warm tropical surface water poleward. The greatest heat loss anywhere in the ocean occurs when the warm cores of these currents reach the poleward side of the subtropical ocean circulation.

The currents are so energetic that they meander with time and shed warm- and cold-core rings. The rings themselves, once formed and separated from the current, can also transport heat from one ocean region to another.

The Agulhas Current is unique among the world's western boundary currents because the African continent ends in the middle of the subtropical latitude band. This means that the continent ends where the interior and Agulhas flow are still large. As a result, the Agulhas shoots past the southern tip of Africa as a free jet. The free jet has no western boundary to supply torques to balance increases in angular momentum with latitude. So the angular momentum increase with latitude is balanced instead by

---

[3] The curl of the wind field causes fluid in the surface layer to converge, squeezing the underlying water column. As the height of water parcels in the column decreases, their plan area, and thus their moment of inertia and angular momentum due to the Earth's rotation, tend to increase. To counteract this change, the water parcels move equatorward, along the surface of the spherical Earth, which reduces their angular momentum by reducing the projected plan area that is perpendicular to the Earth's rotation axis.

curvature in the current's path, which turns counterclockwise towards the South Indian Ocean. This southward extension of the Agulhas from the African continent and the great curving loop it makes there, is called the Agulhas Retroflection. The Retroflection is a favored location for meandering and ring-formation. The current that emerges from the Retroflection flowing eastward is called the Agulhas Return Current. Directly south of the Return Current is the Antarctic Circumpolar Current that encircles the Earth in a continuous eastward-flowing band.

The truncation of the African continent within the subtropics also means that the South Indian circulation, including the Agulhas, and the South Atlantic circulation, including the Brazil Current, are not entirely separate. Observations and theories both indicate that part of the Agulhas flows around the tip of Africa from the Indian Ocean to the Atlantic Ocean, although the magnitude and time-variability of this flow are not known. As the warmest Agulhas water is considerably warmer than any other water found in the southeast South Atlantic, this flow may be important in the heat balance for the two oceans and may have far-reaching climatic consequences. These issues are not well-understood at present.

This thesis presents measurements taken in early 1985 in and around the Agulhas Current. During a month-long cruise, temperature, salinity, pressure, and oxygen measurements were taken from the ocean surface to the bottom at 2 m intervals,[4] at almost a hundred stations separated by 20 - 50 km in the horizontal, arranged in several lines across the current and across some of its associated rings. The subsurface path of the current was followed for 2500 km by navigating along the intersection of a depth surface and a sloping temperature surface. Satellite infrared images of sea surface temperature from the same time period were also obtained.

Some of the less technical conclusions of the thesis are as follows. The surface temperature is not related in an entirely simple way to sub-surface temperature patterns and the current transport field. Knowledge of this relationship is important for

---

[4]The raw data actually consists of digital signals transmitted from an array of sensors and includes samples over intervals much smaller than 2 m. The sampling interval depends on the rate the instrument is lowered and on characteristics of the sensors. The raw data is averaged into 2 m bins that provide more than sufficient resolution for studies of ocean circulation such as this thesis. Other investigators and instruments address themselves to oceanic fine- (10 cm) and micro- (<1 cm) structure measurements.

interpreting the vast majority of satellite infrared images that are not complemented by subsurface measurements. Satellite infrared images have been interpreted previously as showing only gentle turns in the path of the current. The current path shown by the new survey's subsurface measurements includes several very abrupt ninety-degree or greater turns. Also, the flow pattern that would be inferred from the satellite images taken during the survey is rather different from the pattern computed from the subsurface measurements. The image and the subsurface measurements can be reconciled, but they each tell only part of the story.

This new survey shows the current flowing directly over the relatively shallow (<3000 m) Agulhas Plateau instead of around it as in all previous observations. This implies that the current is not steered by bottom topography as strongly as was previously thought.

The current flow is larger than the estimated returning ocean interior flow by a factor of almost two. Similar recirculation has been observed in the Gulf Stream and in numerical models of the ocean, though the dynamics of this recirculation are not well understood.

The Retroflection was found to have not one but two distinct branches during the survey. The survey also found a large cold-core ring within the Retroflection itself, an entirely novel observation. The ring is not detectable in the contemporaneous satellite infrared images of sea surface temperature. A comparison of the satellite images and the other measurements suggests that the warm core of the current seems to follow the branch of the Retroflection farthest upstream. The comparison also suggests that the upstream branch is slowly moving towards the southwest. This movement is similar in direction and rate to previous satellite observations of Agulhas path movement.

Signs of several warm rings were seen to the west of the Retroflection in this, as in previous, surveys.

Net transport from the Indian to the Atlantic Ocean is calculated from this 1985 survey, but the amount is only one-fourth of the value calculated from data taken in 1983. The net calculated transport is shown to depend on how far the calculation is carried across rings near the coast.

Taken together, existing analytical and numerical models make reasonable predictions for the gross scale of the Retroflection, and for the magnitude of the recirculating transport. They also show, in general agreement with observations, enhanced ring formation at the Retroflection, and Indian to Atlantic transport via both

steady flow and rings. Other phenomena are depicted less well or not at all by the models: the influence of bottom topography on the course of the Agulhas, the interaction of the Retroflection and the Antarctic Circumpolar Current, and the effect on the Agulhas of time-dependence in the winds over the ocean interior.

We do not yet know how some of the oceanic phenomena mimicked by the numerical models work. What sets the intensity of the recirculation? How does the boundary current join to the interior flow? How does the boundary current affect the structure of the interior circulation? How do Agulhas rings form? What determines their trajectory after separation?

Further, how do the world's boundary currents compare to each other? Will such a comparison provide any clues to their dynamics? Future graduate students will answer these and other interesting questions.

ACKNOWLEDGEMENTS

Physical oceanographers and meteorologists include in their intellectual lineage not only classical physicists and mathematicians, but also members of the gentler, unnamed fraternity of farmers, sailors, fishers, and all those who have watched and measured weather, waves, and currents. Those of us who work on very large scale phenomena can also claim kinship with mapmakers, geologists, astronauts, environmentalists - all those who think about the Earth beyond their immediate space-time horizons. I respectfully acknowledge this lineage and tradition as the inspiration and source of my education.

My metamorphosis from prospective graduate student to oceanographer was most influenced by three people, and a sailing vessel. I list them here in the order I met them. Bruce Howell and *Passage of Tiree* first took me out on the open sea, where I felt more fear, delight, and peacefulness than I thought possible. Mike McCartney, my first friend and constant mentor at WHOI, freely shared his scientific insights, and supported and encouraged me throughout my graduate studies. John Toole, my advisor, supported me financially and personally with patience and good humor. I hope having a first graduate student of a temperament so different from his own did not shorten his life expectancy too much.

My decision to return to graduate school in oceanography (*physical* oceanography) was the chance result of seeing Val Worthington on the PBS television show *Nova* back when I lived in Berkeley, California. I knew I wanted to continue my studies . . . and that I was interested in the ocean . . . but I first learned the name for my future occupation one afternoon when I came home from work and flicked on the TV to see "Dr. Valentine Worthington, Physical Oceanographer, Woods Hole Oceanographic Institution" talking about the Gulf Stream. That's what I want to do! I thought. Several years later I got up the nerve to tell Val this story, during a pre-cruise visit with Mike McCartney to Val and wife Ruth's summer home in Chipping Camden, near Stratford-upon-Avon; Mike and I had run into Val on the street in front of the Royal Shakespeare Theatre the day before. But Val insisted that I must be mistaken about seeing him on *Nova*! Later he relented: "you know, I do remember some TV cameras, but I never knew they'd used any of it." Val had been Mike's postdoctoral sponsor at WHOI. It is a privilege to carry on their tradition, and I hope I prove worthy of them.

While writing this thesis, I came to think of the new data set I was analyzing as the Agulhas Retroflection equivalent of the Gulf Stream '60 survey. It would be an

oversight not to acknowledge the late Fritz Fuglister, whose thoughtful analysis of the '60 data in many ways set a standard to which I aspired. Mr. Fuglister had long been an emeritus scientist at WHOI when I arrived here. Though we never discussed science, his presence kept me in mind of the foundations upon which I was building. And it must be said, our ideas of progress notwithstanding, computer graphics can only aspire someday to imitate Mr. Fuglister's gorgeous free-hand contouring

I wish to thank the scientists and crew on *R/V Thomas Washington*, Marathon Cruise 3, legs 11 and 12, for collecting the data used in this thesis. Maggie Francis of the WHOI CTD Group, one of those who participated in the cruise, brought the data into usable form. Swami Steve Rintoul set up the inverse model programs and taught me how to use them. Kelly Luetkemeyer provided the registered satellite images. Nick Fofonoff showed me how to use make slides of the images, and made helpful comments concerning the then newborn buoyancy potential vorticity conservation equation.

Pierre Flament generously gave me unlimited access to his SUN computer, which allowed me to finish the data processing quite painlessly, including recompositing the satellite images. Pierre's enthusiasm for and impatience with science and life provided much fun during the grind of writing up. Benedict Dousset and Io's afternoon visits to play with the penguins ('again!') also helped.

I also wish to thank all my friends involved with the WHOI Committee on Human Resources who encouraged and educated me in so many ways. It was a privilege to work with such a fine group of people. And thanks to the Killer B's (volleyball team), the Geotones ('50s band), Ron LaFreniere (running coach), and Amnesty International Group 77 of Falmouth for keeping me connected with the real world outside the ivory tower.

Donna Carson and Vicki Cullen graciously let me use their laser printer whenever I wanted, without charge. Barbara Grant at MIT, Ruth Gorski, Cyndy Lanyon, Mary Woodgate-Jones, Jan Zemba, Carol Alessi, and Mike Caruso helped me learn how to use programs on the MIT IBM system, the WHOI VAXes, and the SUNs. Colleen Hurter of Library Services always found the articles I needed with amazing speed. Dan Kelley gave many hugs, sliced through Gordian rhetorical knots, convinced me to get the Apple Macintosh computer on which this thesis was written, and then wrote superb graphics programs ('gr' and 'gri') for it and gave me copies, which I used

to make many of the figures that appear here. The cheerful assistance of all these individuals was essential and is much appreciated.

While a student, I participated in three cruises – Barbados to Recife, Brazil in 1983; Azores to Recife, Brazil in 1984; and Mauritius to Cape Town, South Africa in 1987. I wish to thank Mike McCartney and Jim Luyten, the chief scientists, other members of the scientific parties, officers, and crew members aboard the *R/V Oceanus, R/V Knorr,* and the *RRS Discovery* for many interesting and enjoyable weeks at sea.

My thesis committee at the time of my thesis defense included John Toole, chairman, Harry Bryden via TELEMAIL from his sabbatical post in the UK, Ray Schmitt, Bill Schmitz, and Glen Flierl representing MIT and JCPO. Joe Pedlosky, Bob Weller, and Bill Young at MIT participated at earlier stages. Jim Luyten ably chaired a painless defense. I thank them all for their helpful comments.

Thanks also to Jim Luyten, Kathie Kelly, Rana Fine and Don Olson at Miami, Arnold Gordon at Lamont, and Carl Wunsch at MIT for helpful discussions.

I note that my advisor, John Toole, studied under Terry Joyce, a student of Bob Beardsley, himself a student of Carl Wunsch, who studied with Henry Stommel. I think this makes me the first great-great-great-grand-student of the MIT/WHOI physical oceanography Joint (and pre-Joint) Program.

Funding was provided by the Office of Naval Research under contract numbers N00014-84-C-0134 (NR083-400), N00014-85-C-0001 (NR083-004), and N00014-87-K-0007 (NR083-004).

LIST OF FIGURES

FIGURE *PAGE*

CHAPTER 1. Introduction

CHAPTER 2. Path of the Currents

CHAPTER 3. Current transport and interior circulation

CHAPTER 4. Tracer fields

CHAPTER 5. Velocity and vorticity

CHAPTER 6. Retroflection Models

CHAPTER 7. Cold core ring

CHAPTER 8. Interbasin exchange and the Cape Town Eddies

LIST OF TABLES

Chapter 1: Introduction

The Agulhas Current is the western boundary current found flowing along the eastern coast of southern Africa. It separates from the coast near the southern tip of the continental slope. South of the continent, as a free jet, it curves around in a large loop called the Agulhas Retroflection. The jet emerges from the Retroflection flowing east as the Agulhas Return Current.

The Agulhas Current separates from the western boundary and flows out into the ocean as a free jet near the latitude where the wind-driven interior transport is at a maximum, since the African continent's southern tip lies near the middle of the subtropical anticyclonic wind-stress curl zone. This unique arrangement - all other western boundary currents separate from meridional coasts that continue poleward - gives rise to the Retroflection. After separation, planetary vorticity changes experienced by the free jet as it crosses latitude lines are balanced, on average, with jet curvature vorticity. Only a very small part of the jet transport, derived from its inshore side and governed by linear dynamics, flows into the South Atlantic ocean instead of retroflecting *(de Ruijter, 1982)*. The free jet injects a large amount of heat, kinetic, and potential energy into the region just south of Africa, making it one of the ocean's most dynamically active and interesting areas.

The word 'retroflect' was first given to the abrupt turn of the Agulhas south of Africa by Nils Bang *(Bang and Pearce, 1970)* after the first synoptic survey of the area in March 1969. Fig. 1.1 and 1.2 reproduce figures from *Harris and van Foreest (1978)* where the 1969 survey final results were reported. In the 1969 survey, a warm core ring was observed off Cape Town.

During the next survey of the region in November-December 1983, the Retroflection and a warm core ring off Cape Town were seen in positions very similar

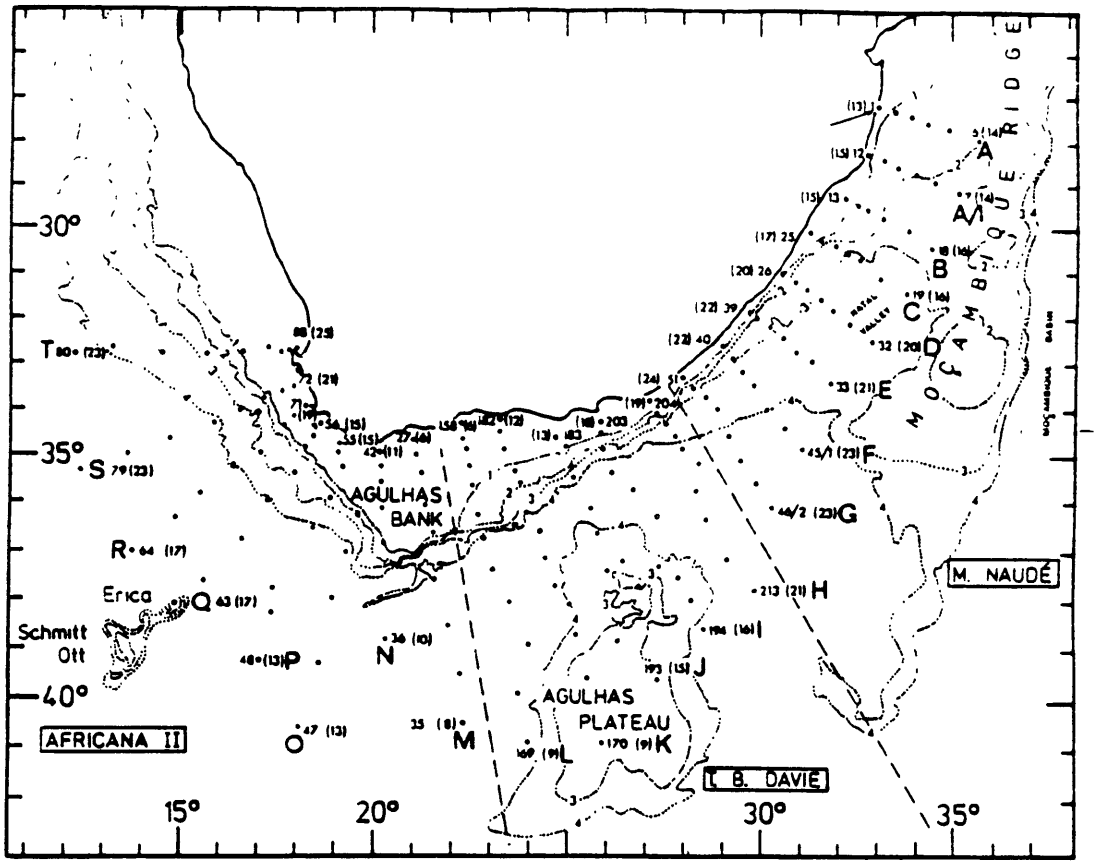

Fig. 1.1 – Agulhas Retroflection region, March 1969 hydrographic survey, station locations and bottom topography. This is a reproduction of Fig. 1 of *Harris and van Foreest (1978).*

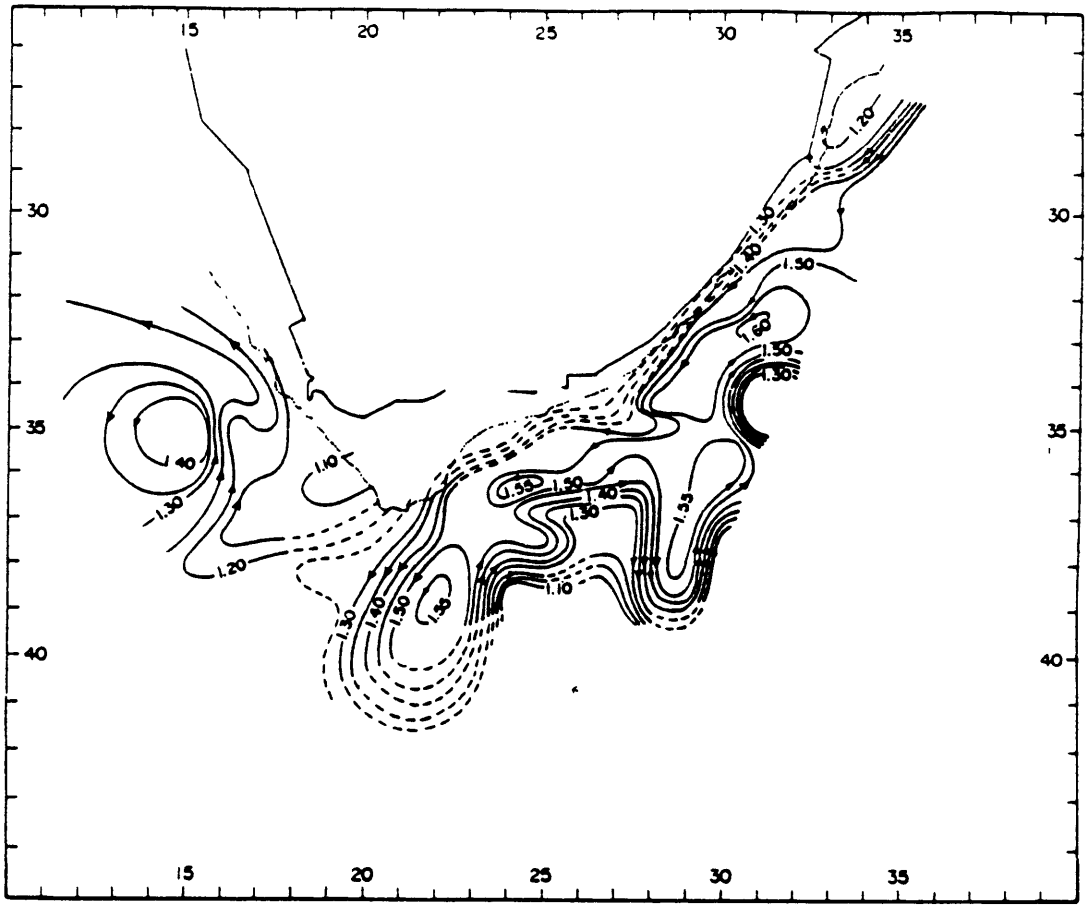

Fig. 1.2 – Agulhas Retroflection region, March 1969, acceleration potential on the 26.6 σ_t surface relative to 1000 m. This is a reproduction of Fig. 5 of *Harris and van Foreest (1978)*. The warm core ring off Cape Town is centered near 35°S, 15°E.

to those of the 1969 survey. Fig. 3.13 and 3.14 in Chapter 3 reproduce figures from *Gordon* et al. *(1987).*

From these two surveys alone one might conclude that the Retroflection is a nearly steady region. In fact, satellite infrared and altimeter observations indicate that the Retroflection location, at least, varies considerably with time. Sea surface temperature images derived from satellite infrared measurements for the period 1984–1985 show considerable variation in the location of Agulhas surface temperature signature *(Lutjeharms and van Ballegooyen, 1988).* Variability in sea surface height along a track cutting through the Retroflection was observed during repeated satellite altimeter passes *(Cheney* et al., *1983).*

This thesis presents the results of a survey of the Retroflection region in February/March 1985 performed by John M. Toole and James R. Luyten. This survey includes three independent, synoptic elements:

- an extensive grid of closely-spaced, full-water-depth hydrographic stations, including several transects of the Agulhas and Agulhas Return Currents (Fig. 1.3),

- a continuous survey of the path of the currents (Fig. 1.4), and

- a contemporaneous and relatively cloud-free sea surface temperature image from satellite infrared measurements (Fig. 1.5).

This is the first hydrographic survey of this region in which nearly all stations reach to within 200 m of the bottom and the first continuous path survey of the Agulhas and Return Currents.

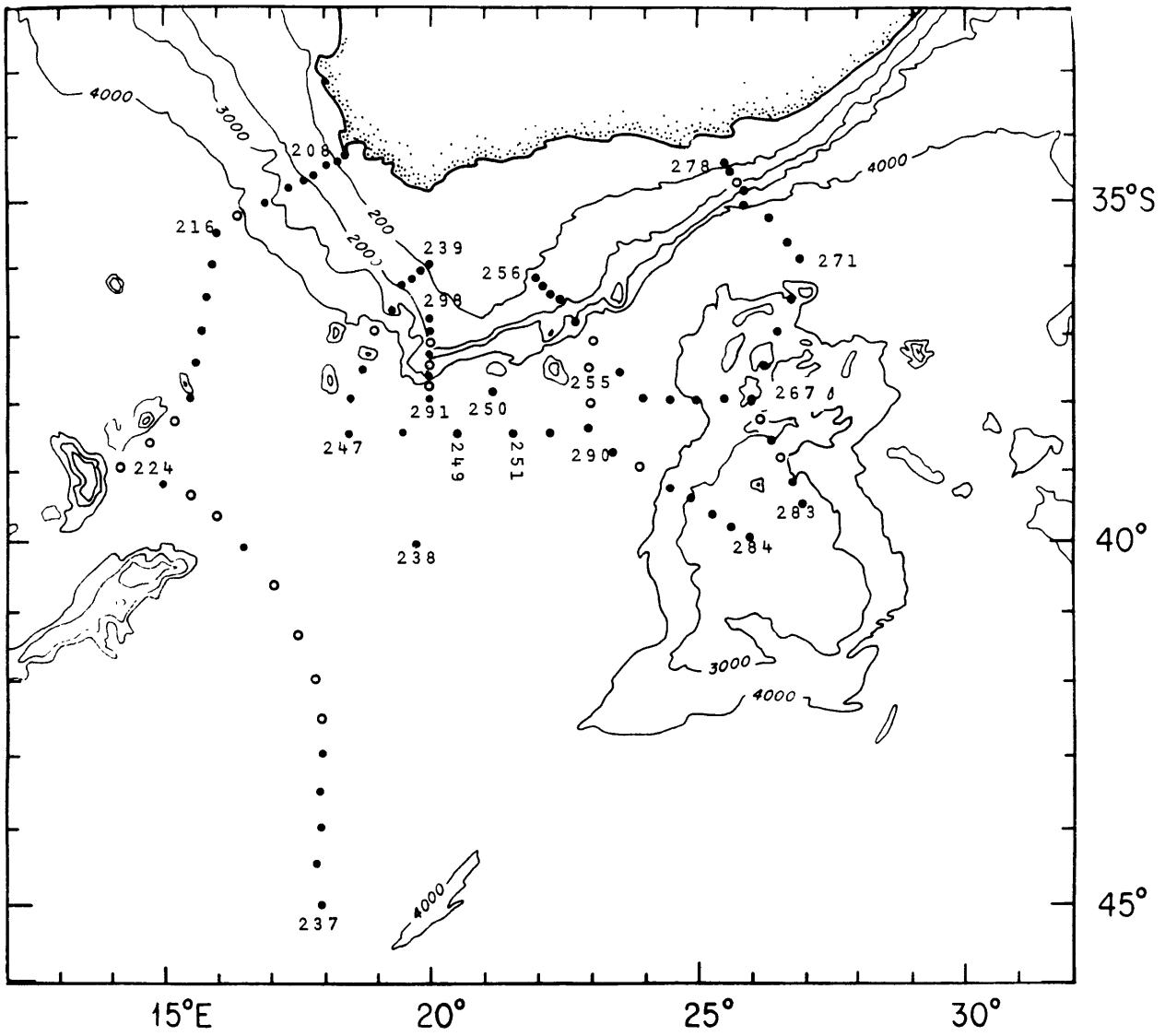

Fig. 1.3 – Agulhas Retroflection region, February/March 1985 hydrographic (CTD/O_2) survey, station locations and bottom topography. Stations marked with solid dots reach to within 200 m of the bottom.

The maximum depth and bottom depth at stations marked with open circles are:

Sta.	End (m)	Bottom (m)	Sta.	End (m)	Bottom (m)	Sta.	End (m)	Bottom (m)
215	4081	4415	230	4033	4741	276	2105	2414
222	4705	4907	231	4537	4793	279	2531	2865
223	4807	5013	232	5009	5481	281	2615	3085
224	4305	4644	244	4005	4347	289	4001	5013
226	3243	4960	254	4885	5488	292	1231	4591
227	3607	5013	255	5003	5402	294	1007	3819
229	2679	5108	261	3311	5381	296	1263	2113

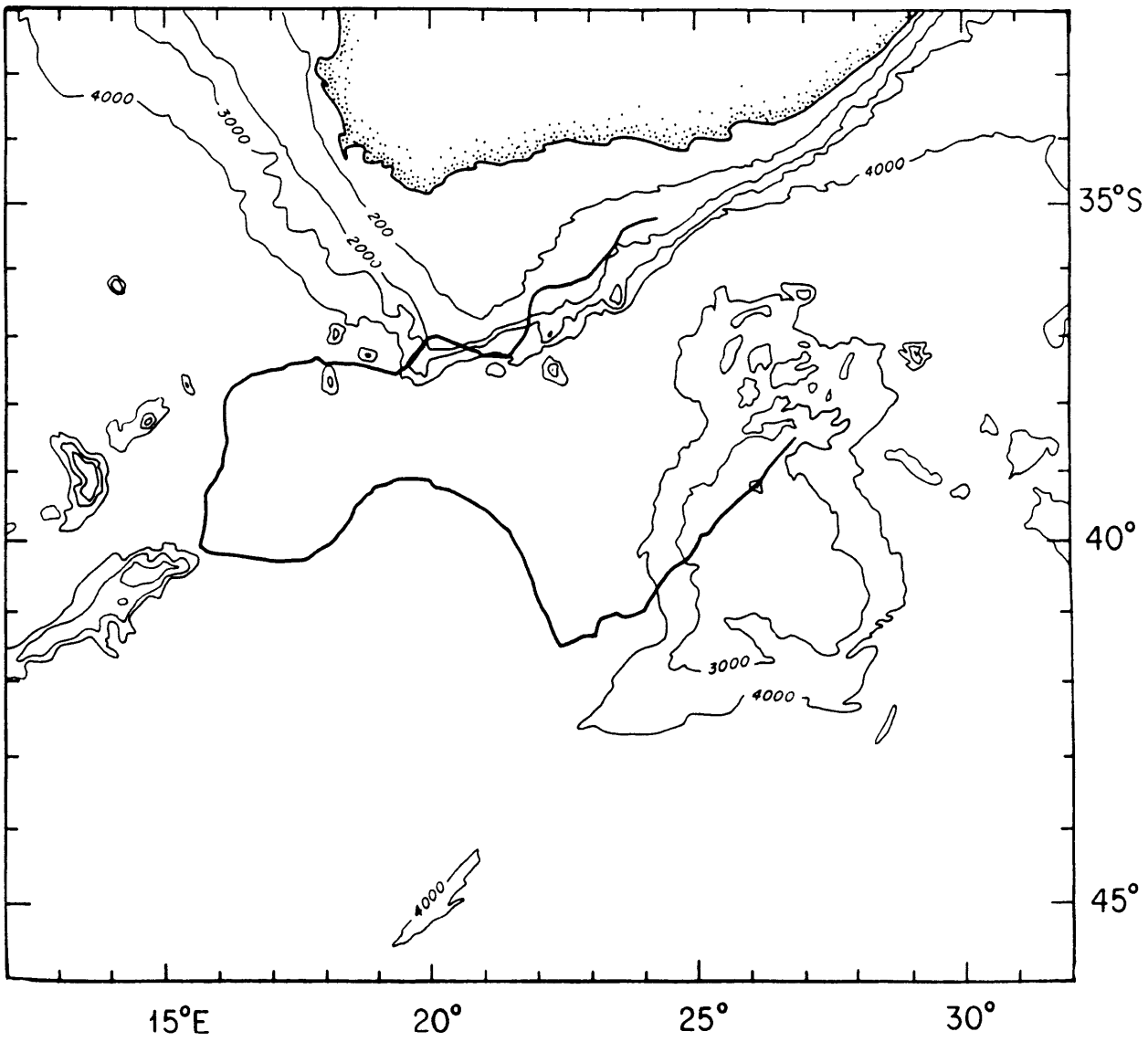

Fig. 1.4 – Agulhas Retroflection region, February/March 1985, continuous survey of the path of the current, produced by navigating along the intersection of the 15 C isotherm and the 200 m depth surface.

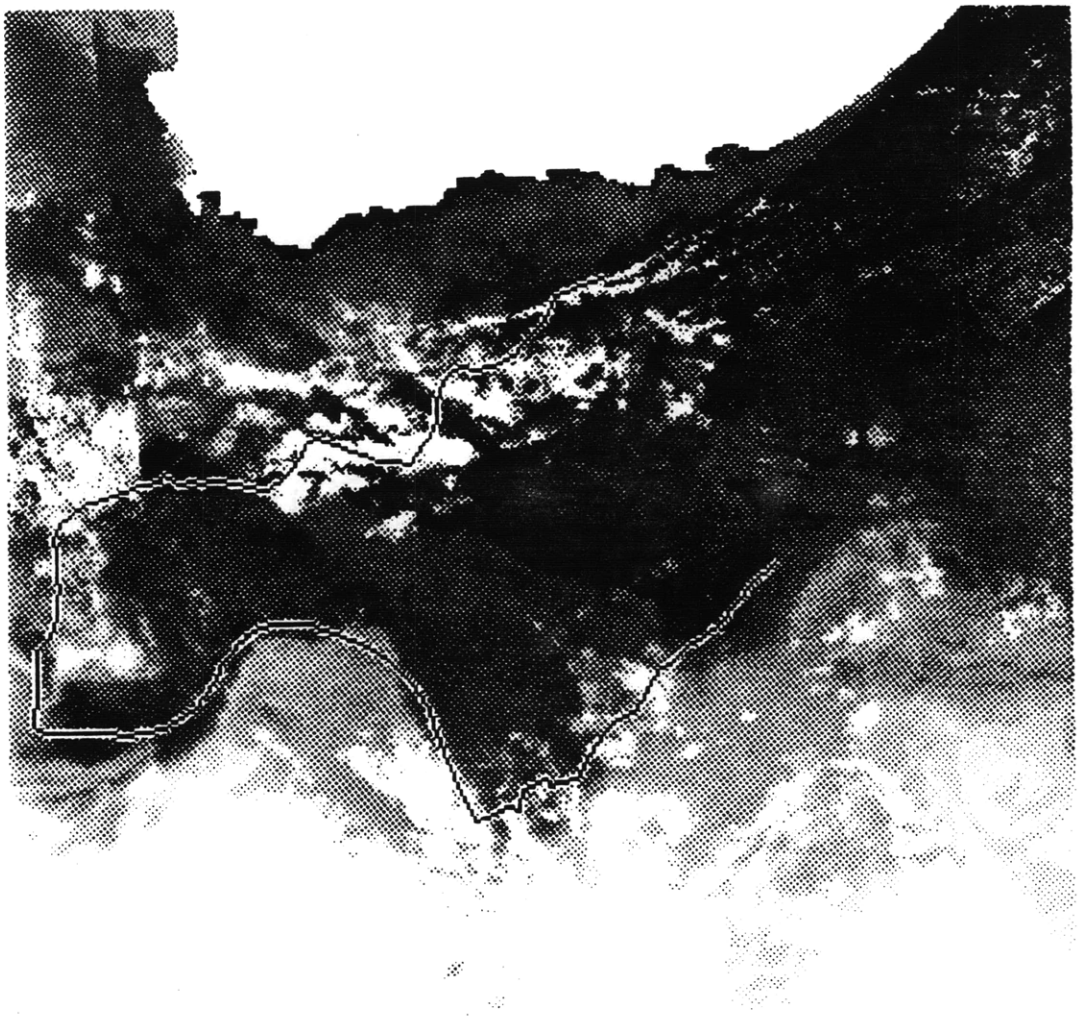

Fig. 1.5 – Agulhas Retroflection region, 25 – 27 March 1985, composite satellite infrared image of sea surface temperature. Warm sea surface areas appear black, and colder clouds appear white. Black on white line is the continuous survey of the intersection of the 15 C isotherm and the 200 m depth surface. Black band extending diagonally across image is the warm core of current, which is following the smaller upstream Retroflection branch. Some black warm core water is seen along the survey line also. Note patch of warmer water off Cape Town near the surface expression of the warm-core ring. The surface temperature front and survey line are in good agreement along the westward-flowing Agulhas Return Current (southern half of continuous survey). Cold-core ring within the Retroflection is not visible in this image (cf. Figs. 1.7 and 1.8). Straight vertical line in upper left is a remnant of the edge of one of the daily satellite images. This image is enlarged 116% relative to the regional maps.

This thesis uses these three survey elements independently and in combination to answer a number of questions about the characteristics and dynamics of the Retroflection region. For the *first time in this region*:

- The *subsurface* path of the Agulhas and Agulhas Return Currents is characterized. The subsurface current path is compared to the current path inferred (i) from the accompanying 1985 hydrographic survey, (ii) from the accompanying 1985 satellite infrared image of sea surface temperature, (iii) from previous hydrographic and satellite surface temperature measurements, and (iv) from dynamical models.

- Information about *bottom and reference level velocities, recirculation* (transport in excess of estimated returning interior ocean transport), and *flow bifurcation* is inferred from transport balances within closed grid boxes, computed relative to a deep level.

- The *top-to-bottom* structure of the current is examined at *repeated synoptic* hydrographic transects. Sections are presented of temperature, salinity, oxygen, potential density and velocity on pressure surfaces; and of pressure, salinity, oxygen, and planetary potential vorticity on potential density surfaces. Characteristics at this new set of transects are related to characteristics at previous (single or intermediate-depth) transects in the Agulhas and to characteristics observed in the interior South Indian, South Atlantic, and Circumpolar Oceans.

- Terms in the expression for *total potential vorticity* in natural isopycnal coordinates (derived here) are computed as data coverage permits: the stratification and isopycnal shear are estimated at the hydrographic transects, curvature is estimated along the subsurface current path survey, and curvature vorticity is estimated at the intersections of the transects and the path survey.

- A cold-core ring was observed for the first time within the Retroflection. Its structure, transport, and contribution to South Indian heat, salt, and vorticity balances are characterized.

These results are compared with their Gulf Stream analogs where appropriate. Also, *interbasin exchange* between the South Indian and South Atlantic oceans *(Gordon, 1986)* is reconsidered in light of the new hydrographic data and a recent inverse model *(Rintoul, 1988)*. One of the 1985 transects and one of Gordon's 1983 transects cross warm-core rings situated just southwest of the tip of Africa.

February/March 1985 measurements

The 1985 hydrographic survey is composed of 92 CTD/O_2 stations (conductivity-temperature-depth-oxygen). Stations 207 to 279 were taken between 20 February and 16 March; the remaining stations 280 to 298 were taken between 22 and 26 March. (Fig. 1.3). Of these stations, 71 reach to within 200 m of the bottom.[1] Most stations are organized into survey lines that enclose four boxes suitable for calculating flux balances. The survey includes four transects of the Agulhas Current, two of the Agulhas Return Current, a transect of a cold core eddy within the Retroflection, and of a warm core eddy off Cape Town. Horizontal resolution along transects is 20-60 km.

The continuous survey of the path of the currents (Fig. 1.4) was made in the period 16 to 22 March, during the break in the hydrographic survey. The path was surveyed by following the intersection of an isotherm and a depth surface, a method developed and first used in the Gulf Stream by *Fuglister and Voorhis (1965)*. In the

[1]The 21 stations ending >200 m above the bottom are marked with open circles in Fig. 1.1. The figure caption lists the maximum pressures and bottom depths at these stations.

1985 survey of the Agulhas, the intersection of the 15 C isotherm and the 200 m depth surface was followed for 2500 km, from the southern African slope at 35°S, 24°E through the Retroflection to the northeast flank of the Agulhas Plateau. This was accomplished by navigating the ship downstream according to temperature profiles produced by XBTs (expendable bathythermographs) deployed every 15 - 20 minutes for the 6 day period of the path survey.

The sea surface temperature image from satellite infrared measurements was composited from three images taken by the Advanced High Resolution Radiometer (AVHRR) onboard a NOAA TIROS-N sun-synchronous satellite. The three images used here were collected on 25, 26, and 27 March 1985. The thermal infrared radiation intensity measurements taken by radiometer channel 4 (wavelengths 10.5 - 11.3 μm) were used.[2] First each image was registered to identical geographical coordinates *(Luetkemeyer, 1987)* and then a single relatively cloud-free image (Fig. 1.5) was generated by retaining the warmest value from each 4 km x 4 km pixel .

Overview of February/March 1985 Retroflection circulation

A consistent picture of the Retroflection in February/March 1985 emerges from the analysis. According to the transport field, the Agulhas retroflected in two branches, one several hundred kilometers to the north of, and the other several hundred kilometers to the southwest of, the southern tip of the continental slope. The continuous survey of the path of the current followed the larger downstream branch that accounted for most of the transport. On the other hand, most of the Current's warm core followed the smaller upstream branch, judging from the satellite sea surface temperature image. The Agulhas

[2]The channel 3 images for the 25, 26, 27 March 1988 could not be used for cloud removal because of sun glint (*K. Kelly*, pers. comm.)

immediately downstream from the smaller branch was found displaced far up onto the continental slope with substantially reduced transport. The stagnation point between the two branches was occupied by a large cold core ring that could be seen in the subsurface fields but not in the satellite or hydrographic sea surface temperature fields (Figs. 1.5 and 1.6 *vs.* Figs. 1.7 and 1.8). This is the first time a cold-core ring has been observed, by any type of measurement, within the Retroflection loop, though such rings are not uncommon in the subtropical gyre east of the Agulhas Plateau. Both of the Retroflection branches and the cold-core ring appear to have been propagating to the west. A large warm core ring was observed off Cape Town, similar in position and size to rings observed in 1983 and 1969. Other warm features were grazed by the westernmost line of the hydrographic survey.

The continuous survey of the path of the currents included many surprising features. The Agulhas meandered up onto the upper continental slope as far as the 400 m isobath, even though the current's geostrophic shear extends to depths greater than 2000 m. After a series of meanders across the slope, the current separated from it at its southernmost extension and proceeded due west from the separation point, rather than south, for several hundred kilometers. No existing dynamical model of the Retroflection and no previous observations exhibit separated westward flow. Nevertheless, the current did finally turn abruptly south, despite its lack of southward momentum and thus motion across latitude lines. After several hundred kilometers of southward flow, the current turned again rather abruptly, this time to the east, executed a gentle north-south meander and made a final turn, sharper than the previous two, that sent it over the central Agulhas Plateau. The current previously had been observed and modelled always flowing around, rather than over, this relatively shallow (<3000 m) feature.

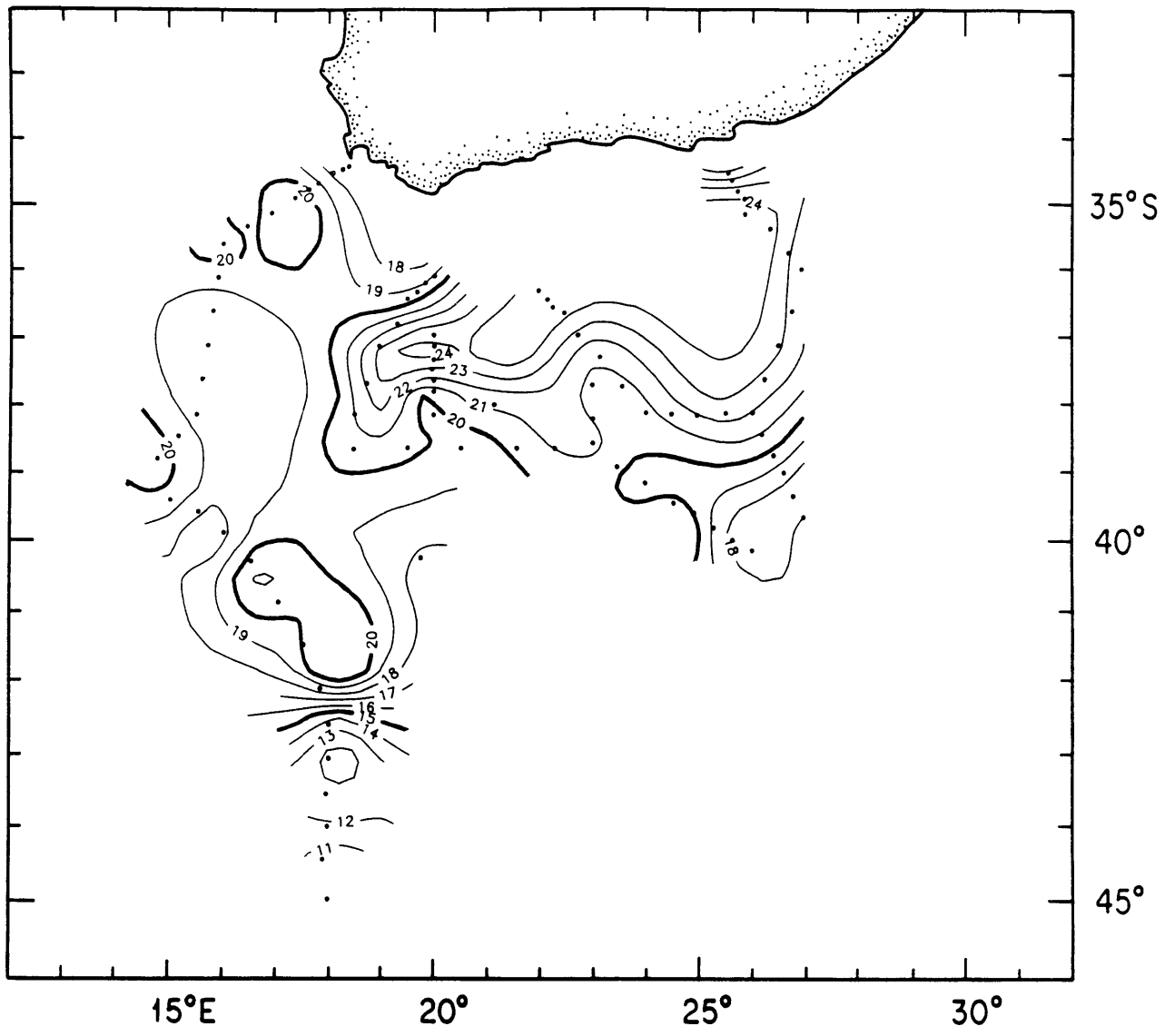

Fig. 1.6 – Agulhas Retroflection region, February/March 1985, temperature at nominal sea surface (6 dbar) from CTD/O_2 station data. Again, cold-core ring is not visible (cf. Figs. 1.7 and 1.8). Discrepancies between this figure and the satellite infrared image of sea surface temperature are due to propagation of features (see Chapter 2). Contour shapes away from stations locations indicated by dots are highly subjective.

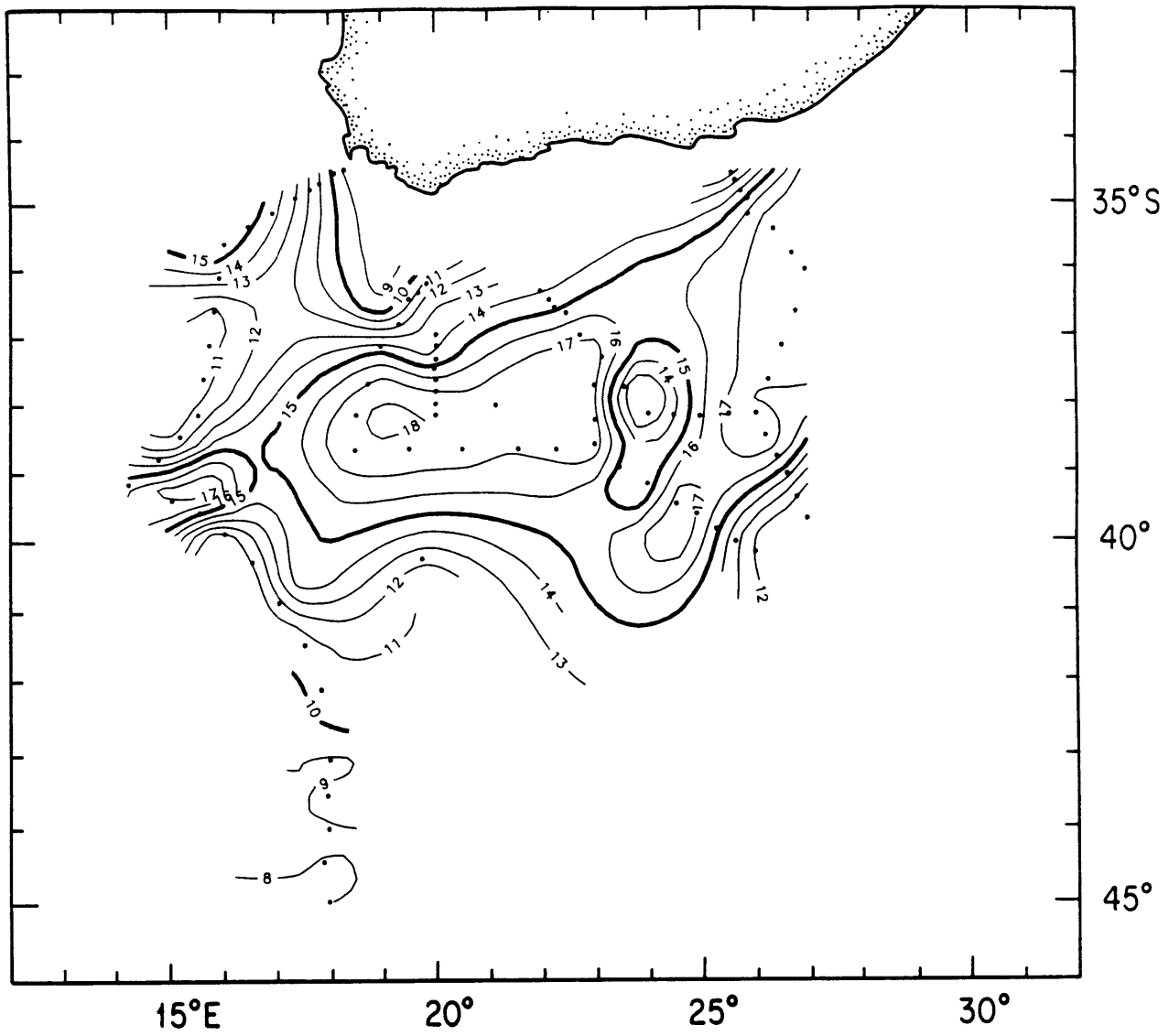

Fig. 1.7 – Agulhas Retroflection region, February/March 1985, temperature on 200 dbar surface from CTD/O_2 station data. The warm-core ring off Cape Town is centered at 35°S, 15°E; the cold-core ring within the Retroflection is centered at 37°S, 27°E. Small upstream branch of Retroflection is at about 26°E, and larger downstream branch is west of 17°E. Contour shapes away from station locations indicated by dots are highly subjective. This can be seen by comparing the 15 C isotherm of this figure with the continuous survey of 15 C at 200 dbar shown in Fig. 1.4. Some propagation of features is also evident (where temperatures at station locations differ between the two surveys).

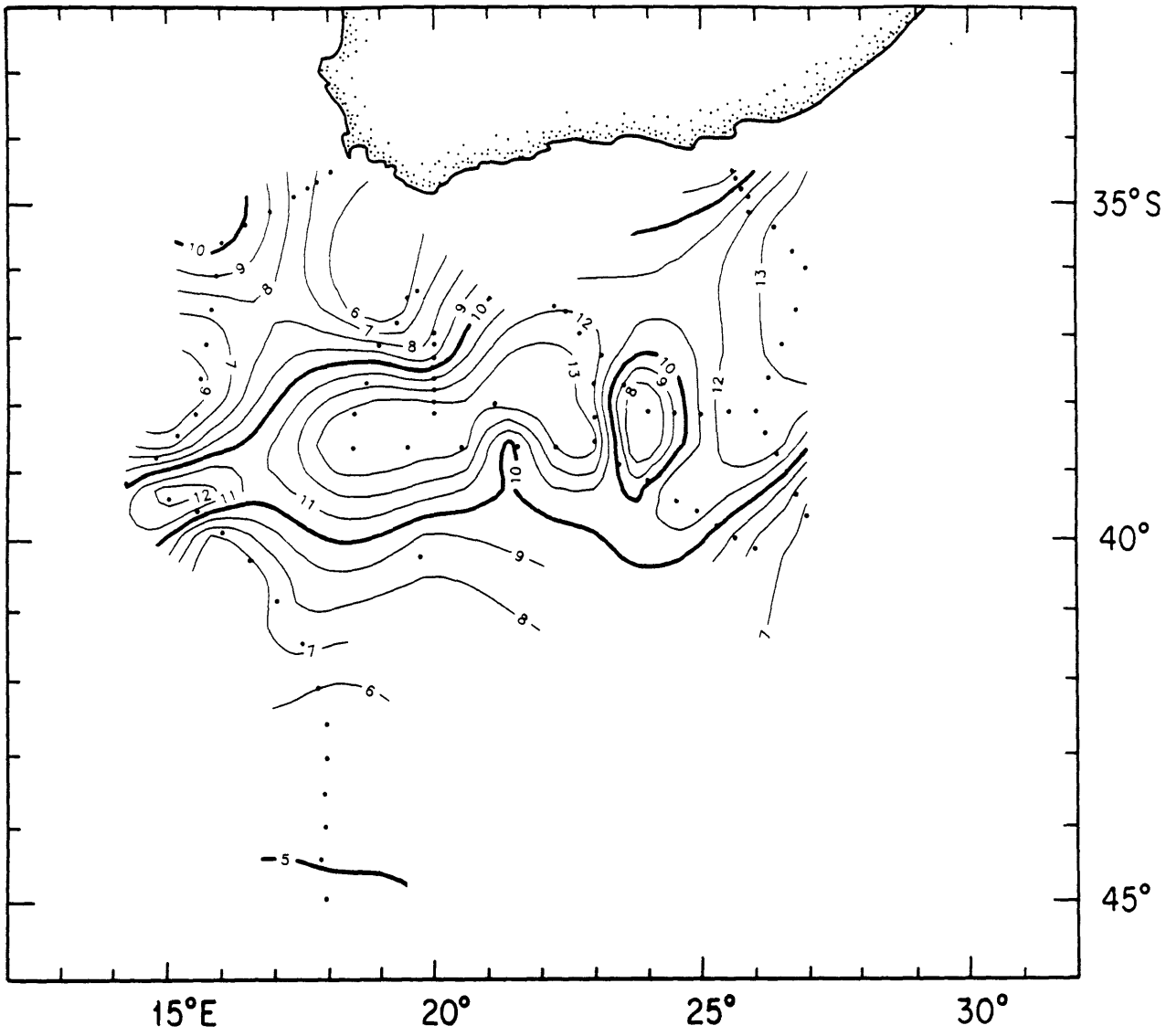

Fig. 1.8 – Agulhas Retroflection region, February/March 1985, temperature on 500 dbar surface from CTD/O_2 station data. The warm-core and cold-core rings visible at 200 dbar (see previous figure) are also visible here. Contour shapes away from stations locations indicated by dots are highly subjective.

The Retroflection loop in 1985 extended westward to 15.5°E, 350 km west of its position at 20°E during the 1969 and 1983 hydrographic surveys. The 1985 Retroflection position happens to be at the westernmost, and the 1969/83 positions at the easternmost, of the range of Retroflection positions seen in satellite infrared images from 1984 - 1985 (*Lutjeharms and van Ballegooyen, 1988;* their figure showing the satellite-derived Retroflection positions is reproduced as Fig. 2.10 in Chapter 2). The westernmost retroflecting flow observed so far was found at 13°E: a drifter *Gründlingh (1978)* deployed in the Agulhas Current proceeded west to this longitude, looped around once in a 150 km diameter circuit there, and then returned east in the Return Current.

Overview of thesis

A great deal of new information is provided by the 1985 measurements. This thesis presents the analysis of these new measurements, integrating them into the existing descriptive and theoretical ideas about the region. Many of the conjectures and conclusions derived from earlier surveys and from modelling efforts based upon them are confirmed and quantified by the picture of the Retroflection in February/March 1985 that emerges here. In other cases, unexpected characteristics of the Retroflection in 1985 contradict our preconceptions.

The path of the Agulhas and Agulhas Return Currents in February/March 1985 is discussed in Chapter 2. The continuous survey of the path of the current following the intersection of the 15 C isotherm and the 200 m depth surface, the satellite infrared image of sea surface temperature, and the hydrographic survey provide complementary information about the course of the current.

The current transport field and the interior circulation are discussed in Chapter 3. At three of the four 1985 Agulhas Current transects, the Agulhas transport,

computed relative to the shallowest reference level consistent with tracer fields, exceeded the maximum returning interior transport, estimated from wind-stress and a measure of the thermohaline circulation,[3] by as much as a factor of two. The transport at the remaining transect, which is located between the two Retroflection branches, was considerably reduced as a result of the current being narrower and displaced inshore over the upper continental slope. The calculated transport at this transect, after adjusting it upward to eliminate mass flux convergence in the adjacent survey boxes, is slightly less than the maximum returning interior transport.

The current structure and tracer fields are discussed in Chapter 4. The four Agulhas and two Agulhas Return Current CTD/O_2 transects - the first set of Retroflection transects to date with fine horizontal resolution and uniform full water column coverage - yield important new information about current structure and its variability. In particular, the impact of the two Retroflection branches on the tracer field can be seen. Vertical extrema of water mass properties (salt, oxygen, and planetary potential vorticity) and cross-frontal property gradients on isopycnals are discussed and related to previous observations in the Agulhas, and in the Indian and Circumpolar Oceans.

The velocity and total potential vorticity of the current is discussed in Chapter 5. It is found that potential vorticity due to the *horizontal* component of relative vorticity (u_z) can be as large as the potential vorticity due to the *vertical* component of relative vorticity ($-u_y$) in the Agulhas. Vortex stretching near a strong front on isopycnals in planetary vorticity (*i.e.*, in stratification) may balance curvature vorticity as the current meanders along the slope.

Existing dynamical models of the Retroflection are discussed, with reference to the new observations, in Chapter 6. The asymptotic linear and nonlinear models of *de Ruijter (1982)*, the inertial/coastline curvature model of *Ou and de Ruijter (1986)*,

[3]Thermocline slope at the eastern boundary *(Veronis, 1973)*; see Chapter 3.

the inertial jet models of *Darbyshire (1972)* and *Lutjeharms and van Ballegooyen (1984)*, and the numerical experiments of *de Ruijter and Boudra (1985)* and *Boudra and de Ruijter (1986)* are discussed and compared to observations.

The characteristics of the cold core ring found within the Retroflection are discussed in Chapter 7. Volume, kinetic, and potential energy anomalies are estimated.

The 1983 and 1985 Cape Town Eddies southwest of the tip of Africa and interbasin exchange estimates are discussed in Chapter 8.

Conclusions are presented in Chapter 9. An atlas of all the contoured sections and several appendices follow. Appendix A gives the derivation of the potential vorticity equation in isopycnal natural coordinates. Appendix B presents the exact conservation for the form of potential vorticity plotted in the Atlas, one based upon the buoyancy frequency; its relationship to neutral surface potential vorticity *(McDougall, 1988, 1987)* is also derived.

Chapter 2: The path of the Agulhas and Agulhas Return Currents

2.1 Introduction

The path of the Agulhas and Agulhas Return Currents provides important information about the Currents' dynamics. The bounding latitude and longitude of the Retroflection, the relationship of the current path to topographic features, and the path curvature are each important dynamical parameters. Also, the angle between the current path and a transect across the current affects estimates at the transect of current width, momentum transport, energy transport, and relative vorticity.

The path of the Agulhas and Agulhas Return Current in March 1985 is inferred from three independent data sets taken over a 20 day period, 8 to 27 March:

- a survey of a temperature/depth contour (Fig. 1.4),
- a composite satellite infrared image of sea-surface temperature (Fig. 1.5), and
- the geostrophic transport field relative to a deep level, computed from a grid of full-water column hydrographic (CTD/O_2) stations (Fig. 2.12).

The most comprehensive synoptic picture of the Retroflection available to date emerges from these complementary, contemporaneous measurements. The Agulhas was found to retroflect in two branches. The farther upstream of the two branches was followed by the current's warm core, evident in the satellite image, and by about a third of the current transport. The other branch was followed by the current's surface temperature front, evident in the satellite image, by the temperature/depth contour survey, and by the remaining two-thirds of the current transport.

This chapter presents the observational evidence for the current paths just described. A large cold-core ring found between the first and second Retroflection branches is described in Appendix B. A large warm-core ring observed off Cape Town is described in Appendix C.

Temperature field characteristics of western boundary currents. Western boundary currents have two distinct temperature signatures, both mentioned above. The current's warm core is a surface temperature maximum found at and just below the sea surface. It is composed of warm water advected from low latitudes poleward more quickly than it can equilibrate to the changing local atmospheric temperature. The Agulhas warm core is a shallow feature, confined to the upper 100 m at the 1985 transects (see Atlas).

The second signature of the western boundary current is a large horizontal temperature gradient at all levels at and above the thermocline, including the sea surface; it decays with depth beneath the thermocline. The relationship between the horizontal temperature front and the current is the consequence of several conditions:

(i) the downstream flow is geostrophic and hydrostatic;

(ii) the relationship between potential temperature and salinity is nearly single-valued (i.e., a tight potential temperature/salinity relation $\theta(s)$ is found) in the current, so density can be inferred from temperature and pressure alone;

Conditions (i) and (ii) yield the thermal wind relation between the vertical shear of alongstream velocity , $\frac{\partial u}{\partial z}$, and the horizontal temperature gradient, $\frac{\partial T}{\partial y}$:

$$\frac{\partial u}{\partial z} \sim \frac{-1}{\rho} \frac{\partial \rho}{\partial \theta(s)} \frac{-1}{g\rho f} \frac{\partial T}{\partial y} \qquad (2.1)$$

where g is the gravitational acceleration, ρ is density, f is the Coriolis parameter, and T is temperature.

One further condition is required in order for the velocity and temperature fields of the current to share a single geographic location. For the horizontal temperature front position at all levels and the current's high velocity core at all levels to be found at the same place,

(iii) the horizontal position of maximum horizontal temperature gradients must vary little with depth.

The validity and implications of these assumptions in the Agulhas is discussed below. For the moment it may be said that the maximum horizontal temperature gradient and the horizontal maximum of velocity at all levels are observed to fall within at most a 50 km cross-stream interval.

Temperature/depth contour survey. The March 1985 Agulhas horizontal temperature front was surveyed by following the intersection of a constant temperature surface (isotherm) and a constant depth surface. This temperature/depth contour technique was invented and first used in the Gulf Stream by *Fuglister and Voorhis (1965)* . The temperature/depth contour they used was the intersection of the 15 C isotherm and the 200 m depth surface, chosen because their towed instrument operated at 200 m depth, where they found the Stream's maximum horizontal temperature gradient centered at 15 C. A temperature/depth contour follows the current if the assumptions listed in the preceding paragraph are satisfied, and the contour temperature lies within the high horizontal temperature gradient of the current all along the current's path. A temperature/depth contour survey can provide information about only one

branch of the current. If in fact the current splits, no information will be provided about the other branch.

The 1985 Agulhas temperature/depth contour followed the main larger-transport branch of the Agulhas. The Agulhas path revealed by the contour exhibited several unexpected characteristics, not previously seen in either observations or models of the current: strong across-slope meanders; westward flow just beyond the separation of the current separated from the slope; extremely sharp turns; and flow directly over the central Agulhas Plateau, which rises to ~3000 m from the ~5000 m basin floor.

Satellite image. The March 1985 Agulhas horizontal temperature front and the warm core are visible in a composite satellite infrared image formed from three daily images taken 25, 26, and 27 March. Satellite infrared images have been much used to locate western boundary current paths *(Cornillon, 1982; Lutjeharms and van Ballegooyen, 1988).* These images provide high resolution instantaneous snapshots of the surface temperature field of large ocean areas, generated at regular frequent intervals. The images suffer from two important limitations. Clouds obscure the sea surface for long periods in some regions. Only about 50 of the daily images from the period 1985-6 have clear area over the Return Current region *(Flament, pers. comm.)*, though additional clear area under broken cloud can be reclaimed by merging successive images. Another limitation of satellite images is that they see only the sea surface. Atmospheric heating and cooling at the sea surface or surface-trapped currents can decouple the surface temperature from the underlying thermal signature of geostrophic currents. Cold-core rings in the Gulf Stream and, with this data set, in the Agulhas, have weak or no surface thermal signature in summer.

Current transects. The March 1985 Agulhas horizontal temperature front and warm core can also be seen in the CTD/O_2 transects across the current. Requiring mass to balance in the closed survey boxes through which the current flows yields a transport

streamfunction (relative to an arbitrary reference level) that quantifies the relative size of flow branches. The CTD data also provides information on the temperature-salinity relationship [mentioned in assumption (ii) above].

The current was not steady during the period of time covered by the three survey elements (temperature/depth contour, satellite image, and hydrographic survey). Propagation of features can be deduced by comparing measurements taken in the same area at different times. The chronology of the survey is given in Table 2.a, and illustrated in Fig. 2.1, to facilitate these comparisons.

2.2 Temperature/depth contour survey: analysis and discussion

The temperature/depth contour defined by the intersection of the 15 C isotherm and the 200 m depth surface was followed for over 2500 km during the period 16-22 March. This was accomplished by deploying expendable bathythermographs (XBTs) every 15 minutes or so and correcting the ship's heading based on the temperature at 200 m. Each XBT generated a 0 to 700 m temperature profile.

The maximum horizontal temperature gradient in the Gulf Stream, where the temperature/depth contour technique was developed, is centered near 15 C at 200 m, as determined from continuous temperature measurements taken by an instrument towed across the Stream at that level *(Fuglister and Voorhis, 1965)*.

The maximum horizontal temperature gradient in the Agulhas and Agulhas Return Currents seems to be centered near 13.5 C at 200 m, with large temperature gradients observed for the range 12.5 - 16.0 C. These estimates are derived from the six 1985 Agulhas and Agulhas CTD transects (see Fig. 2.2 and Atlas sections of potential temperature). The 15 C/200 m temperature/depth contour does lie within the

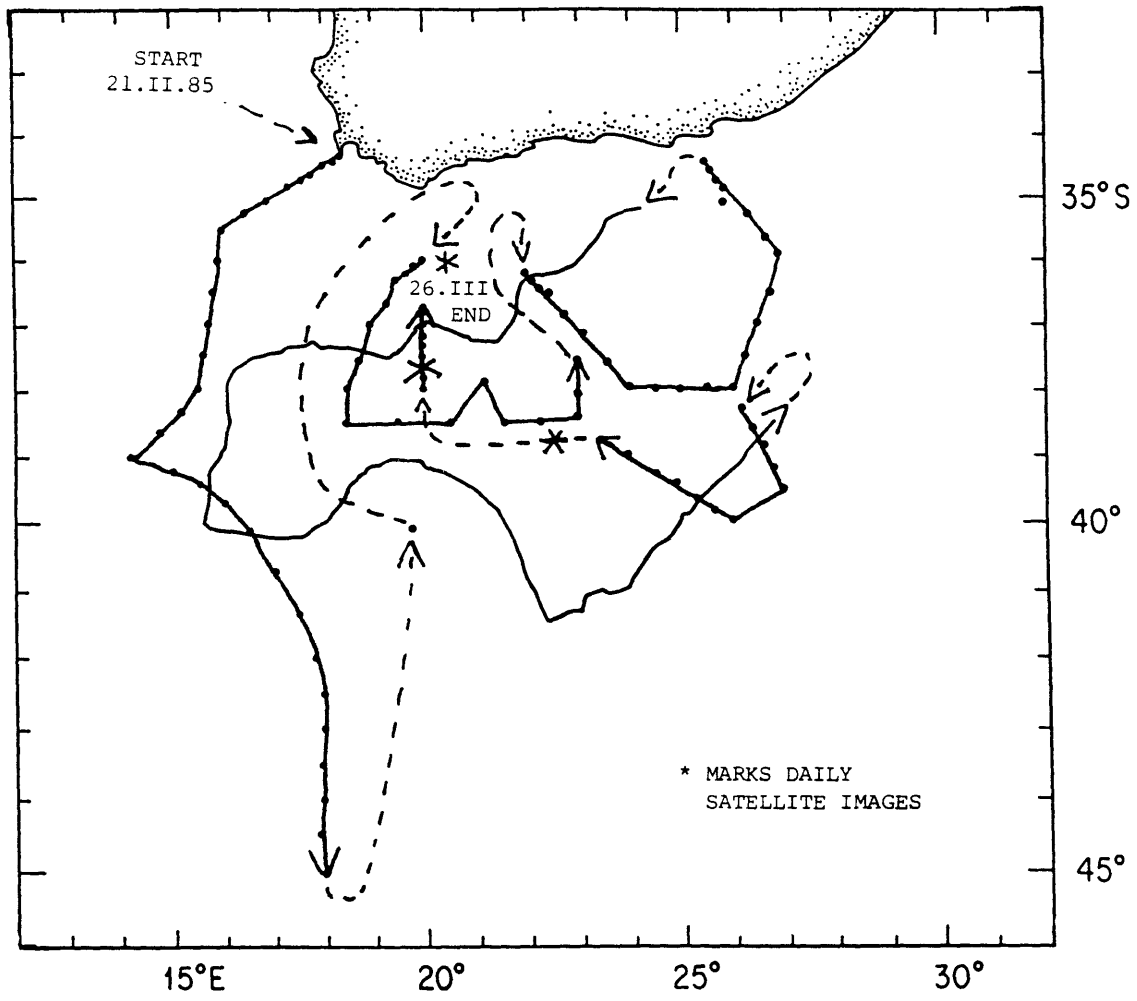

Fig. 2.1 – Chronology of the 1985 survey.

Table 2.a – Dates of 1985 Agulhas Retroflection survey elements.

Date	Time line	Survey element
20 February		Cape Town warm-core ring transect
21		
22		
. . .		
8 March		Agulhas transect D
9		
10		
11		
12		Agulhas transect B and cold-core ring transect
13		
14		Northernmost station of Return Current transect F (sta. 267)
		Agulhas transect A (proceeding onshore)
15		
16		Temperature/depth contour survey
17		
18		
19		
20		
21		
22		Return Current transect F (except sta. 267)
23		
23		Return Current transect E
24		
25		Satellite images
26		Agulhas transect C
27		

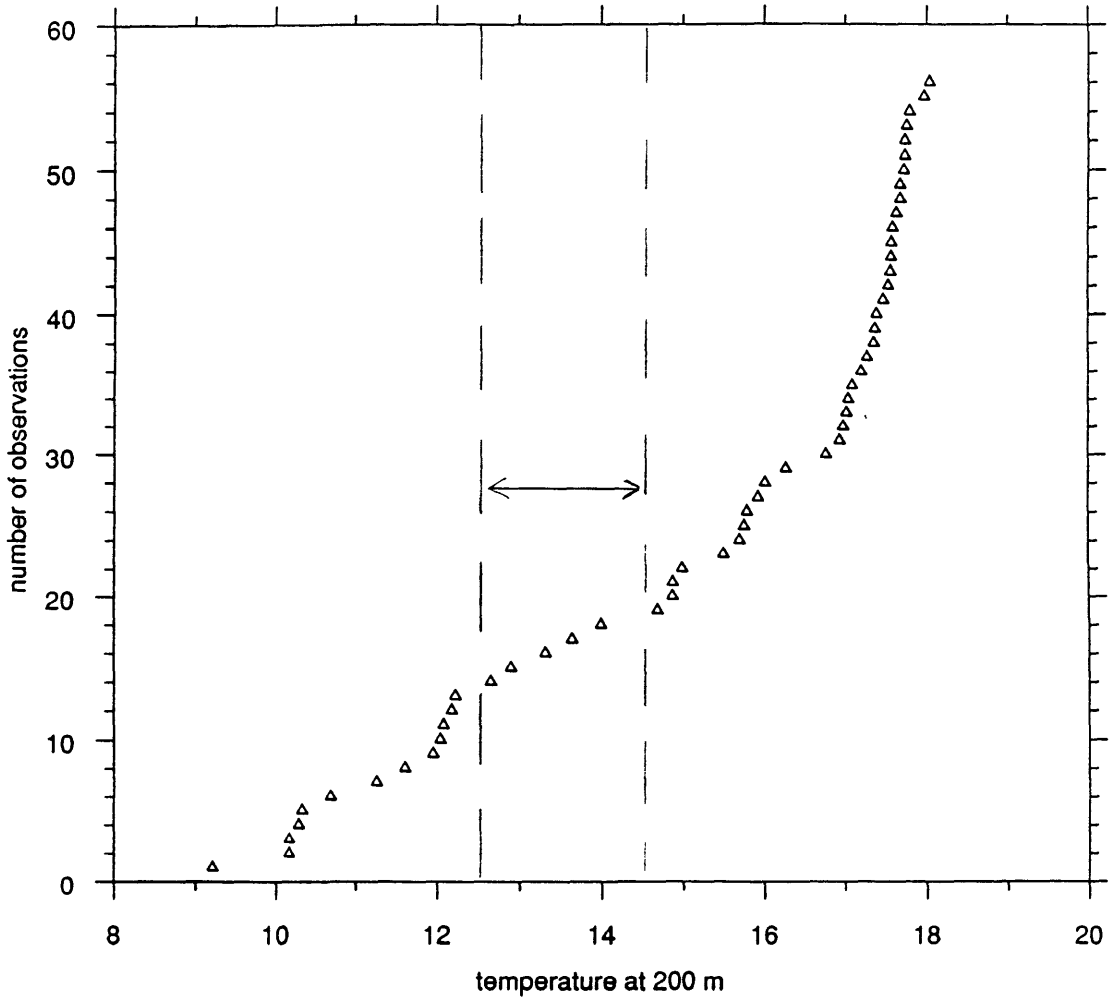

Fig. 2.2 – Temperature at 200 m, 1985 CTD/O_2 Agulhas and Agulhas Return Current transect stations. The high temperature gradient at 200 m appears to be centered at approximately 13.5 C, the central temperature of the interval 12.5 - 14.5 C where few temperature observations at 200 m fall. This is, in effect, a Monte Carlo method for finding the temperature range of the high temperature gradient at 200 m, in the absence of continuous temperature measurements across the front.

high temperature gradient region of the Agulhas and Agulhas Return Currents, slightly to the warm side of the maximum gradient.

Extraction of temperature/depth contour. The temperature/depth contour (Fig. 1.4 and elsewhere) was extracted from the raw ship track (Fig. 2.3) and the XBT temperatures at 200 m. Extracting the real temperature/depth contour from the raw ship track was important for three reasons:

- A meaningful along-contour distance can be computed from the extracted temperature/depth contour, but not from the raw ship track, along which navigation noise accumulates at a variable rate.

- The sharpness of the major turns in the current can be verified to be real features of the current, rather than an artifact of the navigation. The current's compass heading and radius of curvature can be computed directly from the temperature/depth contour, but not from the raw ship track.

- The shape of smaller features in the current (like the meanders along the continental slope) can be seen more clearly after the navigation noise has been removed.

The extraction of the temperature/depth contour was accomplished in a two-step interpolation process. The location of each XBT drop was determined in the first step, by linearly interpolating between pairs of position fixes (X) that bracketed XBT drops, using time (τ) as the interpolation parameter:

$$X_{XBT} = X_{FIX-} + \frac{\tau_{XBT} - \tau_{FIX-}}{\tau_{FIX+} - \tau_{FIX-}} (X_{FIX+} - X_{FIX-}) \qquad (2.2)$$

The subscripts FIX-, XBT, and FIX+ correspond to the position fix preceding the XBT drop, the XBT drop, and the position fix following the drop. Position fixes were

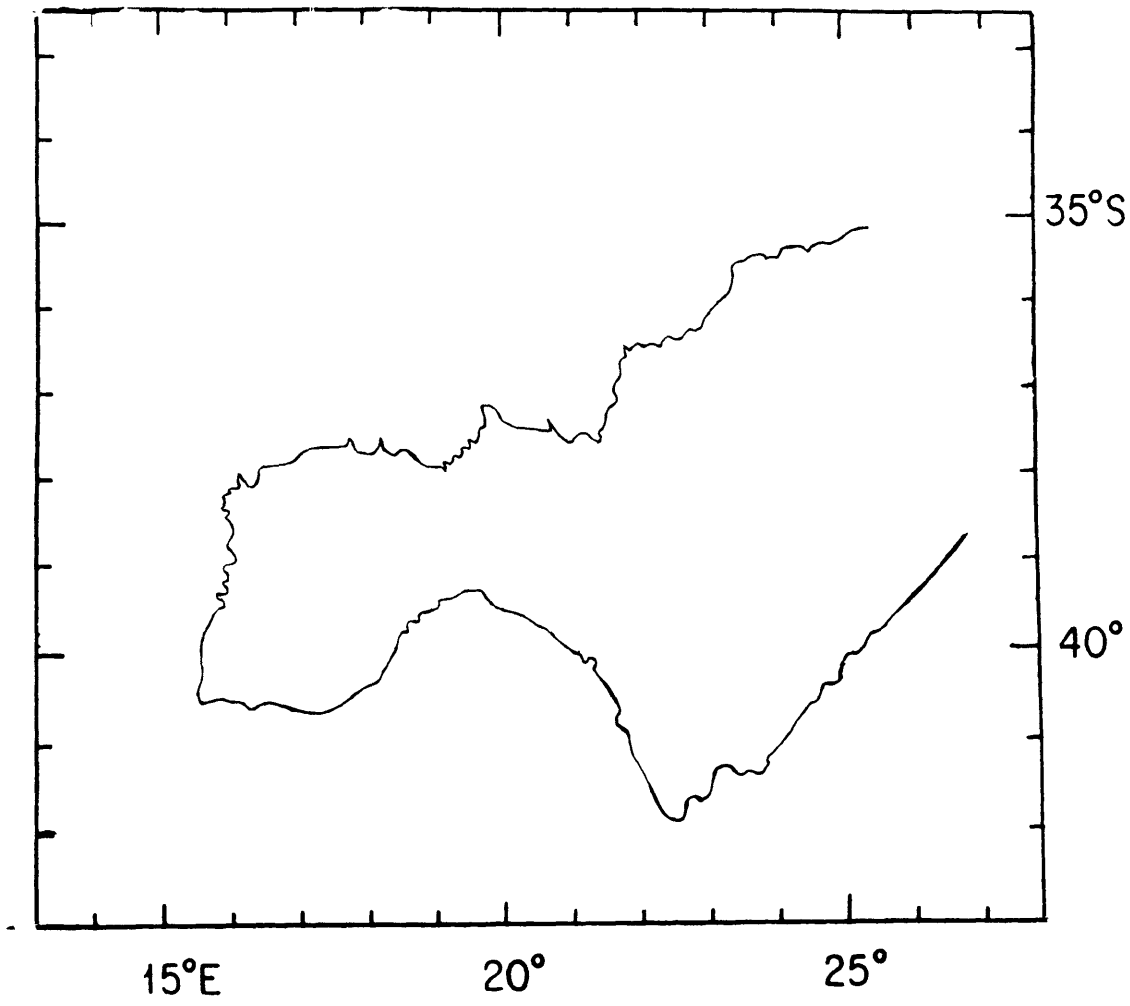

Fig. 2.3 – Raw ship track from which temperature/depth contour was extracted (see text).

received from transit satellites every 2-3 hours and the Global Positioning System (GPS) with an accuracy of better than 1 km. Errors in dead reckoning between fixes are at most 2 m s^{-1} (maximum current speed error plus allowance for windage) over three hours, or about 20 km.

The second extraction/interpolation step was to find the position of the 15 C isotherm at 200 m, $X_{15/200}$, by linearly interpolating between positions of XBTs that bracketed the isotherm, using temperature (T) at 200 m as the interpolation parameter:

$$X_{15/200} = X_{XBT-} + \frac{15\ C - T_{XBT-}}{T_{XBT+} - T_{XBT-}}(X_{XBT+} - X_{XBT-}) \qquad (2.3)$$

The surface temperature and the 10 C depth at the contour were interpolated in a similar way.

Contour location errors and remaining small-scale jaggedness. The resulting contour position, shown in Fig. 1.4 and elsewhere, is geographically accurate to about 30 km, estimating from the dead reckoning error plus smaller uncorrelated errors in satellite fixes, temperature measurements, and in the interpolation procedure. The scale of the remaining small-scale jaggedness in the contour suggests that position errors are in fact smaller than this.

The largest amplitude (about 20 km cross stream) small-scale jaggedness in the contour occurs as the Return Current approaches the Agulhas Plateau. This jaggedness is not an artifact of any of the errors listed above: examining individual XBT traces reveals that it is the real signal of thermohaline interleaving between warm, salty Retroflection water and cold, fresh Circumpolar water across the Return Current. The interleaving means that temperature and density at constant depth are not related through a perfectly single-valued temperature-salinity relation, but the relation is sufficiently tight that the resulting cross-stream displacements are too small to impair the contour's

usefulness as an indicator of the path of the current. Another indication of the thermohaline interleaving at 15 C is shown by the 10 C isotherm depth along the temperature/depth contour (Fig. 2.5, middle panel) which oscillates at the small-scale jaggedness in the contour; the interleaving vertical scale is smaller than the distance between the 15 C and 10 C isotherms. Elsewhere in the Return Current the 10 C isotherm depth is relatively constant.

Validity of assumptions. How well are the assumptions underlying the horizontal temperature front/current relationship met in the Retroflection?

Assumption (i) above: how geostrophic is the alongstream flow? Alongstream flow is geostrophic to order 3×10^{-2}, except in the vicinity of sharp turns in the current seen in the temperature/depth contour, where alongstream velocities can be ageostrophic to order 0.5. These are the values of the Rossby number, $\varepsilon = \frac{U}{fL}$, where U is the alongstream velocity, f the Coriolis parameter, and L the alongstream length scale (radius of curvature), using the values $U = 1$ m s^{-1}, $f = 10^{-4}$ s^{-1}, $L = 300$ km away from the sharp turns, and $L = 20$ km near them. The satellite image is at least partially obscured by clouds at each of the sharp turns in the contour, so unfortunately there is no independent information on the flow at these locations. Sharp meander crests have been found to be preferred locations for cross-frontal motion in an analysis of isopycnal float tracks in the Gulf Stream *(Bower, 1988)*, in agreement with this scaling.

Assumption (ii) above: how tight is the potential temperature/salinity relation, *i.e.*, how well can density be inferred from temperature and pressure alone? The largest variation in salinity on the 15 C isotherm is in the Return Current, as mentioned above, where strong thermohaline interleaving is occurring. The interleaving is strong enough to displace the temperature/depth contour 20 km cross-stream from the density/depth contour to which it corresponds in the mean. The potential temperature and salinity at CTD stations bracketing the 15 C temperature/200 m depth contour in the Agulhas

Current is shown in Fig. 2.4. Here, variations of about 0.1 salinity are observed at 15 C, corresponding to a density difference of about 0.08 kg m^{-3}. The 15 C isotherm falls just about at the boundary between the tight South Indian Central Water temperature/salinity relation at cooler temperatures, and the Tropical Thermocline/Subtropical Surface Water temperature/salinity front at warmer temperatures *(Gordon,* et al., *1987).*

Assumption (iii) above: how well does the high velocity current core line up vertically? The horizontal temperature gradient maximum, the horizontal velocity maximum, at all levels, and the 15 C temperature/200 m depth location are all found within a 50 km cross-stream interval at the CTD/O_2 transects. The velocity sections (see Atlas) show the Agulhas Current horizontal velocity maximum leaning slightly towards the continental slope, with the velocity maximum at depth 10 - 50 km further offshore than the surface maximum. Downstream bottom velocities on the upper slope would move the velocity maximum at all levels further onshore. The mass transport balance implies that such bottom velocities occur at some transects (see Chapter 3). The Return Current horizontal velocity maximum leans south at one of the two CTD transects and north at the other, both by small amounts. The 15 C temperature/200 m depth location at the transects lies between 40 km on the cold side and 20 km on the warm side of the surface velocity maximum.

To summarize, the underlying assumptions relating the current's velocity, temperature gradient field, and the temperature/depth contour are all met fairly well, except at the sharp turns in the contour where ageostrophic flow may not be negligible. An isopycnal float experiment could be designed to test the hypothesis that cross-frontal motion is greatest at sharp turns in the Retroflection.

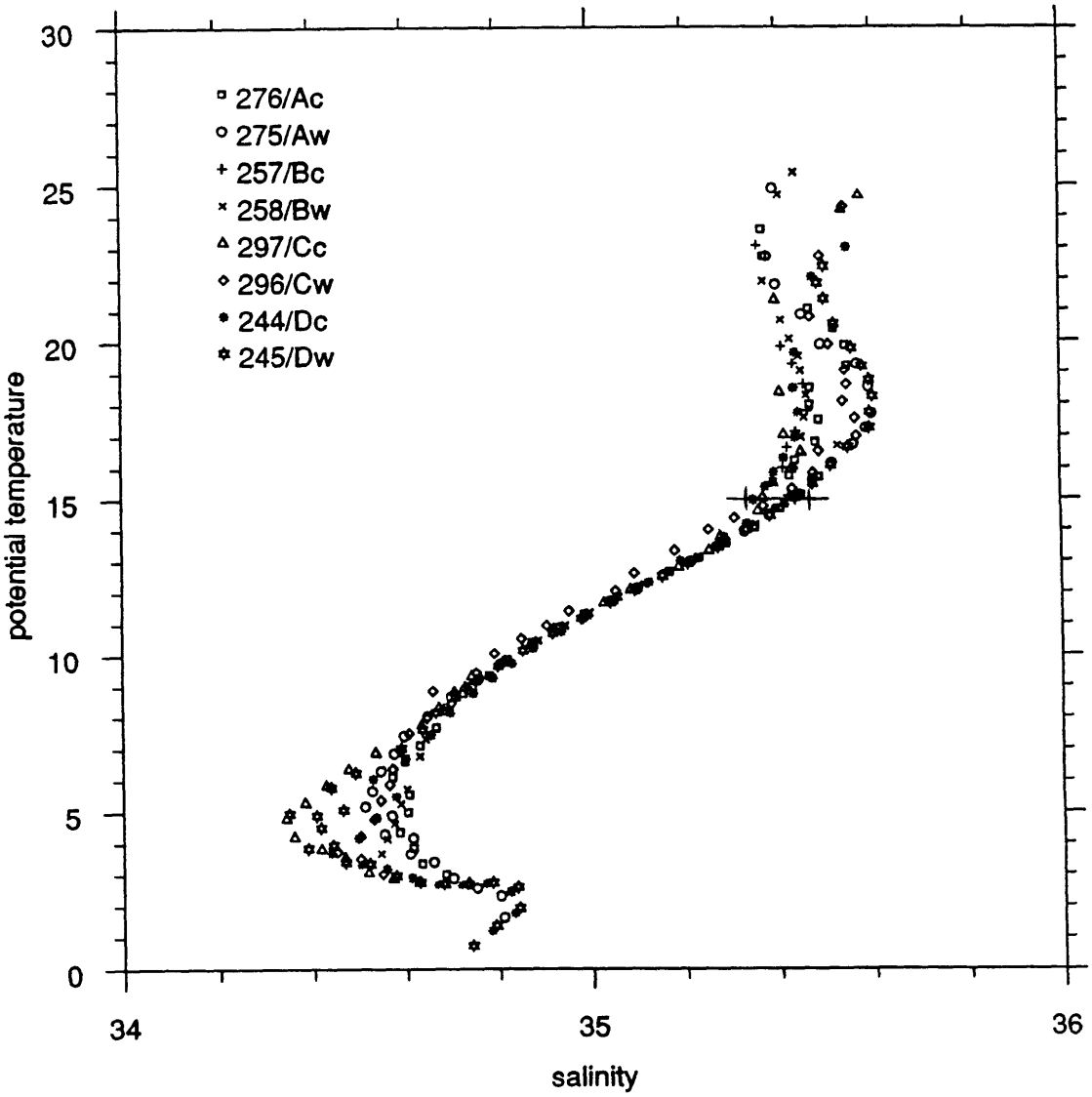

Fig. 2.4 – Potential temperature *vs.* salinity at CTD stations bracketing 15 C temperature/200 m depth location in Agulhas Current. Capital letters A-D refer to the transect name used in the Atlas. Stations marked with a 'c' are on the cold, inshore side of the current, while those marked with a 'w' are on the warm, offshore side. Salinity variation at 15 C is marked. Note the relatively fresh thermocline water at the warm side of Transect C, evidently South Atlantic water that has entered from the south with the local recirculation located between the cold-core ring and the second Retroflection branch (see transport pattern discussion).

2.3 Composite satellite image: processing and discussion of observations

The two Retroflection branches can be seen clearly over much of their length in a composite satellite image (Fig. 1.5) contemporaneous with the March 1985 survey program. The warm core follows the first upstream branch, appearing as a dark streak along the continental slope and in a northwest-to-southeast band cutting across the middle of the image. A strong surface temperature gradient follows the second downstream branch, paralleling the temperature/depth contour location. The cold-core ring has no surface temperature signature; North Atlantic cold-core rings in summer are similarly invisible to satellite imagery.

As was mentioned in the Introduction, the composite satellite infrared sea surface temperature image was constructed from three daily images collected on 25, 26, and 27 March 1985 by the Advanced High Resolution Radiometer (AVHRR) on board a NOAA TIROS-N sun-synchronous satellite. Radiometer channel 4 (wavelengths 10.5 - 11.3 μm) thermal infrared radiation intensity measurements were registered to geographical coordinates *(Luetkemeyer, 1987)*. The composite image was generated by retaining the warmest daily value in each 4 km x 4 km pixel to produce a single relatively cloud-free image (Fig. 1.5).

Relationship between image brightness and temperature. Temperature values corresponding to satellite image brightness values can be inferred by comparing

(i) surface temperature values along the temperature/depth contour (Fig. 2.5, upper panel), and

(ii) brightness values along the temperature/depth contour (Fig. 2.6).

The warm core temperature is ≤ 24.5 C (≥ 135 brightness). Cloud and sea surface temperature brightness values appear as two distinct peaks in a histogram of brightness

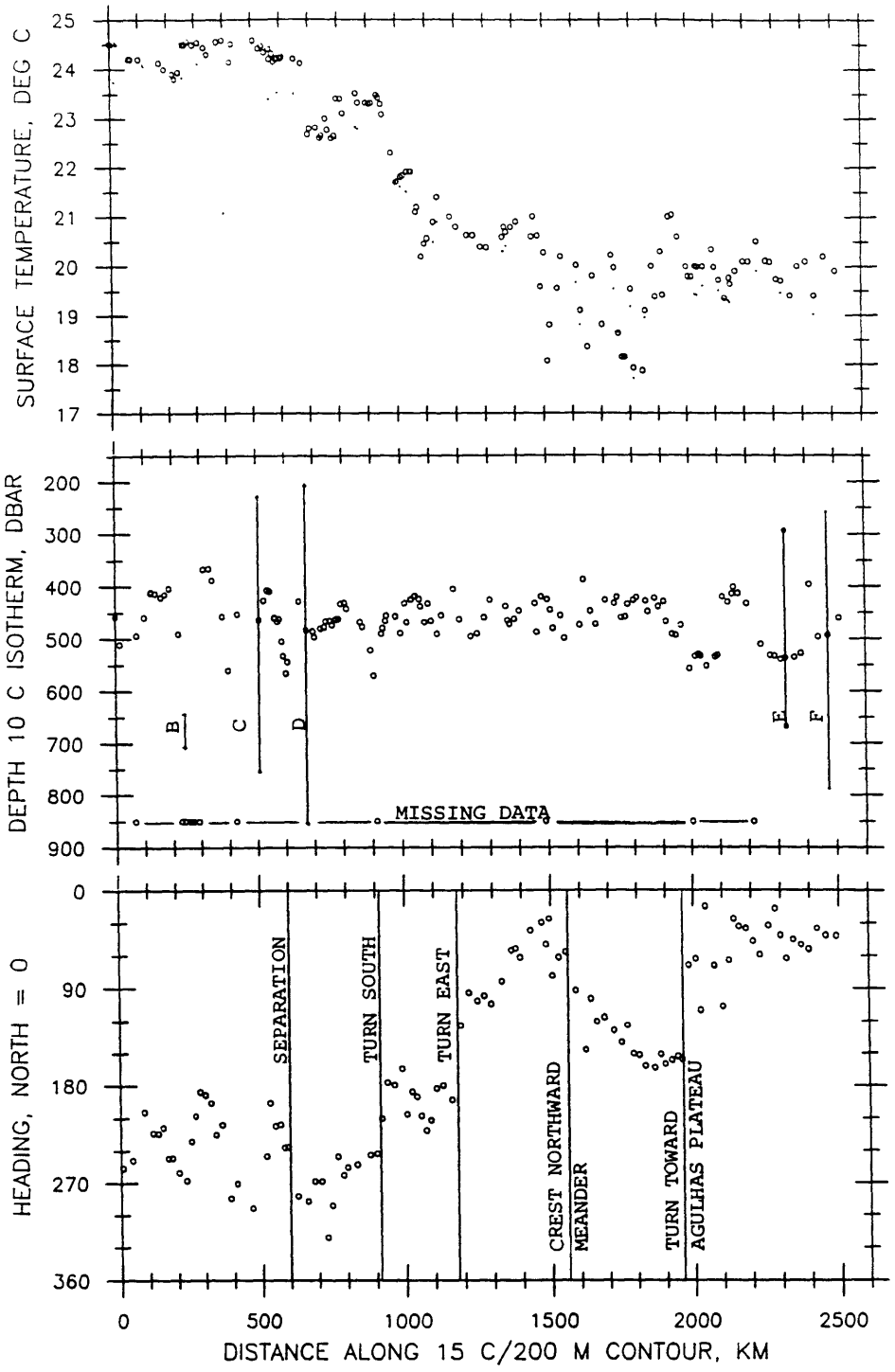

Fig. 2.5 – Surface temperature, 10 C isotherm depth, and 15 C temperature/ 200 m depth contour heading, plotted as a function of along-contour distance. (Caption continues on next page of text as a footnote).

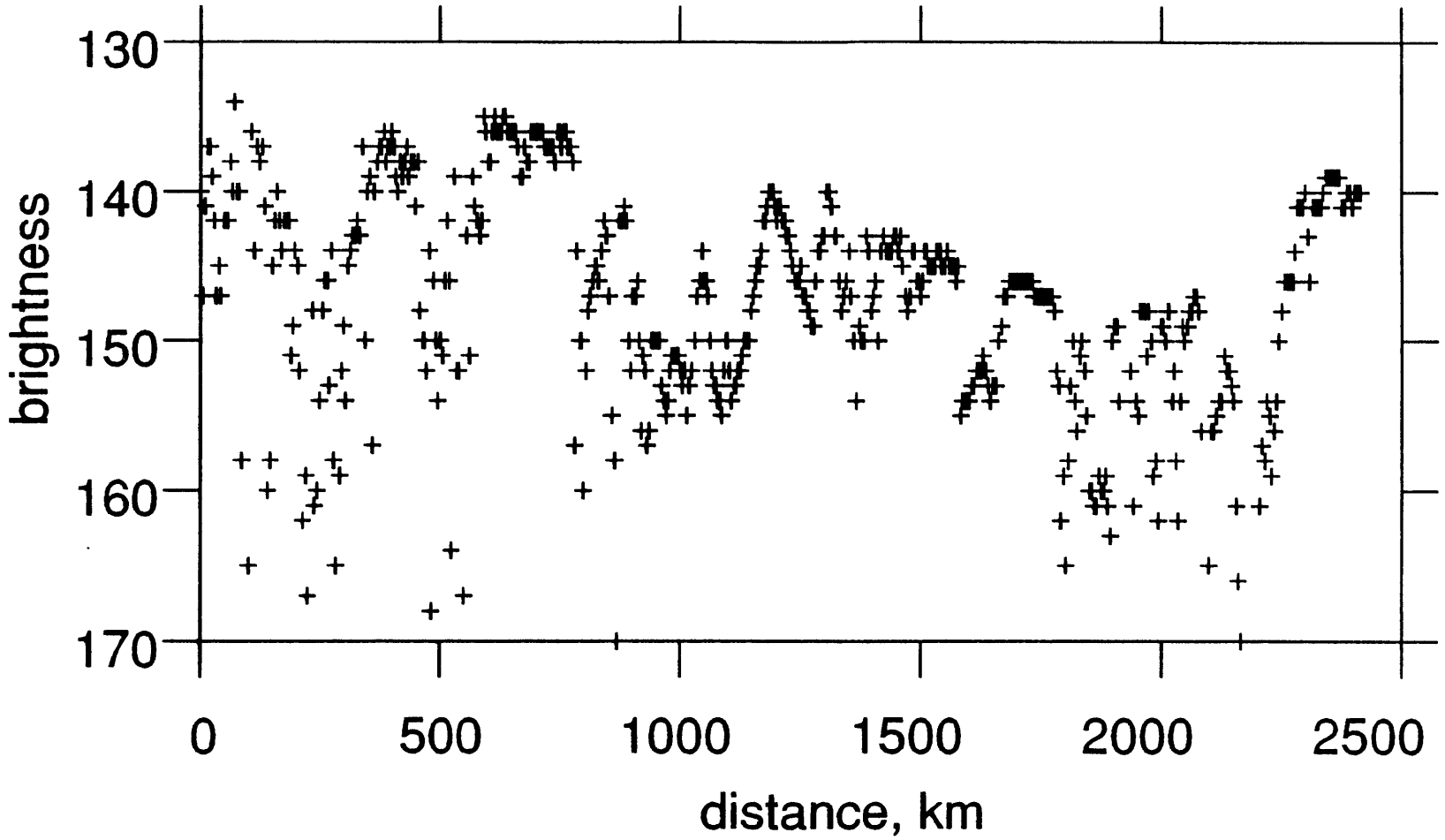

Fig. 2.6 – Brightness values along the temperature/depth contour, median filtered to remove some clouds. Plotted as a function of along-contour distance.

values from the three daily images (Fig. 2.7). The colder clouds peak at 175-200 brightness while the warmer sea surface peaks at 135-165 brightness. Sea surface temperature values for the CTD survey are shown in Fig. 1.6.

Warm core displacement during time between XBT survey and satellite image. The satellite brightness and XBT surface temperature curves are fairly similar in overall shape, except (1) at the very end of the contour at about 2300 km along-contour distance and (2) where the satellite brightness is still contaminated by low cloud (brightness values >170). Near the end of the contour, the brightness drops (*i.e.*, satellite-derived temperature rises) abruptly almost to the value observed at the beginning of the contour, while the XBT temperature stays relatively constant. This suggests that the warm core moved southwestward about 150 km onto the contour, over the 4-5 days between the end of the XBT survey on 22 March and the satellite image taken 26 March when this area was not obscured by clouds. The northeastern side of the cold-core ring (see Fig. 1.7 and 1.8) parallels the first retroflection branch on which the warm core rides. This ring was moving southwestwards also, judging

---

Fig. 2.4 caption, continued:

Upper panel: surface temperature values temperature/depth contour. Open circles: interpolated from surface temperature measured by the XBTs to the temperature/depth contour location. Dots: bucket temperatures.

Middle panel: depth of 10 C isotherm along the temperature/depth contour. Vertical lines denote location of CTD transects B-F across the current; lines extend over 10 C depth range observed at transect. Transect letter-names same as those used in Atlas and elsewhere. Transect A is upstream of beginning of contour. Dots at 850 m denote missing data. Note missing data clustered around Transect B, where contour and current meandered up onto the continental slope as far as the ~400 m isobath.

Bottom panel: contour heading, with north = 0 degrees. Radius of curvature can be estimated from this plot. Vertical lines denote sharp turns in the current path, and other features: separation of current from continental slope at 600 km, abrupt southward turn at 900 km, abrupt eastward turn at 1200 km, crest of broad northward meander at 1600 km, and sharp turn towards the Agulhas Plateau at 2000 km.

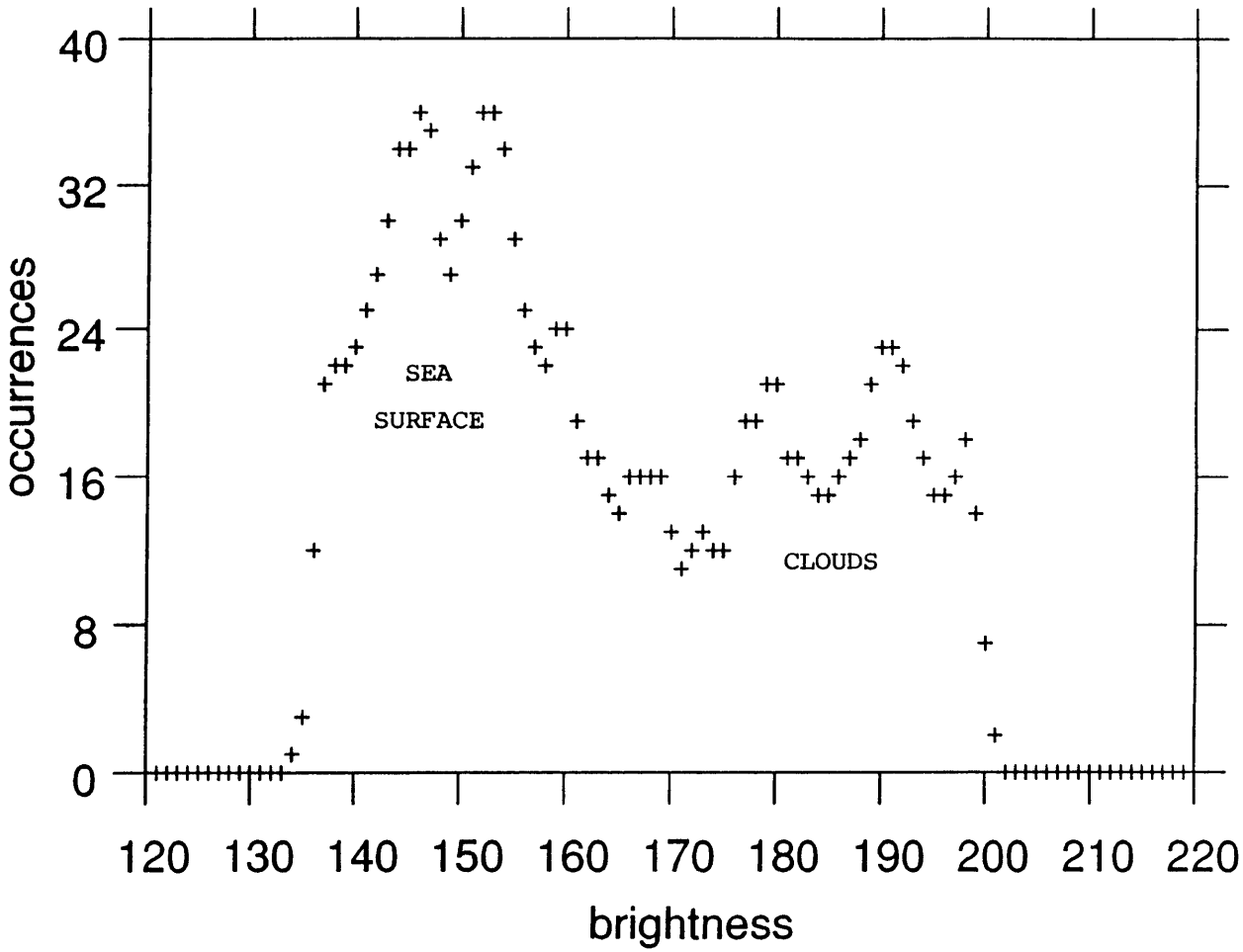

Fig. 2.7 – Histogram of brightness values from three daily NOAA TIROS-N satellite images, taken March 25, 26, and 27 1985. Cloud and sea surface temperature brightness values appear as two distinct peaks. Colder clouds peak at 175-200 brightness while warmer sea surface peaks at 135-165 brightness.

from the density field at two CTD/O_2 transects across the ring that were taken 10 days apart.

The nominal displacement speed implied by comparison of the XBT and satellite surface temperature patterns is 0.3 - 0.4 m s^{-1}. A Rossby number ε for the displacement is U_a/U_g, with a value of 0.3 to 0.4, assuming that the warm-core displacement southwestwards is due entirely to cross-stream ageostrophic velocity U_a, and that the downstream geostrophic velocity U_g is 1 m s^{-1}. This value for ε is similar to values at sharp turns in the current path (see above), and from isopycnal shear and curvature vorticity at the CTD transects (see Chapter 5).

2.4 Sea surface temperature

Comparison with climatology. The ≥24 C warm core in this image extends considerably farther west and southeast than the 24 C isotherm in the climatological monthly average for February (the warmest month; Fig. 2.8). This is not surprising, given that the warm Retroflection is extending about as far to the west and southeast as it has ever been seen to do *(Lutjeharms and van Ballegooyen, 1988).* Representative positions derived from subjective contouring of unregistered satellite images are shown in Fig. 2.9 and 2.10.

Seasonal surface temperature variation vs. variations due to meandering. The seasonal difference between the warmest (February) and coldest (August; not shown) months - is about 4 C everywhere. Variations in surface temperature over shorter time scales, associated with changes in the current location (meandering), can be over twice as large: the sea surface temperature drop, from the warm core across the Agulhas/Agulhas Return Current, is 6 to 9 C (from 24 C to 13 - 18 C) in the 1985 observations, a subrange of the 6 to 13 C range observed in repeated Return Current crossings analyzed by *Lutjeharms and Valentine (1984).* The largest values are

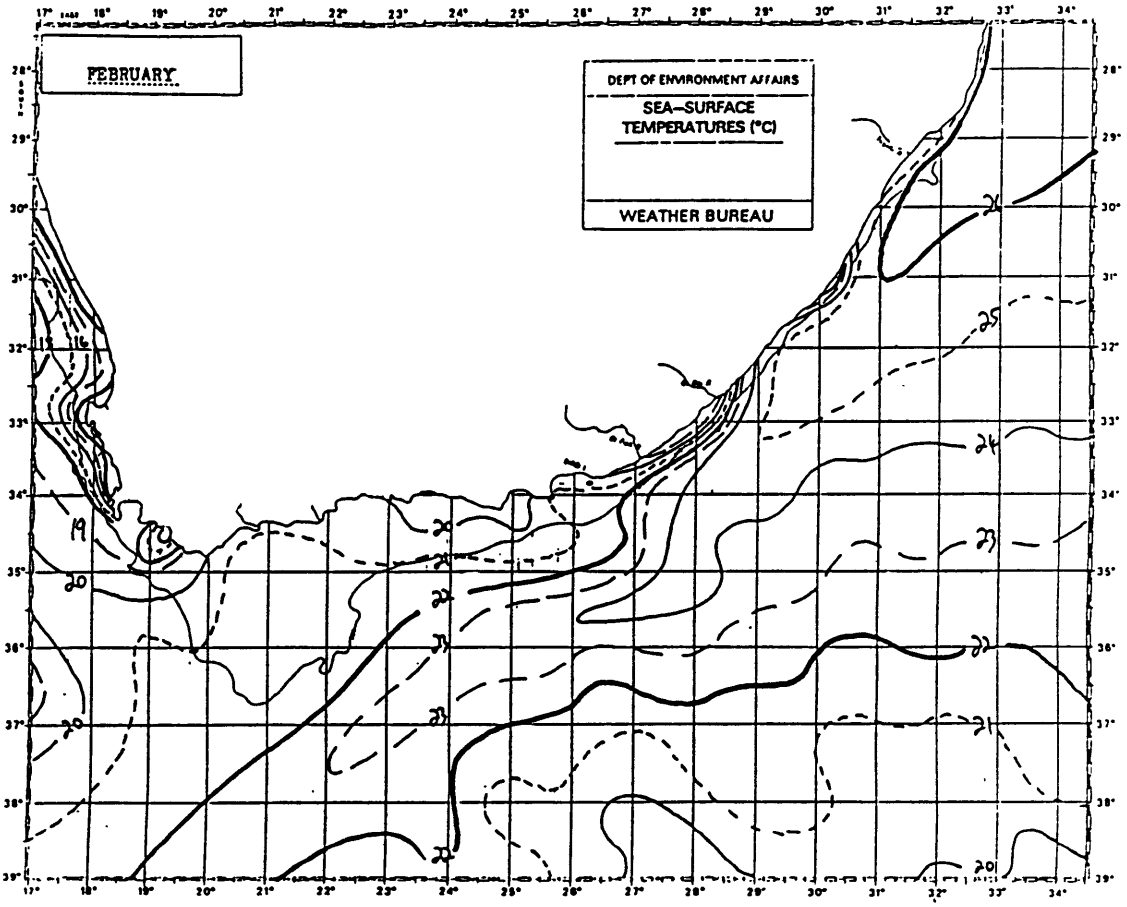

Fig. 2.8 – Climatological average sea surface for February, the warmest month. Compare to sea surface temperature along temperature/depth contour (Fig. 2.5), and to sea surface temperature from CTD/O_2 survey (Fig. 1.6).

observed when the Subtropical Convergence (a strong surface temperature front found south of the Retroflection) coalesces with the Return Current. Retroflection size variation itself was once thought to be mainly seasonal, based on an analysis of a limited number of satellite images (Fig. 2.9; *Lutjeharms and Valentine, 1984*), but mesoscale ring formation events were found to dominate in later work by the same principal author using many more images (Fig. 2.10 and 2.11; *Lutjeharms and van Ballegooyen, 1988*).

Surface temperature gradients along temperature/depth contour. The temperature gradient along the temperature/depth contour is one piece of evidence for the Agulhas Current bifurcation. The warm core evidently peels off with the first smaller-transport Retroflection branch, while the temperature/depth contour follows the larger-transport second branch. Could the temperature gradient along the contour be caused by direct heat loss to the atmosphere? Consider a slab mixed layer of constant depth h, and vertically uniform temperature T, moving along the temperature/depth contour with speed $u = \frac{dl}{dt}$; l is distance along the contour. The rate of air-sea heat flux, $\frac{DQ}{Dt}$, per unit surface area, A, from the slab is given by

$$\frac{1}{A}\frac{DQ}{Dt} = \int_{-h}^{0} \rho C_p \; u \frac{dT}{dl}\, dz \qquad (2.4)$$

The relevant Agulhas values are:

- $h \sim 50$ m, determined by examining XBT traces,
- $u \geq 1$ m s^{-1}, from velocity computed relative to 2400 dbar (see Atlas sections of velocity), and
- $\frac{dT}{dl} = -4$ C/600 km, from the observed drop in XBT surface temperature between 600 and 1200 km along-contour distance (see Fig. 2.5, upper panel).

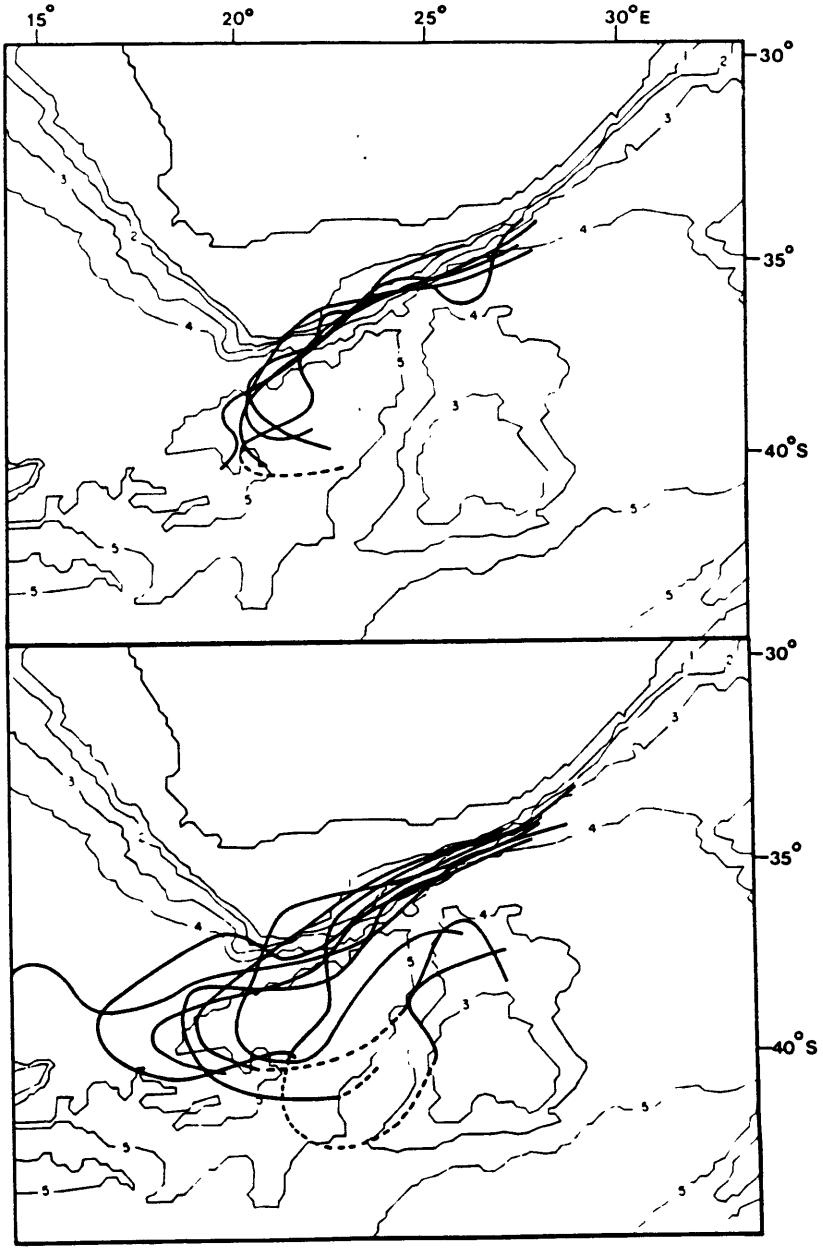

Fig. 2.9 – 1978 to 1982 Agulhas and Agulhas Return Current paths, traced by hand from satellite infrared images of sea surface temperature obtained from a METEOSAT satellite during that period. Upper panel, southern hemisphere winter months; lower panel, southern hemisphere summer months. This is a reproduction of Fig. 6 of *Lutjeharms and Valentine (1984)*.

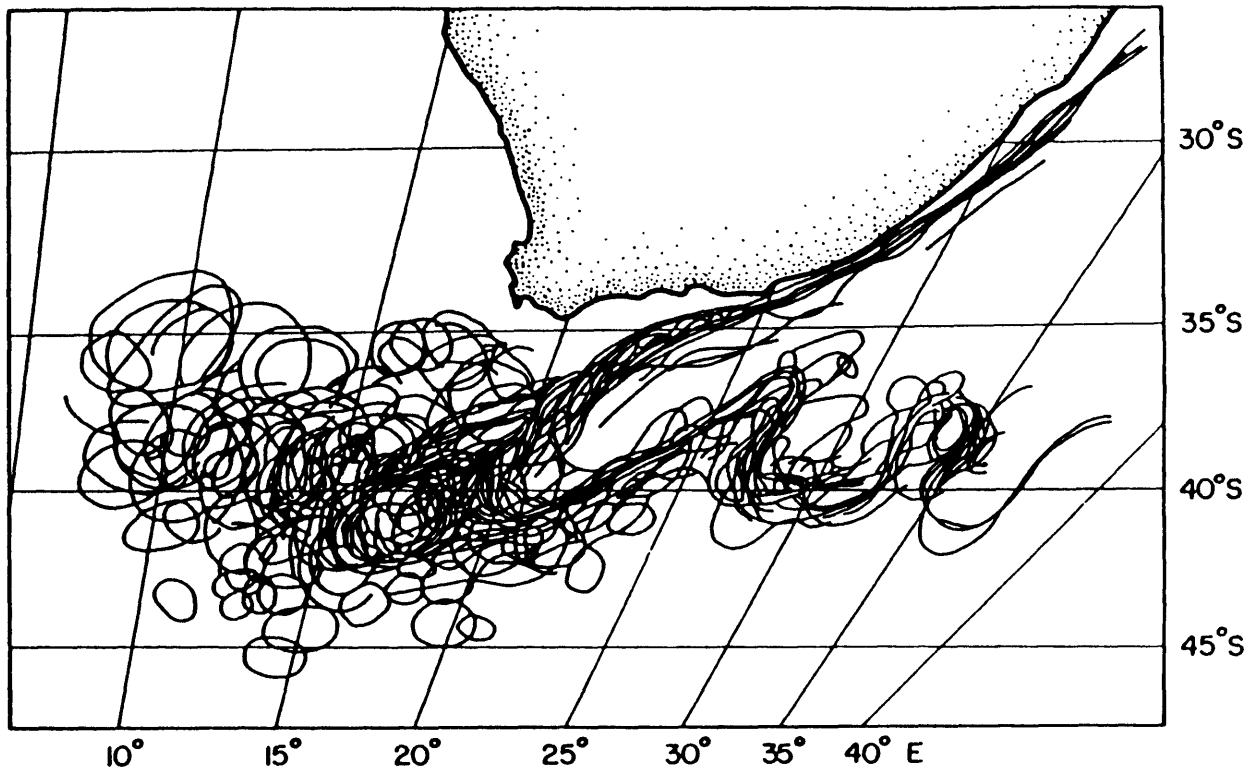

Fig. 2.10 – 1984 to 1985, Agulhas and Agulhas Return Current paths, traced by hand from METEOSAT satellite infrared images of sea surface temperature obtained for that period. This is a reproduction of Fig. 3 of *Lutjeharms and van Ballegooyen (1988)*.

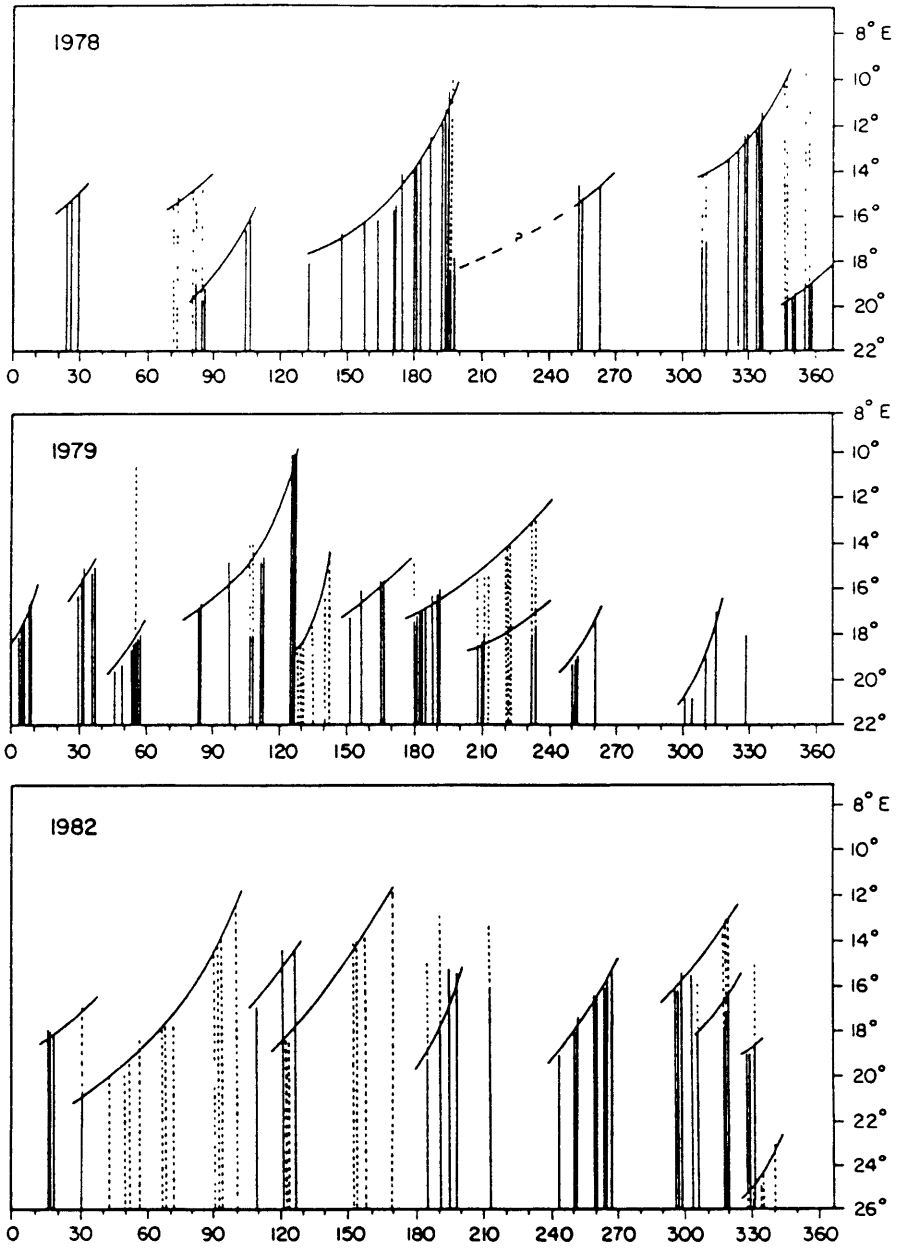

Fig. 2.11 – Zonal location of the westernmost limit of Agulhas Retroflection for 1978, 1979, and 1982, plotted as a function of time in days. Solid lines denote a warm feature that is visibly attached to the Retroflection. Dotted lines denote warm features that are either visibly detached, or whose attachment cannot be determined due to clouds. This is a reproduction of Fig. 7 of *Lutjeharms and van Ballegooyen (1988).*

The rate of air-sea heat flux per unit area that results from Eq. (2.4) and these values is $\leq$-1200 W m^{-2}. This implies an air-sea temperature difference ΔT of $\leq$-30 C, (and thus an air temperature of $\geq$54 C!) estimated from an empirical parametric formula *(Haney, 1971)*

$$\frac{1}{A}\frac{Dq}{Dt} = G(\lambda)\,\Delta T \qquad (2.5)$$

where G = 43 W m^{-2} C^{-1} at λ = 40° latitude; G varies by only 20% over all latitudes. This air-sea temperature difference is too large by an order of magnitude, with the climatological mean ΔT_c only ~-3 C. The air-sea heat flux maximum in the Retroflection reported by *Bunker (1980)* is -130 W m^{-2}. Thus we may conclude that changes in surface temperature along the temperature/depth contour must not be forced principally by atmospheric forcing.

2.5 Transport pattern

Only those transport field characteristics relevant to the path of the current and the surface temperature pattern are presented here; see Chapter 3 for further discussion of transport.

The surface warm core as seen in the satellite image retroflects at or west of the first Retroflection transport branch. The two Retroflection branches can be seen in the overall transport pattern (Fig. 2.12) derived from the CTD survey. Stations used in constructing this pattern were taken during 8-16 and 22-26 March.

The current, as has been mentioned, retroflected in two unequal branches, the first with 35 Sv and the second with 55 Sv transport (plus a 40 Sv locally recirculating component), relative to 2400 dbar. The location of first Retroflection branch in the transport field is displaced $\geq$300 km to the northeast of the warm core location in the satellite image. The transport observations preceded the satellite image by 9 - 15 days,

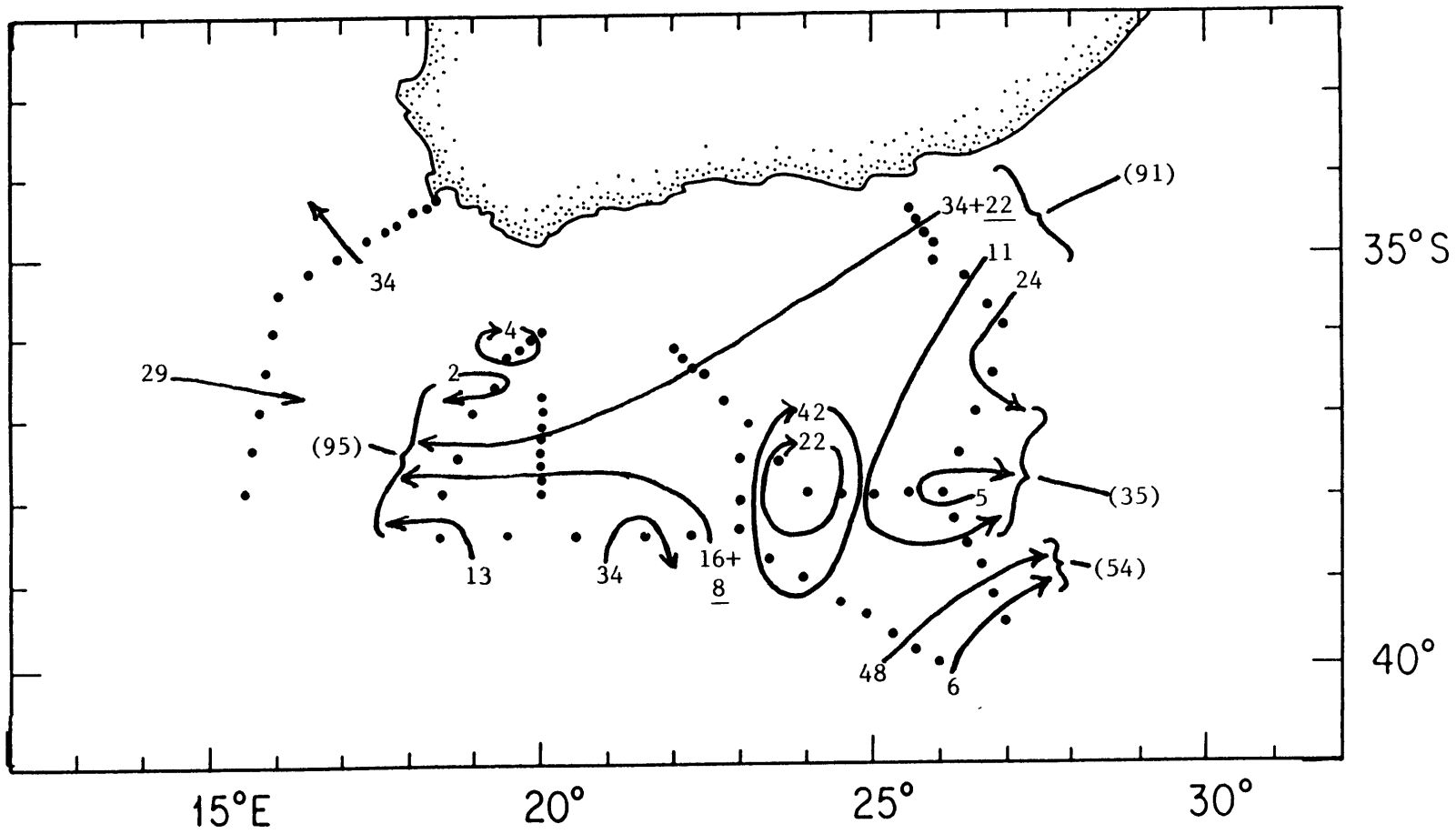

Fig. 2.12 – Schematic transport pattern for March 1985 CTD/O_2 survey. Undadorned numbers denote transport in Sverdrups relative to 2400 dbar for each line with arrowhead. Underlined numbers denote transport in Sverdrups added to make boxes balance. Numbers in parentheses give totals for Agulhas Current inflow (91 Sv), first Retroflection branch (35 Sv), Agulhas Current outflow (95 Sv), and Return Current (54 Sv). Details of transport calculations are given in Chapter 3 and in Appendices B and C.

with the CTD/O_2 stations used to determine the transport of the first branch taken 12 - 16 March, and the composite satellite image taken 25 - 27 March. For the main northwest-southeast trending warm core to have followed the first Retroflection branch, the first branch would have to have moved southwestward at a speed of 0.2 - 0.4 m s^{-1}. This is similar to the range of 0.3 - 0.4 m s^{-1} estimated above (Sec. 2.3) from the movement of the front during the time between the XBT surface temperatures and the satellite image.

2.6 Conclusions

The Agulhas Current in 1985 retroflected in two branches. The current's warm core (≥24 C) followed the first branch, which had a transport of about 35 Sv. The 15 C temperature/200 m depth contour followed the second branch, which had a maximum observed transport of 95 Sv, composed of 55 Sv supplied by the Agulhas Current, and 40 Sv supplied by local recirculation. Transports were computed relative to 2400 dbar.

The first branch moved southwestward at a speed of 0.2 - 0.4 m s^{-1}, estimating from differences between the three survey elements (temperature/depth contour, satellite image, and transport pattern) taken at slightly different times. The displacement has a Rossby number of 0.2 - 0.4, assuming it was purely ageostrophic.

The temperature/depth contour survey gives an accurate picture of the location of the current's high velocities and high horizontal temperature gradients. The contour and the current core at all vertical levels are found within 50 km cross-stream in the six transects across the current. The largest small-scale jaggedness in the contour is due to thermohaline interleaving; its cross-stream amplitude is too small (≥20 km) to distort the contour significantly. The 15 C temperature/200 m depth contour lies within the large temperature gradient region of the Agulhas and Agulhas Return Currents, judging

from the six transects across the current, with the maximum horizontal temperature gradient at 200 m centered near 13.5 C, and large gradients observed in the range 12.5 - 16.0 C.

The contour shows much of the current curvature to be concentrated in three sharp turns in the current path. The turns seem to be a likely location for enhanced cross-frontal motion, since alongstream velocity is ageostrophic to order 0.5 at the turns, but the dynamics of the turns and the current structure in their vicinity are open questions.

The observed surface temperature field is considerably warmer than the climatological monthly average for the warmest month. This is a consequence of the Retroflection's position near the western and southeastern limit of its range. The large surface temperature gradient along the temperature/depth contour is caused by the current bifurcation, with most of the warm core retroflecting at or just west of the first Retroflection branch. The surface temperature gradient along the contour is an order of magnitude too large to be caused by direct heat loss to the atmosphere.

3.1 Introduction

Here we consider several questions concerning the transport field:

- How large is the Agulhas Current transport compared to the wind- and thermohaline-driven transport in the interior of the South Indian subtropical gyre? How does transport vary with the reference level used for the transport integral? What factors constrain reference level choice?

- Does Agulhas Current transport always increase monotonically downstream until the current separates from the coast? Current transport deduced from wind and thermohaline interior forcing increases monotonically, and positive values for transport change per downstream distance were reported by previous authors *(Harris and van Foreest, 1978; Gordon* et al., *1987)* based upon a few widely-spaced transport measurements.

- What is the Return Current transport? How far south must transport be integrated for Return Current transport to balance Agulhas Current transport?

The transport field in the 1985 Cape Town Eddy and the warm water link between the South Indian and South Atlantic Oceans *(Gordon, 1985, 1986)* are considered in Chs. 6 and 8. The transport field in the cold core ring found within the Retroflection in 1985 is discussed in Ch. 7.

Transects across the Agulhas Current and Agulhas Return Current taken during the 1985 Retroflection and historical transects will be compared throughout the present chapter. There are eight historical Agulhas Current transects to the west of the Agulhas Plateau eastern flank (28°E). Six of these transects were taken at intervals down the coast to a depth of 1500 m during the 1969 survey ; these are discussed by *Harris and van Foreest (1978).* The other two transects, both composed of CTD stations covering

the full water depth, were obtained at 21°E by *Jacobs and Georgi (1977),* and at 23°E by *Gordon* et al. *(1987).*

There are four historical Agulhas Return Current transects. Two of these are located at 21°E near the separation of the current from the coast, one taken by *Jacobs and Georgi (1977),* covering the full water depth, and the other just grazing the Retroflection by *Gordon* et al. *(1987),* with most stations to 1500 m. The remaining two transects are located further downstream on the northwestern flank of the Agulhas Plateau, taken by *Harris and van Foreest (1978)* to 1500 m and *Gordon* et al. *(1987)* covering the full water column.

The 1985 survey substantially increases the number of Agulhas and Agulhas Return Current transects in the Retroflection area, especially the number of full-water-column transects. The four 1985 Agulhas Current transects are labelled A through D, proceeding downstream. The two 1985 Agulhas Return Current transects are labelled E and F, again proceeding downstream. Fig. 3.1 shows the locations of the transects, along with the bottom topography, and the location of the 15 C temperature/200 m depth contour as shown by the XBT survey. Table 3.a gives, for each transect station, station number, deepest observed values, bottom depth, along-transect distance, depth of the 15 C isotherm, and the latitude, longitude, and date of observation. Along-transect distance is given with positive values on the warm side of the current, relative to an origin at the 15 C temperature/200 m depth location, chosen for consistency with the XBT survey of the 15 C temperature/200 m depth contour. End point stations in the transects that are outside the current (as defined by isopycnal tilts and transports) are shown in parentheses.[1]

[1]Transect C as shown in the atlas includes stations 291-298. Transport calculations at transect C add on station 248 or 249, ~70 km away.

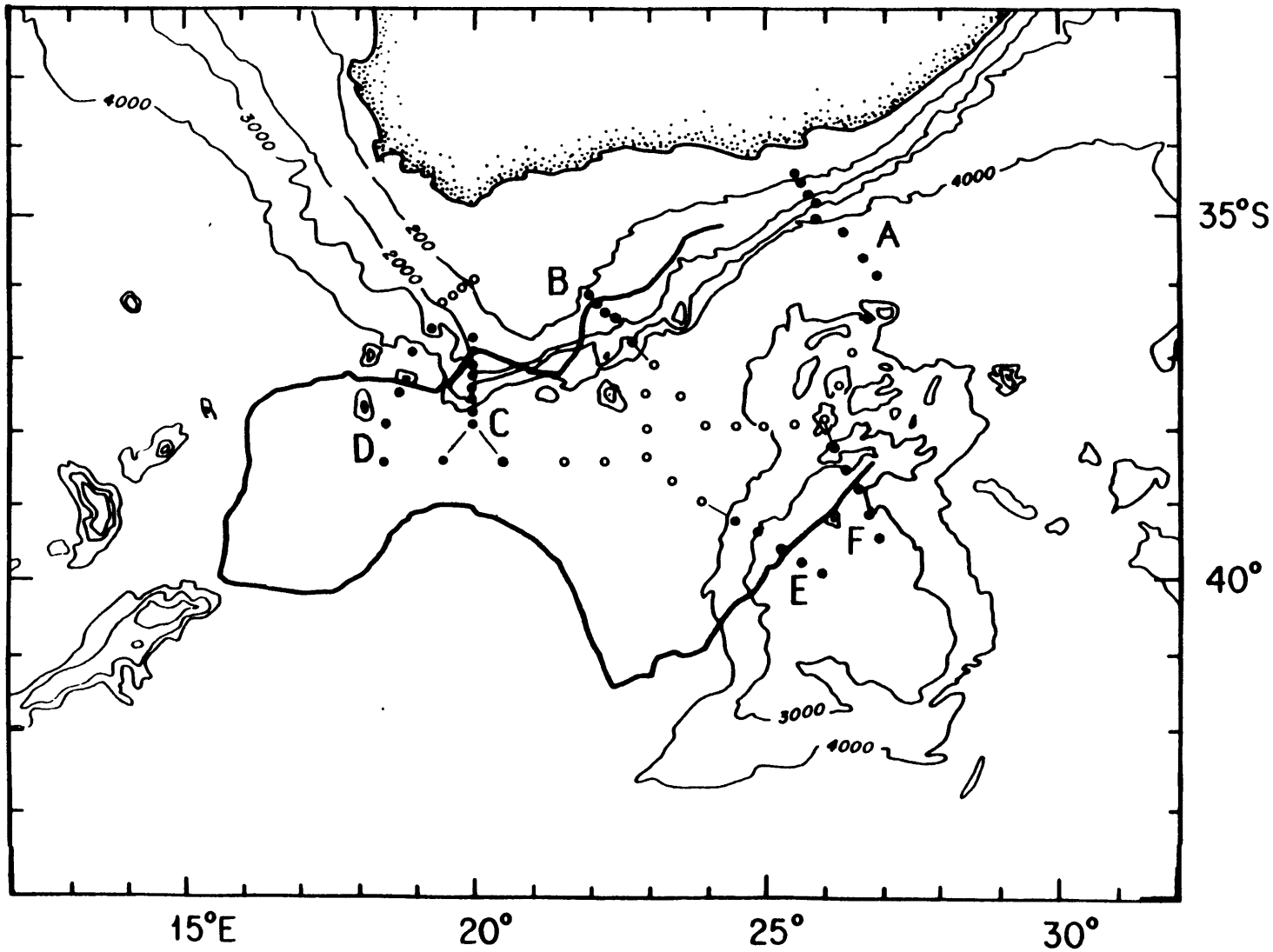

Fig. 3.1 – Map showing Agulhas and Agulhas Return Current transect stations and letter-names, 15 C/200 m contour, and bottom topography. Stations marked with closed dots are used in current transport calculations, and in Atlas sections. Stations in adjacent counterflow are marked with open circles. Lines at southern end of transect C connect to two alternative stations used for transport calculations. Lines at northern ends of Return Current transects E and F connect to stations shown in contoured Atlas sections but not used in transport calculations.

Table 3.a Deepest observations and station summary, Transects A – F. Endpoint stations in the transects that lie outside the current as defined by transports and isopycnal tilts are shown in parentheses.

	sta no.		pres dbar	temp deg c	salt	oxyg ml/l	ptmp deg c	bottom dbar	x-stream dist, km	15C pres dbar	day	mo	lat	long
	270		3549.0	1.996	34.869	5.02	1.712	3629.	239.3	401.	14	3	-36 30.39	26 45.70
	271		4689.0	1.032	34.732	4.99	0.650	4695.	170.1	390.	15	3	-35 54.26	26 56.15
	272		4635.0	0.956	34.728	5.00	0.582	4695.	136.0	387.	15	3	-35 40.14	26 41.20
	273		4225.0	0.963	34.731	5.06	0.635	4275.	86.4	369.	15	3	-35 19.29	26 20.58
A	274		4131.0	1.030	34.738	5.03	0.710	4171.	36.9	297.	15	3	-35 6.30	25 52.01
	275		3501.0	1.891	34.806	5.10	1.614	3676.	12.1	240.	15	3	-34 52.93	25 51.72
	276		2103.0	2.592	34.781	4.54	2.437	2415.	-4.9	184.	16	3	-34 46.36	25 43.91
	277		1715.0	2.852	34.723	4.65	2.727	1756.	-24.7	166.	16	3	-34 37.13	25 37.32
	278		607.0	8.183	34.692	4.38	8.119	606.	-38.3	53.	16	3	-34 30.65	25 33.10
	(262)		5425.0	0.768	34.708	5.11	0.388	5410.	189.6	91.	13	3	-37 35.89	23 32.59
	261		3309.0	2.113	34.830	5.17	1.851	5383.	128.9	330.	12	3	-37 9.96	23 7.42
	260		2477.0	2.472	34.833	4.98	2.284	2415.	78.2	322.	12	3	-36 51.82	22 42.67
B	259		2267.0	2.767	34.821	4.86	2.594	2272.	35.7	288.	12	3	-36 31.77	22 27.11
	258		915.0	3.659	34.547	3.90	3.592	954.	14.5	248.	12	3	-36 26.96	22 14.19
	257		405.0	10.966	34.957	4.76	10.916	420.	-0.9	197.	12	3	-36 20.31	22 8.04
	256		211.0	12.039	35.072	4.34	12.011	243.	-21.7	49.	12	3	-36 12.44	21 58.11
	291		4829.0	0.999	34.731	5.02	0.662	4849.	98.4	375.	26	3	-38 0.16	19 59.57
	292	S	1229.0	3.865	34.458	4.26	3.771	4592.	80.2	367.	26	3	-37 50.38	19 59.35
	293		4397.0	0.955	34.731	5.00	0.608	4435.	60.3	370.	26	3	-37 39.64	19 59.69
C	294	S	1005.0	5.965	34.563	4.14	5.874	3820.	41.9	314.	26	3	-37 29.69	19 59.47
	295		2659.0	2.401	34.860	5.29	2.197	2880.	23.6	233.	26	3	-37 19.92	19 57.59
	296	S	1263.0	3.037	34.573	4.83	2.948	2114.	7.9	225.	26	3	-37 11.60	19 59.48
	297		1705.0	2.882	34.752	4.45	2.758	1679.	-13.7	157.	26	3	-36 59.97	20 0.02
	298		1569.0	2.874	34.731	4.47	2.767	1658.	-31.9	81.	26	3	-36 50.17	19 59.6

Table 3.a

	sta no.	pres dbar	temp deg c	salt	oxyg ml/l	ptmp deg c	bottom dbar	x-stream dist, km	15C pres dbar	day	mo	lat	long
	247	4739.0	0.901	34.723	5.06	0.517	4905.	161.9	416.	9	3	-38 30.72	18 29.00
	246	4605.0	0.994	34.732	5.03	0.622	4747.	105.8	357.	8	3	-38 0.45	18 30.30
D	245	4557.0	1.007	34.734	4.96	0.641	4695.	51.5	299.	8	3	-37 33.24	18 43.99
	244	4003.0	1.279	34.759	4.99	0.965	4348.	-13.3	174.	8	3	-37 0.56	18 57.68
	243	3617.0	1.960	34.829	5.10	1.669	3805.	-60.0	55.	8	3	-36 41.34	19 18.05
	(289)	3999.0	1.293	34.758	5.03	0.980	5013.	145.9	197.	24	3	-38 59.82	23 58.46
	288	3533.0	1.889	34.805	5.06	1.608	3550.	89.1	320.	24	3	-39 17.31	24 30.96
E	287	2961.0	2.094	34.822	5.13	1.867	3013.	52.1	260.	24	3	-39 26.23	24 54.05
	286	2709.0	1.963	34.812	5.11	1.763	2778.	12.2	250.	23	3	-39 39.32	25 16.20
	285	2501.0	2.090	34.812	5.08	1.907	2521.	-24.4	86.	23	3	-39 50.06	25 37.74
	284	2337.0	2.331	34.824	5.04	2.159	2420.	-60.6	85.	23	3	-39 59.36	26 0.12
	(267)	2979.0	2.172	34.824	5.05	1.942	3027.	96.5	332.	14	3	-37 58.92	26 1.40
	279	2529.0	2.443	34.826	5.10	2.251	2876.	58.4	357.	22	3	-38 17.84	26 11.62
F	280	2807.0	1.770	34.799	5.14	1.565	2880.	19.4	290.	22	3	-38 36.34	26 24.43
	281	2613.0	2.377	34.830	5.04	2.178	3096.	-13.1	139.	23	3	-38 51.41	26 35.99
	282	3009.0	1.999	34.816	5.15	1.769	3030.	-53.9	98.	23	3	-39 11.82	26 46.56
	283	2611.0	2.203	34.830	5.16	2.008	2623.	-92.3	78.	23	3	-39 30.46	26 58.22

All six 1985 CTD/O_2 transects are nearly perpendicular ($90 \pm 20°$) to the axis of the flow, so cross-stream and along-transect distance can be used interchangeably; their ratio is always >0.94 [*i.e.*, sin $(90 \pm 20°)$]. Five of the six transects cross current axis (see Ch. 2) at approximately right angles, judging from angle between the transects and the 15 C temperature/200 m depth contour (see Ch. 2).[1] The sixth transect is upstream of the beginning of the XBT survey, perpendicular to the continental slope from which the current has not yet begun separating.

3.2 Agulhas Current transports and the interior circulation

Previous Agulhas Current transport observations show transport increasing rather steadily for 1200 km downstream, from about 35 Sv at 30°S to almost 140 Sv at the southern tip of Africa where the current separates from the continental slope. The historical transport observations, taken by *Toole and Raymer (1985), Gründlingh (1980), Gordon* et al., *(1987),* and *Jacobs and Georgi (1977),* in downstream order, are shown in Fig. 3.2 and Table 3.b. The 1985 transports are also shown in Fig. 3.2 and in Table 3.c.

The increase in transport downstream was estimated by *Gründlingh* to be 6 Sv per 100 km, between his own 75 Sv matched[2] transport to the bottom at 31°S and *Jacobs and Georgi's* 137 Sv geostrophic transport relative to a bottom reference level at 19°E off the Agulhas Bank. The increase was re-estimated by *Gordon* et al. to be

---

[1]Since the current axis may have moved during the time it took to make the CTD/O_2 and the XBT 15 C/200 m contour surveys, each transect/current axis crossing angle was estimated from (a) the transect heading and (b) the range of headings of the XBT 15 C/200 m contour over a distance of $2\ v\ \tau_n$, centered on the transect/contour intersection; v is the local meander propagation speed ($\sim \pm 20$ km day^{-1}, *Gründlingh, 1978*) and τ_n is the time elapsed between the crossing of the CTD/O_2 transect n and the XBT contour. The factor of 2 implies that the sign of v is not known.
[2]See note, Table 3.b.

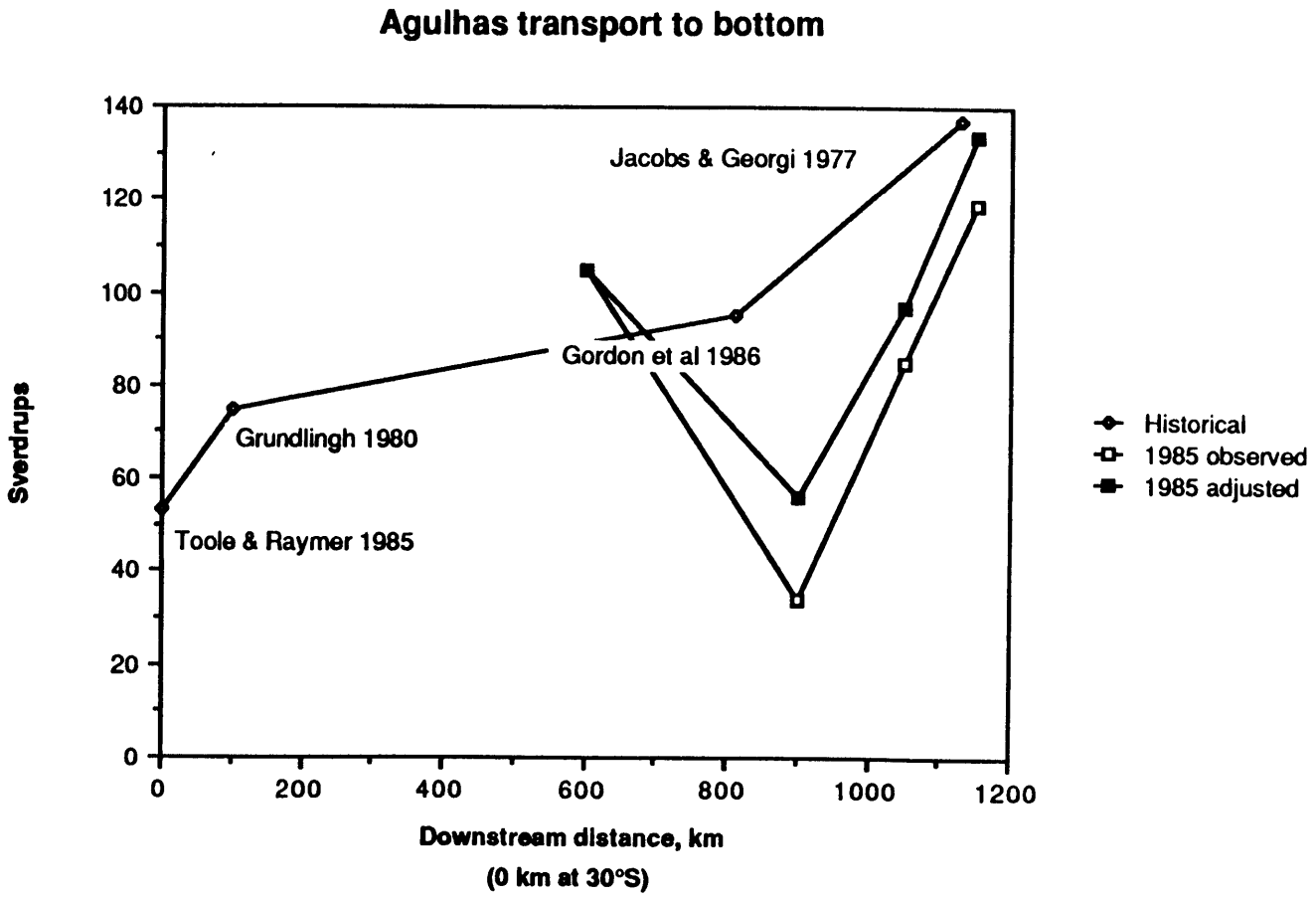

Fig. 3.2 Agulhas Current transport to bottom/deepest common level, historical and 1985 values. See Tables 3.b and 3.c for notes on how individual values were derived.

Table 3.b – Historical Agulhas Current transports

Source	Location	Transports (Sv) above reference level (dbar) 1000 db	1500 db	2400 dbar	Bottom
Toole and Raymer, 1985	Durban, 30°S				44[a]
Gründlingh, 1980	Port Edwards, 31°S	62[c]			75[b,c]
Gordon et al., 1987	Agulhas Passage, 23°E		70[d]	83[d,e]	95[d]
Jacobs and Georgi, 1977	Agulhas Bank, 21°E	80[f]			137
Harris and van Foreest, 1978	20 - 28°E, south of 33°S	30-40[g]			

[a]derived from a composite thermal wind/density field to the ocean bottom within 100 km of the coast, referenced to composite absolute velocity data in the upper 50 m.

[b]computed by multiplying 0 – 1000 m transport by 1.20, *Duncan's (1970)* ratio of total to 0 – 1000 m transport. My calculation in square brackets.

[c]derived from geostrophic shear measured to 1000 m, referenced to direct velocity measurements from a current meter suspended at 100 m depth.

[d]includes 21 Sv from transport extrapolation inshore of station 49.

[e]my calculation.

[f]relative to 900 m.

[g]Estimated from their Fig. 3; transports are computed relative to 1100 dbar (or the '27.2 σ_t level'?), not 1000 dbar.

Table 3.c – Agulhas Current transports, Luyten & Toole survey, Feb. - Mar. 1985, *R/V Thomas Washington*, Cruise 3

		Transports (Sv) above&below reference level (dbar)							
Section	stations	1000 db		1500 db		2400 d		Bottom[a]	
A (26°E)	277-270	38	-80	69	-31	91	-17	105	
B (22°E)	256-260	14	-21	26	-8	34 (56)[b]	0	34 (56)[b]	
C (20°E)	291/3/5/7/8	30	-55	49	-19	65	-2	71	
C'	C + 249	33	-67	55	-29	76 [87][c]	-4	85 [97][c]	
C''	C + 248	34	-68	57	-28	79 [90][c]	-3	83 [95][c]	
D (19°E)	243-247	42	-83	73	-49	99 [111][c]	-21	116 [131][c]	

[a]Deepest common level of station pairs; no extrapolation of shear to actual bottom depth.

[b]Transects A and B plus other stations form a closed box; adjusted transport at transect B to balance the box is shown in parentheses.

[c]Value in brackets includes an estimate of missed transport obtained by extrapolating observed transport per unit width (see text).

2.7 Sv per 100 km downstream between *Gründlingh's* observation and their own at 23°E, and 13 Sv per 100 km between their observation and *Jacobs and Georgi's.*

The 1985 transport observations exhibit transport values comparable the historical observations – except for drastically reduced transport at Transect B (Fig. 3.2 and Table 3.c). Some of this reduction persists at the next transect downstream, Transect C.

How do the historical and 1985 Agulhas Current transports and downstream changes in transport compare with values for a linear western boundary current that simply balances the net ocean interior transport? Interior transport, and thus the linear western boundary current flow, is estimated here from *Veronis' (1973)* two-layer world ocean circulation model. The interior transport has two parts: *(i)* Sverdrup transport derived from wind field observations and *(ii)* net eastern boundary transports, derived from alongshore thermocline slope representing the effects of basin-wide thermohaline forcing, plus an adjustment for Sverdrup transport impinging on the eastern boundary. The western boundary (Agulhas) current transport is just equal and opposite to the zonally-integrated meridional interior transport.

According to *Veronis's* calculations, the western boundary current transport grows from zero at 21°S to a maximum of 72 Sv at 36°S. This includes 5 Sv from eastern boundary transport due to thermohaline forcing. Transport increase per downstream distance in the modelled Agulhas Current reaches a maximum of 9 Sv per degree of latitude at about 25°S, decreasing to zero at 37°S. A degree of latitude corresponds to ~200 km downstream distance along the African continental slope south of 30°S, since the slope runs northeast to southwest there.

Veronis's transport and transport increase values should be revised downward in light of more recent wind stress observations. Wind stress values available to *Veronis* seem to have significantly overestimated the strength of the westerlies in the 35

to 60°S latitude band. The maximum zonally-averaged westerly wind stress in *Hellerman and Rosenstein (1983)* is half as strong (0.1 instead of 0.2 N m^{-2}, with a standard error of 0.05 N m^{-2}) and 2–3° further north of the analogous feature in *Hellerman (1967). Hellerman and Rosenstein* report 40 ± 8 Sv in January and 60 Sv (no error reported) in July, both at at 32°S, for the maximum Sverdrup transport integrated across the S. Indian Ocean. The sum of the thermohaline component (5 Sv) and the average of the January and July values (50 ± >8 Sv) is 55 ± >8 Sv, significantly less than *Veronis'* value of 72 Sv.

The increase in transport downstream is 3 Sv per 100 km, using *Veronis'* wind values, and 2 Sv per 100 km using the new wind observations, at the latitudes (31 to 37°S) of the transects cited in Fig. 3.2 and Table 3.b.

The observed transport exceeds its maximum forced value of 55 ± >8 Sv at all 1985 and historical transects, except Transect B, for 2400 dbar and deepest common reference levels[3] (Fig. 3.3). The maximum observed transport (*Jacobs and Georgi's* value computed to deepest common levels) is over twice the maximum forced value. A reference level choice of less than 1500 dbar would be required to bring transport at Transect D in line with the maximum forced value, and of less than 1000 dbar to reduce transport at *Jacobs and Georgi's* transect to this value. But reference levels this shallow are implausible: the deep oxygen minimum of S. Indian Ocean origin found at 850 – 1800 dbar in the Current is strong evidence for a reference level at greater depths. Reference level choice is discussed further below.

The downstream change in transport expected from interior circulation theory has been compared by previous authors to the observed alongstream change in

[3]*E. g.*, the deepest common level (dcl)of a pair of stations ending at 1000 m and 1300 m is 1300 m. Density and derived fields are sometimes extrapolated from the dcl to the bottom, a procedure called Helland-Hansening *(Helland-Hansen, 1905)*.

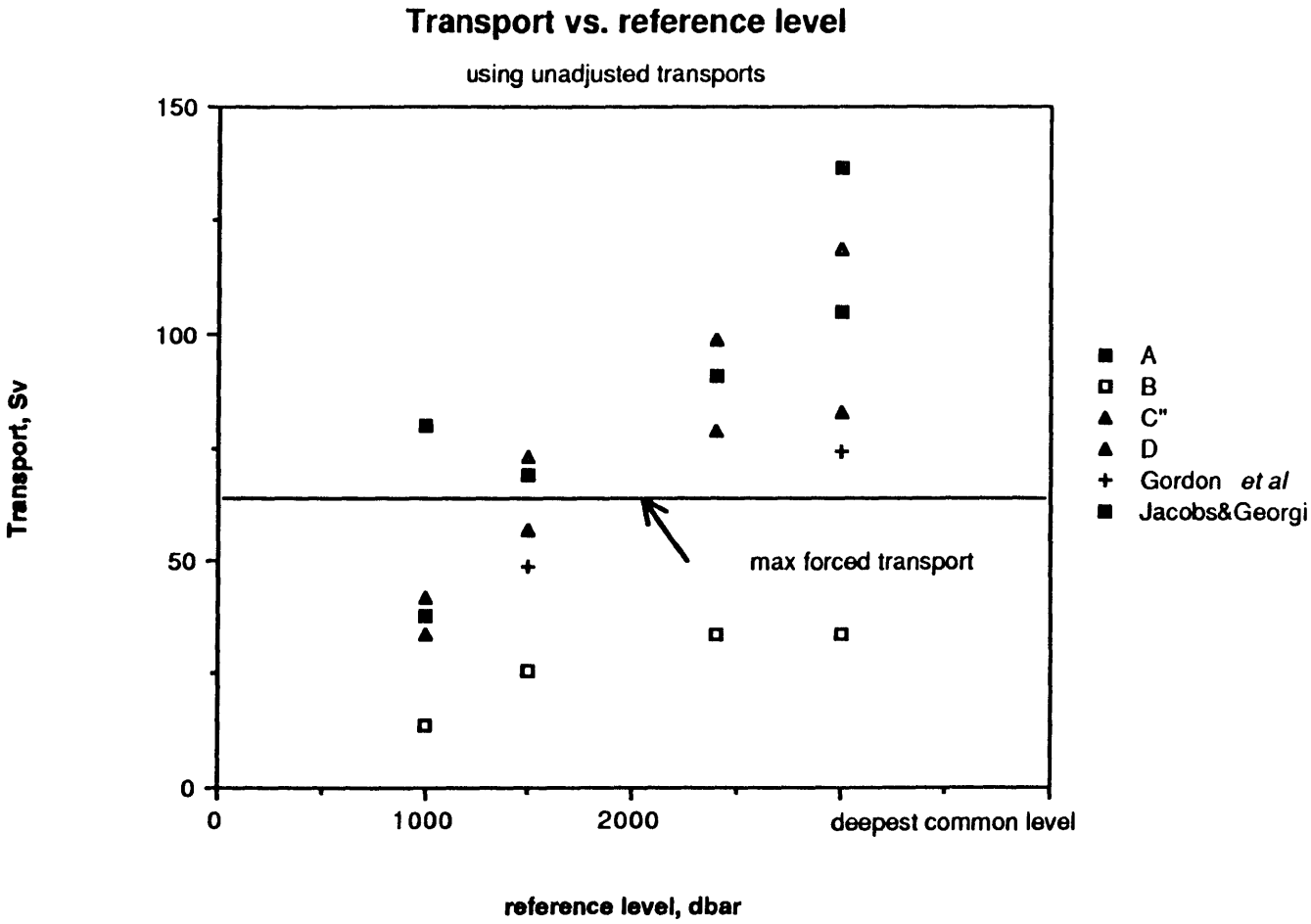

Fig. 3.3 Agulhas Current transport *vs.* reference level. Transport values are *un*adjusted values from Tables 3.b and 3.c.

transport. *Gründlingh (1980)* noted that the 6 Sv per 100 km increase between his and *Jacobs and Georgi's* transports agreed with the transport increase value in *Veronis'* model; and *Gordon* et al. discussed possible interpretations of the rather different rates of alongstream increase between *Gründlingh's* observation and theirs (2.7 Sv per 100 km), and between theirs and *Jacobs and Georgi's* (13 Sv per 100 km).

Possibly the *rates* of observed and modelled increase were compared rather than the transports themselves with the idea that changes in transport were less sensitive than the transports themselves to reference level choice. This is not the case. The two quantities both vary with reference level: at each transect or pair of transects, the value of either quantity for a bottom reference level is 2–4 times the value for a 1000 dbar reference level (Fig. 3.3 – 3.5). Note that Fig. 3.3 shows observed transport values only, while Fig. 3.4 and 3.5 show transport change values derived from both observed and adjusted transport values. The observed transport is just the integrated geostrophic flow between CTD/O_2 stations, while the adjusted transport includes horizontal extrapolation of the transport per unit width function where transects did not completely cross the current, and adjustments for mass balance within boxes enclosed by the CTD/O_2 survey and the slope (explained further below). Transport adjustments in deep water were assumed to have the same variation with reference level as observed transport.

Nearly all the downstream transport change magnitudes exceed the <u>maximum</u> forced value of 9 Sv per 100 km found 1000 km to the north at 25°S, by up to a factor of six (Fig. 3.4 – 3.5); the forced value at the transect latitudes is only 2 Sv per 100 km . Also, transport <u>decreases</u> between Transects A and B, opposite in sign from the transport increase expected from the returning interior transport. The

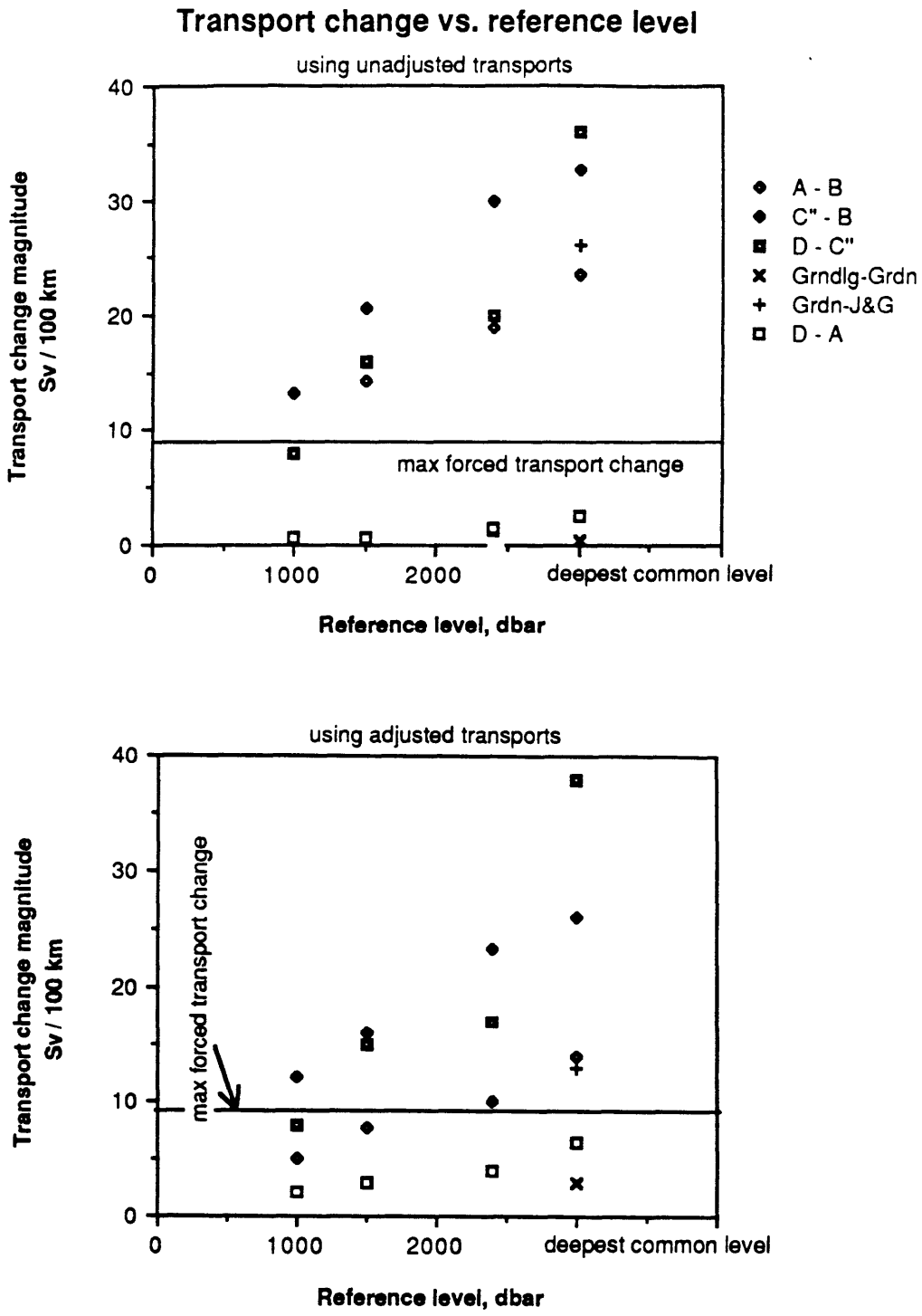

Fig. 3.4 Agulhas Current downstream transport change magnitudes. Computed from *un*adjusted transport values in Table 3.b and 3.c.

Fig. 3.5 Agulhas Current downstream transport change magnitudes. Computed from adjusted transport values in Table 3.b and 3.c.

Gründlingh – Gordon et al. value of 2.7 Sv per 100 km turns out to have the smallest magnitude of all the (adjusted) estimates.[4]

Even generous error estimates cannot account for the observed transport changes in excess of the forced rates. The transport change is a gradient quantity and thus sensitive to errors such as missed transport, particularly at small transect separations alongstream. Even so, the difference between transport change computed from observed and from adjusted transports is still small compared to their difference from the expected forced value. The relatively low values of alongstream increase between A – D (Fig. 3.4 and 3.5) are, in effect, the result of aliasing errors.

Evidently, then, the Agulhas transport is significantly larger and more variable alongstream than predicted by purely linear, thermohaline- and wind-driven dynamics. This indicates that *(i)* the Retroflection is recirculating vigorously, and *(ii)* that the alongstream length scale of the transport is much smaller than the length scale over which the interior forcing varies, and, in fact, smaller than the scale of the Retroflection itself. As we shall see, the downstream variation in tracer quantities supports both of these conclusions.

---

[4]It is tempting to call either $\left(\frac{\Delta T_{obs}}{\Delta T_{forced}}\right)$ or $\left(\frac{T_{obs}}{T_{forced}}\right)$ the recirculation index, but *Rhines (1983)* has already used this name for the ratio of (a) the meridional velocity scale implied by Ekman pumping and continuity to (b) the meridional velocity scale implied by the Sverdrup relation. (Observed transport represented by T_{obs}, and the returning interior transport by T_{forced}, and Δ denotes the downstream change per unit distance.)

Recirculation has still other special meanings: in thermocline theory, "if the fluid . . . recirculates many times . . . before having its properties reset at the surface outcrop . . . a layer [is] considered to be unventilated " (*Keffer, 1985*). The 'Gulf Stream recirculation' refers to that part of the N. Atlantic subtropical gyre interior circulation that impinges upon the Gulf Stream north of Florida Straits. The Peclet number – ratio of velocities *along* to velocities *across* tracer isopleths – is sometimes called the 'index of recirculation' in advective-diffusive models. 'Recirculation' also can refer – as it does in this thesis – to the western boundary current transport in excess of the wind– and thermohaline–driven interior transport *(Munk and Carrier, 1950)*.

These ideas are not entirely new. *Gründlingh (1978)* suggested that the Agulhas and Agulhas Return Current flow may be composed of a series of linked anticyclonic eddies, and *Harris and van Foreest (1978)* noted the premature retroflection of some dynamic isobars upstream of the main Retroflection in the 1969 survey. The 1985 survey confirms the existence of these phenomena, and provides quantitative measures of their importance and sensitivity to reference level.

3.3 Reference level choice

A deepest common reference level (level of no motion) has the practical advantage of producing a single number for transport, instead of two numbers, one above and one below the reference level. Such a reference level produces the maximum above–reference–level thermal wind velocities and transport magnitudes when monotonic vertical shear strongly predominates at all levels, as it does in the Agulhas. (Downstream bottom velocities, of course, increase the velocities and transports above the purely thermal-wind values.)

A reference level in the vicinity of 2500 dbar is suggested by several traditional lines of reasoning:

- *Water mass cores.* The deep oxygen minimum at 850–1800 dbar from S. Indian Ocean sources loses strength proceeding downstream, east to west, in the Agulhas. The deep salinity maximum at 2300 – 3100 dbar of N. Atlantic origin loses strength from west to east throughout the Retroflection (see Chapter 4). This implies a velocity reference level between these two levels, with westward property advection at the oxygen minimum and eastward property advection at the salinity minimum. However, this evidence is not conclusive, since processes other than mean advection are important in maintaining the extrema field. In the Retroflection region, eddy energies are as high as anywhere in the world ocean (*Cheney* et

al., *1983)* so stirring due to unsteady advection undoubtedly plays an important role.

- *Topographic constraints.* Flow from the bottom up to 2500-3000 m is connected more directly to S. Atlantic and Circumpolar than to S. Indian sources of mass, momentum, and water mass characteristics. This is because the Natal Valley through which the Agulhas Current flows is a cul-de-sac opening to the southwest. The Valley is bounded, north of 35°S and below 3000 m, to the west by the African slope, to the north by the Moçambique Channel, and to the east by the Moçambique Plateau. A 2500 m reference level in the Retroflection implies deep eastward flow along the African continental slope, bringing water from S. Atlantic sources into the Natal Valley.

- *Topographic steering.* Finally, the fact that the Agulhas and Agulhas Return Currents are located over topography as shallow as 2500 m (Transects B, E, and F) suggests that velocities at and below 2500 m are too weak to couple the flow to the topography. Better understanding of topographic control dynamics is necessary to quantify this impression.

The use of a 2500 m reference level was suggested by *Duncan (1970),* who mentioned the water mass cores and the topographic constraint of the Moçambique Channel.[6] *Duncan* assumed, however, that the Agulhas was supplied through the Channel itself. More recent studies *(Harris, 1972, Saetre and Jorge da Silvia, 1984,* and *Fu, 1986,* discussed by *Gordon* et al., *1987)* found only 0 – 10 Sv throughflow, implying that the Agulhas is supplied principally from the east over the Moçambique Plateau.

---

[6]Since *Duncan* had a limited amount of deep data, he computed the ratio $\left(\frac{\text{transport above 1500 m}}{\text{transport above 2500 m}}\right)$ at the deep station pairs, for transport computed relative to 2500 m. Then, transport relative to 1500 m at shallow (~1500 m) station pairs was divided by this ratio (0.80) to get transport relative to 2500 m.

Agulhas transport integrated across the current above a 2400 dbar reference level is 85 – 100% of the transport above deepest common levels at the 1985 Agulhas transects. The 100% value occurs at Transect B where the depth is ≤ 2400 dbar all the way across the Current. The ratio at individual station pairs in the Agulhas of transport above a 2400 dbar reference to transport above deepest common levels is 65 – 100%. The 100% value occurs where the depth is ≤ 2400 dbar.[7]

3.4 Agulhas Current transport

Transport at the four Agulhas transects is considered in conjunction with mass convergence in closed boxes defined by the CTD/O_2 survey lines. Transports are reported here computed relative to *(a)* the deepest common level of each station pair, and *(b)* 2400 dbar (or the deepest common level if it is < 2400 dbar).[8] Table 3.c shows the Agulhas transport at the 1985 transects. Fig. 3.6 shows transport per unit width and bottom topography. Fig. 3.7 shows the boxes used for mass convergence calculations. Figs. 3.8 – 3.10 show the transports along the box boundaries. These may be compared to the simplified transport schematic shown in Fig. 2.12 above.

[7] *Gordon* et al. reported the ratio of (a) transport between 1500 and 3000 dbar to (b) transport above 1500 dbar, with *both* transports computed relative to a deep level, to have a value of 0.15 – 0.25.

[8]The MIT inverse model programs (discussed in Appendix A) and the WHOI transport programs are set up such that the reference level must be chosen from a set of discrete levels. The two sets of levels are slightly different, so 2400 dbar was used at WHOI and 2500 dbar at MIT. The differences in net transport using these two levels are negligible (order 1 Sv).

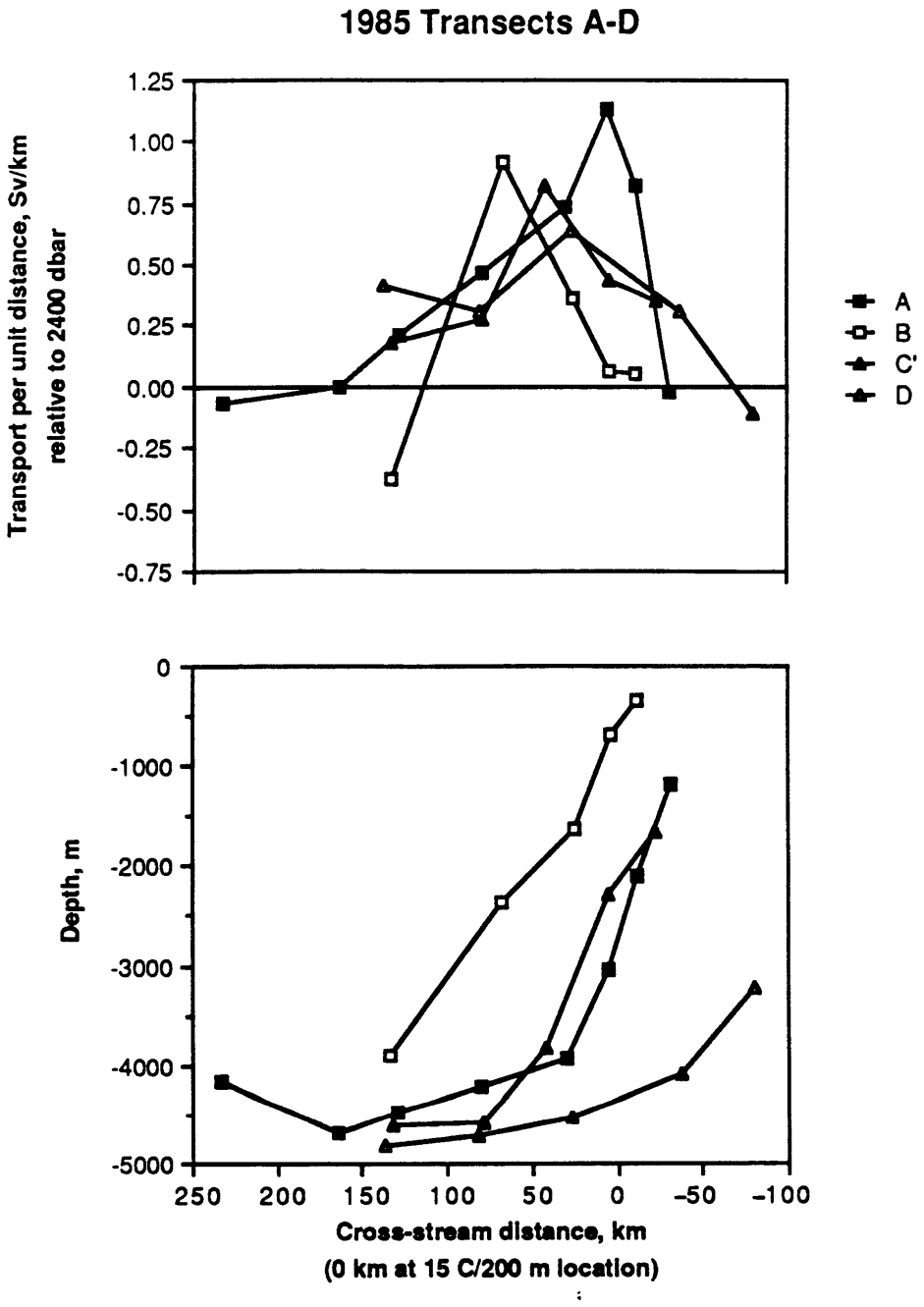

Fig. 3.6 Agulhas Current: (a) transport per unit cross-stream distance, 1985 transects A-D, looking downstream. Transport is computed relative to 2400 dbar or the deepest common level of station pairs, whichever is deeper. (b) depth of bottom beneath current. For both plots, origin of cross-stream distance is at transects' 15 C/200 m location.

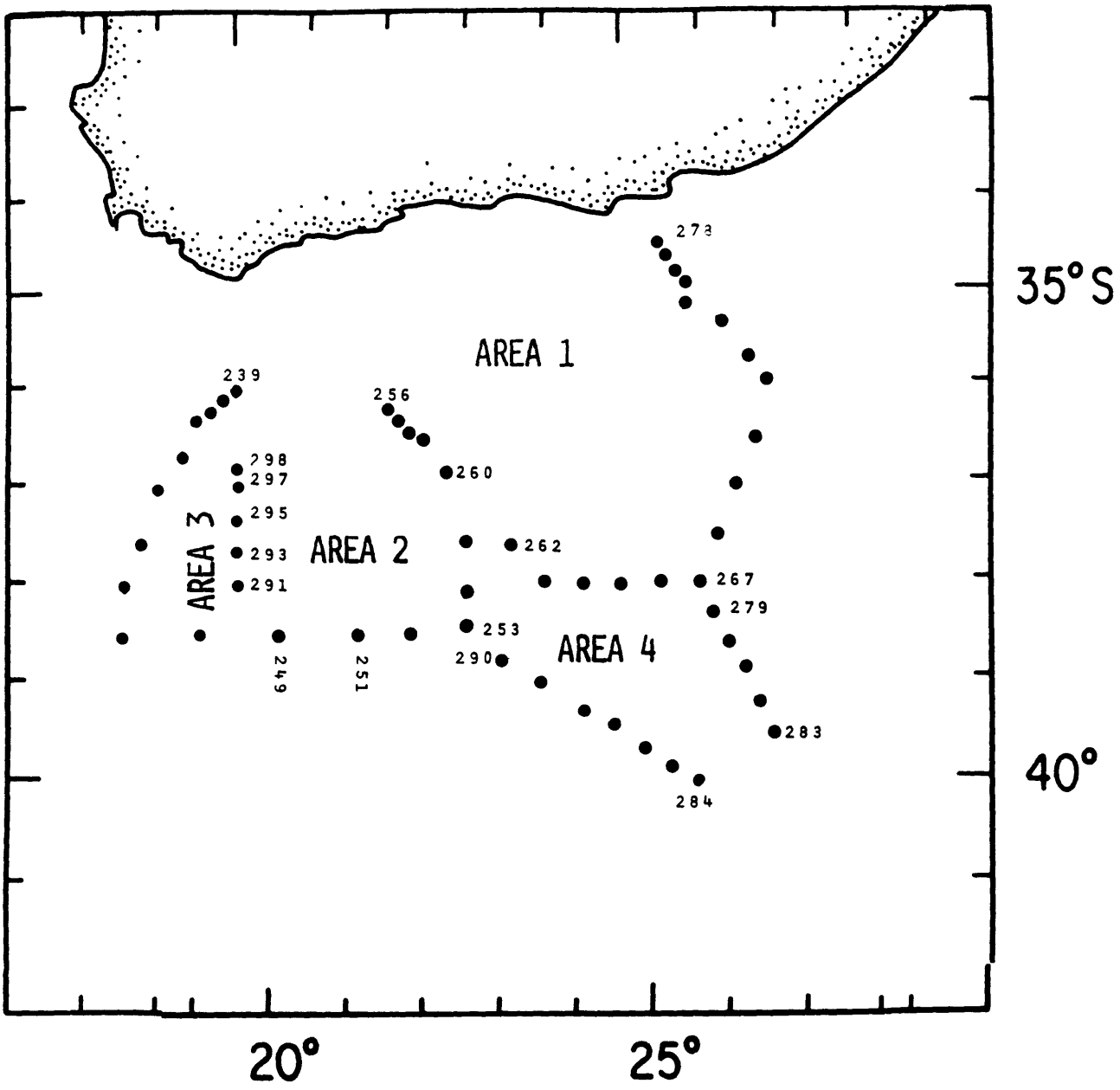

Fig. 3.7 Plan view, closed areas defined by CTD/O_2 survey used for transport calculations.

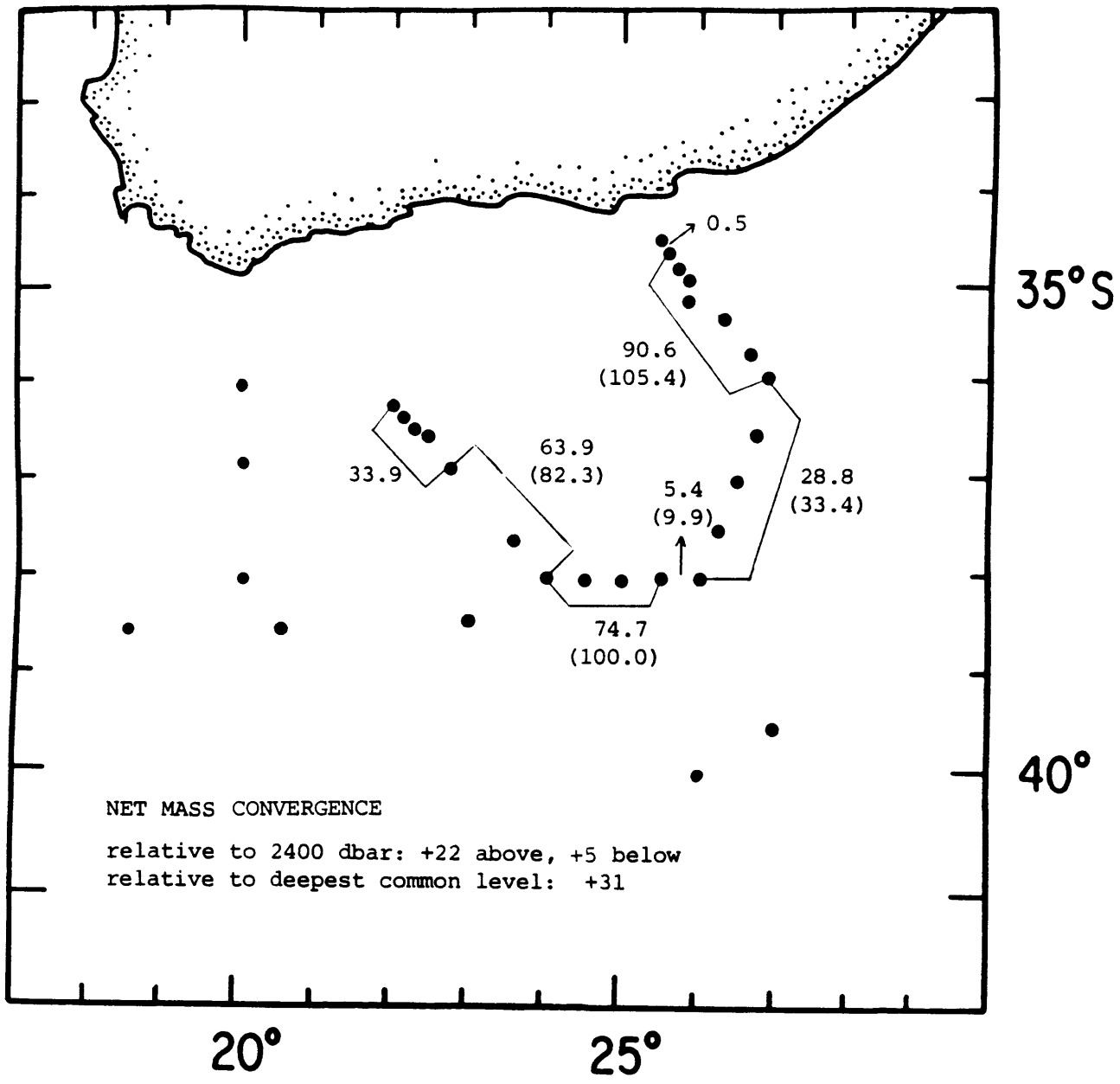

Fig. 3.8 Mass imbalance schematic, Area 1: transports above 2400 dbar reference level (transports above bottom reference level in parentheses; values omitted if same as transport above 2400 dbar.)

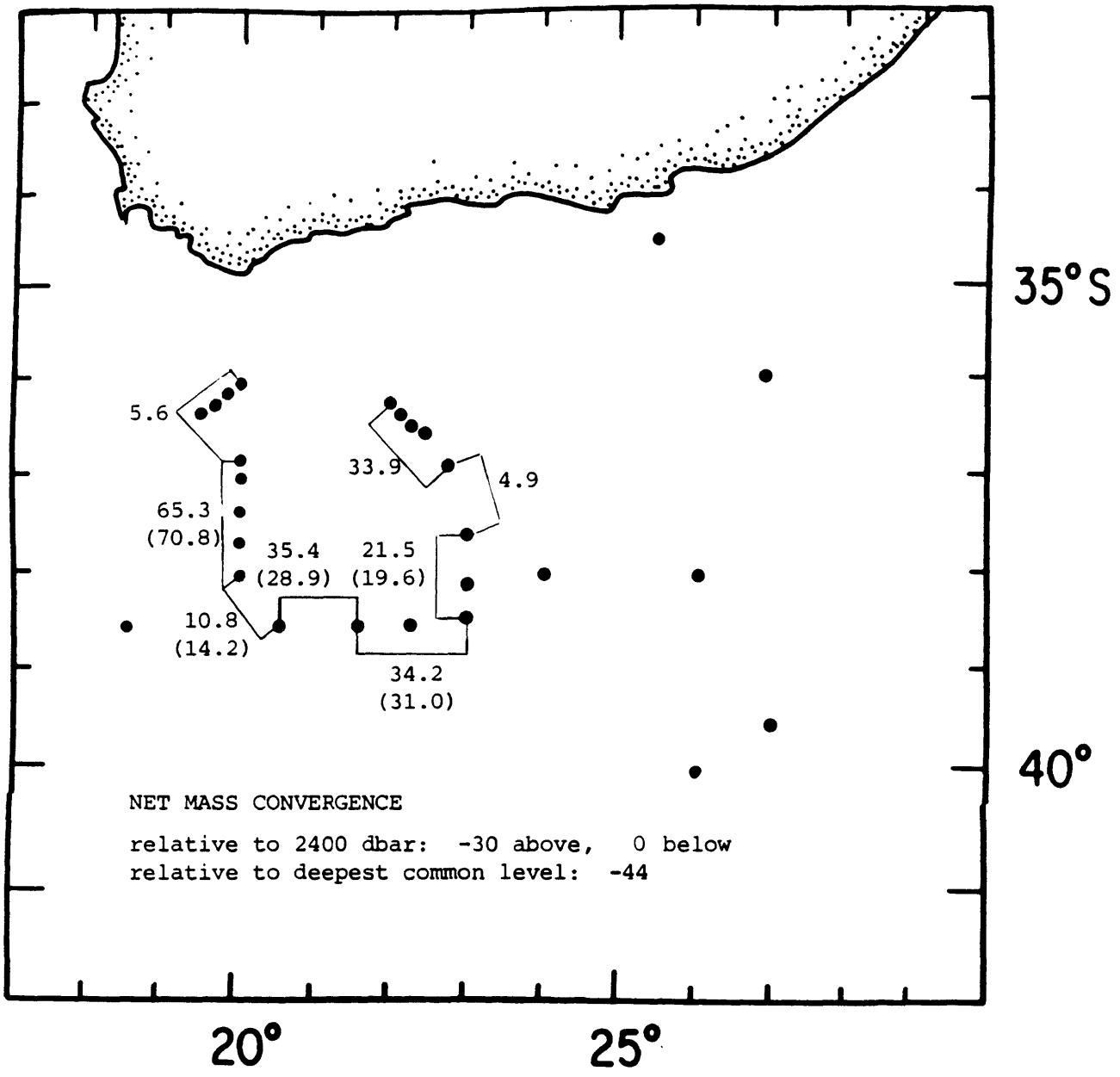

Fig. 3.9 Mass imbalance schematic, Area 2: transports above 2400 dbar reference level (transports above bottom reference level in parentheses; values omitted if same as transport above 2400 dbar.)

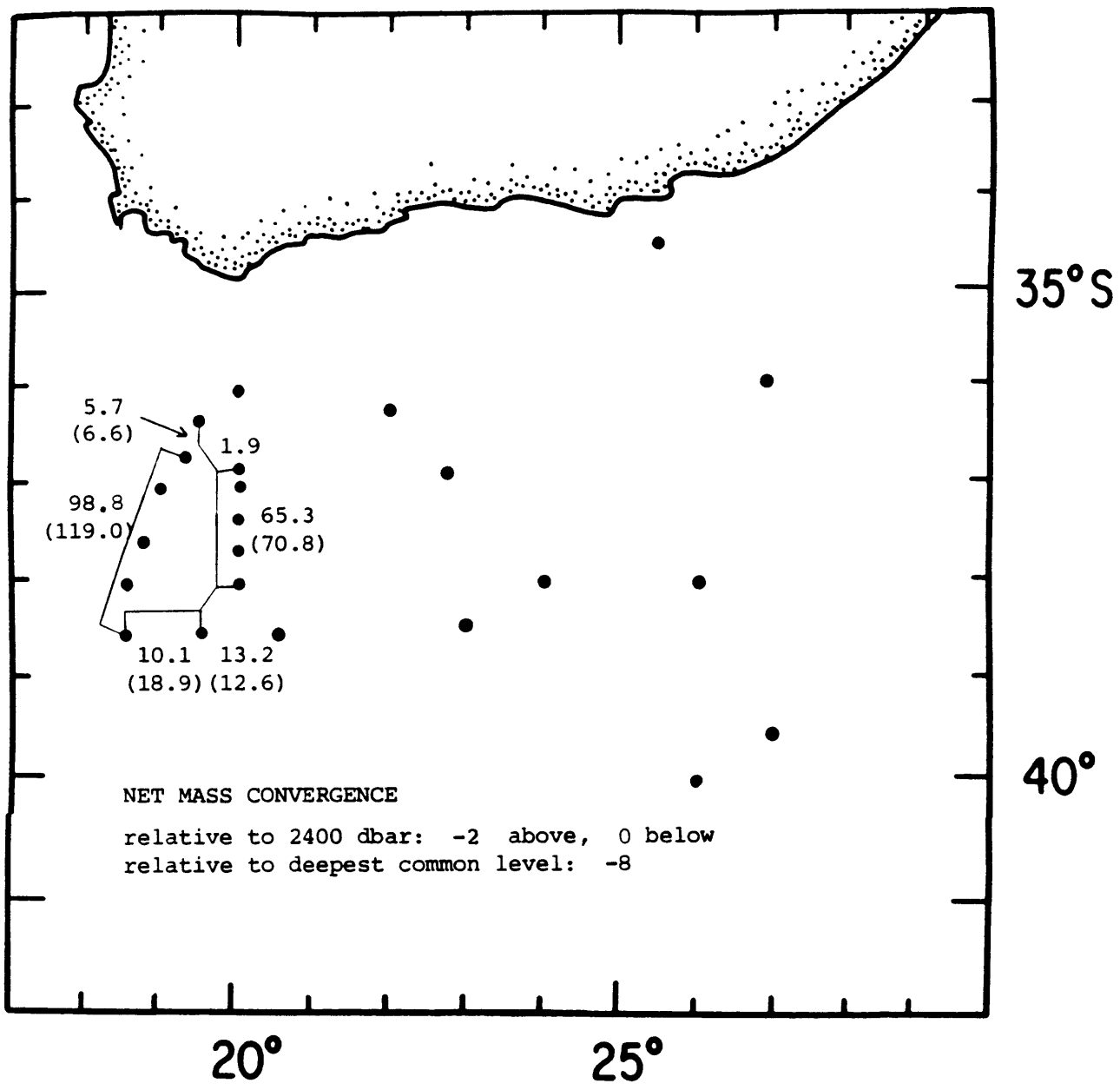

Fig. 3.10 Mass imbalance schematic, Area 3: transports above 2400 dbar reference level (transports above bottom reference level in parentheses; values omitted if same as transport above 2400 dbar.)

Transect A. Transport at transect A relative to the deepest common level is 105 Sv. The transport per unit width function (Fig. 3.6) exhibits several characteristics in agreement with previous theoretical and observational idealizations of Agulhas structure:

- three indicators of the Current's main axis – the transport per unit width maximum, the 15 C/200 m contour location (origin of cross-stream distance on the Figure; see also Chapter 2), and the 2000 m isobath – line up (within 15 km) vertically;
- the cyclonic (cold, right-hand) side is much narrower than the anticyclonic side; and
- transport increases and decreases smoothly across the current.

It is apparent that the transect completely crosses the Current, but that station spacing does not fully resolve the transport per unit width maximum, which may thus be somewhat underestimated.

Transect B and Area 1. Transport at transect B relative to the deepest common level is 34 Sv, only 30% of the value given by linear interpolation of alongstream adjacent historical and 1985 transport values. Transports at all other 1985 transects are 70 – 110% of the historical values. There is *no* deep flow beneath 2500 m at transect B, unlike all other deep Agulhas transects west of 28°E, both historical and in the 1985 survey. The current transport at transect B has been displaced up-slope entirely inshore of the 2500 m isobath (Fig. 3.6).

A mass imbalance of only +31 Sv is observed for Area 1 (Fig. 3.7), despite the 71 Sv mismatch between transects A and B for a deepest common reference level. Inflow at transect A contributes +105 Sv. Outflow south of transect A removes −33 Sv in a broad northward extension of the Return Current, between stations 270–267.

Inflow at station pair 267–266 adds +10 Sv. Net outflow across the cold core ring removes −18 Sv (stations 260, 262–266[9], discussed in Ch. 7). Finally, outflow at transect B removes −34 Sv (Fig. 3.8). Imbalances are +22 and +5 Sv above and below a 2400 dbar reference level.

The missed transport inshore of transect A is small and uncertain in sign. transect A ends in 600 m of water on its inshore side. Isopycnal tilts reverse below 200 m between the last two stations (277 – 278), producing a small (0.5 Sv) outflow there. A missed transport of only ±2 Sv is implied by assuming an average velocity of ±10 cm s^{-1}, 20 km between the 600 and 200 m isobaths, and 100 km between the 200 m isobath and the coast.

The true reference and deepest common level (dcl) velocities are, of course, unknown. Nevertheless, we can still ask if a plausible dcl velocity field can effect mass balance in Area 1. It seems reasonable to expect enhanced dcl velocities at transect B where the Current is displaced onshore and transport is reduced compared to the other transects. Transport at transect B increases 1.5 Sv per 1 cm s^{-1} dcl velocity, assuming for the moment that dcl velocity is constant across the transect, where, recall, the maximum bottom depth is 2380 m at station 260. Rather large dcl velocities of 15 cm s^{-1} uniformly across the current would bring the Area 1 mass transport above a 2400 dbar reference level into balance. Alternatively, dcl velocities of, say, 70 cm s^{-1} where the dcl is 200 – 400 m (station pairs 256 – 258), and of 7 cm s^{-1} where the dcl is 400 – 2400 m (remaining station pairs 258 – 260), also bring the transport above the 2400 dbar reference level into balance. Such velocity magnitudes seem plausible in light of recent direct measurements in the Retroflection region (*Luyten*, pers. comm.) that gave velocity means and standard deviations of up to 8 ± 15 cm s^{-1}

[9]Station 261 is not used for transport calculation because it stops 2000 m above the bottom.

at 1500 dbar and 5 ± 10 cm s^{-1} at 4000 dbar, for 2 year records. Mass transport below 2400 dbar can be balanced with smaller adjustments at transect B and at other station pairs in the box. Transport errors and layer-by-layer imbalances are discussed with the inverse model below.

The adjusted Agulhas Current transport at transect B to balance Area 1, then, is about 56 Sv. This translates into a downstream decrease in transport of −16 Sv per 100 km between transects A and B. The revised value at B is 50% of the interpolated historical and 1985 transports. Just 60% of the transport at transect A continues on in the Agulhas proper to B. The rest exits Area 1 in two branches; one branch retroflects back eastward south of transect A, and the other branch flows southward on the eastern side of the cold core ring. These two flow paths short-circuit the main retroflection farther downstream. Such a partial retroflection was also noted by *Harris and van Foreest (1978).*

The observed decrease in transport at transect B occurs in close proximity to the strong cold–core ring observed in the southern approach to the Agulhas Passage, just offshore of the Current at transect B (visible in *e.g.* Fig. 1.7). Eastward flow in the northern side of the ring may be entraining water from the westward-flowing Agulhas. The ring is discussed further in Chapter 7.

Transect C. Transect C, plus either station 249 or 248, gives a transport of 83 – 85 Sv relative to the deepest common level. A plot of transport per unit width at the transect (Fig. 3.6) shows that the current core was fully crossed, but that the transect does not extend all the way to the edges of the current. The transect extends onshore only as far as the 1600 m isobath (station 298).

The missed transport on the inshore and offshore sides can be estimated from the transport per unit width figure (Fig. 3.6). At each edge of the transect, the transport

per unit width function can be extrapolated to zero graphically with a line of slope s over a distance of d kilometers. The estimate of missed transport, M, is given by

$$M = \int_0^d \frac{s\,x}{d}\,dx = \frac{sd^2}{2} \tag{3.1}$$

On the inshore side of transect C, $s = 7.0 \cdot 10^{-3}$ Sv km^{-2}, and $d = 50$ km, so $M = 9$ Sv. This agrees fairly well with the 6 Sv transport between stations 239 - 242 and 298 on the inshore side of C.

On the offshore side, $s = 1.5 \cdot 10^{-2}$ Sv km^{-2}, and $d = 20$ km, so $M = 3$ Sv. The transport at C becomes 95 – 97 Sv with these adjustments.

The transport relative to the deepest common level at transect C with (without) adjustment is 80% (70%) of the linear interpolation of the along-stream adjacent historical values. The downstream adjusted (unadjusted) transport increase between transects B and C is 27 Sv (33 Sv) per 100 km.

Area 2. A mass imbalance of −44 Sv relative to deepest common reference levels (−30 Sv above and 0 Sv below 2400 dbar) is observed for Area 2, the closed area that includes transects B and C (Fig. 3.7 and 3.9). Recall that Area 1 had an imbalance of +31 Sv (+22 Sv and −8 Sv below 2400 dbar), and that a plausible adjustment in transport at transect B was shown to bring mass above 2400 dbar into balance in Area 1. This same adjustment also reduces the imbalance in Area 2 above 2400 dbar to −8 Sv. The transport at transect B was adjusted for the smaller of the Area 1 and Area 2 imbalances, since this gives a more conservative estimate of the adjustment and of the transect B transport.

The unadjusted flow at the perimeter of Area 2 is shown in Fig. 3.9: relative to deepest common levels, the Agulhas at transect B contributes 34 Sv. Eastward flow in

the northwest side of the cold core ring, which is just grazed by the survey, removes 5 Sv. Westward inflow south of the ring contributes 20 Sv, composed of 5 Sv that balances the cold-core ring outflow and 15 Sv of Return Current transport that enters Area 4 from the west and exits into Area 2 (Fig. 3.11 and Sec. 3.5). Weak westward flow removes 6 Sv north of transect C proper (*i.e.*, north of station 298) on the western side of Area 2. The Agulhas at transect C and station 249 removes 85 Sv. The Agulhas Return Current meandering north along the southern side of the box brings 29 Sv into the box between stations 249 and 251, and then removes 31 Sv between stations 251 and 253.

Transect D. Transport at transect D is 119 Sv relative to the deepest common levels. Transport per unit width (Fig. 3.6) shows that transect D extends over the northern edge of the current and across the current core but stops short of the current's southern edge: counterflow is observed north of the current at station pair 242–243 (−80 km on Fig. 3.6), but at the southernmost station pair (246-247), isopycnals still descend to the south (Atl. 3.28). Perhaps not too much transport was missed. At station 247, the 10 C isotherm reaches its maximum depth of the entire survey; and this station happens to fall near the center of the Retroflection loop defined by XBT 15 C/200 m contour (Fig. 1.3). Extrapolating using Fig. 3.6 as before gives parameters for Eq. 3.1 of $s = 3.0 \cdot 10^{-3}$ Sv km^{-2} and $d = 100$ km at the offshore side of transect D, so $M = 15$ Sv there.

Transport relative to the deepest common level at transect D with (without) adjustment is 96% (87%) of *Jacobs and Georgi's* transport at their section taken nearby. The downstream transport increase between transects C and D is 39 Sv per 100 km (23 or 50 Sv per 100 km using an adjusted value at C or D only).

Current transport at transect D lies entirely in deep (>3000 m) water, unlike transport at transects A–C, so the largest difference is observed at D between transport

computed to the deepest common level and transport computed to a 2400 dbar reference level. Transport above a 2400 dbar reference level is 99 Sv (111 Sv with adjustment for transport missed at the offshore edge); transport below the reference level is –7 Sv. Transport above 2400 dbar increases 22 Sv per 100 km (10 or 33 Sv using an adjusted value at C or D only).

Area 3. A mass imbalance of –8 Sv relative to deepest common reference levels (–2 above and 0 Sv below 2400 dbar) is observed for the closed area that includes transects B and C (Area 3 in Fig. 3.7).

The flow at the perimeter of Area 3 is shown in Fig. 3.10. The Agulhas contributes 85 Sv, relative to a deepest common level and summed over transect C, C's southern end and station 248, and C's northern end and station 242. Northward flow along the southern end of the box (stations 247 - 248) adds 19 Sv . The Agulhas at transect D removes 119 Sv. Eastward counterflow north of D adds 6 Sv (stations 242 and 243).

Summary. Evidence from water mass extrema, topographic constraints, and topographic steering suggest a reference level near 2500 dbar in the Retroflection region. Transports computed relative to this and other levels at the Agulhas transects are reported in Table 3.c, with relatively small adjustments as suggested by the transport per unit width function shown in Fig. 3.6.

Nearly matched transport surplus and deficit in the closed areas separated by transect B were used to infer an upward adjustment to the extremely low transport at this transect. Such an adjustment requires bottom velocities that fall within ranges derived from current meter measurements in this area. The imbalances in the three areas remaining after these adjustments are very small compared to the fluxes due to the Agulhas Current and the cold-core ring.

3.5 Agulhas Return Current transport

Transport at historical transects across the Agulhas Return Current (Table 3.d) and at the two 1985 Agulhas Return Current transects (transects E and F in Table 3.e and Fig. 11) is considered in conjunction with mass convergence in the fourth closed box of the CTD/O_2 survey (Fig. 3.07 and 3.12). A Return Current transect from *Gordon* et. al's 1983 Retroflection survey is included here for comparison (also shown in Fig. 11). Their transect is composed of three stations in the Return Current and six adjacent stations, all taken to the bottom (stations 50–58 in Figs. 3.13 and 3.14, which are a reproductions of *Gordon* et al.'s Figs. 1 and 2).

The Return Current crossed directly over the heart of the Agulhas Plateau during the 1985 survey, so transports relative to 2400 dbar and to deepest common levels are nearly equal. The 2500 – 3600 dbar depths beneath Transects E and F can be seen in Fig. 3.11. The Current followed a very different path, deflecting northwest around the Plateau following its flank, during both previous surveys that crossed the Return Current near the Plateau, *(Harris and van Foreest, 1978,* and *Gordon* et al., *1987).* The 15 C temperature /200 m depth contour in both of the 1985 transects lies above the 2700 dbar isobath, while in the 1983 transect it lies above the 4200 m isobath. The depth difference corresponds to an approximately 300 km horizontal displacement of the Return Current up onto the Agulhas Plateau; the flank of the Plateau has fairly constant slope.

Return Current transport is not as unambiguously defined as Agulhas Current transport. There is no geostrophic shear reversal and no coastline to define the southern limit of the Return Current transport, since the eastward flow of the Circumpolar Ocean lies at the southern side of the eastward-flowing Return Current. Return Current

Table 3.d – Historical Agulhas Return Current transports

Source	Location	Transports (Sv) above reference level (dbar) 1000 db	1500 db	2400 db	Bottom
Gordon et al., 1986	separated southward flow, 21°E		64		
Jacobs and Georgi, 1977	south of Agulhas Bank, 21°E				129[a]
Harris and van Foreest, 1978	20 - 28°E, north flank Plateau	35[b]			
Gordon et al., 1986	24° E, north flank Plateau		54	78[c]	98[c]

[a]Estimated from their Fig. 15a.

[b]Estimated from their Fig. 3; transports are computed relative to 1100 dbar (or the '27.2 σ_t level'?), not 1000 dbar.

[c]My calculation using Gordon's data.

Table 3.e – Agulhas Return Current transports, Luyten & Toole survey, Feb. - Mar. 1985, R.V. *Thomas Washington,* Cruise 3

		Transports above/below (Sv) reference level (dbar)							
Section	stations	1000 db		1500 db		2400 db		Bottom
E	284-288	22	-21	34	-6	48	0	50
E^	283-283 extended[a]					54	0	56
F	283-279	30	-35	50	-10	73	0	75
F^	F extended[a]					75		77
F^'	F^ + 267-271[b]					94	0	96

[a]Extended to 110 km (southern boundary of *Gordon* et al. 1983 transect) south of the 15 C/200 m location, using transport per unit width value at last station pair. See text.

[b]Additional stations cross net eastward flow between Transect F and Transect A.

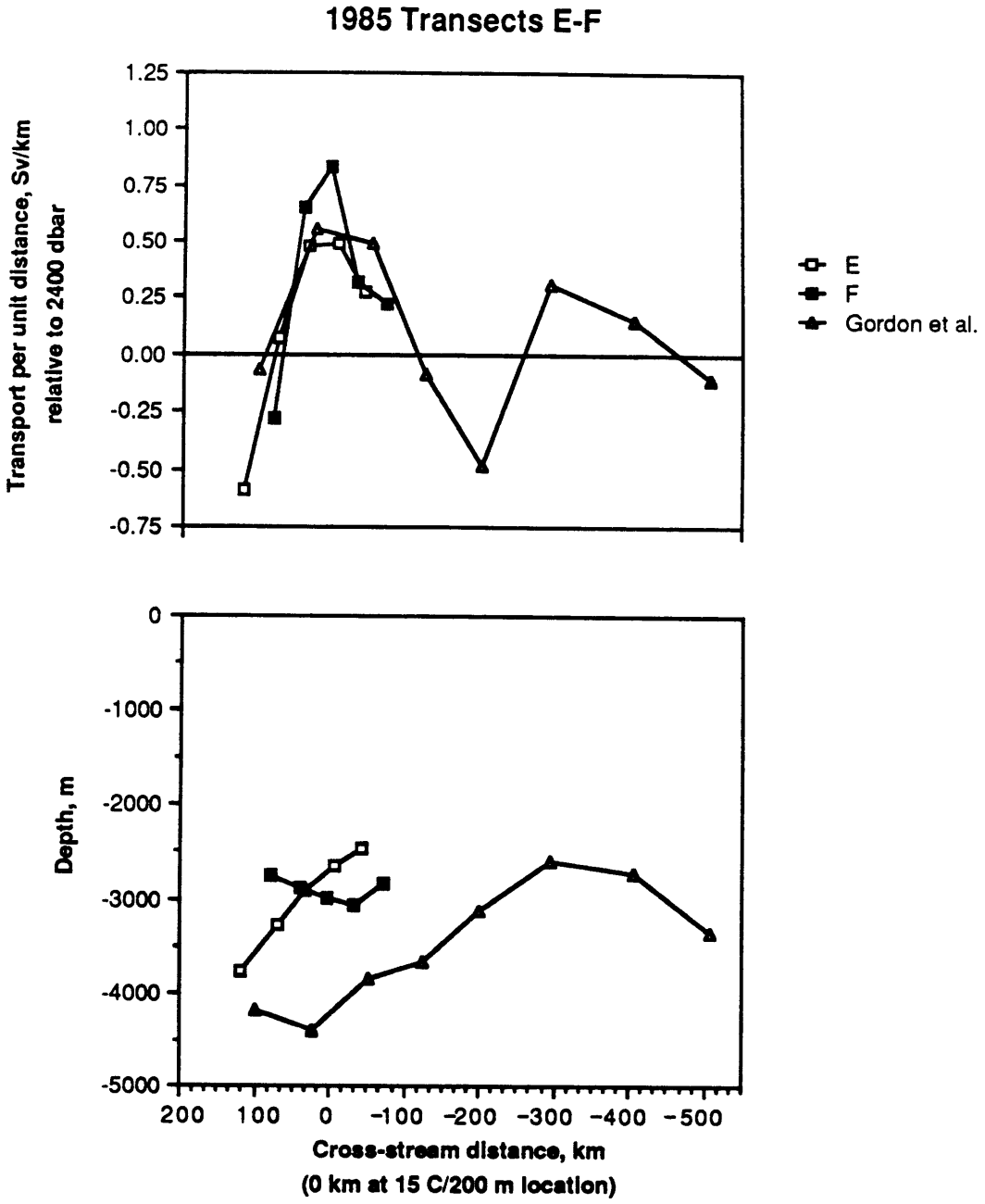

Fig. 3.11 – Agulhas Return Current: (a) transport per unit cross-stream distance, 1985 transects E-F, looking downstream. Transport is computed relative to 2400 dbar or the deepest common level of station pairs, whichever is deeper. (b) depth beneath Current. For both plots, origin of cross-stream distance is at transects' 15 C/200 m location.

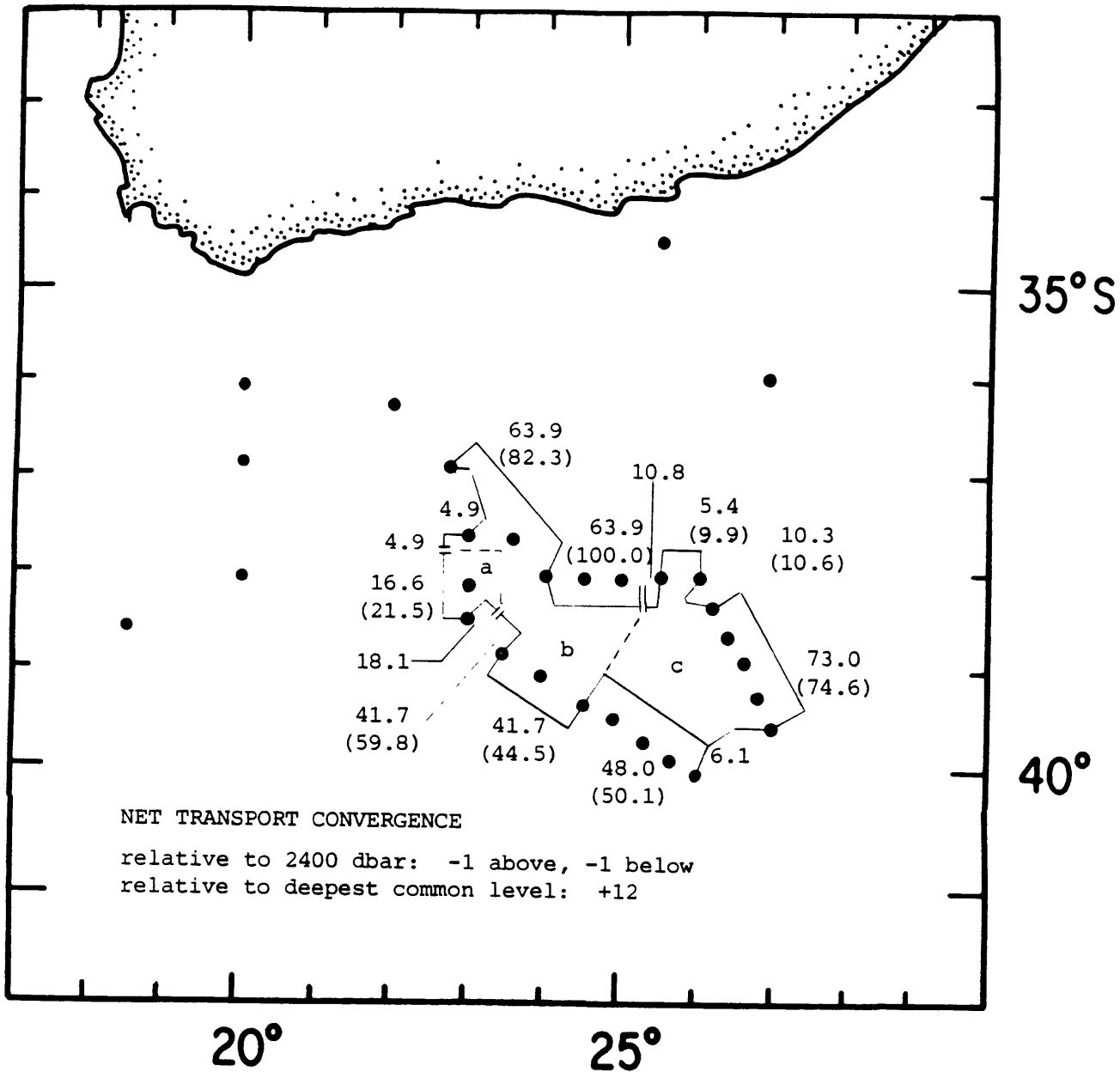

Fig. 3.12 – Mass imbalance schematic, Area 4: transports above 2400 dbar reference level (transports above bottom reference level in parentheses; values omitted if same as transport above 2400 dbar.) Two transport numbers relative to 2400 dbar are shown for split station pairs (see text).

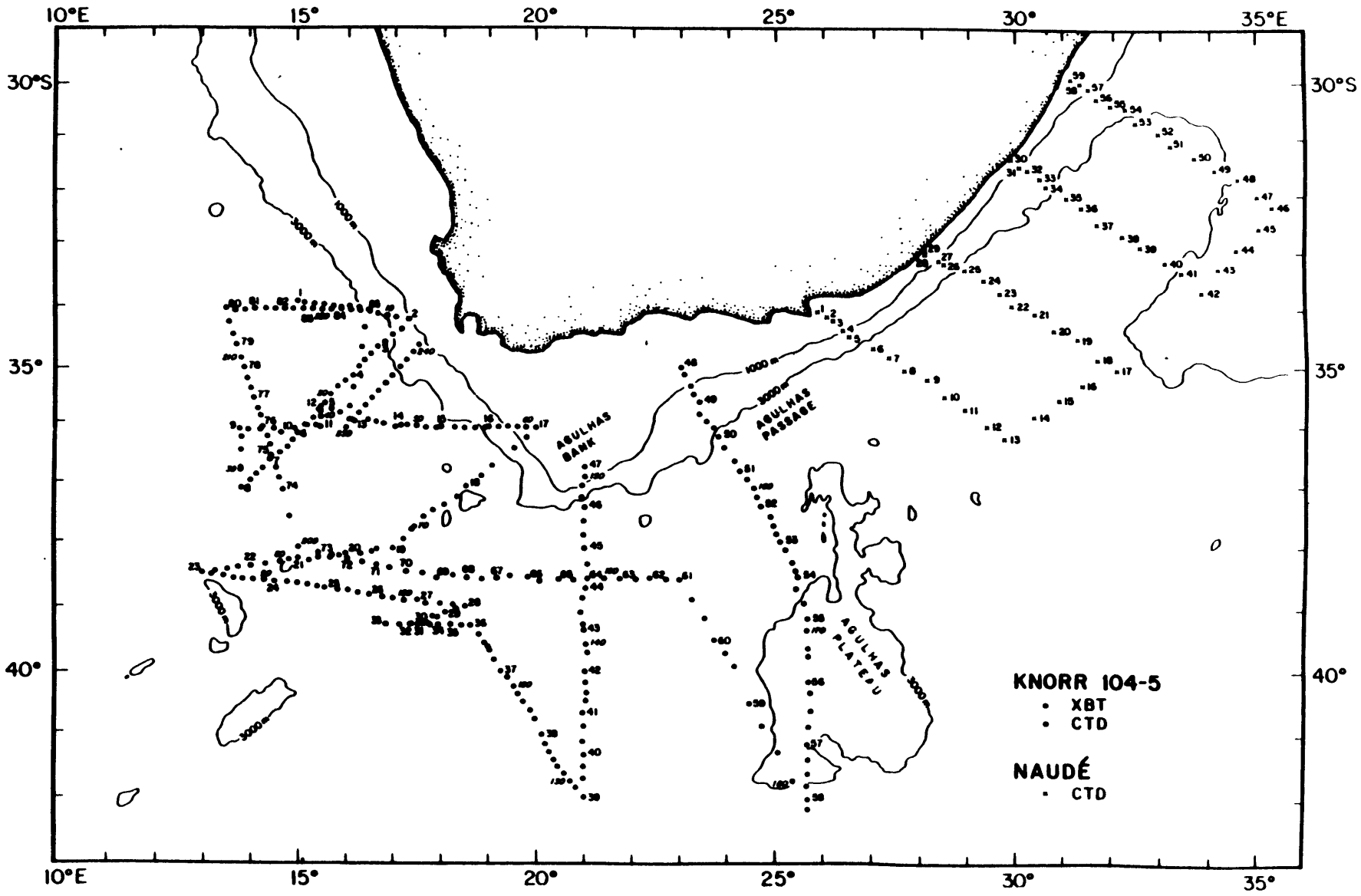

Fig. 3.13 – CTD station locations and topography, R.V. *Knorr*, November-December, 1983, and R.V. *Mering Naude*, October 1983. Reproduction of *Gordon* et al., *1987*, Fig. 1.

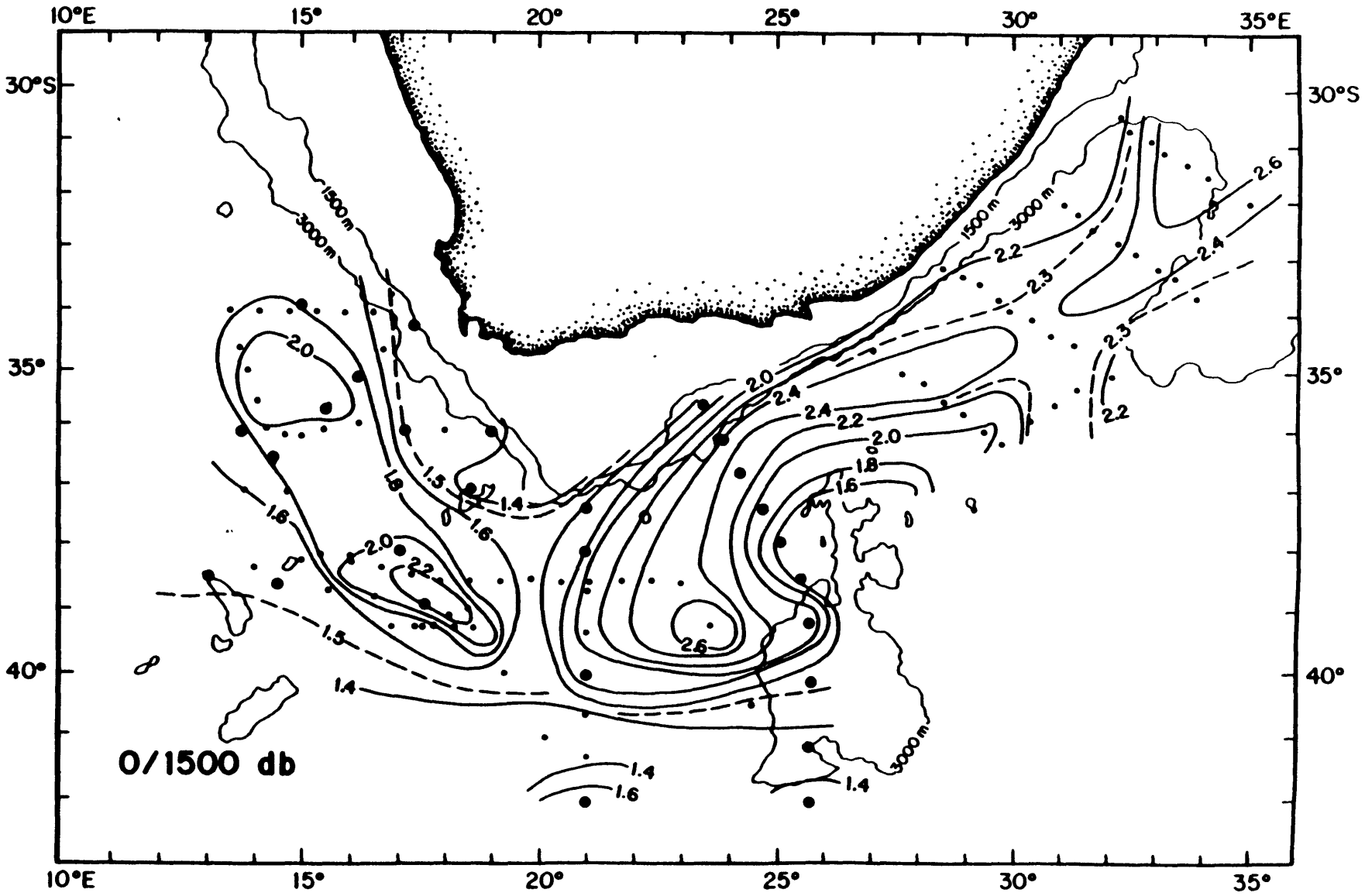

Fig. 3.14 – Dynamic height anomaly of the sea surface relative to 1500 dbar computed from CTD stations taken from R.V. *Knorr*, November-December 1983, and from R.V. *Mering Naude*, October 1983. R.V. *Knorr* stations extending to near the bottom are marked with large circles (my addition). Reproduction of *Gordon* et al., *1987*, Fig. 2.

transport continues to accumulate slowly as stations are added to the south – unless and until a transport reversal associated with an anticyclonic feature is encountered.

Transport per unit width at the 1985 transects E and F and at the 1983 transect reaches a maximum value between 10 and 30 km on the warm, northern, side of the 15 temperature/200 m depth contour (Fig. 3.11). The sharp reversal from positive to negative transport 50 km north of the 15 C/200 m contour signals the northern limit of Return Current transport. The warm, anticyclonic, northern side of the Agulhas Return Current is narrower than the cold side, the reverse of the situation in the Agulhas Current.

1983 Return Current transect. Transport at the 1983 Return Current transect is 78 Sv (98 Sv) relative to 2400 dbar (deepest common level). The transect grazed the Retroflection loop south of the Return Current: note the nearly-matched positive and negative transport lobes between −100 and −400 km in Fig. 3.11. These correspond to the dynamic height reversal seen in *Gordon* et al.'s map, reproduced here as Fig. 3.14.

Return Current transport at the 1983 transect extends to −110 km. The two 1985 transects end at −61 and −92 km, before encountering westward counterflow. The 1985 transports will be extrapolated to −110 km to facilitate comparison with the 1983 transport value. Transport per unit width is about 0.25 Sv per km at the southern side of all three transects, so defining the southern limit of the Return Current differently changes the transport by *e.g.* 13 Sv for a 50 km southward shift.

Transect E. Transport at Transect E (stations 284–288) is 48 Sv (50 Sv) relative to 2400 dbar (deepest common levels). The last station south of the transect falls at −61 km, south of the 15 C/200 m location. After using Eq. 3.1 between −61 and −110 km (the end of the 1983 transect), the transport becomes 54 Sv (56 Sv).

Transect F. Transport at Transect F (stations 283–279) is 73 Sv (75 Sv) relative to 2400 dbar (deepest common levels). The last station of the transect falls

92 km south of the 15 C/200 m location. Again, after using Eq. 3.1 between −92 and −110 km, the transport becomes 75 Sv (77 Sv).

There is additional net eastward flow of 19 Sv (23 Sv) relative to 2400 dbar (deepest common level) between Transect F and Transect A to the north, *i.e.* between stations 267 and 271.

Area 4. A mass imbalance of +12 Sv relative to deepest common reference levels (−1 Sv above and +1 Sv below 2400 dbar) is observed for the closed area that includes Transects E and F (Area 4 in Fig. 3.7).

The flow at the perimeter of Area 4 is shown in Fig. 3.11. The cold-core ring cuts across the middle of Area 3, isolating two subregions of Return Current transport from each other. The area was divided up into three distinct subregions, labelled *a*, *b*, and *c*, in order to clarify the situation. A recirculation of Return Current transport entering from the west and exiting to the east into Area 2 occupies subregion *a*. The cold-core ring occupies subregion *b*. The Return Current proper transits subregion *c*. Transports at three station pairs have each been split between two subregions so that each subregion's transport nearly balances – the details of the splitting are not, of course, unique. The stations are too far apart to resolve the circulation.

The adjacent stations 253 and 290 on the western edge of Area 4, at the boundary of subregions *a* and *b*, were taken 13 days apart, the longest elapsed time for adjacent stations in the entire survey. Propagation of the cold-core ring during the time elapsed between the two stations evidently caused a drop in the dynamic height (increase in mean density) at the location of the southern station of the pair (station 290), judging from the large transport per unit width (1.10 Sv km^{-1} relative to 2400 dbar; the maximum for the entire survey is 1.17 Sv km^{-1} at Transect A). Non-synoptic data is sometimes blamed for anomalously large mass imbalances in closed boxes *(Wunsch, 1978)*. The non-synopticity of the data in this case has not noticeably increased the

mass imbalance of Area 4, which is comparable to the mass imbalances in the other areas.

Agulhas vs. Agulhas Return Current transports. Keeping in mind that the southern boundary of the Return Current is not sharply defined, we can ask how the Return Current transports compare with the corresponding Agulhas Current transports. The fully adjusted values relative to 2400 dbar are summarized in Table 3.f.

This is exactly the same as asking if transport relative to 2400 dbar, plus transport due to the bottom velocity adjustment at Transect B, vanishes when integrated between the coast of southern Africa and 100 km south of the 15 C/200 m contour in the Return Current.

The agreement is quite good at all the transects. This suggests that 100 km south of the 15 C/200 m contour in the Return Current is (fortuitously?) not a bad choice for its southern boundary, assuming that the Agulhas and Agulhas Return Currents must roughly balance – except for 5 to 15 Sv that may leak into the S. Atlantic and ultimately return to the S. Indian via straits in the Indonesian archipelago (suggested by *Gordon, 1985, 1986*).

This comparison is, in effect, an independent check on the bottom velocity adjustment at Transect B: the Agulhas Current/Return Current transect pair involving Transect B looks about as well matched as the other two pairs, which suggests that the transport adjustment at Transect B is appropriate.

Summary. The Return Current as it appears in the 1983 and 1985 transects has a transport of 54 to 94 Sv (56 to 98 Sv) relative to 2400 dbar (deepest common levels), having integrated the Return Current eastward transport south to 110 km south of the 15 C temperature/200 m depth location. A small extrapolation was necessary on both 1985 transects. The Return Current transports defined in this way correlate well with the transport at corresponding Agulhas Current transects. Since the adjusted

Table 3.f – Agulhas and Agulhas Return Current transports at corresponding transects

Agulhas Current transect	Agulhas Return Current transect	Agulhas transport (Sv)[a]	Return Current transport (Sv)[a]
1983	1983	83	78
A	F	91	94
B	E	56	54

[a]Fully adjusted transport values relative to 2400 dbar are shown.

Agulhas Current transport at Transect B falls in line with the other values, this increases confidence in the adjustment procedure.

Mass transport imbalances in the closed area (Area 4) crossed by the Return Current are only −1 Sv above and −1 Sv below 2400 dbar, despite non-synoptic data (13 days between two adjacent stations) and the presence of a strong cold-core ring that was evidently propagating across the edge of the box.

3.6 Conclusions

The overall 1985 Retroflection transport pattern is shown at the end of the previous chapter (Fig. 2.12).

The Agulhas transport is significantly larger and more variable alongstream than the returning wind- and thermohaline-forced interior flow. The Agulhas transport is between about 55 and 135 Sv at the 1985 transects' latitude range, while the returning interior flow accounts for no more than 55 ± 8 Sv. Apparently as little as 0.4 of the Agulhas transport is directly forced.

The alongstream variation in Agulhas transport, upstream of the current's separation from the African continental slope, has values from about -20 to +30 Sv per 100 km. Returning interior transport computed from wind stress curl and an estimate of thermohaline circulation, varies alongstream by only +2 to +3 Sv per 100 km at Retroflection latitudes (31 - 37°S). The maximum alongstream increase is +9 Sv at 25°S much further north.

Both observed transport and observed alongstream transport variation increase with reference level. Transport and transport variation can be reduced to levels expected from the wind- and thermohaline forcing by moving the reference level upward to ≤1500 dbar. However, this reference level is above the deep oxygen minimum of

South Indian origin and would result in this water mass flowing towards its source in the South Indian Ocean.

Agulhas transport decreases dramatically between transects A and B, from 90 Sv at transect A to about 55 Sv at transect B. This decrease is associated with a 35 Sv partial retroflection, located just upstream of a large cold ring found on the northwestern flank of the Agulhas Plateau. The Agulhas at transect B is found entirely inshore of the 2400 m isobath.

The 56 Sv transport value at transect B includes 34 Sv from geostrophic shear, plus 22 Sv corresponding to 70 cm s^{-1} bottom velocities at depths of 200 - 400 m, and 7 cm s^{-1} at depths of 400 - 2400 m. Deep bottom velocities of the latter magnitude are comparable to directly measured velocities at similar depths in the Retroflection.

The Agulhas Current transport consistently matches Return Current transport immediately to the south, to within ±5 Sv for three pairs of Agulhas/Return Current transects, when transport is integrated from the African coast to 110 km south of the 15 C temperature/200 m depth contour in the Return Current. Two of the transect pairs (transects A/F and B/E) were taken from the 1985 survey, and the third from the 1983 survey. The B/E pair balances about as well as the other two pairs. This provides independent confirmation that the bottom-velocity/transport adjustment at transect B is reasonable.

Chapter 4: Tracer fields in the Agulhas and Agulhas Return Currents

4.1 Introduction

Synoptic tracer gradients in a streamwise coordinate frame in the Agulhas and Agulhas Return Currents are discussed in this chapter. Four 1985 transects across the Agulhas and two 1985 transects across the Return Current are used for this purpose (the transect and station locations are shown in Fig. 3.1). The 1983 Agulhas transect *(Gordon* et al., *1987)* is also included. The tracers discussed here are potential temperature, salt, oxygen, and planetary potential vorticity.

The 1985 transects provide the first high vertical and horizontal resolution synoptic snapshot of cross-stream and along-stream tracer gradients in the Agulhas and Agulhas Return Currents. Previous presentations of Retroflection region tracer data were restricted to consideration of regional-scale or coarse features of the tracer field, as seen in *(i)* a single deep Agulhas/Return Current transect *(Jacobs and Georgi, 1977,* and *Gordon* et al., *1987), (ii)* several transects of coarsely spaced Nansen casts to intermediate depth *(Harris and van Foreest, 1978),* and *(iii)* an ensemble of non-synoptic hydrographic stations *(Wyrtki, 1971).*

Tracer variation over small along-stream scales in the Retroflection has important implications. Fluxes of heat, salt, and potential vorticity across the Retroflection can be incorrectly estimated or interpreted, if tracer characteristics at a transect across the current are dominated by local processes but are treated as if they represented characteristics over some large distance along-stream. These fluxes can play an significant role in gyre and global scale dynamic and thermodynamic balances *(Gordon, 1985, 1986).*

The biggest surprise in the new set of transects is, in fact, how rapidly the current can change in the along-stream direction. The simple thin jet/boundary layer

scaling $\delta L << L$, where δL is the cross-stream scale and L the downstream scale, might lead one to expect that tracers and transport would vary more slowly in the along-stream than in the cross-stream direction.

But the thin jet/boundary layer scaling breaks down in the Retroflection, as can be seen in the 1985 synoptic transport (the overall transport pattern is shown in Fig. 2.12). Transport, as discussed in the previous chapter, can increase by over one-half its value (from 55 Sv to 90 Sv between 1985 transects B and C), within about two and a half current widths (current width ~100 km). Evidently, each transect accurately characterizes the current over an along-stream distance that is not much larger than the current width – and, it must be added, for only a limited time, judging from the time-dependence of surface temperature in satellite infrared images *(Lutjeharms and van Ballegooyen, 1988)*, sea surface height in satellite altimeter measurements *(Cheney* et al., *1983)*, and velocity directly measured with current meters (*Luyten,* pers. comm.).

Along-stream tracer field variations at and above intermediate levels (≤ 2000 dbar) are well-correlated with the along-stream transport changes due to the partial retroflection and the intense, partially isolated recirculation of the Retroflection itself. Many features of the intermediate to upper level tracer fields are, in fact, hardly understandable without reference to the transport field.[1]

The new data provides fresh insights into circulation ideas developed in previous investigations of this part of the ocean. As we shall see, the Subantarctic Mode Water (SAMW) potential vorticity minimum varies in core density across the current consistent with *McCartney's (1982)* ideas about SAMW formation and circulation.

[1]Using the transport field to understand aspects of the tracer field is to be distinguished from classical core layer analysis, in which the tracer extrema patterns are used to choose the reference level for the large-scale geostrophic transport; a deep (~2400 dbar) Retroflection reference level was inferred in the previous chapter in this way.

S. Atlantic/Circumpolar thermocline water swept into the Retroflection in 1985 as it was in 1983 *(Gordon* et al., *1987)*, can be closely linked, as was alluded to above, to the high-resolution 1985 synoptic transport field. The high-salinity influence found at intermediate depths of the Red Sea Water (RSW), defined by a salinity maximum in the Indian Ocean, can be traced even further downstream in the Agulhas than in previous observations *(Wyrtki, 1971, Gordon* et al. and *Gründlingh, 1985)*, beyond its separation from the coast. The supply route to the Retroflection of the highest salinities in the North Atlantic Deep Water (NADW) deep maximum, considered by *Wyrtki (1971), Jacobs and Georgi (1977),* and *Reid (pers. comm.)*, is found to be tightly pressed up against the African continental slope.

The new high horizontal resolution transects show a sharp water mass boundary on isopycnal surfaces in the Agulhas near-surface (<300 m) layer near the current core. Tropical Thermocline Water is found on the cyclonic, inshore side of Agulhas, with low oxygen, and salinity and stratification decreasing monotonically with depth. Characteristics changing rather sharply across the core to those of Subtropical Surface Water, defined by a slight subsurface salinity maximum, and Subtropical Mode Water, defined by a potential vorticity minimum and associated oxygen maximum. This tracer boundary, and a similar but less sharp boundary at intermediate levels marking the offshore extent of Red Sea Water influence, is used to generate a simple estimate of steady east-west upper (<2000 m)level heat flux across the Retroflection, by balancing the TTW flow with return flow on the south side of the Return Current.

4.2 Overview of tracer extrema

Tracer extrema, like the NADW deep salinity maximum and others already mentioned, are of particular interest. Each can, in principle, be traced back through the

gyre and global circulation to its source region, usually an area of enhanced air-sea interaction at the sea surface or in a marginal sea.

A water mass name is customarily given to the layer around a tracer extremum, *e.g.* the name 'North Atlantic Deep Water' (NADW) to the layer around the deep salinity maximum. A few water masses label other tracer configuration types: 'Central Water' is the name given to the parts of the various subtropical gyres' regional potential temperature/salinity curves that are nearly single-valued and, as was noticed long after the original naming, have constant density ratio *(Schmitt, 1981)*.

Each Retroflection region tracer extremum discussed here has been used previously in Indian Ocean/Retroflection circulation studies (salt and oxygen extrema, *Wyrtki, 1971*, and *Warren, 1981;* South Indian Subantarctic Mode Water, *McCartney, 1982;* Benguela oxygen minimum, *Chapman and Shannon, 1985;* local Subtropical Mode Water plus all other previously used extrema, *Gordon* et al., *1987)*. The tracer vertical extrema are, from top to bottom:

- Shallow (50 – 300 dbar):
  Salinity maximum core of the S. Indian Subtropical Surface Water (SSW).
  Potential vorticity minimum core of the local Subtropical Mode Water (STMW).
  Oxygen maximum associated with the STMW.
  Oxygen minimum associated with the S. Indian Tropical Thermocline Water (TTW).
  Oxygen minimum associated with Benguela shelf bottom water (observed only on the 1985 Cape Town Eddy transect; see Ch. 8).

- Thermocline (200 – 800 dbar):
  Potential vorticity minimum core of the S. Indian Subantarctic Mode Water (SAMW).
  Oxygen maximum associated with the SAMW.

- Intermediate (600 – 1800 dbar):
  Salinity minimum core of the Antarctic Intermediate Water (AAIW).
  'Deep' oxygen minimum emanating from the northern Indian Ocean.

- Deep (2000 dbar – bottom):
  Oxygen minimum core of the Upper Circumpolar Deep Water (UCDW).
  Salinity maximum core of the North Atlantic Deep Water (NADW).
  Oxygen maximum associated with the NADW.
  Oxygen minimum core of the Lower Circumpolar Deep Water (LCDW).

The Agulhas warm core, the only purely horizontal extremum in the region, should perhaps be mentioned with this list. It is discussed in Ch. 2.

The Central Water found in the Retroflection is the South Indian Central Water (SICW) which occupies the entire South Indian main thermocline and includes the SAMW.

The oxygen minima of the Upper and Lower CDW are just barely observable in the Retroflection and is mentioned here only for completeness. Fresher, higher-oxygen Antarctic Bottom water lies between the Lower Circumpolar Deep Water and the bottom.

Water-mass names for all the extrema are shown on contoured sections across the Agulhas in Fig. 4.1 - 4.3. Water-mass names for the salt and oxygen cores are shown on potential temperature/salinity and potential temperature/oxygen diagrams in Figs. 7.7 and 7.8 in the cold ring chapter, Ch. 7.

Mode Waters are the products of wintertime deep convection at the sea surface, thus their anomalously thick isopycnals (weak stratification) and the oxygen maxima associated with them. Oxygen minima are associated with enhanced biological oxygen utilization and/or relatively poorly ventilated layers. Salinity minima emanate from zones of excess precipitation over evaporation at the sea surface (*e.g.* the Antarctic

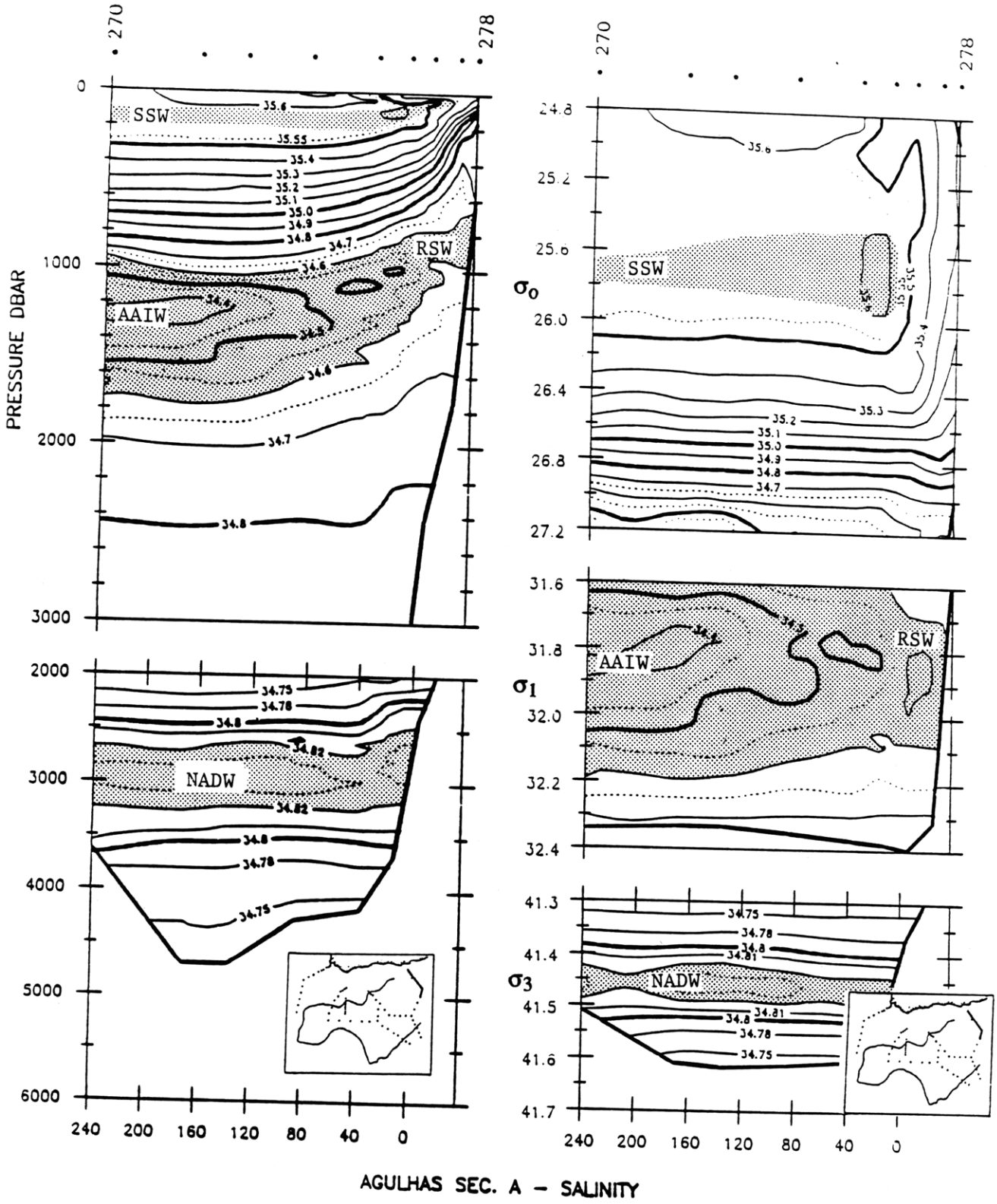

Fig. 4.1 – Salinity sections across the Agulhas showing names of salinity extremum layers: Subtropical Surface Water (SSW) maximum, Antarctic Intermediate Water (AAIW) minimum, and North Atlantic Deep Water (NADW) maximum.

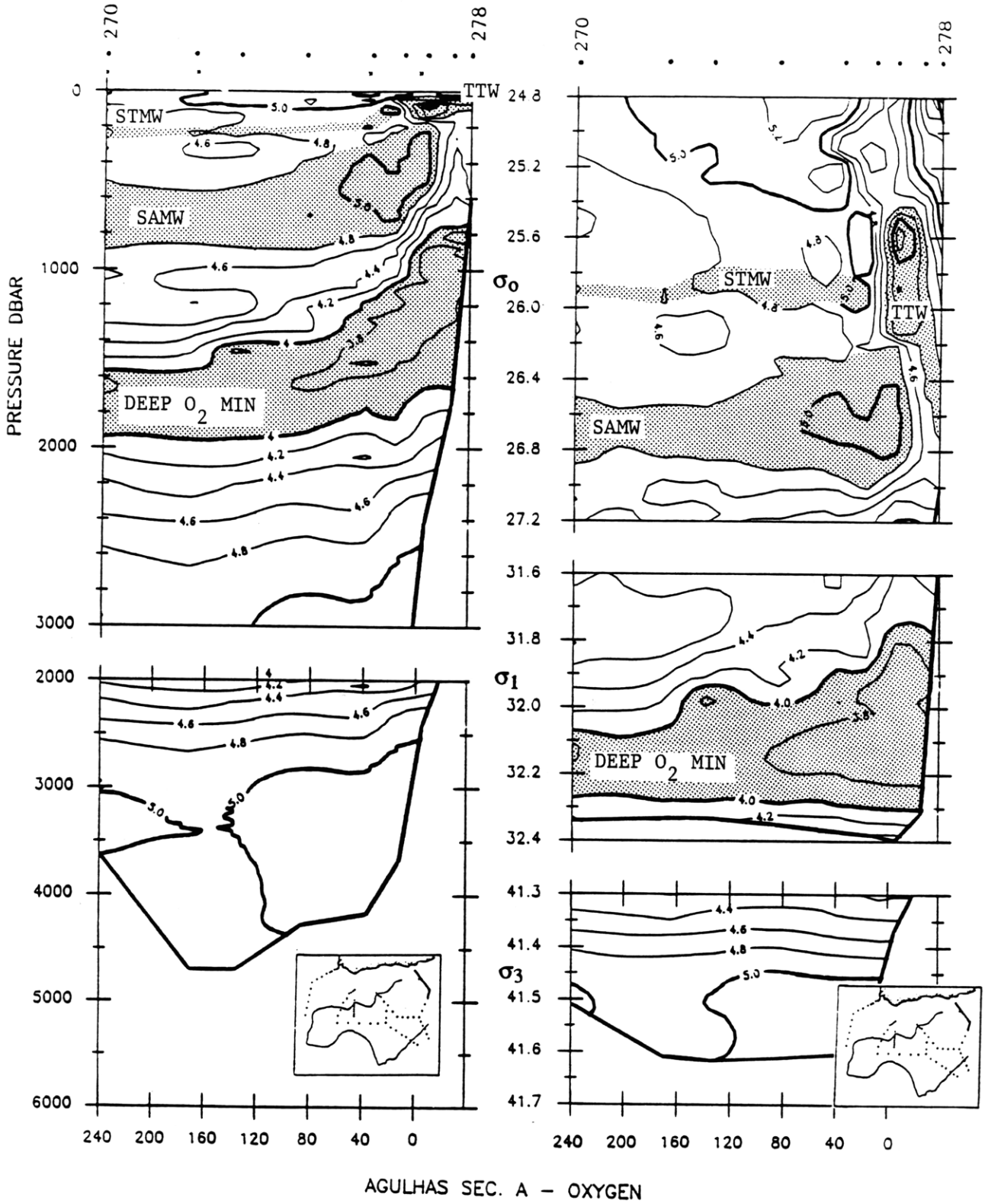

Fig. 4.2 – Oxygen sections across the Agulhas showing names of oxygen extremum layers: Tropical Thermocline Water (TTW) minimum, oxygen maximum associated with the Subtropical Mode Water (STMW), oxygen maximum associated with the Subantarctic Mode Water (SAMW), deep oxygen minimum of northern Indian Ocean origin. Upper and Lower Circumpolar Deep Water minima are very faint or absent in the Retroflection.

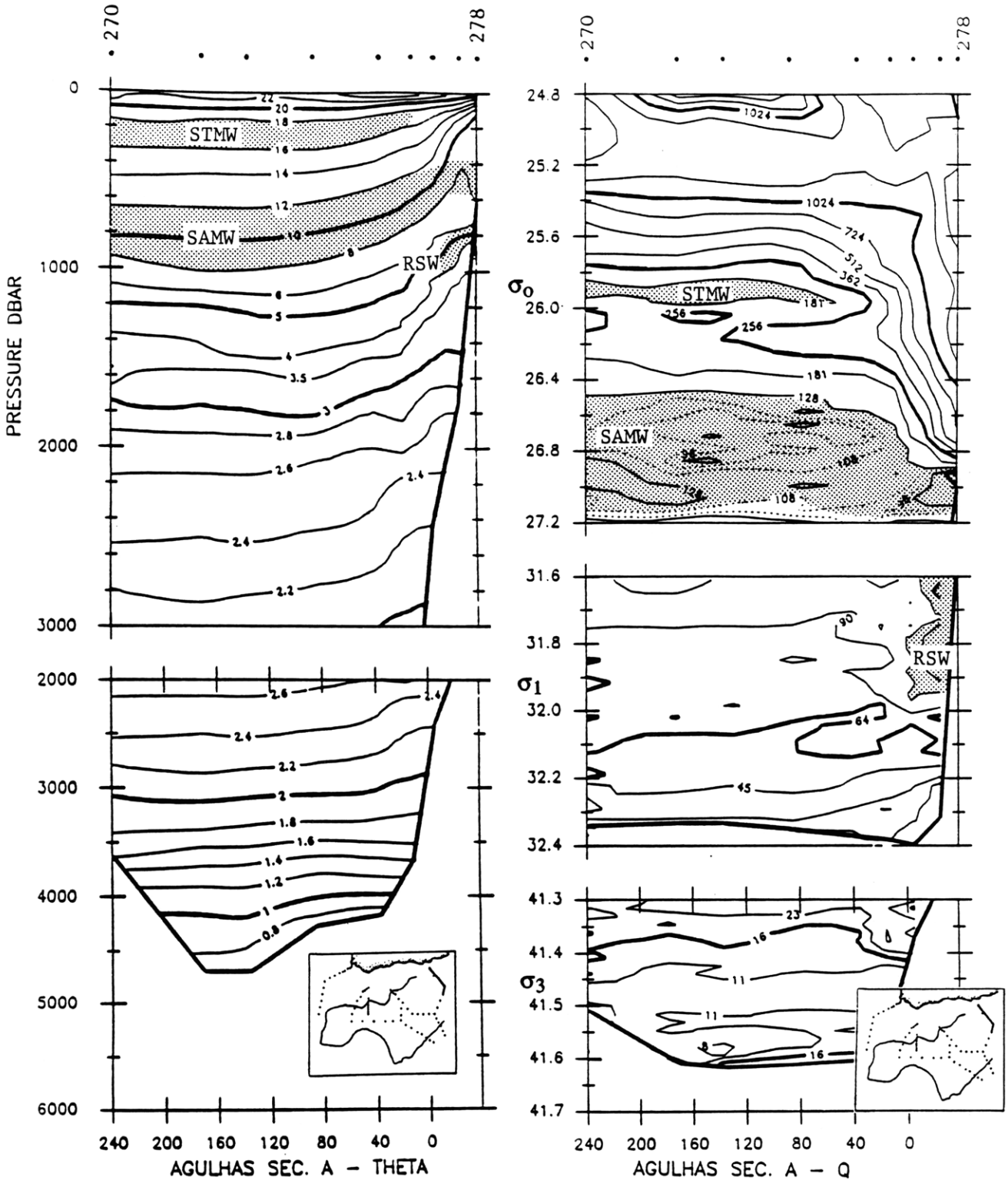

Fig. 4.3 – Potential temperature and planetary potential vorticity ($\bar{q}$) sections across the Agulhas showing names of $\bar{q}$ extremum layers: Subtropical Mode Water (STMW) minimum, Subantarctic Mode Water (SAMW) minimum.

Intermediate Water formation zone in the Subantarctic, *McCartney, 1977*), and, conversely, salinity maxima from zones of excess evaporation over precipitation, often marginal seas (*e.g.* the North Atlantic Deep Water formation zone in the Norwegian/Greenland Seas) or gyre interiors (*e.g.* the Subtropical Surface Water formation zone at the surface of the South Indian subtropical gyre). Extrema exist only relative to adjacent layers with less extreme characteristics, of course, and thus can be obscured if the characteristics of adjacent layers change.

Scatter plots of tracer values at extrema as a function of potential density (Fig. 4.4), extrema lists (Table 4.a), and contoured tracer sections (Atlas, after the last thesis chapter)[2] are used in the discussions to follow. These presentations are used rather than contoured tracer maps because *(i)* extrema are not found on surfaces of any constant quantity (pressure, potential density, *etc.*), and *(ii)* the horizontal correlation of the extrema values is often on the order of the station spacing, in part because they are gradient quantities susceptible to features of arbitrarily small vertical and, by implication, horizontal, scales. Vertical smoothing produces reasonable-looking contoured maps, but choosing the smoothing scale is problematic since extrema thickness vary considerably with depth and from station to station. Traditional interpretations of extrema, seen through the filter of Nansen cast vertical resolution (~100 m in the thermocline, more in the deep ocean), saw these extrema as rather broad features steadily spreading away from their formation zones. The analysis used here acknowledges that small blobs of anomalous water are a common feature of the ocean, and presumes that the most anomalous have advected most rapidly away from their

[2]Since the contoured sections and the extrema tabulation were prepared using slightly different subsampling and smoothing schemes, weak extrema may appear in one presentation and not the other, This occurs most often in the oxygen field, because of its relatively weak, noisy signal in this region, and in the potential vorticity field, because it is a gradient quantity sensitive to filtering details. The UCDW and LCDW oxygen minima are not tabulated.

source region. This analysis represents only a best guess as to how oceanic tracer dispersion, (a subject of active research) really works, especially in highly energetic regions.

Table 4.a also lists mean values and standard deviations for each extremum and for the extremum's pressure, potential density, *etc.*, in addition to the the individual extremum observations. These values were extracted from the CTD/O_2 data using standard criteria, followed in ambiguous cases by subjective editing.

Tracer fields in the cold ring and the 1985 Cape Town Eddy are discussed in Chs. 7 and 8 respectively.

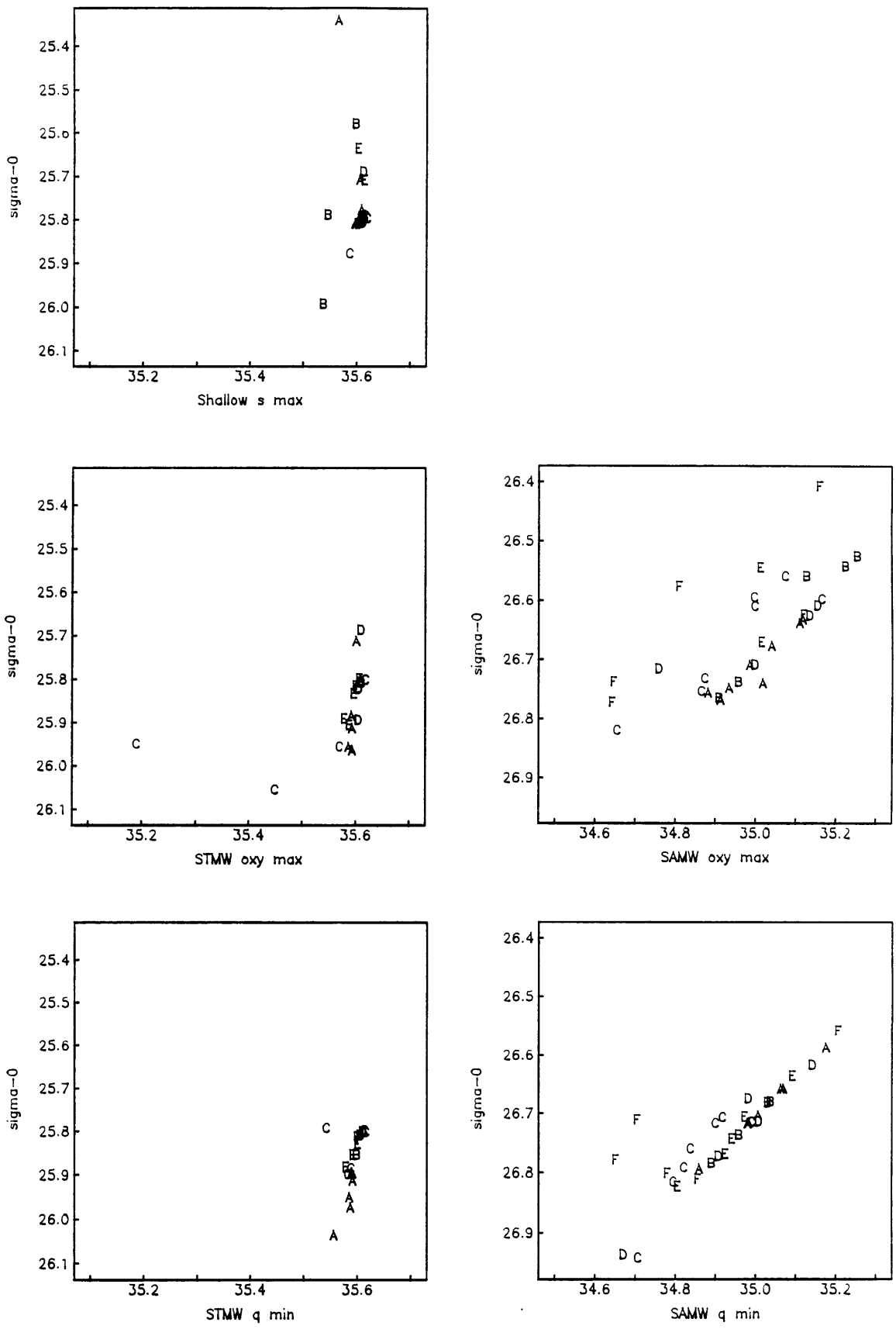

Fig. 4.4 – Scatter plots of salinity and potential density at tracer extrema. See caption next page.

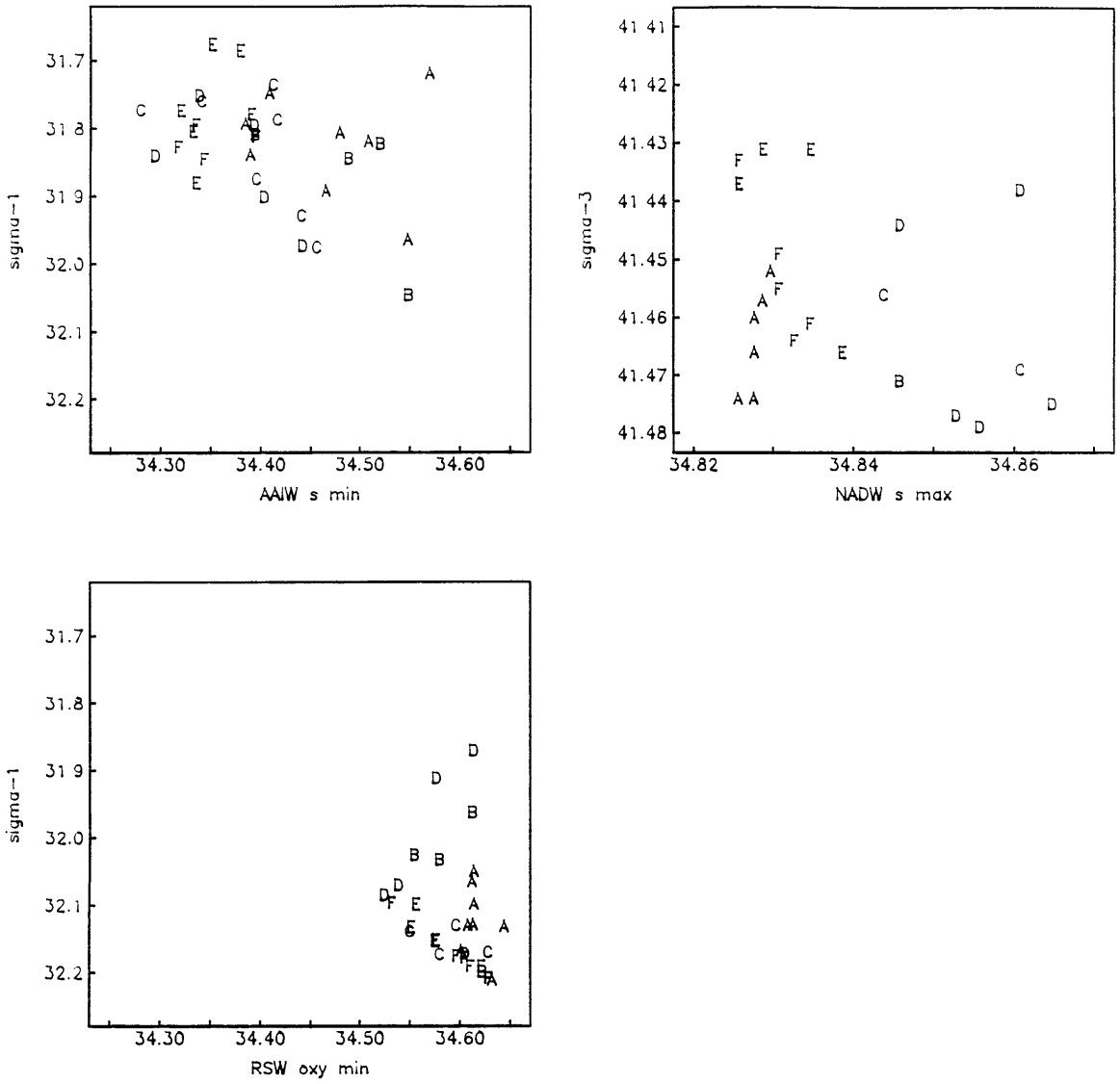

Fig. 4.4, continued – Scatter plots of salinity and potential density at the major tracer extrema observed in the Retroflection (see Table 4.a for list of values, station numbers, *etc.*) The plotting symbol for each extremum observation is the letter of the Agulhas or Agulhas Return Current transect from which it comes. Refer to Table 4.a to identify station numbers of points with anomalous properties.

The left-hand column of plots on the previous page shows the upper layer extrema. The right-hand column shows the extrema associated with the Subantarctic Mode Water (SAMW).

The left-hand column on the this page shows the intermediate layer Antarctic Intermediate Water (AAIW) salinity minimum and the 'deep' oxygen minimum (labelled here 'RSW' for Red Sea Water). The right-hand column shows the North Atlantic Deep Water (NADW) salinity maximum. The Upper and Lower Circumpolar deep water oxygen minima are very faint or absent in the Retroflection, so they are omitted here.

Shallow salinity maximum, mean characteristics

	x−(s*t)	x	x+(s*t)	s*t	x min	x max	obsvns
sig−θ, kg/m	25.52061	25.77186	26.02311	0.25125	25.35181	26.00254	23
salt, psu	35.54678	35.59087	35.63497	0.04410	35.52900	35.61100	23
pres, dbar	72.40909	152.21739	232.02570	79.80830	55.00000	211.00000	23
temp, C	16.81730	17.83508	18.85287	1.01778	16.68200	19.38700	23
salt, psu	35.54678	35.59087	35.63497	0.04410	35.52900	35.61100	23
oxy, ml/l	4.36030	4.79565	5.23100	0.43535	4.19500	5.15600	23
ptemp, C	16.78402	17.80909	18.83416	1.02507	16.65800	19.37700	23

Oxygen maximum near STMW, mean characteristics

	x−(s*t)	x	x+(s*t)	s*t	x min	x max	obsvns
sig−θ, kg/m	25.68676	25.87095	26.05514	0.18419	25.69729	26.06459	21
oxy, ml/l	4.43776	4.92610	5.41443	0.48834	4.01800	5.20600	21
pres, dbar	94.13887	180.61905	267.09924	86.48018	99.00000	261.00000	21
temp, C	16.14274	17.34681	18.55088	1.20407	15.71700	18.17100	21
salt, psu	35.36836	35.56419	35.76002	0.19583	35.18200	35.61000	21
oxy, ml/l	4.43776	4.92610	5.41443	0.48834	4.01800	5.20600	21
ptemp, C	16.11183	17.31643	18.52103	1.20460	15.68700	18.14600	21

Table 4.a (continued on following pages) – Observations of tracer extrema at the 1985 Agulhas and Agulhas Return Current transects A – F.

Mean characteristics pages give means (x) , means plus and minus the 95% confidence limits ($s*t$), minimum and maximum value observed (x min, x max), and number of observations. Planetary potential vorticity units (q) are 10^{-12} $m^{-1}s^{-1}$, not 10^{-13} $m^{-1}s^{-1}$ as labelled.

The observation pages show the actual values at each station. These are plotted in Fig. 4.4.

Shallow salinity maximum, observations

sec	sta	lat	long	x	sig-0	salt	press	temp	salt	oxy	ptemp
	270	-36.50	26.76	239.3	25.820	35.591	191.000	17.648	35.591	4.722	17.615
	271	-35.90	26.93	170.5	25.820	35.589	179.000	17.642	35.589	4.738	17.612
	272	-35.66	26.68	136.0	25.810	35.595	183.000	17.700	35.595	4.851	17.669
A	273	-35.32	26.34	86.4	25.813	35.602	189.000	17.712	35.602	4.989	17.680
	274	-35.10	25.86	36.9	25.719	35.598	125.000	18.070	35.598	4.815	18.048
	275	-34.88	25.86	12.1	25.788	35.601	105.000	17.797	35.601	4.849	17.779
	276	-34.77	25.73	-4.9	25.352	35.558	55.000	19.387	35.558	4.619	19.377
	261	-37.16	23.12	128.9	25.817	35.600	169.000	17.687	35.600	4.940	17.659
B	260	-36.85	22.71	78.2	25.590	35.589	135.000	18.562	35.589	4.763	18.538
	259	-36.52	22.45	35.7	25.799	35.537	149.000	17.558	35.537	4.195	17.532
	258	-36.44	22.23	14.5	26.003	35.529	149.000	16.682	35.529	4.534	16.658
	292	-37.84	19.98	80.2	25.807	35.611	195.000	17.767	35.611	4.997	17.734
C	293	-37.66	19.99	60.3	25.800	35.605	161.000	17.769	35.605	4.992	17.742
	294	-37.49	19.99	41.9	25.808	35.601	147.000	17.721	35.601	4.887	17.696
	296	-37.19	19.99	7.9	25.888	35.578	145.000	17.320	35.578	4.855	17.296
	247	-38.51	18.48	161.9	25.809	35.605	211.000	17.744	35.605	4.927	17.708
D	246	-38.00	18.50	105.8	25.814	35.602	185.000	17.709	35.602	5.156	17.677
	245	-37.55	18.73	51.5	25.700	35.603	149.000	18.168	35.603	4.692	18.142
	288	-39.28	24.51	89.1	25.803	35.602	151.000	17.746	35.602	4.835	17.720
E	287	-39.43	24.90	52.1	25.719	35.606	137.000	18.096	35.606	4.508	18.072
	286	-39.65	25.27	12.2	25.647	35.594	69.000	18.339	35.594	4.549	18.327
F	279	-38.29	26.19	58.4	25.821	35.594	187.000	17.655	35.594	4.915	17.623
	280	-38.60	26.40	19.4	25.805	35.600	135.000	17.728	35.600	4.972	17.705

Table 4.a, continued

Oxygen maximum near STMW, observations

sec	sta	lat	long	x	sig-0	oxy	press	temp	salt	oxy	ptemp
	270	-36.50	26.76	239.3	25.895	4.886	229.000	17.329	35.585	4.886	17.290
	271	-35.90	26.93	170.5	25.968	4.874	261.000	17.009	35.579	4.874	16.966
A	272	-35.66	26.68	136.0	25.924	4.954	243.000	17.213	35.586	4.954	17.172
	273	-35.32	26.34	86.4	25.810	5.039	187.000	17.724	35.602	5.039	17.692
	274	-35.10	25.86	36.9	25.975	5.087	191.000	16.989	35.586	5.087	16.957
	275	-34.88	25.86	12.1	25.723	5.005	99.000	18.039	35.594	5.005	18.021
B	261	-37.16	23.12	128.9	25.817	4.940	169.000	17.687	35.600	4.940	17.659
	292	-37.84	19.98	80.2	25.811	5.029	199.000	17.749	35.610	5.029	17.715
	293	-37.66	19.99	60.3	25.818	5.022	181.000	17.690	35.602	5.022	17.660
C	294	-37.49	19.99	41.9	25.834	4.890	155.000	17.595	35.594	4.890	17.568
	295	-37.33	19.96	23.6	25.960	5.193	193.000	15.717	35.182	5.193	15.687
	296	-37.19	19.99	7.9	25.966	4.960	167.000	16.945	35.561	4.960	16.918
	297	-37.00	20.00	-13.7	26.065	4.018	119.000	16.120	35.441	4.018	16.101
	247	-38.51	18.48	161.9	25.831	5.039	229.000	17.629	35.597	5.039	17.590
D	246	-38.00	18.50	105.8	25.697	5.206	143.000	18.171	35.601	5.206	18.146
	245	-37.55	18.73	51.5	25.904	4.860	195.000	17.318	35.596	4.860	17.285
	288	-39.28	24.51	89.1	25.915	4.877	211.000	17.226	35.580	4.877	17.191
E	287	-39.43	24.90	52.1	25.843	4.825	165.000	17.544	35.589	4.825	17.516
	286	-39.65	25.27	12.2	25.901	4.784	129.000	17.242	35.571	4.784	17.221
F	279	-38.29	26.19	58.4	25.825	4.975	191.000	17.635	35.593	4.975	17.602
	280	-38.60	26.40	19.4	25.809	4.985	137.000	17.712	35.599	4.985	17.688

Table 4.a, continued

STMW q minimum, mean characteristics

		x-(s*t)	x	x+(s*t)	s*t	x min	x max	obsvns
sig-0,	kg/m	25.73596	25.87823	26.02049	0.14226	25.80162	26.04725	19
q,	1E-13/ms	67.79399	152.21359	341.75565	189.54205	83.49399	331.30093	19
pres,	dbar	114.58342	188.68419	262.78497	74.10077	121.00000	257.00000	19
temp,	C	16.72852	17.38274	18.03695	0.65422	16.56000	17.73900	19
salt,	psu	35.54559	35.58316	35.62073	0.03757	35.53400	35.60700	19
oxy,	ml/l	4.60633	4.88332	5.16030	0.27698	4.50700	5.05700	19
ptemp,	C	16.69551	17.35105	18.00660	0.65555	16.53300	17.71000	19

q maximum beneath STMW, mean characteristics

		x-(s*t)	x	x+(s*t)	s*t	x min	x max	obsvns
sig-0,	kg/m	25.82226	26.06676	26.31126	0.24450	25.73764	26.21123	19
q,	1E-13/ms	227.68124	374.24817	615.16571	240.91754	276.84293	610.00690	19
pres,	dbar	128.54454	255.52632	382.50812	126.98179	155.00000	367.00000	19
temp,	C	14.85067	16.30521	17.75975	1.45454	14.96300	18.00400	19
salt,	psu	35.33781	35.49563	35.65346	0.15783	35.23900	35.59900	19
oxy,	ml/l	4.35863	4.67421	4.98979	0.31558	4.40200	5.06400	19
ptemp,	C	14.80132	16.26405	17.72679	1.46274	14.92700	17.97700	19

Table 4.a, continued

STMW q minimum, observations

sec	sta	lat	long	x	sig-0	q	press	temp	salt	oxy	ptemp
	270	-36.50	26.76	239.3	25.906	99.355	239.000	17.277	35.583	4.879	17.237
	271	-35.90	26.93	170.5	25.961	130.573	257.000	17.033	35.578	4.859	16.990
A	272	-35.66	26.68	136.0	25.923	110.030	241.000	17.212	35.584	4.928	17.172
	273	-35.32	26.34	86.4	25.907	148.047	229.000	17.268	35.582	4.987	17.229
	274	-35.10	25.86	36.9	25.984	124.098	199.000	16.933	35.580	5.025	16.900
	275	-34.88	25.86	12.1	26.047	258.299	167.000	16.560	35.549	4.803	16.533
B	261	-37.16	23.12	128.9	25.864	186.077	191.000	17.464	35.590	4.824	17.432
	292	-37.84	19.98	80.2	25.811	93.632	199.000	17.739	35.607	5.029	17.705
	293	-37.66	19.99	60.3	25.807	83.494	169.000	17.738	35.604	5.002	17.710
C	294	-37.49	19.99	41.9	25.895	190.585	179.000	17.305	35.580	4.804	17.275
	295	-37.33	19.96	23.6	25.802	315.014	153.000	17.539	35.534	4.507	17.514
	296	-37.19	19.99	7.9	25.908	331.301	153.000	17.226	35.574	4.905	17.200
D	247	-38.51	18.48	161.9	25.810	111.076	213.000	17.729	35.602	4.951	17.692
	246	-38.00	18.50	105.8	25.819	131.686	189.000	17.671	35.597	5.057	17.639
	288	-39.28	24.51	89.1	25.839	136.137	175.000	17.576	35.593	4.830	17.546
E	287	-39.43	24.90	52.1	25.864	208.389	175.000	17.444	35.584	4.761	17.415
	286	-39.65	25.27	12.2	25.892	158.688	121.000	17.276	35.571	4.725	17.256
F	279	-38.29	26.19	58.4	25.822	149.161	189.000	17.644	35.592	4.935	17.612
	280	-38.60	26.40	19.4	25.825	152.108	147.000	17.638	35.596	4.972	17.613

Table 4.a, continued

Oxygen maximum near SAMW, mean characteristics

		x-(s*t)	x	x+(s*t)	s*t	x min	x max	obsvns
sig-0,	kg/m	26.47319	26.66741	26.86163	0.19422	26.41461	26.82695	31
oxy,	ml/l	4.72871	5.05590	5.38310	0.32719	4.67500	5.38200	31
pres,	dbar	119.11090	486.22586	853.34082	367.11496	167.00000	769.00000	31
temp,	C	9.23780	11.51184	13.78587	2.27403	9.16600	13.51500	31
salt,	psu	34.64218	34.97464	35.30709	0.33246	34.63400	35.24200	31
oxy,	ml/l	4.72871	5.05590	5.38310	0.32719	4.67500	5.38200	31
ptemp,	C	9.16835	11.44955	13.73074	2.28119	9.08400	13.46400	31

SAMW q minimum, mean characteristics

		x-(s*t)	x	x+(s*t)	s*t	x min	x max	obsvns
sig-0,	kg/m	26.57075	26.74122	26.91169	0.17047	26.56621	26.94885	33
q,	1E-13/ms	39.70758	67.58800	115.04449	47.45649	23.92000	107.91003	33
pres,	dbar	188.73990	517.84851	846.95715	329.10861	259.00000	807.00000	33
temp,	C	8.72692	10.87476	13.02259	2.14783	8.44800	12.95800	33
salt,	psu	34.63363	34.91860	35.20358	0.28498	34.64200	35.19600	33
oxy,	ml/l	4.56897	4.92088	5.27279	0.35191	4.42700	5.22700	33
ptemp,	C	8.67655	10.81003	12.94351	2.13348	8.41700	12.89600	33

q maximum beneath SAMW, mean characteristics

		x-(s*t)	x	x+(s*t)	s*t	x min	x max	obsvns
sig-0,	kg/m	26.64589	26.91020	27.17452	0.26432	26.59245	27.12684	33
q,	1E-13/ms	121.88159	172.47221	244.06198	71.58977	115.04202	261.81906	33
pres,	dbar	251.83871	667.84845	1083.85815	416.00974	305.00000	1081.00000	33
temp,	C	5.93989	8.88079	11.82168	2.94089	6.76700	12.62500	33
salt,	psu	34.42749	34.70903	34.99057	0.28154	34.49500	35.14400	33
oxy,	ml/l	4.27147	4.75542	5.23938	0.48396	4.18700	5.20400	33
ptemp,	C	5.86519	8.80755	11.74991	2.94236	6.71600	12.56200	33

Table 4.a, continued

SAMW q minimum, observations

sec	sta	lat	long	x	sig-0	q	press	temp	salt	oxy	ptemp
	270	-36.50	26.76	293.3	26.801	66.879	807.000	10.295	34.850	4.919	10.197
	271	-35.90	26.93	170.5	26.666	66.348	671.000	11.904	35.053	4.881	11.815
	272	-35.66	26.68	136.0	26.724	76.066	729.000	11.261	34.973	4.895	11.167
A	273	-35.32	26.34	86.4	26.666	62.742	633.000	11.922	35.059	4.997	11.838
	274	-35.10	25.86	36.9	26.725	61.164	595.000	11.228	34.970	5.066	11.153
	275	-34.88	25.86	12.1	26.711	73.906	509.000	11.405	34.997	5.038	11.339
	276	-34.77	25.73	-4.9	26.595	79.273	331.000	12.682	35.166	5.072	12.637
	261	-37.16	23.12	128.9	26.687	67.474	565.000	11.665	35.026	4.907	11.591
B	260	-36.85	22.71	78.2	26.689	54.019	569.000	11.626	35.019	4.940	11.552
	259	-36.52	22.45	35.7	26.792	87.998	637.000	10.458	34.879	4.962	10.380
	258	-36.44	22.23	14.5	26.744	46.300	575.000	11.020	34.947	5.042	10.948
	292	-37.84	19.98	80.2	26.722	68.294	641.000	11.291	34.979	5.051	11.209
	293	-37.66	19.99	60.3	26.714	80.843	627.000	11.019	34.907	5.002	10.940
	294	-37.49	19.99	41.9	26.799	53.868	619.000	10.109	34.811	4.999	10.035
C	295	-37.33	19.96	23.6	26.724	93.886	453.000	10.865	34.889	4.947	10.809
	296	-37.19	19.99	7.9	26.767	85.766	429.000	10.341	34.827	5.070	10.290
	297	-37.00	20.00	-13.7	26.949	58.650	441.000	8.614	34.696	4.427	8.567
	298	-36.83	19.99	-31.9	26.823	23.920	259.000	9.800	34.784	4.657	9.770
	247	-38.51	18.48	161.9	26.780	70.178	807.000	10.625	34.896	4.864	10.525
	246	-38.00	18.50	105.8	26.682	61.530	625.000	11.468	34.970	5.163	11.387
D	245	-37.55	18.73	51.5	26.625	65.378	487.000	12.404	35.130	4.859	12.338
	244	-37.00	18.96	-13.3	26.721	88.199	355.000	11.331	34.996	4.671	11.287
	243	-36.68	19.30	-60.0	26.944	74.562	293.000	8.448	34.660	4.544	8.417
	288	-39.28	24.51	89.1	26.750	89.956	611.000	10.921	34.930	4.909	10.844
	287	-39.43	24.90	52.1	26.713	57.667	575.000	11.257	34.962	4.873	11.184
E	286	-39.65	25.27	12.2	26.776	67.549	477.000	10.679	34.913	4.764	10.620
	285	-39.83	25.62	-24.4	26.643	58.352	271.000	12.084	35.081	4.841	12.048
	284	-39.98	26.00	-60.6	26.830	83.625	317.000	9.813	34.795	4.800	9.777
	279	-38.29	26.19	58.4	26.818	63.604	775.000	10.176	34.846	4.973	10.083
	280	-38.60	26.40	19.4	26.566	60.085	443.000	12.958	35.196	4.998	12.896
F	281	-38.85	26.60	-13.1	26.786	66.438	401.000	9.370	34.642	5.227	9.325
	282	-39.19	26.77	-53.9	26.718	73.806	275.000	10.010	34.695	5.201	9.978
	283	-39.50	26.97	-92.2	26.809	107.910	287.000	9.818	34.770	4.830	9.785

Table 4.a, continued

AAIW salinity minimum, mean characteristics

		x−(s*t)	x	x+(s*t)	s*t	x min	x max	obsvns
sig−1,	kg/m	31.66457	31.83425	32.00392	0.16967	31.68506	32.05380	34
salt,	psu	34.24825	34.40156	34.55487	0.15331	34.27500	34.56500	34
pres,	dbar	571.60986	983.17651	1394.74316	411.56665	605.00000	1359.00000	34
temp,	C	3.44082	4.65059	5.86035	1.20976	3.72600	6.26800	34
salt,	psu	34.24825	34.40156	34.55487	0.15331	34.27500	34.56500	34
oxy,	ml/l	3.85736	4.62253	5.38770	0.76517	3.83300	5.28300	34
ptemp,	C	3.37086	4.57123	5.77161	1.20037	3.66000	6.19500	34

Oxygen minimum near RSW, mean characteristics

		x−(s*t)	x	x+(s*t)	s*t	x min	x max	obsvns
sig−1,	kg/m	31.95017	32.12108	32.29199	0.17091	31.87858	32.21894	31
oxy,	ml/l	3.45831	3.83716	4.21601	0.37885	3.46100	4.23800	31
pres,	dbar	829.52985	1343.70972	1857.88965	514.17987	823.00000	1823.00000	31
temp,	C	2.30770	3.58806	4.86843	1.28037	3.00500	5.53000	31
salt,	psu	34.52197	34.58720	34.65244	0.06524	34.51900	34.63900	31
oxy,	ml/l	3.45831	3.83716	4.21601	0.37885	3.46100	4.23800	31
ptemp,	C	2.19695	3.48700	4.77705	1.29005	2.92200	5.42100	31

Table 4.a, continued

AAIW salinity minimum, observations

sec	sta	lat	long	x	sig-1	salt	press	temp	salt	oxy	ptemp
	270	-36.50	26.76	239.3	31.847	34.385	1265.000	4.499	34.385	4.700	4.396
	271	-35.90	26.93	170.5	31.801	34.380	1251.000	4.808	34.380	4.721	4.703
	272	-35.66	26.68	136.0	31.756	34.404	1215.000	5.268	34.404	4.704	5.162
A	273	-35.32	26.34	86.4	31.901	34.461	1309.000	4.547	34.461	4.300	4.440
	274	-35.10	25.86	36.9	31.815	34.475	1101.000	5.232	34.475	4.309	5.138
	275	-34.88	25.86	12.1	31.828	34.504	999.000	5.289	34.504	4.158	5.203
	276	-34.77	25.73	-4.9	31.729	34.565	799.000	6.268	34.565	4.045	6.195
	277	-34.61	25.62	-24.7	31.972	34.543	843.000	4.455	34.543	3.833	4.389
	261	-37.16	23.12	128.9	31.817	34.389	1083.000	4.727	34.389	4.726	4.639
B	260	-36.85	22.71	78.2	31.853	34.483	1157.000	5.010	34.483	4.229	4.912
	259	-36.52	22.45	35.7	31.832	34.515	1059.000	5.332	34.515	4.049	5.241
	258	-36.44	22.23	14.5	32.054	34.543	865.000	3.826	34.543	3.881	3.763
	292	-37.84	19.98	80.2	31.937	34.435	1163.000	4.099	34.435	4.412	4.009
	293	-37.66	19.99	60.3	31.795	34.411	1071.000	5.010	34.411	4.566	4.920
	294	-37.49	19.99	41.9	31.743	34.407	969.000	5.350	34.407	4.788	5.267
C	295	-37.33	19.96	23.6	31.883	34.390	959.000	4.223	34.390	4.523	4.150
	296	-37.19	19.99	7.9	31.984	34.450	963.000	3.809	34.450	4.200	3.737
	297	-37.00	20.00	-13.7	31.768	34.336	689.000	4.746	34.336	4.814	4.692
	298	-36.83	19.99	-31.9	31.781	34.275	609.000	4.283	34.275	5.283	4.237
	247	-38.51	18.48	161.9	31.910	34.398	1359.000	4.099	34.398	4.649	3.991
	246	-38.00	18.50	105.8	31.803	34.388	1149.000	4.831	34.388	4.757	4.735
D	245	-37.55	18.73	51.5	31.760	34.334	997.000	4.821	34.334	5.053	4.740
	244	-37.00	18.96	-13.3	31.982	34.436	909.000	3.726	34.436	4.265	3.660
	243	-36.68	19.30	-60.0	31.849	34.290	639.000	3.850	34.290	5.032	3.804
	288	-39.28	24.51	89.1	31.813	34.328	1063.000	4.394	34.328	4.977	4.310
	287	-39.43	24.90	52.1	31.694	34.375	945.000	5.516	34.375	4.892	5.434
E	286	-39.65	25.27	12.2	31.782	34.316	885.000	4.545	34.316	5.000	4.476
	285	-39.83	25.62	-24.4	31.889	34.331	921.000	3.815	34.331	4.843	3.747
	284	-39.98	26.20	-60.6	31.685	34.347	605.000	5.395	34.347	5.097	5.345
	279	-38.29	26.19	58.4	31.787	34.386	1143.000	4.937	34.386	4.898	4.842
	280	-38.60	26.40	19.4	31.854	34.339	1105.000	4.152	34.339	4.946	4.066
F	281	-38.85	26.60	-13.1	31.836	34.313	893.000	4.113	34.313	4.960	4.046
	282	-39.19	26.77	-53.9	31.820	34.390	765.000	4.685	34.390	4.645	4.625
	283	-39.50	26.97	-92.3	31.803	34.331	681.000	4.460	34.331	4.911	4.408

Table 4.a, continued

Oxygen minimum near RSW, observations

sec	sta	lat	long	x	sig-1	oxy	press	temp	salt	oxy	ptemp
	270	-36.50	26.76	239.3	32.137	3.700	1651.000	3.640	34.608	3.700	3.512
	271	-35.90	26.93	170.5	32.219	3.859	1823.000	3.094	34.627	3.859	2.957
	272	-35.66	26.68	136.0	32.176	3.822	1743.000	3.243	34.596	3.822	3.112
A	273	-35.32	26.34	86.4	32.138	3.761	1619.000	3.594	34.603	3.761	3.469
	274	-35.10	25.86	36.9	32.140	3.617	1475.000	3.793	34.639	3.617	3.678
	275	-34.88	25.86	12.1	32.058	3.559	1239.000	4.228	34.609	3.559	4.129
	276	-34.77	25.73	-4.9	32.073	3.597	1101.000	4.089	34.607	3.597	4.004
	277	-34.61	25.62	-24.7	32.106	3.637	999.000	3.833	34.609	3.637	3.758
	261	-37.16	23.12	128.9	32.207	3.903	1551.000	3.097	34.616	3.903	2.984
B	260	-36.85	22.71	78.2	32.041	3.627	1357.000	4.156	34.574	3.627	4.048
	259	-36.52	22.45	35.7	31.971	3.489	1159.000	4.864	34.607	3.489	4.767
	258	-36.44	22.23	14.5	32.034	3.851	855.000	4.021	34.549	3.851	3.957
	293	-37.66	19.99	60.3	32.178	3.830	1471.000	3.376	34.622	3.830	3.266
C	295	-37.33	19.96	23.6	32.138	3.792	1303.000	3.485	34.590	3.792	3.389
	297	-37.00	20.00	-13.7	32.147	3.907	1179.000	3.089	34.544	3.907	3.006
	298	-36.83	19.99	-31.9	32.181	4.027	1191.000	3.005	34.574	4.027	2.922
	247	-38.51	18.48	161.9	32.180	3.904	1697.000	3.228	34.599	3.904	3.100
	246	-38.00	18.50	105.8	31.879	3.461	1219.000	5.530	34.608	3.461	5.421
D	245	-37.55	18.73	51.5	32.093	3.962	1327.000	3.395	34.519	3.962	3.297
	244	-37.00	18.96	-13.3	31.920	3.667	823.000	4.997	34.571	3.667	4.930
	243	-36.68	19.30	-60.0	32.079	3.892	947.000	3.570	34.533	3.892	3.501
	288	-39.28	24.51	89.1	32.161	3.944	1533.000	3.176	34.570	3.944	3.064
	287	-39.43	24.90	52.1	32.160	3.942	1505.000	3.187	34.571	3.942	3.076
E	286	-39.65	25.27	12.2	32.107	3.963	1311.000	3.486	34.551	3.963	3.389
	285	-39.83	25.62	-24.4	32.141	3.976	1249.000	3.166	34.546	3.976	3.077
	284	-39.98	26.20	-60.6	32.199	3.936	1301.000	3.143	34.616	3.936	3.050
	279	-38.29	26.19	58.4	32.105	4.238	1531.000	3.362	34.527	4.238	3.247
	280	-38.60	26.40	19.4	32.216	4.106	1593.000	3.069	34.623	4.106	2.952
F	281	-38.85	26.60	-13.1	32.186	4.028	1379.000	3.144	34.599	4.028	3.044
	282	-39.19	26.77	-53.9	32.184	4.018	1289.000	3.106	34.591	4.018	3.014
	283	-39.50	26.97	-92.3	32.199	3.937	1235.000	3.064	34.605	3.937	2.977

Table 4.a, continued

NADW salinity maximum, mean characteristics

		x-(s*t)	x	x+(s*t)	s*t	x min	x max	obsvns
sig-3,	kg/m	41.42527	41.45757	41.48986	0.03230	41.43212	41.47988	24
salt,	psu	34.81067	34.83700	34.86333	0.02633	34.82500	34.86400	24
pres,	dbar	2281.19116	2729.00024	3176.80933	447.80899	2295.00000	3137.00000	24
temp,	C	2.20992	2.38358	2.55724	0.17366	2.23800	2.59500	24
salt,	psu	34.81067	34.83700	34.86333	0.02633	34.82500	34.86400	24
oxy,	ml/l	4.92140	5.08054	5.23968	0.15914	4.96500	5.27900	24
ptemp,	C	1.98199	2.17325	2.36451	0.19126	2.00800	2.39200	24

Table 4.a, continued

NADW salinity maximum, observations

sec	sta	lat	long	x	sig-3	salt	press	temp	salt	oxy	ptemp
	270	-36.50	26.76	239.3	41.461	34.827	2919.000	2.335	34.827	4.965	2.107
	271	-35.90	26.93	170.5	41.467	34.827	3049.000	2.306	34.827	4.977	2.066
A	272	-35.66	26.68	136.0	41.458	34.828	2909.000	2.357	34.828	4.967	2.130
	273	-35.32	26.34	86.4	41.453	34.829	2851.000	2.383	34.829	5.018	2.161
	274	-35.10	25.86	36.9	41.475	34.825	2987.000	2.240	34.825	5.052	2.008
	275	-34.88	25.86	12.1	41.475	34.827	2843.000	2.238	34.827	5.062	2.020
B	261	-37.16	23.12	128.9	41.472	34.845	2893.000	2.350	34.845	5.157	2.124
C	293	-37.66	19.99	60.3	41.457	34.843	2825.000	2.429	34.843	5.160	2.209
	295	-37.33	19.96	41.9	41.470	34.860	2609.000	2.403	34.860	5.279	2.204
	247	-38.51	18.48	161.9	41.445	34.845	2817.000	2.507	34.845	5.105	2.285
	246	-38.00	18.50	105.8	41.480	34.855	3137.000	2.373	34.855	5.200	2.122
D	245	-37.55	18.73	51.5	41.439	34.860	2605.000	2.595	34.860	5.073	2.392
	244	-37.00	18.96	-13.3	41.478	34.852	2831.000	2.336	34.852	5.153	2.117
	243	-36.68	19.30	-60.0	41.476	34.864	2703.000	2.398	34.864	5.165	2.190
	288	-39.28	24.51	89.1	41.467	34.838	2927.000	2.349	34.838	5.104	2.120
	287	-39.43	24.90	52.1	41.432	34.834	2619.000	2.515	34.834	5.039	2.313
E	286	-39.65	25.27	12.2	41.432	34.828	2517.000	2.478	34.828	5.016	2.286
	285	-39.83	25.62	-24.4	41.438	34.825	2395.000	2.416	34.825	5.025	2.238
	284	-39.98	26.20	-60.6	41.438	34.825	2295.000	2.404	34.825	5.034	2.235
	279	-38.29	26.19	58.4	41.434	34.825	2523.000	2.450	34.825	5.094	2.259
	280	-38.60	26.40	19.4	41.456	34.830	2541.000	2.338	34.830	5.067	2.146
F	281	-38.85	26.60	-13.1	41.450	34.830	2571.000	2.383	34.830	5.036	2.188
	282	-39.19	26.77	-53.9	41.465	34.832	2647.000	2.304	34.832	5.065	2.104
	283	-39.50	26.97	-92.3	41.462	34.834	2483.000	2.319	34.834	5.120	2.134

Table 4.a, continued

4.3 Tracer extrema and anomalies in the upper ~300 dbar

Basic structure. The upper layer at all the 1983 and 1985 Agulhas Current transects displays a sharp transition in characteristics near the core of the Current. Inshore, the nearly-isohaline, highly stratified Tropical Thermocline Water and its intense subsurface oxygen minimum are found. Offshore, in the Retroflection interior, the Subtropical Mode Water potential vorticity minimum and faint subsurface oxygen maximum, and the Subtropical Surface Water subsurface salinity maximum are found.

The transition from inshore to Retroflection interior water mass characteristics, is located within 20 km of the 15 C temperature/200 m depth contour on transects A, C, and D. At transect B, water-mass transitions at the various extrema and the velocity maximum are shifted 40 - 120 km offshore relative to their positions at other transects, spreading out the band of inshore characteristics and confining the offshore characteristics to a narrower band. This offshore shift occurs in conjunction with considerable current transport reduction and onshore displacement, at transect B, relative to all the other Agulhas Current transects (see Ch. 3).

The horizontal maximum of velocity is found near the water-mass boundary at transects A, B, and D, while at transect C two velocity maxima straddle the water-mass boundary. The near-surface velocity at transect C has two horizontal maxima due to interaction of the shear associated with the surface warm core and an underlying layer of rather uneven shear.[3]

---

[3]On transect C, surface velocity maxima of 1.12 m s^{-1} is found between the northernmost pair of stations, 298-7, and another of 0.87 m s^{-1} between stations 295-3, separated by a velocity of 0.61 m s^{-1} at the intervening station pair, 297-5 (stations 294 and 296 stopped at mid-depths and so were omitted from velocity calculations). Note that these occur at lighter densities than are shown on the velocity *vs.* potential density sections.

The upper layer in the two 1985 Return Current transects also displays a sharp transition near the current core (*i.e.*, near the 15 C temperature/200 m depth contour location and the horizontal maximum of velocity, which coincide at the two Return Current transects). Retroflection interior water-mass characteristics are found on the northern side of the Return Current and fresher, more highly oxygenated, less well stratified water on the southern, Circumpolar side of the Current.

An intrusion of fresh, highly oxygenated water from south of the Return Current is seen in the Agulhas Current, in the upper layer at $\sigma_o \sim 26.0$ on transect C, stations 295 and 296, 10 km inshore from the velocity maximum, which is 40 km offshore from the 15 C temperature/200 m depth contour. This intrusion presumably resulted from entrainment of Return Current water from the south into the Agulhas Current. This is consistent with the transport pattern, which shows such entrainment taking place between transects B and C (transport pattern shown in Fig. 2.12).

Individual extrema. The Subtropical Surface Water salinity maximum, formed in the center of the South Indian subtropical gyre (*Wyrtki, 1971*, pp. 274-276), appears at all Agulhas and Agulhas Return Current transects at at least two stations. It has the most uniform characteristics of all the extrema in the region, as can be seen in Fig. 4.4. Most SSW observations are clustered around $s = 35.60$ psu, $\theta = 17.7$ C, and $\sigma_o = 25.80$. This is virtually identical to the 1983 Retroflection observations. The nearest section of *Wyrtki's* 35.6 psu contour is over 3000 km away near 55°E, 30°S, but this can likely be ascribed to his 0.2 psu contour interval and the Nansen-bottle data's limited vertical resolution, which could miss either the thin >35.6 psu extremum, or the thin, fresher <35.6 psu cap over it.

The lateral boundary of the SSW salinity maximum appears as a near-vertical isohaline on the 1985 and 1983 salinity/potential density sections. It falls within ten kilometers of the 15 C temperature/200 m depth location at all 1985 Agulhas and

Agulhas Return Current transects except transect B, where it is found 40 km farther offshore. Perhaps at B mixing is enhanced in the current core, eroding away the SSW salinity maximum; or perhaps the salinity maximum moves offshore as part of an adjustment or instability process in the onshore meander. The SSW lateral boundary in the 1983 Agulhas transect is found at the first station on the warm side of the 15 C temperature/200 m depth contour, which falls 40 km offshore of the contour.

The most anomalous SSW points are observed at stations just inside the lateral boundary: the warmest SSW observation occurs at station 276, transect A, and the coldest observation at station 258 (Atlas, transect A and B, salinity on potential density surfaces).

The Subtropical Mode Water potential vorticity minimum appears at all 1985 Agulhas and Agulhas Return Current transects, and at the 1983 Agulhas transect, at slightly fewer stations than the SSW salinity maximum. The potential vorticity at the minimum has values ranging from 100 to 350 x 10^{-12} m^{-1} s^{-1}, and is found at $s = 35.58 \pm 0.04$ psu and $\theta = 17.4 \pm 0.7$ C. The potential vorticity minimum values tend to increase onshore in the Agulhas, *i.e.* the anomalously thick Mode Water wedge thins towards the African continental slope. The STMW potential vorticity minimum is found 50 to 100 m beneath the SSW salinity maximum at stations where both are present, which is usually the case. The potential vorticity minimum disappears either a station or two offshore from, or at the same station as, the SSW salinity maximum disappearance. The SAMW potential vorticity minimum is present at just one station on transect B, station 261, located 120 km south of the 15 C temperature/200 m depth location.

The STMW oxygen maximum is found with values of about 4.8 - 5.2 ml l^{-1}, generally within 20 - 40 m of the STMW potential vorticity minimum. The STMW oxygen maximum signal is noisy and at the threshold of the oxygen measurement

accuracy (~0.25 ml l^{-1}), so the Atlas contoured sections do not show it very well. For example, the (questionable and only) oxygen maximum on Agulhas Current transect B, station 261, appears on the oxygen/potential density section as a dot, actually a tiny closed 5.0 ml l^{-1} contour.

The shallow oxygen extrema patterns are most complicated on the inshore side of the Agulhas where low oxygen values associated with the Tropical Thermocline Water are found. An example of this is the 4.0 ml l^{-1} oxygen maximum (!) value listed in Table 3.a for the inshore side of the Agulhas Current at transect C, station 297. This maximum is locally 'produced' between two lower-oxygen Tropical Thermocline Water layers above and below; it is not associated with the STMW at all.

The Tropical Thermocline Water oxygen minima appears at stations at and just inshore of the Agulhas Current in 1985 transects A - D and in the 1983 Agulhas transect. The minimum reaches values of less than 3.8 ml l^{-1} at a station or two on each 1985 Agulhas transect,[4] and less than 4.2 ml l^{-1} at station 49 on the 1983 Agulhas transect. It is confined inshore of 40 km on the warm side of the 15 C temperature/200 m contour, and does not appear at all on the Agulhas Return Current transects.

4.4 Tracer extrema and anomalies at thermocline levels

Basic structure. The thermocline layer at all the 1985 Agulhas Current transects is occupied by South Indian Central Water (SICW), plus intrusions of colder, fresher water from south of the Return Current. The SAMW potential vorticity minimum lies at 10 to 12 C within the 6 to 16 C potential temperature range of the SICW; the potential vorticity minimum is found on every station in the Agulhas and Agulhas Return Current

[4]The Tropical Thermocline Water oxygen minimum appears at the very top of the transect B oxygen/potential density section, on the right-hand side. It does have a higher oxygen cap, at densities lighter than those shown in the section.

that reaches SAMW densities. The SAMW oxygen maximum is also found on every station that reaches SAMW densities, except for several stations in the Return Current where increased oxygen in the overlying layer obscures it.

Individual extrema. The Subantarctic Mode Water potential vorticity minimum has values ranging from 24 to 110 10^{-12} m^{-1} s^{-1}, with most observations found within the ranges $34.8 \leq s \leq 35.2$ psu, $10 \leq \theta \leq 12$ C, and $26.6 \leq \sigma_\theta \leq 26.8$. These ranges agree almost perfectly with observations of SAMW at 18 and 32°S in the South Indian Ocean *(McCartney, 1982)*. The SAMW extends all the way across the Agulhas Current to the continental slope, ~50 km further inshore than the STMW is found, and all the way across the Return Current transects (Fig. 4.5; also Atlas contoured sections of potential vorticity). The SAMW core density changes abruptly near the slope at transects A and B, perhaps because the continental slope side/bottom boundary is a source of frictional torques and enhanced mixing.

McCartney (1977, 1982) argued that the SAMW is injected northward into the S. Indian from its Subantarctic surface formation zone, and that its core density increases from west to east in the South Indian because the SAMW continues to cool and convect while travelling eastward in the Circumpolar flow. Now, if the subtropical gyre streamlines wrap around into the western boundary current in an orderly way, we may expect to find the heaviest SAMW cores on the Retroflection side of the Agulhas and Agulhas Return Currents. This expectation is faintly fulfilled by the SAMW core potential density on transects B - D (see Table 4.a). Also, the $\bar{q}$ isopleth just above the SAMW $\bar{q}$ minimum does tilt upward, relative to density surfaces, across the current into the Retroflection on transects C - F. This can be seen in the Atlas sections of $\bar{q}$ *vs.* potential density.

The SAMW oxygen maximum is found with values from 4.9 - 5.4 ml l^{-1}, generally within ±100 m of the SAMW potential vorticity minimum. A couple of lower

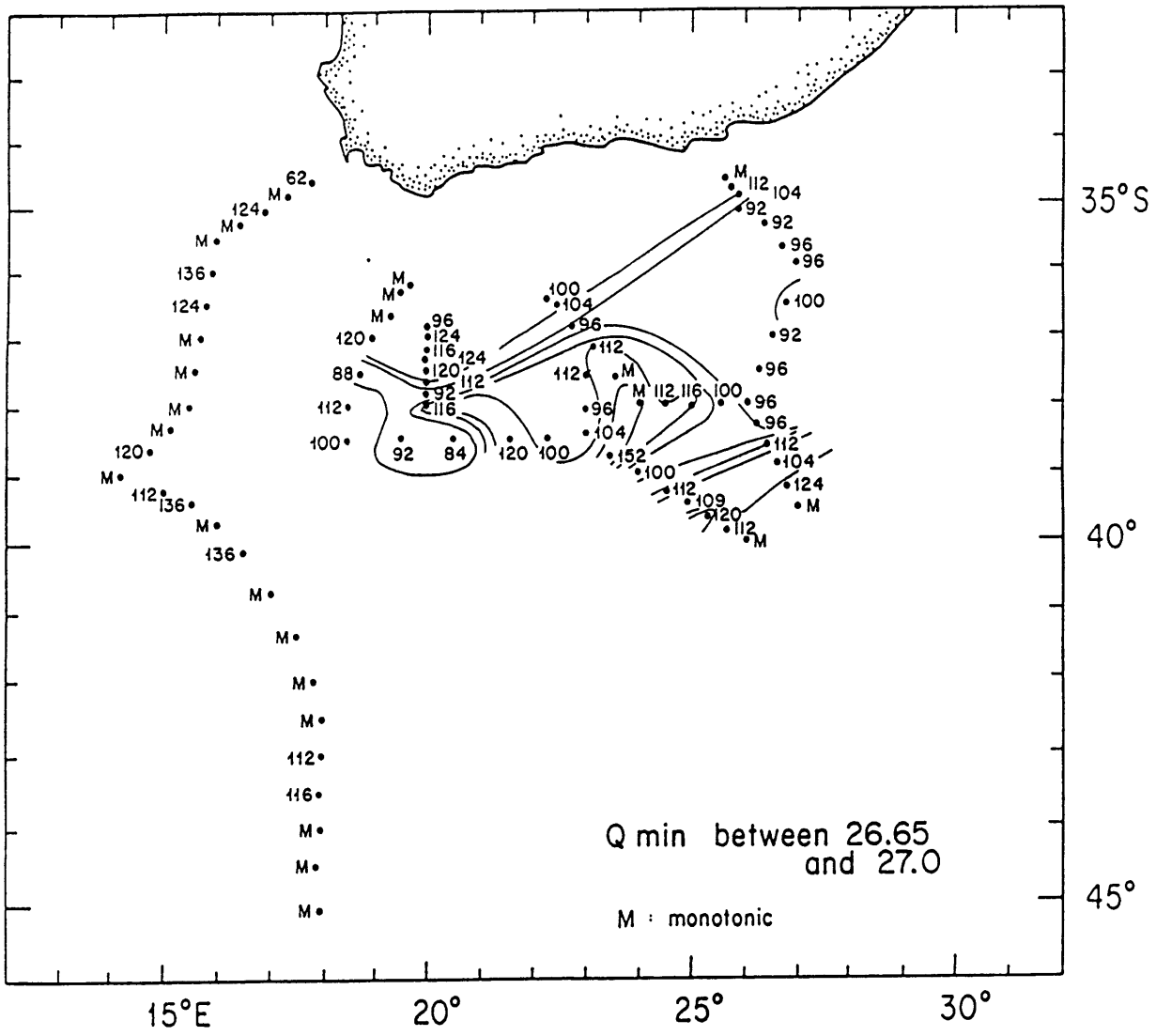

Fig. 4.5 – Map of Subantarctic Mode Water (SAMW) potential vorticity minimum values, in 10^{-12} m^{-1} s^{-1}, at 1985 survey CTD station locations. No SAMW minimum was observed at locations marked with an 'M' for monotonic. Note that monotonic stations are mainly observed outside the Retroflection and Retroflection warm rings: inshore of the Agulhas up on the continental slope, outside the warm features west of the Retroflection, south of the Agulhas Return Current, and within the cold ring.

values are observed on the inshore side of the Agulhas, at transects A and C, probably the result of tropical thermocline influence. The oxygen minimum layer between the STMW and SAMW oxygen maxima is always less than 4.8 ml l^{-1} in the Agulhas Current, so the two maxima are definitely distinct there. The upper layer and thermocline in the Return Current have more uniformly high oxygen values due to infusion of water from the south, which tends to mask the STMW and SAMW oxygen maxima.

Fig. 4.4 shows that most oxygen maximum observations at transects C - F are anomalously fresh compared to the SICW, indicating that downstream of transect B high oxygen water was entrained into the Agulhas from the south side of the Return Current. The anomalously salty oxygen maximum observation at transect A, station 277, is on the inshore side of the Agulhas and indicates Red Sea Water high salinity influence, discussed further in the next section.

4.5 Tracer extrema and anomalies at intermediate levels

Basic structure. The intermediate level salinity field provides striking tracer evidence for entrainment of water into the Agulhas Current from the south side of the Return Current downstream of the partial retroflection, and for separation of the current from the continental slope north of the slope's southern tip.

Oxygen and salinity values are strongly anti-correlated in this layer, with high salinities and low oxygens matching almost perfectly, even at interleaving vertical scales.

Salty, low oxygen Red Sea Water is found at the most inshore stations on transects A and B across the Agulhas Current. Further downstream, fresh, high oxygen water is found at the most inshore stations on transects C and D across the Agulhas Current, evidently from cold eastward inflow just north of the Agulhas at transect D.

The saltiest water on transects C and D is seen just offshore of this thin fresh ribbon. A confused mixture of fresh and salty water is seen at the rest of the transect C and D stations, presumably a mixture of saltier water from the Agulhas at transect B, and fresher Return Current water entrained from the across Retroflection between transects B and C.

The Return Current AAIW is generally fresher than that in the Agulhas Current, $s \sim 34.35$ psu as compared to 34.50 psu.

Oxygen at the deep oxygen minimum increases downstream through the Agulhas Current and Return Current, from $3.5 < O_2 < 3.9$ ml l^{-1} at transect A to $3.9 < O_2 < 4.2$ ml l^{-1} at transect F.

Individual extrema. Salinity in the Antarctic Intermediate Water salinity minimum decreases relatively smoothly offshore in the Agulhas Current at transects A and B, from $s > 34.6$ psu close inshore to $s < 34.4$ psu offshore, at $\theta \sim 4.6$ C and $\sigma_1 \sim 31.8$. Temperature/salinity interleaving is superimposed on the overall decrease in salinity proceeding offshore, with temperature/salinity at a station varying between the temperature/salinity curves at neighboring stations.

The RSW-influenced high salinity ribbon close onshore has significantly higher $\bar{q}$ than the fresher salinity minimum immediately offshore (>128 *vs.* <90 x 10^{-12} m^{-1} s^{-1}). The RSW appears as a salinity maximum further north in the Indian Ocean with values of 38.0 psu at the Red Sea, weakening southward to ~34.7 psu at the maximum's southernmost extent in the Moçambique Channel *(Wyrtki, 1971, Gründlingh, 1985).*

The AAIW salinity minimum itself weakens northward in the South Indian sector from values of 34.2 psu at ~50°S to 34.6 psu at the southern end of the Moçambique Channel.

The smooth decrease in intermediate level salinities proceeding offshore at transects A and B gives over to intense, confused gradients at transects C and D. The AAIW salinity minimum itself generally increases offshore at transects C and D, from s = 34.27 to 34.43 psu at transect C and from s = 34.29 to 34.40 at transect D, except for the saltiest observation at these transects. The saltiest water appears at two stations on transect C, and one station on transect D, offshore from the freshest, most inshore station. This rather strange arrangement can be reconciled, amazingly, with the transport field. A thin counterflow, the southern limb of a tiny anticyclonic eddy between stations 242 and 243 inshore of the Agulhas Current at transect D introduces fresh water from the South Atlantic into the regime inshore of the Agulhas Current at transects C and D - thus the freshest minimum values are observed at the most inshore stations. The strongest remnant of the RSW would seem to account for the saltiest minima a station or two offshore. The fresh, noisy, minimum observations further offshore, relative to values at transects A and B, are evidently a mixture of AAIW from the Agulhas Current at transect B and from the part of the Return Current entrained between transects B and C (see Fig. 2.12). This is no doubt a simplified interpretation, with very intense interleaving observed at all transect C and D stations.

The pattern just described at the minimum itself is consistent with patterns in the 2 - 3 C layer immediately above; the s = 34.5 psu contour undergoes striking vertical excursions at both transect C and D on sections with salinity plotted as a function of potential density.

The AAIW in the Return Current is fresher than most of the Agulhas Current observations and has smaller lateral gradients, with less than half the salinity variation at the minimum, just $34.31 \leq s \leq 34.39$ (Fig. 4.4). Interleaving of similarly reduced intensity occurs over smaller and more regular vertical scales than in the Agulhas Current.

The 'deep' oxygen minimum, underlying the AAIW, is mostly observed in the range $32.1 \leq \sigma_I \leq 32.2$, with values from 3.5 to 4.2 ml l^{-1} generally increasing downstream.

4.6 Tracer extrema and anomalies at deep levels

Consistent with its Atlantic origin, the deep salinity maximum of the North Atlantic Deep Water decreases in intensity from the Atlantic into and across the Indian Ocean to the east *(Wyrtki, 1971)*. The details of its circulation in the Retroflection region and in the Cape Basin west of southern Africa and south of Walvis Ridge are only now being studied. Preliminary examination of data in the Cape Basin suggests that there is a deep cyclonic circulation there *(J. Reid,* pers. comm.). The western limb of this deep circulation, flowing south along the western African continental slope, would supply NADW to the western edge of the Retroflection at the slope's southern tip.

This, in fact, is exactly where the saltiest NADW is observed, on the inshore side of the Agulhas Current at transect D, with $s = 34.864$ psu. Salty NADW, $s \geq 34.860$ psu, is also seen at the next Agulhas Current transect upstream, transect C, and beneath the 1983 and 1985 Cape Town eddies. This is not the first time that the saltiest water has been found at the tip of Africa; an $s = 34.862$ psu measurement was taken by *Jacobs and Georgi (1977)* at the tip of the continental slope,[5] and *Deacon (1937)*, also quoted in *Jacobs and Georgi* , remarked of the *Meteor* observations that the NADW core lies "close round the Cape of Good Hope."

The deep geostrophic shear fields beneath the 1985 Cape Town eddy and at transects D and C (moving along the weakening NADW core towards the Indian Ocean) are quite active, with over 200 dbar net vertical isopycnals displacements at

[5]STD 269, *R/V Conrad* January-April 1974.

NADW levels (~2700 dbar). The deep shear field seems somewhat decoupled from the overlying Cape Town eddy shear, with the deep field differently shaped and shifted onshore compared to the upper level field. At transect D it underlies and tilts the same way as thermocline Agulhas Current isopycnals, giving monotonic shear from the bottom to the surface.

The Agulhas Current at transect B is so far onshore and upslope that only one station in the current (as defined by the transport field) is deep enough to reach the NADW. NADW is found beneath the cold ring, just offshore, with the deep NADW isopycnals rising in the middle of the ring, following the pattern of the overlying shear. Superimposed on this, however, between the continental slope to the north and the Agulhas Plateau, is a net increase in the depth of NADW isopycnals of, again, over 200 dbar. This means that the isopycnals slope the same way and change depth the same amount in the Agulhas Passage beneath transect B and the cold ring as under the Agulhas Current at transects C and D. Salinity at the NADW maximum decreases to $s \leq 34.845$ psu at transect B and beneath the cold ring.

Some NADW may be carried in east in the Return Current, with the saltiest value on transect E, $s = 34.838$ psu seen on the flank of the Agulhas Plateau. Transect F crossed the Return Current as it passed directly over the Agulhas Plateau, and the NADW signal is clearly disturbed by the >3000 dbar topography.

Values drop still further, to $s \leq 34.830$ psu, beneath the Agulhas Current at transect A and at stations 268 - 271 between transects A and F, despite the fact that the channel between Africa and the Agulhas Plateau is over 4000 m deep.

4.7 Steady heat flux across the Retroflection, part I: upper level exchange

Can we estimate the steady east-west heat flux across the Retroflection from the 1985 hydrography? First let us imagine transport between Africa and Antarctica

partitioned into a Circumpolar part and a Retroflection part, with the Circumpolar transport set equal to the transport at Drake Passage. The northern limit of Circumpolar transport is found by integrating meridionally northward from Antarctica until the Drake Passage transport value is reached. The remaining zonal transport in the passage between Antarctica and Africa is then associated with the Retroflection. The Retroflection's net east-west transport must be zero, neglecting transport cells involving Bering Strait, since the Atlantic is (almost) closed to the north. Any net transport from the Pacific Ocean to the Indian Ocean through the Indonesian straits must be balanced by return transport south of Australia.

This implies that we can estimate steady heat flux across the Retroflection by integrating heat flux meridionally southward from Africa across the Agulhas and Agulhas Return Currents until the net mass transport is zero. This steady heat flux estimate *(i)* excludes heat flux due to eddies and rings, and *(ii)* depends on a prescribed thermohaline overturning (upper-layer-to-lower-layer water mass conversion) in the Atlantic north of the Circumpolar Current. When the estimate is made from hydrographic observations, it also *(iii)* presumes that the synoptic fields represent the steady fields, and *(iv)* depends on the arbitrary reference level/bottom velocities supplied to the transport integration.

An estimate of the heat flux due to steady upper-level ($z < 2000$ m) exchange, with thermohaline overturning set to zero, is the only estimate that can be gotten from the 1985 hydrographic observations alone. Fluxes per unit overturning transport are discussed separately below; water diverted into the overturning cell for conversion to lower layer water will be subtracted out of the upper-layer exchange.

The steady upper-level estimate represents a lower bound on the total Retroflection heat exchanges since all the other exchange mechanisms increase heat flux to the west. The other mechanisms include release of warm Retroflection rings to the

west and incorporation of cold rings into the Retroflection [*(i)* above]; net warm-to-cold overturning in the Atlantic [*(ii)* above]; and increased steady upper-layer heat fluxes due to the likely downstream reference level/bottom velocities beneath the Agulhas on the continental slope [*(iv)* above].

To estimate the steady upper-level tracer fluxes across the Retroflection, we exploit the water-mass boundary found near the velocity maximum in the Agulhas: the westward Tropical Thermocline Water- and Red Sea Water-influenced transport on the northern side of the Agulhas water-mass boundary is balanced by eastward S. Atlantic/Circumpolar-influenced transport on the southern side of the Return Current. Heat fluxes due to circulation of Retroflection interior water are neglected.

There are several reasons for estimating the steady upper-level fluxes this way. First, the anomalous water found on the Agulhas inshore side is not observed returning east with the Return Current. Second, water on the cyclonic, inshore side of the Agulhas seems dynamically less likely to retroflect, due to its reduced velocity, the potential vorticity source at the lateral boundary, and mass and momentum exchanges with the adjacent S. Atlantic/Circumpolar water. Lastly, heat flux due to circulation of the Retroflection interior water, which is relatively homogeneous laterally, is probably negligible compared to the heat flux due to exchange of Agulhas inshore water with Return Current water of very different properties.

Tracer characteristics in the westward transport on the northern side of the Agulhas are represented by stations 276 and 259 on Agulhas transects A and B. Tracer characteristics in the eastward transport on the Return Current south side, just north of the southern Retroflection transport integration limit,[6] are represented by the observations at stations 284 and 283 from transects E and F. The velocity profiles on

[6] At about 110 km south of the 15 C/200 m contour in the Return Current; see Ch. 3.

the Agulhas inshore side are represented by station pairs 276-5 and 259-60 at Agulhas Current transects A and B's northern ends and at station pairs 282-3 and 284-5 at Return Current transects E and F's southern ends. It is assumed for simplicity that the transport exchange takes place between columns of water that extend from the surface to 2000 m. In reality, Agulhas water inshore of the water mass boundary on the continental slope is confined to shallower columns, but adjusting the heat flux calculation to take this into account would require arbitrarily specifying the level at which this water is returned. Any adjustment for topography would tend to increase the heat flux, so the values given below are, if anything, underestimates.

The exchanged transport is conservatively and uncertainly estimated at $M = 12 \pm 8$ Sv; Agulhas transport inshore of the water-mass boundary and velocity maximum is in general 20 Sv or more.

Cross-stream distance Δx is given for each velocity profile v by $\Delta x = M \left(\int_{z_o}^{o} v \, dz \right)^{-1}$. The steady upper-level heat flux Q is thus given by:

$$Q(M) = \rho C_p \left[\Delta x_N(M) \int_{z_o}^{o} v_N \, \theta \, dz + \Delta x_S(M) \int_{z_o}^{o} v_S \, \theta \, dz \right] \qquad (4.1)$$

assuming, for the moment, that there is no net overturning. The sign of Q is negative because warmer water is flowing west and colder water is returning to the east.

The steady upper level heat flux range for $4 \leq M \leq 20$ Sv works out to be $-0.045 \geq Q(M) \geq -0.22$ PW (PW = 10^{15} W) for Agulhas transect A paired with Return Current transect F, and $-0.029 \geq Q(M) \geq -0.15$ PW for Agulhas transect B

paired with Return Current transect E. Calculations are shown in spreadsheet form in Table 4.b. The difference between the two transect pairs is small compared to the uncertainty in the exchanged transport.

This heat flux may have a significant effect on Atlantic Ocean heat convergence within the Retroflection latitude band: it corresponds to between 0.04 and 0.32 of *Hastenrath's (1982)* 0.69 PW estimate of northward heat transport across 32°S in the South Atlantic. One wonders what the effect on box budget (*e.g.* inverse) calculations is of using hydrographic data that does not fully resolve the flow on the upper continental slope!

The steady upper-level exchange may also be compared to the heat lost at the sea surface in the Retroflection, west of the transect-pair longitudes. A total heat loss of -0.015 PW to the atmosphere corresponds to the local rate of ~ -100 W m^{-2} *(Bunker, 1982)* times a nominal area of 4° x 4° (1.6×10^{11} m^2). This is only 50% of the smallest value estimated for $Q(M)$, so the steady upper-level heat flux must be balanced by more remote heat sinks.

Finally, the steady upper layer exchange may be compared to a similar calculation by *Gordon (1985)* across the 1983 Cape Town Eddy (CTE) at ~35°S, which gave a value of 0.023 PW for a steady upper layer exchange of 13.5 Sv. The values for $Q(M = 13.5$ Sv) in the Retroflection are 0.15 PW and 0.10 PW, a factor of 4 to 6 larger. Thus, taking all these estimates at face value, it appears that most of the heat flux westward across the Retroflection does not simply turn the corner in the upper layer into the S. Atlantic north of 35°S.

4.8 Steady heat flux across the Retroflection, part II: the Atlantic Ocean NADW overturning cell

So far this calculation presumes, as was mentioned above, that zero upper-to-lower layer conversion is occurring in the Atlantic, and, equivalently, that transport above 2000 m balances across the Retroflection and across the Circumpolar Current. But the deep salinity influence of the North Atlantic Deep Water extending over the

		Velocity, cm s-1				
Depth, m		Transect F	Transect A	Transect E	Transect B	
50		27.12	139.00	41.02	49.05	
100		24.44	134.24	38.03	49.00	
500		15.67	99.70	20.55	39.40	
1000		10.19	50.69	8.71	31.94	
1500		4.83	14.20	3.66	10.45	
2000		1.48	1.63	1.25	0.10	
		Velocity * dz, m2 s-1				
Depth, m	dz, m	Transect F	Transect A	Transect E	Transect B	
50	50	13.56	69.50	20.51	24.53	
100	50	12.22	67.12	19.02	24.50	
500	400	62.68	398.80	82.20	157.60	
1000	500	50.95	253.45	43.55	159.70	
1500	500	24.15	71.00	18.30	52.25	
2000	500	7.40	8.15	6.25	0.50	
		Running sum v*dz, m2 s-1				
Depth, m		Transect F	Transect A	Transect E	Transect B	
50		13.56	69.50	20.51	24.53	
100		25.78	136.62	39.53	49.03	
500		88.46	535.42	121.73	206.63	
1000		139.41	788.87	165.28	366.33	
1500		163.56	859.87	183.58	418.58	
2000		170.96	868.02	189.83	419.08	
		dx, m Sv-1				
		Transect F	Transect A	Transect E	Transect B	
		5.85E+03	1.15E+03	5.27E+03	2.39E+03	
		Potential temperature, deg C				
Depth, m		Transect F	Transect A	Transect E	Transect B	
50		16.89	19.76	17.16	21.99	
100		13.38	17.03	13.36	19.21	
500		6.91	10.26	7.68	12.01	
1000		3.50	4.31	3.68	5.95	
1500		2.66	2.99	2.72	2.70	
2000		2.40	2.50	2.45	2.65	
		v * dz * pot temp * dx, C m3 s-1 Sv-1				
Depth, m		trans F	trans A	trans E	trans B	
50		1.34E+06	1.58E+06	1.85E+06	1.29E+06	
100		9.56E+05	1.32E+06	1.34E+06	1.12E+06	
500		2.53E+06	4.71E+06	3.33E+06	4.52E+06	
1000		1.04E+06	1.26E+06	8.45E+05	2.27E+06	
1500		3.75E+05	2.45E+05	2.62E+05	3.36E+05	
2000		1.04E+05	2.35E+04	8.08E+04	3.16E+03	

Table 4.b – Spreadsheet summary of upper layer heat exchange calculations. Continued on following page.

		Running sum v*pot temp*dz*dx, C m3 s-1 Sv-1				
depth, m		trans F	trans A	trans E	trans B	
50		1.34E+06	1.58E+06	1.85E+06	1.29E+06	
100		2.30E+06	2.90E+06	3.19E+06	2.41E+06	
500		4.83E+06	7.61E+06	6.52E+06	6.93E+06	
1000		5.87E+06	8.87E+06	7.36E+06	9.19E+06	
1500		6.25E+06	9.12E+06	7.62E+06	9.53E+06	
2000		6.35E+06	9.14E+06	7.71E+06	9.53E+06	
		Difference of running sums v*pot temp*dz*dx, C m3 s-1 Sv-1				
		Transects F - A		Transects E - B		
		-2.79E+06		-1.83E+06		
		...times rho*Cp, J Sv-1				
		-1.11E+13		-7.31E+12		
		Q 4 Sv, 20 Sv				
		-4.46E+13		-2.93E+13		
		-2.23E+14		-1.46E+14		

world deep ocean indicates that there is a net export of lower layer NADW from the Atlantic.

The return flow into the Atlantic balancing export of NADW must be composed of thermocline, intermediate, and/or bottom water. Renewed interest in their relative contributions to the return flow have been fueled by speculation about possible climatic implications of return flow composition. *Gordon (1985, 1986)* estimated an entirely warm return flow from estimates of NADW transport and of ocean heat flux, both across 30°S in the Atlantic. This warm ($\geq$ 9 C) return flow would have to make its way back to the Atlantic *via* the Indonesian straits from the Pacific Ocean, and *via* the Agulhas Retroflection from the Indian Ocean, since the warmest water in Drake Passage is 8 C. Local geological or physical changes at the Indonesian straits or the Retroflection might, in this scenario, have global climatic implications through modulation of the global thermohaline circulation.

The warm water path hypothesis was subsequently tested by *Rintoul (1988)*, using an inverse model of South Atlantic observations. *Rintoul* first found that NADW transport across 30°S and heat flux across 30°S were closely related: prescribing higher heat flux caused the inverse model to produce a more vigorous NADW overturning cell. The inverse model's northward return flow across 30°S had stable composition over the entire range of reasonable heat flux values, of about half intermediate and bottom water, and half thermocline water.

Rintoul then forced the inverse model to produce *Gordon's* net warm water flow from the Indian Ocean into the Atlantic. This produced a model circulation with unreasonable characteristics, including substantial heat convergence (1 PW) in the S. Atlantic between 32°S and the Weddell-Scotia Sea and model reference level velocities an order of magnitude higher than those in the inverse model without imposed warm flow. *Rintoul* concluded that NADW transport and heat flux across 30°S could

not be specified independently, and that the warm water path was an artifact of *Gordon's* having specified both heat flux across 30°S (0.69 PW) and an NADW transport across 30°S (16 Sv) that was much lower than the NADW transport produced by the inverse model (27 Sv) for the same heat flux.

Taking all of this into consideration, here we simply estimate the additional heat flux per unit overturning transport. Overturning transport refers to water that leaves the Retroflection on the north side of the Agulhas and returns as NADW, rather than as upper-layer water in the Return Current. The NADW potential temperature is $\theta = 2.2$ C, which is 4.8 C colder than the transport-weighted Return Current upper level potential temperature $\theta = 7.0$ C, for a resulting increase in westward heat flux of -0.019 PW Sv^{-1} ($Sv = 10^6\ m^3\ s^{-1}$), expressed as energy per unit transport diverted from the upper-level exchange cell into the NADW overturning cell. The total heat flux associated with transforming upper layer water leaving the Retroflection into NADW is -0.030 PJ Sv^{-1}.[7]

To summarize, a steady upper-level ($z < 2000$ m) heat flux of between -0.029 and -0.22 PW (westward) is associated with westward upper-layer transport of 12 ± 8 Sv inshore of the Agulhas water-mass boundary and an eastward return transport of equal magnitude on the south side of the Return Current. Westward heat flux increases by -0.019 PW for every Sv diverted from this upper-level exchange into overturning exchange between upper-level water and North Atlantic Deep Water.

[7]Note that the 'horizontal circulation' involving the Brazil Current and its interior return flow have been omitted from this discussion. It should be noted in particular that the heat flux across 30°S corresponds not to the NADW overturning alone, but to the combined NADW overturning and Brazil Current cells.

4.9 Conclusions

Consistent water mass boundaries in the upper 300 dbar are observed near the velocity maximum in all the Agulhas and Agulhas Return Current transects. Tropical Thermocline Water (low oxygen, constant or decreasing salinity with depth) is observed on the inshore side of the Agulhas, and Subtropical Surface Water (SSW, salinity maximum) and Subtropical Mode Water (STMW, potential vorticity minimum, oxygen maximum) on the offshore side.

The Agulhas undergoes a complicated adjustment in structure at transect B. Current narrowing and offshore shift of the water-mass boundary and velocity maximum at transect B increases the width of the inshore regime, both in absolute distance and as a proportion of the current cross-section, and severely reduces the width of the offshore regime, confining it to a smaller proportion of a narrower current. Relative to all the other transects, transport, total width, and the width of the offshore side of the current are decreased at transect B, while the width of the onshore side of the current is increased.

A water-mass boundary is also observed in the two 1985 Agulhas Return Current transects, between the Retroflection interior water-masses (SSW and STMW) on the current's northern side and fresher, more highly oxygenated South Atlantic/Circumpolar water on the southern side.

Tracer properties at the thermocline and intermediate levels at transects C and D exhibit signs of input from the south side of the Return Current, evidently entrained into the Agulhas Current between Agulhas transects B and C, in the onshore limb of the Retroflection recirculation cell found downstream from the partial retroflection and the cold ring. Water from the south also intruded directly across into the Return Current, as it did in 1983 *(Gordon,* et al., *1987).*

The Subantarctic Mode Water (SAMW) $\bar{q}$ minimum values and core densities are in good agreement with *McCartney's (1982)* SAMW observations on zonal sections across the South Indian Ocean. SAMW core density increases, faintly, towards the outer edges of the Retroflection, consistent with *McCartney's* analysis of the SAMW formation mechanism.

Some disruption in the the Subantarctic Mode Water core density and thermocline potential vorticity field, perhaps due to boundary mixing or torques, is observed hard by the continental slope in the Agulhas.

Red Sea Water high-salinity, low-oxygen influence at intermediate levels is seen pressed up against the slope on Agulhas transects A and B. Further downstream, at transects C and D, the strongest RSW influence is separated from the slope by a ribbon of fresh Antarctic Intermediate Water (AAIW) of S. Atlantic origin.

The North Atlantic Deep Water salinity maximum is found pressed up against the foot of the continental slope, beneath the 1983 and 1985 Cape Town Eddies, and transect D at the southern tip of the slope. The salinity maximum decreases in intensity from west to east. The shear is consistent with a shallower reference level and flow to the east: isopycnals descend fairly consistently ~200 m from north to south beneath the Agulhas (and the cold ring) in the Agulhas Passage, and more across transect D, west of the Passage. They ascend ~200 m across the 1985 Cape Town Eddy, but a shallower reference level is still necessary for the saltiest water to be flowing southward.

If the westward flow of water inshore of the Agulhas water mass boundary is balanced by eastward flow of water on the south side of the Return Current, a steady east-west heat flux across the Retroflection results. The exchanged transport was first estimated to be between 4 and 20 Sv, and it was assumed that both flows were composed of 2000 m deep water columns. A range of heat flux values between -0.029

and -0.22 PW (with eastward positive) was then computed from selected stations at two sets of paired transects. If indeed this exchange is a reasonable model of what is really happening, this would seem to be a low estimate: balancing warm, shallow columns flowing west with deep columns flowing east, for example, would increase it. The heat flux estimated here is 4 to 6 times greater than the values computed by *Gordon* et al. *(1987)* using a similar method across the 1983 Cape Town Eddy.

Every Sv (10^6 m s^3) that flows west and returns east in the North Atlantic Deep Water layer instead of returning at <2000 m depths in the Return Current increases the westward heat flux by -0.019 PW Sv^{-1}.

Chapter 5: Velocity and total potential vorticity

5.1 Introduction

So far we have examined the path of the current and its transport and tracer fields. This examination has yielded new insights into the Agulhas Retroflection circulation, confirming some existing ideas about its characteristics, challenging others, and suggesting new questions. The current path, as we have seen, can turn more sharply and cut across isobaths more strongly than expected from previous observations and models. Current transport definitely reaches values that are greater than the upper limit of the range predicted by linear theory from observed winds, but does not, as was often tacitly assumed, increase monotonically downstream. In fact, the current retroflection can occur in two branches (at least) having comparable transport, with substantial recirculation beyond the first branch and rapid along-stream transport variation between them.

Sharp tracer fronts are found in the near-surface layer (<300 m) near the current's velocity maximum: nearly-isohaline, low-oxygen, highly stratified water from the tropical thermocline is found on the inshore side of the Agulhas; slight salinity maximum, high-oxygen, relatively homogeneous Mode Water created at the surface within the subtropical gyre is found within the Retroflection; and fresher, high oxygen water from the S. Atlantic/Circumpolar regime is found south of the Return Current. At intermediate levels ($1000 < z < 2000$ m), a thin ribbon of anomalously salty, low-oxygen, highly stratified water from northern Indian Ocean sources is found pressed up against the continental slope. Another thin ribbon, of the saltiest deep water from the Atlantic, enters the Indian Ocean pressed up against the foot of the continental slope around the tip of Africa.

Ultimately, one wants to understand the dynamics of these features, many of which were observed or observed clearly for the first time by the 1985 hydrographic survey. The next step towards this goal, having completed the characterization of the overall circulation, is an examination of the velocity and total potential vorticity fields of the currents.

In this chapter:

- The geostrophic velocity field is discussed (Sec. 5.2).
- An expression for potential vorticity in natural, along- and across-stream, isopycnal coordinates is introduced (Sec. 5.3).
- The relationship between a Rossby number ε_k, based on the total velocity and parcel trajectory curvature, and a Rossby number ε_g, based on geostrophic velocity and geostrophic streamline curvature, is explored (Sec. 5.4).
- The magnitudes of individual potential vorticity terms in the Agulhas and Agulhas Return Current are estimated, and some remarks are made about possible dynamical balances (Sec. 5.5).
- The Agulhas and Agulhas Return Current potential vorticity cross-stream gradients are computed, to determine if and in what way they meet the necessary conditions for baroclinic and barotropic instability (Sec. 5.6 and Sec. 5.8).
- The relationship of the Agulhas and Agulhas Return Current (and Gulf Stream) potential vorticity cross-stream gradients to the local Mode Waters is discussed (Sec. 5.7).

These investigations characterize the Currents, and prepare the way for an examination in the next chapter of Agulhas Current and Retroflection models, their dynamics, scales, geometry, assumptions, and simplifications.

5.2 Geostrophic velocity

Some intrinsically interesting features of the current's geostrophic velocity field are described here. Geostrophic velocity sections across the Agulhas and Agulhas Return Currents are shown in the Atlas. Note that average geostrophic velocity between the two hydrographic stations is the quantity discussed below. It tends to underestimate the magnitude of geostrophic velocity extrema, and may differ significantly from the total velocity when trajectory curvatures are not small (see Sec. 5.4).

Surface and near surface velocity. The maximum surface velocity at the Agulhas Current transects is:

1.78 m s^{-1} at transect A relative to a 1700 m deepest common level (dcl),
0.83 m s^{-1} at transect B relative to a 900 m dcl,
1.13 m s^{-1} at transect C relative to a 1500 m dcl, and
0.96 m s^{-1} at transect D relative to 2400 dbar.

Surface velocity values as high as 2.60 m s^{-1} (averaged over 24 hours) have been observed directly in the Agulhas using satellite-tracked drifters and current meter measurements from a drifting ship within radio positioning range of the coast *(Gründlingh, 1977).*

The surface velocity maximum at transect B would be 1.44 m s^{-1} if the bottom velocity beneath it were 0.61 m s^{-1}, the maximum velocity at 900 m on transect A, found one station pair offshore from the surface velocity maximum there. The maximum at transect C was found at the most inshore station pair and is the sum of

0.56 m s^{-1} due to the 1500 to 200 m shear, plus a huge 0.57 m s^{-1} due to shear in the upper 200 m, within the onshore side of the current's superficial warm core.

There is a second surface velocity maximum at transect C which overlies the main velocity maximum at deeper levels. The double maximum structure arises from an onshore shift in the warm core location relative to the underlying current. The second maximum has a value of 0.85 m s^{-1} relative to 2400 dbar, and is separated laterally from the larger maximum listed above by a local minimum of 0.61 m s^{-1}. This maximum arises mostly from strong upper deep and intermediate level shears, which are well correlated with tracer anomalies at these levels. Velocity actually increases with depth here, from 0.85 m s^{-1} at the surface to 1.00 m s^{-1} at 150 m, since the surface warm core shear is opposite in sign to the underlying shear. Subsurface velocity maxima occur in the upper 200 m or so at some of the other Agulhas station pairs as well.

The maximum surface velocity at the Agulhas Return Current transects is:

0.68 m s^{-1} at transect E relative to a 2400 dbar reference level, and
1.28 m s^{-1} at transect F relative to a 2400 dbar reference level.

This apparent downstream increase in maximum surface velocity from transect E to transect F is not surprising, given that transport at transect F is about $1\frac{1}{2}$ times as large as transport at transect E: Return Current transport at transect E is joined by the first Agulhas Current retroflection branch between transects E and F.

The velocity maximum at transect E was probably significantly underestimated, as a result of station positioning: the maximum velocity value was observed at two consecutive station pairs, involving three consecutive stations. It seems likely that stations offset by half a station spacing width would have better resolved the maximum.

Further, note that minimum station spacing in the Return Current is twice as large as minimum spacing in the Agulhas.

Horizontal maximum of velocity at other depths. The velocity maximum tends to shift inshore with height at Agulhas Current transects A, B and C (as can be seen in the Atlas contoured sections of velocity). This means that the velocity maximum line parallels the continental slope over the whole water column, keeping the width of the jet's cyclonic side relatively constant with depth. As if to confirm this point, the velocity shifts onshore with height only in the upper 200 m at transect D, where the current has separated away from the slope. A similar onshore shift with height is also observed in the Kuroshio and Gulf Stream, the other large western boundary currents *(Worthington and Kawai, 1972).*

Intermediate and deep boundary currents. Tracer anomalies at intermediate and deep levels are found near the high velocity core at all the Agulhas Current transects (compare Atlas contoured sections of salt, oxygen, and velocity). The anomalously salty, low-oxygen Red Sea Water from the Indian Ocean and the salty North Atlantic Deep Water are found in layers of enhanced shear, suggesting deep western boundary currents for these water masses.

5.3 Vorticity in natural isopycnal coordinates

It is desirable to look at the vorticity in a coordinate system in which each term has an invariant physical interpretation. Along- and across-stream coordinates are customarily used in studies of western boundary currents *(Kawai, 1957, Chew, 1974).* These so-called natural coordinates transform the velocity from arbitrary Cartesian components into along- and across-stream components. Relative vorticity is transformed from three shear terms in the three Cartesian directions into a single cross-stream shear term and a single curvature vorticity term.

Natural coordinates were also used by *Hall (1985)*, who estimated cross-stream shear but not curvature vorticity. *Hall* also estimated vorticity due to vertical shear of along-stream velocity and isopycnal tilt.[1] Small vorticity terms due to curl of vertical velocity are all dropped in these natural coordinate formulations; we shall do the same here.

The vorticity due to vertical shear of along-stream velocity, included in *Hall's* estimates but not in *Kawai's* and *Chew's* expressions for jet vorticity, is not necessarily negligible in western boundary currents compared to horizontal shear vorticity. In fact, vorticity terms due to vertical and horizontal shear have comparable maximum values in the Gulf Stream, as *Hall* demonstrated using direct measurements of velocity and temperature. These vertical shear vorticity terms are non-quasi-geostrophic, and are dropped from the quasi-geostrophic equations. The ratio of vertical shear vorticity to horizontal shear vorticity is εS^{-1}, in terms of the usual non-dimensional numbers ε, the Rossby number, $\frac{V'}{fL}$, and S, the Burger number, $\frac{N^2H^2}{f^2L^2}$, with f the Coriolis parameter, L the length scale of the motion, N the buoyancy frequency, and H the water depth. As is shown in the derivation of the vorticity equation in isopycnal natural coordinates in Appendix A, εS^{-1} is just $\Delta h/H$, where Δh is the depth variation on an isopycnal over the cross-stream distance, and H is the depth over which the velocity varies. Gulf Stream and Agulhas values of εS^{-1} are comparable, both being about 1.

Isopycnal natural coordinates, derived in Appendix A, can be used to combine cross-stream shear vorticity and along-stream vertical shear vorticity into a single

---

[1]The vorticity terms due to vertical shear arise from the dot product:

$$\frac{\partial \boldsymbol{u}}{\partial z} \cdot \nabla_H \lambda$$

where λ is usually potential density or potential temperature *(Pedlosky, 1979)*.

isopycnal shear vorticity term without further approximation, simply by taking the cross-stream coordinate along isopycnals instead of along a horizontal surface.

Total potential vorticity, q, then becomes:

$$q \sim \left(f + K_s v' - \frac{\partial v'}{\partial n'} \right) \frac{\partial \lambda}{\partial z} \tag{5.1}$$

calling the isopycnal cross-stream coordinate n', the path curvature K_s , and the tracer used to mark the location of material surfaces λ (usually potential density or potential temperature in practice). Along- and across-stream flow directions vary with depth, defined by $\boldsymbol{u}$. The only terms neglected in deriving Eq. (5.1) are *(a)* vorticity due to curl of vertical velocity (negligible since $W/L << U/H$) and *(b)* planetary vorticity variation with latitudinal isopycnal tilt, which in western boundary currents is ~0.01 compared to the planetary vorticity itself.

5.4 Some interesting consequences of path curvature

We now briefly examine the effects of curvature of geostrophic streamlines and parcel trajectories. Path curvature can lead to significant differences between purely geostrophic velocity v'_g and total velocity v'. There can also be differences between the curvature of geostrophic streamlines K_g (intersection of pressure and depth surfaces) and curvature of actual parcel trajectories K_s.

The degree and nature of the differences, when time-dependence can be neglected, is illustrated by the relationship between a curvature Rossby number based on the geostrophic velocity, $\varepsilon_g = \frac{K_g v'_g}{f}$, and a curvature Rossby number based on the total velocity, $\varepsilon_k = \frac{K_s v'}{f}$ (the prime is used here to denote the along-stream isopycnal

velocity). Taking the gradient wind equation *(Holton, 1979)*, from which time-dependent terms have been dropped, and solving quadratically for ε_k gives:

$$\varepsilon_k = \frac{-1}{2}\left\{1 \pm \sqrt{\left(1 + 4\,\frac{K_s}{K_g}\varepsilon_g\right)}\right\} \tag{5.2}$$

Setting $K_s = K_g$, appropriate for a steady ring, the relationship of ε_k and ε_g (and thus v_g' and v') may be plotted (Fig. 5.1).

The expression Eq. (5.2) includes three cases:

(i) Inertial flow, in which the pressure gradient and thus v_g' and ε_g vanish. The two roots are *(a)* ε_k and v' both vanish (trivial root), or *(b)* $\varepsilon_k = -1$, $v' = \frac{-f}{K_s}$ (physical root).

(ii) Gradient wind flow. The physical root giving $\varepsilon_k \sim \varepsilon_g$ arises from subtracting the radical. The minimum allowed value of ε_k is -0.5, and real values of ε_k require $\frac{K_s}{K_g}\varepsilon_g \geq -0.25$, K_g and K_s having the same sign.

(iii) Here $\left|\frac{K_s}{K_g}\right|\varepsilon_g < -0.25$, and trajectory curvature and geostrophic curvature have opposite signs so that ε_k has real roots: parcels flow cyclonically around intense high pressure centers. Again, the physical root giving $\varepsilon_k \sim \varepsilon_g$ arises from subtracting the radical.

The second and third of these cases are relevant to the Agulhas path and rings. Where $K_s = K_g$ is appropriate, as in steady rings, the relationship between the total velocity and geostrophic velocity magnitudes is straightforward (Fig. 5.1). Total velocity is less than (greater than) geostrophic velocity in cyclonic rings with $\varepsilon_k > 0$ (anticyclonic rings with $\varepsilon_k < 0$), since the pressure gradient is partially balanced by the centrifugal acceleration term: for example, when $\varepsilon_g = 0.25$, $\varepsilon_k = 0.21$, and $v' = 0.83\ v_g'$. The greatest discrepancy between total and geostrophic velocity

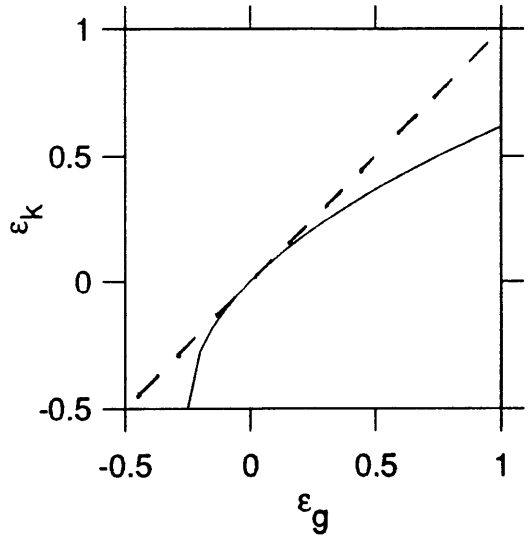

Fig. 5.1 – Curvature vorticity Rossby number $\varepsilon_k = K_s v'/f$, based on curvature of actual parcel trajectories K_s and total velocity v', plotted (solid line) as a function of geostrophic curvature Rossby number $\varepsilon_g = K_g v_g'/f$, based on geostrophic curvature K_g and geostrophic velocity v_g', for $K_s = K_g$, *e.g.* steady ring. The dashed line shows the $\varepsilon_g = \varepsilon_k$ curve.

magnitude occurs when $\varepsilon_g = -0.25$ and the radical in Eq. (5.2) vanishes (the tightest anticyclonic rings allowed), giving $\varepsilon_k = -0.5$ and $v' = 2v_g'$.

More generally, for cyclonic and small anticyclonic values of geostrophic curvature vorticity in a meandering current, a parcel can follow a trajectory that is more or less tightly curved than the geostrophic path. Parcels may 'spin out' of steepening anticyclonic meanders as the centripetal acceleration plus the pressure gradient overcomes the opposing Coriolis acceleration [as in case *(iii)* above]. Significant cross-frontal motion, and thus departure of real curvature from geostrophic curvature, was observed throughout Gulf Stream meander patterns by *Bower (1988).*

What are the geostrophic curvature and geostrophic Rossby numbers in the Agulhas? At the 1985 Agulhas transects, geostrophic curvature K_g is essentially zero at transects A, D, E and F, and anticyclonic (>0 anticyclonic in the southern hemisphere) with a nominal value of 0.028 km^{-1} (80° in 50 km and 95° in 60 km, respectively) at transects B and C, judging from the satellite image of sea surface temperature at transect A and the 15 C temperature/200 m depth contour at transects B - F.

Geostrophic curvature vorticity at transects B and C is $K_g v_g' \sim 2.0 \times 10^{-5}\ s^{-1}$, based on the 15 C/200 m contour curvature and velocities at the contour in the upper 200 m of $\geq 0.7\ m\ s^{-1}$. The Coriolis parameter f is $-8.3 \times 10^{-5}\ s^{-1}$, which gives a value for ε_g of -0.24. By Eq. (5.2), $\frac{K_s}{K_g}\varepsilon_g$ must be greater than -0.25, so these meanders are just above the critical value of $\varepsilon_g = -0.25$ beyond which K_s must be smaller than K_g. Again, time-dependence has been neglected here for the sake of discussion. In reality, time-dependence may well be important. The observations necessary to quantify it are lacking from the 1985 survey.

The even larger curvatures in the Agulhas Current beyond its separation from the continental slope and in the Return Current, if accompanied by similar velocities (regrettably, there are no measurements of velocity at the sharp turns), would have ε_g

values much less than -0.25 and thus considerable cross-stream velocities, or considerable time-dependence.

5.5 Estimates of potential vorticity terms in the Agulhas from the 1985 hydrography

Having had a preliminary look at the curvature vorticity, now the other vorticity and potential vorticity terms are estimated as completely as possible from the 1985 observations. Recall from Eq. (5.1) that there are three vorticity terms: a Coriolis term f due to planetary rotation, a curvature term $K_s v'$, and an isopycnal shear term $\partial v'/\partial n'$. The planetary vorticity is just the sum of these three terms, weighted by the vertical separation of material surfaces, customarily indicated by the vertical gradient of a suitably conserved tracer. Estimates from the near-surface layer, where the two relative vorticity terms are largest, are discussed below and summarized in the conclusions to this chapter (Sec. 5.9).

The Coriolis parameter, f, is -9.0×10^{-5} s^{-1} at the mean latitude of the Retroflection region, 38°S. This value is equivalent to cross-stream isopycnal shear of -3.6 m s^{-1} over 40 km, the separation of cross-stream distance tic marks in Atlas sections of velocity, and to a radius of curvature at unit velocity R_1 of -11 km per 1 m s^{-1} (cyclonic <0, southern hemisphere).

The Coriolis parameter variation, δf over the latitude range occupied by the Retroflection during the 1985 survey, 34.5 - 41.5°S, is $\pm 0.08\,|f_o|$, where f_o is the Coriolis parameter in the middle of the latitude range. This variation in f is equivalent to cross-stream isopycnal shear of ± 0.28 m s^{-1} over 40 km, and to an R_1 of ± 36 km per 1 m s^{-1}.

Geostrophic velocity cross-stream isopycnal shear, $-\frac{\partial v'_g}{\partial n'}$, can be estimated only at the CTD transects. Anticyclonic isopycnal shear ($-\frac{\partial v'_g}{\partial n'} > 0$, n' pointing into the Retroflection) has an observed maximum on the warm, offshore side of the Agulhas at

transects A, B, and C, of 0.60 m s^{-1} over 40 km. This corresponds to a geostrophic shear Rossby number of -0.17. Anticyclonic isopycnal shear is smaller at transect D, corresponding to a Rossby number of -0.10.

Anticyclonic isopycnal shear cannot be reliably estimated at the Return Current transects E and F because stations at the warm northern ends of these transects were not taken consecutively. Very high values of apparent isopycnal shear are observed between the non-consecutive stations.

Cyclonic isopycnal shear, $-\frac{\partial v_g'}{\partial n'} < 0$, has an observed minimum above the ~1500 m isobath on the inshore side of the Agulhas at transect A, with a value of -1.5 m s^{-1} over 17 km (-3.5 m s^{-1} over 40 km), corresponding to a geostrophic shear Rossby number of 0.98. Unknown deepest common level (dcl) velocities may make a significant contribution to isopycnal shear here, since water depths range from 600 to 2100 m beneath the strongest cyclonic shear.

Geostrophic path curvature, K_g, can be estimated at 200 m from the 15 C temperature/200 m depth contour heading (Fig. 2.5). Path curvature varies from -0.046 km^{-1} (-70° over 30 km), in cyclonic meanders of the Agulhas Current along the continental slope, to +0.14 km^{-1} (130° over 20 km), where the Agulhas Return Current turns anticyclonically northeast toward the Agulhas Plateau. The radius of curvature, R_s, ranges from -∞ to -25 km and from +10 to +∞ km.

Geostrophic path curvature vorticity, $K_g v_g'$, can be estimated only at the intersection of transects B - F and the 15 C/200 m contour, where both K_g and v_g' can be estimated. Agulhas transects B and C are located at the crests of successive anticyclonic meanders, with fairly similar values of K_g andv_g' (see Sec. 5.4 above) giving a geostrophic curvature Rossby number of ε_g = -0.24. The path curves very gently at transect D, for a geostrophic curvature Rossby number of ~ 0.04. Path curvature at transects E and F is effectively zero.

At the sharpest turn in the path, where the Agulhas Return Current turns northeast towards the Agulhas Plateau, there is no way, unfortunately, to estimate velocity, not from a *CTD* transect nor even from the satellite sea surface temperature image.[2] If the velocity value from the intersection of transect E and the 15 C/200 m contour 350 km downstream were used (v_g' is 0.50 m s^{-1} there), ε_g would be -0.78.

The sum of the planetary vorticity, the curvature vorticity, and the isopycnal shear vorticity are all weighted by the vertical gradient of a suitably conserved tracer. If this gradient decreases (increases) following a fluid parcel, vortex tubes are stretched (squashed), which implies changes in the planetary or relative vorticity or external torques. Vortex stretching ($\partial w/\partial z$) is, through continuity, linked to horizontal divergence ($\partial u/\partial x + \partial v/\partial y$).

The Atlas contoured sections of planetary potential vorticity show the varying thickness of isopycnal sheets (the planetary vorticity gradient itself, β, makes only a small contribution). Where planetary potential vorticity values are low, vertical gradients are weak, and vortex tubes are relatively long. Strong gradients of vortex length are observed at upper levels across all the Agulhas and Agulhas Return Current transects, with relatively weakly stratified water observed within the Retroflection and more strongly stratified water observed on cold onshore side of the Agulhas, and on the cold southern side of the Return Current. A parcel's vortex length, like salinity, oxygen, and other tracers, is set initially in the surface mixed layers, with the thickest layers, the Mode Waters, coming from regions where deep convection occurs; the vortex length is then modified as it circulates by mixing, torques, and variations in absolute vorticity.

---

[2]Velocity estimates might, in principle, be derived from the off-15 C/200 m contour XBTs, but position errors, limited spatial data coverage, strong thermohaline interleaving across the Return Current, and the shallow maximum depth, 700 m for these XBTs, would introduce large uncertainties.

Significant isopycnal vortex length gradients are observed from sea surface isopycnals down to $\sigma_1 \sim 32.2$ (~1800 m) in the Agulhas Current, and down to $\sigma_0 \sim 27.2$ (~1200 m) in the Agulhas Return Current. The greater depth to which gradients extend in the Agulhas is due to contrasts between Indian origin water on the inshore side and Atlantic/Circumpolar origin water on the offshore side of the Current at Antarctic Intermediate Water and deep oxygen minimum levels.

The largest cross-stream gradients occur at the Subtropical Mode Water potential vorticity minimum level near 200 m depth, in both the Agulhas and Agulhas Return Currents. Planetary potential vorticity increases by up to a factor of 8 (*i.e.*, 6 contour intervals of $\sqrt{2}$ each) onshore across the Agulhas over a distance of 50 - 100 km. If a parcel were to traverse the front moving onshore at this level, in the absence of torques, it would acquire cyclonic planetary vorticity of $7f$!

The cyclonic isopycnal cross-stream shear at transect A is, recall, as strong as observed at any of the transects and as large as f. The potential vorticity due to cross-stream isopycnal shear at transect A is shown in Fig. 5.2; it may compared with the Atlas contoured section of planetary potential vorticity at transect A. The cross-stream gradients of the two quantities both increase onshore, with comparable magnitudes there. Thus tremendously strong potential vorticity changes accompany any cross-stream motion. Evidently, in the upper level Agulhas and Return Currents (where a similar if less intense arrangement is observed), potential vorticity conservation presents a formidable barrier to cross-frontal motion.

It appears that curvature potential vorticity variations following a fluid parcel can be balanced by small cross-frontal displacements. The curvature vorticity Rossby number varies along a geostrophic streamline from +0.3 to -0.8. At the level of the Subtropical Mode Water, where potential vorticity gradients are largest, this variation can be balanced by a cross-frontal displacement across one-seventh the total potential

vorticity gradient. This means that curvature vorticity can be balanced by cross-frontal parcel displacements of one-seventh of the front width, *i.e.*, 20 km displacements across a 140 km wide front, if we use a linear gradient as an approximation. Vertical excursions of ~100 m along isopycnals sloping up by ~700 m would be associated with parcels experiencing such cross-frontal displacements. Indeed, vertical excursions of this type (upward and onshore in meander crests, downward and offshore in meander troughs) have been measured directly using quasi-isopycnal floats in the in the Gulf Stream *(Bower, 1988).* And *Chew (1974)* notes that for dynamical reasons curvature and shear vorticity tend to offset each other, as they do here, with anticyclonic meanders moving onshore into a higher cyclonic shear region (and shorter vortex lengths).

5.6 Agulhas and Agulhas Return Current instability – I. Baroclinic conditions

Instabilities of ocean currents have been subjected to extensive theoretical study, including the work of *Gill* et al. *(1974), Robinson* et al. *(1975), Talley (1982),* and many others. Here, *Johns's (1988)* recent paper, which includes a good review of previous work, is taken as a starting point.

Johns, following the work of *Bryden (1979)* and *Wright (1981)* in the Drake Passage, compared the results of a simple baroclinic instability model to dispersion relations and growth rates of Gulf Stream meanders, estimated from inverted echo sounder (IES) time-series observations of thermocline depth. The model is linear, one-dimensional, purely baroclinic, and confined to a channel, with quasi-geostrophic scaling; the equations are by now standard and will not be reproduced here. The limited correspondence between solutions to this one-dimensional (z only) model, solutions to layered models, and solutions to a fully two-dimensional (y, z) model have been noted by *Killworth (1980).* However, since the model still seems to have been useful in

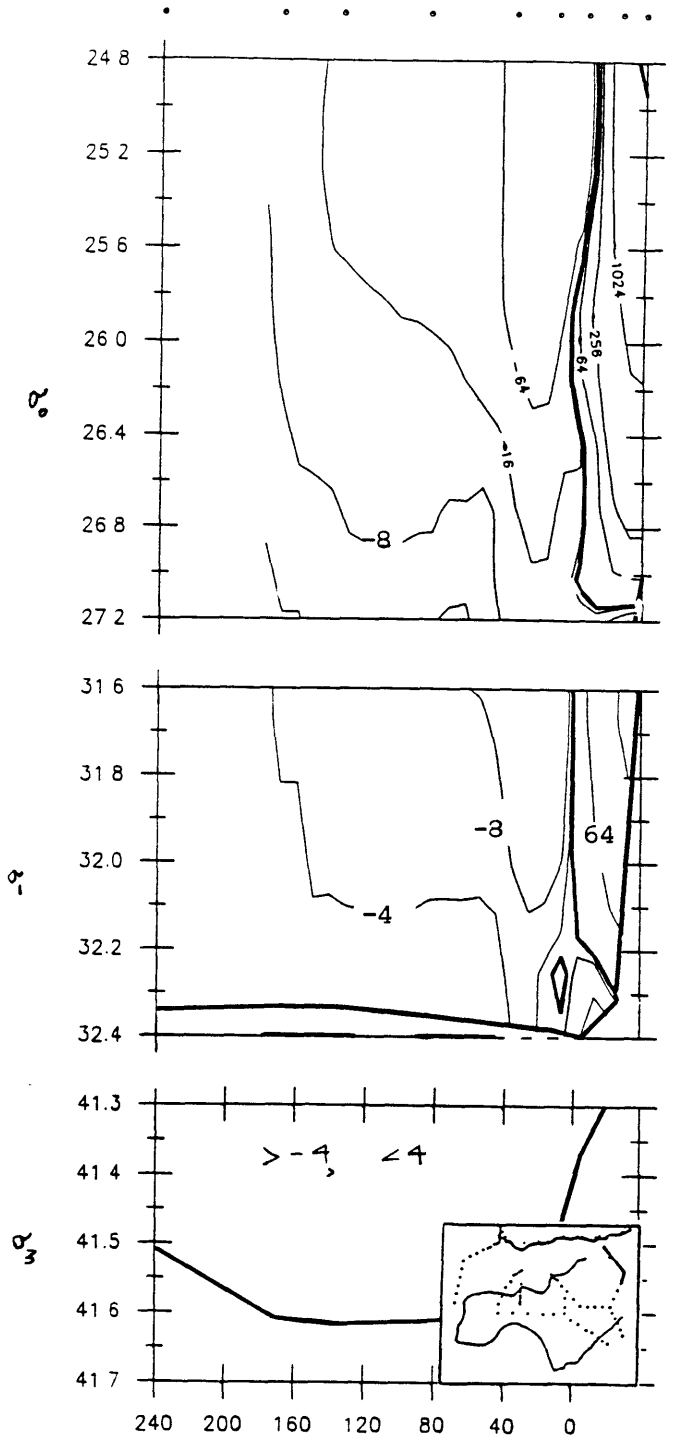

Fig. 5.2 – Buoyancy potential vorticity due to cross-stream isopycnal shear, $\frac{\partial v'}{\partial n'}\frac{N^2}{g}$, at the most upstream Agulhas Current transect, transect A (transect location shown on tiny map). The reader should compare this figure to the transect A contoured section of planetary buoyancy potential vorticity shown in the Atlas. Units here, as in the Atlas, are 10^{-12} m^{-1} s^{-1}. Here cyclonic potential vorticity values are greater than zero, and anticyclonic values are less than zero (opposite from Atlas). Cyclonic values seen here are the largest of the 1985 survey.

understanding time-series observations in the Gulf Stream and in the Drake Passage, it seems worthwhile to compute the model input profiles for the Agulhas, in anticipation of their use in modelling forthcoming time-series observations in the Agulhas [*e.g.* the 1985-7 Retroflection current meter observations of *Luyten (pers. comm.)*].

The Agulhas and Gulf Stream velocity and mean potential vorticity gradient (Q_y) profiles are remarkably similar. The Agulhas Q_y profiles are even more similar to a synthetic profile whose instability characteristics *Johns* explored, so intelligent speculation on the likely results of a linear baroclinic model solved for realistic Agulhas profiles is possible. Comparison of these speculations with time-series observations in the Agulhas will soon be possible using the 1985-7 current meter records now being analyzed by *Luyten (pers. comm.)*

The model's input profiles are the mean (averaged in y) geostrophic velocity U, the mean buoyancy frequency squared N^2, and mean cross-stream gradient of the basic state potential vorticity, $Q_y = \beta - U_{yy} - \frac{\partial}{\partial z}\left(\frac{f^2}{N^2}U_z\right)$. As *Johns* notes, the last, baroclinic, term of Q_y corresponds to vertical gradients of isopycnal slope, using thermal wind to get $\frac{\partial}{\partial z}\left(\frac{f^2}{N^2}U_z\right) = \frac{\partial}{\partial z}\left(f\,\frac{\partial z}{\partial y}\Big|_\rho\right)$.

Note that the U_{yy} (barotropic) term is neglected in the y-averaged problem. *Johns* points out that for a parabolic jet profile, U_{yy} is proportional to $-\bar{U}(z)$ and has its largest magnitude, of $O(-4 \times 10^{-10}\ m^{-1}\ s^{-1})$ for a Gulf Stream with 50 km half-width, near the surface. The U_{yy} term thus shifts the Q_y profile in the negative direction everywhere, most near the surface; as the various profiles in the Gulf Stream and the Agulhas will show, this does not change the basic structure of Q_y very much. Note that these remarks apply only to Q_y across the intense, central part of the jet: the barotropic term across the entire Agulhas jet is briefly discussed in Section 5.8.

It must be noted that the relative importance of barotropic and baroclinic mechanisms in producing current fluctuations cannot be assessed from linear, pure baroclinic or pure barotropic models and hydrographic data alone; this question must be addressed with more sophisticated models and time-series observations. It should also be noted that, as always, the potential vorticity gradient profiles called for by the models and the observed profiles are not necessarily the same thing: the observed profiles may be contaminated by the instability processes to some degree, relative to the model profiles. All that can be said is that the observed profiles give some indication of the potential for further instability.

The necessary conditions for instability are:

(1) Q_y changes sign between the top and bottom boundaries;
(2) Q_y at some level has the opposite sign from U_z at the surface; or
(3) Q_y at some level has the same sign as $U_z\,(1 - h_y^*)$ at the bottom, where h_y^* is the ratio of bottom slope h_y to the slope of deep isopycnals.

The Gulf Stream profiles are reproduced here as Fig. 5.3 (*John's* Fig. 1). All three of the necessary conditions are met in the Gulf Stream since Q_y changes sign. *Johns* notes that that the instabilities produced by the model are basically interior in type [necessary condition *(1)*], since their steering levels fall in the 600 - 1500 m range, far from the top and bottom boundaries, so the boundary terms that give rise to necessary conditions *(2)* and *(3)* make relatively small contributions. Note also that β is negligible, since it is as much as two orders of magnitude smaller than the baroclinic term of Q_y.

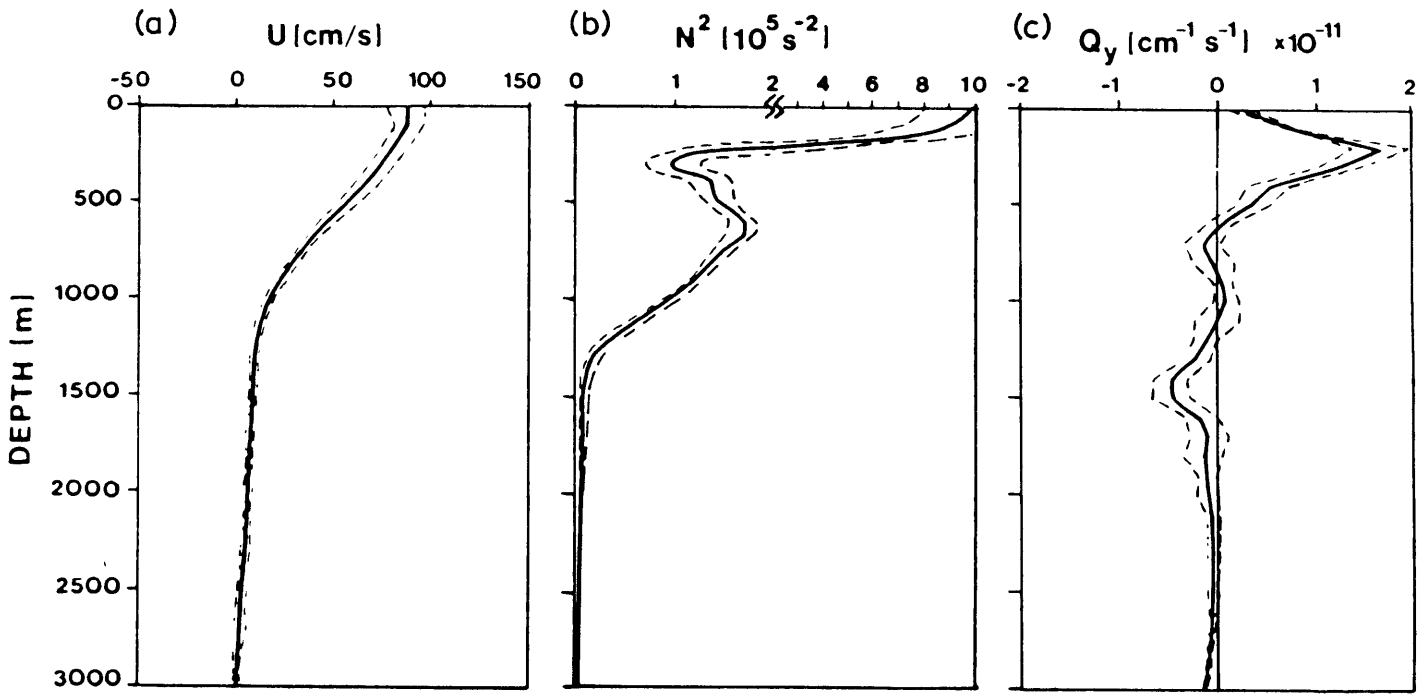

Fig. 5.3 – Laterally-, ensemble-averaged profiles across the Gulf Stream of: *(a)* velocity, U; *(b)* Brunt-Väisäla frequency squared, N_2, *(c)* potential vorticity gradient, Q_y. This is a reproduction of *Johns (1988)* Fig. 1.

The Agulhas and Agulhas Return Current profiles[3] of u, u_z, N^2, $f\frac{\partial z}{\partial y}|_\rho$, and Q_y are shown in Fig. 5.4 - 5.15. Agulhas and Agulhas Return Current Q_y profiles are shown at each current transect (Fig. 5.4 - 5.7) averaged laterally on *(1)* depth surfaces (solid Q_y curves) plotted *vs.* depth, and *(2)* potential density surfaces (gray Q_y curves) plotted *vs.* mean isopycnal depths. The depth-averaged and density-averaged Q_y profiles are generally similar in shape, but since the density-averaged curves give better resolution in the upper water column and less noise in the lower water column, they are used for the discussion that follows. Some of the differences between the two types of curves, especially the greater noise in the deep depth-averaged curves are the result of the necessarily different vertical smoothing schemes: the depth-averaged curves were smoothed using a Gaussian of constant width in depth units, while the density-averaged curves were smoothed by averaging into potential density bins of constant width in density units, within each potential density parameter (σ_o, σ_1, σ_3) range; this effectively smooths over a larger depth interval when stratification is small. The relationship between the shape of the profiles and the local Mode Waters is discussed briefly in the next section.

The Agulhas and Agulhas Return Current Q_y profiles all change sign at least once, thereby meeting the necessary conditions for baroclinic instability. In fact, there is

---

[3]The stations used in the averages are:

Transect	Stations	
A	272 - 277	
B	260 - 257	
C	293/5/7/8	(intervening stations end at mid-depth)
D	247 - 243	
E	284 - 287	
F	282 - 279	

Stations that bracketed significant downstream transport were included. Profiles are plotted with east positive, so $U<0$ in the Agulhas Current and $U>0$ in the Return Current and in the Gulf Stream. Note that the problem is symmetric in x in the Agulhas and Gulf Stream, since β is negligible.

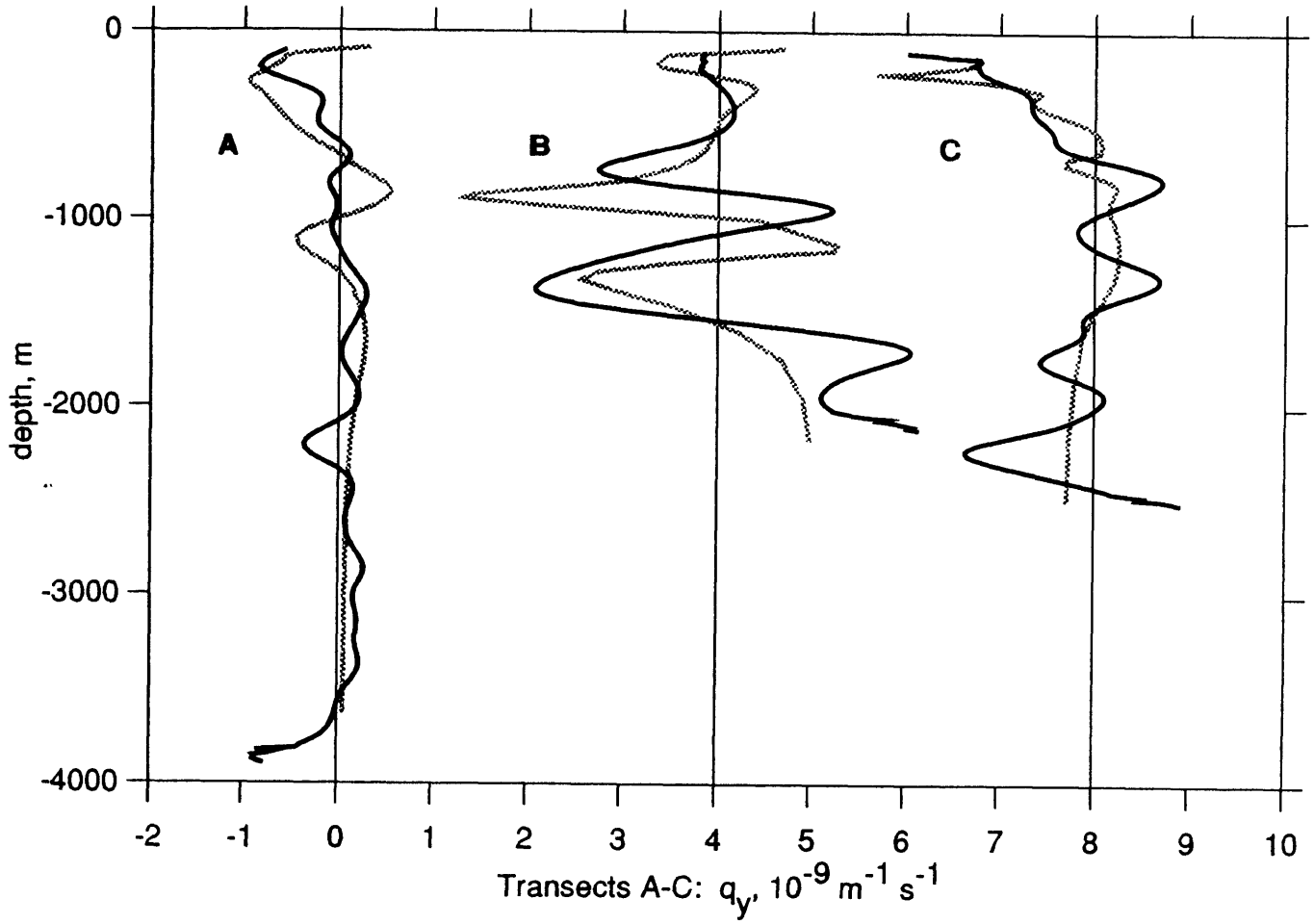

Fig. 5.4 – Potential vorticity gradient, Q_y, across the Agulhas Current at transects A, B, and C. Solid curves - averaged on depth surfaces; gray curves - averaged on potential density surfaces (σ_o between 0 and ~700 m, σ_1 between 700 and 2000 m, and σ_3 between 2000 m and the bottom). Curves are offset incrementally in the x direction by 4×10^{-9} m^{-1} s^{-1}.

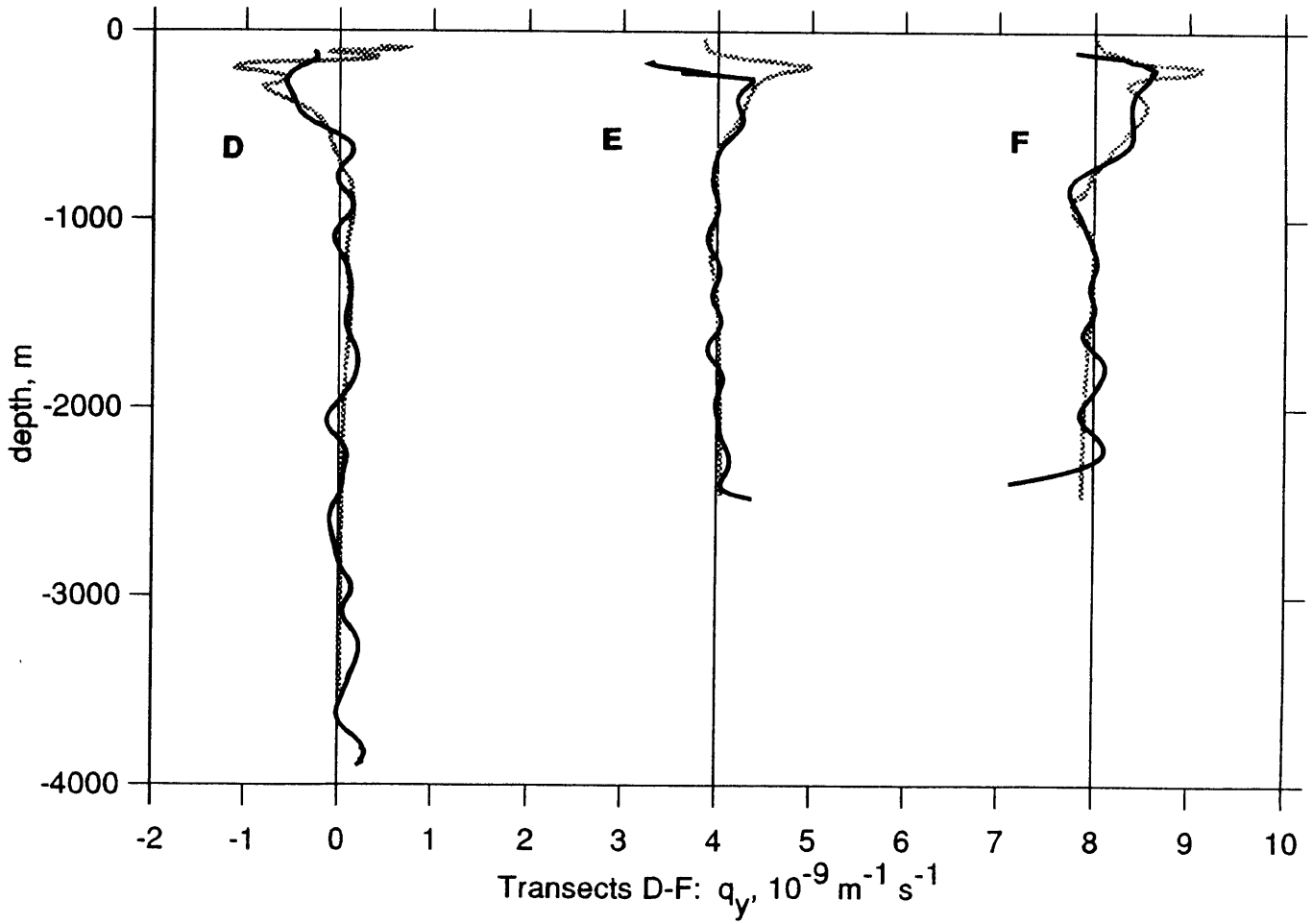

Fig. 5.5 – Potential vorticity gradient, Q_y, across the Agulhas Current at transect D, and the Agulhas Return Currents at transects E, and F. Solid curves - averaged on depth surfaces; gray curves - averaged on potential density surfaces (σ_o between 0 and ~700 m, σ_1 between 700 and 2000 m, and σ_3 between 2000 m and the bottom). Curves are offset incrementally in the x direction by 4×10^{-9} m^{-1} s^{-1}.

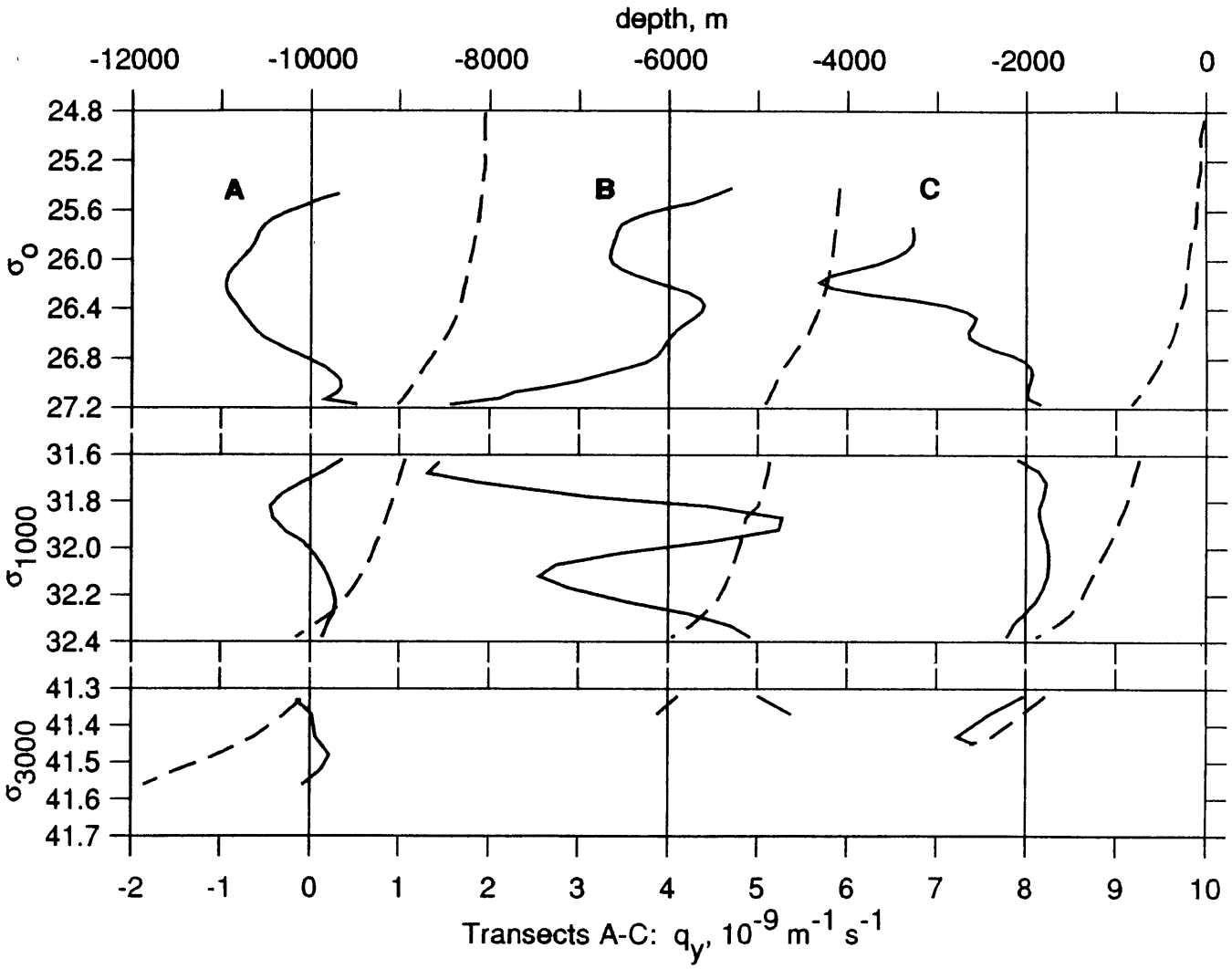

Fig. 5.6 – Potential vorticity gradient, Q_y, (solid curves) and depth of isopycnals (dashed curves), averaged across the Agulhas Current at transects A, B, and C, plotted as a function of potential density. Curves are offset incrementally in the x direction by 4×10^{-9} m^{-1} s^{-1}.

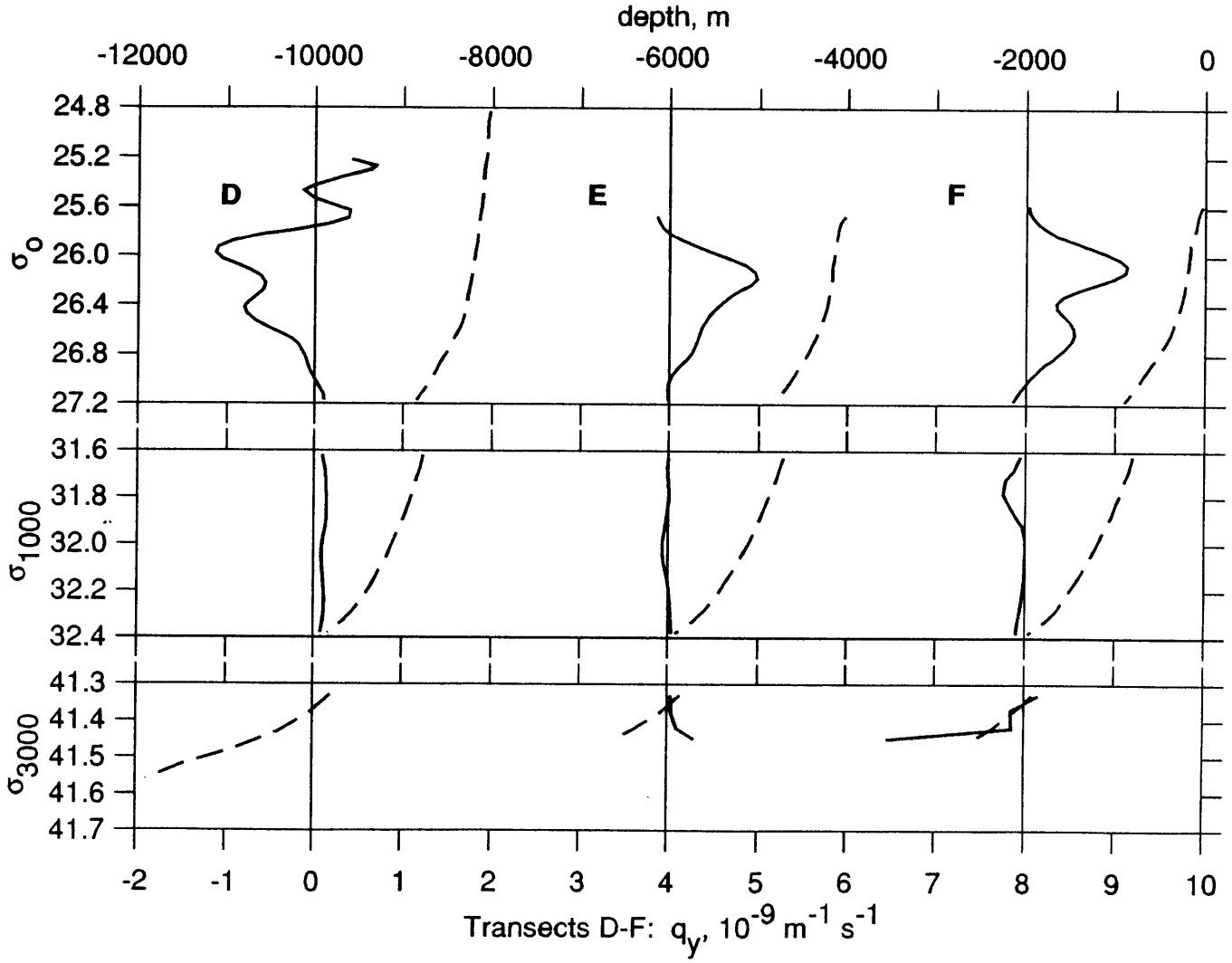

Fig. 5.7 – Potential vorticity gradient, Q_y, (solid curves) and depth of isopycnals (dashed curves), averaged across the Agulhas Current at transect D and the Agulhas Return Current at transects E and F, plotted as a function of potential density. Curves are offset incrementally in the x direction by 4×10^{-9} m^{-1} s^{-1}.

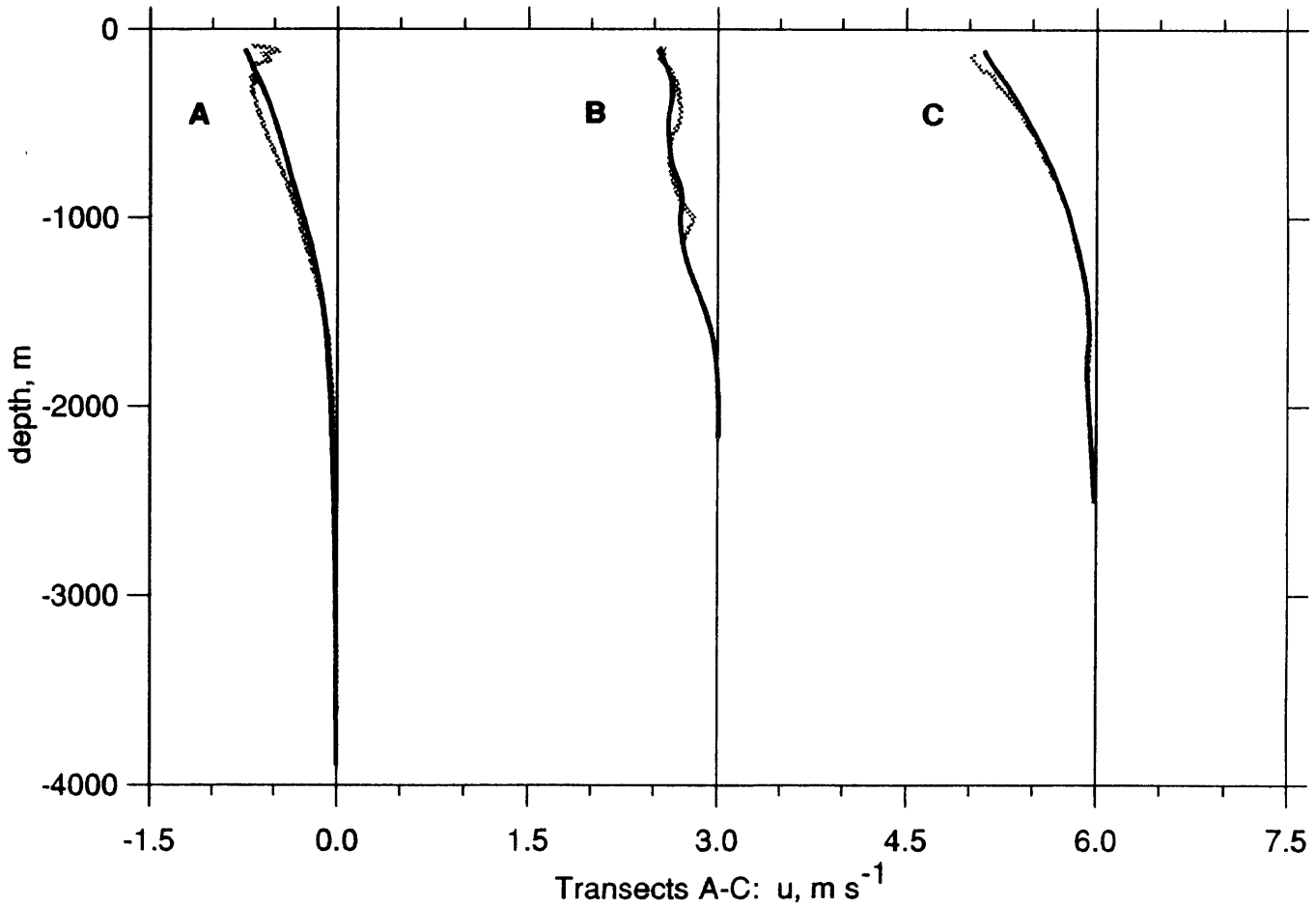

Fig. 5.8 – Velocity, u, averaged across the Agulhas Current at transects A, B, and C. Solid curves - averaged on depth surfaces; gray curves - averaged on potential density surfaces (σ_0 between 0 and ~700 m, σ_1 between 700 and 2000 m, and σ_3 between 2000 m and the bottom). Curves are offset incrementally in the x direction by 3 m s^{-1}.

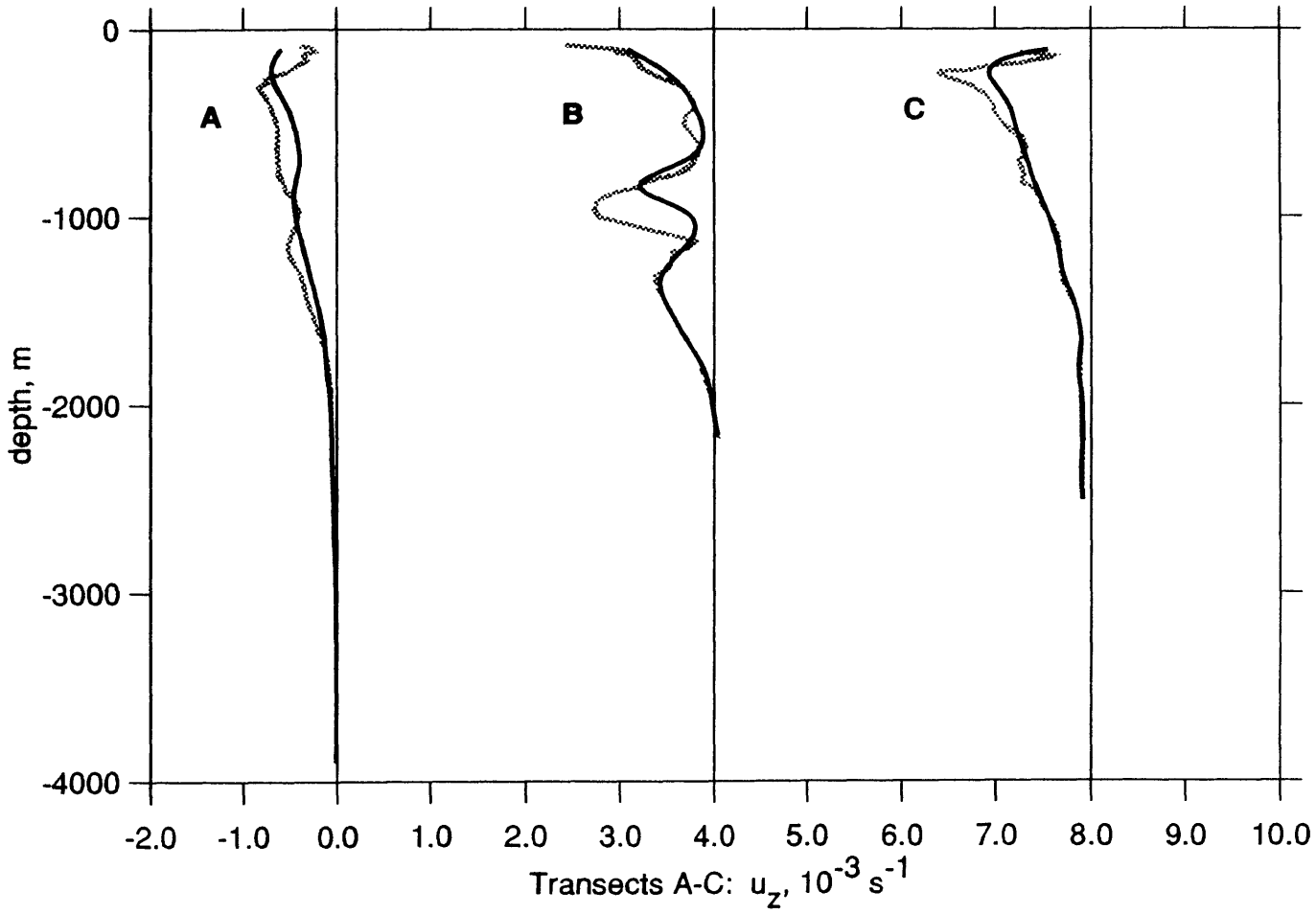

Fig. 5.9 – Vertical shear of velocity, u_z, averaged across the Agulhas Current at transects A, B, and C. Solid curves - averaged on depth surfaces; gray curves - averaged on potential density surfaces (σ_0 between 0 and ~700 m, σ_1 between 700 and 2000 m, and σ_3 between 2000 m and the bottom). Curves are offset incrementally in the x direction by 4×10^{-3} s^{-1}.

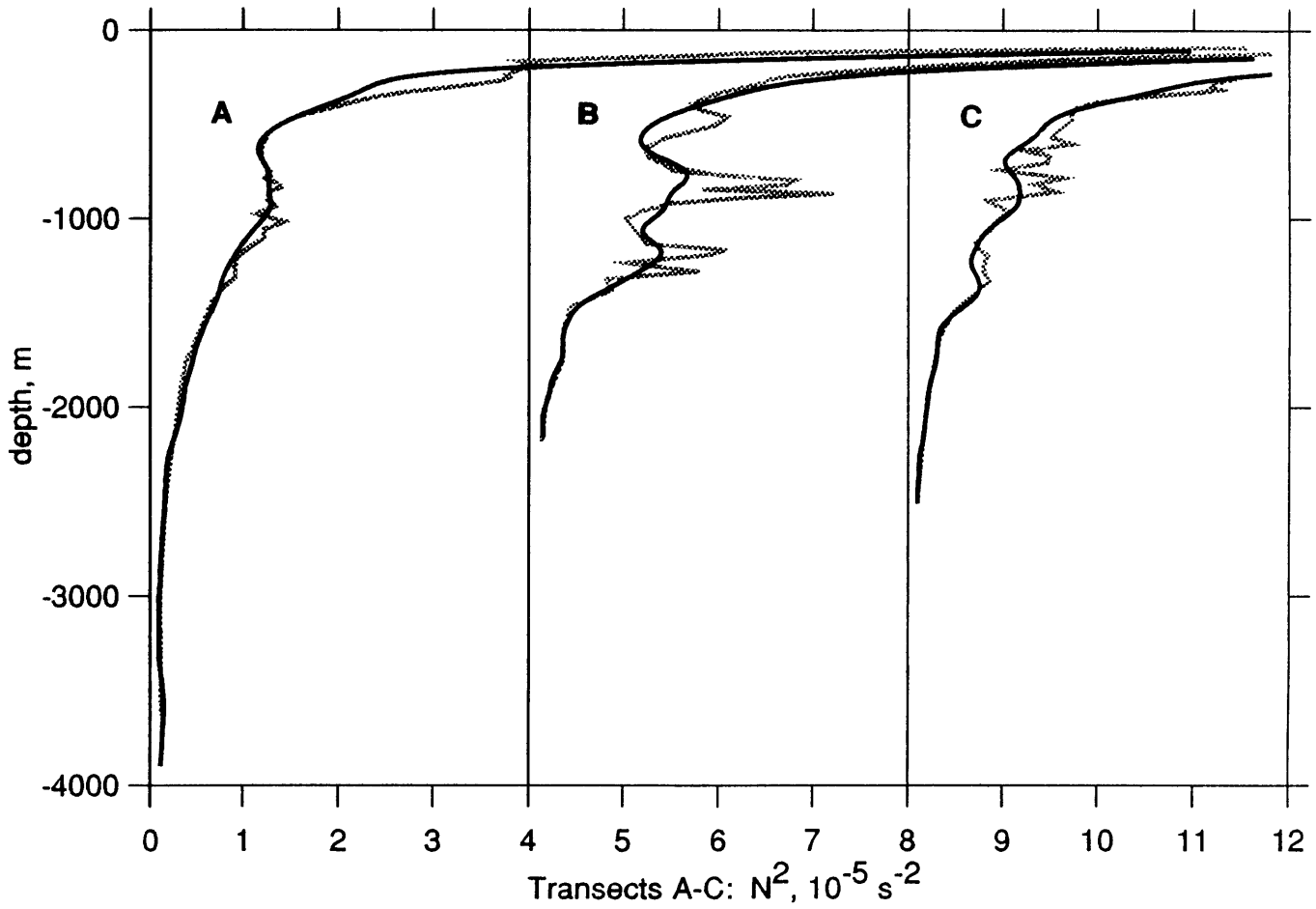

Fig. 5.10 – Brunt-Väisäla frequency squared, N^2, averaged across the Agulhas Current at transects A, B, and C. Solid curves - averaged on depth surfaces; gray curves - averaged on potential density surfaces (σ_o between 0 and ~700 m, σ_1 between 700 and 2000 m, and σ_3 between 2000 m and the bottom). Curves are offset incrementally in the x direction by 4×10^{-5} s^{-2}.

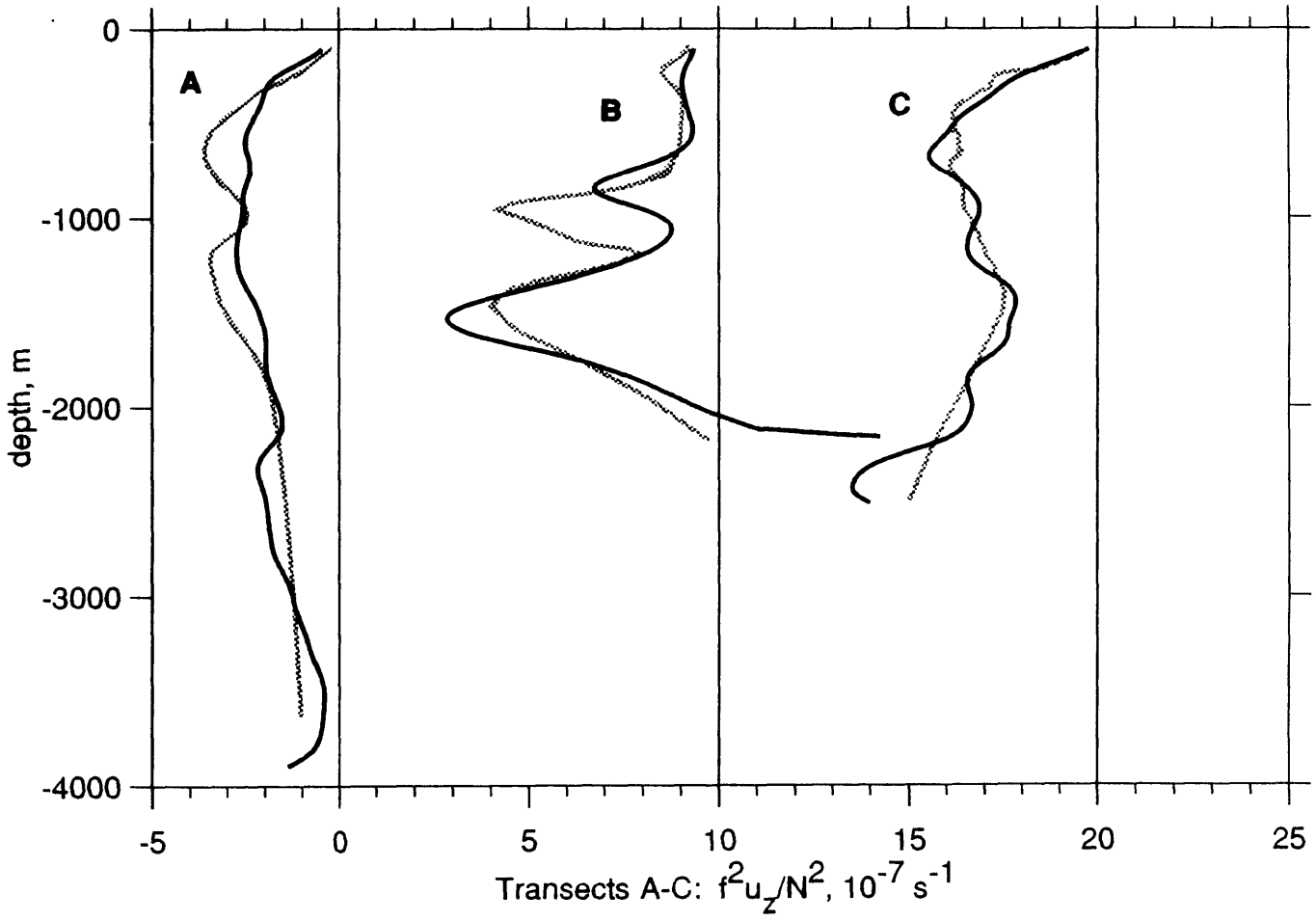

Fig. 5.11 – Isopycnal slope times f, $f^2 u_z/N^2$, across the Agulhas Current at transects A, B, and C. Solid curves - averaged on depth surfaces; gray curves - averaged on potential density surfaces (σ_o between 0 and ~700 m, σ_1 between 700 and 2000 m, and σ_3 between 2000 m and the bottom). Curves are offset incrementally in the x direction by 10×10^{-7} s^{-2}.

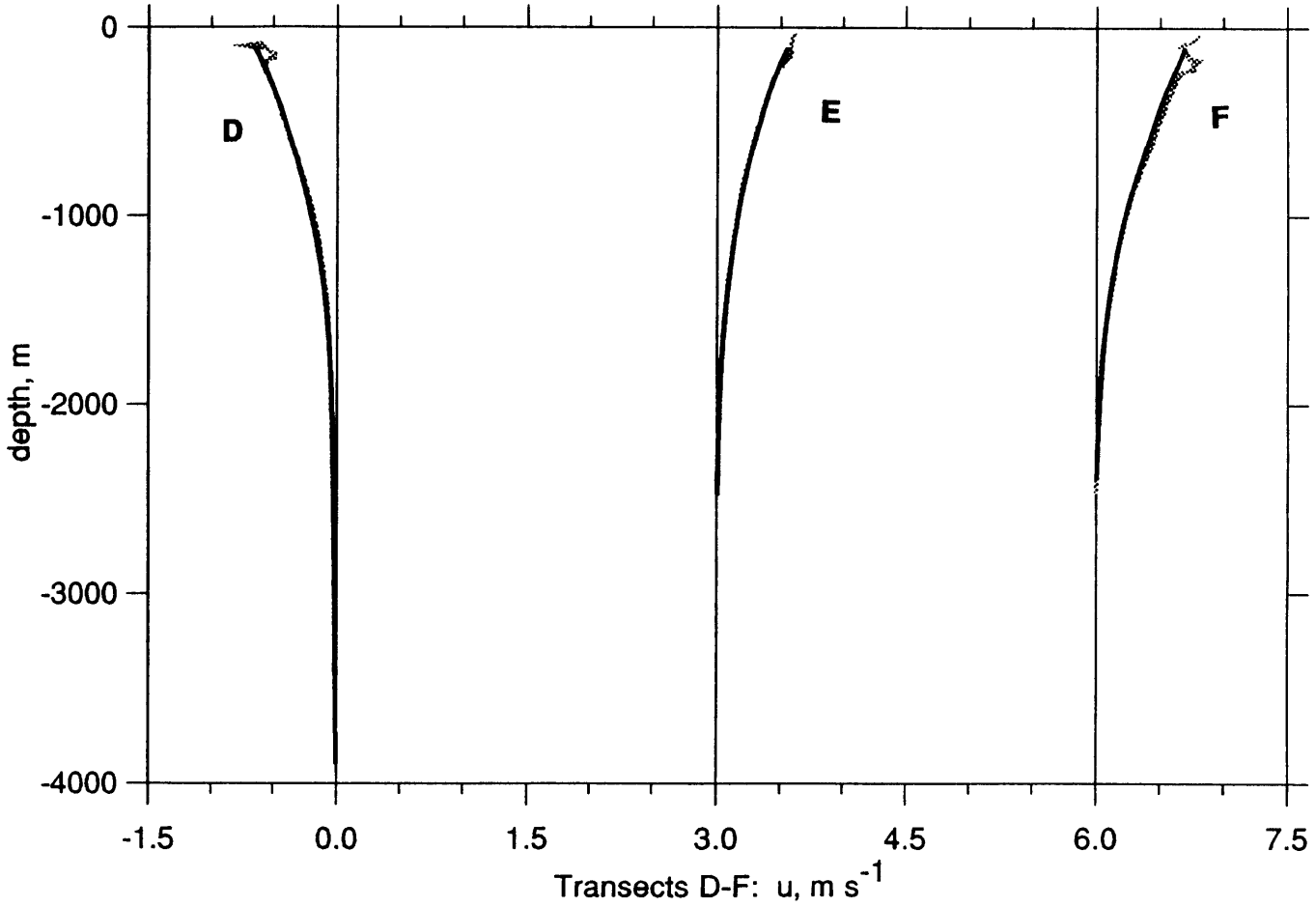

Fig. 5.12 – Velocity, u, averaged across the Agulhas Current at transect D and the Agulhas Return Currents at transects E, and F. Solid curves - averaged on depth surfaces; gray curves - averaged on potential density surfaces (σ_o between 0 and ~700 m, σ_1 between 700 and 2000 m, and σ_3 between 2000 m and the bottom). Curves are offset incrementally in the x direction by 3 m s^{-1}.

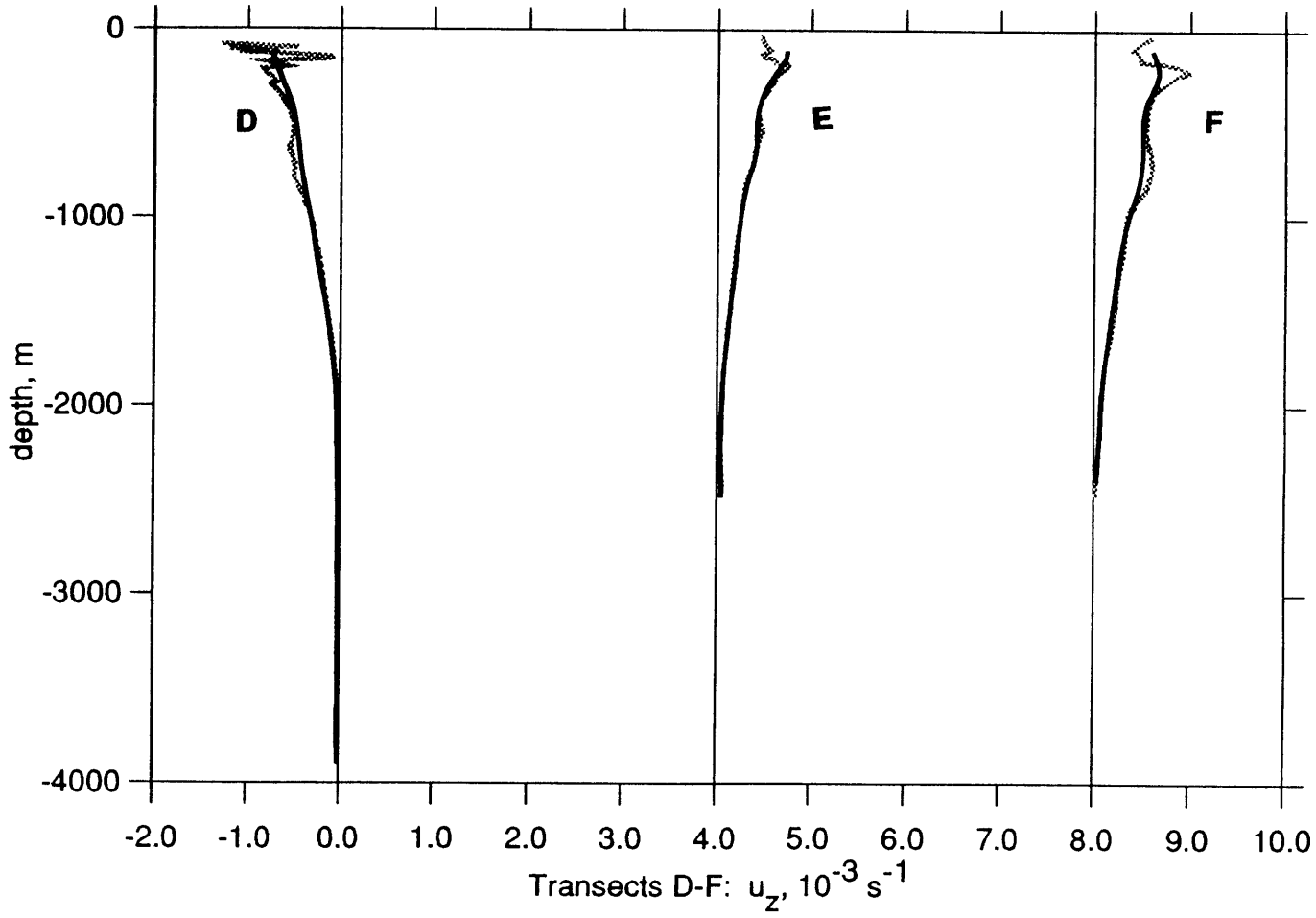

Fig. 5.13 – Vertical shear of velocity, u_z, averaged across the Agulhas Current at transect D and the Agulhas Return Currents at transects E, and F. Solid curves - averaged on depth surfaces; gray curves - averaged on potential density surfaces (σ_0 between 0 and ~700 m, σ_1 between 700 and 2000 m, and σ_3 between 2000 m and the bottom). Curves are offset incrementally in the x direction by 4×10^{-3} s^{-1}.

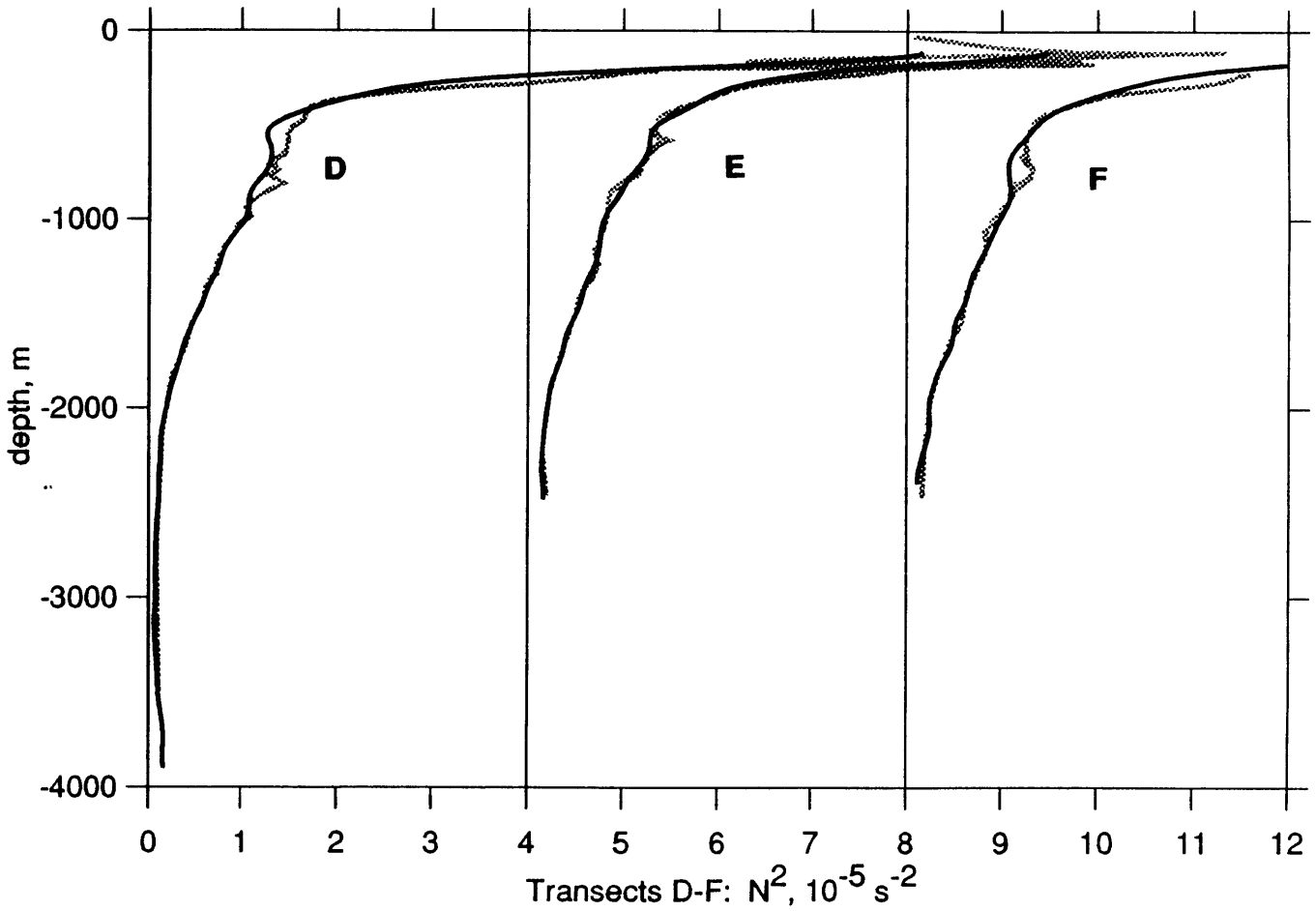

Fig. 5.14 – Brunt-Väisäla frequency squared, N^2, averaged across the Agulhas Current at transect D, and the Agulhas Return Currents at transects E, and F. Solid curves - averaged on depth surfaces; gray curves - averaged on potential density surfaces (σ_0 between 0 and ~700 m, σ_1 between 700 and 2000 m, and σ_3 between 2000 m and the bottom). Curves are offset incrementally in the x direction by 4×10^{-5} s^{-2}.

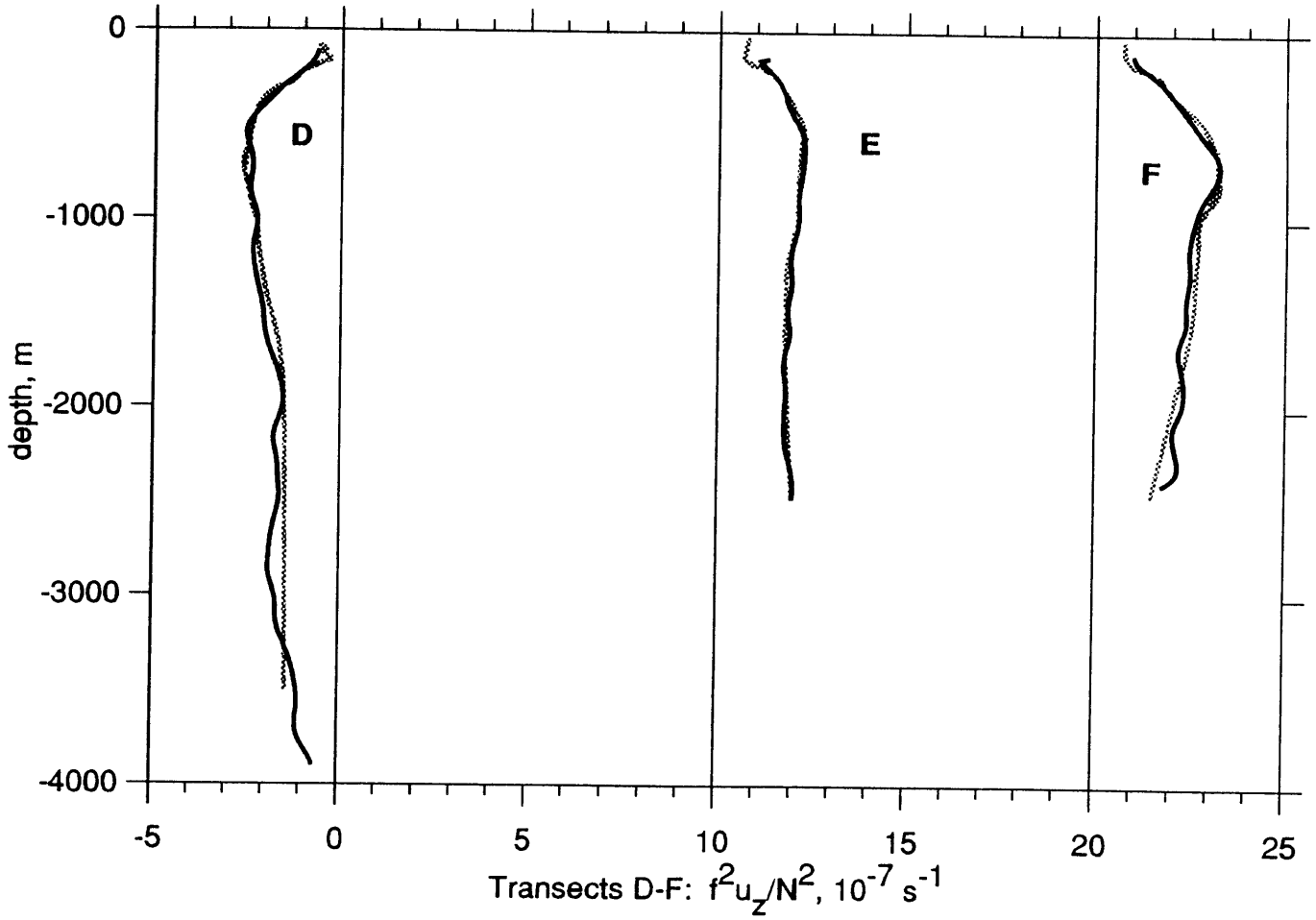

Fig. 5.15 – Isopycnal slope times f, f^2u_z/N^2, across the Agulhas Current at transect D, and the Agulhas Return Currents at transects E, and F. Solid curves - averaged on depth surfaces; gray curves - averaged on potential density surfaces (σ_0 between 0 and ~700 m, σ_1 between 700 and 2000 m, and σ_3 between 2000 m and the bottom). Curves are offset incrementally in the x direction by 10×10^{-7} s^{-1}.

remarkable similarity in overall shape between the Gulf Stream, Agulhas, and Agulhas Return Current Q_y profiles - except for the Agulhas Current transect B profile, which is wildly different. This is hardly surprising, given that the Current at transect B displays numerous other radical differences from current structure at all the other transects: the current at transect B is displaced far up onto the upper slope, has much reduced transport, and displays related changes in physical structure and tracer fields (see Chs. 3 and 4).

Each of the similar profiles has: *(1)* positive Q_y increasing with depth, taking the downstream direction as positive, from near the surface to about 200 m; *(2)* positive Q_y decreasing with depth between 200 m and a remarkably consistent zero crossing level of 650 m in the Agulhas and 600 m in the Gulf Stream; and *(3)* negative Q_y between 600 - 650 m and at least 1500 m, except for a weak positive lobe near 1000 m in the Gulf Stream whose ±1 standard deviation envelope grazes the z-axis. The zero crossing the Agulhas at 650 m in the depth-averaged appears slightly deeper at 700 m in the plots of Q_y averaged on isopycnals and average isopycnal depth (Fig. 5.6 and 5.7).

The greatest differences between the Gulf Stream and the Agulhas/Agulhas Return Currents profiles are *(1)* the pronounced negative bump in the Gulf Stream Q_y profile near 1500 m, which is not seen in the Agulhas profiles, and *(2)* the definitely negative values everywhere between 1500 and 3000 m in the Gulf Stream, where both positive and negative values seem equally likely in the Agulhas. The origin of the negative Q_y bump in the Gulf Stream is discussed in the next section.

The instability model gives growth rate peaks at three distinct frequencies for the Gulf Stream profiles. *Johns* also ran the model for a synthetic profile corresponding to the mean Gulf Stream Q_y profile minus its standard deviation, in which the weak positive Q_y values near 1000 m is eliminated, as it is in the Agulhas. For this Agulhas-

like profile (except for the deep Q_y values, which are still more negative than in the Agulhas), the model gives a single broad peak in growth rate, corresponding to steering levels anywhere between the Q_y zero crossing and 1800 m or so. The dispersion curves for the mean Gulf Stream profile and for a one-zero-crossing profile are reproduced here as Fig. 5.16 (*Johns's* Fig. 3). The effects of a deep (>1500 m) zero crossing to positive Q_y values, as seen on the transect C and F Q_y profiles, was not explored by *Johns*. He found that changing the channel width (here 150 km), an external parameter imposed upon the linear baroclinic model, shifted the results in wavenumber space, otherwise having little effect.

For the Agulhas-like profile, along-stream wavelengths range from 250 km to 650 km at the broad growth rate peak of about 0.12 d^{-1} at frequencies from 0.15 to 0.055 cpd (Fig. 5.16). Observed Return Current meander wavelengths are about 600 km (see, for example, Fig. 2.10, Agulhas Return Current paths traced from satellite images), within the model range. What role baroclinic instability really plays in these meanders is an open question, particularly at and in the lee of the Agulhas Plateau, where topographic Rossby waves are possible *(Harris and Bang, 1974)*. Growth rate and phase speed are quite sensitive to h_y^* (the ratio between bottom slope and deep isopycnal slope), especially at lower frequencies, with decreasing bottom slope tending to give faster growth rates and phase speeds. The dispersion curves shown here are all for $h_y^* = 2$, *i.e.*, bottom slope twice that of deep isopycnals. This is much too small for the Agulhas at transects C - E, and too large at transect F. The sensitivity to bottom slope could make this type of model hard to use in the Agulhas, where bottom slope encountered by the current varies strongly as the current meanders.

The possible effects of the Retroflection curvature should be mentioned. Rings tend to be stabilized relative to a jet with the same cross-stream Q gradients, because an integral number of unstable modes must fit around the ring - so long as the ring is

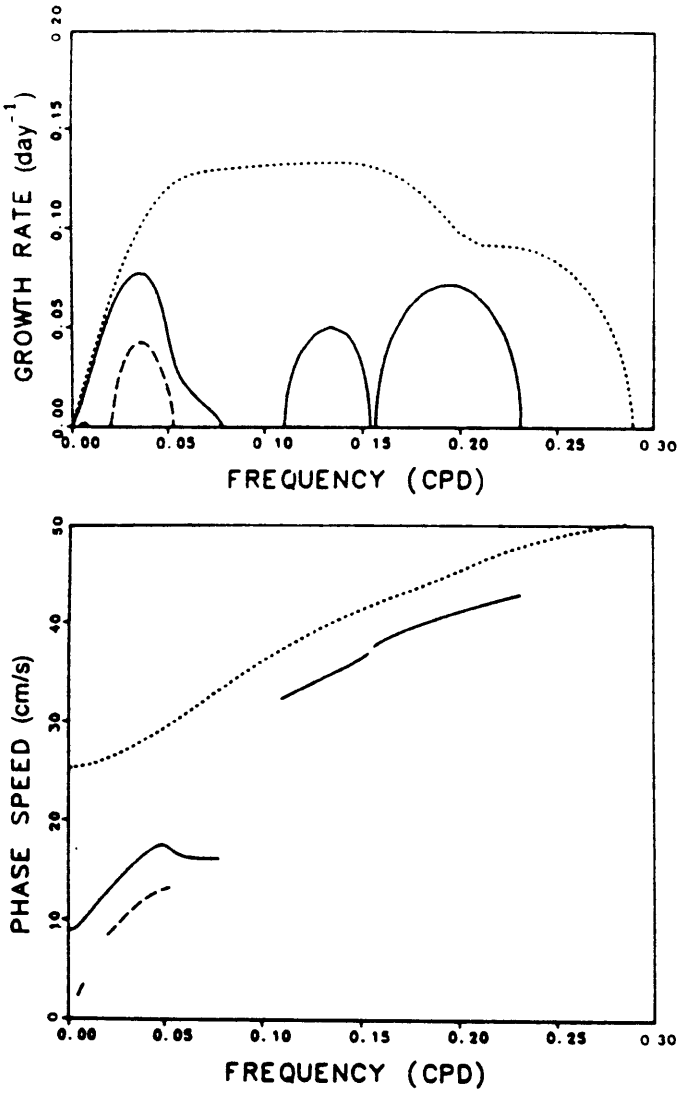

Fig. 5.16 – Reproduction of *Johns's* Fig. 3: dispersion diagram for the Gulf Stream profiles shown above in Fig. 5.3, with channel width $2L$ = 150 km and $h_y^* = 2$. The upper panel shows growth rate kc_i and the lower panel the phase speed as a function of frequency. Solid lines correspond to the mean ($\bar{x}$) Gulf Stream profiles, dotted lines to the left-hand ($\bar{x}$ - s) profile, and dashed lines to the right-hand ($\bar{x}$ + s) profile; s is the standard deviation. The dotted line, which has positive values of Q_y only down to about 600 m, is probably the most relevant to the Agulhas. The other profiles have positive values deeper into the water column, which seems to limit the growth of higher frequency waves.

small enough that information can propagate around the ring in good time to quantize the instability; a small instability on a large ring will simply see the ring as a front *(Pedlosky, 1985)*. In any case, the Retroflection curvature cannot affect the instability problem in this particular way, since the Retroflection is an open, U-shaped structure, not a closed ring.

To summarize, similar Q_y profiles are evident in the Gulf Stream, the separated Agulhas Current, and the Agulhas Return Current: the Q_y profiles are all positive above 600 m or so, and mostly negative below, with comparable magnitudes through most of the water column. These profiles meet all three necessary conditions for instability since Q_y changes sign at 600 m, with the interior condition seeming to be most important.

Johns's numerical solutions to the linear one-dimensional baroclinic problem using the Gulf Stream Q_y and related profiles appear to be directly relevant to the Agulhas. For a Q_y curve similar to the Agulhas's in structure (i.e., with a single zero crossing at the correct level), wavelengths and phase speeds at the broad peak in fastest growing waves match observed Return Current meander characteristics. It would be worthwhile to check these preliminary results by redoing *Johns's* calculation with the Agulhas profiles, including an examination of different deep Q_y values, the effect of another Q_y zero crossing in deep water, with different bottom slopes. The best test of the model will be a comparison with time-series observations in the Agulhas for fluctuations corresponding to the instabilities predicted by the model.

5.7 *Sloping isopycnals, local Mode Waters, and the mean baroclinic potential vorticity gradient*

The original motivation for computing density-averaged Q_y profiles was an interest in *(1)* the effect of large vertical excursions of isopycnals on the Q_y profile, and

in *(2)* the relationship between the Q_y profile and water masses, in particular the low N^2 Mode Waters. These Q_y profiles are evidently the first computed by averaging along isopycnals for any ocean current, although plots of potential vorticity on potential density or potential temperature surfaces are now usual (*e.g. McCartney, 1982, Watts, 1983, and Hall, 1985).*

The effect of vertical excursions of isopycnals is of interest because the quasi-geostrophic scaling of the linear baroclinic model formally requires that such vertical excursions be much less than the thermocline depth - which is clearly not the case in Drake Passage, the Gulf Stream and the Agulhas and Agulhas Return Currents. *Johns* and *Wright* both assumed that large isopycnal excursions did not matter much to the instability problem. The overall similarity between the depth-averaged and density-averaged profiles in the Agulhas and Agulhas Return Currents provides the first direct observation confirmation that the mean Q_y profile can be estimated adequately while ignoring large isopycnal excursions. This does not, however, guarantee that other aspects of the instability process are equally insensitive to the excursions.

The density-averaged profiles reveal an interesting relationship between the Agulhas and Agulhas Return Currents' Q_y profiles and the Subantarctic Mode Water. The change in the sign of Q_y occurs at or below this layer: isopycnal tilts increase with depth (Q_y positive) above and in the SAMW, and then decrease with depth (Q_y negative) below it. The characteristics of the Subantarctic Mode Water core are $\sigma_o = 26.74 \pm 0.17$, $s = 34.9 \pm 0.28$ psu, $\theta = 10.9 \pm 2.1$ C, and it is found at depths ranging from 250 m to 800 m.

The relationship between maximum isopycnal slope and the base of the SAMW is also evident in a plot of the pressure variation on isopycnals taken for all stations of the 1985 survey (Fig. 5.17), which shows the largest pressure variation on the $\sigma_o = 26.9$ isopycnal, across the various current and ring transect.

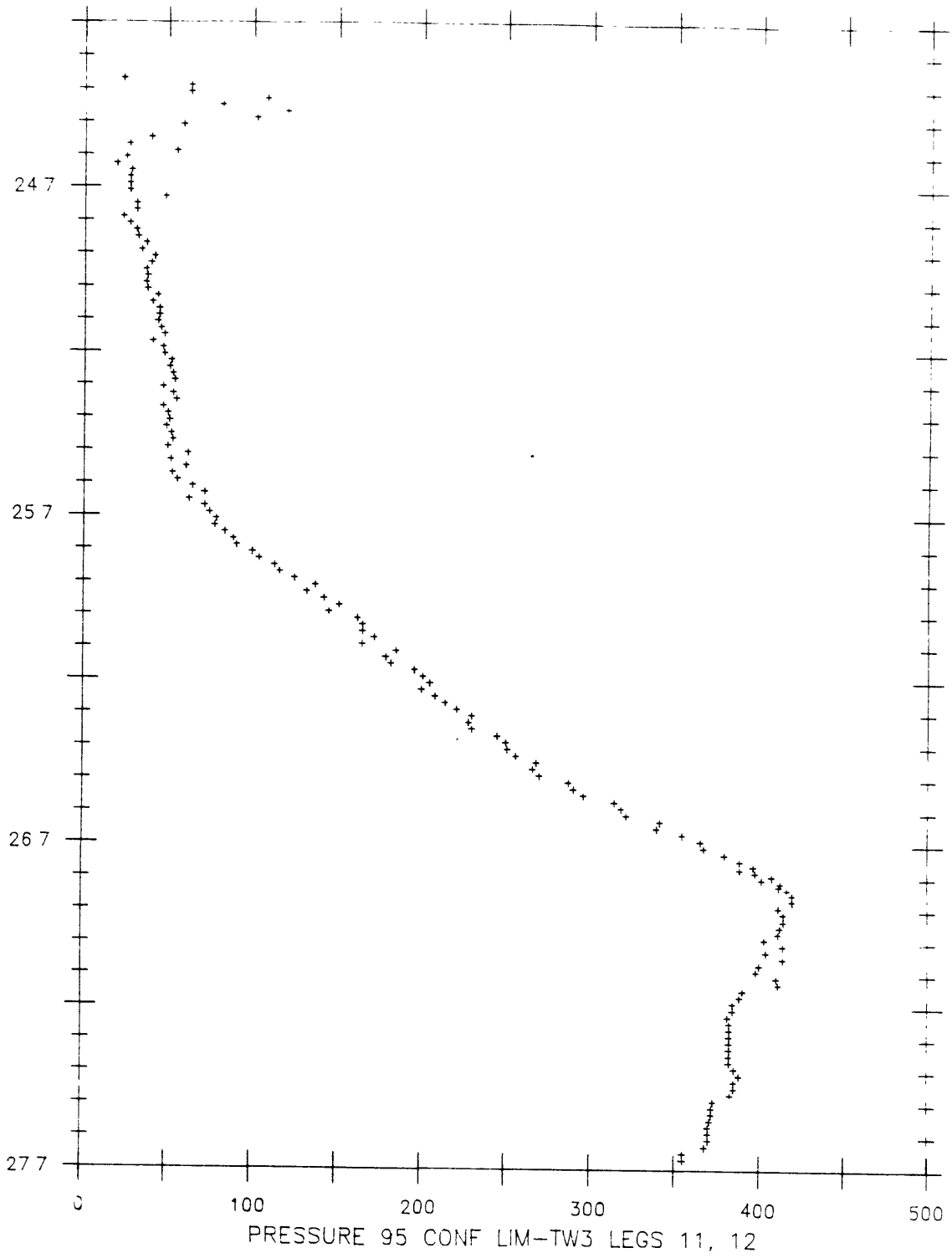

Fig. 5.17 - Pressure variation on isopycnals (x axis), as a function of potential density (y axis), showing maximum pressure variation on $\sigma_o = 26.85$. (The x quantity plotted is the 95% confidence limit on mean pressure of isopycnals, averaging over all the 1985 stations.

The Agulhas Subtropical Mode Water is too weak (or at least it was in 1985) to produce even an inflection in the lateral average N^2 profiles (Fig. 5.10 and 5.14).

The similarity between the Gulf Stream and Agulhas Q_y profiles above 1200 m or so seems attributable to the similarity of their dominant upper-level Mode Waters. The Gulf Stream system exhibits a strong Subtropical Mode Water layer (the 18 C water) that extends to almost the same depth as the Retroflection SAMW. The Gulf Stream STMW corresponds to the minimum observed between 100 and 600 m or so in the Gulf Stream N^2 profile (Fig. 5.3).

Deeper down in the water column, the Gulf Stream Q_y profile exhibits a negative bump at ~1500 m. A similar feature does not appear in the Agulhas Q_y profiles. The bump corresponds to isopycnal slopes decreasing with depth, more rapidly than anywhere else in the water column, and is found near the level of the Labrador Sea Water, a subpolar mode water of the North Atlantic found 'flowing west and south [from the Grand Banks] inshore of or under the Gulf Stream' *(Talley and McCartney, 1982)*. The details of the relationship between the Q_y bump and the LSW stratification minimum are not clear, in the absence of density-averaged profiles and sections of potential vorticity contoured on density: is the Q_y bump above, at, or below the LSW at in the Gulf Stream at 73°W? The lack of a similar Q_y bump in the Agulhas profile is perhaps due to the lack of a deep mode water.

To summarize, isopycnal slope increases with depth from the surface down to the base of the SAMW in the Agulhas and the STMW in the Gulf Stream, while isopycnal slope decreases rapidly with depth in the Gulf Stream near the LSW. Superficially, this looks contradictory. But Mode Waters, vertical minima in stratification, influence the lateral mean Q_y profile only insofar as they give rise to cross-stream variations in stratification. The SAMW and STMW are found within the subtropical gyres, on the warm side of the Agulhas, while the LSW is found 'inshore'

(or under) the Gulf Stream. Thus the SAMW and STMW wedges appear to push the thermocline down on the warm side of the jet to 650 and 600 m depth respectively, so isopycnals slopes increase with depth above and in the wedges. The least stratified LSW on the inshore side of the the Gulf Stream pushes deep isopycnals down there, so that isopycnal slopes across the current flatten out rapidly with depth above and in the LSW.

It would appear then, that mode water formation helps to create conditions favorable to baroclinic instability. It would be interesting to know what the Q_y profile of the Brazil Current looks like, given that the South Atlantic thermocline mode water is extremely weak.

5.8 Agulhas and Agulhas Return Current instability – I. Barotropic conditions

The Agulhas and Agulhas Return Currents also satisfy the purely barotropic condition for instability, with β - U_{yy} changing sign in the shoulders of the jet [in fact β is, as for the baroclinic condition, negligible to $O(10^{-2})$]. Figs. 5.18 - 5.19 show the barotropic part, U_{yy}, of the mean potential vorticity gradient Q_y across the Agulhas and Agulhas Return Currents at the sea surface; we may anticipate that the magnitude of U_{yy} decays rapidly, as U, with depth. Again, Q_y changes sign, opposite in sign from the jet velocity within the jet, and same-sign in the shoulders of the jet. The largest values are found within the jet, reaching magnitudes in excess of 2×10^{-9} m^{-1} s^{-1} at transect A; extreme values on the order of $\pm 1 \times 10^{-9}$ m^{-1} s^{-1} are usual, comparable to the extreme observed values for the baroclinic part of Q_y.

The barotropic gradient of Q_y within the current, when added to the baroclinic Q_y gradient, shifts it such that the whole profile is shifted in the upstream direction, decreasing magnitudes above the baroclinic zero crossing, increasing magnitudes below it, and tending to move the zero crossing up in the water column. The smaller barotropic gradient of Q_y in the shoulders of the current has the opposite effect. The

barotropic contribution to Q_y might shift the fastest growing waves away from the scales produced by the purely baroclinic model, particularly near the surface.

5.9 *Conclusions*

In this chapter, the Agulhas and Agulhas Return Currents' velocity, shear, and potential vorticity fields, and baroclinic and barotropic instability conditions have all been characterized, based on the March 1985 observations. Here is a brief summary of the results.

Geostrophic velocity, Sec. 5.2

- The Agulhas Current velocity maximum ranges from 0.8 to 1.8 m s^{-1} at the four transects.
- The Agulhas Return Current velocity maximum is 0.8 and 1.2 m s^{-1} at the two transects.
- As the Agulhas Current flows along the continental slope, the maximum velocity and velocity shear tends to shift onshore with height, as has been observed in the Gulf Stream and Kuroshio, instead of lining up vertically.
- Enhanced shear at deeper levels tends to be found near tracer extrema (*e.g.* Red Sea Water and North Atlantic Deep Water high salinities), suggesting deep western boundary currents for these water masses.

Isopycnal natural coordinates, Sec. 5.3

- As in the Gulf Stream, in the Agulhas vorticity due to vertical shear was found to be nearly as large as vorticity due to horizontal shear. Their ratio, formally the Rossby number ε divided by the Burger number S, estimated here directly from the observed velocity, has a value of about 1 in the Agulhas, similar to the Gulf Stream value computed by *Hall (1985)*.
- Isopycnal natural coordinates (derived in Appendix A) allow vertical shear vorticity to be retained, combined in a single, physically meaningful, cross-stream isopycnal shear term with the horizontal shear vorticity, without approximation beyond that required by natural coordinates.

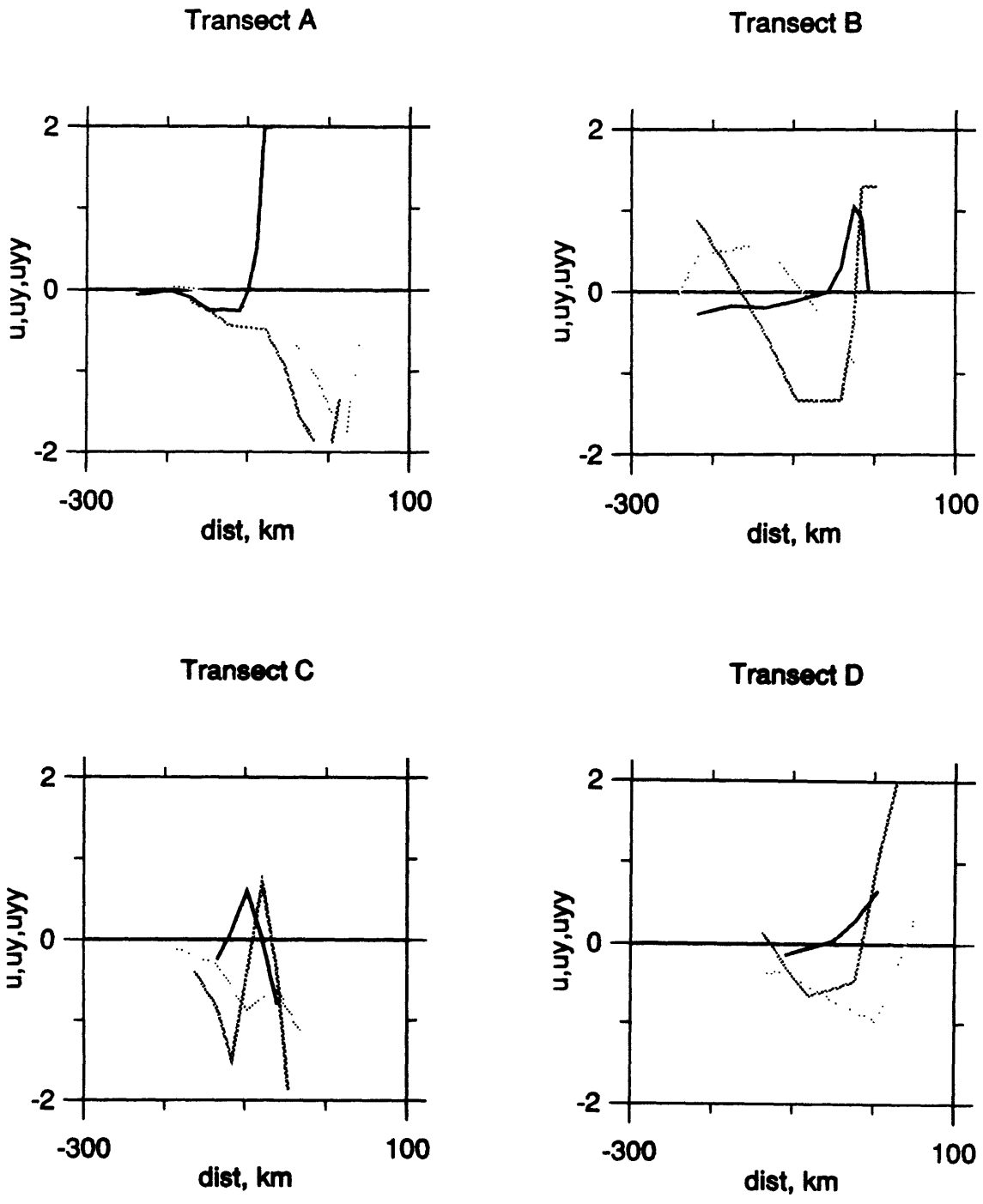

Fig. 5.18 - See caption next page.

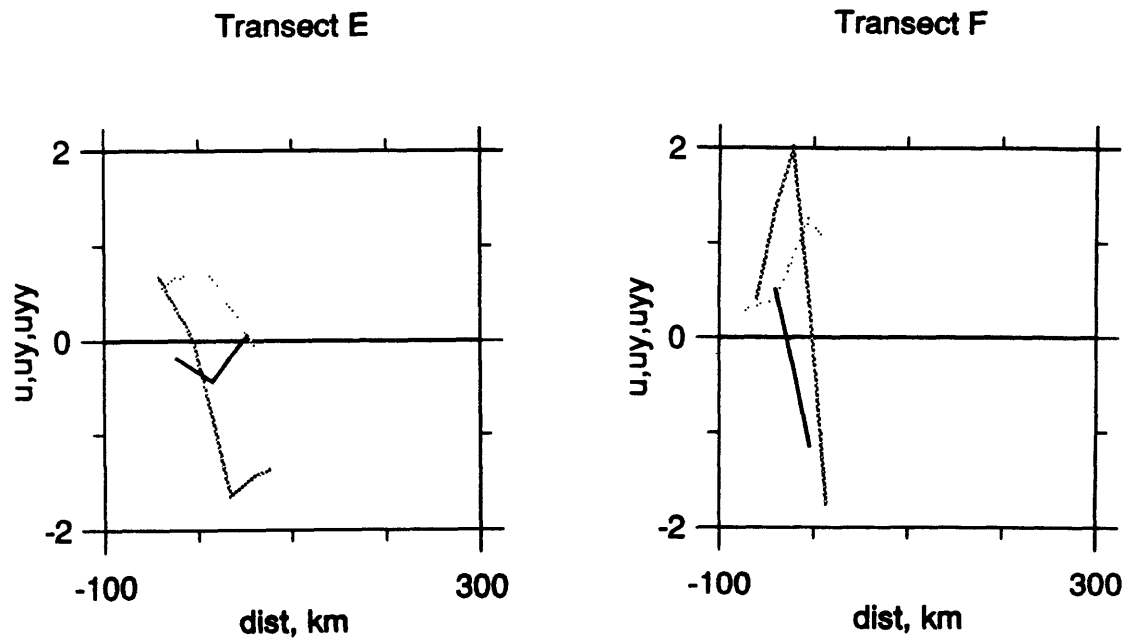

Fig. 5.18 - See previous page. Agulhas Current transects A, B, and C, at the sea surface as a function of cross stream distance: velocity (u, light gray curves, m s^{-1}), horizontal shear (u_y, dark gray curves, 10^{-5} s^{-1}), and barotropic contribution to q_y (u_{yy}, black curves, 10^{-9} $m^{-1}s^{-1}$). Note that the largest barotropic q_y is similar in magnitude to the largest baroclinic q_y (Figs. 5.4 - 5.7), implying that overall Burger number S is similar in size to the Rossby number ε. Cross-stream distance is plotted north positive, looking westward; origin of cross-stream distance is approximately at the 15 C temperature/200 m depth location. Velocity is plotted with west negative (downstream). Note that q_y is large and positive in the current at transects A, B, and D, and small and negative on the current's warm anticyclonic far side. Transect C is different, with two distinct velocity maximum, due to an onshore displacement of the warm core relative to the underlying shear. The curves persist in shape with depth and decrease in magnitude.

Fig. 5.19 - Agulhas Return Current transects E and F, at the sea surface as a function of cross stream distance: see Fig. 5.18 caption above. Cross-stream distance is still plotted north positive, looking westward (which is now upstream but still negative). Both transects show upstream values within the current, as in the Agulhas Current, and zero crossings on the northern side of transect E) and on the southern side of transect F.

- Potential vorticity in isopycnal natural coordinates is:

$$q \sim \left(f + K_s v' - \frac{\partial v'}{\partial n'}\right) \frac{\partial \lambda}{\partial z}$$

The three terms in parentheses are planetary vorticity, curvature vorticity, and cross-stream shear along an isopycnal, weighted by the vertical gradient of a suitable tracer λ, *e.g.* potential temperature or potential density.

Consequences of path curvature, Sec. 5.4

- The gradient wind equation was rewritten as a quadratic for a Rossby number based on the total velocity field, ε_k, as a function of the curvature of geostrophic streamlines, K_g, curvature of parcel trajectories, K_s, and a Rossby number based on the geostrophic field, ε_g. For the case of geostrophic and parcel trajectory curvature equal, Fig. 5.1 shows that ε_g substantially underestimates ε_k for anticyclonic features, and overestimates ε_k for cyclonic features - just as geostrophic velocity underestimates total velocity in anticyclonic features, and overestimates it in cyclonic features.
- The pressure gradient and centrifugal acceleration overcome the Coriolis force in anticyclonic meanders as $|K_s\varepsilon_g/K_g|$ increases beyond 0.25, when ε_g is negative (anticyclonic), and K_s and K_g have the same sign. Values for ε_g of -0.24 are observed in the Agulhas meanders over the continental slope evident in the 15 C temperature/200 m depth contour.

Estimates of Agulhas potential vorticity terms and balances, Sec. 5.5

- Variation in Coriolis parameter f over the Retroflection latitude range is $\pm 0.08 f_o$, with f_o the mean Coriolis parameter.
- The largest cyclonic geostrophic curvature observed was -70° over 30 km (smallest cyclonic radius of curvature 25 km).
- The largest anticyclonic geostrophic curvature observed was +130° over 20 km (smallest anticyclonic radius of curvature 10 km).
- The largest anticyclonic geostrophic curvature vorticity observed was $-0.24 f_o$, in the Agulhas at the intersections of the 15 C temperature/200 m contour with transects B and C. Anticyclonic vorticity at the sharpest turn in the contour, southwest of the Agulhas Plateau, would be $-0.78 f_o$, if velocity there was

0.5 m s^{-1} as at transects E and F. No cyclonic curvature vorticity estimates were made, since no transect/contour intersection fell at a cyclonic meander.

- The largest cyclonic isopycnal shear vorticity observed was $+0.98f_o$, seen on the cold side of the Agulhas Current at transect A (see Fig. 5.2).
- The largest anticyclonic isopycnal shear vorticity observed was $-0.17f_o$, seen on the warm side of the Agulhas Current at transects A, B, and C.
- The largest potential vortex stretching (also called horizontal divergence, planetary potential vorticity variation) observed was a factor of 8 thinning of isopycnal sheets onshore at the level of the Subtropical Mode Water.
- Cross-frontal contrasts in planetary potential vorticity persist from the surface down to ~1800 m in the Agulhas Current, and down to ~1200 m in the Agulhas Return Current.
- It appears that the observed alongstream variation of curvature vorticity can be balanced by planetary potential vorticity variations, if parcels make excursions along sloping isopycnals across the planetary potential vorticity gradient , of *e.g.* ~20 km in the horizontal and ~100 m in the vertical.

Agulhas baroclinic instability, Sec. 5.6

- The mean baroclinic potential vorticity gradient profiles across the Agulhas Current and the Agulhas Return Current transects (Fig. 5.4 - 5.7) consistently change sign, thereby meeting the necessary conditions for baroclinic instability.
- The largest values of the isopycnal thickness gradient $f^2 U_{zz}/N^2$ are $\sim 2 \times 10^{-9}$ m^{-1} s^{-1}, two orders of magnitude larger than the planetary vorticity gradient β.
- The Agulhas and Agulhas Return Current mean baroclinic potential vorticity gradient, Q_y, profiles at all transects except B are quite similar to the mean Gulf Stream profile (Fig. 5.3) reported by *Johns (1988)*, with large values of the same sign as U above ~600 m, a zero crossing at ~600 m, and values opposite in sign from U below. The transect B profile, like many other characteristics of the current at transect B, is wildly different from the profiles at all the other transects.
- Observed Agulhas Return Current meander wavelengths of ~600 km fall within the 250 to 650 km range for fastest growing waves produced by the baroclinic instability model for *Johns's* most Agulhas-like profile. This suggests that baroclinic instability may play a role in Agulhas Current meandering.
- The Agulhas (omitting transect B) and Gulf Stream profiles do differ in what appear to be details, judging from the various profiles whose baroclinic instability behaviors were explored by *Johns*. The Gulf Stream profile has a region of very

weak positive values near 1000 m, the Agulhas does not. The Agulhas is as likely as not to have another weak zero crossing below ~1500 m. Finally, the Gulf Stream exhibits a lobe of enhanced Q_y values near 1500 m; magnitudes in the Agulhas decay fairly uniformly below the zero crossing at ~600 m.

- Formally, the quasi-geostrophic scaling of the linear baroclinic instability problem requires that isopycnal depth variations be small compared to layer (thermocline) depth, clearly not the case in the Agulhas, Gulf Stream, or Drake Passage *(Wright, 1980)*. Nevertheless, horizontally and isopycnally averaged profiles of Q_y computed across the Agulhas and Agulhas Return Currents were found to be quite similar, thus it partly substantiates *Johns'* and *Wright's* belief that large isopycnal slopes may be neglected, at least in estimating the Q_y mean gradient.

Baroclinic potential vorticity gradient and Mode Waters, Sec. 5.7

- The Q_y zero crossing at ~600 m lies near the base of the North Atlantic Subtropical Mode Water in the Gulf Stream, and near the base of the South Indian Subantarctic Mode Water in the Agulhas. Isopycnal slopes increase with depth above ~600 m and decrease below it, a signature of the thick Mode Water wedge in the thermocline on the warm side of the current. This can be seen in the Agulhas by comparing contour plots of planetary potential vorticity showing the Mode Water minimum (see Atlas) with *(i)* isopycnally averaged Q_y plotted as a function of potential density (Fig. 5.6 - 5.7) and *(ii)* a plot of pressure variation on Retroflection isopycnals, Fig. 5.16.

- The lobe of enhanced Q_y values at ~1500 m in the Gulf Stream lies near the level of the Labrador Sea Water (LSW), one of the subpolar mode waters of the North Atlantic; no similar feature is seen in the Agulhas. Isopycnal slopes <u>decrease</u> very rapidly with depth in the LSW, a signature of the thick Mode Water wedge beneath the thermocline on the <u>cold</u> side of the current.

Barotropic instability, Sec. 5.8

- The barotropic potential vorticity gradient, U_{yy}, across the Agulhas Current and the Agulhas Return Current transects (Fig. 5.18 - 5.19) consistently changes sign, thereby meeting the necessary conditions for barotropic instability. The largest values of U_{yy} are found near the surface, and are comparable in magnitude to the largest values of the baroclinic potential vorticity gradient. Formally, the ratio of U_{yy} to f^2U_{zz}/N^2 is S^2, where S is the Burger number NH/fL.

- The barotropic part of the mean Q_y gradient modifies the baroclinic gradient and thus may modify the purely baroclinic instability solutions. Values of U_{yy} <u>within</u> the current are <u>opposite</u> in sign from the baroclinic term f^2U_{zz}/N^2 above the baroclinic

zero crossing at ~600 m, and similar in sign below it. This tends to place the zero crossing of the total Q_y above the baroclinic zero crossing. The situation is reversed for U_{yy} in the shoulders of the current: U_{yy} and $f^2 U_{zz}/N^2$ have the same sign above, and the opposite sign below ~600 m; Q_y crosses zero below ~600 m.

Analyses of other types of observations will be needed to understand the kinematics and dynamics of the intense anticyclonic meanders found over the continental slope and in the separated Agulhas, to test the predictions of the linear baroclinic instability model, and to quantify eddy energy and heat fluxes out of the Retroflection.

Chapter 6: Re-evaluation of dynamical models

6.1 Introduction

The most striking feature of the Retroflection is, of course, the fact that it retroflects at all. We may ask of dynamical models of the Retroflection:

- why does the flow retroflect?
- what determines the latitude, y_R, of the Retroflection's southern extension?
- what determines the longitude, x_R, of the Retroflection's western extension?
- what determines the path of the Current, s(x,y), relative to topographic features and latitude lines?

The Current is sometimes modelled as a cohesive jet, and the Retroflection as a simple material boundary between the S. Indian and S. Atlantic gyres. Observations suggest, however, that rings and flow bifurcation(s) are characteristic of this region, and that these phenomena may play an important role in the exchange of mass, heat, salt, and vorticity between the two oceans. Again, we may ask of the models:

- what determines the total Agulhas Current transport which includes both the returning interior Sverdrup transport and a locally recirculating component?
- what determines the portion of the Agulhas Current transport that circulates around the combined S. Atlantic/S. Indian subtropical gyres?
- what determines the size and spawning frequency of Retroflection rings?
- what determines the contrasts in heat, salt, and vorticity between exiting S. Indian-to-S. Atlantic outflow and the returning S. Atlantic-to-S. Indian inflow?

The structure of the Agulhas Current as it flows along the continental slope of southern Africa is also of interest:

- what determines the wavelength and amplitude of observed meanders?

What existing models of the Retroflection have to say about these questions is discussed below. First, the classical western boundary current models are briefly reviewed, in order to illustrate the basic dynamical balances. This leads naturally into a discussion of the simple analytical models of the Retroflection developed by *de Ruijter (1982)* and *Ou and de Ruijter (1986)*. Parameter values used in western boundary current models and the resulting width scales are summarized in Table 6.a.

The 1985 observations can be compared to the results of realistic numerical models, including *Lutjeharms and van Ballegooyen's (1984)* numerical solutions to an inertial-jet model, and the one- and two-layer numerical models of *de Ruijter and Boudra (1985)* and *Boudra and de Ruijter (1986)*.

It should be noted that there is nothing particularly mysterious or complicated (no more so than anything else in rotating fluid dynamics, anyway) about the basic, underlying dynamics of the Retroflection itself. The asymptotic model of *de Ruijter* gives a rather clear explanation. The model, which is steady and thus characterizes the time-mean flow (but not, it must be said, the instantaneous field of any single synoptic survey) shows that the Retroflection is a fundamentally non-linear feature. To retroflect, the current must have momentum enough to overshoot the tip of the boundary. Having done so, it balances increasing planetary potential vorticity with curvature vorticity of the opposite sense. A complete explanation of the model is given in Sec. 6.3.

6.2 Classical western boundary current models

The classical models of *Stommel (1948)*, *Munk (1950)*, and *Charney (1955)*, reviewed by *Pedlosky (1979)* and *Gill (1982)*, illustrate the three basic two-term vorticity balances possible in homogeneous steady (western) boundary currents: advection of planetary vorticity balanced by bottom friction, side friction, and relative

Table 6.a – Summary of parameter values used in western boundary current models.

Parameter	Definition	value(s)	units	description
A_H		10^2 - 10^4	m^2s^{-1}	lateral eddy viscosity
A_V		10^{-4} - 10^{-1}	m^2s^{-1}	diapycnal eddy viscosity
a_r		6.4 x 10^6	m	Earth radius
Ω		7.3 x 10^{-5}	s^{-1}	Earth rotation rate
f	$2\Omega sin\varphi$	1 x 10^{-4}	s^{-1}	Coriolis parameter; φ is latitude
β	$2\Omega cos\varphi/a_r$	1.9 x 10^{-11}	$m^{-1}s^{-1}$	variation of Coriolis parameter with latitude
u_i		0.01 - 0.1	ms^{-1}	interior velocity
H		5 x 10^3	m	water depth
r^{-1}	$(\frac{fA_v}{2H^2})^{-1/2}$	7.0 x 10^7	s	spin-down time due to bottom Ekman layer (80 days)
W_B	r/β	1 - 20	km	Scale width of classical bottom-frictional boundary current
W_H	$(\frac{A_H}{\beta})^{1/3}$	20 - 80	km	Scale width of classical side-frictional boundary current
W_I	$(\frac{u_i}{\beta})^{1/2}$	20 - 70	km	Scale width of classical inertial boundary current
ε_b	$u_i/a_r\Omega$	2.0 x 10^{-4}	none	Rossby number*
E	$A_H/\Omega a_r^2$	2.8 x 10^{-6}	none	Ekman number*
W_{HS}	$(a_rA_H/\Omega)^{1/3}$	90	km	Scale width of side-frictional, and mixed side-frictional/inertial boundary currents*
W_{RS}	$W_{HS}\,\varepsilon_b^{-1/6}$	370	km	Scale width of free-inertial Retroflection/S. Atlantic free jet regime*

*As defined in *de Ruijter (1982).*

vorticity respectively. Each balance has a characteristic scale width and implies restrictions on where the boundary current can be located; as is usual in boundary layer problems, the balance with the largest scale width dominates. Characteristics of the simple numerical models of *Bryan (1963)* are also briefly mentioned.

Classical bottom frictional wbc model. The vorticity balance in the bottom-frictional western boundary current (wbc) model is between advection of planetary vorticity and vortex stretching due to Ekman pumping at the bottom boundary layer:

$$\beta \frac{\partial \psi_B}{\partial x} = -\frac{f}{H} w_E\Big|_{z=-h} = -r \frac{\partial^2 \psi_B}{\partial x^2} \tag{6.1}$$

where β is the variation of the Coriolis parameter f with latitude; ψ_B is the boundary layer streamfunction; $w_E\Big|_{z=-h}$ is the vertical velocity at the top of the bottom Ekman layer; $r^{-1} = (\frac{fA_v}{2H^2})^{-1/2}$ is the spin down time associated with the bottom Ekman layer; A_v the vertical component of the effective viscosity, and H the fluid depth.

The width scale for this balance is $W_v = \frac{r}{\beta}$, which has a value of only 1 to 20 km, when we use the values given in Table 6.a. This range of current widths is much thinner than the observed 60 to >100 km e-folding scales in the 1985 Agulhas transect velocity fields, and much thinner than the side-frictional and inertial widths derived below. As the balance with the largest width scale dominates dynamically, it appears that bottom friction is relatively unimportant in the western boundary current.

Bottom-frictional boundary layer solutions are possible only on the western side of the basin: if we introduce a boundary layer variable for the eastern wall (stretched, shifted, and opposite in sign from x) and require that the boundary layer vanish as we move away from the wall, we find that the eastern boundary layer solution must be identically zero.

A bottom-frictional wbc solution can be constructed to satisfy the boundary condition of no flow into the western wall. It cannot also satisfy a no-slip condition since the vorticity equation's highest order term, horizontal friction, has been dropped, a singular perturbation which leaves insufficient degrees of freedom to satisfy the full set of boundary conditions.

Classical side frictional model. The vorticity balance in the side-frictional wbc model is between advection of planetary vorticity and diffusion across the wbc of frictional torques from the side wall:

$$\beta \frac{\partial \psi_B}{\partial x} = A_H \frac{\partial^4 \psi_B}{\partial x^4} \tag{6.2}$$

where A_H is the horizontal component of the effective viscosity.

The wbc scale width for this balance is $W_H = (\frac{A_H}{\beta})^{1/3}$. The relevant range of A_H is $2 \times 10^2 \leq A_H \leq 10^4$ m^{2}s^{-1}, giving values for W_H from 20 to 80 km.[1] The observed e-folding scales in the 1985 Agulhas transect velocity fields are slightly larger, varying, as was mentioned above, from 60 to 100 km.

The side-frictional boundary layer solution is the product of an oscillating and a decaying function, while the bottom frictional and inertial layers are strictly decaying functions. The first zero of the oscillating part occurs at an offshore distance of $\frac{2\pi}{\sqrt{3}} W_H$ (about $3.6 W_H$). This corresponds to the distance across the current from

---

[1]Oceanic A_H estimates range from 10 to 10^4 m^{2}s^{-1} (e.g., *Pedlosky, 1979*). We also must require that $W_H \geq W_I$, in order for side-friction to appear in the dominant dynamic balance; W_I is the inertial boundary current width (see next subsection). This requirement, with the definitions of W_H and W_I, translates into the condition $A_H \geq \sqrt{\frac{u_i^3}{\beta}}$, where u_i is the interior velocity. For $u_i = 0.01$ ms^{-1}, we require $A_H \geq 2 \times 10^2$ m^{2}s^{-1}.

the coast to the the location where the boundary-current velocity vanishes. The range of first-zero locations corresponding to the range of W_H given above is 70 to 300 km. This is similar to the observed first-zero locations in the Agulhas of 120 to >250 km.

The side-frictional boundary current includes a recirculating component due to the oscillating structure, giving a total transport of about 1.2 times the interior Sverdrup transport. The S. Indian interior transport estimated from wind-stress observations and a model of *Veronis (1973)* is 55±8 Sv, and 1.2 times this is 66±10 Sv. Observed Agulhas transports range from 0.9 to 1.8 times the interior transport values. [Observed values are 56 to 111 Sv above a reference level of 2400 dbar; beneath this level transports are generally small (order 1 Sv) and opposite in direction.]

Again, boundary layer solutions are possible only on the western side of the basin; reasoning as above, it may be deduced that the interior flow itself must satisfy the no normal flow condition on the eastern boundary.

Classical inertial boundary current model. The vorticity balance in the inertial wbc model is between advection of planetary vorticity and relative vorticity in the current:

$$u_i \frac{\partial^2 \psi_B}{\partial x^2} + \beta \psi_B = 0 \qquad (6.3)$$

where u_i is the zonal (on/offshore) component of the interior velocity. The wbc scale width for this balance is $W_I = \left(\frac{u_i}{\beta}\right)^{1/2}$, which has a value of 20 to 70 km when we use 0.01 to 0.1 m s^{-1} for the interior velocity. These values overlap the low end of the observed range of *e*-folding scales (60 to >100 km) seen in the 1985 Agulhas transect velocity fields.

The boundary layer in this case need *not* be on the western side of the basin. Rather, the inertial boundary current can decay away from either an the eastern or western wall provided that the interior velocity is westward. This solution cannot satisfy a no-slip boundary condition for the same reason the bottom-frictional wbc could not: lateral friction has been omitted.

Mixed inertial/side frictional wbc. It is likely that both the inertial and side-frictional terms contribute significantly, given that the scale widths, an indication of their relative importance, are comparable. Both terms contribute desirable properties to the solution: inertia gives a scale width that is independent of the poorly-known effective viscosity coefficients, and as the numerical models discussed later show, it also allows the current path to exhibit characteristics seen in nature that are impossible in a purely frictional model, including path curvature and overshooting the latitude where the Sverdrup interior transport vanishes. Frictional processes of some kind must also play an important role in the wbc system somewhere, dissipating the boundary current's relative vorticity so that it can merge with the quiet ocean interior; friction is also necessary to dissipate the energy input from wind stress. In combination the terms give damped Rossby waves where the wbc rejoins the interior, and total transport in excess of the interior wind-driven transport (again their ratio is about 1.2, for $\frac{W_I}{W_H}$=1.3; *Bryan, 1963*) as seen in the purely side-frictional solution is retained by the mixed solution.

6.3 Agulhas Retroflection asymptotic models part I: de Ruijter's model

The most obvious difference between the classical wbc models and the Agulhas Retroflection region is the fact that the African continent ends in the middle of the anticyclonic subtropical wind-stress curl zone. The asymptotic models of *de Ruijter (1982)* address the question of a western boundary terminating in mid-gyre. He reformulates the classical linear, side-frictional, and mixed inertial/side-frictional

models mentioned above in spherical geometry with a partition midway across the basin ending in mid-gyre. A cartoon of the S. Indian/S. Atlantic circulation is given in Fig. 6.1. The elements of the cartoon are discussed in detail in the next section. Sketches relevant to *de Ruijter's* models are shown in Figs. 6.2 - 6.3.

Side-frictional Retroflection model. The essential result of the classical side-frictional wbc model reformulation is that the side-frictional wbc scale width W_{HS} is itself the largest scale found anywhere near the boundary . This model does <u>not</u> produce a larger scale width over which a Retroflection-type feature can occur.

The value of W_{HS} is 90 km, using *de Ruijter's* value for lateral eddy viscosity A_H of 8.4 x 10^3 m^2s^{-1}. This is within the range of *e*-folding scales observed in the 1985 Agulhas transect velocity fields (60 to >100 km). The scale width W_{HS} is defined by $W_{HS} = \left(\frac{a_r}{\Omega} A_H\right)^{1/3}$, where a_r is the radius of the Earth and Ω is the rotation frequency.[2] This differs a bit from the classical side-frictional wbc scale width $W_H = \left(\frac{A_H}{\beta}\right)^{1/3}$, as a consequence of *de Ruijter*'s non-dimensionalizing the problem in spherical geometry. The ratio $\frac{W_H}{W_{HS}} = (2\cos\varphi)^{-1/3}$ is ~0.85 at mid-latitudes; recall φ is the latitude and $\beta = \frac{2\Omega\cos\varphi}{a_r}$.

The circulation pattern produced by this model is shown in Fig. 6.2 (*de Ruijter's* Fig. 3.c). The side-frictional wbcs of the S. Indian and S. Atlantic Oceans, plus a free viscous shear layer extending across the S. Atlantic at the partition tip latitude, passively close the Sverdrup interior circulation. The free viscous layer and the matching region where it joins onto the wbc have the same scale width as the wbc itself, that is, W_{HS}.

---

[2]The definition can also be written $W_{HS} = a_r E^{1/3}$, with the Ekman number E given by $\frac{A_H}{\Omega a_r^2}$.

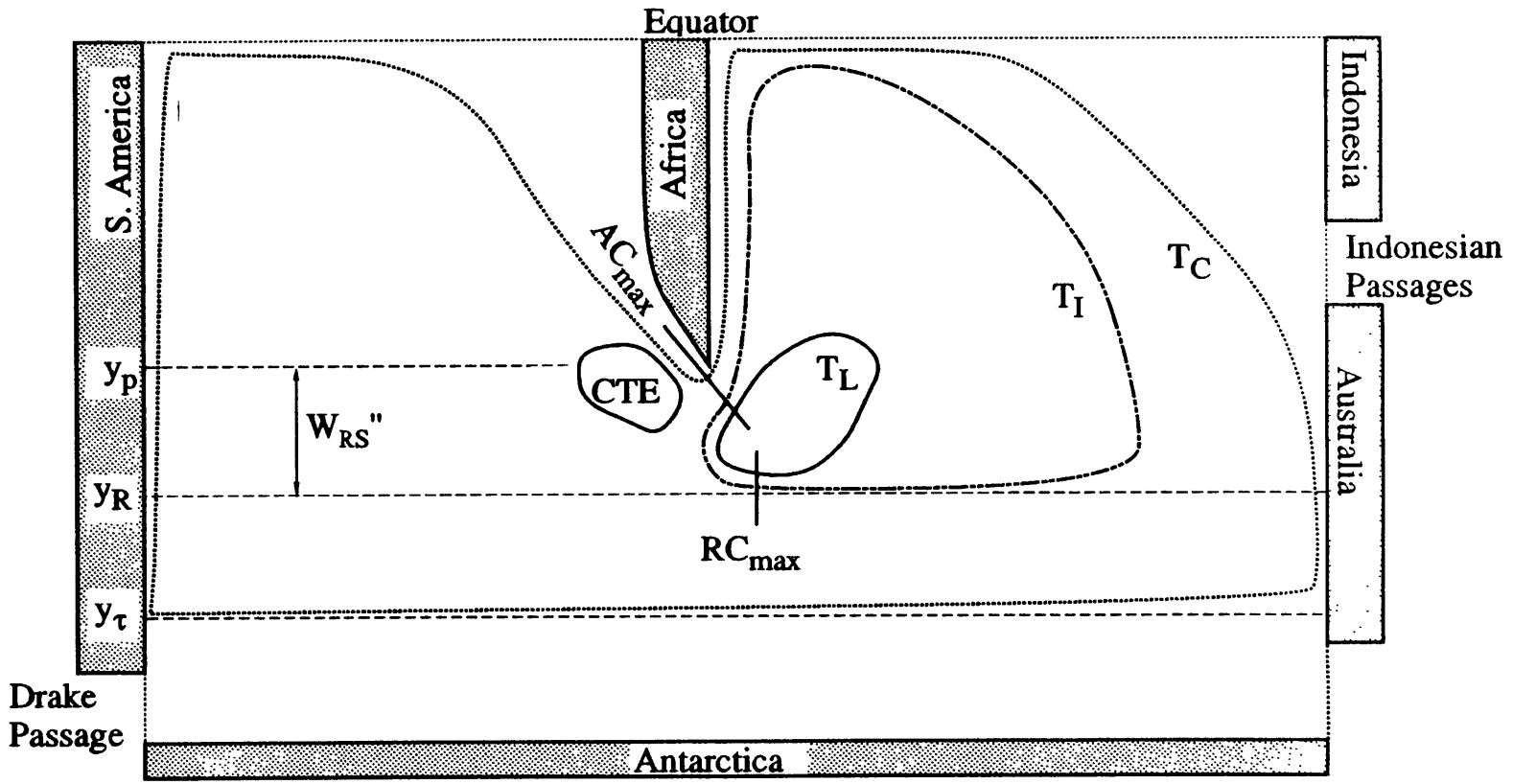

Fig. 6.1 - Cartoon (not to scale) of S. Indian/S. Atlantic circulation. Latitudes of the African partition southern tip, y_p, of the Retroflection southern boundary, y_R, and of the southern wind stress curl zero, y_τ, are marked. Solid streamlines correspond to the outer edges of the Retroflection local recirculation, which has transport T_L, and to the Cape Town eddy, CTE. Double-dashed streamline corresponds to the outer edge of S. Indian inner gyre, which has transport T_I. Dotted streamline corresponds to the outer edge of the combined S. Indian/S. Atlantic super-gyre, which has transport T_C. The maximum Agulhas Current transport, AC_{max}, the maximum Agulhas Return Current transport, RC_{max} is marked. Note the ambiguity in RC_{max} depending on the choice of its southern limit. Not shown: flow across the equator, flow through the Indonesian and Drake Passages and south of Australia, and S. Atlantic local recirculation and inner gyre streamlines.

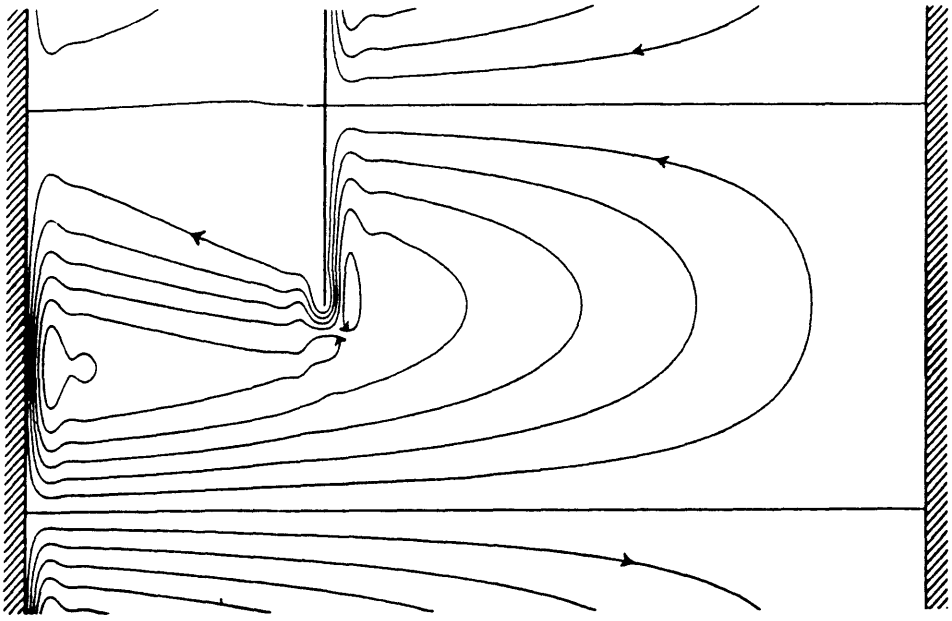

Fig. 6.2 – First approximation of transport stream function for linear side-fictional model (*de Ruijter's* Fig. 3c.). Wind-stress curl is $sin\,(9\varphi + \pi/4)$, approximating observed winds. The zeroes of the wind-stress curl are located at 25° and 45°S (marked by straight lines across both basins), and the maximum at 35°S. The partition tip is also located at 35°S.

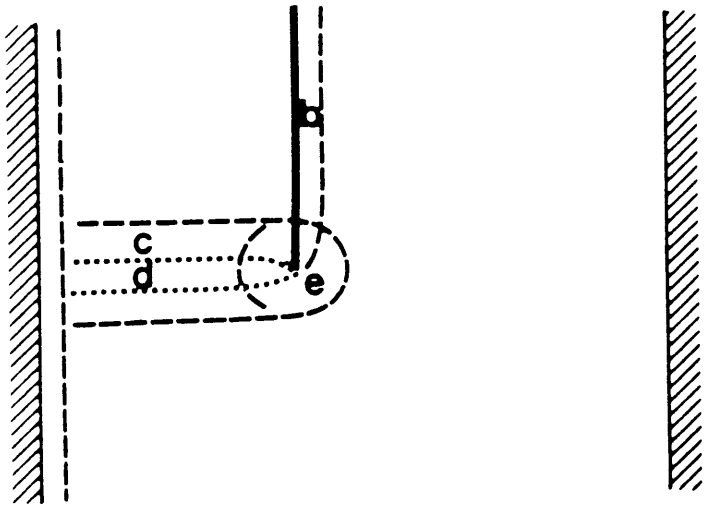

Fig. 6.3 – Boundary layers emerging from the mixed inertial-side frictional Retroflection model (*de Ruijter's* Fig. 5.). Labels refer to:

(b) mixed inertial/frictional boundary layer.
(c) free inertial boundary layer.
(d) free inertial frictional sub-boundary layer.
(e) inertial tip region and its western zonal extension.

There are three circulation regimes: an inner South Atlantic gyre, an inner South Indian gyre, and an outer super-gyre that encircles both inner gyres. The transport of the combined outer gyre, T_C, is just the integral of the Sverdrup interior transport across the basin from the partition longitude to the eastern boundary, along the latitude of the viscous shear layer offshore edge as it flows west south of the partition tip. The transport of the respective inner gyres, as a function of latitude, is given by the integral of the Sverdrup interior transport between the eastern and western boundaries of South Atlantic and South Indian Oceans, minus the outer gyre transport - to which the small recirculating transport associated with the oscillatory character of the side-frictional boundary current may be added as before.

Mixed inertial/side-frictional Retroflection model. The second part of *de Ruijter's* analysis includes both lateral friction and inertia. The assumption that neither of these balances overshadows the other implies that $W_{HS} \sim W_I$, *i.e.*, that the scale width of the mixed wbc is $W_{MS} \sim \alpha W_{HS}$, where α is an order-one scaling factor; W_{HS} is defined above.

A fundamentally new free-inertial regime appears in a circular region of radius W_{RS} surrounding the tip of the partition and in a $2W_{RS}$-wide band centered on the partition tip latitude that extends across the South Atlantic Ocean to its western boundary (Fig. 6.3, *de Ruijter's* Fig. 5). The vorticity balance in the free-inertial regime is between planetary and relative vorticity (from *de Rujter's* Eq. B7), which includes jet axis curvature. Any poleward component of fluid motion in the free inertial jet is accompanied by increased cyclonic planetary vorticity and increased anticyclonic relative vorticity, including axis curvature to the east.

Retroflection scale radius. The scale of W_{RS} is $a_r \varepsilon_b^{1/3}$ (again, from *de Rujter's* Eq. B7) or equivalently $W_{HS}\varepsilon_b^{-1/6}$, where ε_b is the basin-scale Rossby number $\frac{u_i}{\Omega a_r}$.

The value of $\varepsilon_b^{1/3}$ is 5.8×10^{-2} when $\varepsilon_b = 2.0 \times 10^{-4}$ and $u_i = 0.093$ m s^{-1}. Now u_i is the scale of the maximum interior zonal velocity, which itself depends upon the wind-stress curl maximum $curl\ \underset{\sim}{\tau}_{max}$.

De Ruijter adjusts the Retroflection scale radius to the local interior zonal velocity in the vicinity of the partition tip by taking the cube root of the product of W_{RS} and the ratio $\dfrac{curl\ \underset{\sim}{\tau}(y_p)}{curl\ \underset{\sim}{\tau}_{max}}$, where $curl\ \underset{\sim}{\tau}(y_p)$ is the zonally-averaged wind stress curl at the partition tip latitude. The adjusted value, W_{RS}', is $0.9 - 1.0 W_{RS}$, estimating from maps of Sverdrup transport computed from wind stress curl *(Hellerman and Rosenstein, 1983)*. The maximum Sverdrup transport is found very near the partition tip latitude in the July map and >200 km to the south in the January map [the spatial resolution is limited by the averaging of the wind data over 2° x 2° (220 km north-south x 180 km east-west) squares].

The value of W_{RS} is 370 km using *de Ruijter's* values: 90 km for W_{HS} (see above); 2.0×10^{-4} for the Rossby number ε_b; and $\alpha = 1$. The scale W_{RS}' after adjusting for the wind-stress curl is 340 - 370 km. The model thus predicts fairly intense Current and Return Current flow within 340 - 370 km of the partition tip.

Apparent western boundary tip latitude. There are three circulation regimes, as for the purely side-frictional model. Now, however, the Retroflection free-inertial jet regime extends the apparent western boundary southward, to $y_R = y_p + W_{RS}'$, where y_p is the partition tip latitude. The super-gyre transport integral now must be taken further south at y_R. This decreases the super-gyre transport, if the Sverdrup interior transport decreases to the south as is the case south of the partition tip in the South Indian Ocean, and increases the inner gyre transports. Further increases in the inner gyre transports may arise from additional recirculation associated with the inertial terms.

6.4 Agulhas Retroflection asymptotic models part II: an adjustment to de Ruijter s model and comparison with observations

So far I have followed *de Ruijter's* arguments. A further adjustment to W_{RS}' may be rationalized as follows. The observed Retroflection includes a recirculating component that nearly doubles its transport above the maximum interior value. This suggests the adjustment $W_{RS}'' = W_{RS}'\left(\frac{u_r}{u_i}\right)^{1/3}$, where u_r is an interior velocity scale that includes the recirculating component. The observed range of the ratio of Agulhas transport and maximum Sverdrup interior transport is 0.9 - 1.8, which gives a range of values for W_{RS}'' of 330 - 440 km. Asymptotic model parameters and adjustments are summarized in Table 6.b.

Adjusting W_{RS}' in this way implies a prediction: that the Retroflection is largest when the transport is greatest, assuming that transport of the Agulhas does indeed vary. This adjustment also implies that changes in the recirculation strength are self-reinforcing, so long as the Retroflection southern boundary is north of the zero wind-stress curl latitude. As the recirculation increases, the Retroflection expands to the south and incorporates more South Indian anticyclonic streamlines into the South Indian inner gyre, which increases the energy supply to the recirculation, and presumably tends to spin it up further. The dynamics of the recirculating transport component itself are, obviously, sidestepped here.

Comparison with observed Retroflection radius. If we take W_{RS}'' to represent the *e*-folding scale of the meridional velocity, then the Return current axis should be south of the partition tip latitude by $1.1W_{RS}''$ (Fig. 6.4). The 1985 observations of the Agulhas and Agulhas Return Current axis (represented by the 15 C/200 m contour) show it lying within about 500 km of the tip of the Agulhas Bank. This is just above the $1.1W_{RS}''$ range of 360 - 480 km.

Table 6.b – Summary of parameter values used in asymptotic Retroflection models and comparison with observation.

Parameter	Definition	value(s)	units	description
W_{RS}	$W_{HS}\,\varepsilon_b^{-1/6}$	370	km	Scale width of free-inertial regime
c	$\dfrac{\int curl\ \underset{\sim}{\tau}(y_p)\,dx}{\int curl\ \underset{\sim}{\tau}_{max}\,dx}$	0.8 - 1.0	none	ratio of wind-stress curls
W_{RS}'	$c^{1/3}W_{RS}$	340 - 370	km	de Ruijter's Retroflection scale width/radius
u_r/u_i		0.9 - 1.8	none	ratio of recirculating and Sverdrup interior velocities
W_{RS}''	$\left(\frac{u_r}{u_i}\right)^{1/3}W_{RS}'$	330 - 440	km	Retroflection scale width with recirculation adjustment
γ_e		68	deg	change in Agulhas heading over which meridional velocity falls to e^{-1} of alongstream velocity
R	$W_{RS}''/sin\ \gamma_e$	360 - 480	km	Retroflection radius
R_{obs}		500	km	observed Retroflection radius
y_p		37°S	lat	observed partition tip latitude
y_R		41.5°	lat	observed Retroflection southern boundary latitude

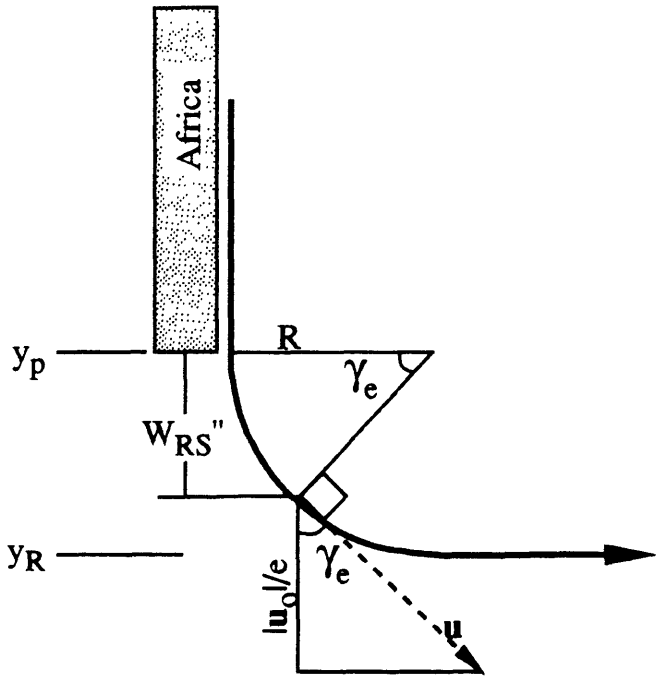

Fig. 6.4 - Sketch (not to scale; see below) showing e-folding scale of meridional component of velocity. The Retroflection scale width, W_{RS}", radius of the Retroflection, R, current heading, γ, partition tip latitude, y_p, and southern boundary of the Retroflection , $y_R = y_p - R$, are shown; the velocity **u** is imagined to have constant magnitude $|\mathbf{u}_0|$. When the heading is γ_e degrees east of south, the meridional component has decreased to e^{-1} times its y_p value. (The angle γ_e used here is about 45 degrees, to leave room for labels; the correct value is 68 degrees. The correct ratio between W_{RS}" and R is 0.93.)

Note that the partition tip latitude *de Ruijter* used (35° S) corresponds to the southernmost point on the African shoreline. But the continental shelf, *i.e.* the Agulhas Bank, is 200 km wide here. Thus we have used 37°S, the southernmost latitude of the continental slope (specifically, the 400 - 4000 m isobath range) along which the Agulhas flows. Zonally integrated Sverdrup transport computed from wind-stress curl varies by at least 20% between 35° and 37°S.

South Indian to South Atlantic transport. The Agulhas Current probably bifurcates to some degree, as yet poorly known, in the Retroflection. One branch turns west into the S. Atlantic ocean, and the other east into the S. Indian as the Return Current. First, we note that the transport of the Agulhas Current at y_p, $T_A(y_p)$, is given by an integral of the Sverdrup interior transport across the South Indian basin at the latitude y_p, plus the locally recirculating transport T_L:

$$T_A(y_p) = \int_{x_R}^{x_E} \frac{curl\ \underset{\sim}{\tau}(y_p)}{\rho\beta}\, dx \quad + \quad T_L \tag{6.4}$$

where x_R and x_E are the longitudes of the Retroflection and Australia at y_p. The maximum South Indian interior transport at latitudes near y_p is 63 Sv, which gives us a maximum value for the integral. The maximum observed Agulhas geostrophic transport at the 1985 transects relative to 2400 dbar is 98 Sv, which gives a value for T_A. Evidently the recirculating transport T_L was at least 35 Sv.

Now the transport of the super-gyre streamlines, T_C, representing water transported from the South Indian to the South Atlantic, is just the interior transport integrated across the South Indian basin at the latitude y_R of the southern boundary of the Retroflection. This is given by an integral analogous to the one appearing in

Eq. (6.4) evaluated at y_R, the Retroflection southern boundary. The Retroflection southern boundary is related to the partition tip latitude y_p by $y_R = y_p + W_{RS}''$.

The value of T_C estimated from the wind field at y_R is about 30 Sv, with a standard error of at least 8 Sv, again using *Hellerman and Rosenstein's (1983)* maps of Sverdrup transport computed from wind stress curl. It must be noted that this value comes from the southernmost edge of their maps where errors are largest.

The observed values of interbasin transport are:

- 13.5 Sv (relative to 1500 dbar, 1983 observation),
- 19.2 Sv (relative to the bottom, 1984 observation, possible incomplete transect),
- 6.7 Sv (relative to 1500 dbar, 1985 observation),
- 5.0 Sv (relative to 2400 dbar, same 1985 observation), and
- 11.8 Sv (relative to deepest common levels, same 1985 observation).

These values are consistently smaller than the 30 ± 8 Sv inferred from the wind observations. The interbasin transport of warm water is discussed further in Chapter 8.

Return Current transport. The transport of the Return Current that flows directly eastward into the S. Indian Ocean in the Agulhas Return Current is given by

$$T_I = [T_A - T_C] \tag{6.5}$$

where T_A is the transport of the Agulhas Current at y_p, and T_C is the net flow past the tip of Africa from the Indian Ocean into the Atlantic Ocean.

If the maximum observed Agulhas Current transport T_A is 98 Sv, and the maximum observed Indian to Atlantic flow T_C is 5 - 19 Sv, then the direct Agulhas Return Current transport T_I is evidently at most 93 Sv. There are two transects of the Return Current in the 1985 survey with transports of 54 and 94 Sv, but observed Return Current transports cannot compared directly to T_I, however, since there is no

way of knowing where the Return Current 'ends,' since eastward transport persists to the south in the Antarctic Circumpolar Current (which includes the super-gyre streamlines).

Southern limit of the super-gyre. Where is the southernmost streamline of the combined S. Atlantic/S. Indian super-gyre? Geostrophic transport calculations across the Agulhas and Agulhas Return Currents show that the net east-west transport is less than 5 Sv, if the integration is taken from the African coast out to 110 km beyond the Return Current 15 C/200 m contour. This implies that the outer streamline of the super-gyre is at about this location. The smallest paired Agulhas and Return Current transports have values of 54 and 56 Sv. These values agree very well (if fortuitously) with the maximum transport value of 63 Sv expected from the returning interior transport alone, with no recirculating component.

6.5 Role of coastline curvature

The general question of an inertial jet separating from a curving coastline was considered by *Ou and de Ruijter (1986)*. They used a $1\frac{1}{2}$layer inertial jet model bounded offshore by a free streamline to show that the separation point from the coast, where the interface between the two layers surfaces, was a function of the current's transport, the coastline curvature, and the Coriolis parameter.

Increasing transport decreases the interface depth at the coast, h_L. For a given transport, increasing cyclonic coastline curvature and/or increasing f also decreases h_L (Fig. 6.5). Again, once h_L reaches zero, the interface breaks the surface, and the current separates from the coast. After separation, the jet follows a path dictated by the vorticity balance between path curvature vorticity and planetary vorticity (the 'separation curve' on Fig. 6.5).

This model clearly illustrates, as did the asymptotic models, the balance of curvature vorticity and the planetary vorticity in a free western boundary current extension. The calculated path for a free jet is shown in Fig. 6.6, with the interface at the 10 C isotherm, a dimensional upper layer transport of 60 Sv, and zero path curvature at 35°S. These parameter values and the corresponding calculated path compare well to the observed Agulhas path during 1983 survey (see Fig. 3.14).

The transport value and the zero path curvature location for 1985 would be hard to chose, since transport varies from 26 Sv at transect B to 73 at transect D! (relative to 1500 m, as for the 1983 observations). Since the separation point is at a higher latitude in 1985 than in 1983, the logic of the model would demand a smaller transport in 1985 - a point with which we can neither agree nor argue. *Ou and de Ruijter* found that the Agulhas went around the tip of Africa without separating (something which has never been observed) for a transport that is just 10% less than 69 Sv, the 1983 value used in generating Fig. 6.5. If the current does not separate, the utter lack of friction in the model becomes a rather serious deficiency - given that a purely inertial jet is just as happy on an eastern boundary as on a western boundary *(Pedlosky, 1979)*.

This model gives a clear picture of the underlying physics of the Retroflection, but in the absence of time-dependence, transport variation alongstream, and friction, it cannot be compared to the observations in detail.

6.6 Topographic inertial jet model

The topographic inertial jet model originally formulated by *Warren (1963)* includes topographic stretching to the vorticity balance, in addition to the relative and planetary vorticity terms retained in the jet model discussed in the previous section. Again, there is no friction, so in some cases the current does not separate from the continental slope even after it turns into an eastern boundary. This model was

Fig. 6.5 – Scaled interface depth at the coast as a function of Coriolis parameter and jet curvature. Reproduction of Fig. 5, *Ou and de Ruijter (1986).*

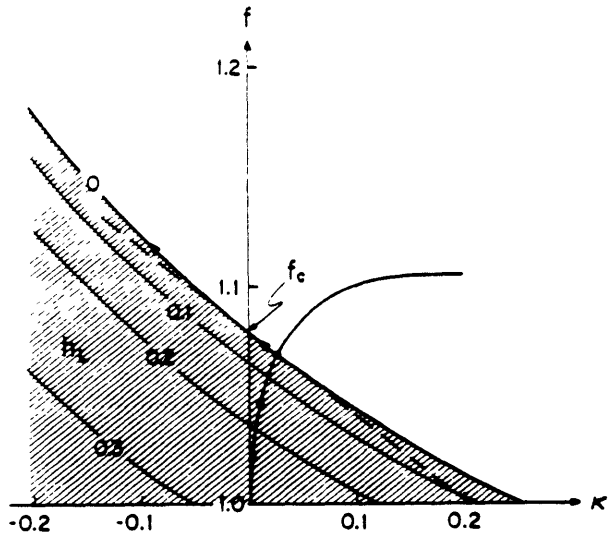

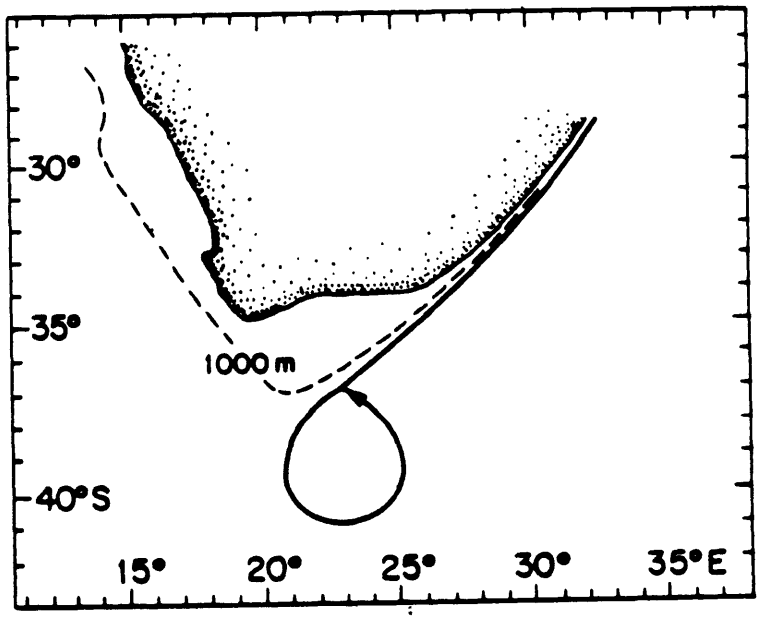

Fig. 6.6 – Agulhas Current path, calculated from $1\frac{1}{2}$ layer model, for a transport of 60 Sv, with zero jet curvature at 33°S

subsequently applied to the Agulhas Current and Return Current by *Darbyshire (1972)* and then by *Lutjeharms and van Ballegooyen (1984)*, who added realistic topography.

The parameters of the topographic model are the initial depth or latitude upstream, the integrated volume mass and momentum transport, and bottom velocity, which together imply a scale for the vertical shear. This allows a somewhat bewildering array of paths to be generated (Fig. 6.7), displaying strong sensitivity to the model parameters.

The model itself has several restrictions that make it difficult to take the dependence of the path on the model parameters too seriously in the Agulhas. Mass transport is constant alongstream and there is no time-dependence, as for *Ou and de Ruijter's* path/coastline curvature model. Momentum, bottom velocity, and vertical structure are also held fixed alongstream. It must be further assumed that the velocity direction does not vary much from top to bottom, so that vortex stretching accompanying flow across isobaths at the bottom boundary can be transmitted to the water column above. And again, in the absence of friction, a purely inertial eastern boundary current can arise. All of these restrictions seem to fit rather badly on the Agulhas: along-stream mass transport can increase and decrease by a factor of two or so, rings spawned out of the Retroflection loop, and velocity seems to veer strongly with depth.

Certainly this model does no worse than the simpler *Ou and de Ruijter* model. But the greater complication, restrictions, and sensitivity to poorly known or highly variable parameters make it rather unattractive.

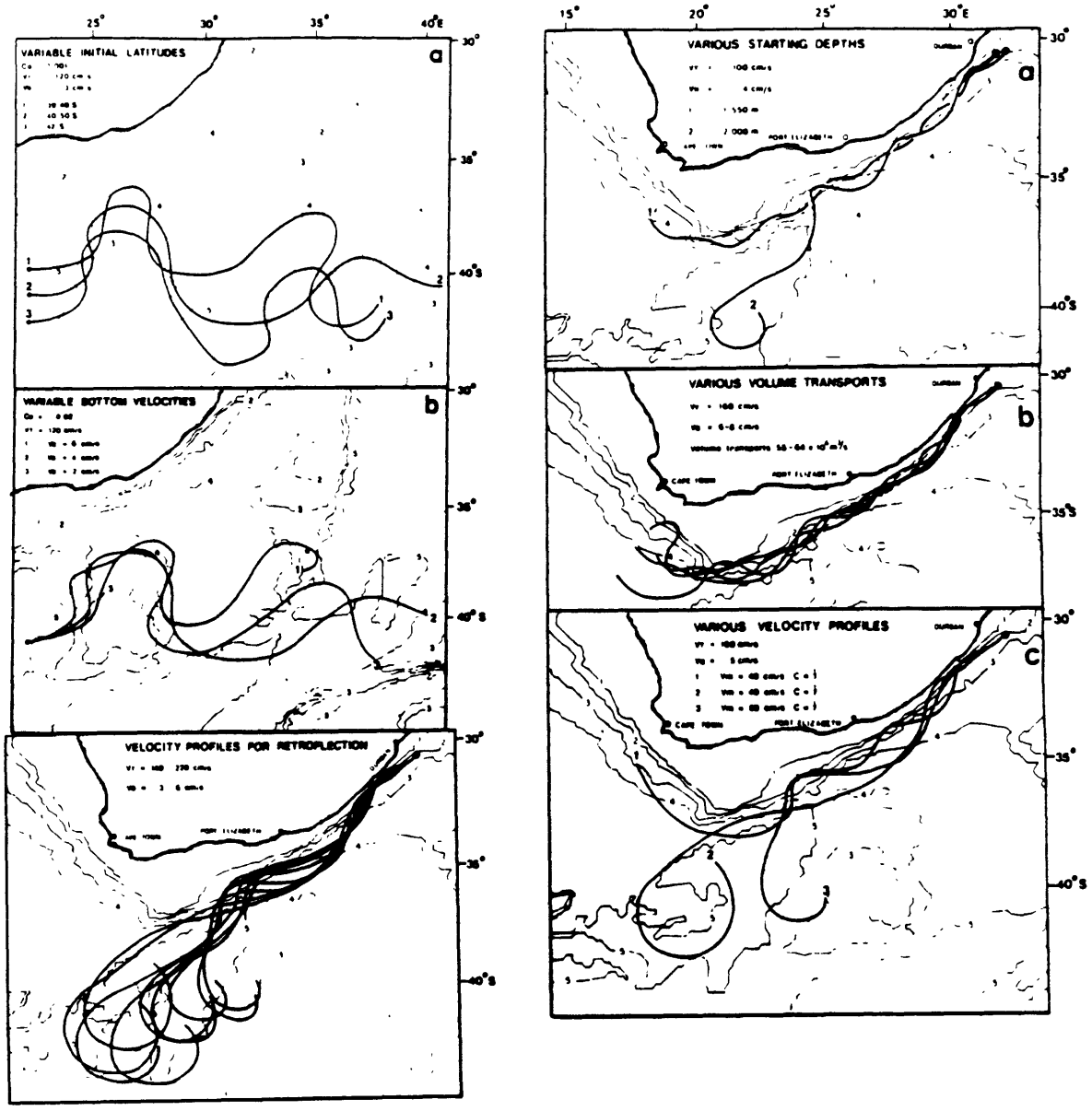

Fig. 6.7 – Inertial jet model results, parameters as noted. Reproduction of a figure from *Lutjeharms and van Ballegooyen (1984)*.

6.7 *Eddy-resolving numerical models*

A series of eddy-resolving numerical model experiments have been performed by *de Ruijter and Boudra (1985), Boudra and de Ruijter (1986),* and very recently by *Boudra and Chassignet (1988)* and *Chassignet and Boudra (1988).*

Each of these investigations models a double gyre basin with a partition ending in mid-anticyclonic-gyre. The models have progressed from one layer with a north-south partition, to three layers with a north-south partition, to models with a more realistic northeast-southwest oriented boundary. The basin is still rather small (see Fig. 6.8), and the bottom flat, but the results are encouraging and seem in harmony with our still rather limited observational experience in this area.

The dynamics of the models thus now approaches those of the ocean in complexity. Yet certain robust results stand out. First, increasing the nonlinearity of the model upper layer decreases the amount of flow into the Atlantic around the tip of Africa (Fig. 6.8), as in the asymptotic model. Second, recirculating Agulhas transport in excess of the Sverdrup interior flow occurs as non-linearity increases. Third, rings and partial/multiple retroflections are seen to form (Fig. 6.9). Finally, the models are highly time-dependent even in the presence of steady wind forcing. Clearly these models are fairly successful in replicating known ocean behaviors.

The greatest deficiency of the models would seem to be in representing the Antarctic Circumpolar Current. Maps of the Southern Ocean strongly suggest interaction between the ACC and the Agulhas Return Current, yet in some of the numerical models the southern subpolar gyre (in the absence of a true circumpolar current) can be shut down by anticyclonic vorticity input from the retroflection.

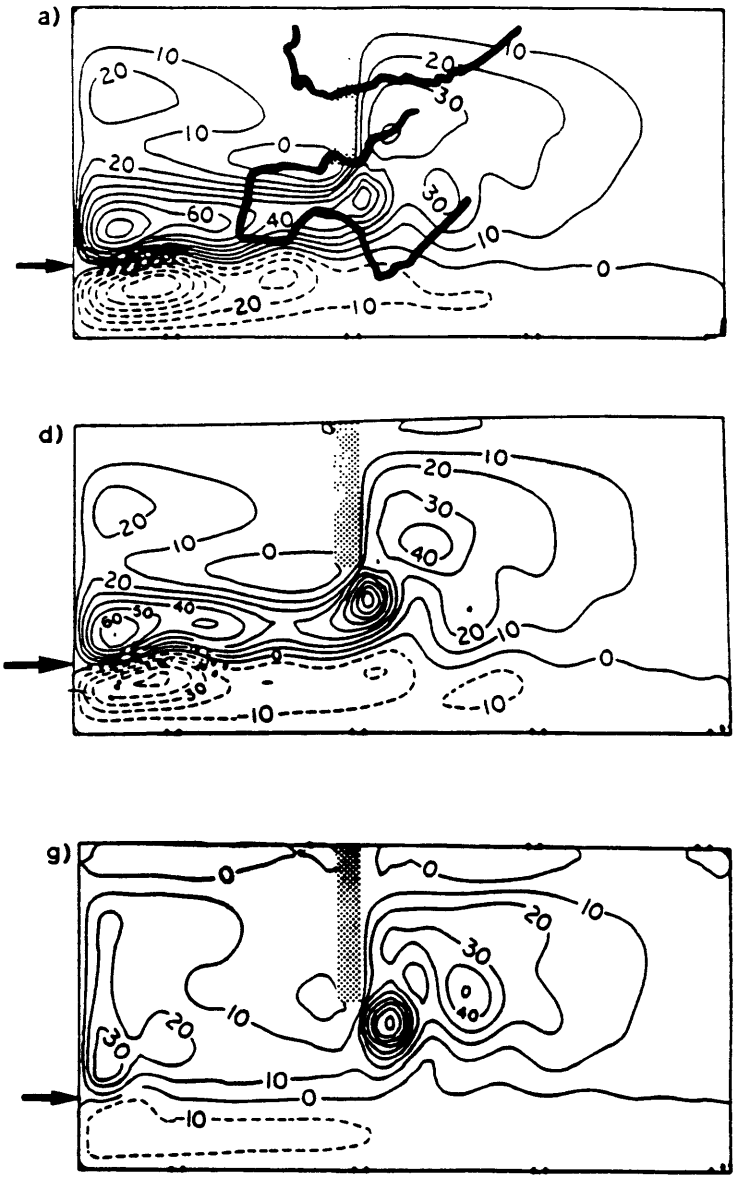

Fig. 6.8 – Agulhas Retroflection time-averaged, vertically integrated streamfunction from a three layer eddy-resolving model. Upper layer depth decreases and Rossby number increases going from panels labelled (a) to (d) to (g). Top panel has the African coastline and the 1985 15 C temperature/200 m contour overlaid. Reproduced from *Boudra and de Ruijter (1986).*

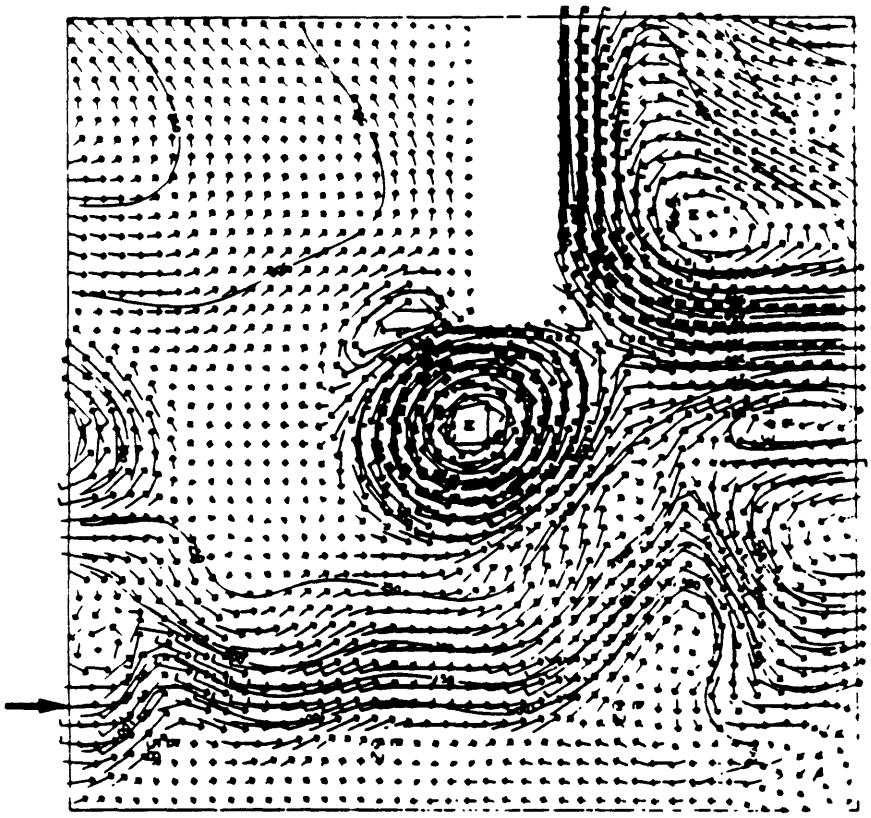

Fig. 6.9 – Instantaneous snapshot of upper layer showing ring formation and partial retroflection, from a three layer eddy-resolving model. Reproduced from *Boudra and de Ruijter (1986).*

6.8 Conclusions

A number of questions were posed at the beginning of this chapter, concerning the dynamics of observed phenomena in the Agulhas and Agulhas Return Currents. The models developed so far answer only some of these questions.

Most importantly, the basic dynamics of the Retroflection itself can be clearly understood from the asymptotic models, and from the very simple and rather elegant coastline/jet curvature model. As the current overshoots the tip of the continent, it crosses latitude lines and must balance increasing cyclonic planetary vorticity with anticyclonic curvature vorticity. The latitude to which the current overshoots is well estimated from these simple models. The longitude to which the current extends to the west, by contrast, is not constrained by planetary vorticity variation and thus might be expected to be, and in fact is, much more variable.

The path of the current relative to topographic features remains an open question, given the rather unsatisfying character of solutions to the topographic inertial jet problem with realistic topography, and the as yet flat bottom in the numerical model experiments.

Total Agulhas transport in excess of the wind-driven value is observed in the more non-linear numerical experiments. The amount of Agulhas transport that turns into the South Atlantic decreases with increasing non-linearity, in the asymptotic model and the numerical models.

Retroflection rings and partial/multiple retroflections play a role only in the numerical experiments; in the coastline/jet curvature and topographic inertial jet models, such features and in fact any time-dependence explicitly violates the model assumptions.

As to the vorticity, heat, and salt contrasts between Indian-to-Atlantic flow and the return flow, the models, not surprisingly, have little yet to offer. For this we must stick to observations for a while still.

Chapter 7: Characteristics of a cold-core ring within the Retroflection loop

7.1 Introduction

No cold-core ring had ever been observed within the Agulhas Retroflection loop before the March 1985 survey, that is, within the area bounded by the Agulhas and Agulhas Return Currents on the north, west, and south, and by the Agulhas Plateau on the east. The 1985 Agulhas Retroflection cold ring appears centered near 38S, 24E, on the northwest flank of the Agulhas Plateau, between the Agulhas and Agulhas Return Currents. The ring can be seen in maps of temperature on the 200 m and 500 m depth surfaces (Fig. 1.7 and 1.8), and in contoured sections of the ring included in the Atlas[1]. The ring is not visible in the CTD/O_2 surface temperature field (Fig. 1.6), in the satellite infrared image, nor in the XBT survey of the 15 C/200 m contour.

The ring was ≥130 km in diameter, defining this as the distance between the observed 15 C temperature/200 m depth locations at the ring edges. The ring had surface velocities ≤1.2 m s^{-1} and transported about 65 Sv (see Fig. 2.12), both relative to 2400 dbar (relative to deepest common levels, surface velocities were ≤1.3 m s^{-1} and transport was about 80 Sv). The Rossby number, estimated from the gradient wind relation, may be as high as ~0.5. These estimates, derived from the CTD/O_2 transect across the ring, are lower bounds because the orientation of the transect relative to the ring is entirely unknown; the transect may have passed through

[1] A single northwest-to-southeast Africa/Agulhas/cold ring/Return Current section for each contoured property can be constructed by concatenating sections from Agulhas transect B, the cold ring transect, and the Return Current transect F. The Return Current transect must first inverted left-to-right (north-south), since it is displayed looking east while the Agulhas and cold ring are displayed looking west. Note that there is a 10 day gap between the two northern-most stations of transect F [transect A, the ring transect, and the northernmost station of transect F were taken 12-13 March, while the rest of transect F was taken 22-23 March].

ring center, or just grazed its outer edge. Isopycnals at mid-depth do dome up in the ring to depths shallower than those observed at the southern ends of the Return Current transects; for example, $\sigma_o \sim 27.0$ kg m^{-3} domes up to ~400 m in the ring, but only to ~450 m at the southern ends of Return Current transects E and F. Assuming that the cold ring did form from a meander of the Return Current, the ring isotherm topography suggests that the cold ring transect came close to the center of the ring, and that the ring has the full strength of the current from which it was formed.

Several questions about this unusual feature will be addressed here:

- Evidence is presented that the feature is indeed a cold ring, not just a northward meander of the Return Current. This includes a discussion of why the ring lacks a signature in the sea surface temperature field (Sec. 7.2).

- The origin of the water within the ring is discussed (Sec. 7.3).

- The Retroflection cold ring is compared to cold rings observed farther east in the South Indian ocean (Sec. 7.4).

- The Retroflection cold ring's contribution to the heat/salt/vorticity balances of the South Indian and Circumpolar Oceans and the Retroflection are roughly estimated (Sec. 7.5).

Results are summarized in Sec. 7.6.

7.2 Cold ring or northward meander?

Could the observations be interpreted as showing a northward meander of the Return Current instead of a cold ring? Suppose that the 'cold ring' CTD/O_2 transect (stations 261-266, taken 12-13 March) in fact crossed a northward meander of the Return Current. Suppose also that the meander propagated east after the transect was

completed, such that the meander's western side was sampled again, by the last CTD/O_2 Return Current transect (labelled 'F' in the Atlas), and by the part of the temperature/depth contour survey that is located between the contour's last sharp turn at 42S, 22E and the contour's downstream end.

The western side of the Return Current meander, in this interpretation, was located on 12 March near 38S, 23E ('cold ring' transect), and on 22 March near 39S, 26E (intersection of transect F and the temperature/depth survey). This implies a meander propagation rate comparable in magnitude, and opposite in sign, to other propagation rates estimated from this data set (cf. Chapter 2): 300 km eastward over the 9 days between (i) the 'cold ring' transect and (ii) Transect F and the temperature/depth survey, or 0.4 m s^{-1}. If the cold feature were a meander propagating in the manner described, the data set would be seriously contaminated with spatial/temporal aliasing, and plan-view maps (like Figs. 1.6-8) contoured as if the data were synoptic would be quite misleading.[2]

Fortunately, however, there are two pieces of evidence that have not yet been mentioned which preclude the Return Current meander interpretation and support the closed cold ring interpretation. First, ring tracer anomalies and transport can also be seen at the three stations 288-290 which lie on the northern end of Return Current transect E (the Atlas contoured sections end at sta. 289, since the flow reverses at station pair 288-9). These three stations were taken on 24 March, just two days after the conclusion of the temperature/depth survey, and a day before the first daily satellite image. The transport at the station pairs 288-289 and 289-290 is about 0.6 of the ring transport inferred from the main cold ring transect taken 12-13 March. Either

---

[2]Thanks to Jerry Miller, Rosenstiel School of Marine Science, University of Miami, for his seminar question that contained this alternative interpretation.

(i) stas. 288-289 were located further from ring center than the main cold ring transect or (ii) the ring flow field weakened rapidly during the 9 days between the two surveys. There is no observational information available to decide this point.

The second piece of evidence for the cold ring interpretation is provided by the surface temperature field. If the cold feature were a meander of the Return Current, surface temperature along a line across the meander would be expected to drop where the Return Current enters the meander and rise again where the Current exits it. In fact, along the main cold ring transect surface temperature rises almost monotonically from northwest to southeast, from 20 to 22 C (Fig. 1.6). Across the Return Current at transects E and F, by contrast, surface temperature drops by about 2 C, from 20 to 18 C. This suggests that the cold core ring is indeed an isolated feature, whose initial cold surface temperature anomaly has been erased by heat flux from the atmosphere.

How long has the ring been an isolated feature? We may place a lower bound on the ring's age by estimating how long it took for its initial isolated cold surface temperature anomaly (of 18 C compared to the local summer air temperature) to disappear. The decay of the initial air-sea temperature difference ΔT can be estimated using the simple mixed layer model discussed in Chapter 2 (Eq. 2.3 and 2.4). Replacing the advective temperature change $u\frac{\partial T}{\partial x}$ by the time rate of change $\frac{-\partial T}{\partial t}$ and holding the air temperature fixed gives $\Delta T = \Delta T_o e^{-t/\tau}$ with ΔT_o the initial air-sea temperature difference. The time it takes ΔT_o to decay to $e^{-1}\Delta T_o$ in this model is $\tau = \rho C_p h/G$, where, as in Chapter 2, ρ is density, C_p is specific heat of seawater, h is a mixed layer depth of 50 m, and G is an empirical coefficient relating ΔT and heat flux per unit area.

With, as in Chapter 2,

ρ = 1000 kg m^{-3}
C_p = 4 x 10^3 J kg^{-1} K^{-1}
h = 50 m
G = 40 W m^{-2} K^{-1}

the value of τ is 5 x 10^6 s ~ 60 days. This is probably an upper bound on τ; reduced mixed layer depth with heating to, say, 10 m, would reduce τ to 12 days. The 60 day value is consistent with observations of Gulf Stream cold rings, which usually lose any cold surface temperature anomaly over a summer *(Ring Group, 1981)*. So we may estimate very roughly that the ring's age was at least 10-60 days at the time of the main cold ring transect. An inspection of two-week composite satellite infrared images for the two month period preceding the March 1985 survey did not find signs of the cold ring's formation, either because (i) the ring formed at during an earlier period, (iii) the formation event was obscured by clouds, (iv) the formation event was obscured by the infrared image compositing and declouding procedure, or (ii) the ring formed remotely and propagated into the Retroflection after losing its surface temperature signal. [3]

Upper bounds on the ring's age can be derived only by analogy to Gulf Stream cold rings, which can persist for a year or more before being reabsorbed by the Stream *(Ring Group, 1981)*. It seems likely that a cold ring within the Retroflection has a higher likelihood than a Gulf Stream ring of being reabsorbed quickly, given that the ring is closely surrounded on almost all sides by the Agulhas and Agulhas Return Currents. Some but not all Gulf Stream cold rings can still be identified in satellite images by warm streamers advected with the ring's velocity field, even after the ring's

[3]Satellite Group, Rosenstiel School of Marine Science, University of Miami (E. Chassignet, R. Evans, D. Olson), pers. comm. They generously showed me their two-week-average declouded images formed from the 4.4 km x 4.4 km Global Area Coverage NOAA TIROS-N infrared data.

cold surface anomaly has been lost *(Ring Group, 1981)*. The 1985 Agulhas cold ring does not exhibit streamers in the satellite image shown here.

Thus we may conclude that the cold feature is indeed a cold ring, not a northward meander of the Return Current, for two reasons:

- The cold feature was observed near the same location in two CTD/O_2 transects, one taken before and the other after the temperature/depth contour survey. This precludes the interpretation that the cold feature was a meander that moved east after the first CTD/O_2 transect to the Return Current position seen in the temperature/depth contour survey and Return Current transect F.

- The cold feature lacks the cold sea surface temperature anomaly (~18 C) that would be expected within a northward meander of the Return Current, exhibiting instead a nearly monotonic, relatively warm surface temperature gradient (20 C to 22 C northwest to southeast) along the main cold ring transect. A simple model suggests that the cold sea surface temperature anomaly (relative to an atmospheric temperature assumed constant) of a newly-formed cold ring decays to e^{-1} of its initial value over 10-60 days. This suggests that the Retroflection cold ring pinched off from the Return Current at least 10-60 days before the main cold ring transect.

7.3 Ring water characteristics and origins

The cold ring core at upper levels is similar to water found on the south side of the Return Current as would be expected in a feature formed from a cyclonic Return Current meander. The ring's potential temperature/salinity (θ/s) and potential temperature/oxygen (θ/O_2) values above $\sigma_o \sim 26.7$ are similar to values observed on the Return Current's south side (Fig. 7.1 and 7.2) and distinctly different from those observed in the Retroflection interior (Fig. 7.3 and 7.4). The origin of nearly all the ring core water below $\sigma_0 \sim 26.7$ cannot be determined from the available data, since

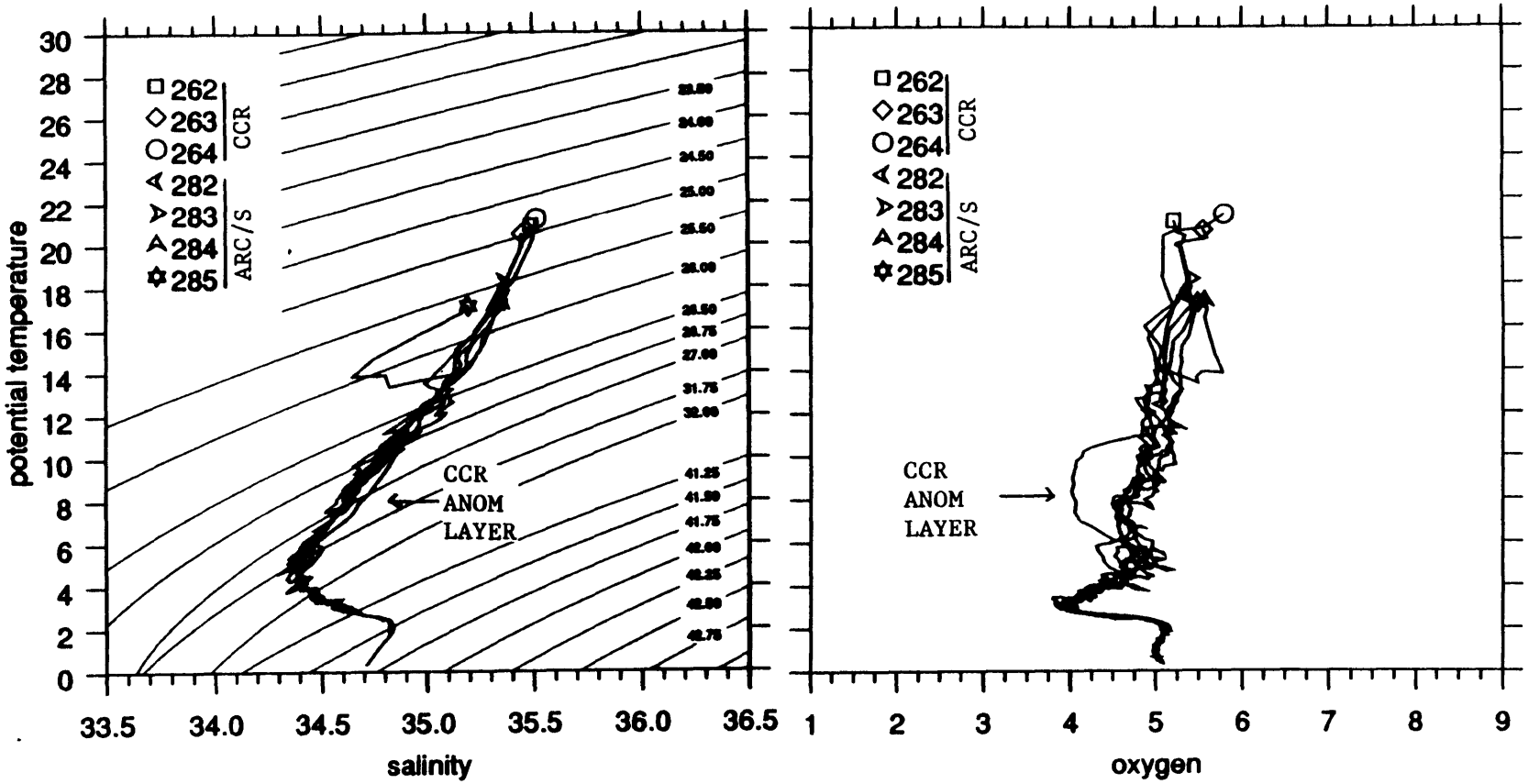

Fig. 7.1 (left panel) – Potential temperature (θ) and salinity (s) values at the cold ring core (CCR), stations 262-4, and the Agulhas Return Current south side (ARC/S), stations 282-5. The CCR and ARC/S θ/s values are similar, except for *(i)* the anomalously fresh near-surface (at $\sigma_0 \sim 26.0$) layer at ARC/S station 285, and *(ii)* the anomalously salty mid-depth layer (at $\sigma_0 \sim 27.0$) on the ring center station 263. Smooth diagonal curves are isopycnals referenced to various pressures: $\sigma_0 \leq 27.0$, $31.75 \leq \sigma_1 \leq 32.0$, and $41.2 \leq \sigma_3 \leq 42.7$.

Fig. 7.2 (right panel) – Potential temperature and oxygen (O_2) values. The CCR and ARC/S θ/O_2 values are similar, except for *(i)* the anomalously high-oxygen near-surface (at 14 C) layer at ARC/S station 285, *(ii)* the anomalously low oxygen mid-depth layer (at 8 C) on the ring center station 263, and *(iii)* the ring surface water ($\theta > 18$ C) which is a bit saltier than the saltiest ARC/S surface water.

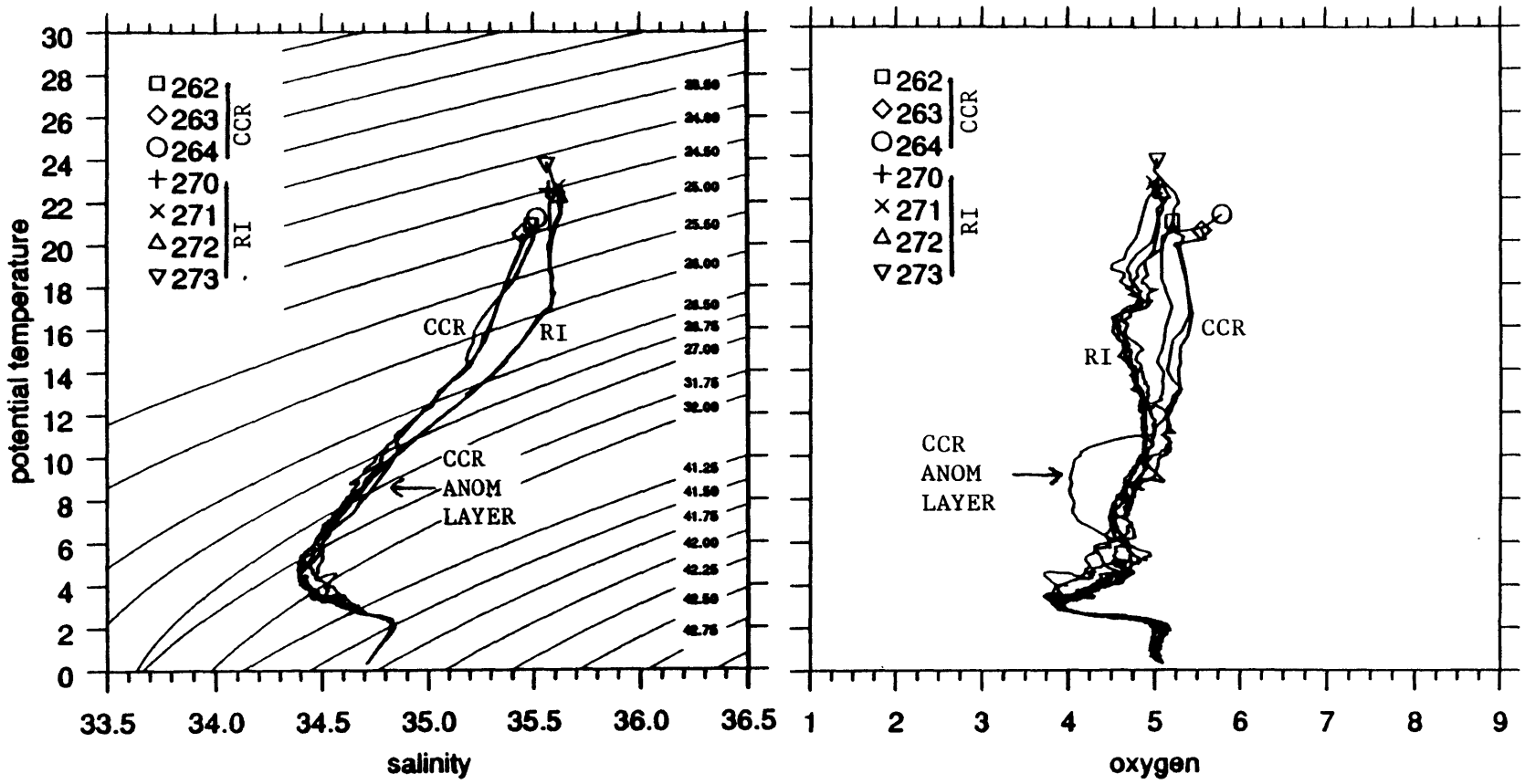

Fig. 7.3 (left panel) – Potential temperature (θ) and salinity (s) values at the cold ring core (CCR), stations 262-4, and the Retroflection interior (RI), stations 270-3. The CCR and RI θ/s values are distinct above $\sigma_o \sim 26.75$. The CCR values lie on the fresh side of the curve down to at least $\sigma_1 \sim 32.0$, except for the anomalously salty mid-depth layer (at $\sigma_o \sim 27.0$) on the ring center station 263. Smooth diagonal curves are isopycnals referenced to various pressures: $\sigma_O \leq 27.0$, $31.75 \leq \sigma_1 \leq 32.0$, and $41.2 \leq \sigma_3 \leq 42.7$.

Fig. 7.4 (right panel) – Potential temperature and oxygen (O_2) values. The CCR and ARC/S θ/O_2 values are distinct down to about 13 C.

most ring core values, the Retroflection interior, and the Return Current south side share the same, if noisy, θ/s and θ/O_2 curves beneath this level.[4]

The ring's potential density/planetary potential vorticity ($\sigma/\bar{q}$)values above $\sigma_o \sim 26.7$ are also similar to values observed on the Return Current 's south side and distinct from Retroflection interior values, taking into account atmospheric sources of $\bar{q}$ in the seasonal thermocline; 'similar' $\bar{q}$ differ by a factor of 2 or less, and 'distinct' values by more than a factor of 2 (see Atlas $\sigma/\bar{q}$ sections, cold ring transect, Agulhas transect A, and Return Current transects E and F; same stations as Figs. 7.1 - 7.4). The three $\sigma/\bar{q}$ fields coalesce below $\sigma_o \sim 26.7$. Relative vorticity is at most ~0.4 times the planetary potential vorticity, with the largest values found near the sea surface in the shoulders of the Agulhas jet (see Chapter 5), so its contribution to potential vorticity anomalies is considerably smaller than the factor of 2 planetary potential vorticity anomalies considered here.

There is one layer beneath $\sigma_o \sim 26.7$ in the ring core with characteristics markedly different from both the Retroflection interior nor the Return Current south side. A layer of extraordinarily salty, low oxygen water was observed at the center station of the ring (station 263), within the density range $26.8 > \sigma_o > 27.2$ kg m^{-3} at depths of $300 < z < 500$ m and $6 < \theta < 10$ C (Figs. 7.1 - 7.4 and Atlas cold ring sections).

---

[4]The Retroflection interior water is characterized here by stations 270-273 at transect A. Transect A crosses the Agulhas farthest upstream, before the Agulhas bifurcates, and before it interacts with the cold core ring. Retroflection interior stations further downstream are all contaminated to some degree by cold, fresh water that has been entrained into the Agulhas transport from the cold ring, the South Atlantic, or the Circumpolar Ocean.

The ring core is characterized by stations are 262-264 from the main ring transect; stations 289-290 from the northern end of transect F graze the ring edge.

The cold side of the Return Current is is characterized by stations 282-283 on the cold side of transect F, and 284-285 on the cold side of transect E.

The layer's salt anomaly is significant despite its smallness (Fig. 7.5). Relative to the Retroflection region's saltiest/warmest volumetrically important thermocline water, the South Indian Central Water (SICW), the anomaly is at most +0.10 psu on constant isopycnal surfaces; the SICW is characterized by a tight, stable θ/s relation at thermocline temperatures (about 8 - 13 C; see Fig. 7.3). The anomalous cold ring layer is as salty as any water observed at comparable densities during the entire 1985 and 1983 Retroflection surveys. The θ/s values at the salty cold ring core station (station 262) and at other salty stations in the $26.8 > \sigma_o > 27.2$ density range of the 1985 survey (stations 277 and 278 in Fig. 7.5) may be compared to the entire 1983 *Knorr* CTD data set *(Gordon* et al., *1987),* shown in Fig. 7.7. These two stations show Red Sea Water remnants entering the Retroflection region on the continental slope inshore of the Agulhas Current axis.

The layer's oxygen anomaly is striking (Fig. 7.6).[5] The layer oxygen values are 0.5 ml l^{-1} less than all the 1983 Retroflection observations at comparable potential temperatures (Fig. 7.8). They are as much as -0.75 ml l^{-1} lower than the lowest values observed during the 1985 survey south of the Return Current or in the Retroflection interior. Lower oxygen was observed in 1985 at these temperatures on the inshore side of the Cape Town Eddy (Fig. 7.6). The Eddy is just south of St. Helena Bay, the southernmost area of the Benguela coastal upwelling regime, in which oxygen-deprived water is produced at the local bottom density on the continental shelf ($\sigma_o \sim 26.8$ kg m^{-3} in St. Helena) as a result of the upwelling-enhanced biological activity and oxygen utilization rates (shown in Fig. 7.9, reproduced from *Chapman and Shannon, 1985*). Oxygen values less than 4.0 ml l^{-1} were found on the Cape Town Eddy transect within 100 km of the shelf break, at stations 207, 208,

[5]The CTD/O_2 measurements of low oxygen in the layer are confirmed by a titrated value of 4.14 ml l^{-1} in a water sample taken at ~400 dbar, 7.8 C, on station 263.

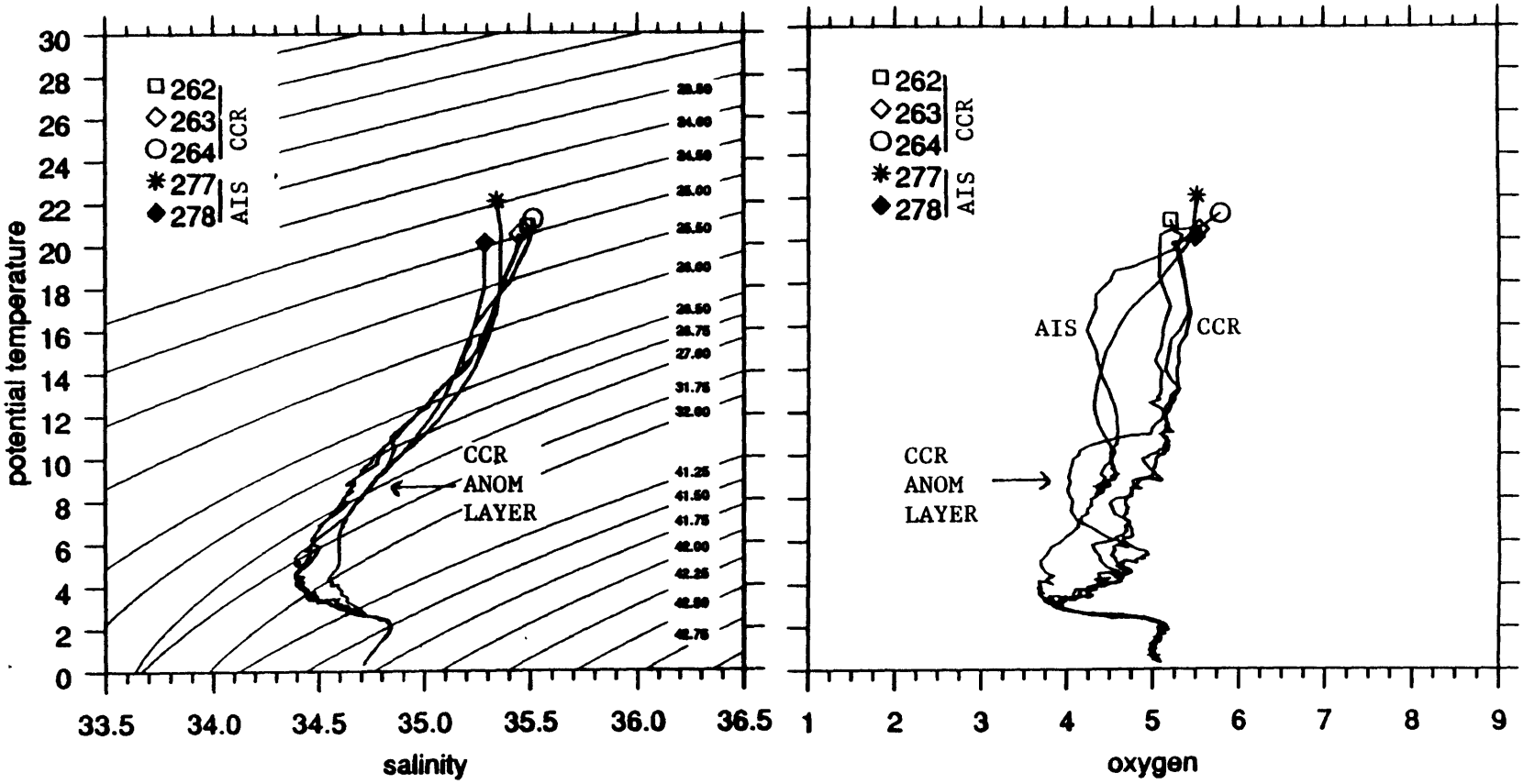

Fig. 7.5 (left panel) – Potential temperature (θ) and salinity (s) values at the cold ring core (CCR), stations 262-4, and the Agulhas Current inshore side (AIS) stations 277-8. The anomalous layer (at $\sigma_o \sim 27.0$) on the ring center station falls on the AIS θ/s curve. Smooth diagonal curves are isopycnals referenced to various pressures: $\sigma_O \leq 27.0$, $31.75 \leq \sigma_1 \leq 32.0$, and $41.2 \leq \sigma_3 \leq 42.7$.

Fig. 7.6 (right panel) – Potential temperature and oxygen (O_2) values. The AIS θ/O_2 curve falls midway between the outer ring core curves (stations 262 and 264) and the anomalous layer (at $\sigma_o \sim 27.0$) on the ring center station 263.

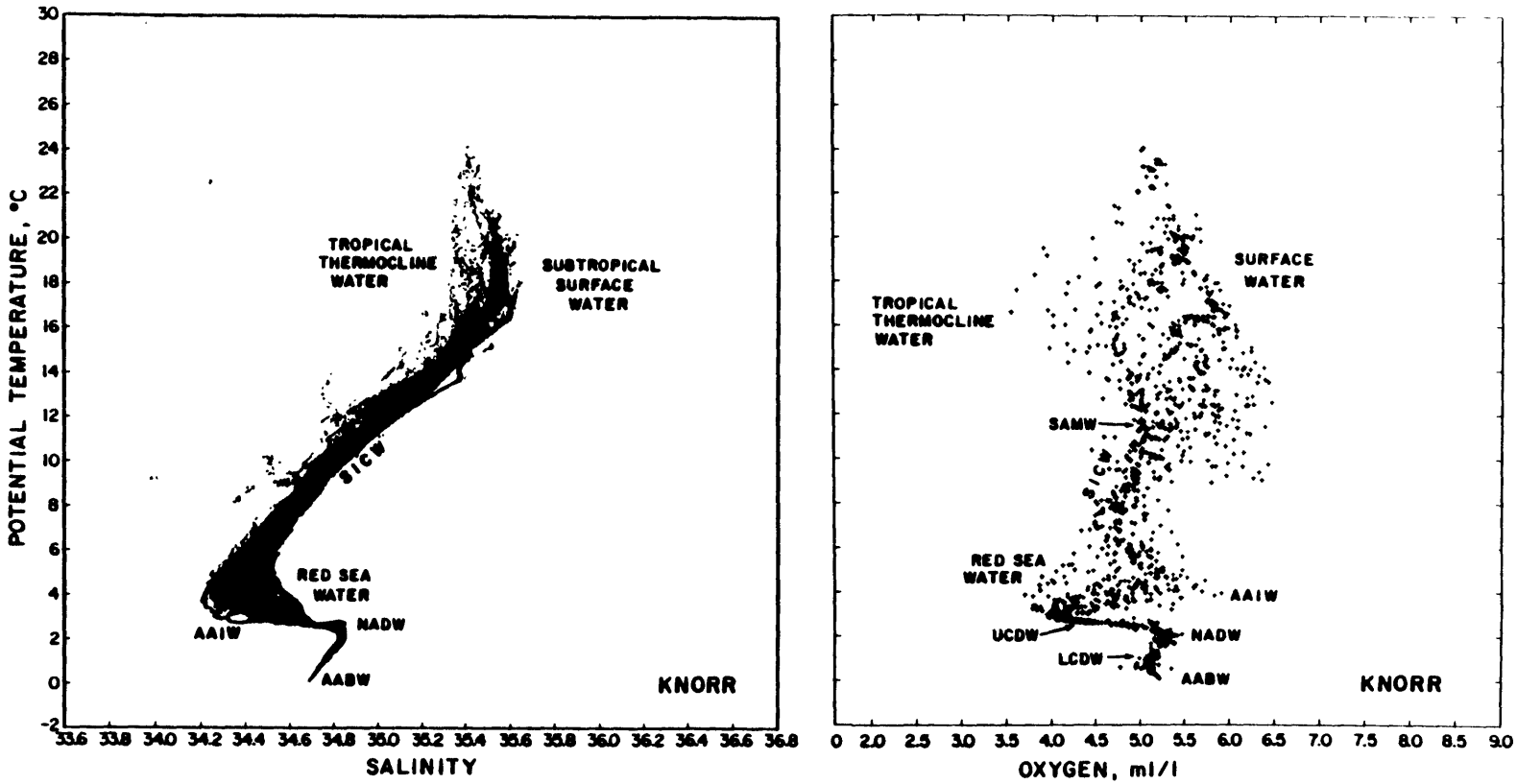

Fig. 7.7 (left panel) – Potential temperature *(θ)* and salinity *(s)* values for the entire 1983 Agulhas Retroflection Cruise, *R/V Knorr* data set. The various water masses are marked: South Indian Central Water (SICW), Antarctic Intermediate Water (AAIW), North Atlantic Deep Water (NADW), and Antarctic Bottom Water (AABW). This figure is a reproduction of Fig. 11(a), *Gordon* et al., *1987*.

Fig. 7.8 (right panel) – Potential temperature and oxygen *(O_2)* bottle-data values, 1983 Agulhas Retroflection Cruise, *R/V Knorr* data set. Water masses as in Fig. B.7, plus: Subantarctic Mode Water (SAMW), and Upper and Lower Circumpolar Deep Water (UCDW and LCDW). This figure is a reproduction of Fig. 11(b), *Gordon* et al., *1987*.

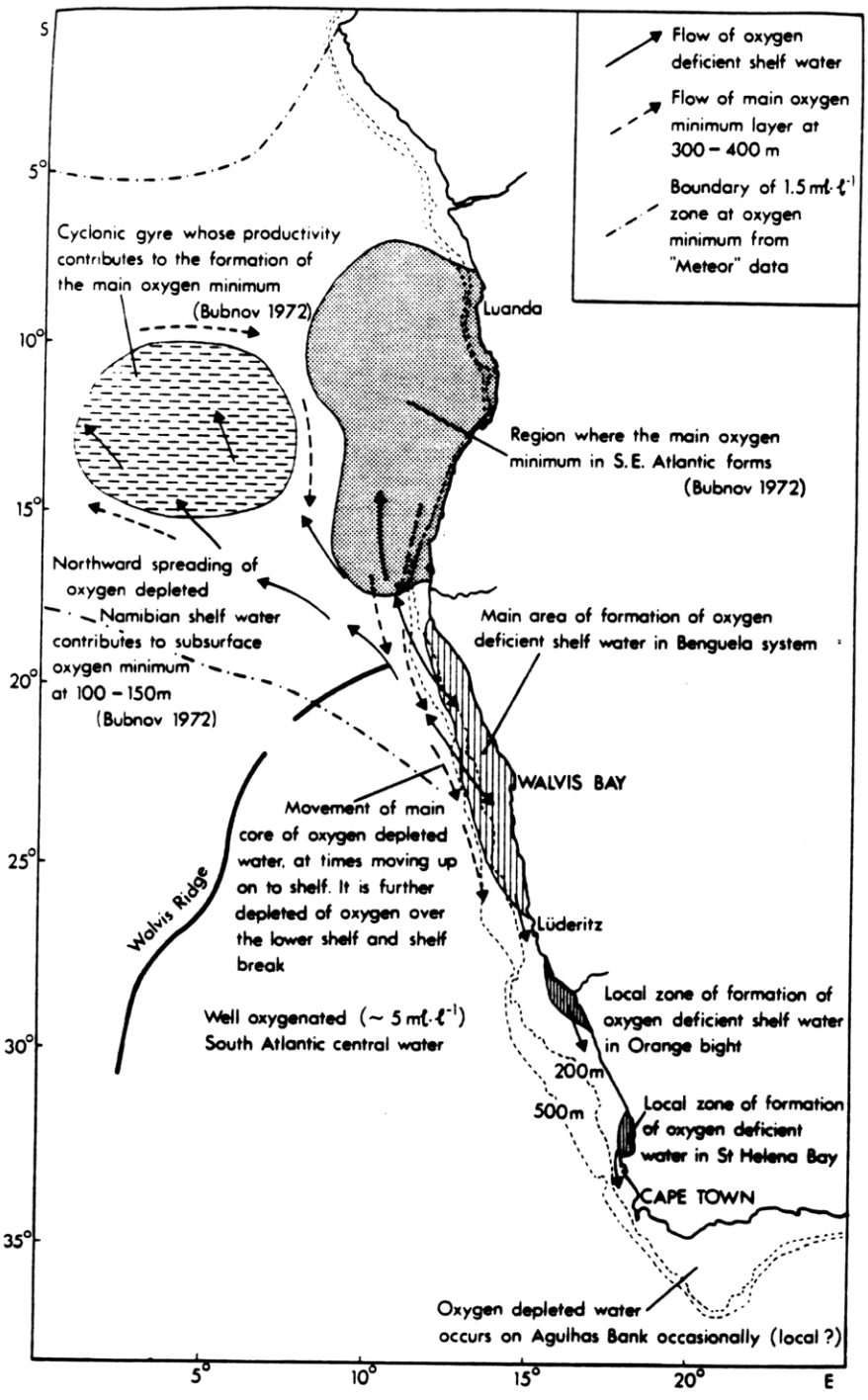

Fig. 7.9 – Sketch showing areas where low oxygen water is formed in the South East Atlantic and its inferred movement. The low oxygen, $\sigma_o \sim 26.8$, water observed on the inshore side of the Cape Town Eddy at stations 207, 208, and 211 (see Atlas sections), is probably produced at shelf bottom densities in St. Helena Bay, the southernmost low-oxygen-water production region shown here, and advected southward in a poleward countercurrent beneath the Benguela Current. This figure is a reproduction of Fig. 6, *Chapman and Shannon, 1985*.

and 211, $100 < z < 400$ m depth and $8.4 < \theta < 9.5$ C potential temperatures. This low-oxygen water has θ/s values very close to those of the SICW, however, so we may rule it out as the source of the anomalous water in the cold ring - not to mention the fact that nothing else in the regional circulation suggests that water mass exchange between the Benguela and cold ring regimes could have occurred.

Evidently, then, the cold ring's anomalously salty, oxygen-poor layer is either *(i)* the product of water mass modification within the ring, *(ii)* an anomalously low-oxygen blob from the inshore side of the Agulhas, or *(iii)* a combination of the two.

First we consider the layer's θ/s anomaly. The θ/s anomaly overlays almost perfectly the Red Sea Water (RSW) remnant observed at stations 277 and 278. There are several possibilities for how the remnant could have been incorporated into the ring core. The remnant could have been advected with the first Agulhas retroflection branch along the ring edge. Alternatively, the remnant could have come in contact with the ring if the ring, or the Return Current meander from which it was formed, cut off the Agulhas Current flow as far inshore as the RSW influence. Once the remnant was brought in contact with the ring, it could then have moved into the ring core as an intrusion, or during ring propagation if core water was imperfectly carried along with the ring. The only other plausible source for the layer's θ/s anomaly is modification of SICW, e.g. SICW cooled ~0.2 C at constant salinity. The mechanism for such modification is not obvious.

Next we consider the layer's θ/O_2 anomaly. Aging Gulf Stream cold core rings have been observed to exhibit decreasing oxygen concentrations in the upper 150 m due to biological activity *(Ring Group, 1981)*. Ring core oxygen concentrations decrease with time at deeper levels due to exchange between the ring core and lower-oxygen Sargasso and Gulf Stream water. The Agulhas ring's anomalous layer occurs at $300 < z < 500$ m, a bit deeper than the level at which biological activity predominates

in Gulf Stream cold rings. However, unlike the Gulf Stream rings, the water outside the Agulhas cold ring core is all higher in oxygen (with the RSW remnant having the lowest values at +0.4 ml l^{-1} relative to the anomalous layer), so the lower oxygen cannot be attributed entirely to exchange. Perhaps in the center of the Agulhas ring a surface convergent secondary circulation similar to that observed in Gulf Stream cold rings concentrates and downwells biological material, depleting oxygen there, most likely from the already low (≤4.7 ml l^{-1}) values of an RSW remnant. Nothing more can be said with the available observations.

7.4 Comparison with Mozambique ridge cold rings

Cold rings have been observed southwest of Madagascar and east of the Mozambique ridge *(Gründlingh, 1985)*. They seem to be distinctly different in structure from the Retroflection cold ring. All Mozambique ridge ring isotherms (above 1800 dbar) are 100-400 m deeper than isotherms in the Retroflection cold ring, at corresponding positions across the rings. Near the surface, isotherms ≤18 C in the Mozambique ridge ring and ≤20 C in the Agulhas ring are nearly flat.

The largest of the Mozambique ridge rings are larger in diameter than the Retroflection cold ring. The Mozambique ridge rings range from 80 to 240 km in diameter (based on the 10 C temperature/650 m depth contour). Quantitative comparison of the ring diameters is not straightforward since Retroflection/Mozambique ring isotherms have very different depth ranges, but, judging subjectively, the Retroflection cold ring has a diameter of 130 km based upon the 15 C temperature/200 m depth contour (assuming that the Retroflection ring transect does nearly bisect the ring).

The maximum geostrophic surface velocities of Mozambique ridge rings are ≤0.6 m s^{-1} and their geostrophic transports range from 20-50 Sv, both relative to

1800 dbar. The Retroflection cold ring though smaller has higher surface velocity and transport of ~1.0 m s^{-1} and ~55 Sv relative to 1800 dbar, respectively.[6]

7.5 Cold ring contribution to Retroflection dynamical and tracer balances

The contribution of cold rings to the Retroflection dynamical and tracer balances, is a function of the rings' volume, V, the strength of the rings' anomalies per unit volume, δ_n, the frequency with which the rings are formed, $2\pi/\tau$, and the ring water's ultimate fate, which may be designated by r, the ratio of ring fluid absorbed by the Retroflection to total ring fluid introduced. The scale rate $\frac{da_n}{dt}$ at which rings deposit a_n in an oceanic region is given by:

$$\frac{da_n}{dt} \sim \frac{2\pi r V \delta_n}{\tau} \tag{7.1}$$

Since only V and δ_n can be estimated from the 1985 cold ring transect, the ring contribution to South Indian/Circumpolar balances can be reported only in dynamical or tracer units per ring formed, *i.e.*, $\delta_n V$, leaving the question of the frequency of ring formation $\frac{2\pi}{\tau}$ and the efficiency of ring water absorption r to later investigators.

The volume and other anomalies are estimated here in terms of the 10 C isotherm depth, following the practice of *Olson and Evans (1986)* in their analysis of Agulhas warm rings. They used this isotherm to represent the interface in a two-layer approximation of ring structure, having found maximum correlation between isotherm depth and dynamic height at this temperature in the *Levitus (1982)* atlas data taken from

[6]Transport linearly interpolated from values (i) relative to 1500 dbar (50 Sv) and 2400 dbar (65 Sv). The transport relative to the bottom and (mistakenly) to 2400 dbar reported elsewhere omitted station 261, which ended near 3300 dbar, ~2000 dbar above the bottom. Inclusion of this station does not significantly change the transport relative to any level.

the 10° x 10° square centered on the Retroflection and the warm ring region west of it. The 10 C isotherm depth/dynamic height *(d, h)* relation within this box is

$$d, \text{ dyn m} = C_o + (0.0018 \pm 0.0001)\ h, \text{ m}$$

with C_o a constant. Since 1 dyn m = 10 $m^2\ s^{-2}$, the reduced gravity g' is 0.018 m s^{-2}.

The 10 C isotherm in the Agulhas cold ring is represented here by a circularly symmetric Gaussian, $h = h_o + A\ e^{-r^2/R^2}$. This is the simplest function that can be easily fit[7] to the observed 10 C depths at stations 261-266 (Fig. 7.10), and will serve as an objective, reproducible way to evaluate integral properties of the ring. The fit produces the values h_o = 750 m for the 10 C depth as the radius r goes to infinity, A = -500 m for the amplitude (the depth anomaly for a cold ring is negative), and R = 93 km for the half-width. The internal Rossby radius of deformation is $L_R = \frac{\sqrt{g'h_o}}{f} \sim 42$ km, and the Rossby number is $\varepsilon = \frac{L_R}{R} \sim 0.45$, using these values.

The upper layer volume anomaly is (Fig. 7.11):

$$V = \int_0^\infty 2\pi r\ [\ h(r) - h_o\ ]\ dr = \pi R^2 A = -14 \text{ x } 10^{12} \text{ m}^3 \qquad (7.2)$$

i.e., the same as a cylinder of radius R and height A. The upper layer volume within a radius c is just $V_u\ (c) = \pi c^2 h_o$ - |V|. It is 6.8 x 10^{12} m^3 within $r = R$.

[7]The nonlinear fitting routine *mrqmin* from *Numerical Recipes in C (Press* et al., *1988)* was used.

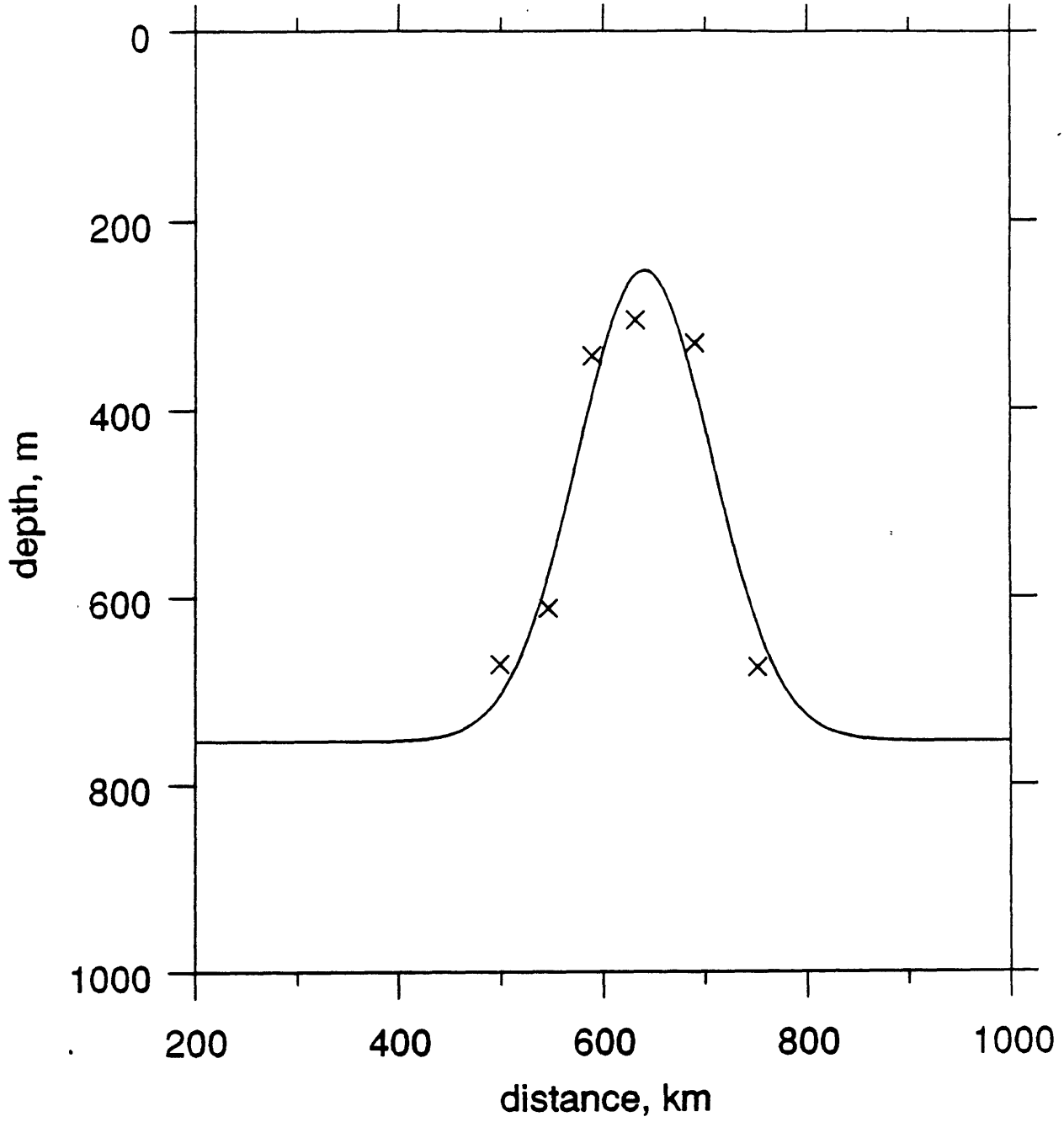

Fig. 7.10 – Depth of 10 C isotherm in the cold core ring. Cross are observed depths at stations 261 – 266 (shown with station 266 farthest on the left), and curve is Gaussian fitted to the observed depths. Note that the far-field is not specified with observations, but results from the near-field fit. The x-axis distance has an offset of about 500 km compared to the distance on the Atlas cold ring transect.

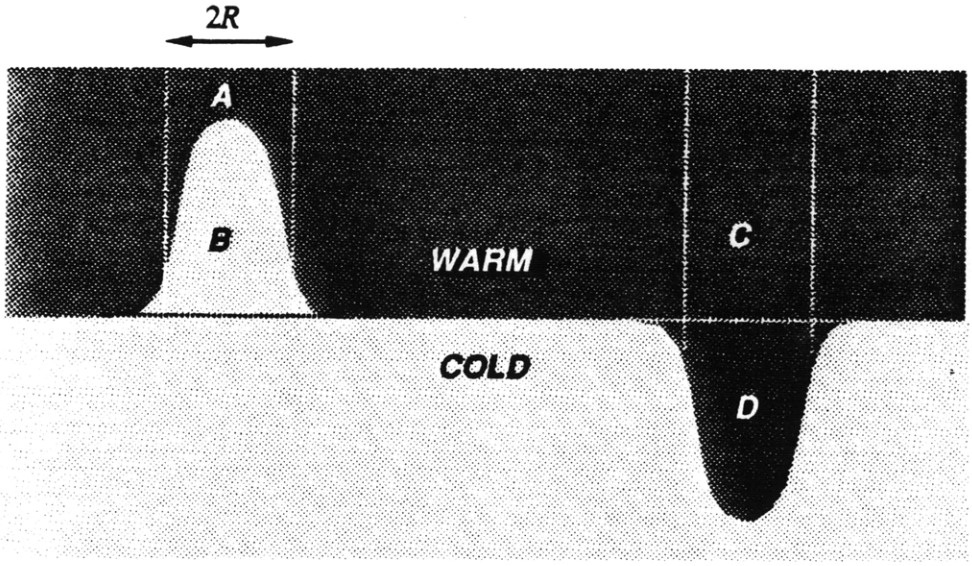

Fig. 7.11 - Cold ring (left) and warm ring (right).
Ring radius labelled *R*.

Cold ring: upper layer volume anomaly is $-B$
Upper layer core volume is A.

Warm ring: upper layer volume anomaly is $+D$
upper layer core volume is $C + D$.

The ring's available potential energy per unit volume, *i.e.*, the potential energy anomaly due to the departure of h from h_o, is APE $= \frac{\rho g'}{2}[\, h(r) - h_o \,]$. Integrating over the upper layer volume anomaly gives:

$$\int dV \,\mathrm{APE} = \int_o^\infty 2\pi r \, \frac{\rho g'}{2} [\, h(r) - h_o \,]^2 \, dr = \tag{7.3}$$

$$= \frac{\rho g' \pi R^2 A^2}{2} = 61 \times 10^{15} \text{ J}$$

again, the same as in a cylinder of radius R and height A.

The ring's kinetic energy per unit volume due to baroclinic velocity in the upper layer is $\mathrm{KE_b} = \frac{1}{2}\rho v_b^2$, where the baroclinic velocity, v_b, obeys the gradient wind relation $\frac{v_b^2}{r} + f v_b = g' \frac{\partial h}{\partial r}$, which is just a quadratic for v_b. The integral of $\mathrm{KE_b}$ over the upper layer volume is:

$$\int dV \;\mathrm{KE_b} = \int_o^\infty \pi r \, h(r) \, \rho \, v_b^2 \, dr \tag{7.4}$$

where

$$v_b = = \frac{rf}{2}\left(\sqrt{\left\{ 1 + \frac{8g'[h(r)-h_o]}{f^2} \right\}} - 1 \right) \tag{7.5}$$

Integrating this numerically gives a value of 8.3×10^{15} J for the ring's integrated $\mathrm{KE_b}$. Note that we specified the $\mathrm{KE_b}$/APE ratio *a priori* by specifying a Gaussian for h. Velocity and thus kinetic energy, unlike volume and available potential energy, are sensitive to the details of the shape of h. Errors in the $\mathrm{KE_b}$ estimate are thus likely to be

larger than errors in the other estimates. Also, of course, any barotropic contribution to the kinetic energy is missing entirely.

The ring's potential vorticity anomaly is

$$\text{PVA} \quad = \frac{g'}{g}\frac{f + \zeta_b}{h} - \frac{f}{h_o} = \frac{g'}{g}\frac{\left[1 - \frac{h}{h_o}\right]f + \zeta_b}{h} \tag{7.6}$$

neglecting barotropic contributions to the relative vorticity $\zeta_b = \frac{v_b}{r} + \frac{\partial v_b}{\partial r}$, and holding f fixed. The factor $\frac{g'}{g}$ is included for consistency with the planetary potential vorticity estimator $\frac{fN^2}{g}$ used in the Atlas contoured sections (and elsewhere in the literature, e.g. *McCartney, 1982*). The ring's total potential vorticity anomaly is obtained by *(i)* using Eq. 7.5 to compute v_b and from it ζ_b, and then *(ii)* integrating Eq. 7.6 numerically over the upper layer volume, as was done for the kinetic energy. This gives an integrated PVA value of 2.8×10^3 m^{2}s^{-1}.

The estimates just discussed quantify the ring's dynamical contribution to the Retroflection. The ring's upper layer (θ >10 C) tracer anomalies, relative to Retroflection interior tracer values, are confined to a volume of approximately

$$V_u(R) \sim \pi R^2 (h_o - |A|) \sim 6.8 \times 10^{12} \text{ m}^3 \tag{7.7}$$

Upper layer salt and heat anomalies on isopycnals are at most +1 C and -0.3 psu relative to Retroflection interior water. The total ring upper-layer anomalies are thus at most 0.3×10^{20} J and -2.1×10^{12} kg salt. These would be the net transfers into the Retroflection if the upper layer volume influx associated with the cold ring were balanced by a withdrawal of Retroflection interior water, in the cores of Retroflection

warm rings, for example. The cold ring's lower layer (θ<10 C) tracer anomalies are negligible (Fig. 7.3-4 and section 7.3).

Table 7.a summarizes the Agulhas cold ring's, and other ring's, characteristics. Estimates of total energy and vorticity supplied by the wind per year to the South Indian Ocean are also shown.

7.6 Conclusions

The 1985 Agulhas Retroflection cold ring, the first such feature observed within the Retroflection loop, was found on the northwest flank of the Agulhas Plateau. This ring is evidently formed from a northward meander of the Return Current that pinched off at least month or two before the 1985 survey, judging from the time it would take to warm the ring's cold surface cap to observed temperatures. The ring's geostrophic field is fully as strong as the Return Current. Subsurface upper layer water in the ring is similar to that found immediately to the south of the Return Current, and is distinctly different from water found in the Retroflection interior. The only exception is a salty, low-oxygen blob evidently entrained from the inshore side of the Agulhas where Red Sea Water remnants with the appropriate characteristics are observed. The blob's oxygen values are lower than any other water observed during the 1983 and 1985 surveys, except for unrelated shelf bottom water from St. Helena Bay at the southern end of the Benguela upwelling regime. This suggests enhanced oxygen utilization within the ring.

The cold ring's upper layer volume anomaly magnitude and its potential energy anomaly are comparable in magnitude to values of these quantities computed for the warm Agulhas rings observed in 1983. The cold ring is about three times as nonlinear as the Agulhas warm rings, and half as nonlinear as a representative Gulf Stream cold ring. The anticyclonic wind stress curl potential vorticity input to the entire

S. Indian subtropical gyre can be balanced by the potential vorticity flux associated if the South Indian and Southern Oceans exchanged approximately 25 warm ring/cold ring pairs each year.

Table B.a – Summary of ring characteristics and related quantities. Notes on following page.

Ring	Radius max vel	Ref lev	Max surf vel	Rossby no	Transp	Upper layer θ>10C						
						Vol anom	Core vol	Tot APE	Tot KE	Tot PVA anom	Tot salt anom	Tot heat anom
	R_{vmx}	p_r	v_{mx}	ε		V	V_u	$\int dV$ APE	$\int dV$ KE	$\int dV$ PVA		
	km	dbar	ms^{-1}	$\frac{v_{mx}}{fR_{vmx}}$	Sv	10^{12}m^3	10^{12}m^3	10^{15}J	10^{15}J	10^3m^{2}s^{-1}	10^{12}kg	10^{20}J
Agulhas cold ring[1]	65 65	2400 dcl	1.2 1.3	0.22 0.24	65 80	-14.	6.8	61.	8.3	2.8	-2.1	-0.3
Mozambique ridge cold ring[2]	65	1800	-0.6	0.12	32-48							
1983 southern warm ring[3]	130	note 3	-0.9	0.08		19.2		51.4	8.7			
1983 northern warm ring[3]/CTE[4]	110	note 3 1500	-0.6	0.07	35-50	15.2		30.0	6.2			
1985 Cape Town Eddy (CTE)[1]	50	2400	-0.4	0.10	29-34							
1982 Gulf Stream warm ring 82B[5]	60	note 5	-0.6	0.11		4.5		4.2	1.0			
1977 Gulf Stream cold ring Bob[6]	40	note 6	1.25	0.37		30.				0.001 s^{-1} note 6	-3.	-5.

Agulhas Retroflection reduced gravity[7]: 0.018 ± 0.001 m s^{-2}
Gulf Stream/Sargasso reduced gravity[8]: 0.0106 ± 0.0003 m s^{-2}
Estimated wind stress energy input to the S. Indian gyre in one year[9]: 3.5 x 10^{17} J
Total Retroflection eddy APE[10]: between 18 x 10^{16} and 52 x 10^{16} J
Estimated wind stess potential vorticity input to the S. Indian gyre in one year[11]: -1.4 x 10^5 m^2 s^{-1}

[1]Radius based on geostrophic velocity. Range of 1985 CTE transport values reflects the fact that the ring is neither isolated or symmetrical, displaying intensified flow on its inshore side.

[2]*Gründlingh, 1985.* Radius estimated from contoured section of temperature.

[3]*Olson and Evans, 1986.* Radius and velocities from two layer model, 10 C and reduced gravity fit to 0/2000 dyn height. Rossby numbers given here are calculated from v_{mx}, R_{vmx} and f at latitudes 35° and 38°S for the northern and southern warm rings respectively. The Rossby numbers reported in *Olson and Evans, 1986,* are 0.07 and 0.04 respectively.

[4]*Gordon et al.*, 1987. Transport values relative to 1500 dbar for the southern ring are taken from this paper. As for 1985 CTE, range of transport values reflects the fact that the ring neither isolated or symmetrical, displaying intensified flow on its inshore side.

[5]*Olson* et al., 1985. Radius and velocities from two layer model, 10 C and reduced gravity fit to 0/2000 dyn height. Volume anomaly given here is taken from *Olson* et al., *1985*, Fig. 4; volume anomaly is reported in *Olson and Evans, 1986*, as 3.9×10^{12} m^3.

[6]*Ring Group, 1981.* Radius and velocities from surface drifter. *Ring Group* did not provide details of how upper layer volume, and salt, heat, and potential vorticity anomaly values were computed. It may be said that the reported volume anomaly corresponds to a cylinder of radius 100 km and height 1 km, thus their salt and heat estimates are high, by as much as a factor of 4, relative to the estimates made using upper layer volume above the 10 C isotherm within a Gaussian half-width radius. They report that their rate of potential vorticity anomaly input from rings is similar in size to 'input from variations in wind stress [that drive most of] the circulation above the thermocline.' The rate given, 0.001 m^2 s^{-2}, is equivalent to the rate of <u>vorticity</u> (not potential vorticity) input given by

$$n \times \iint v\left(1 - \frac{(h - h_o)}{h_o}\right) \frac{f}{h_o}\, dx\, dz$$

with the number of rings $n = 2$, the ring translation speed $v = 0.05$ m s^{-1}, 10 C depth at ring center $h = 500$ m, far-field depth $h_o = 1000$ m, Coriolis parameter $f = 10^{-4}$ s^{-1}, and the integration ranges $0 \le x \le 200$ km and $0 \le z \le 1000$ m.

[7]Calculated from a linear fit of 10 C to 0/2000 dbar dynamic height *(Olson and Evans, 1986)*.

[8]Calculated from a linear fit of 10 C to 100/2000 dbar dynamic height *(Olson* et al., *1985)*.

[9]Calculated as 9.5×10^{-4} W m^{-1} *(Gill, 1974)* times 1.2×10^{13} m^2 (South Indian subtropical gyre between 25 and 37°S) times 3.1×10^7 s y^{-1}.

[10]Calculated as 6.65×10^5 J m^{-2} (maximum APE per unit area in the Retroflection, *Olson and Evans, 1986*, Fig. 6), times π times R^2, the Retroflection scale radius, estimated by $300 \le R \le 500$ km.

[11]Calculated by integrating the curl of the wind stress per unit mass over the South Indian subtropical gyre for a year, scaled by the mean stratification:

$$\frac{g'}{gh} \int\int\int \nabla \times \underset{\sim}{\tau}\, dx\, dy\, dt =$$

$$\frac{C_o g'}{gh} \int_0^{t_o} \int_0^{L_y} \int_0^{\pi L_x} \sin \frac{y}{L}\, dx\, dy\, dt = -1.4 \times 10^5 \text{ m}^2 \text{ s}^{-1}$$

using $C_o = -1. \times 10^{-10}$ m s^{-2}, $L_x = 8.9 \times 10^6$ m and $L_y = 7.0 \times 10^5$ m, $t_o = 1$ y, and constant values for reduced gravity $g' = 0.018$ m s^{-2} and layer thickness $h = 500$ m. The magnitude of $\underset{\sim}{\tau}$ is taken from *Veronis (1973)*, and the shape of $\nabla \times \underset{\sim}{\tau}$ from *de Ruijter (1982)*.

Chapter 8: Interbasin exchange and the 1983 and 1985 Cape Town Eddies

8.1 Introduction

Flow from the Indian to the South Atlantic Ocean around the tip of Africa is suggested by some of the dynamical models just discussed. *Taft (1963)* and *Gordon (1985, 1986)* saw such interbasin exchange as a link in a thermohaline overturning cell of global proportions, supplying warm thermocline water from the Indian Ocean to the North Atlantic for conversion into cold deep water. *Gordon* went on to suggest that changes in the global cell might have remote effects, *e.g.*, if the interbasin exchange rate changed, the deep water formation rate might also change.

The global scale overturning cell proposed by Gordon, based on simple heat and mass budgets, balances the export of North Atlantic Deep Water (10 to 20 Sv) from the Atlantic across 30 S with an import of South Indian Ocean thermocline water around the southern tip of Africa, with a mean temperature in the range 8 to 15.4 C.

The warmest water in Drake Passage is 8 C, as *Gordon* notes. Thus, only water warmer than 8 C must come from the Indian Ocean, in sufficient quantities to raise the mean temperature of the imported water into the 8 to 15.4 C range. Note that there is nothing in the model to distinguish between steady and time-dependent interbasin exchange.

The discussion that follows, then, addresses the question: how much thermocline (warmer than 8 C) water enters the Atlantic Ocean from the Indian Ocean around the tip of Africa and across 30 S? We examine the observational evidence from the 1985 and previous surveys, compute the thermocline water transport, and note sources of uncertainty. The relevant results of a recent inverse model of the South Atlantic sector of the Southern Ocean *(Rintoul, 1988)* are also discussed.

The heat flux across Retroflection longitudes was discussed previously in Secs. 4.7 and 4.8.

8.2 Transport observations west of the tip of Africa

Hydrographic sections were collected in 1983, in 1984, and again in 1985, starting at the tip of Africa and extending several hundred kilometers to the southwest. The 1983 and 1985 sections observed warm eddies situated near the continent. The 1983 warm eddy was dubbed the 'Cape Town Eddy' by *Gordon* et al. *(1987)*. The 1985 Cape Town Eddy (as it came to be called) is not the same ring as in 1983: drifters sowed into the 1983 CTE showed that it move slowly off into the Atlantic Ocean interior (Fig. 2 of *Olson and Evans, 1986*). Contoured sections across both rings are included in the Atlas.

The net northward transport across the 1983 ring was 13.5 Sv relative to 1500 dbar. In 1984, *Whitworth and Nowlin (1987)* found a northward flow of 19.2 Sv 200 km southwest of Cape Town at the last station pair of a short hydrographic line. This area is, however, densely populated with anticyclonic eddies and strong return flow immediately to the south cannot be ruled out. The net northward transport across the 1985 ring was 6.5 Sv relative to 1500 dbar.

The second zero of the transport field was used as the offshore edge of the ring transport in the 1983 and 1985 calculations. This must be regarded as a questionable procedure, especially when there observations of the transport field beyond the second transport zero are limited. This was the case in 1983, when the section was terminated based on evidence of isopycnals descending over 45 km (XBTs 28 and 29, and CTD 8). The accumulated transport *vs.* along-transect distance for the 1983 and 1985 rings is plotted in Fig. 8.1. The 1985 transect, which continued well past the boundary of the 1985 ring, found weak southward transport on its offshore side sufficient to

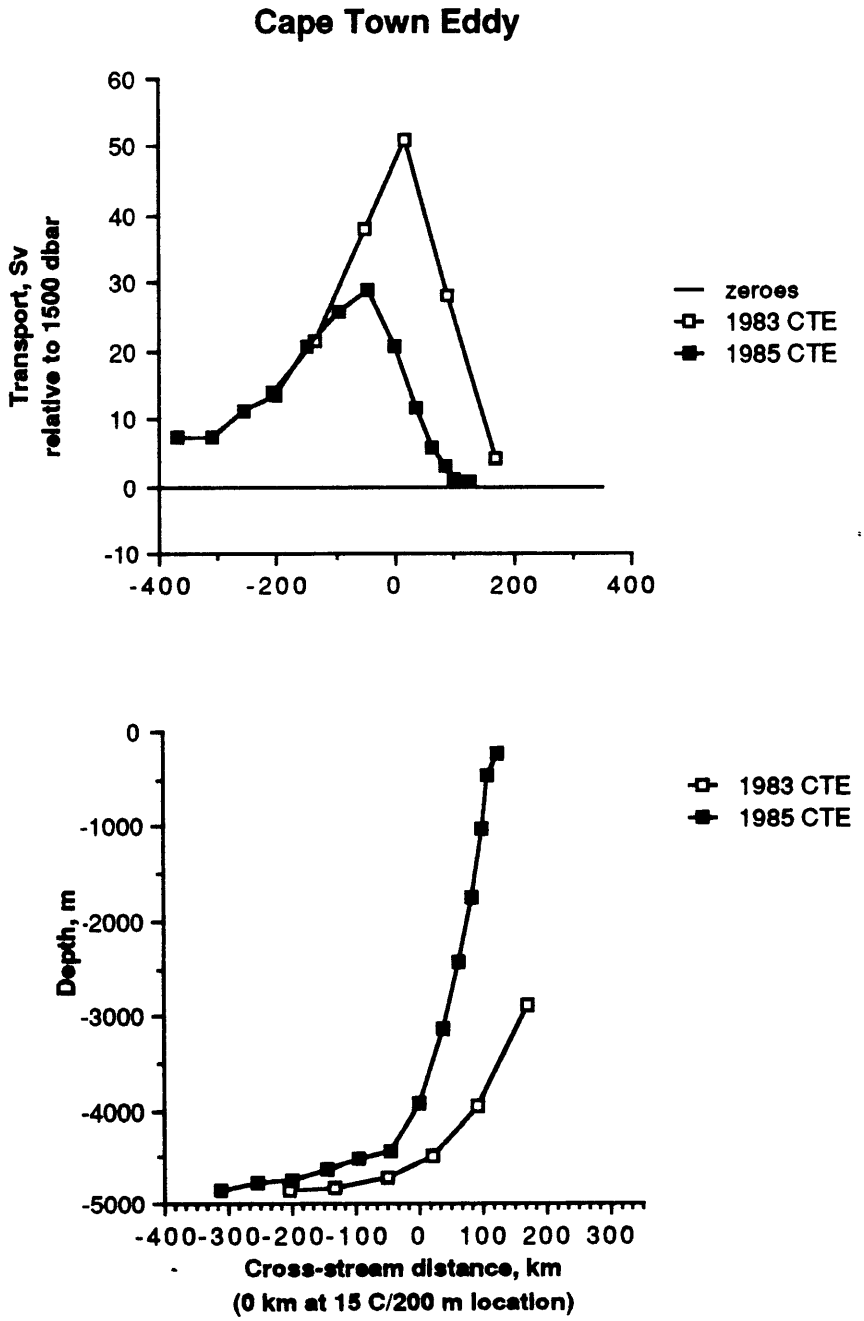

Fig. 8.1 – 1983 and 1985 Cape Town Eddy transects: transport integrated offshore and bottom depth *vs.* along-transect distance; looking northwest. Distance in km, transport in Sv. Transects oriented with 15 C/200 m contours on inshore side of eddies lined up at $x = 0$.

reduce the 1985 net imbalance to one-half the 1983 value. There is no way of knowing if a similar situation also obtained in 1983.

Now, the net transport across the 1983 and 1985 rings above 1500 dbar is almost twice the size of the net transport of water warmer than 8 C. Water this warm is found only above 350 - 450 dbar at the edges of the 1983 and 1985 rings, and above 550 - 850 dbar at their centers. The ratio of ring transport above 8 C to total ring transport is about 0.5, with both transports computed relative to 1500 dbar. The 1983, 1984, and 1985 net northward transports of >8 C water are 6.8 Sv, 9.6 Sv, and 3.3 Sv respectively, again relative to 1500 dbar, if the net transports are reduced to 0.5 of their original values.

Further, slightly more >8 C water flows south than north, since a net descent of isotherms offshore (which is just the thermal wind signature of the net northward transport) is superimposed on the symmetric ring structure. The net transport values should be further reduced by 0.5 Sv (roughly) to 6.3 Sv in 1983 and 2.8 Sv in 1985, having estimated that *(i)* the 8 C isotherm descends 200 m across the rings, *(ii)* the average azimuthal velocity above 8 C is 0.20 m s^{-1}, and *(iii)* the ring radii are on the order of 150 km.

Thus the observed net Indian-to-Atlantic transports of thermocline water, warmer than 8 C, were 6.3, 9.6, and 2.8 Sv in 1983, 1984, and 1985, keeping in mind that the 1984 value is questionable. These transports are 0.63, 0.96, and 0.28 of the lowest NADW export rate of 10 Sv, and 0.32, 0.48, and 0.14 of the highest rate export rate (20 Sv). Discounting the 1984 observation, then, the proportion of the imported transport coming from the Indian thermocline ranges 0.14 to 0.63 of the total import. The remainder of the imported water is colder than 8 C, and may be supplied either from the Indian Ocean or from Drake Passage.

Transports relative to 2400 dbar[1] and relative to the bottom/deepest common levels were also examined for the the 1985 eddy. The net transport above a 2400 dbar reference level is 5.0 Sv. This is slightly less than the net transport above a 1500 dbar reference level. Net transport above deepest common reference levels is 12.7 Sv. Northward bottom velocities over the continental slope would, obviously, increase the net northward transport.

Interestingly, on the inshore side of the 1985 Cape Town Eddy, very low oxygen values are found (see Atlas contoured section of oxygen for this transect). This low oxygen water would seem to originate to the north at shelf bottom densities in St. Helena Bay *(Chapman and Shannon, 1985;* see Fig. 7.9, which is reproduced from this paper and related discussion in Sec. 7.3). There is some possibility of oxygen depleted water forming on the Agulhas Bank; none was seen in the 1983 or 1985 surveys.

Current meter measurements to the southwest of Africa show substantial northwestward transport, *(Luyten, pers. comm)*, but as the moored array is incoherent careful analysis will be required to determine how well the moored measurements represent the entire flow field.

8.3 Indian to Atlantic warm water transport in an inverse model of the South Atlantic sector of the Southern Ocean

The 'warm water path' proposed by *Gordon* was tested by *Rintoul (1988)* using an inverse model. The inverse model solutions for the likely range of Atlantic heat flux values and overturning cell transports balanced the Atlantic NADW export across 30 S with an import of equal parts thermocline (>8 C, $\sigma_0 < 26.8$ or so) and intermediate/bottom water.

---

[1]Reference level used for Agulhas transport calculation, located above the North Atlantic Deep Water salinity maximum.

But the thermocline water is not drawn from the Indian Ocean in the inverse model solutions: all of the thermocline water (3 - 9 Sv) sent north across 30 S, plus some for export to the Indian Ocean (2 - 6 Sv), is manufactured in the South Atlantic subtropical gyre south of 32 S!

The model's thermohaline cell increases its heat flux by increasing the overturning cell transport, not by increasing the proportion of thermocline water in the overturning cell. This led *Rintoul* to suggest that *Gordon's* model overspecified the thermohaline cell by imposing both the Atlantic heat flux and the overturning cell transport.[2]

Rintoul also tested the warm water path directly by imposing on the model a 13 Sv net northward transport into the South Atlantic of water warmer than 8 C. The resulting inverse solution relative to the standard model displayed numerous striking changes, including nearly reversed transport in the Subantarctic Front of the Antarctic Circumpolar Current.

Rintoul's choice of 13 Sv for the northward transport of >8 C water was based on *Gordon's* observation of 13.5 Sv net transport across the 1983 Cape Town Eddy. But, as was discussed above, this value actually pertains to the net transport above 1500 dbar, while the net transport of >8 C water is only about 6.3 Sv.

8.4 Warm water transport by drifting rings

Warm rings spawned by the Agulhas Retroflection drift into the South Atlantic, bringing within themselves a volume of warm water. Each ring contains on the order of 15×10^{12} m^3 water warmer than 10 C *(Olson and Evans, 1986)*, relative to the 10 C isotherm depth in the far field.

---

[2] It must be noted that the hydrographic data used in the inverse model have obvious deficiencies, especially near the southern tip of Africa, and one has to wonder how the inverse solution structure is affected by these deficiencies.

For an NADW export of 10 to 20 Sv to be entirely balanced by the anomalous warm water in ring cores, 20 to 40 rings would have to be produced. The actual number of rings per year on average is unknown, but something on the order of 6 to 12 per year (one every month or two) is suggested by satellite infrared image series (the western limit of the Retroflection retreats eastward about this often, see Fig. 2.11; also *Olson and Evans, pers. comm).*

This works out to a mean eddy warm water transport on the order of 3 to 6 Sv. Net thermocline transport around the tip of Africa measured in 1983 and 1985 was, recall, 6.3 and 2.8 Sv respectively. Thus the rings and the steady flow may make comparable contributions to the Indian-to-Atlantic warm water flow.

One must also ask how the Cape Town Eddies interact with the the northward transport along the western side of the African tip. The 1983 and 1985 net transport along the tip's western side was, after all, measured when a warm ring was present. What is the transport when there is no ring present?

8.5 Conclusions

In 1983, 1984, and 1985 respectively, 6.3, 9.6 (nominally), and 2.8 Sv of water warmer than 8 C flowed from the Indian into the Atlantic Ocean around the southern tip of Africa, based on transport computed relative to 1500 dbar. These values are consistently smaller than the 10 to 20 Sv value proposed by *Gordon (1986)* to balance the export of NADW. The net transport is decreased slightly in 1985 when a deeper reference level just above the North Atlantic Deep Water salinity maximum is used; it would be increased if bottom velocities on the slope were northward. Very low oxygen water on the inshore side of the 1985 eddy would seem to have come from the north, though an Agulhas Bank origin may be possible.

An inverse model *(Rintoul, 1988)* of the South Atlantic sector of the Southern Ocean indicates that the North Atlantic Deep Water overturning cell transport and the Atlantic air-sea heat flux are linked, and that *Gordon's* warm water path may have resulted from specifying both of these variables, at incompatible levels. The inverse model shows the South Atlantic Southern Ocean sector producing warm (>10 C) water for export to both the South Atlantic and the Indian Oceans. *Rintoul* tested the warm water path directly, using *Gordon's* value of 13 Sv for the warm water flow, and found that severely anomalous inverse solutions resulted.

Warm water transported within Retroflection warm rings was estimated to amount to 3 to 6 Sv, using a volume anomaly of 15×10^{12} m^3 and a formation frequency of 6 to 12 rings per year. The effect of the Cape Town Eddies on flow near the African coast is as yet unknown.

9.1 Summary and conclusions

The 1985 hydrographic survey of the Agulhas Retroflection strongly confirms the impression that the Retroflection is a complicated, highly energetic region.

The main current axis (represented by a temperature/depth contour of 15 C at 200 m) meandered strongly across isobaths on the continental slope, parted from the slope at its southernmost point, and then retroflected (turned around to the east) in a series of sharp turns, not in a large smooth loop. The Agulhas Return Current flowed directly over the heart of the relatively shallow Agulhas Plateau, contrary to all previous observations.

About a third of the current transport retroflected far upstream from the main current axis' retroflection. This first, partial, retroflection occurred just upstream of a meander of the Agulhas into extremely shallow water. Just offshore of the shallow meander a large cold core ring was found within the retroflection current loop, giving the appearance of its having played some role in displacing the current up onto the slope. Downstream of the first retroflection, transport increased again, creating a somewhat isolated anticyclonic cell there. The existence of two Retroflection branches means that transport decreased and increased rapidly alongstream in both the Agulhas and Agulhas Return Currents. The current's superficial warm core, visible in satellite infrared images of sea surface temperature, followed the first retroflection branch. A strong temperature gradient, also visible in the images, followed the second retroflection branch. Surface temperature changes along the main current axis are too large by an order of magnitude to be caused by direct heat loss to the atmosphere.

The maximum transport of the Agulhas Current (95 Sv relative to 2400 dbar, 111 Sv relative to deepest common levels) is significantly more than the maximum

interior Sverdrup transport (63 Sv), indicating that much of the Agulhas Current is recirculating locally. The Agulhas transport cannot be reduced to the interior transport value simply by moving the reference level for the geostrophic transport calculation without causing water obviously of South Indian origin to flow back towards its source.

A strong front in tracer (salt, oxygen, potential vorticity) strengths was found in the upper water (above 300 m) of the Agulhas and Agulhas Return Currents, persisting in attenuated form down through intermediate levels.

The thick wedge of the Subantarctic Mode Water potential vorticity minimum is found everywhere within the Retroflection and makes a major contribution to the thermocline structure, with the most strongly sloping isopycnals located at its base.

The most salty Red Sea Water and North Atlantic Deep Water are found in thin ribbons near enhanced geostrophic shear, suggesting deep western boundary currents for these water masses. The RSW ribbon is visible on the northeastern-most Agulhas Current transects, and the NADW ribbon on the southwesternmost Agulhas transect, and beneath a large warm eddy in the South Atlantic just west of the African tip.

The steady westward heat flux across a longitude line east of the tip of Africa, due to exchange of warm Agulhas upper level water flowing west with cooler Return Current water flowing east, was roughly estimated from the hydrography. This heat flux was found to be equivalent to the heat lost from the sea surface, at Retroflection air-sea heat flux values (~-100 W m^2), over a square area of 250 – 550 km on a side. Each Sv (10^6 m^3) of transport that returns to the east as North Atlantic Deep Water instead of upper layer water increases the westward heat transport, by an amount equivalent to another 300 x 300 km square of Retroflection air-sea heat flux.

The geostrophic velocity maxima at transects across the currents ranged from 0.7 to 1.8 m s^{-1}. These values represent the maximum average velocity between

hydrographic stations, so it is not surprising that they are considerably less than the maximum speed yet observed, using drifters, of 2.60 m s^{-1} *(Gründlingh, 1977)*.

Relative vorticity as large as the planetary vorticity f was found on the cyclonic side of the Agulhas Current in the form of cross-stream isopycnal shear. Anticyclonic curvature vorticity, estimated from the geostrophic fields, was found to be one-quarter of f in the Agulhas Current meanders on the slope, the upper limit on anticyclonic curvature vorticity in gradient wind balance.

A natural coordinate, isopycnal form of potential vorticity was found to be usable in the Agulhas. Potential vorticity due to vertical velocity shear is not negligible and is retained in the natural isopycnal potential vorticity formulation.

Cross-stream gradients in vortex tube length (stratification) are as large as a factor of 8 in the upper levels of the Agulhas, suggesting that observed along-stream curvature vorticity variations can be balanced by vortex stretching from small parcel displacements cross-stream. These large cross-stream stratification gradients form a dynamical barrier to large cross-stream displacements. They are associated with large salt and oxygen gradients in the upper water, consistent with their role in inhibiting free cross-stream parcel exchange.

The separated Agulhas Current and Agulhas Return Current meet the necessary conditions for both barotropic and baroclinic instability, separately and when combined together; the contribution of the planetary vorticity gradient β is negligible to order 10^{-2}.

The velocity, mean baroclinic and barotropic potential vorticity gradients, *etc.*, profiles, of both the Agulhas Current once it separates from the coast and of the Agulhas Return Current, are basically similar to Gulf Stream profiles. The mean baroclinic potential vorticity gradient Q_y profiles of both currents have positive (*i.e.*, same sign as downstream velocity) lobes down to ~600 m and negative values below that level. The 600 m zero crossing is found at the base of the local thermocline Mode Waters of the

two systems: isopycnal slope increases with depth down to 600 m and then decreases with depth. Profiles of Q_y and other quantities averaged on horizontal and isopycnal surfaces in the Agulhas and Agulhas Return Currents are very similar, despite the large depth variation on isopycnals.

Since the Gulf Stream and Agulhas profiles are so similar, the results of a linear baroclinic model for the Gulf Stream *(Johns, 1988)* appear to be almost directly applicable to the Agulhas – in particular a version of the model using a mean baroclinic potential vorticity gradient profile Q_y which departs from the Gulf Stream profile in some of the same ways the Agulhas Q_y profile does. Observed Agulhas Return Current meander wavelengths fall in the range of wavelengths associated with the model's fastest growing waves, suggesting that baroclinic instability may play a role in their generation. A run of the model with the Agulhas profiles, and comparison to time-series data in the Agulhas, will be needed to take these speculations further.

Dynamical models of the Retroflection exhibit many of the observed features and help elucidate their underlying dynamics. The simplest models (*de Ruijter, 1982,* and *Ou and de Ruijter, 1986)* show that the Retroflection is a fundamentally non-linear feature, and that the current must have momentum enough to overshoot the tip of the boundary in order to retroflect - otherwise it can flow in a zonal jet across to South America. The overshooting jet balances increasing planetary potential vorticity with curvature vorticity of the opposite sense. The southern penetration latitude of the Retroflection is well estimated by these models. Topographically controlled inertial jet models (*Darbyshire, 1972* and *Lutjeharms and van Ballegooyen, 1984*) can produce realistic-looking current paths, but are very sensitive to initial conditions on the path. Finally, eddy-resolving numerical models in a small basin (*de Ruijter and Boudra, 1985* and *Boudra and de Ruijter, 1986)* confirm the impression that increasing the non-

linearity intensifies the time-average retroflection, while producing reasonable eddy formation and shedding events and baroclinic structure.

The cold core ring observed within the Retroflection loop has mass transport (65 Sv relative to 2400 m, 80 relative to deepest common levels) fully as large as the Return Current from which it was probably formed. The ring is invisible in the satellite infrared image and in the hydrographic surface temperature field due to a warm surface cap, similar to caps observed on Gulf Stream cold rings. The Agulhas ring cap was estimated to have formed over a month or two, judging from a simple model of air/sea heat flux. The ring's subsurface upper layer water is similar to that found south of the Return Current, except for a low oxygen blob near the center. The blob may have been entrained from the warm, low-oxygen, inshore side of the Agulhas, and/or lost oxygen to enhanced biological activity within the ring. Volume and potential energy anomalies are similar to those of some warm Agulhas rings observed in 1983. The cold ring is smaller and spins faster than the warm rings, making it about three times as nonlinear.

The interbasin exchange of mass from the Indian to the Atlantic Ocean around the tip of Africa estimated from the wind field is 30 ± 8 Sv, while the observed geostrophic transport is between 5 and 20 Sv, relative to reference levels ranging from 1500 m to deepest common levels, for transects taken in three consecutive years.

The interbasin exchange of warm water, warmer than any found in Drake Passage, was 6.3 Sv in 1983 and 2.8 Sv in 1985, both computed across warm eddies in the Atlantic just west of the African tip, and both based on transport relative to 1500 m. These amounts of warm water transport balance just one-tenth to one-half of the 10 - 30 Sv of North Atlantic Deep Water exported from the Atlantic Ocean. Further, these warm water transport values are significantly less than the 13 Sv previously estimated from the 1983 observations and tested in an inverse model of the Atlantic sector of the Southern Ocean.

9.2 Future work

An explosively growing data base, both theoretical and observational, created and accompanied by improving measurement and analysis tools and techniques, is creating the promise of an exciting and productive next decade in physical oceanography.

In the Agulhas Retroflection region:

- A tall, incoherent current meter mooring array deployed for two years in the Agulhas and recovered in 1987 will provide a first look at the current's vertical structure and instabilities, including eddy heat fluxes.

- The sharp turns in the Agulhas and Agulhas Return Current's path seem unique in the world ocean. What is their structure in three dimensions? How do they evolve and propagate? Are they preferred sites for cross-frontal flow? How much energy and mass is extracted at the turns?

- It has been suggested that the Agulhas has seasonal cycles in transport, giving rise to seasonal variations in interbasin exchange of mass and warm water. Until the variability of transport and interbasin exchange is understood, extracting mean values for these quantities from isolated observations will continue to be questionable. What part of the variation is seasonal, and what part the product of hydrodynamic instability? Characterizing the variability will require a combination of satellite measurements, *in situ* measurements, and numerical experimentation.

The 1985 hydrographic survey and the results of this thesis provide, it is hoped, a solid characterization of the Retroflection upon which future work can be built.

ATLAS OF CONTOURED SECTIONS

This Atlas contains contoured sections of water mass properties and velocity at transects across the Agulhas Current, the Agulhas Return Current, and Retroflection rings. The station data is taken from the 1985 and 1983 Agulhas Retroflection surveys.

Four 1985 Agulhas Current transects, labelled A - D, and two 1985 Agulhas Return Current transects, labelled E - F, are included. The 1985 transect station locations are shown in Fig. 3.1, and information about station depth, *etc.*, is given in Table 3.a.

Two ring transects from the 1985 survey are also included. One crosses a warm ring located west of Cape Town, labelled the '1985 Cape Town Eddy.' The other crosses a cold ring, located on the northwestern flank of the Agulhas Plateau within the Retroflection loop, labelled the 'cold core eddy.' The locations of the ring stations are shown in Fig. 1.3.

The 1983 Agulhas Current transect, labelled 'Gordon Agulhas,' and the 1983 Cape Town Eddy transect, labelled 'Gordon CT eddy', are also included. The locations of the 1983 Agulhas Retroflection survey stations *(Gordon* et al., *1987)* are shown in Fig. 3.13. The 1983 transects were contoured only down to 1500 dbar, even though all stations of the 1983 Agulhas Current transect, and most stations of the 1983 CTE transect, go to the bottom (most of the remaining 1983 stations do end at 1500 dbar, Fig. 3.14).

All transects have station locations and numbers marked at the top. Stations on transect C marked with an 'S' end at intermediate depths (see Fig. 1.3 for values). The dark line at the bottom connects the station echo sounding depths, converted to pressure, on sections where pressure is the vertical coordinate. The dark line at the top is the surface density (plus the density increment corresponding to the filter half-width

for planetary potential vorticity, $\bar{q}$) on sections with potential density as the vertical coordinate, and the dark line at the bottom is the bottom density (minus the same adjustment as at the surface for $\bar{q}$). Note that caps over near-surface extrema may be missing if the surface potential density is less than $\sigma_0 = 24.8$, the minimum shown.

All current transects are oriented looking downstream, with the cold side of the current on the right. The cross-stream distance is marked in kilometers at the bottom. The origin is located at the 15 C temperature/200 m depth location, the current axis indicator that was followed during the XBT contour survey (see Ch. 2). Distance is positive on the warm, anticyclonic side of the current.

The warm eddy sections are oriented looking northwest, with the African continental slope on the right. The cold eddy section is oriented looking southwest, with the Agulhas Plateau on the left. Distance origin and sign is arbitrary for the ring transects.

Each 1985 contoured section bears a tiny map showing the transect location.

Variables (1) through (5) listed below are contoured in cross-stream *vs.* pressure coordinates. Variables (3) through (7) are contoured in cross-stream *vs.* potential density coordinates:

(1) potential temperature, θ, in degrees Celsius,

(2) potential density referenced to 0, 1000, and 3000 dbar: σ_0, σ_1, and σ_3 respectively, where

$$\sigma_{pr} = \rho\,(s,\ \theta\,(s, T, p; p_r), p_r) - 1000.0 \text{ kg m}^{-3}.$$

(3) salinity, s, in practical salinity units,

(4) oxygen, O_2 in ml l^{-1},

(5) geostrophic velocity[1] relative to deepest common levels, in cm s^{-1}

(6) pressure, in dbar, and

(7) planetary potential vorticity, $\bar{q}$, defined as

$$\bar{q} = f\, g^{-1}\, N^2,\ 10^{-12}\ m^{-1}\ s^{-1}$$

where f is the Coriolis parameter, g the gravitational acceleration, and N the buoyancy frequency.[2] This variable was smoothed with a Gaussian to remove $\lesssim$50 m scales.

The sections were contoured using the PLOT5 program *(Keffer, PLOT5 Ver. 3.4,* unpublished program documentation).

The contoured sections of pressure as a function of potential density are a bit unusual and their use deserves mention: *(i)* They allow the original depth (pressure) of tracer contours plotted as functions of potential density to be easily determined. *(ii)* They show the volumetric extent of tracer anomalies. These anomalies can expand

---

[1]Velocity was contoured only for the 1985 transects, and velocity on potential density surfaces only for the 1985 Agulhas and Return Current transects.

[2]The conservation equation for potential vorticity formed from N^2 is derived in Appendix B. The increment between adjacent solid q contours in the Atlas q sections is

$$ln\ q_{n+1} - ln\ q_n = 0.346\ (\text{const.})$$

where the contour value q_n is given by $2^{n/2}$ (16, 23, 32, 45, 64, 90, 128, *etc.*, in units of 10^{-12} m^{-1} s^{-1}). Dashed contours are introduced near q minima at intervals of $2^{n/4}$. This gives approximately evenly spaced q contours in potential density coordinates, since the basic stratification (proportional to N^2) is about exponential with potential density. This contour increment was chosen to correspond approximately to the smallest mappable q features, consistent with the usual practice of contouring oceanographic variables (for example, oxygen) at slightly above the measurement error.

The buoyancy potential vorticity source term due to changes in pressure following a parcel (see Appendix B), implies that even in the absence of mixing, the buoyancy potential vorticity of a parcel descending on an isopycnal from 0 to 1500 dbar (an extreme case) changes by an amount equal to 2–3 contour intervals, with contour values defined as above. The error accumulates non-linearly with pressure change, so surfaces descending half as far have less than half the error.

and visually dominate contoured sections of tracer as a a function of potential density, when tracer anomalies occur in highly stratified layers. And *(iii)* they show where tracer gradients on isopycnals are located in the water column, which is useful since tracer gradients on isopycnals outcropping into the mixed layer and on subsurface isopycnals are generally produced by different physical mechanisms, *e.g.* local atmospheric forcing (a locally non-conservative process) *vs.* confluence of water from different remote formation regions (locally conservative).

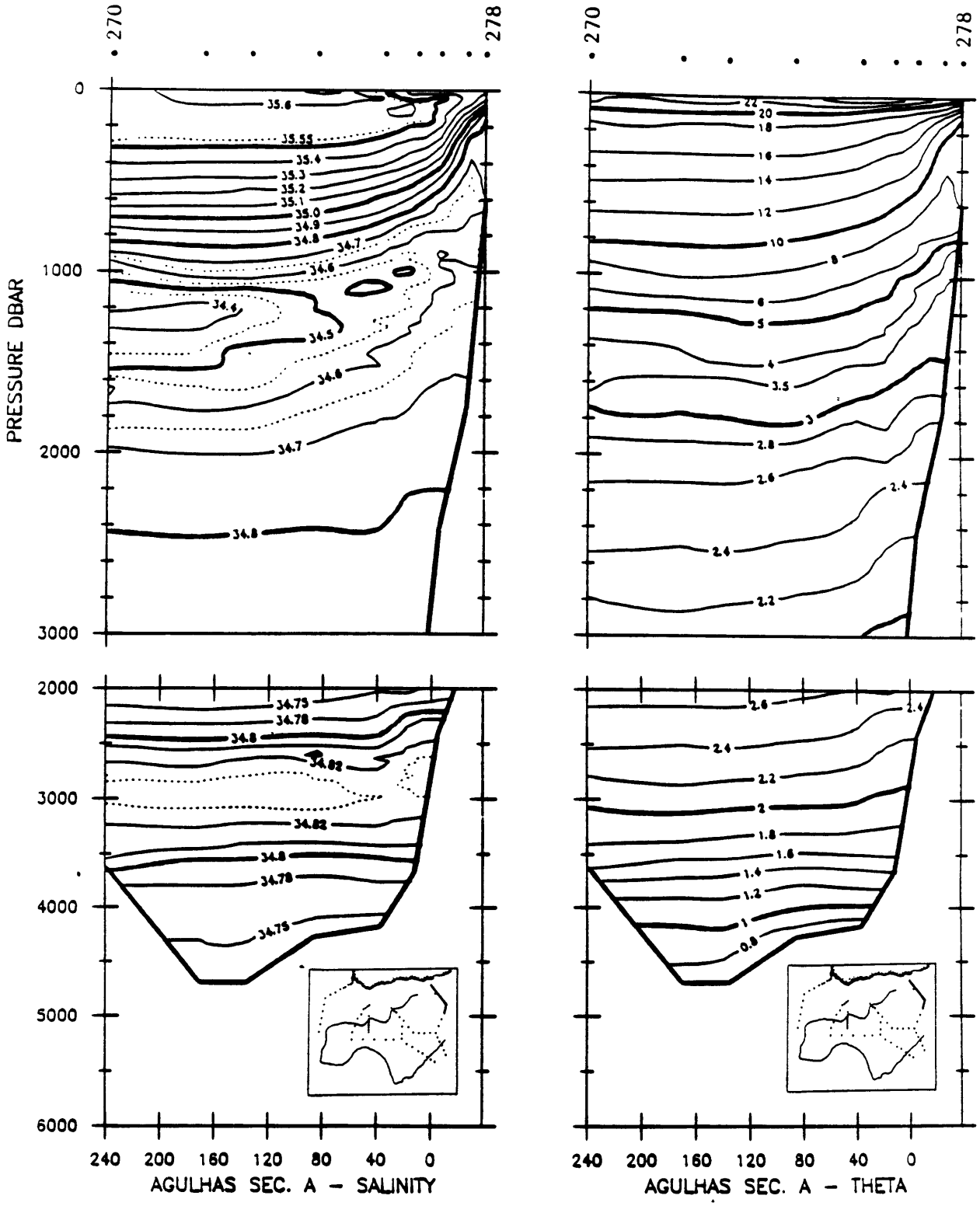
270
278
0
1000
2000
3000
4000
5000
6000
PRESSURE DBAR
35.6
35.55
35.4
35.3
35.2
35.1
35.0
34.9
34.8
34.7
34.6
34.5
34.4
34.75
34.78
34.82
240 200 160 120 80 40 0
AGULHAS SEC. A – SALINITY
22
20
18
16
14
12
10
8
6
5
4
3.5
3
2.8
2.6
2.4
2.2
2
1.8
1.6
1.4
1.2
1
0.8
AGULHAS SEC. A – THETA

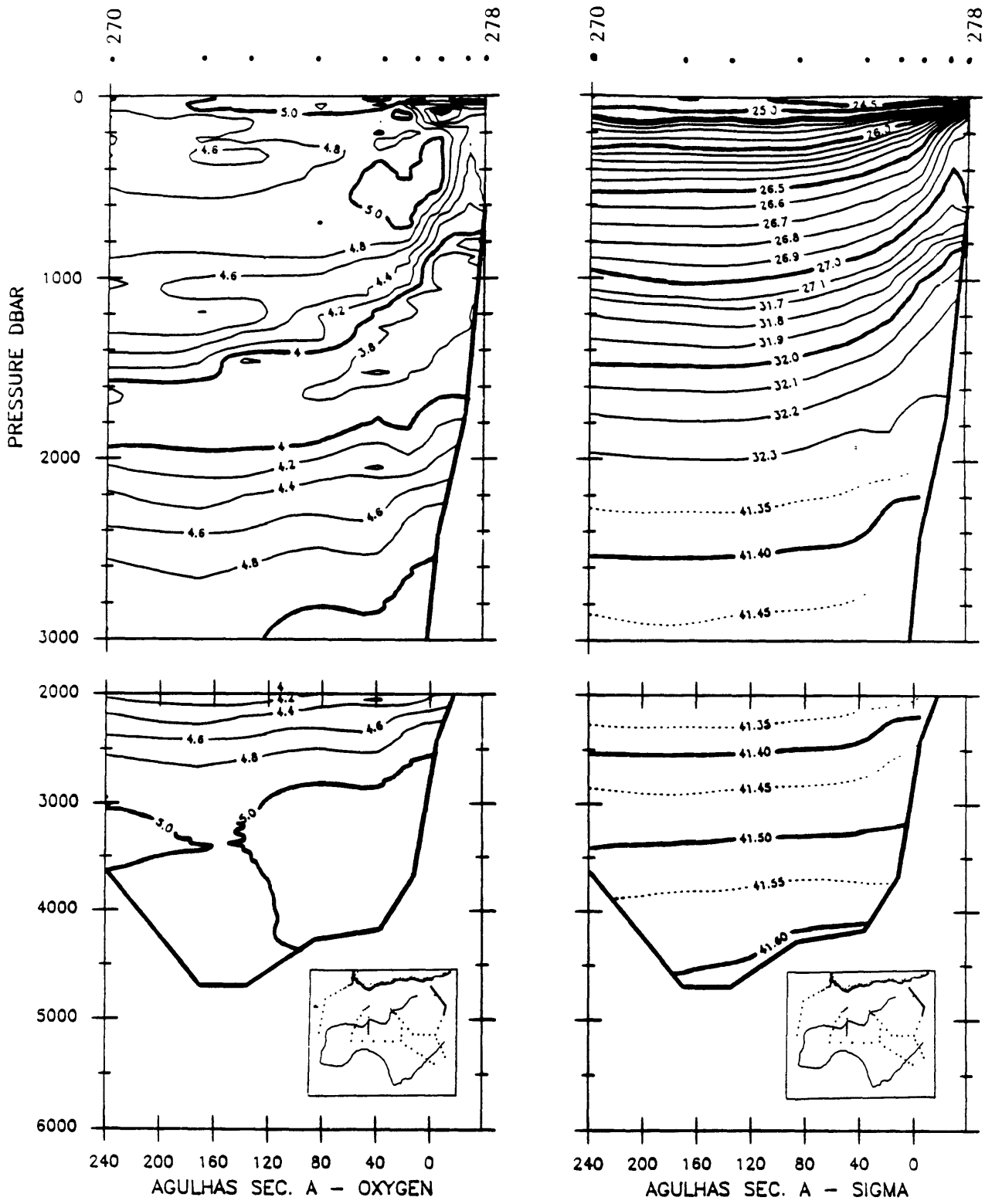
270
278
0
1000
2000
3000
4000
5000
6000
PRESSURE DBAR
5.0
4.8
4.6
4.4
4.2
4
3.8
25.0
24.5
26.5
26.6
26.7
26.8
26.9
27.3
27.1
31.7
31.8
31.9
32.0
32.1
32.2
32.3
41.35
41.40
41.45
41.50
41.55
41.60
240
200
160
120
80
40
0
AGULHAS SEC. A – OXYGEN
AGULHAS SEC. A – SIGMA

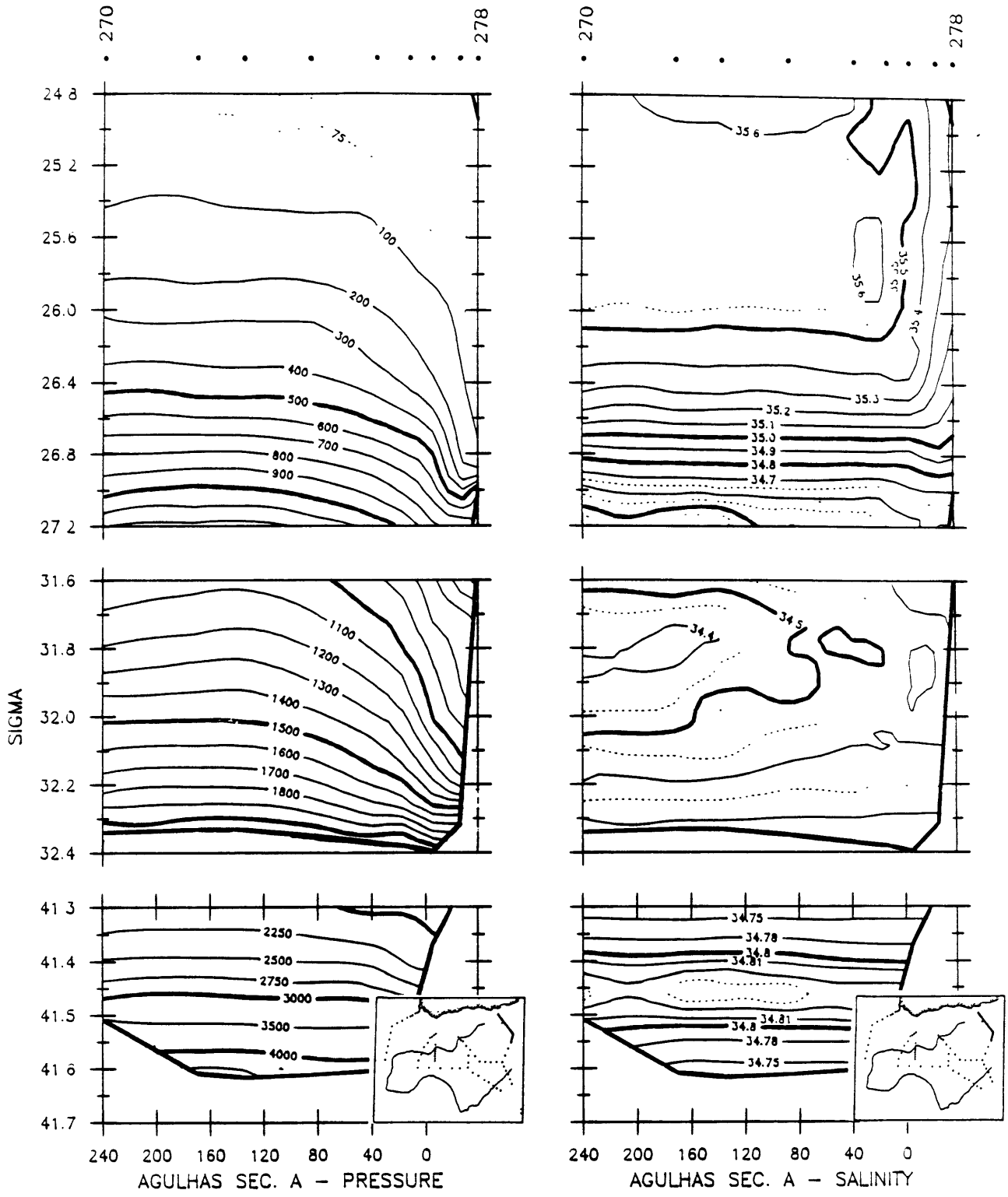
270
278
SIGMA
24.8
25.2
25.6
26.0
26.4
26.8
27.2
31.6
31.8
32.0
32.2
32.4
41.3
41.4
41.5
41.6
41.7
75
100
200
300
400
500
600
700
800
900
1100
1200
1300
1400
1500
1600
1700
1800
2250
2500
2750
3000
3500
4000
35.6
35.4
35.3
35.2
35.1
35.0
34.9
34.8
34.7
34.5
34.4
34.75
34.78
34.8
34.81
240
200
160
120
80
40
0
AGULHAS SEC. A – PRESSURE
AGULHAS SEC. A – SALINITY

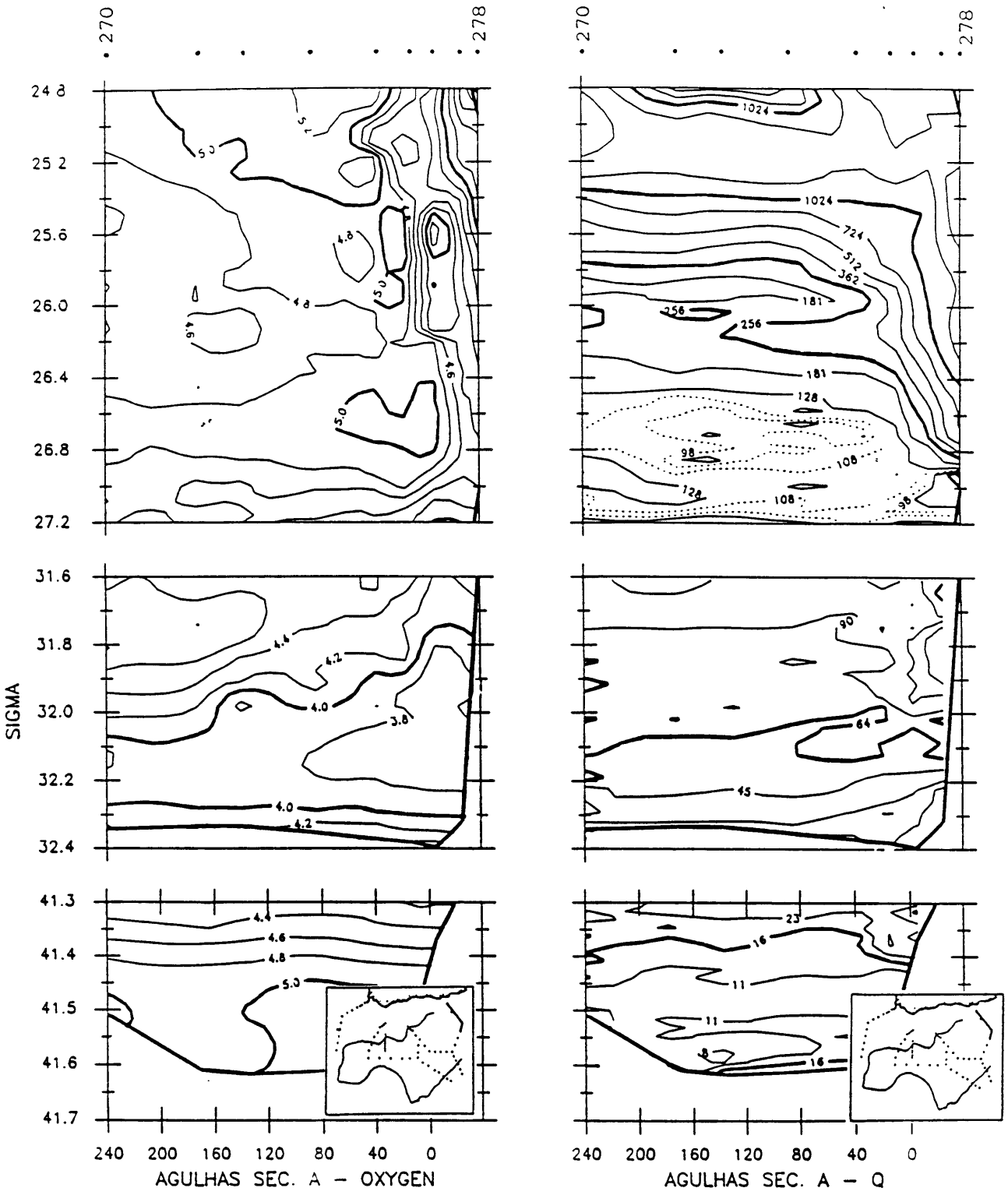
270
278
24.8
25.2
25.6
26.0
26.4
26.8
27.2
31.6
31.8
32.0
32.2
32.4
41.3
41.4
41.5
41.6
41.7
SIGMA
240 200 160 120 80 40 0
AGULHAS SEC. A – OXYGEN
AGULHAS SEC. A – Q

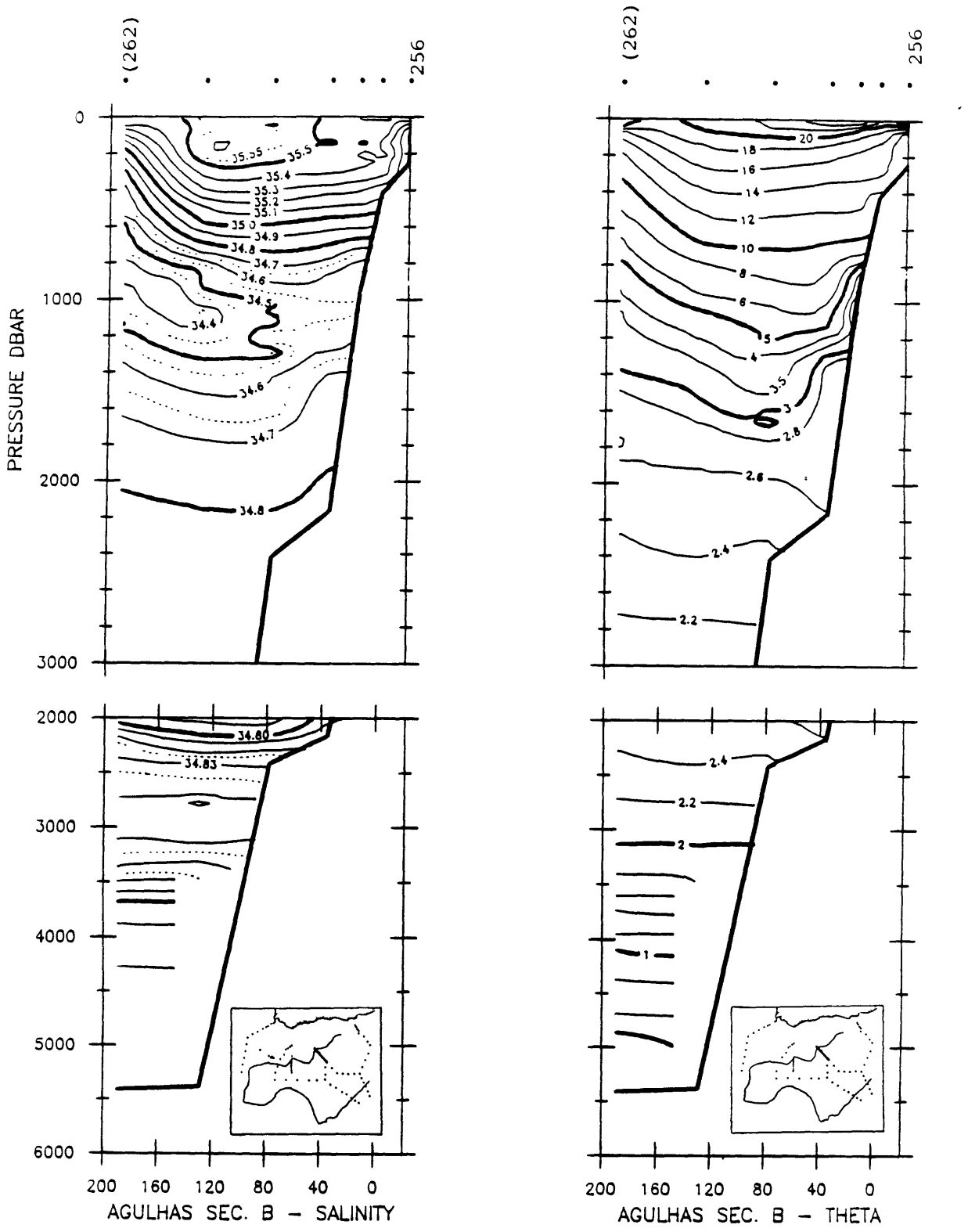
(262)
256
PRESSURE DBAR
0
1000
2000
3000
35.55
35.5
35.4
35.3
35.2
35.1
35.0
34.9
34.8
34.7
34.6
34.5
34.4
34.6
34.7
34.8
20
18
16
14
12
10
8
6
5
4
3.5
3
2.8
2.6
2.4
2.2
2000
3000
4000
5000
6000
34.80
34.83
2.4
2.2
2
1
200 160 120 80 40 0
AGULHAS SEC. B – SALINITY
AGULHAS SEC. B – THETA

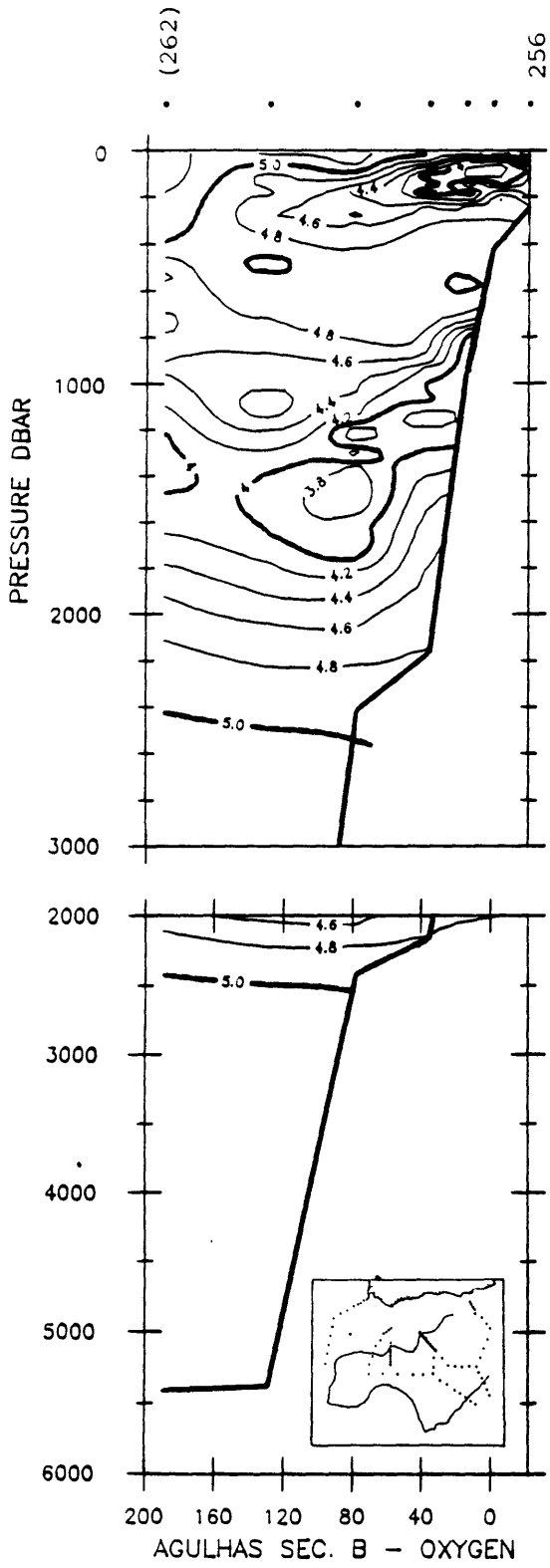
(262)
256
PRESSURE DBAR
0
1000
2000
3000
4000
5000
6000
5.0
4.8
4.6
4.4
4.2
3.8
200 160 120 80 40 0
AGULHAS SEC. B – OXYGEN

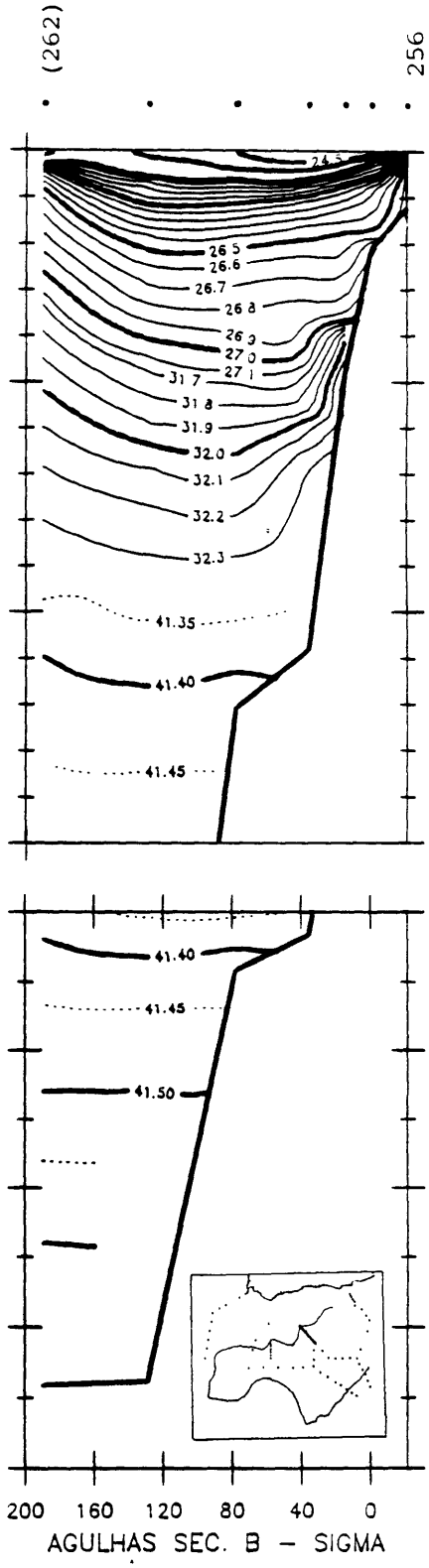
(262)
256
26.5
26.6
26.7
26.8
26.9
27.0
27.1
31.7
31.8
31.9
32.0
32.1
32.2
32.3
41.35
41.40
41.45
41.50
200 160 120 80 40 0
AGULHAS SEC. B – SIGMA

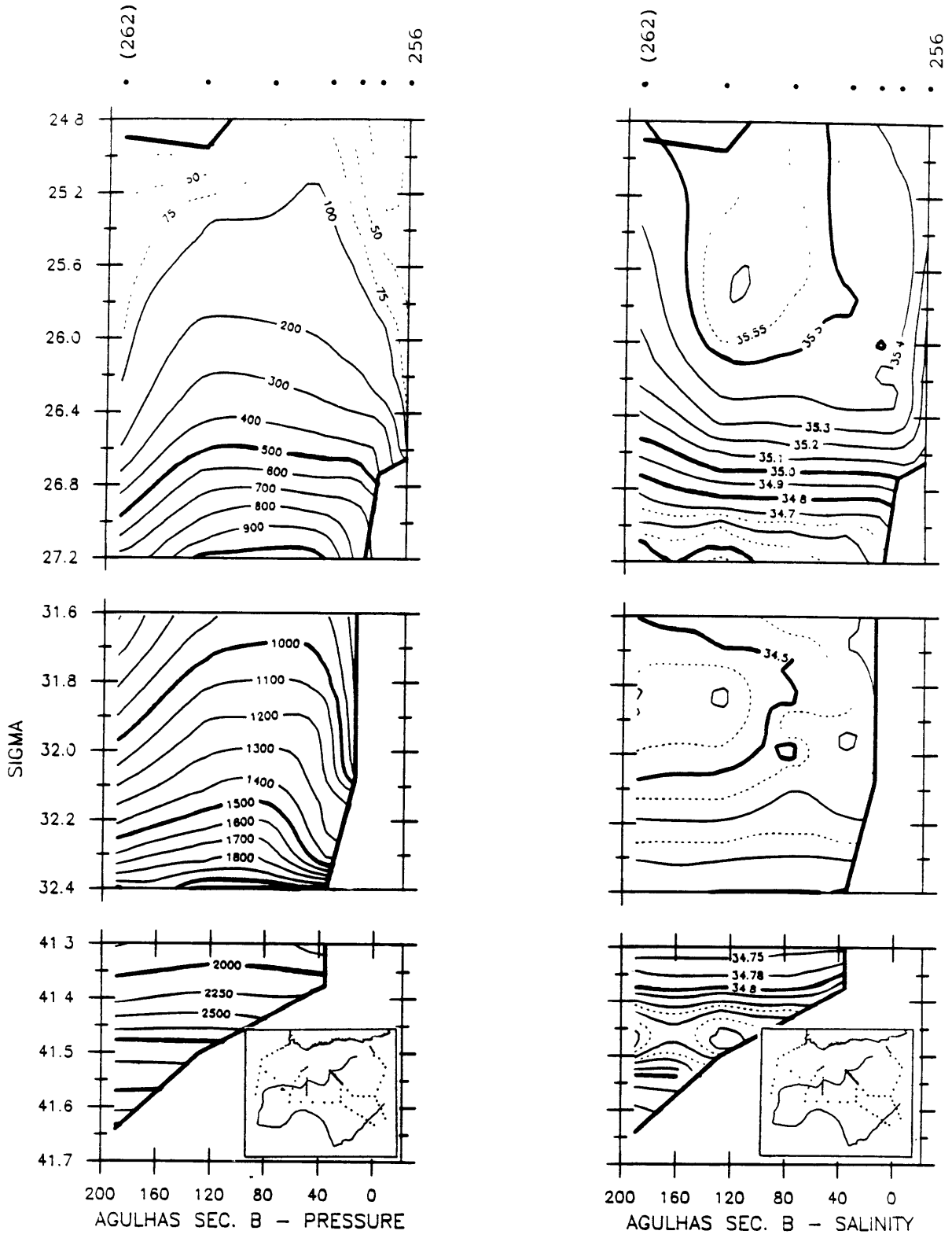
(262)
256
24.8
25.2
25.6
26.0
26.4
26.8
27.2
SIGMA
31.6
31.8
32.0
32.2
32.4
41.3
41.4
41.5
41.6
41.7
200 160 120 80 40 0
AGULHAS SEC. B – PRESSURE
AGULHAS SEC. B – SALINITY

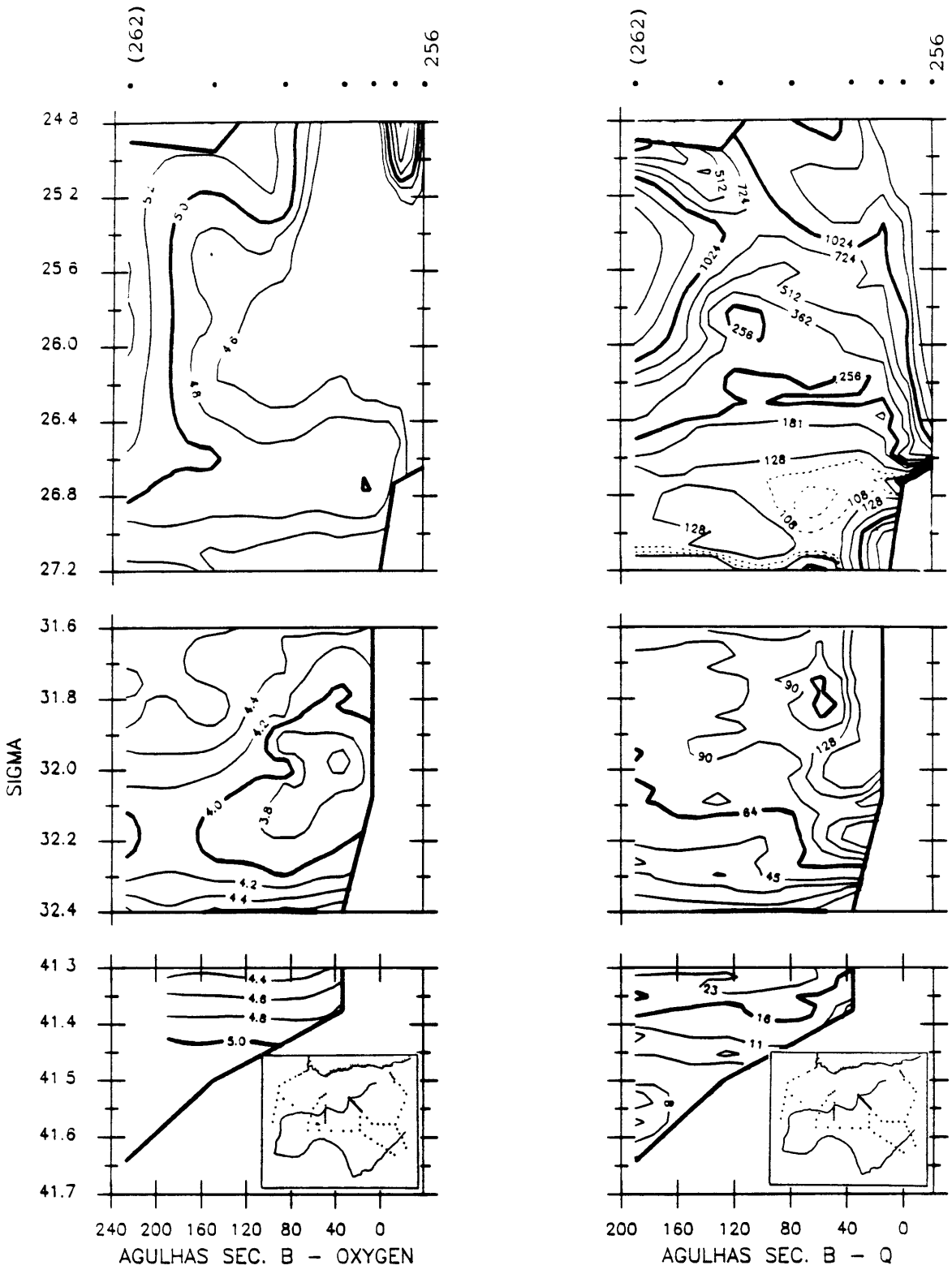
(262)
256
SIGMA
24.8
25.2
25.6
26.0
26.4
26.8
27.2
31.6
31.8
32.0
32.2
32.4
41.3
41.4
41.5
41.6
41.7
240 200 160 120 80 40 0
AGULHAS SEC. B – OXYGEN
200 160 120 80 40 0
AGULHAS SEC. B – Q

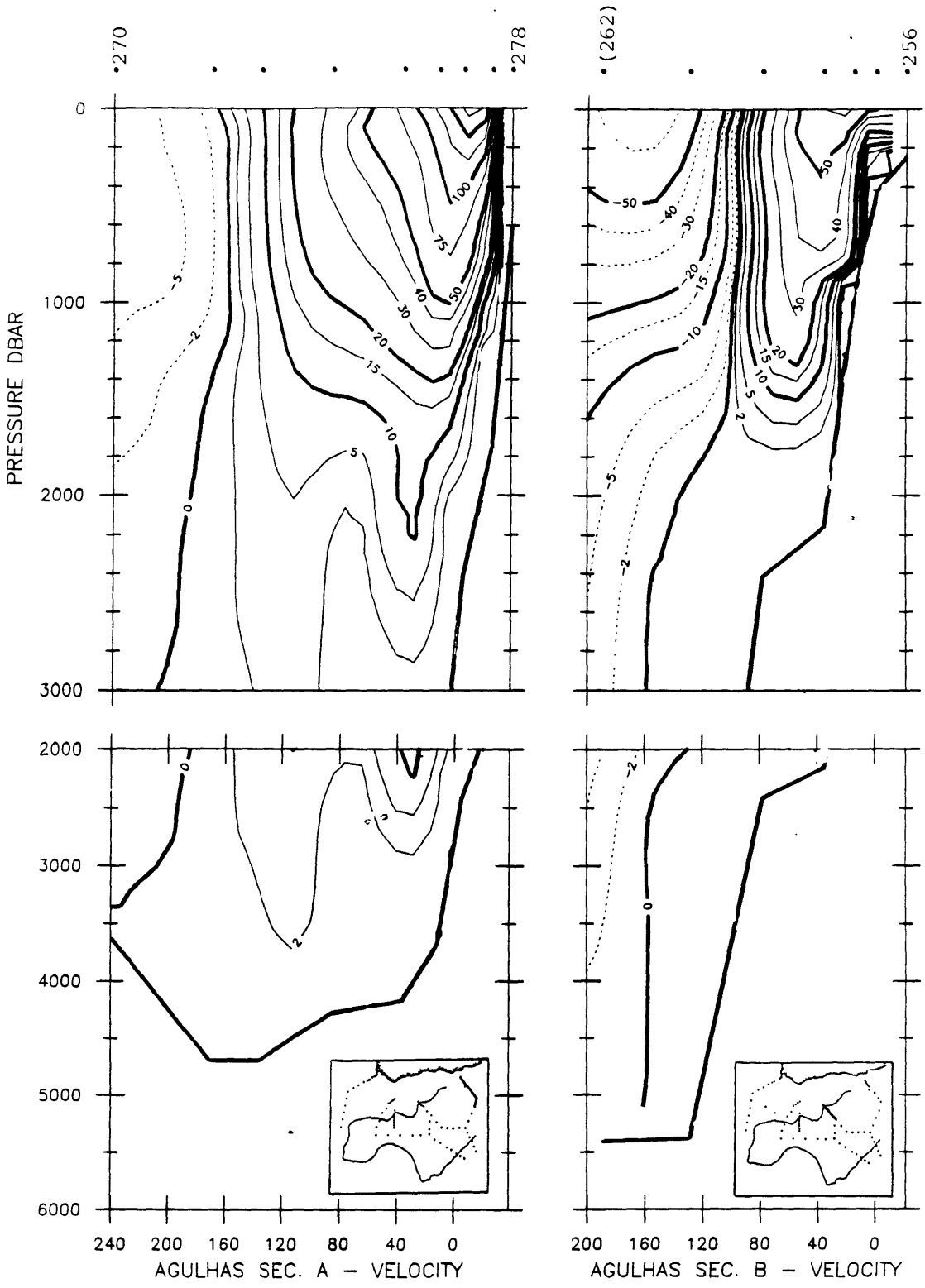
270
278
(262)
256
PRESSURE DBAR
0
1000
2000
3000
4000
5000
6000
240 200 160 120 80 40 0
AGULHAS SEC. A – VELOCITY
200 160 120 80 40 0
AGULHAS SEC. B – VELOCITY

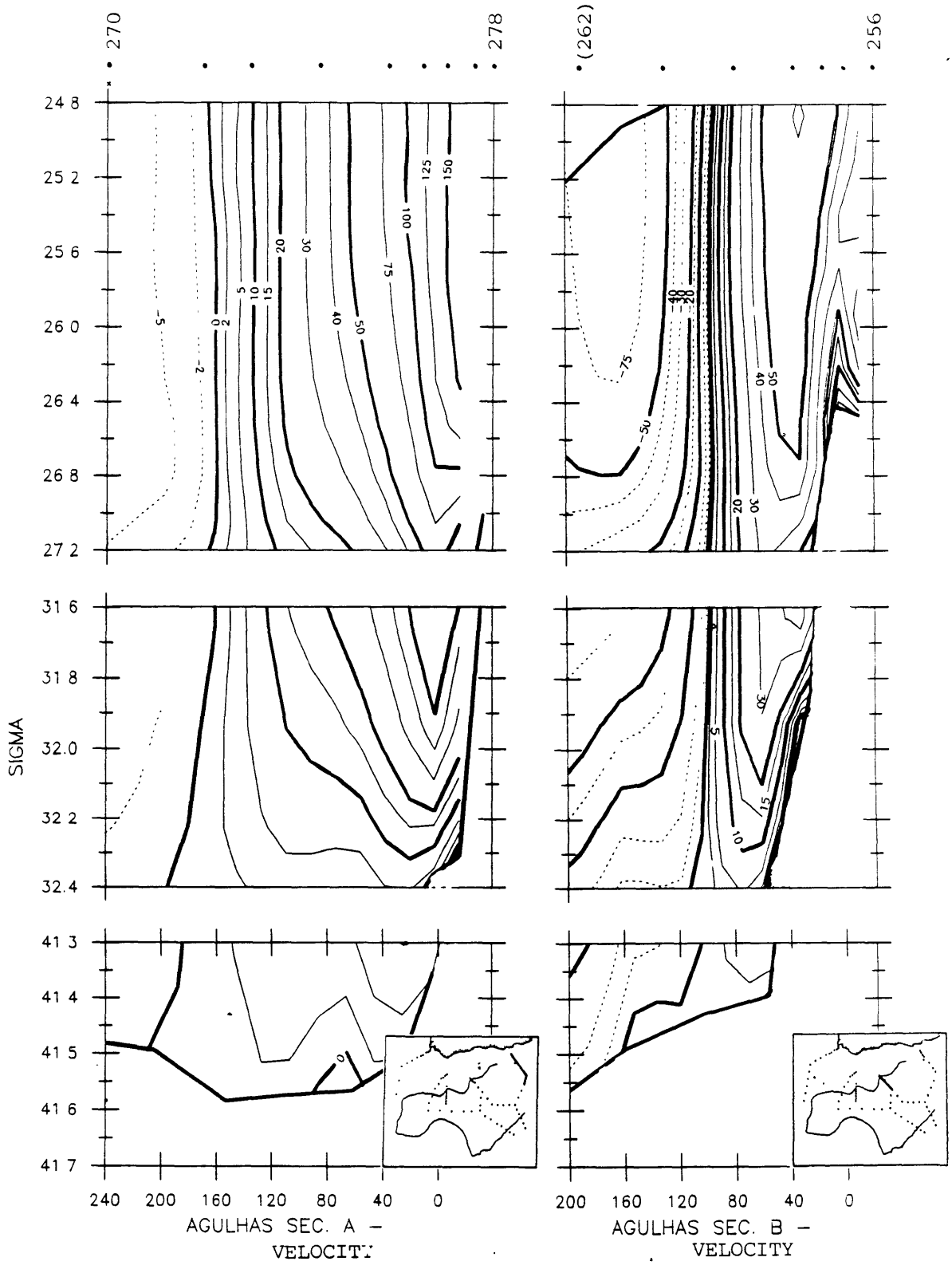
270
278
(262)
256
24 8
25 2
25 6
26 0
26 4
26 8
27 2
31 6
31 8
32.0
32 2
32.4
41 3
41 4
41 5
41 6
41 7
SIGMA
240 200 160 120 80 40 0
AGULHAS SEC. A – VELOCITY
200 160 120 80 40 0
AGULHAS SEC. B – VELOCITY

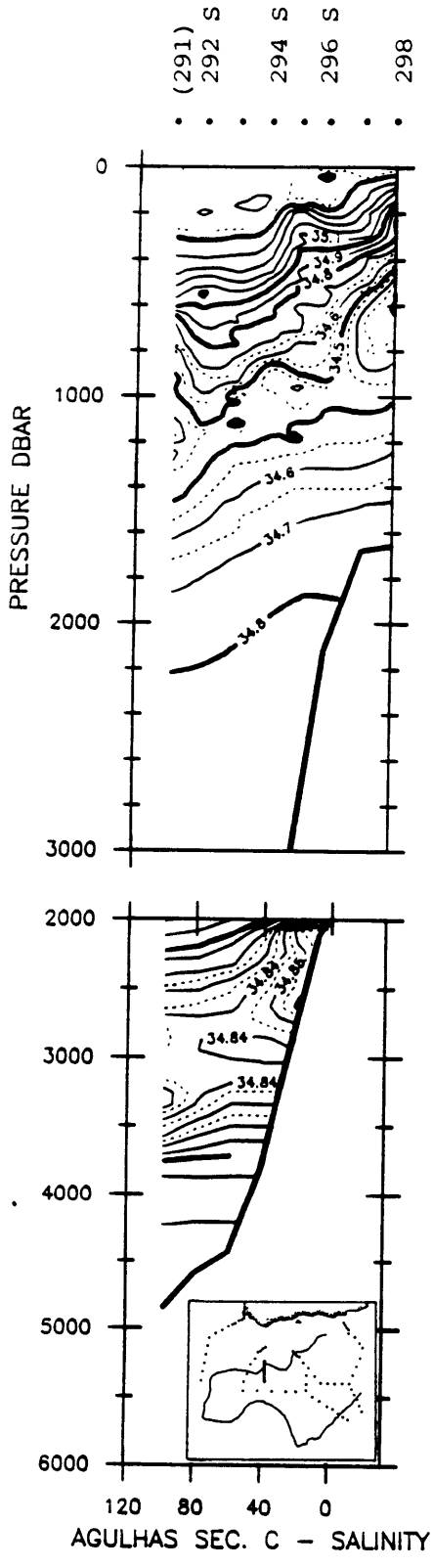
(291)
292 S
294 S
296 S
298
PRESSURE DBAR
0
1000
2000
3000
4000
5000
6000
34.6
34.7
34.8
34.84
120
80
40
0
AGULHAS SEC. C – SALINITY

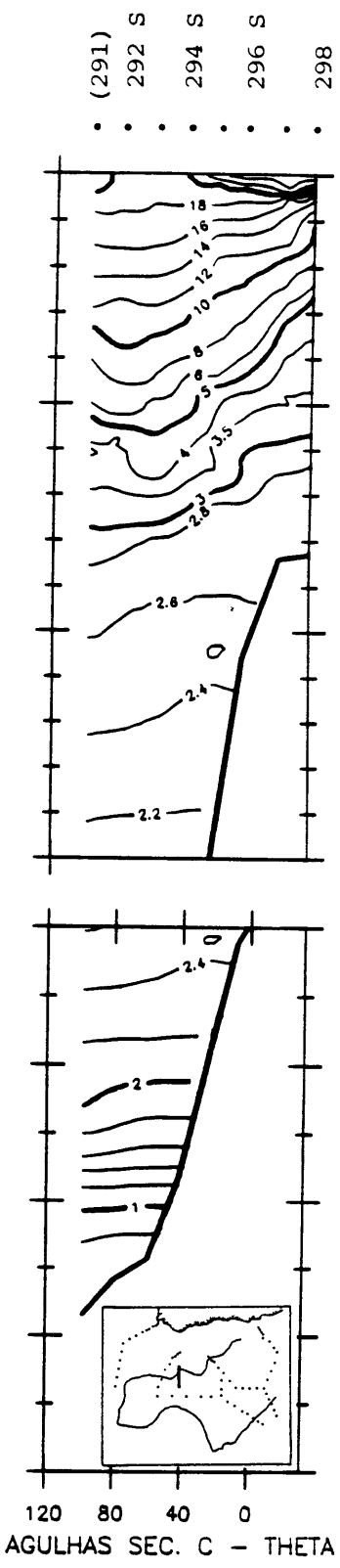
(291)
292 S
294 S
296 S
298
18
16
14
12
10
8
6
5
4
3.5
3
2.8
2.6
2.4
2.2
2
1
0
120
80
40
0
AGULHAS SEC. C – THETA

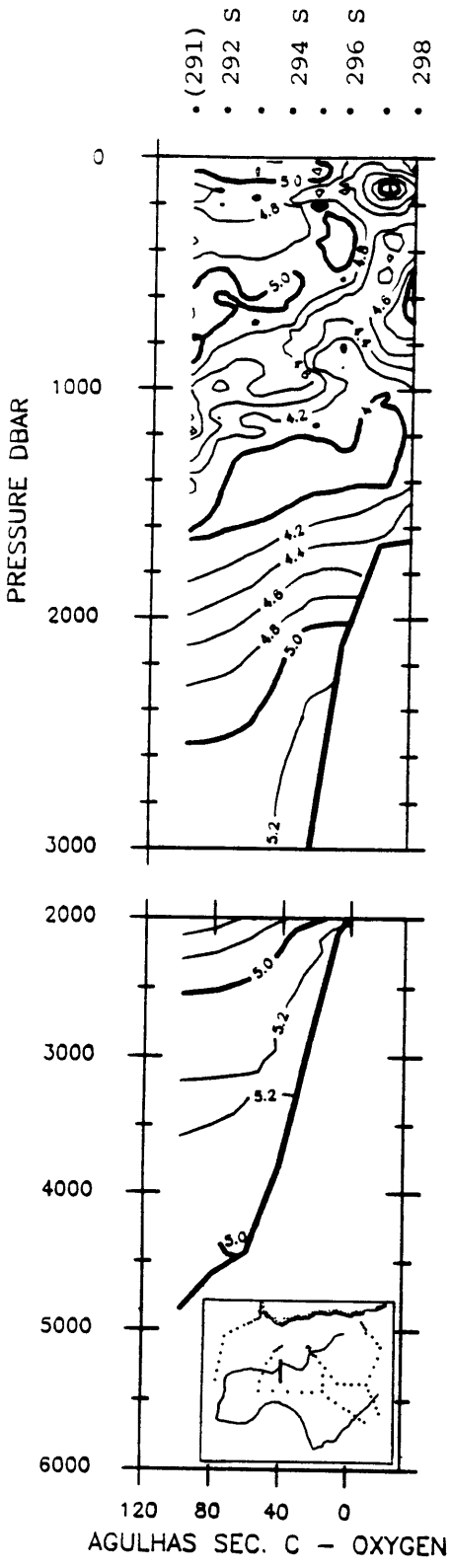
(291)
292 S
294 S
296 S
298
PRESSURE DBAR
0
1000
2000
3000
4000
5000
6000
5.0
4.8
4.6
4.4
4.2
3.2
120
80
40
0
AGULHAS SEC. C – OXYGEN

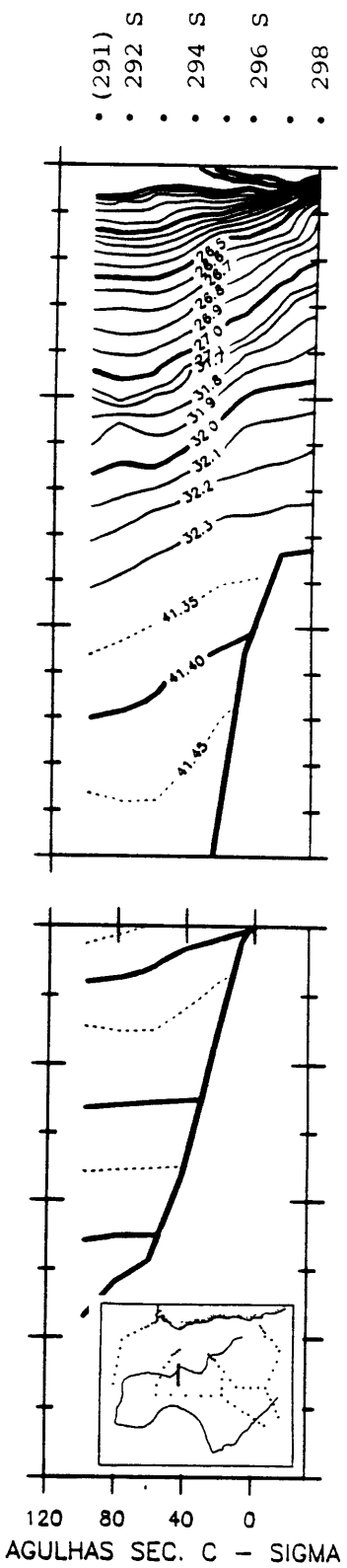
(291)
292 S
294 S
296 S
298
28.5
28.6
28.7
28.8
28.9
29.0
31.7
31.8
31.9
32.0
32.1
32.2
32.3
41.35
41.40
41.45
120
80
40
0
AGULHAS SEC. C – SIGMA

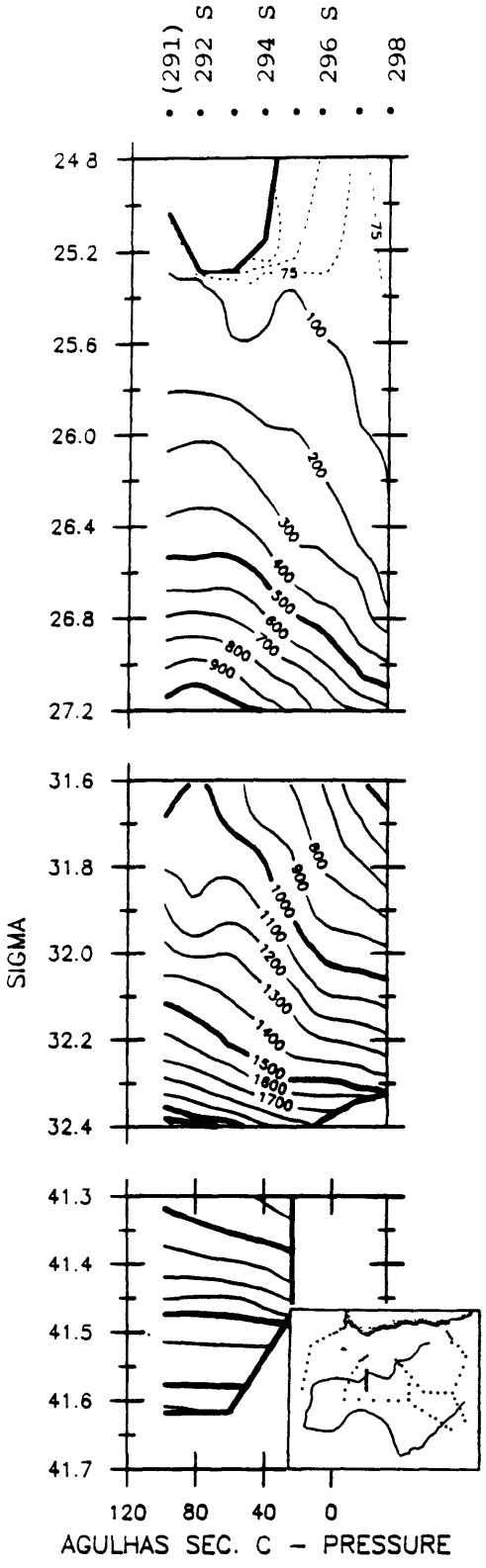
(291)
292 S
294 S
296 S
298
24.8
25.2
25.6
26.0
26.4
26.8
27.2
75
100
200
300
400
500
600
700
800
900
31.6
31.8
32.0
32.2
32.4
SIGMA
800
900
1000
1100
1200
1300
1400
1500
1600
1700
41.3
41.4
41.5
41.6
41.7
120
80
40
0
AGULHAS SEC. C – PRESSURE

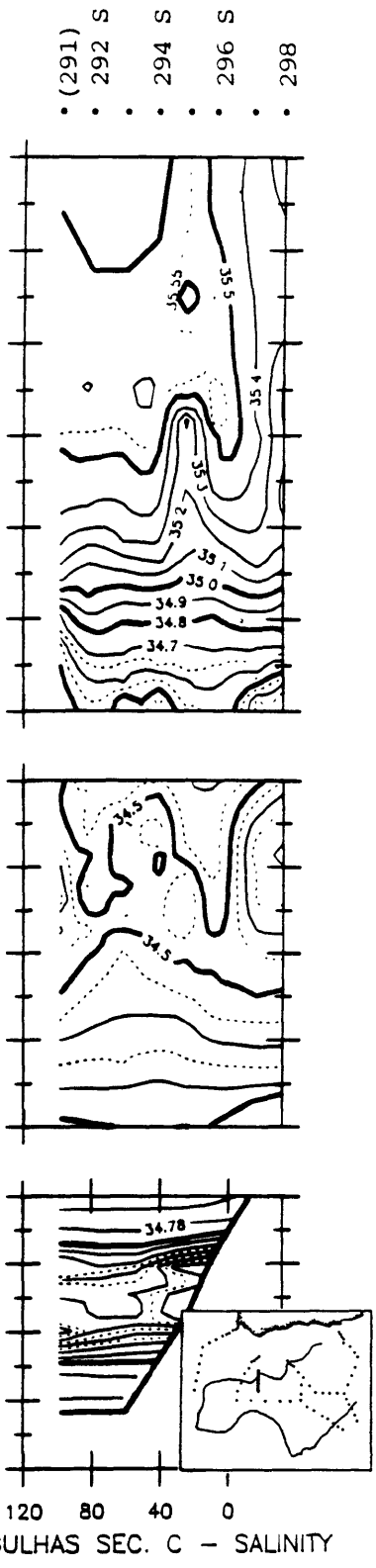
(291)
292 S
294 S
296 S
298
35.5
35.4
35.3
35.2
35.1
35.0
34.9
34.8
34.7
34.5
34.78
120
80
40
0
AGULHAS SEC. C – SALINITY

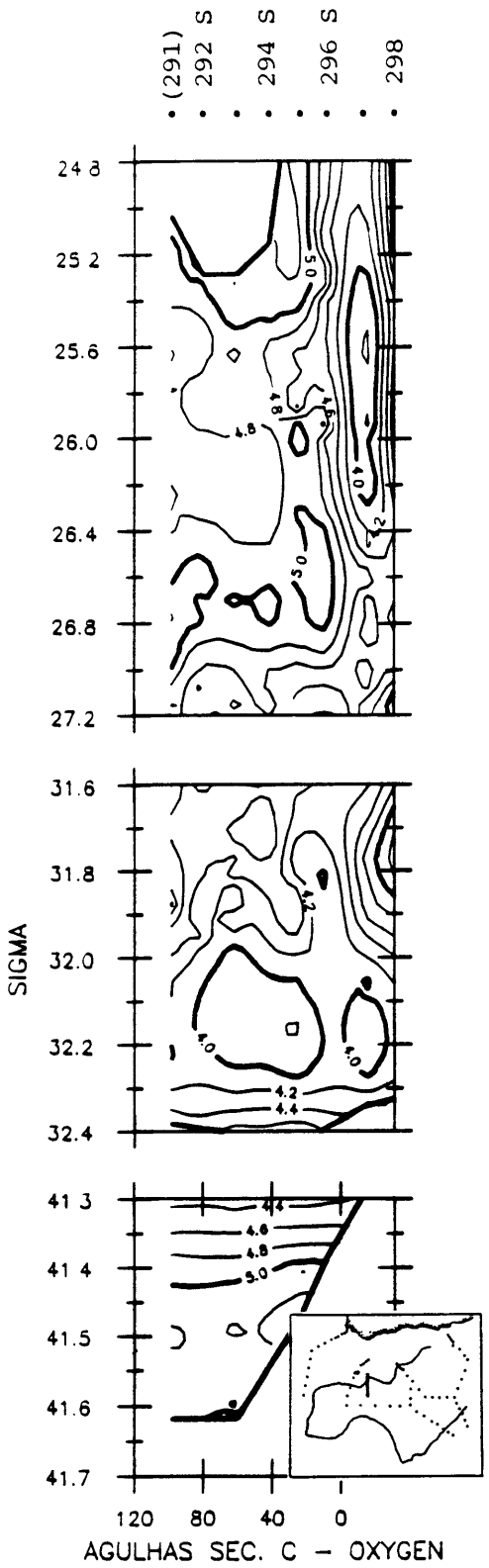
(291)
292 S
294 S
296 S
298
24 8
25 2
25.6
26.0
26.4
26.8
27.2
31.6
31.8
32.0
32.2
32.4
SIGMA
41 3
41 4
41.5
41.6
41.7
120
80
40
0
AGULHAS SEC. C – OXYGEN

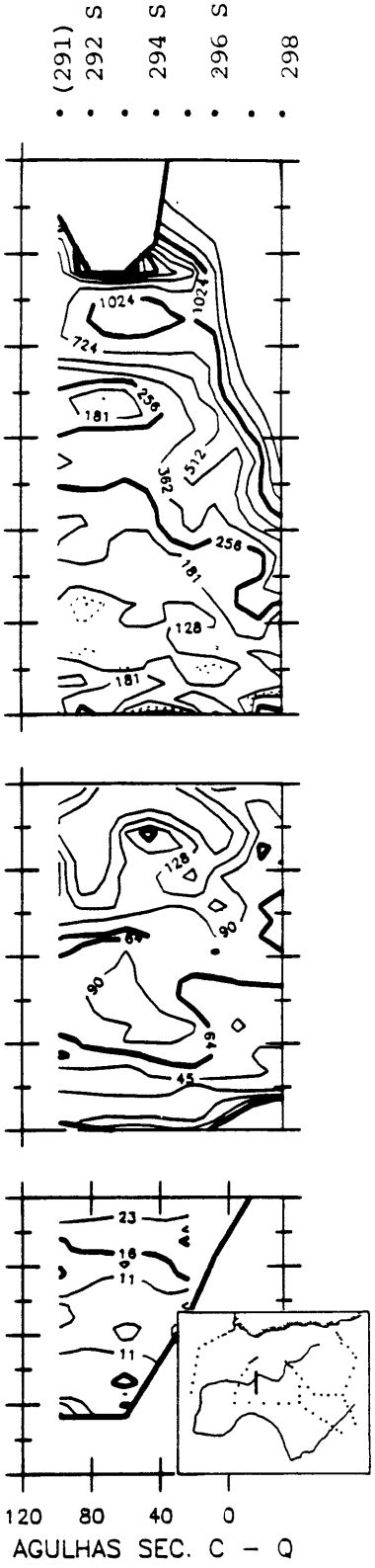
(291)
292 S
294 S
296 S
298
1024
724
256
181
512
128
90
64
45
23
16
11
120
80
40
0
AGULHAS SEC. C – Q

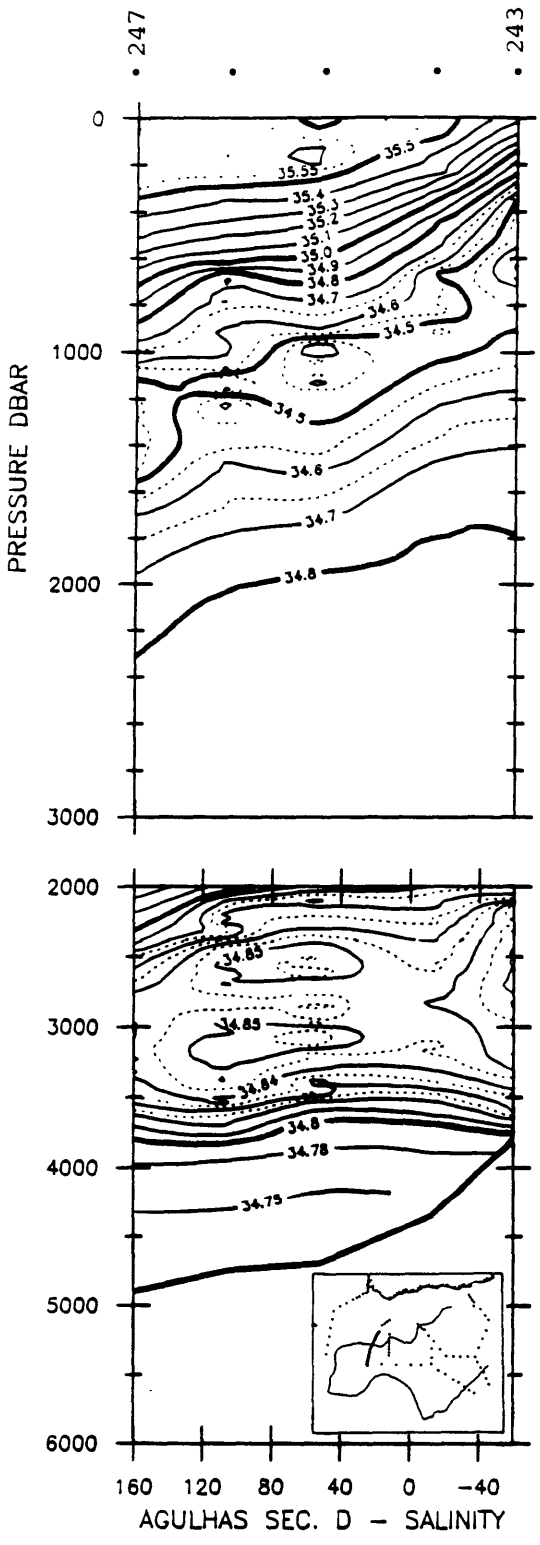
247
243
PRESSURE DBAR
0
1000
2000
3000
4000
5000
6000
35.55
35.5
35.4
35.3
35.2
35.1
35.0
34.9
34.8
34.7
34.6
34.5
34.9
34.6
34.7
34.8
34.85
34.84
34.8
34.78
34.75
160 120 80 40 0 −40
AGULHAS SEC. D – SALINITY

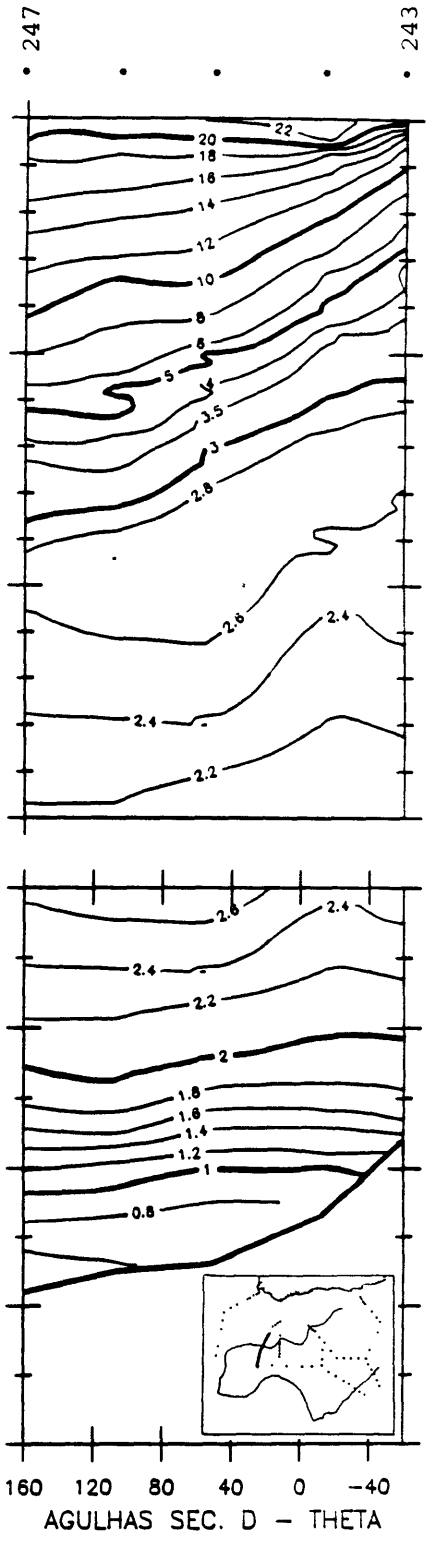
247
243
22
20
18
16
14
12
10
8
6
5
4
3.5
3
2.8
2.6
2.4
2.2
2
1.8
1.6
1.4
1.2
1
0.8
160 120 80 40 0 −40
AGULHAS SEC. D – THETA

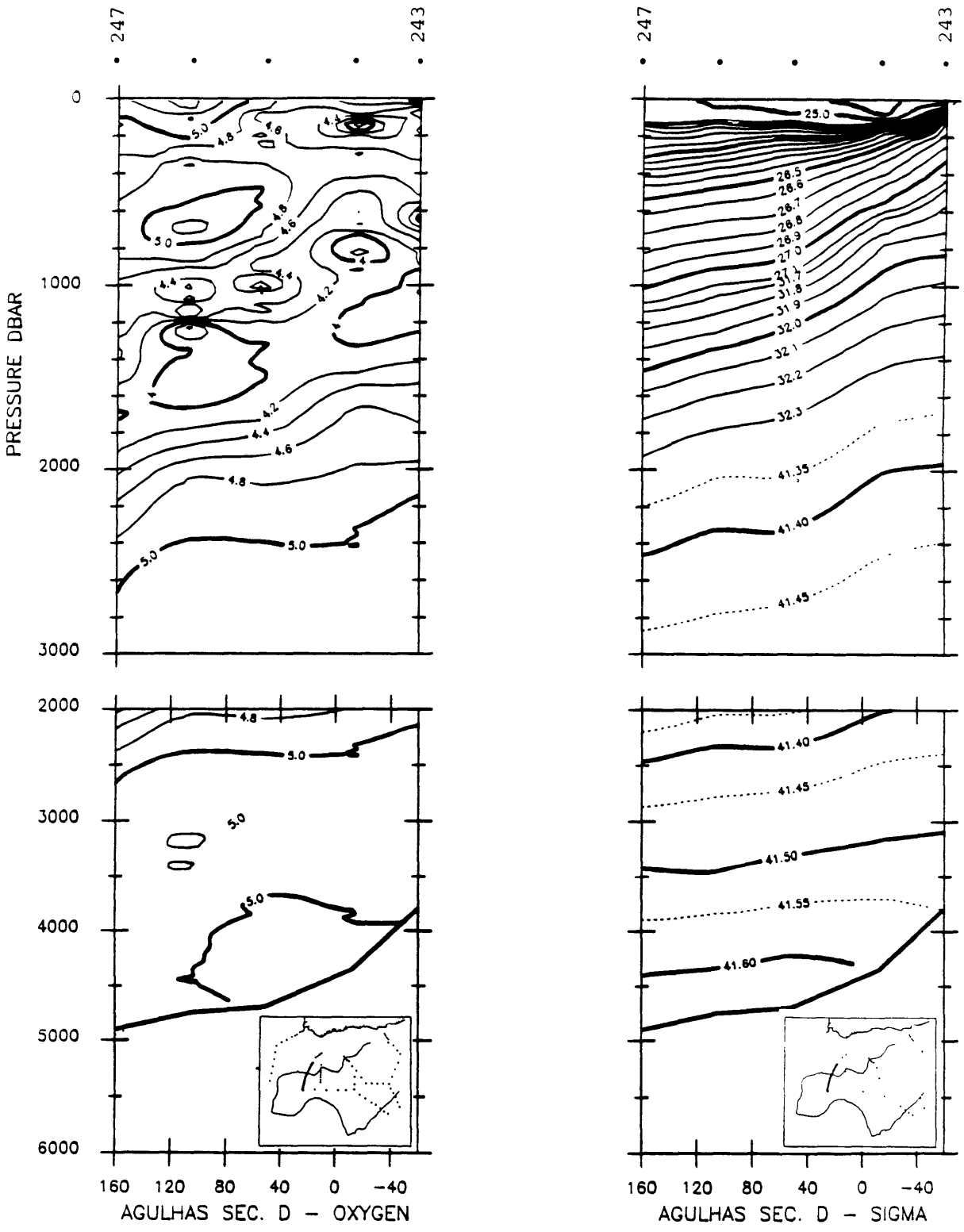
247
243
PRESSURE DBAR
0
1000
2000
3000
4000
5000
6000
4.8
5.0
4.6
4.4
4.2
160 120 80 40 0 -40
AGULHAS SEC. D – OXYGEN
25.0
26.5
26.6
26.7
26.8
26.9
27.0
31.7
31.8
31.9
32.0
32.1
32.2
32.3
41.35
41.40
41.45
41.50
41.55
41.60
AGULHAS SEC. D – SIGMA

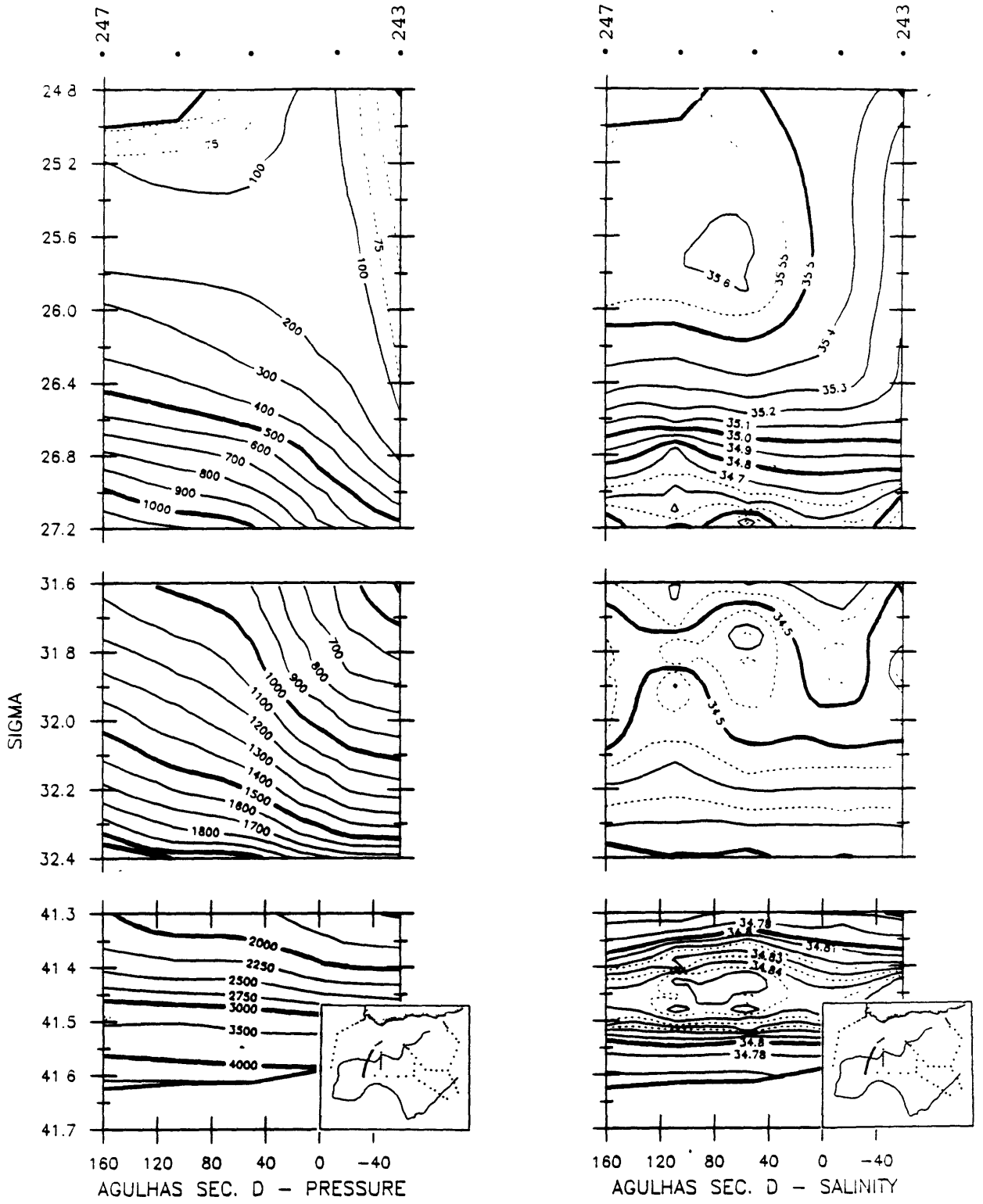
247
243
SIGMA
AGULHAS SEC. D – PRESSURE
AGULHAS SEC. D – SALINITY
160 120 80 40 0 -40

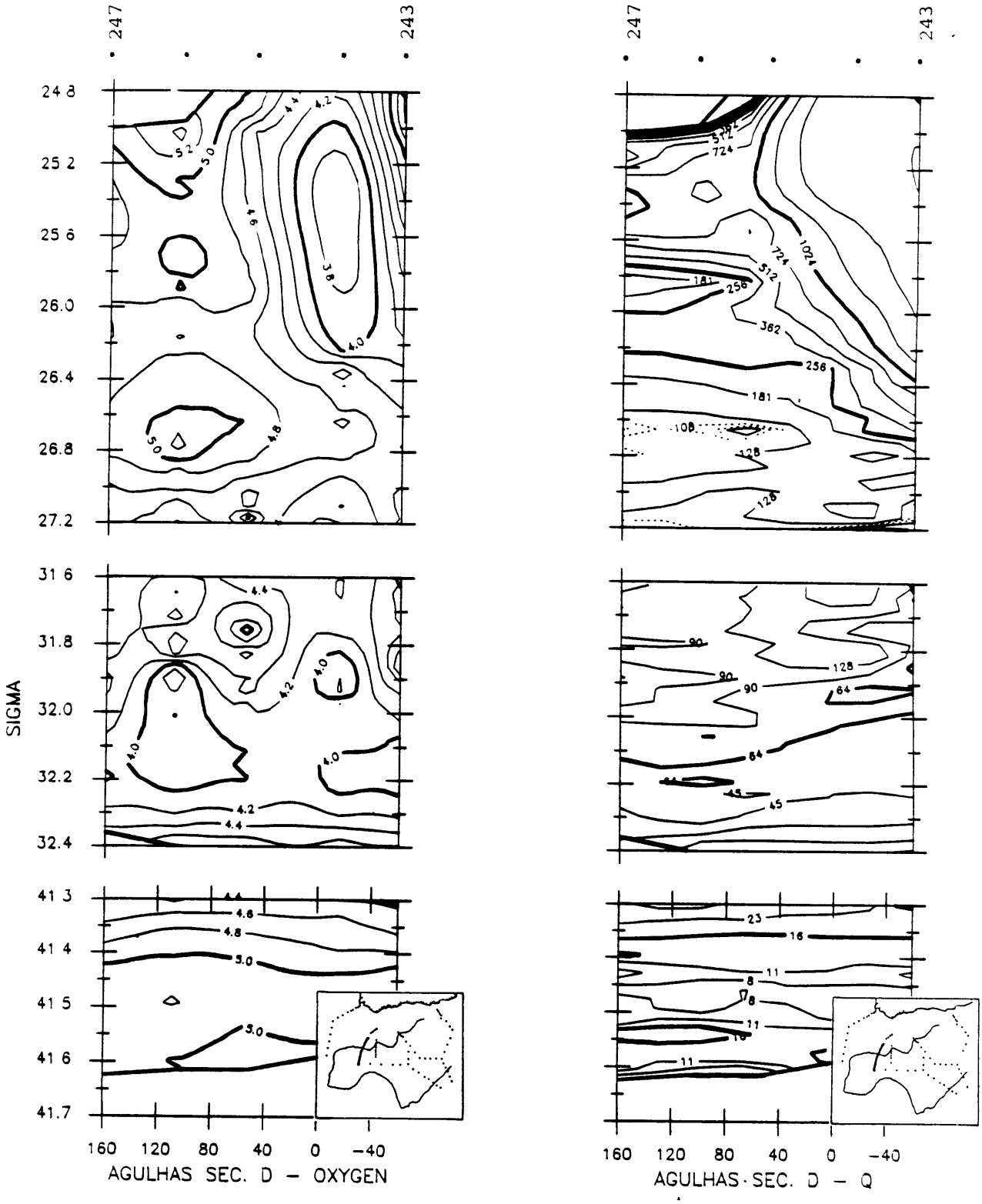
247
243
24.8
25.2
25.6
26.0
26.4
26.8
27.2
31.6
31.8
32.0
32.2
32.4
41.3
41.4
41.5
41.6
41.7
SIGMA
160 120 80 40 0 -40
AGULHAS SEC. D – OXYGEN
AGULHAS SEC. D – Q

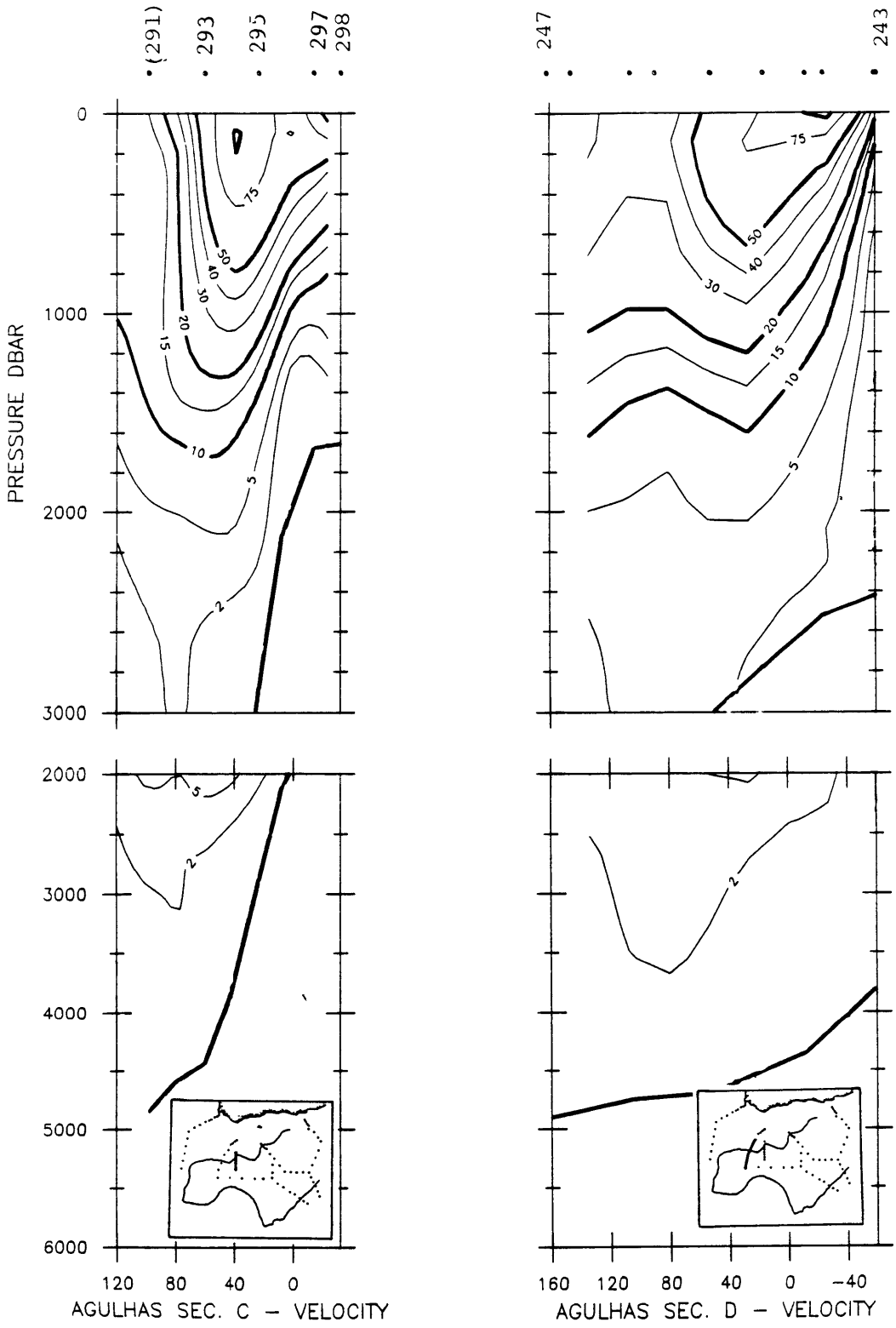
(291)
293
295
297
298
247
243
PRESSURE DBAR
0
1000
2000
3000
4000
5000
6000
120
80
40
0
160
120
80
40
0
-40
AGULHAS SEC. C – VELOCITY
AGULHAS SEC. D – VELOCITY

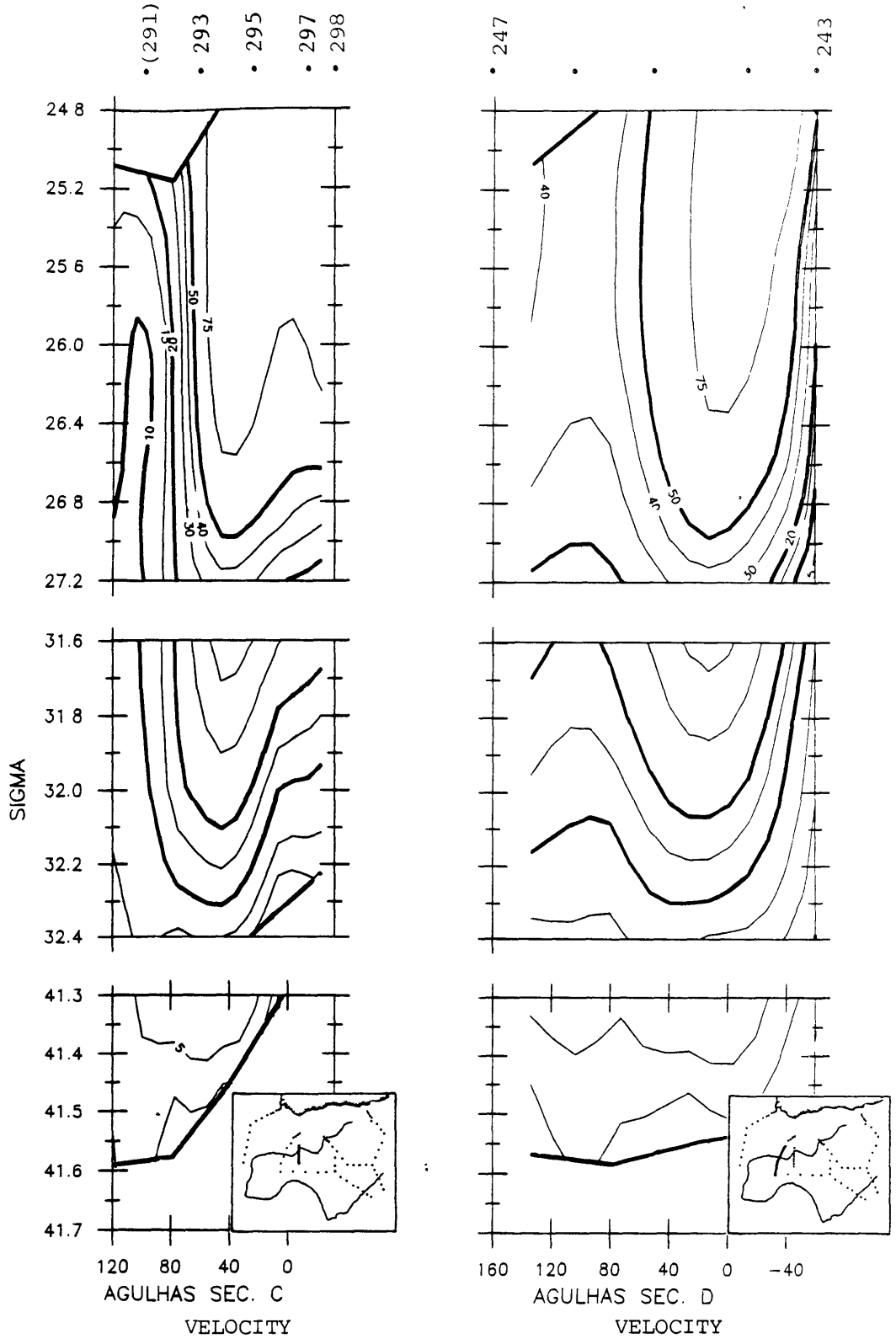
•(291)
• 293
• 295
• 297
• 298
• 247
• 243
24 8
25.2
25 6
26.0
26.4
26 8
27.2
31.6
31 8
32.0
32.2
32.4
41.3
41.4
41.5
41.6
41.7
SIGMA
10
20
30
40
50
75
120 80 40 0
AGULHAS SEC. C
VELOCITY
160 120 80 40 0 -40
AGULHAS SEC. D
VELOCITY

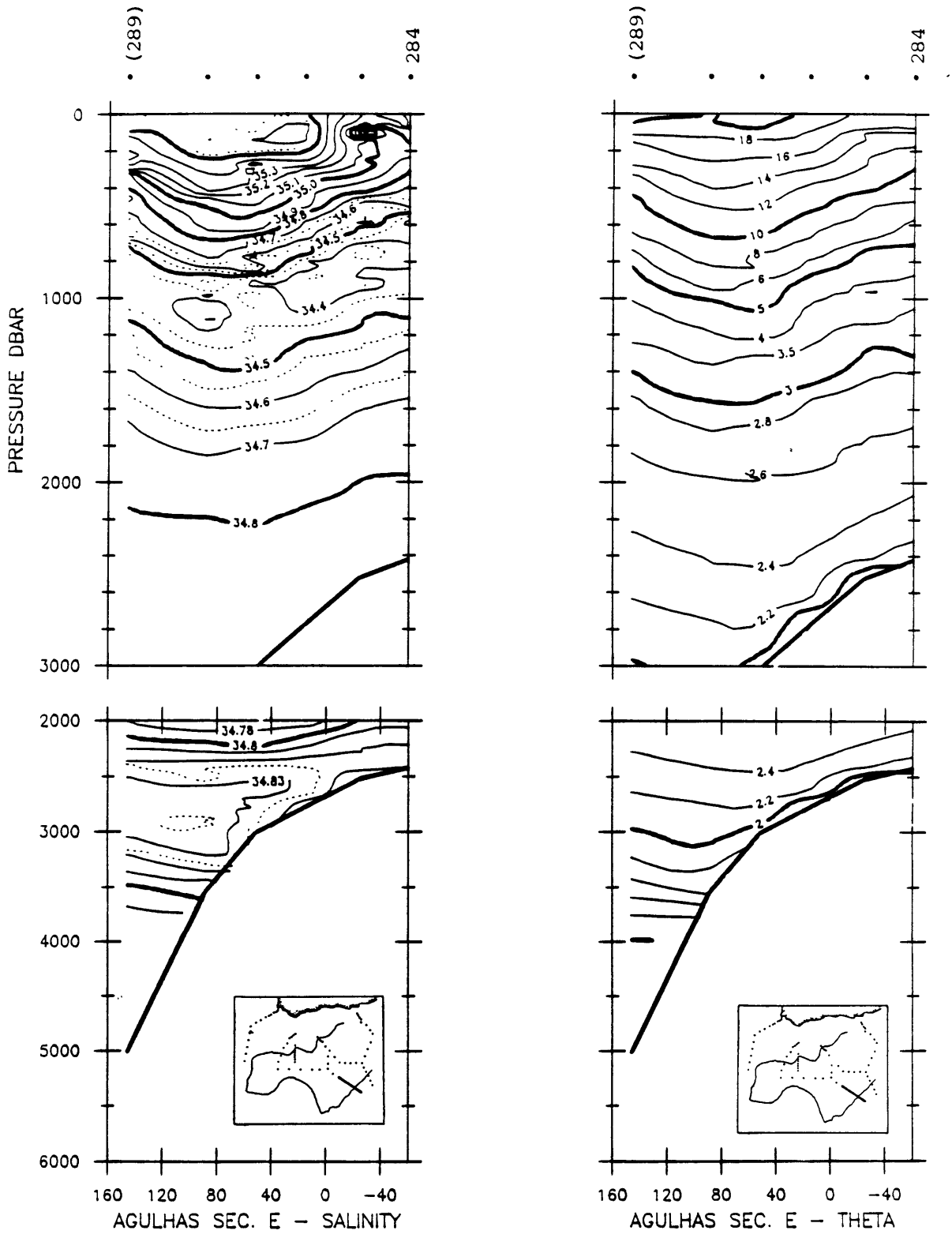
(289)
284
PRESSURE DBAR
0
1000
2000
3000
4000
5000
6000
35.3
35.2
35.1
35.0
34.9
34.8
34.7
34.6
34.5
34.4
34.78
34.8
34.83
18
16
14
12
10
8
6
5
4
3.5
3
2.8
2.6
2.4
2.2
2
160 120 80 40 0 -40
AGULHAS SEC. E – SALINITY
AGULHAS SEC. E – THETA

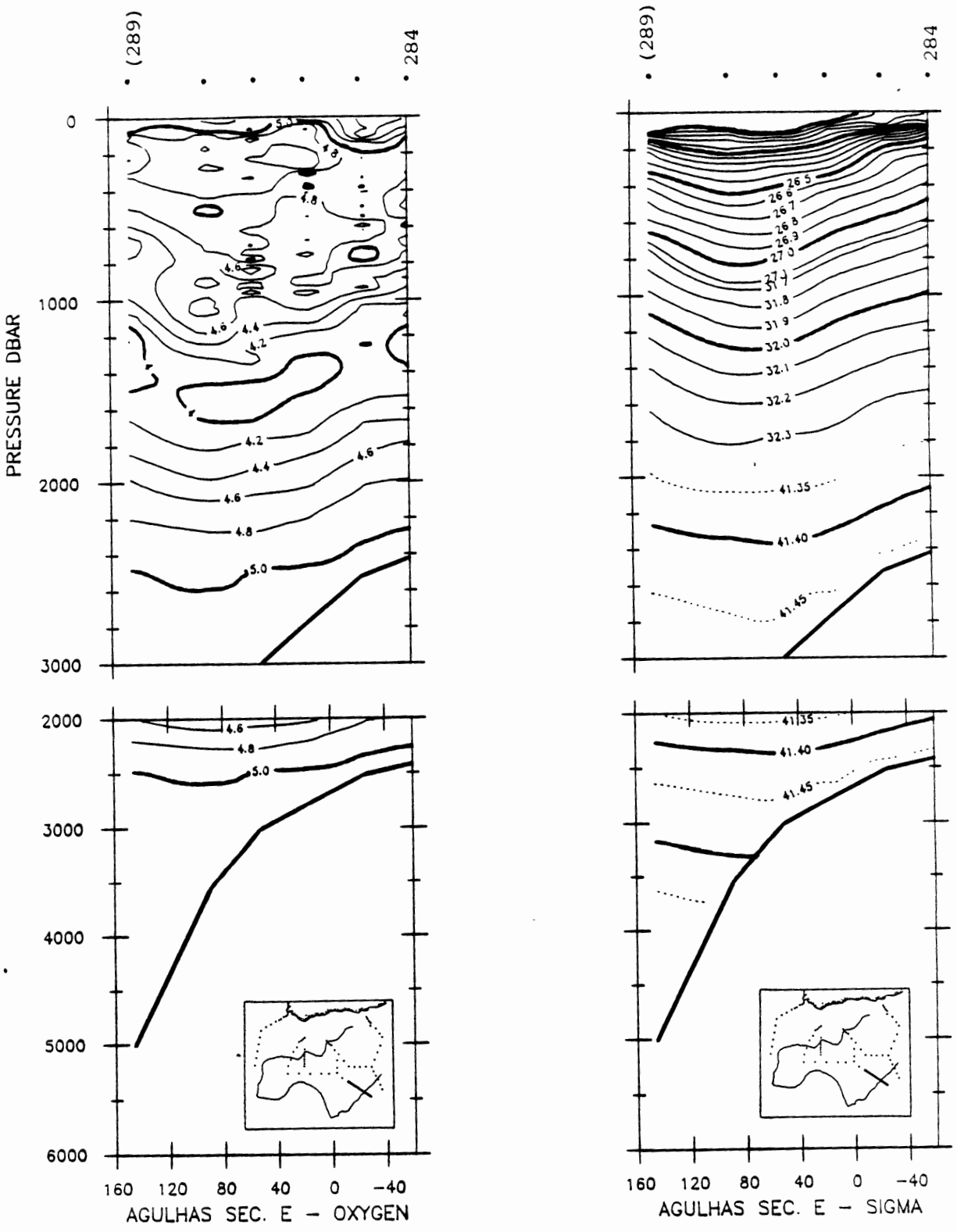
(289)
284
PRESSURE DBAR
0
1000
2000
3000
4000
5000
6000
4.2
4.4
4.6
4.8
5.0
160 120 80 40 0 -40
AGULHAS SEC. E – OXYGEN
26.5
26.6
26.7
26.8
26.9
27.0
27.1
31.7
31.8
31.9
32.0
32.1
32.2
32.3
41.35
41.40
41.45
AGULHAS SEC. E – SIGMA

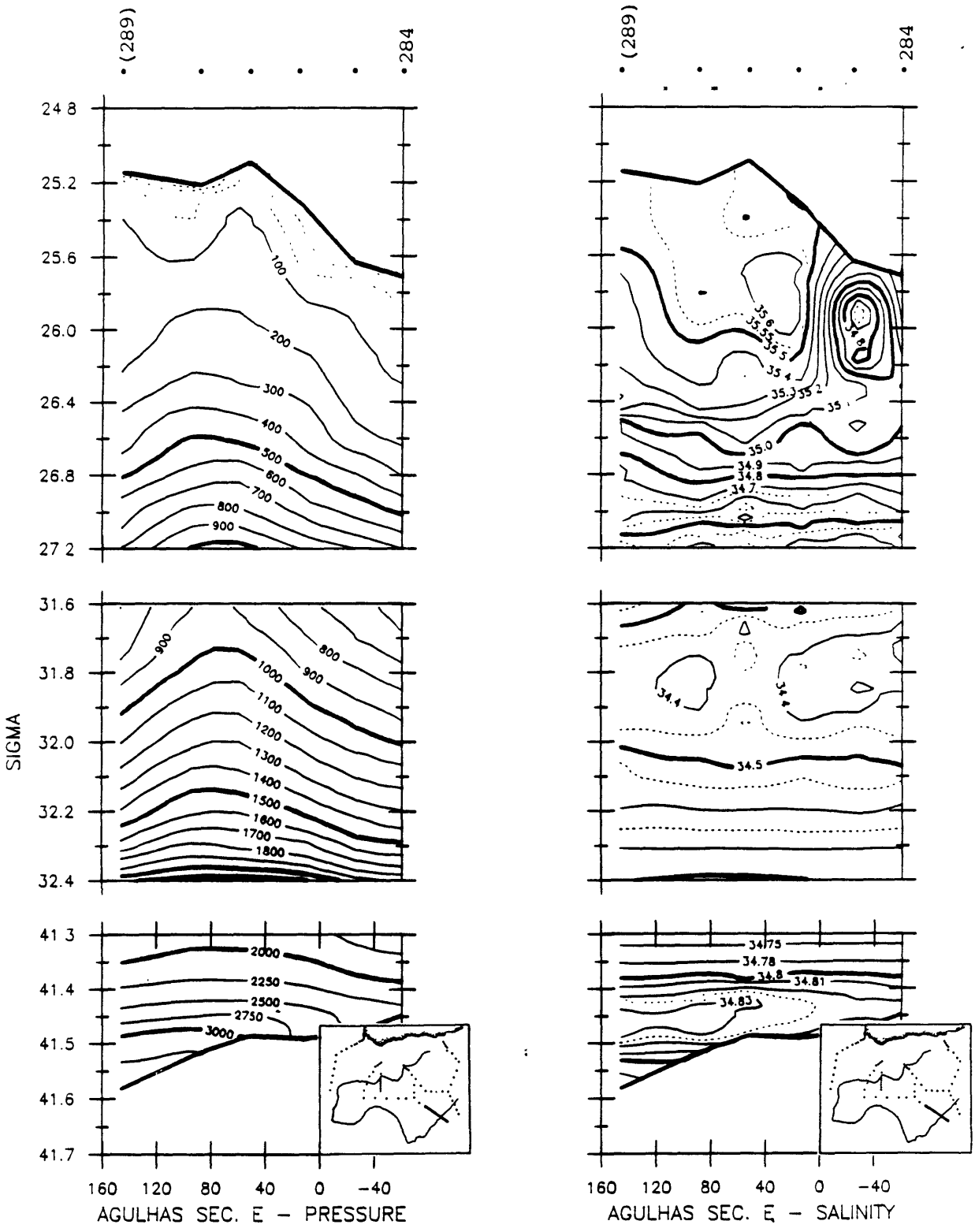
(289)
284
SIGMA
24.8
25.2
25.6
26.0
26.4
26.8
27.2
31.6
31.8
32.0
32.2
32.4
41.3
41.4
41.5
41.6
41.7
100
200
300
400
500
600
700
800
900
1000
1100
1200
1300
1400
1500
1600
1700
1800
2000
2250
2500
2750
3000
34.4
34.5
34.75
34.78
34.8
34.81
34.83
160 120 80 40 0 -40
AGULHAS SEC. E – PRESSURE
AGULHAS SEC. E – SALINITY

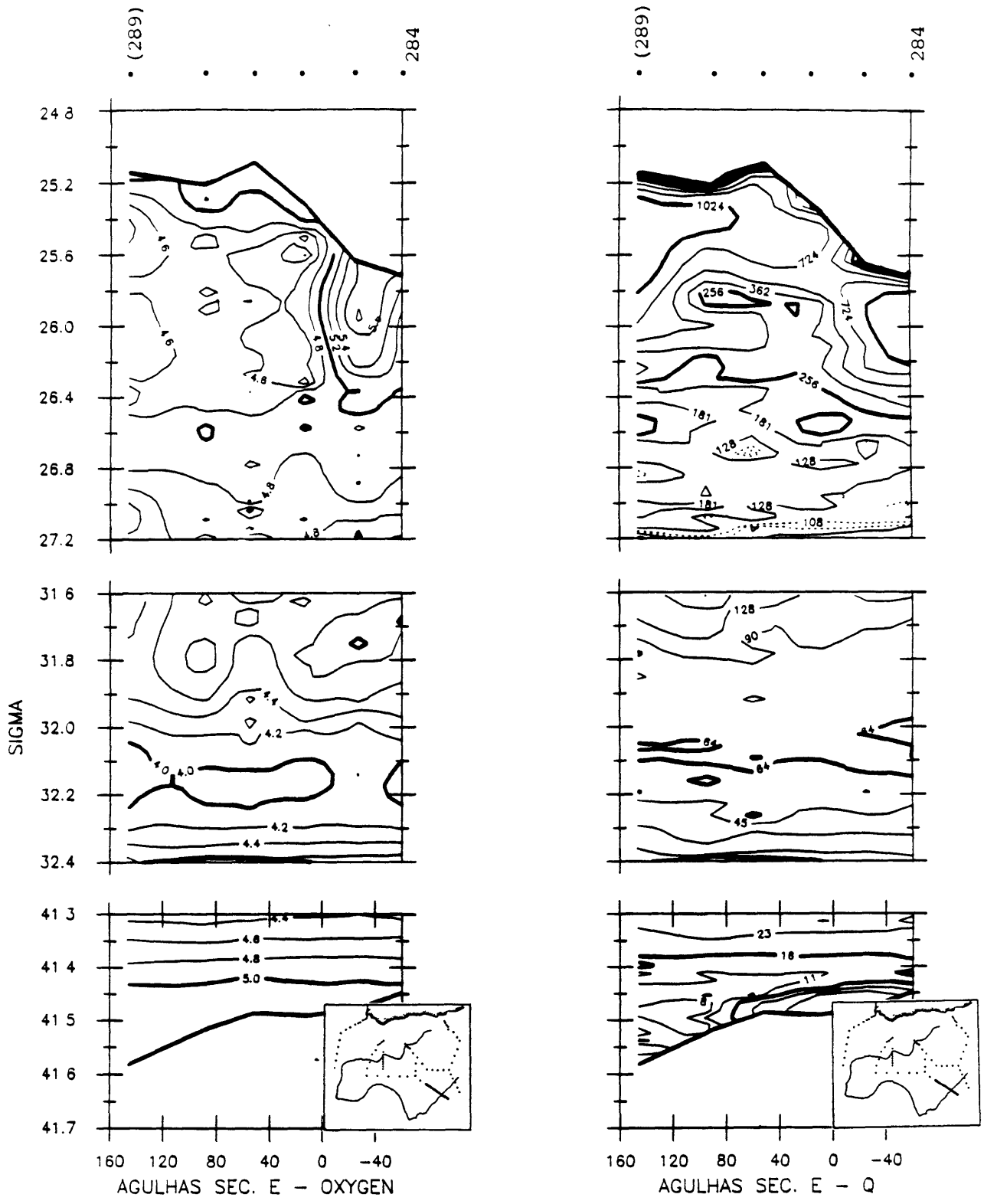
(289)
284
SIGMA
24.8
25.2
25.6
26.0
26.4
26.8
27.2
31.6
31.8
32.0
32.2
32.4
41.3
41.4
41.5
41.6
41.7
160 120 80 40 0 -40
AGULHAS SEC. E – OXYGEN
AGULHAS SEC. E – Q

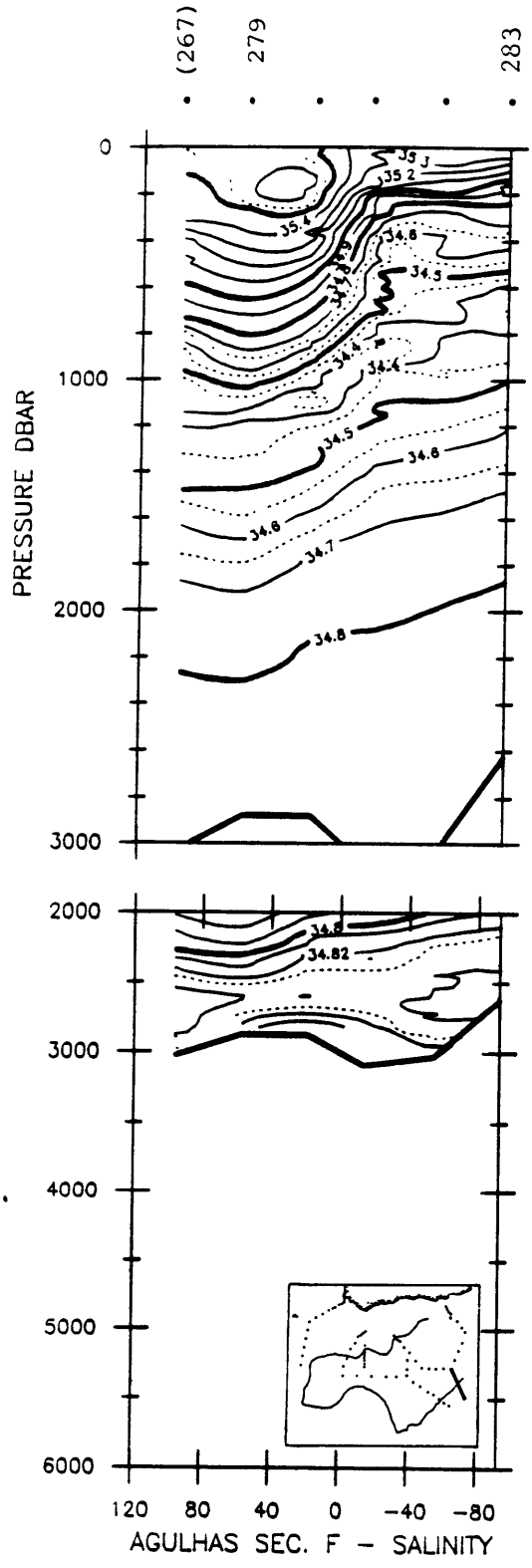
(267)
279
283
PRESSURE DBAR
0
1000
2000
3000
4000
5000
6000
35.1
35.2
35.4
34.6
34.5
34.4
34.5
34.6
34.6
34.7
34.8
34.8
34.82
120 80 40 0 -40 -80
AGULHAS SEC. F – SALINITY

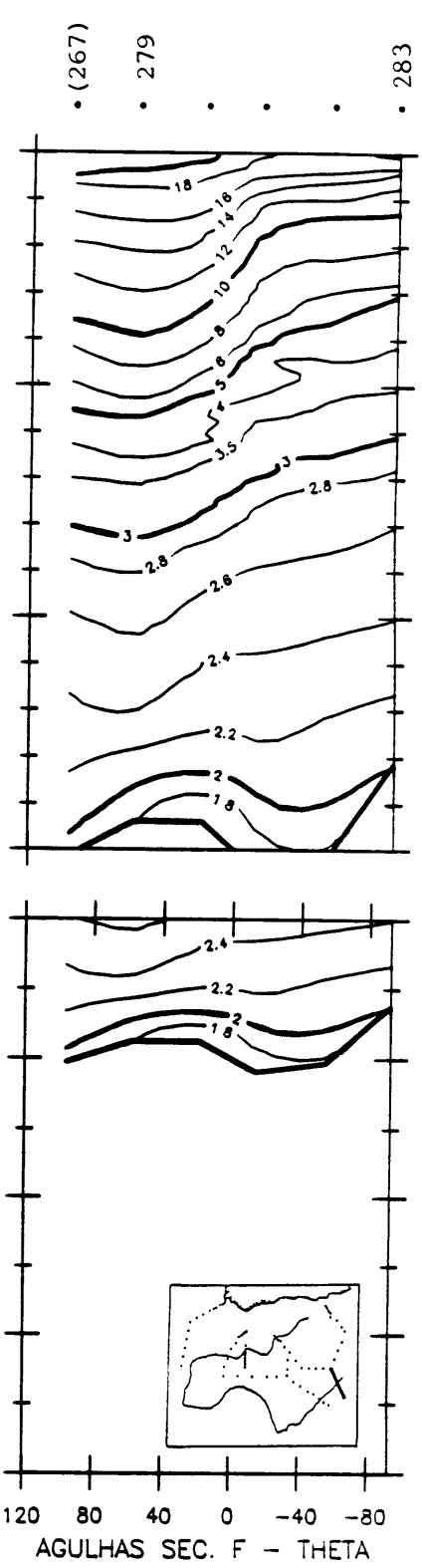
(267)
279
283
18
16
14
12
10
8
6
5
4
3.5
3
2.8
3
2.8
2.8
2.4
2.2
2
1.8
2.4
2.2
2
1.8
120 80 40 0 -40 -80
AGULHAS SEC. F – THETA

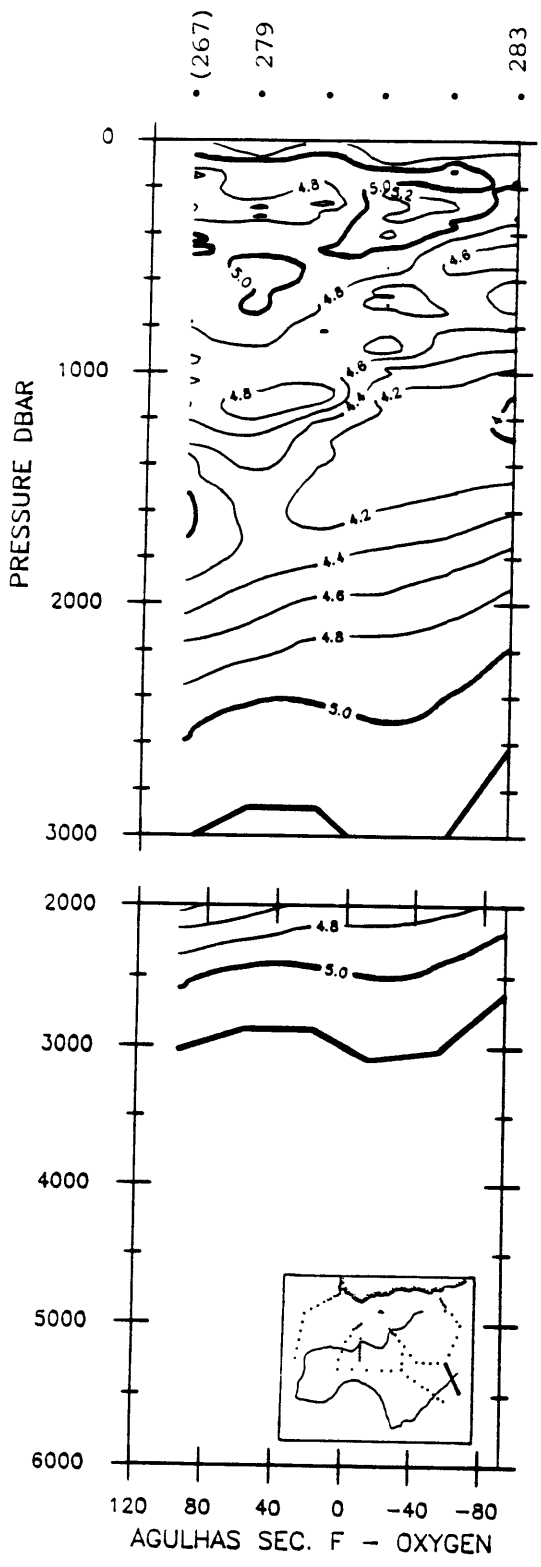
(267)
279
283
PRESSURE DBAR
0
1000
2000
3000
4000
5000
6000
4.8
5.0
5.2
4.6
4.4
4.2
120 80 40 0 -40 -80
AGULHAS SEC. F – OXYGEN

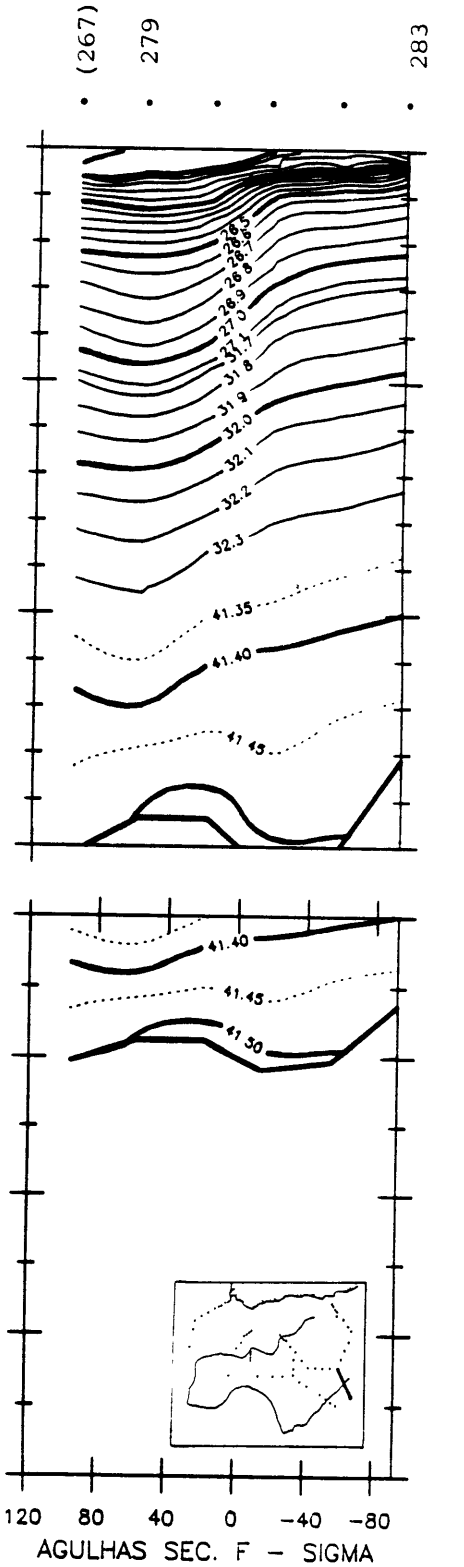
(267)
279
283
28.5
28.6
28.7
28.8
28.9
27.0
31.4
31.8
31.9
32.0
32.1
32.2
32.3
41.35
41.40
41.45
41.50
120 80 40 0 -40 -80
AGULHAS SEC. F – SIGMA

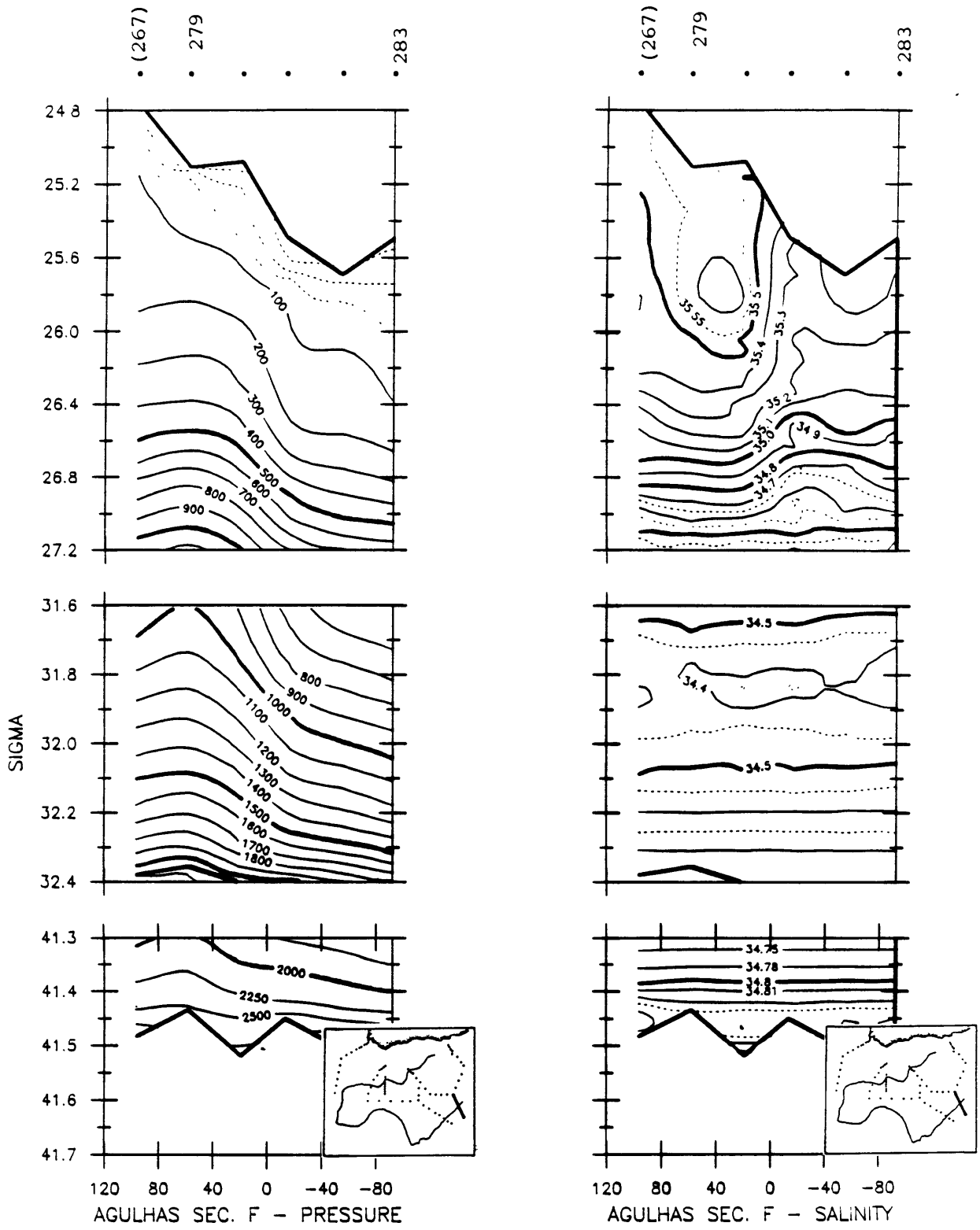
(267)
279
283
SIGMA
24.8
25.2
25.6
26.0
26.4
26.8
27.2
31.6
31.8
32.0
32.2
32.4
41.3
41.4
41.5
41.6
41.7
100
200
300
400
500
600
700
800
900
1000
1100
1200
1300
1400
1500
1600
1700
1800
2000
2250
2500
35.55
35.5
35.4
35.3
35.2
35.1
35.0
34.9
34.8
34.7
34.5
34.4
34.75
34.78
34.8
34.81
120
80
40
0
-40
-80
AGULHAS SEC. F - PRESSURE
AGULHAS SEC. F - SALINITY

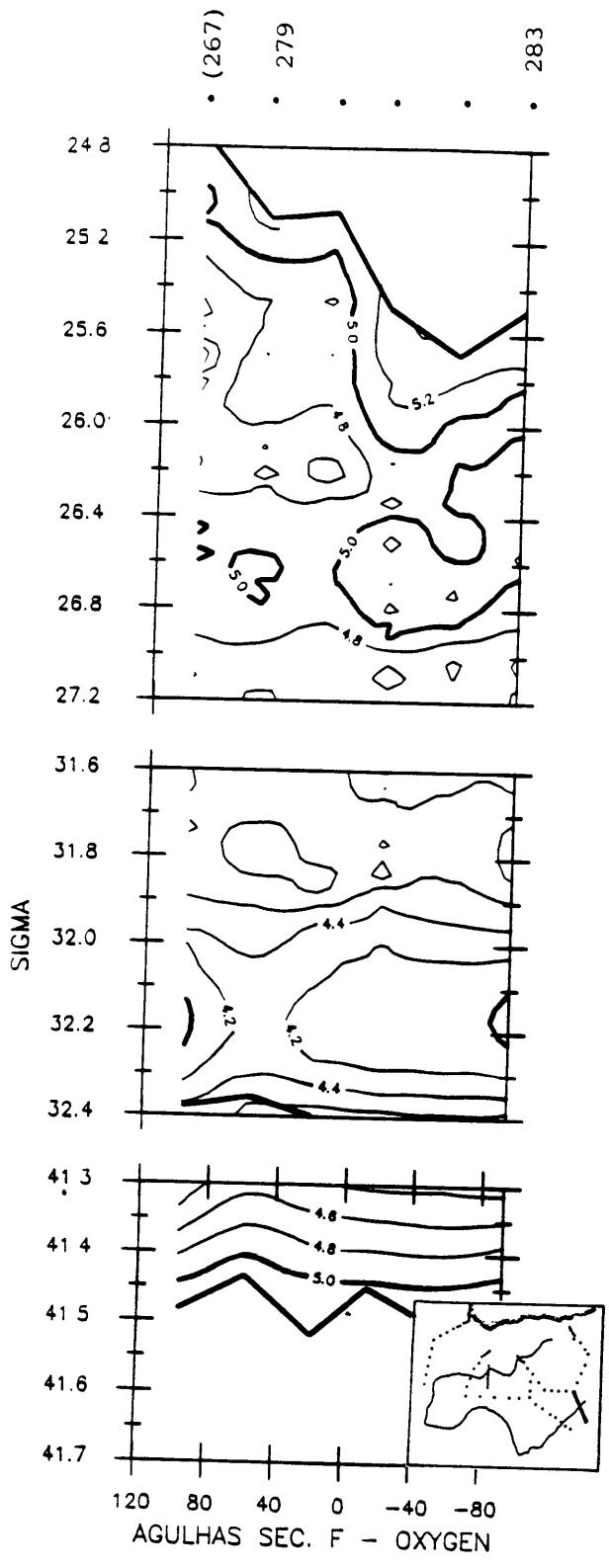
(267)
279
283
24 8
25 2
25.6
26.0
26.4
26.8
27.2
5.0
5.2
4.8
5.0
5.0
4.8
31.6
31.8
32.0
32.2
32.4
SIGMA
4.4
4.2
4.2
4.4
41 3
41 4
41 5
41.6
41.7
4.6
4.8
5.0
120 80 40 0 -40 -80
AGULHAS SEC. F – OXYGEN

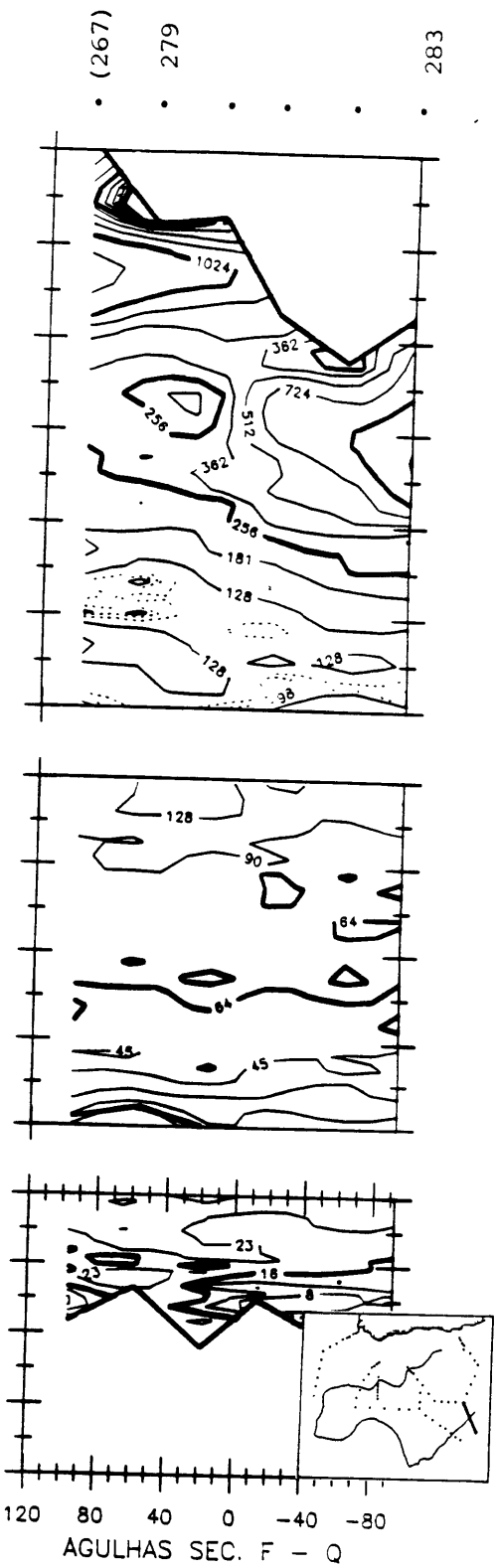
(267)
279
283
1024
362
724
512
256
362
256
181
128
128
128
38
128
90
64
64
45
45
23
23
18
8
120 80 40 0 -40 -80
AGULHAS SEC. F – Q

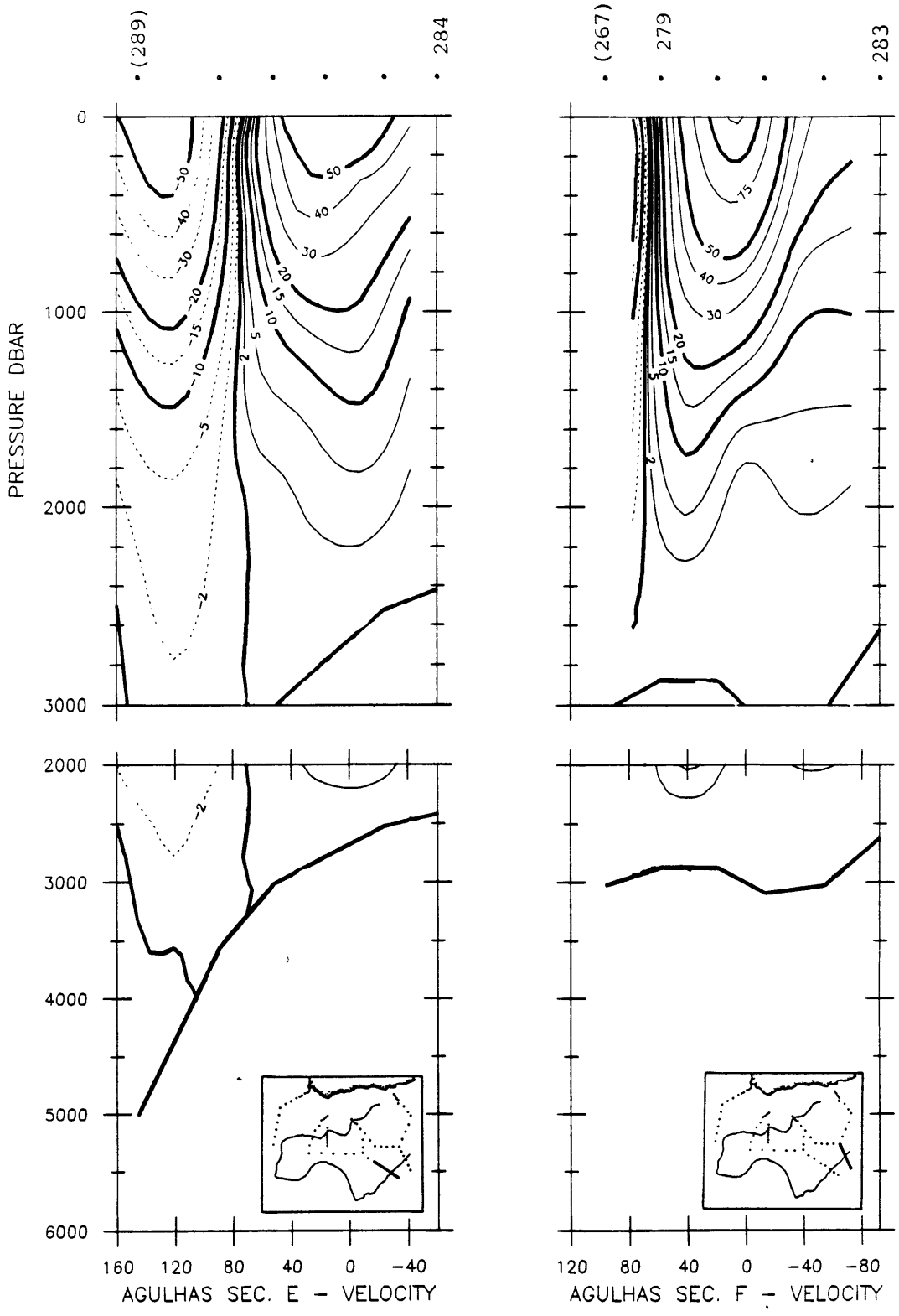
(289)
284
(267)
279
283
PRESSURE DBAR
0
1000
2000
3000
4000
5000
6000
160 120 80 40 0 −40
AGULHAS SEC. E − VELOCITY
120 80 40 0 −40 −80
AGULHAS SEC. F − VELOCITY

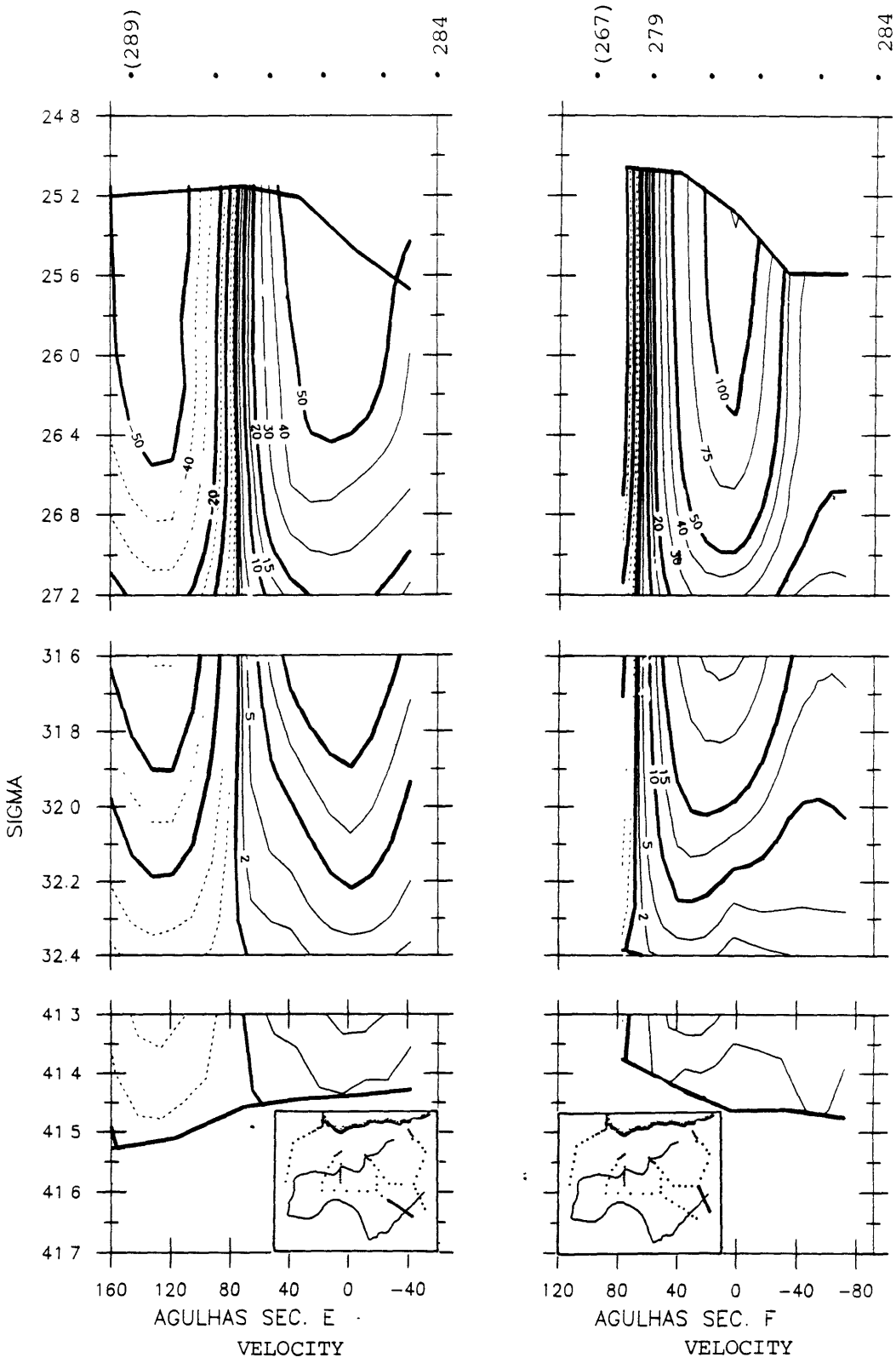
(289)
284
(267)
279
284
24 8
25 2
25 6
26 0
26 4
26 8
27 2
31 6
31 8
32 0
32.2
32.4
41 3
41 4
41 5
41 6
41 7
SIGMA
160 120 80 40 0 -40
AGULHAS SEC. E
VELOCITY
120 80 40 0 -40 -80
AGULHAS SEC. F
VELOCITY

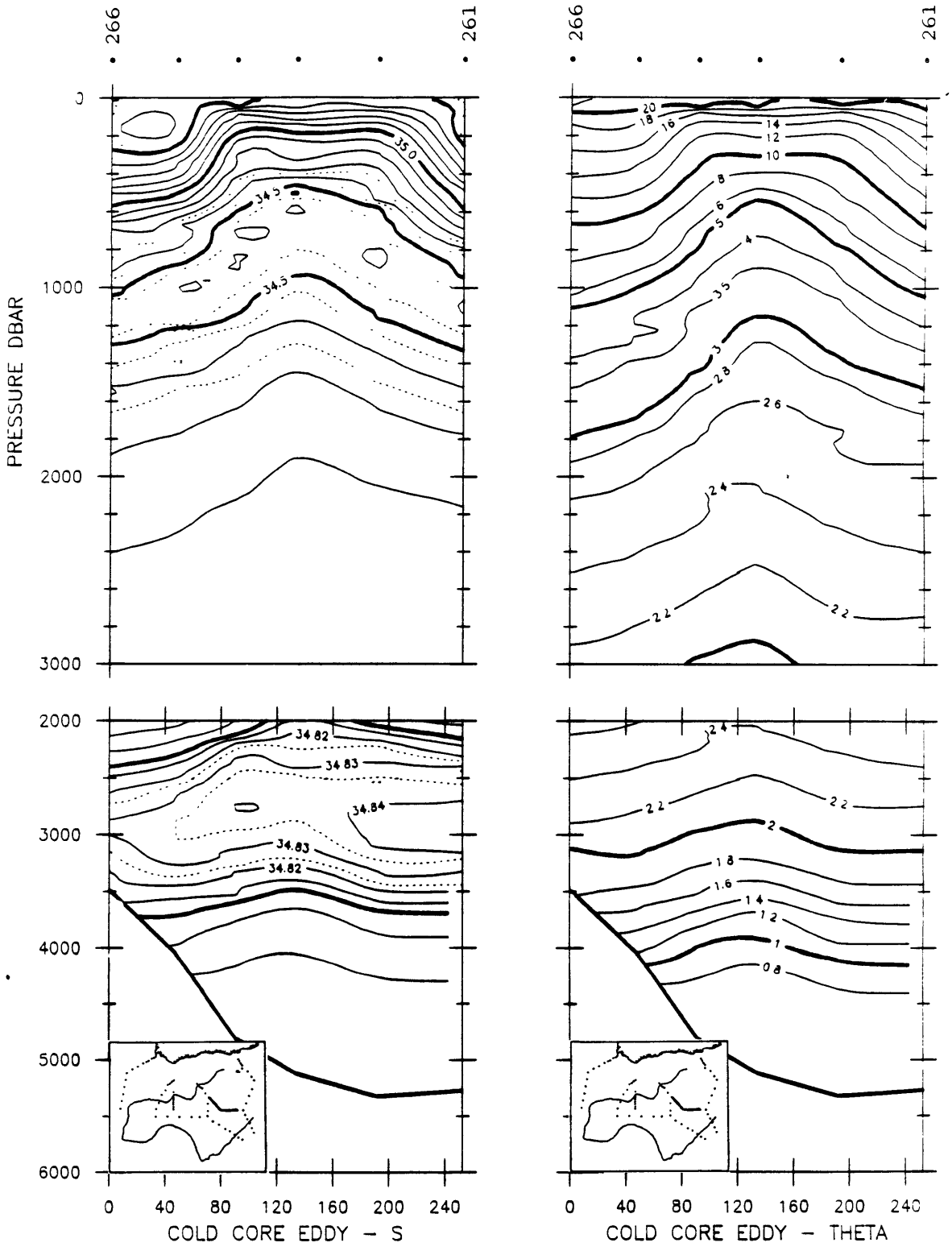
266
261
PRESSURE DBAR
0
1000
2000
3000
4000
5000
6000
35.0
34.5
34.5
34.82
34.83
34.84
34.83
34.82
20
18
16
14
12
10
8
6
5
4
3.5
3
2.8
2.6
2.4
2.2
2.2
2.4
2.2
2
1.8
1.6
1.4
1.2
1
0.8
0
40
80
120
160
200
240
COLD CORE EDDY – S
COLD CORE EDDY – THETA

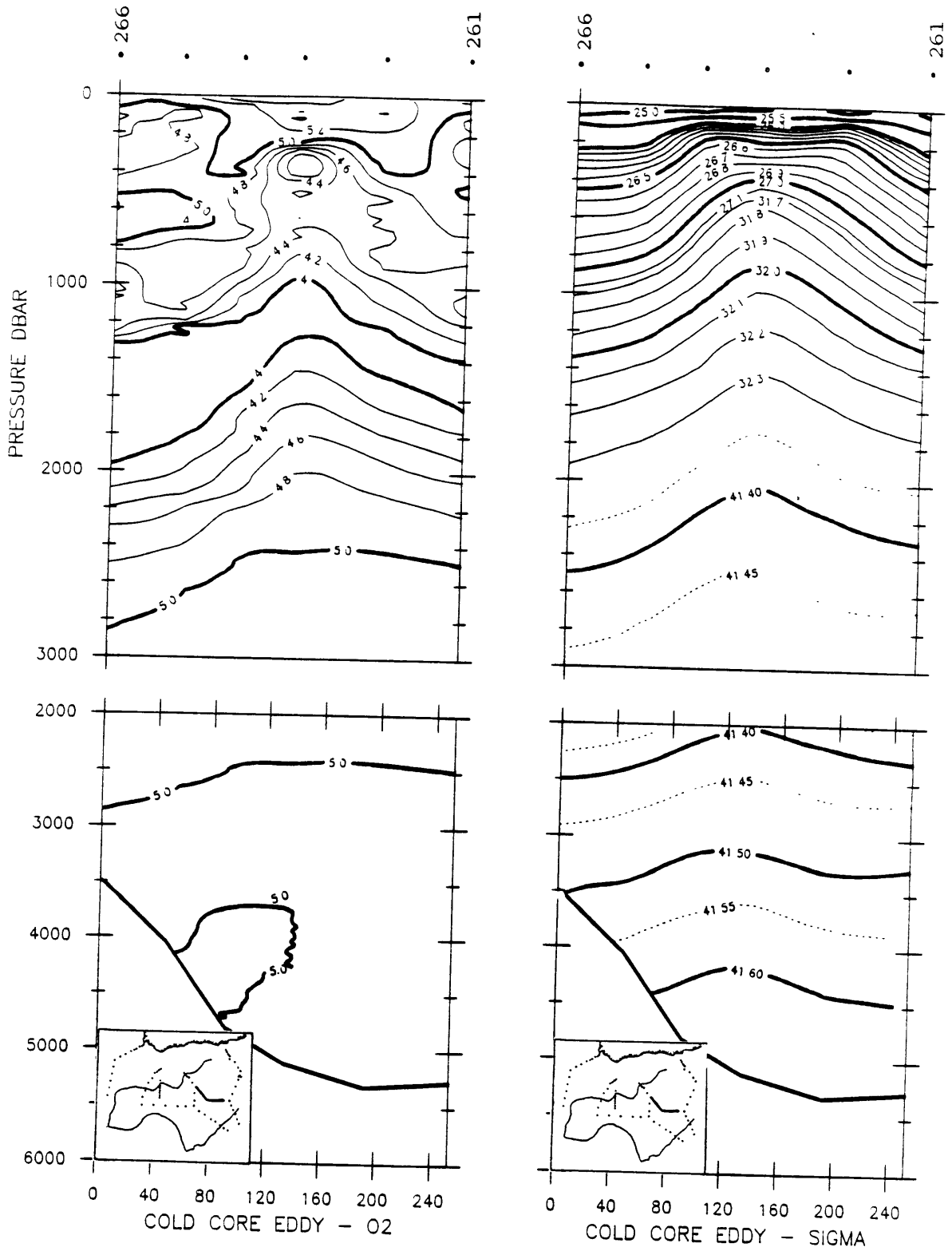
266
261
PRESSURE DBAR
0
1000
2000
3000
4000
5000
6000
0
40
80
120
160
200
240
COLD CORE EDDY – O2
COLD CORE EDDY – SIGMA

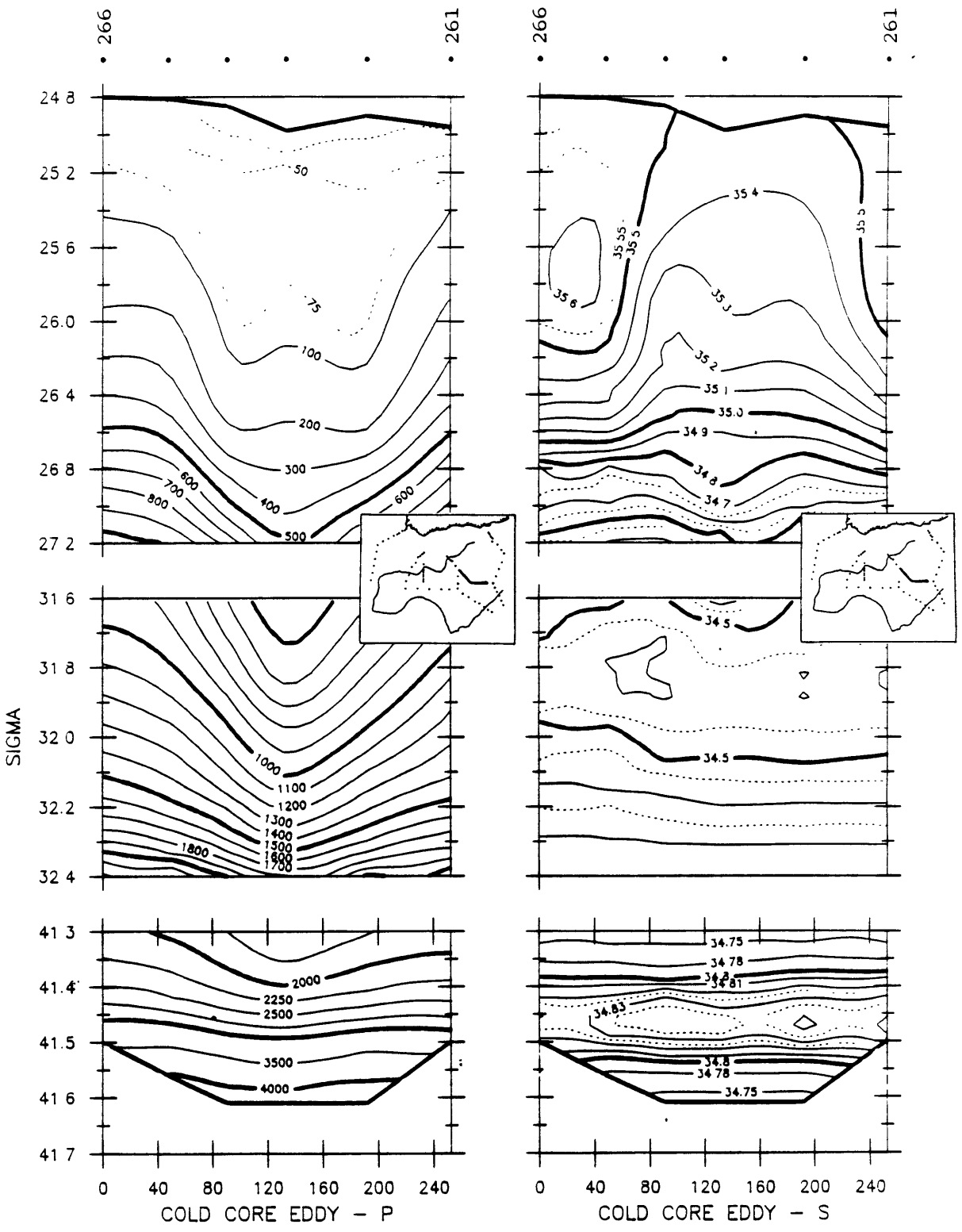
266
261
SIGMA
24 8
25 2
25 6
26.0
26 4
26 8
27 2
31 6
31 8
32 0
32.2
32 4
41 3
41.4
41.5
41 6
41 7
50
75
100
200
300
400
500
600
700
800
900
1000
1100
1200
1300
1400
1500
1600
1700
1800
2000
2250
2500
3500
4000
35 4
35 3
35 2
35 1
35.0
34 9
34 8
34 7
34.5
34.75
34 78
34 81
34.83
34.8
0
40
80
120
160
200
240
COLD CORE EDDY – P
COLD CORE EDDY – S

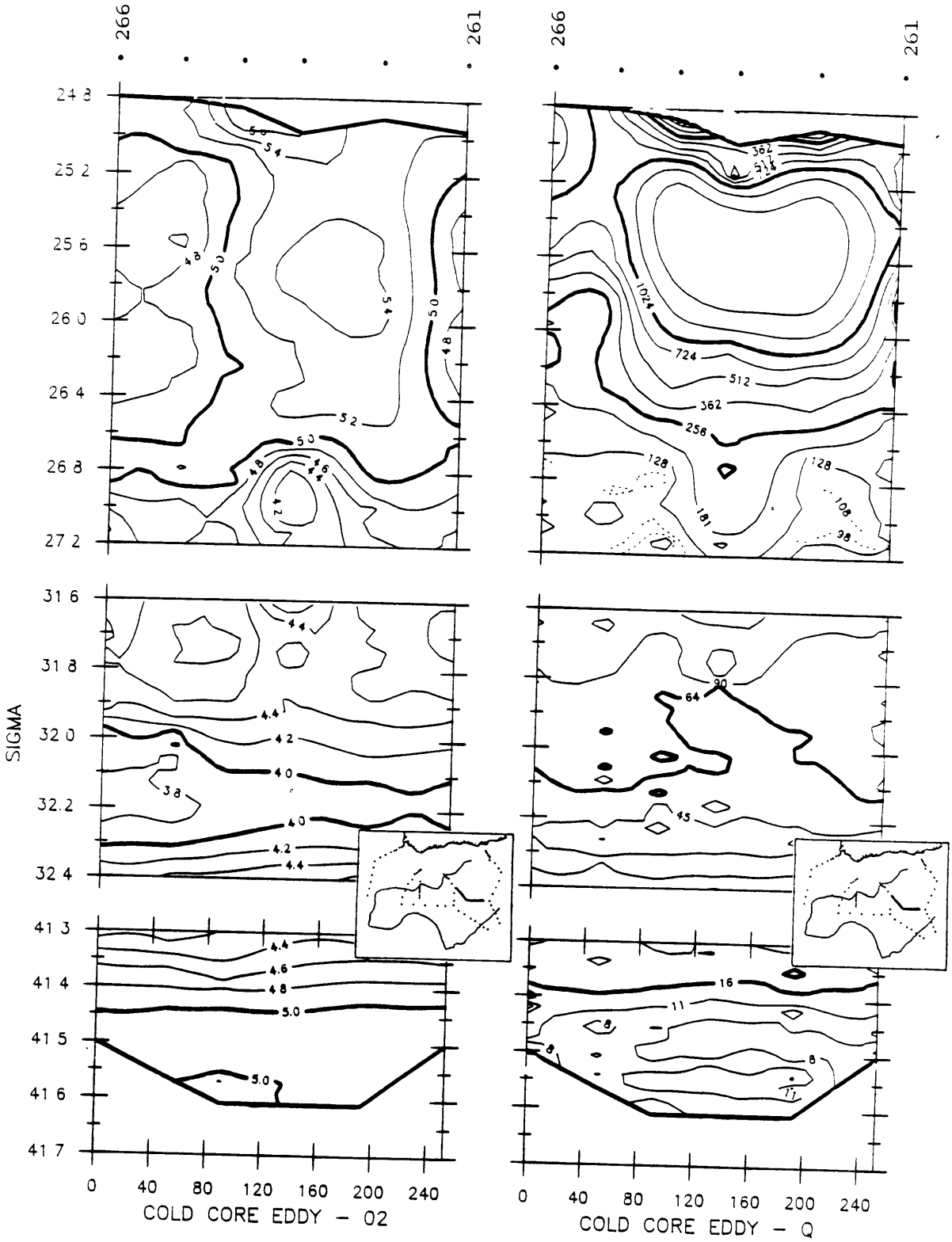
266
261
24 8
25 2
25 6
26 0
26 4
26 8
27 2
5.6
5.4
4.8
5.0
5.4
5.0
4.8
5.2
5.0
4.8
4.6
4.2
362
512
1024
724
512
362
256
128
128
108
181
98
SIGMA
31 6
31 8
32 0
32.2
32 4
41 3
41 4
41 5
41 6
41 7
4.4
4.4
4.2
4.0
3.8
4.0
4.2
4.4
4.4
4.6
4.8
5.0
5.0
90
64
45
16
11
8
8
0
40
80
120
160
200
240
COLD CORE EDDY – 02
COLD CORE EDDY – Q

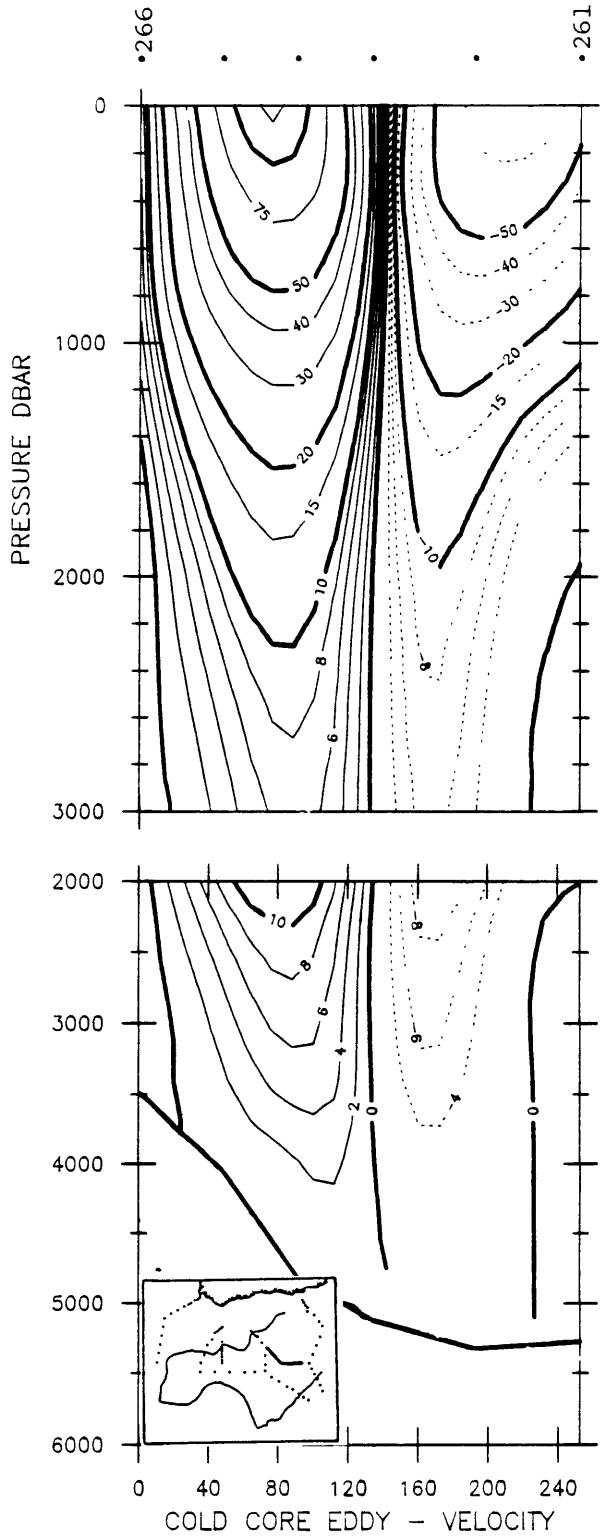
•266
•261
0
1000
2000
3000
4000
5000
6000
PRESSURE DBAR
75
50
40
30
20
15
10
8
6
-50
-40
-30
-20
-15
-10
-8
10
8
6
4
2
0
-8
-6
-4
0
0
40
80
120
160
200
240
COLD CORE EDDY – VELOCITY

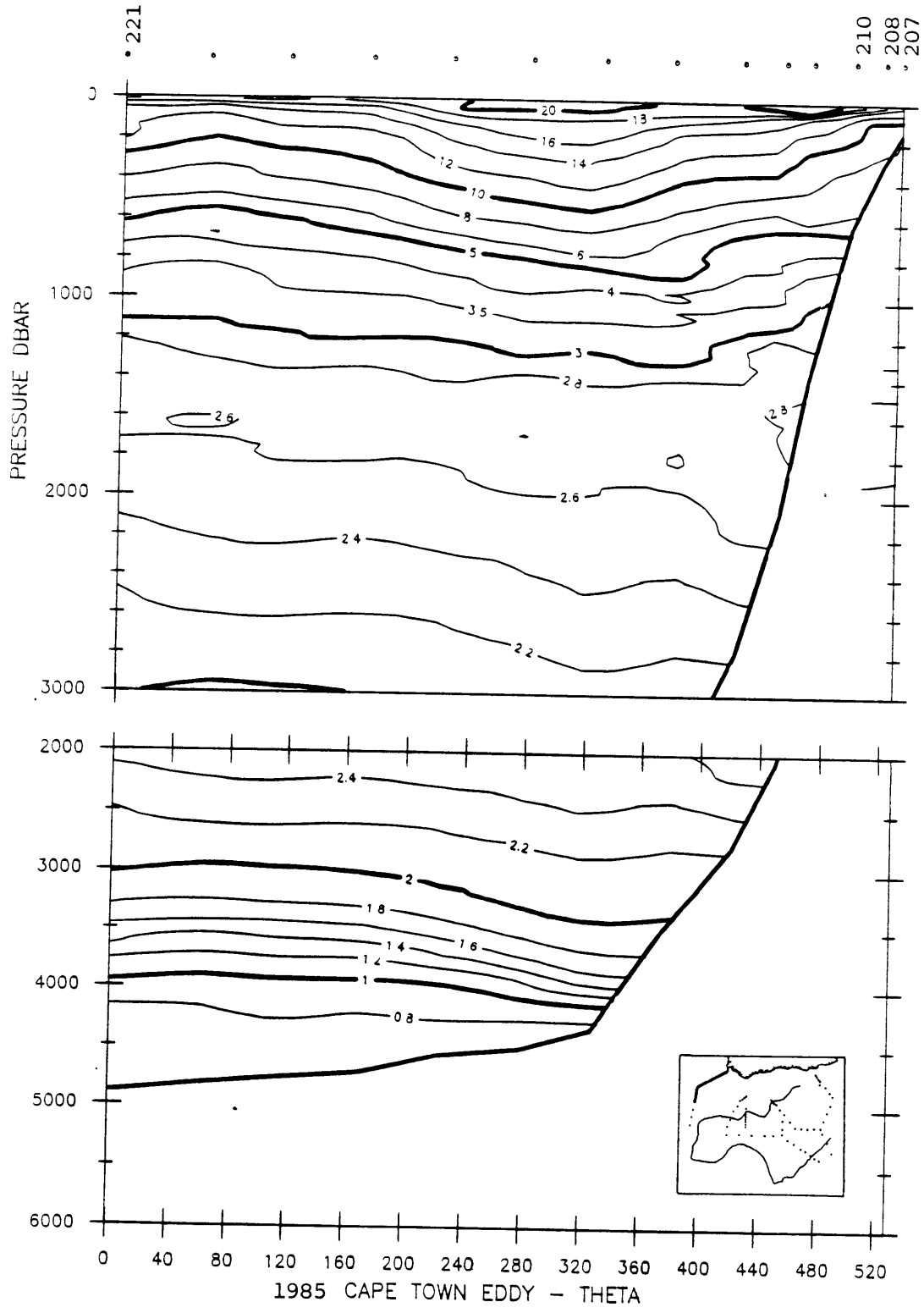
221
210
208
207
0
1000
2000
3000
PRESSURE DBAR
20
18
16
14
12
10
8
6
5
4
3.5
3
2.8
2.6
2.4
2.2
2000
3000
4000
5000
6000
2.4
2.2
2
1.8
1.6
1.4
1.2
1
0.8
0
40
80
120
160
200
240
280
320
360
400
440
480
520
1985 CAPE TOWN EDDY – THETA

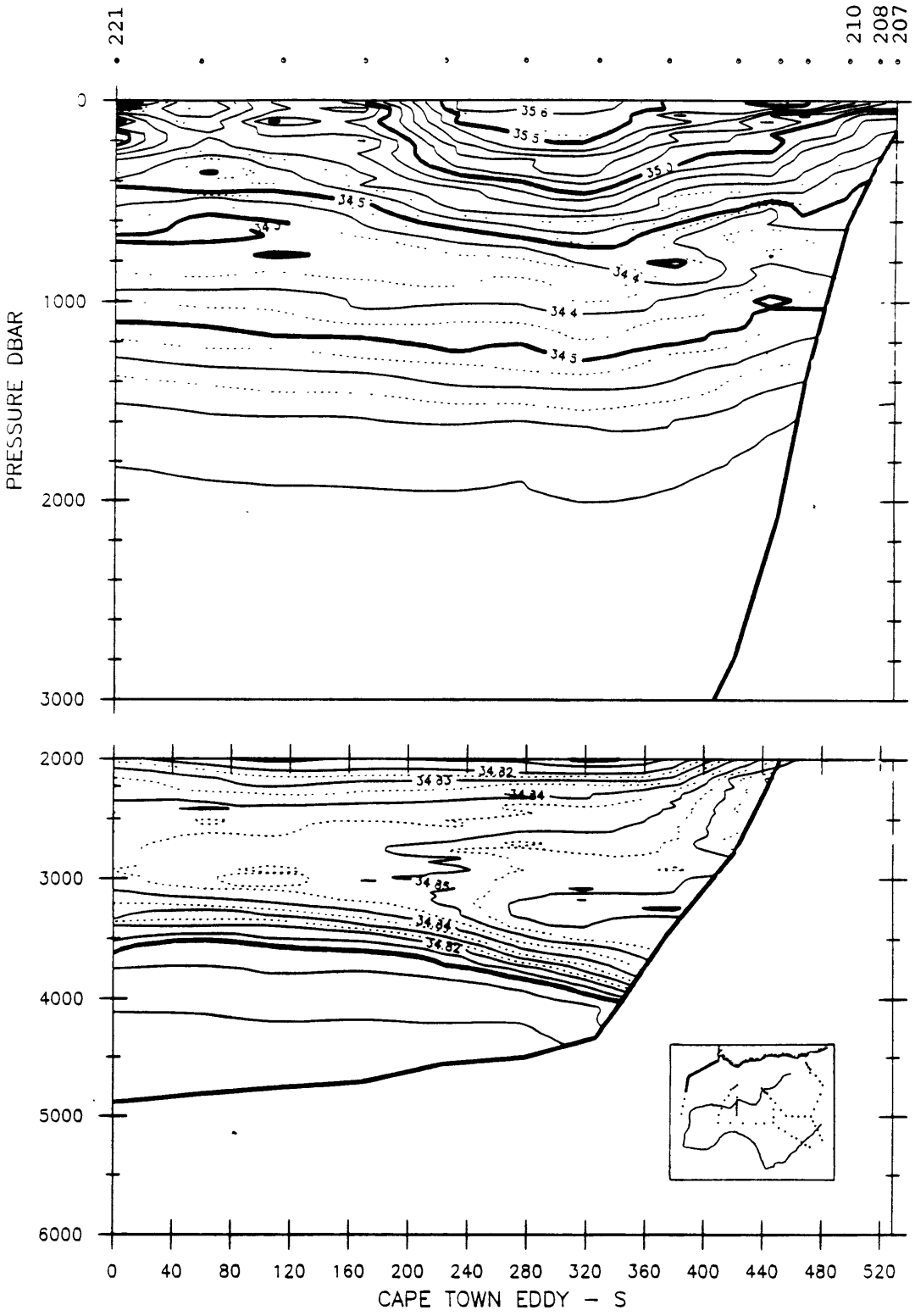
221
210
208
207
0
1000
2000
3000
PRESSURE DBAR
35.6
35.5
35.3
34.5
34.4
34.5
2000
3000
4000
5000
6000
34.83
34.82
34.84
34.85
34.84
34.82
0
40
80
120
160
200
240
280
320
360
400
440
480
520
CAPE TOWN EDDY – S

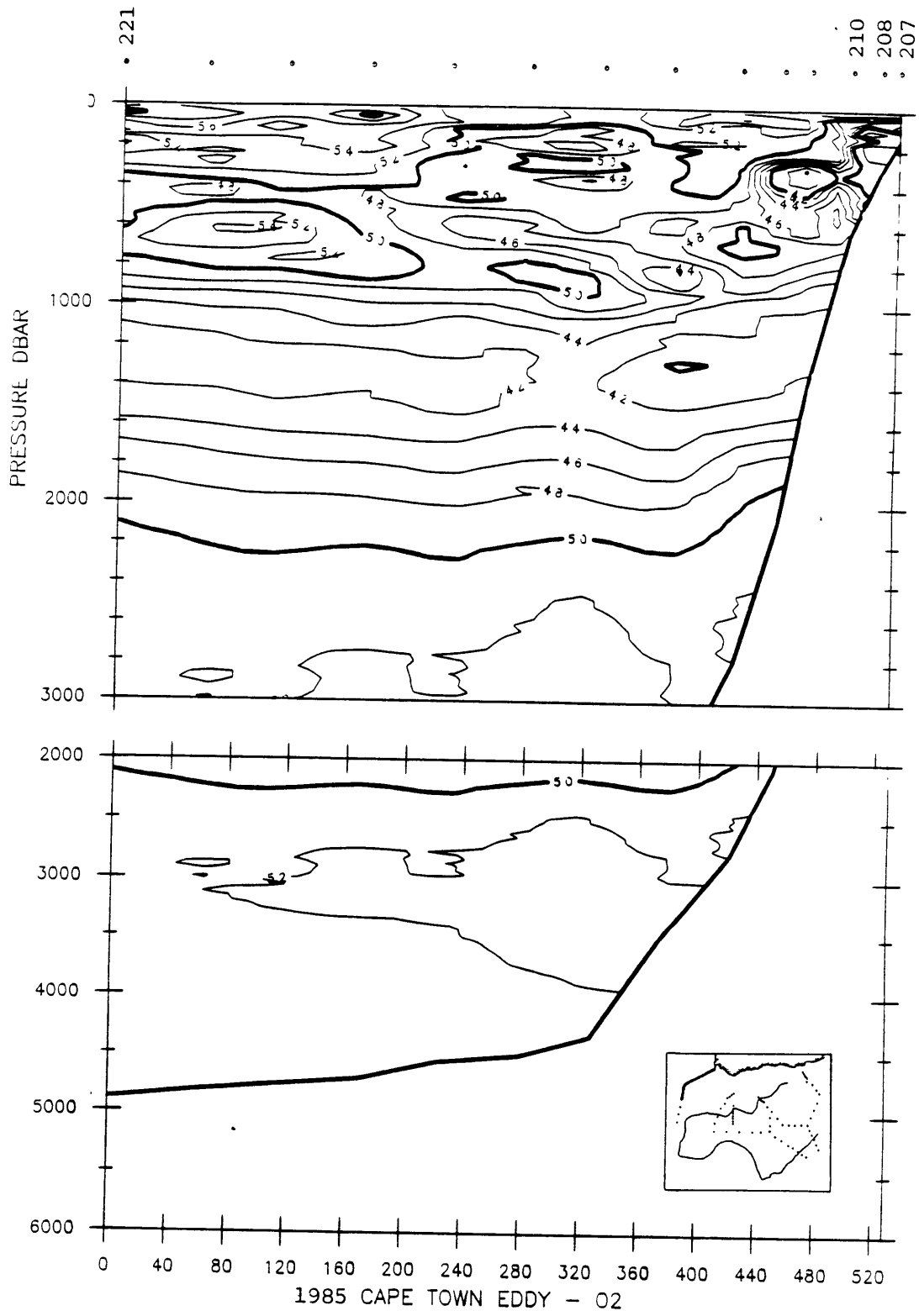
221
210
208
207
PRESSURE DBAR
0
1000
2000
3000
2000
3000
4000
5000
6000
0
40
80
120
160
200
240
280
320
360
400
440
480
520
1985 CAPE TOWN EDDY – 02

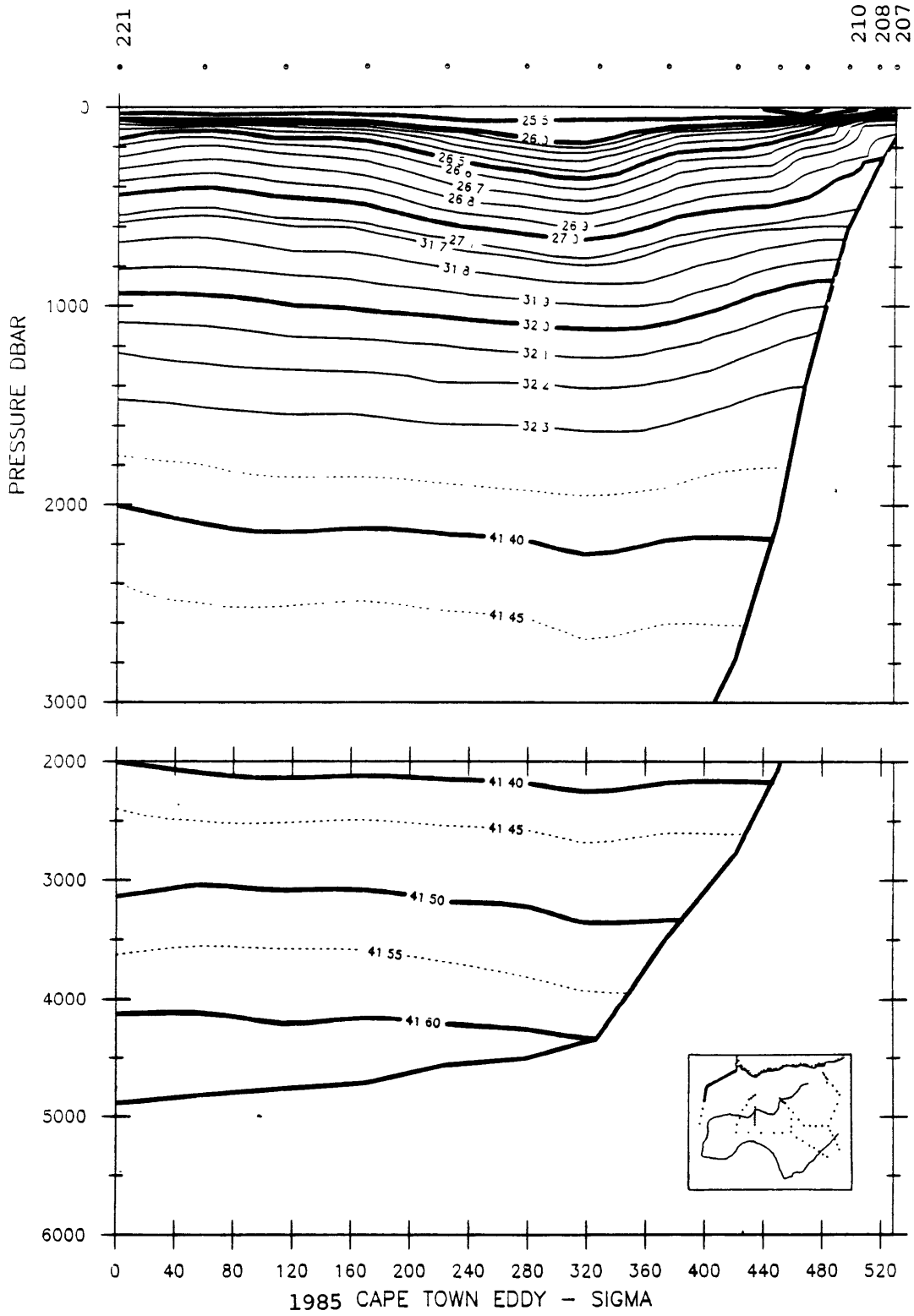
221
210
208
207
PRESSURE DBAR
0
1000
2000
3000
4000
5000
6000
25.5
26.0
26.5
26.6
26.7
26.8
26.9
27.0
27.1
31.8
31.9
32.0
32.1
32.2
32.3
41.40
41.45
41.50
41.55
41.60
0
40
80
120
160
200
240
280
320
360
400
440
480
520
1985 CAPE TOWN EDDY – SIGMA

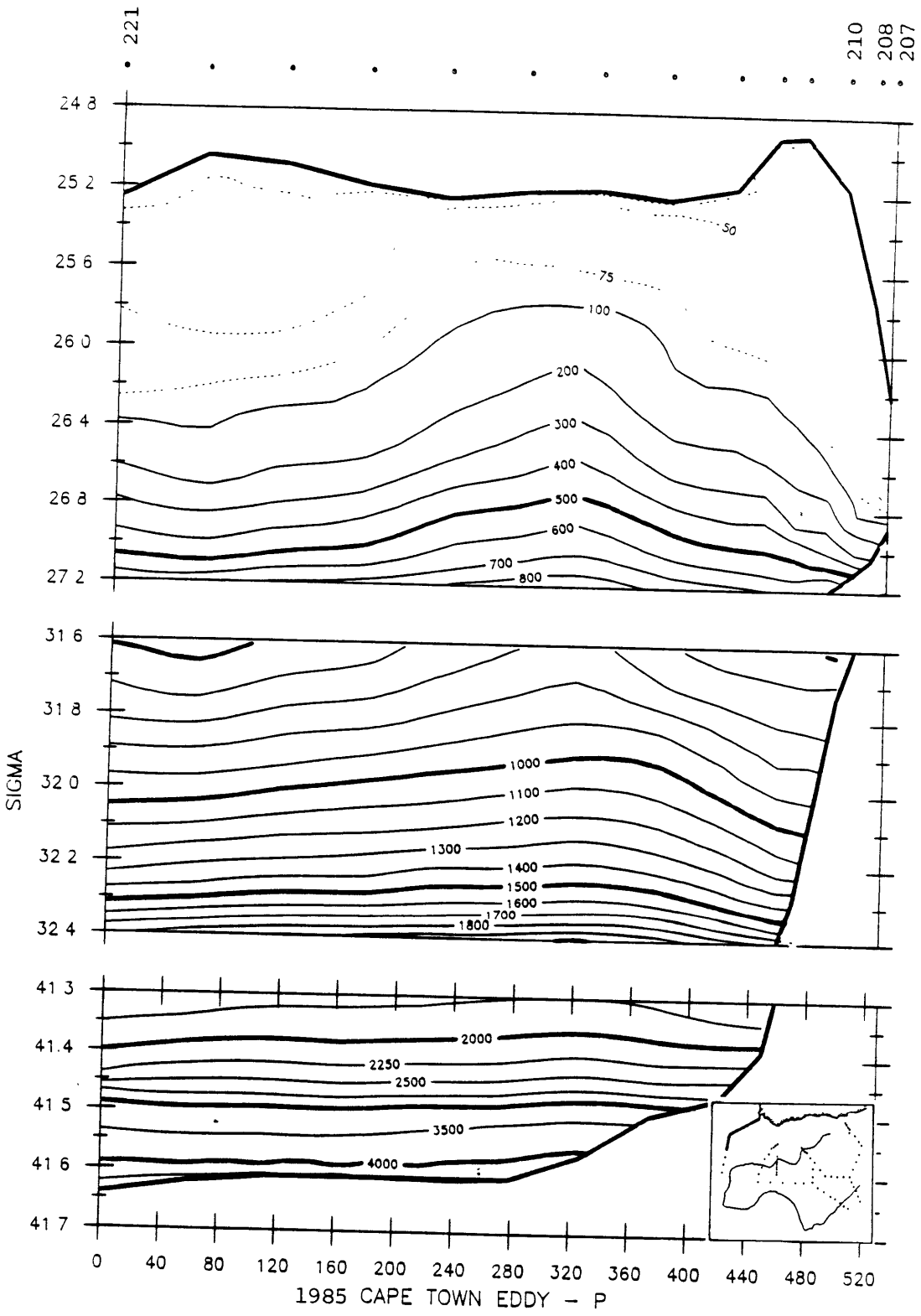
221
210
208
207
24 8
25 2
25 6
26 0
26 4
26 8
27 2
50
75
100
200
300
400
500
600
700
800
31 6
31 8
32 0
32 2
32 4
SIGMA
1000
1100
1200
1300
1400
1500
1600
1700
1800
41 3
41.4
41 5
41 6
41 7
2000
2250
2500
3500
4000
0
40
80
120
160
200
240
280
320
360
400
440
480
520
1985 CAPE TOWN EDDY – P

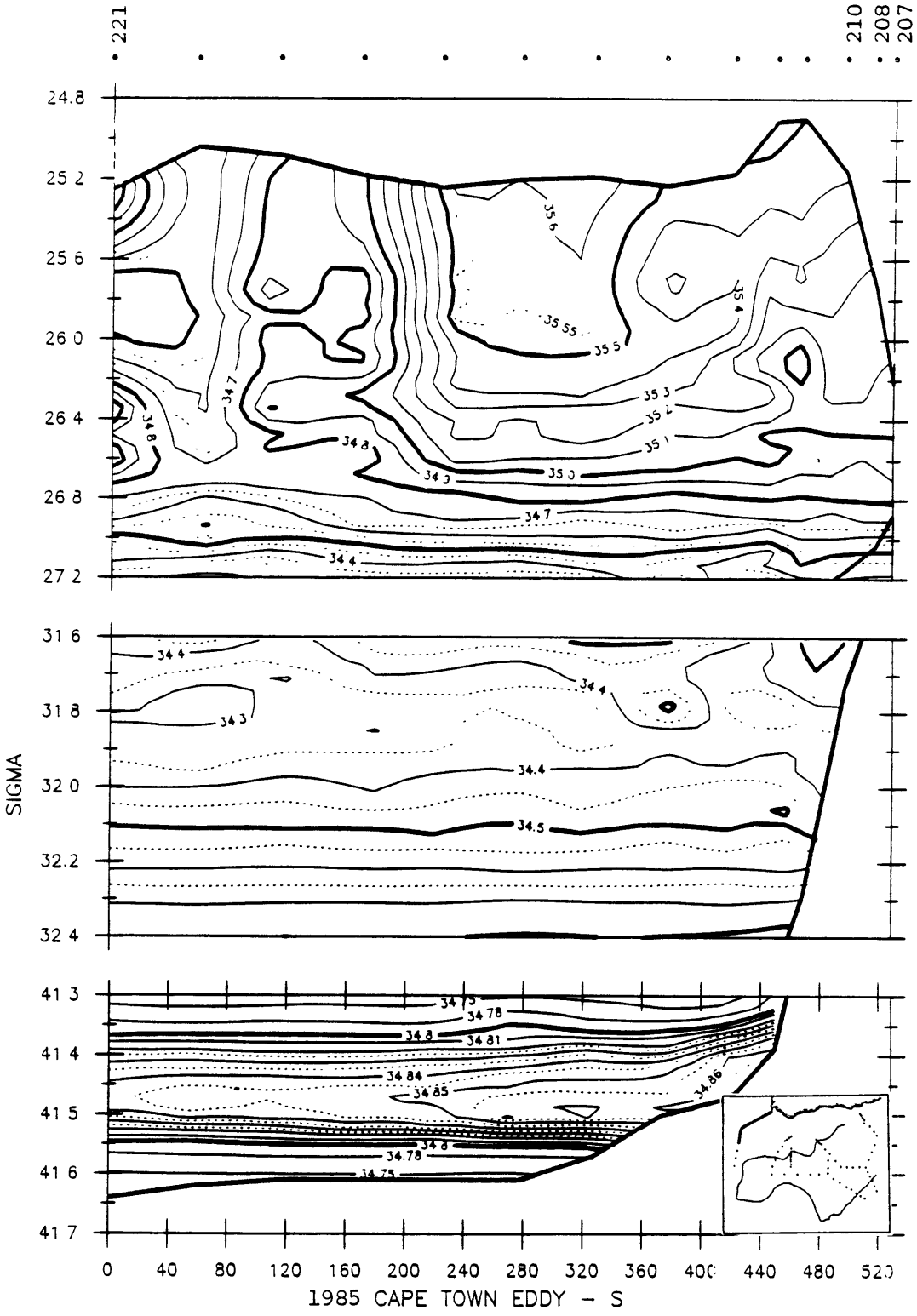
221
210
208
207
24.8
25 2
25 6
26 0
26 4
26 8
27 2
35 6
35 55
35 5
35 4
35 3
35 2
35 1
35 0
34 8
34 7
34 6
34 5
34 4
34 3
31 6
31 8
32 0
32.2
32 4
34.4
34.5
41 3
41 4
41 5
41 6
41 7
34 75
34 78
34 8
34 81
34 84
34 85
34.86
34.78
34.75
SIGMA
0
40
80
120
160
200
240
280
320
360
400
440
480
520
1985 CAPE TOWN EDDY – S

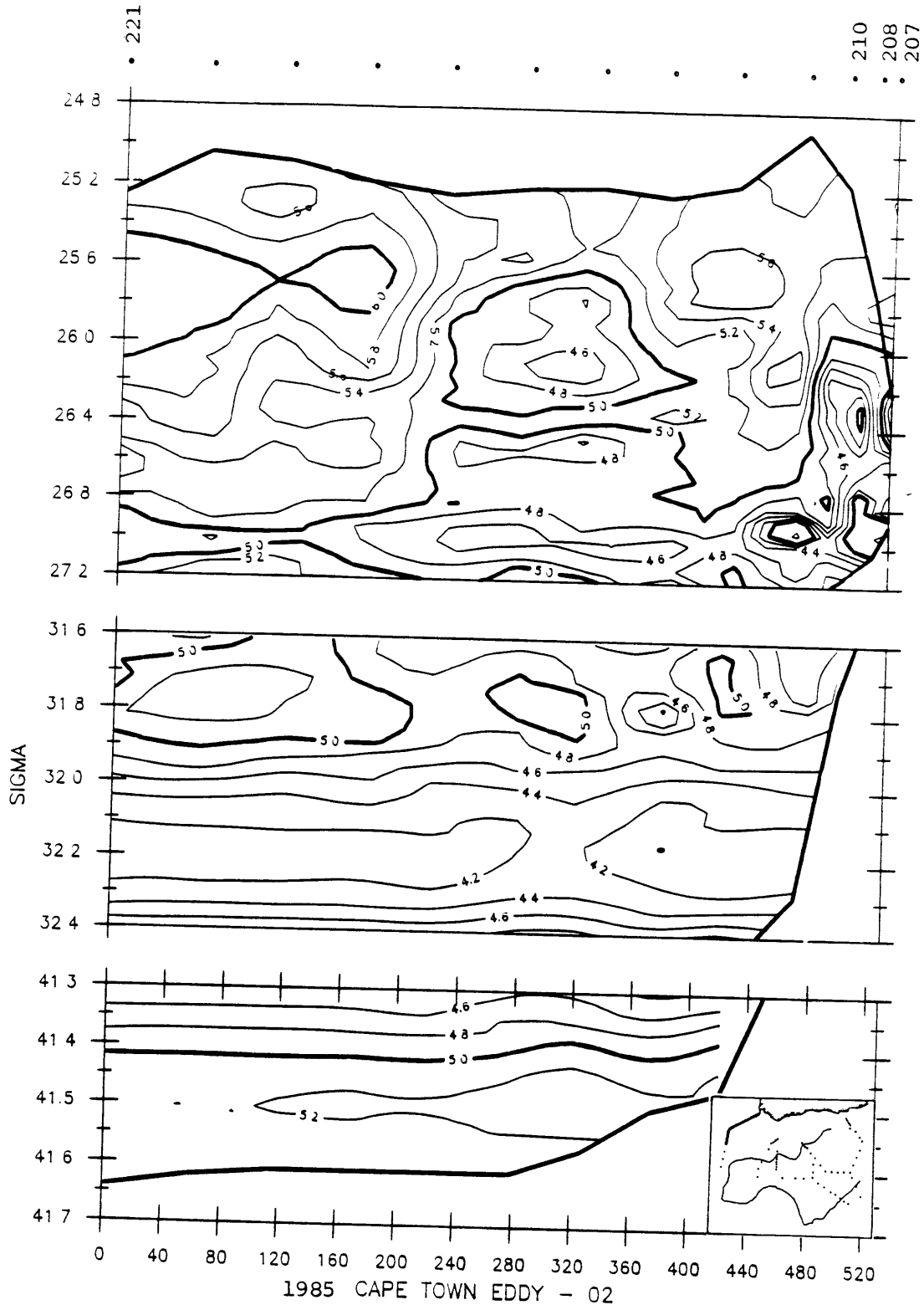
221
210
208
207
24 8
25 2
25 6
26 0
26 4
26 8
27 2
31 6
31 8
32 0
32 2
32 4
SIGMA
41 3
41 4
41.5
41 6
41 7
0
40
80
120
160
200
240
280
320
360
400
440
480
520
1985 CAPE TOWN EDDY – 02

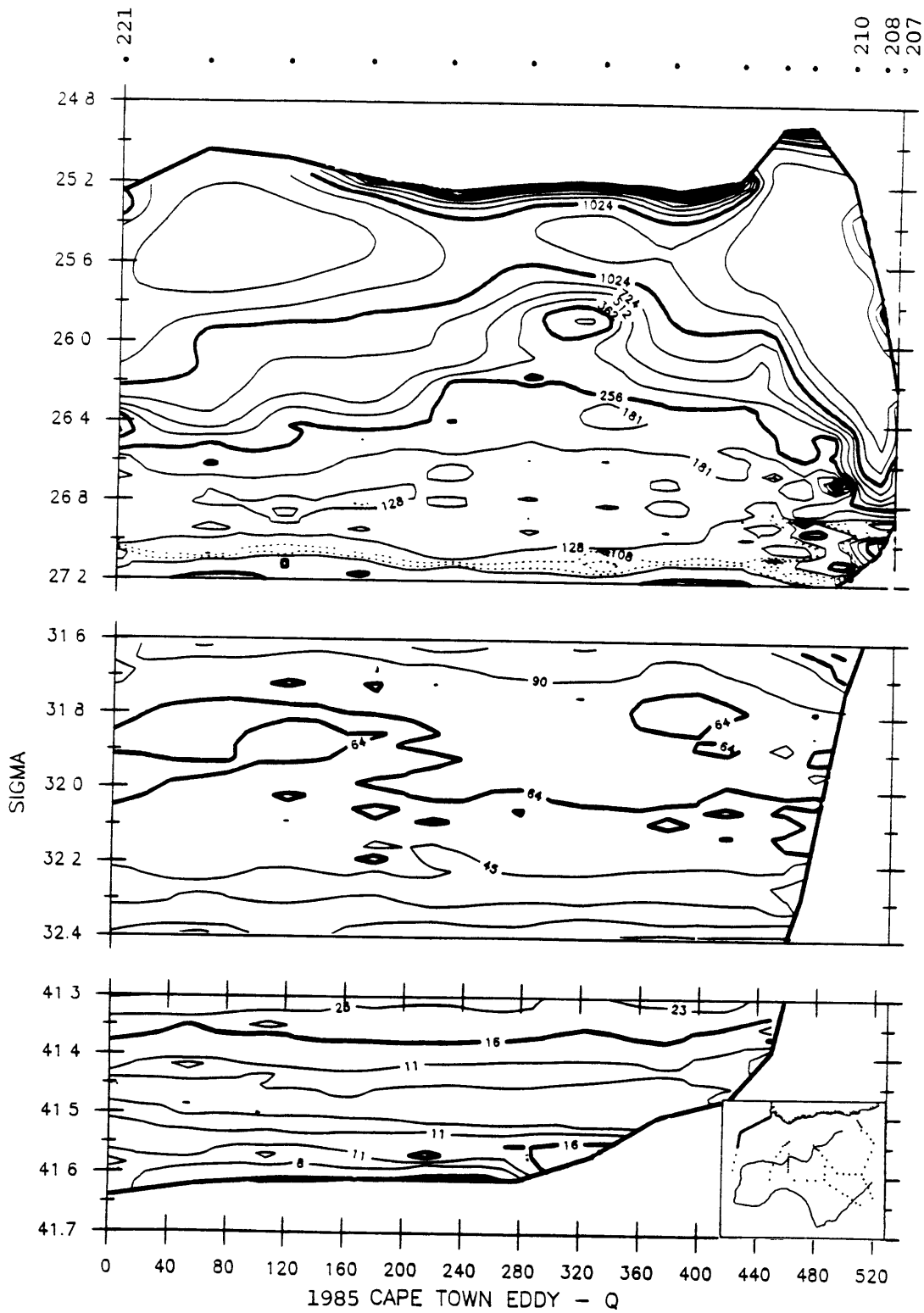
221
210
208
207
24 8
25 2
25 6
26 0
26 4
26 8
27 2
1024
1024
524
256
181
181
128
128
108
0
31 6
31 8
32 0
32 2
32.4
90
64
64
64
64
45
SIGMA
41 3
41 4
41 5
41 6
41.7
25
23
16
11
11
11
16
8
0
40
80
120
160
200
240
280
320
360
400
440
480
520
1985 CAPE TOWN EDDY – Q

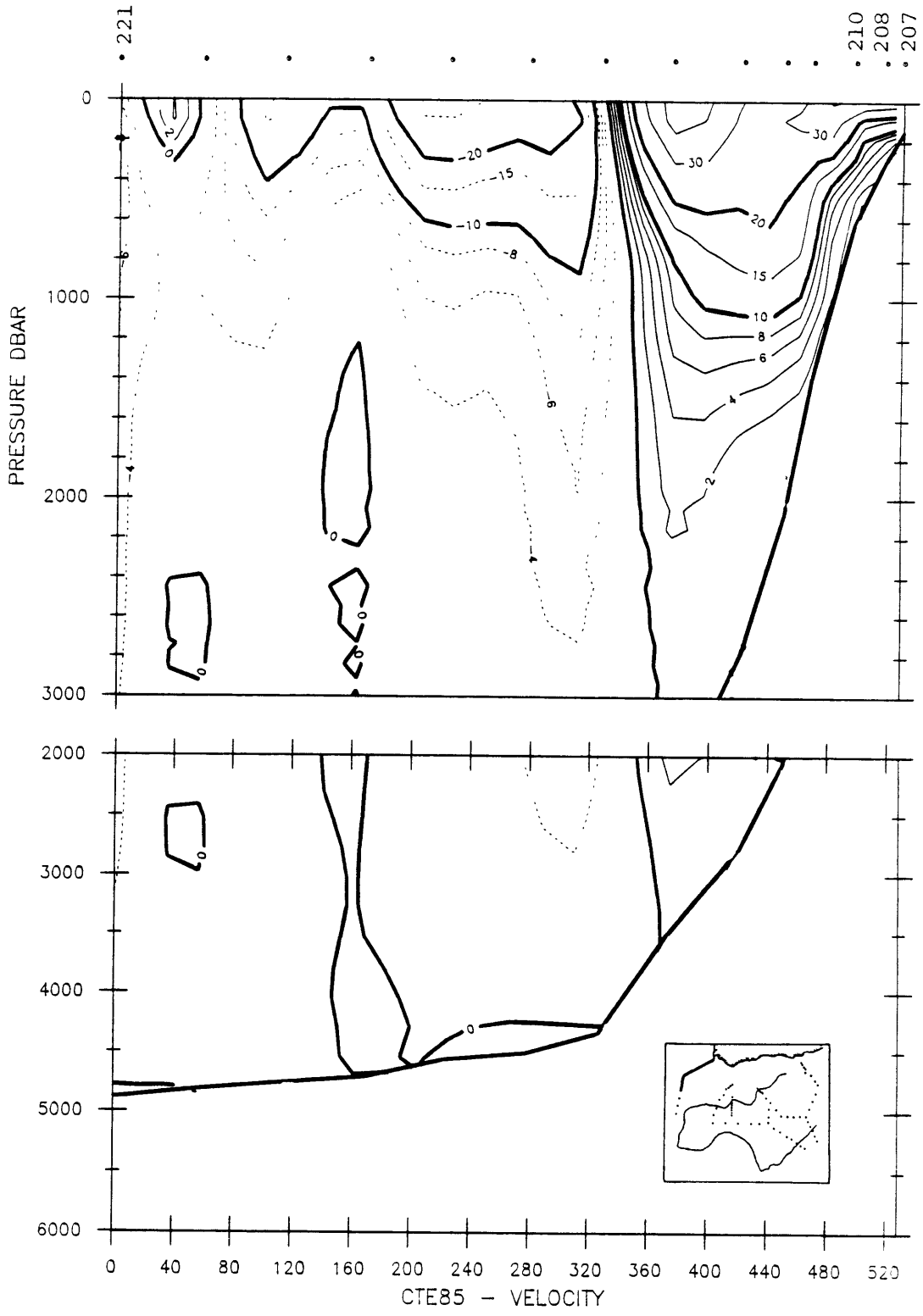
221
210
208
207
PRESSURE DBAR
0
1000
2000
3000
4000
5000
6000
0
40
80
120
160
200
240
280
320
360
400
440
480
520
CTE85 – VELOCITY

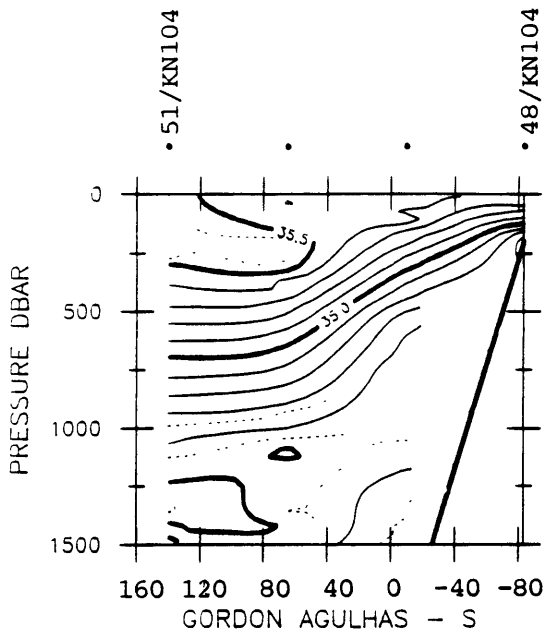
• 51/KN104
• 48/KN104
PRESSURE DBAR
0
500
1000
1500
35.5
35.0
160 120 80 40 0 -40 -80
GORDON AGULHAS – S

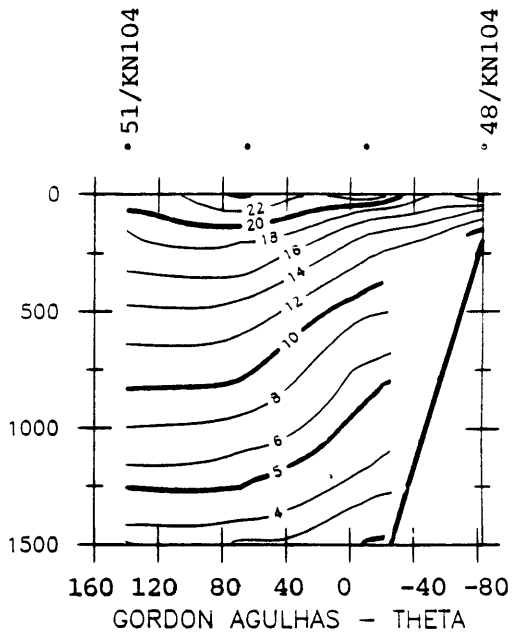
• 51/KN104
• 48/KN104
0
500
1000
1500
22
20
18
16
14
12
10
8
6
5
4
160 120 80 40 0 -40 -80
GORDON AGULHAS – THETA

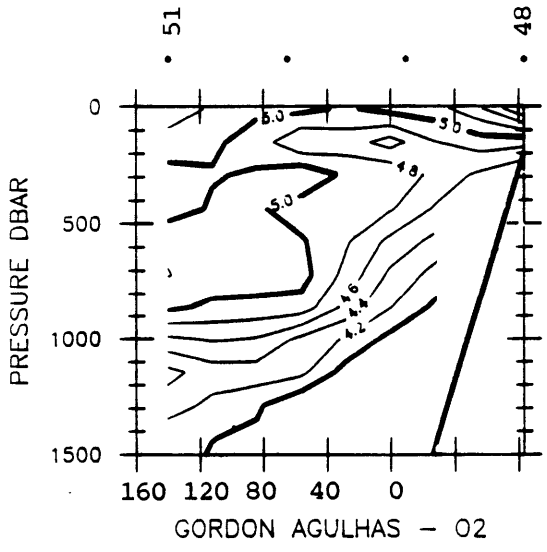
• 51
• 48
PRESSURE DBAR
0
500
1000
1500
5.0
4.8
4.6
4.4
4.2
160 120 80 40 0
GORDON AGULHAS – O2

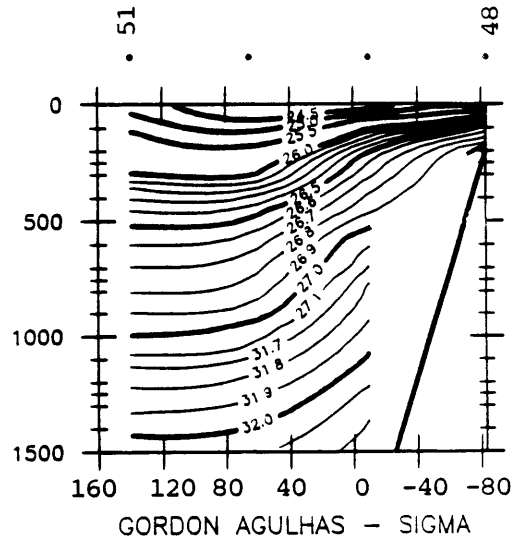
• 51
• 48
0
500
1000
1500
26.0
27.0
27.1
31.7
31.8
31.9
32.0
160 120 80 40 0 -40 -80
GORDON AGULHAS – SIGMA

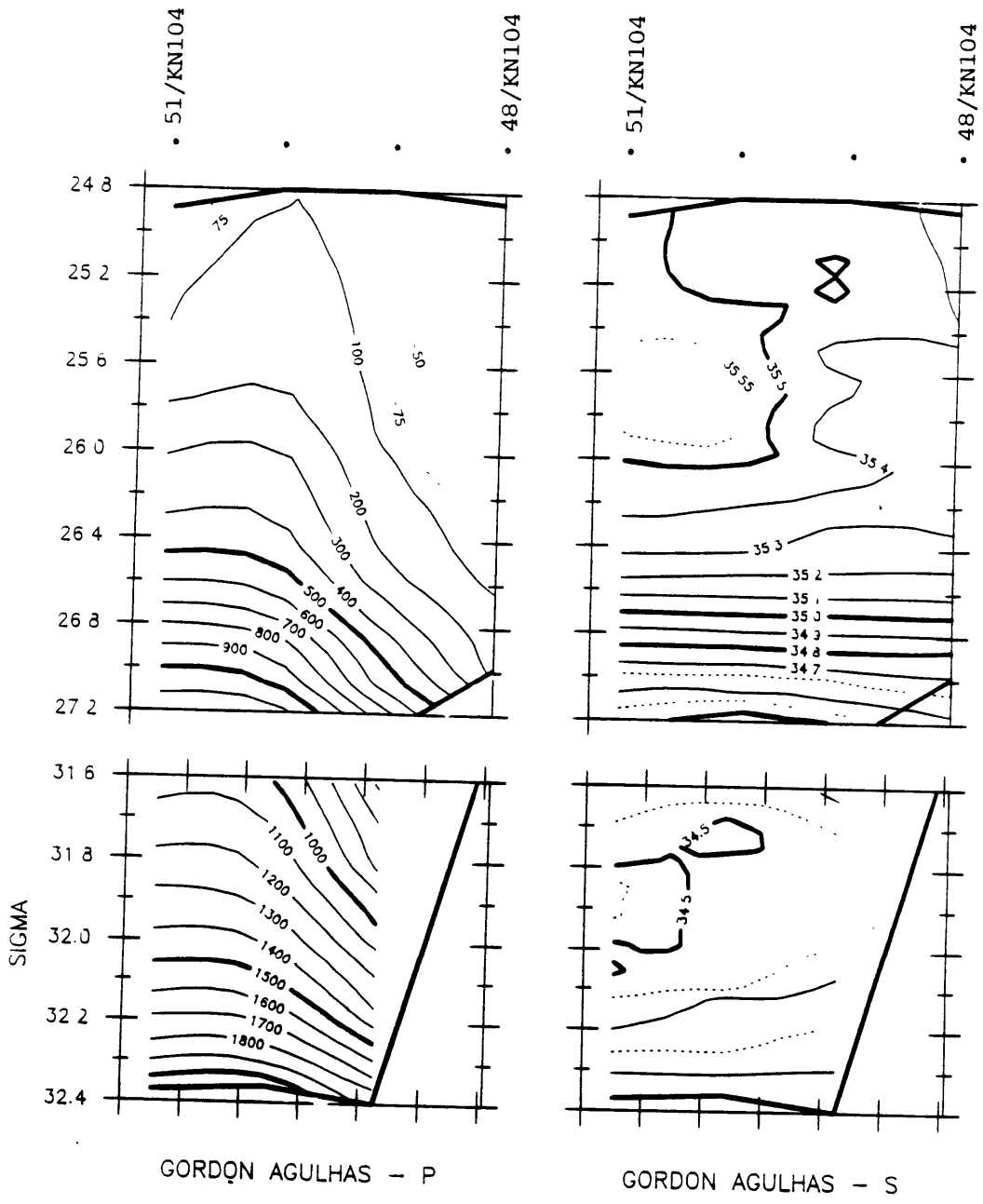
• 51/KN104
• 48/KN104
• 51/KN104
• 48/KN104
24 8
25 2
25 6
26 0
26 4
26 8
27 2
31 6
31 8
32.0
32 2
32.4
SIGMA
75
100
50
75
200
300
500
400
600
700
800
900
1100
1000
1200
1300
1400
1500
1600
1700
1800
35 5
35 55
35 4
35 3
35 2
35 1
35 0
34 9
34 8
34 7
34.5
34 5
GORDON AGULHAS – P
GORDON AGULHAS – S

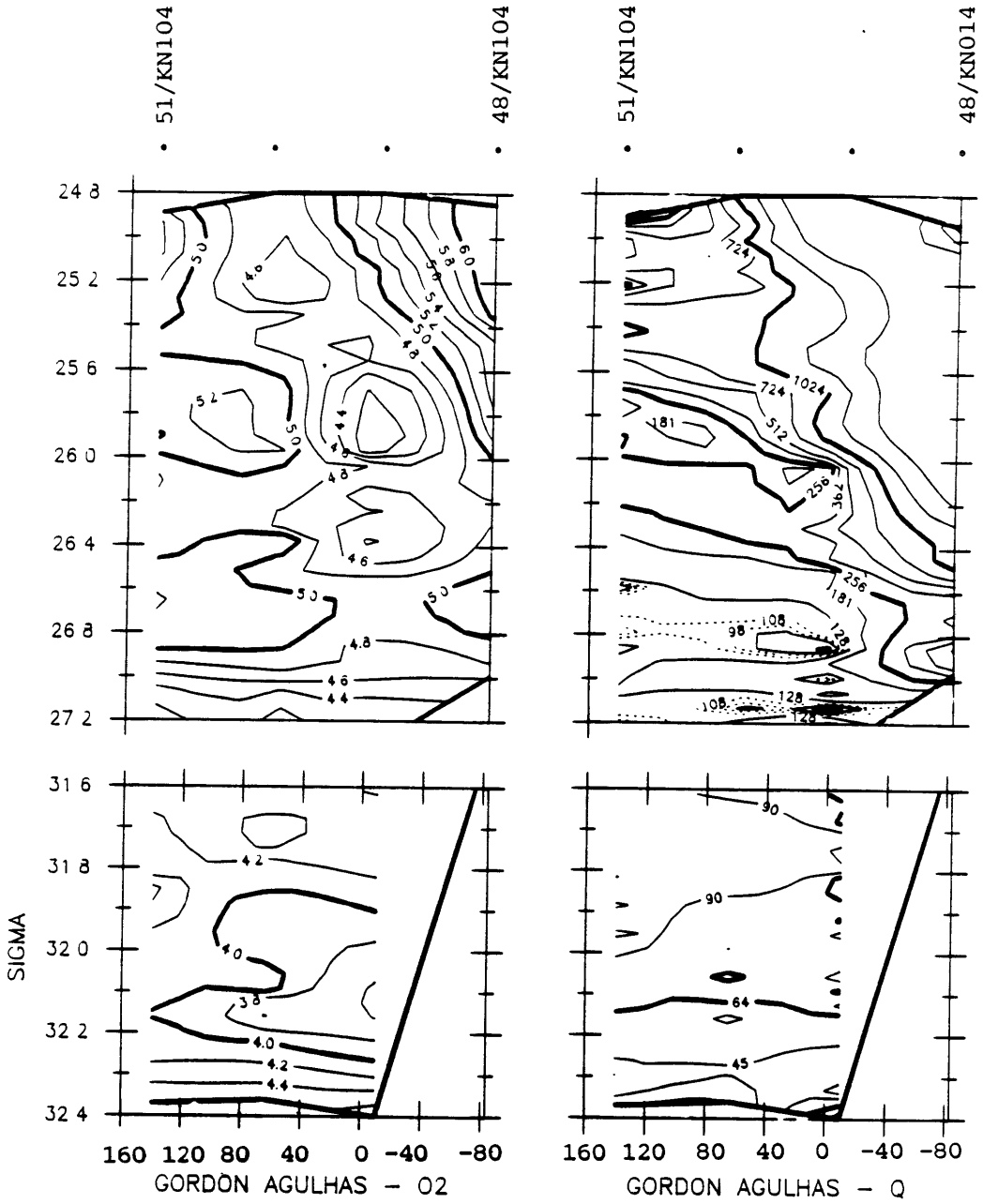
51/KN104
48/KN104
51/KN104
48/KN014
24 8
25 2
25 6
26 0
26 4
26 8
27 2
31 6
31 8
32 0
32 2
32 4
SIGMA
160 120 80 40 0 -40 -80
GORDON AGULHAS - O2
160 120 80 40 0 -40 -80
GORDON AGULHAS - Q

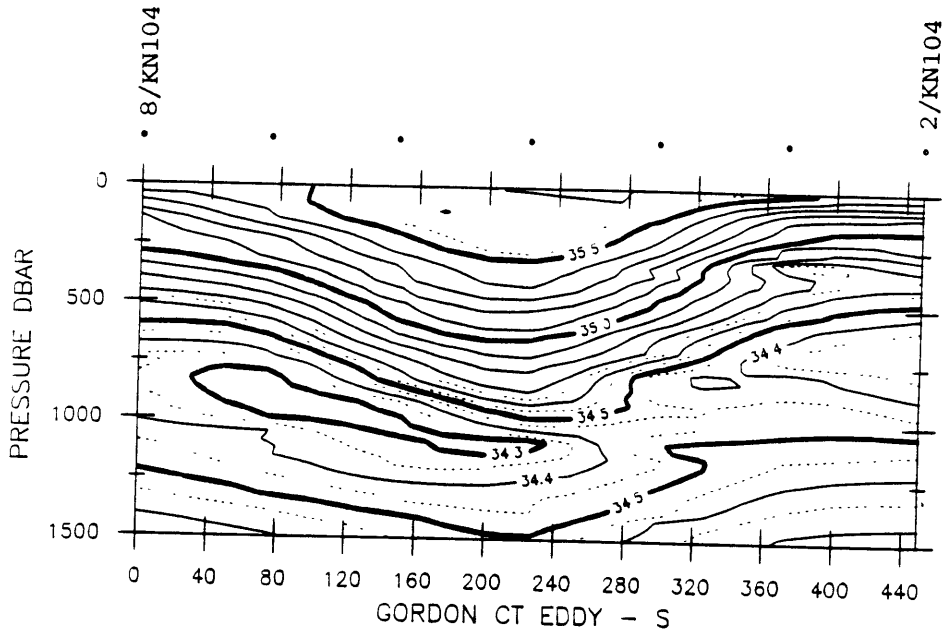
8/KN104
2/KN104
PRESSURE DBAR
0
500
1000
1500
35.5
35.0
34.4
34.5
34.3
34.4
34.5
0
40
80
120
160
200
240
280
320
360
400
440
GORDON CT EDDY – S

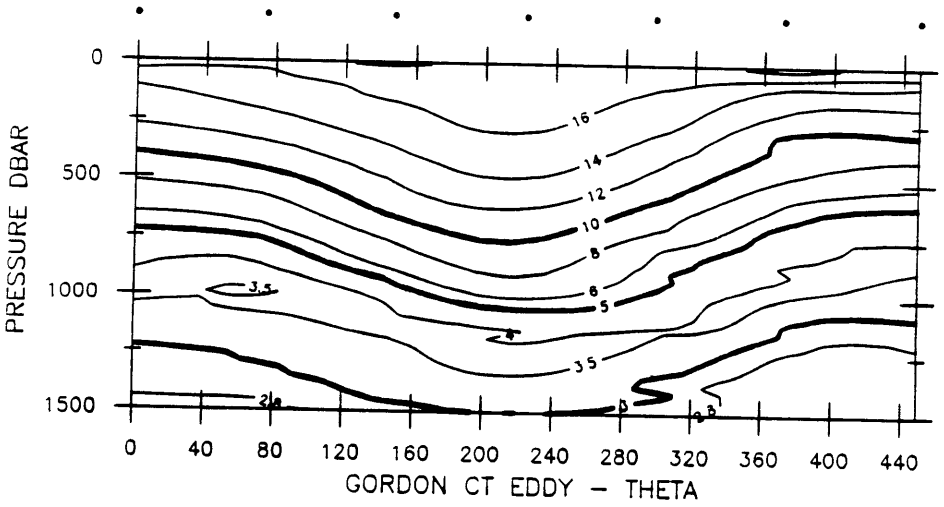
PRESSURE DBAR
0
500
1000
1500
16
14
12
10
8
6
5
4
3.5
3.5
0
40
80
120
160
200
240
280
320
360
400
440
GORDON CT EDDY – THETA

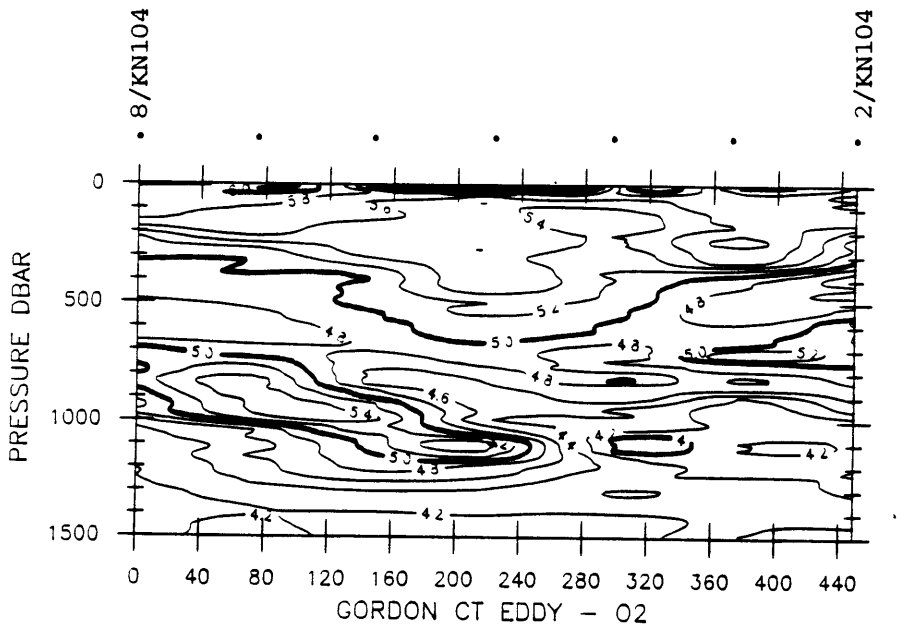
8/KN104
2/KN104
PRESSURE DBAR
0
500
1000
1500
0 40 80 120 160 200 240 280 320 360 400 440
GORDON CT EDDY – O2

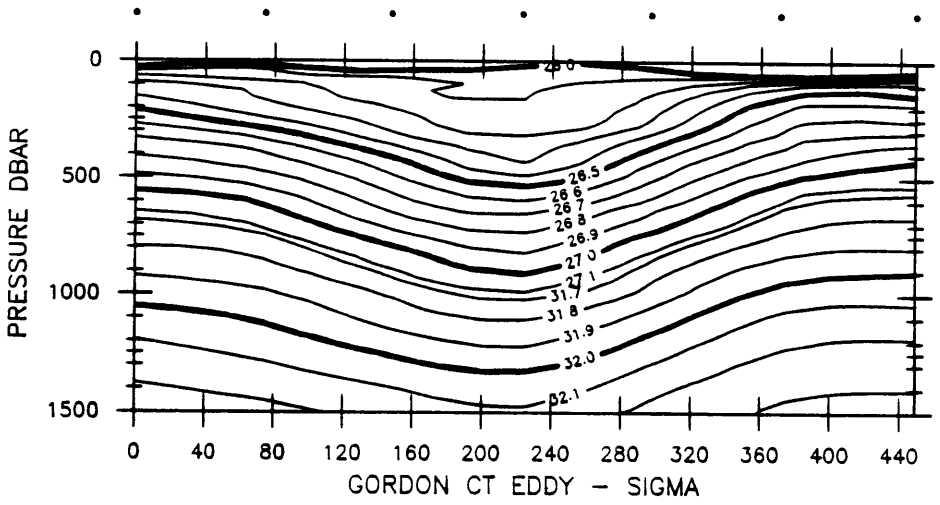
PRESSURE DBAR
0
500
1000
1500
26.5
26.6
26.7
26.8
26.9
27.0
27.1
31.7
31.8
31.9
32.0
32.1
0 40 80 120 160 200 240 280 320 360 400 440
GORDON CT EDDY – SIGMA

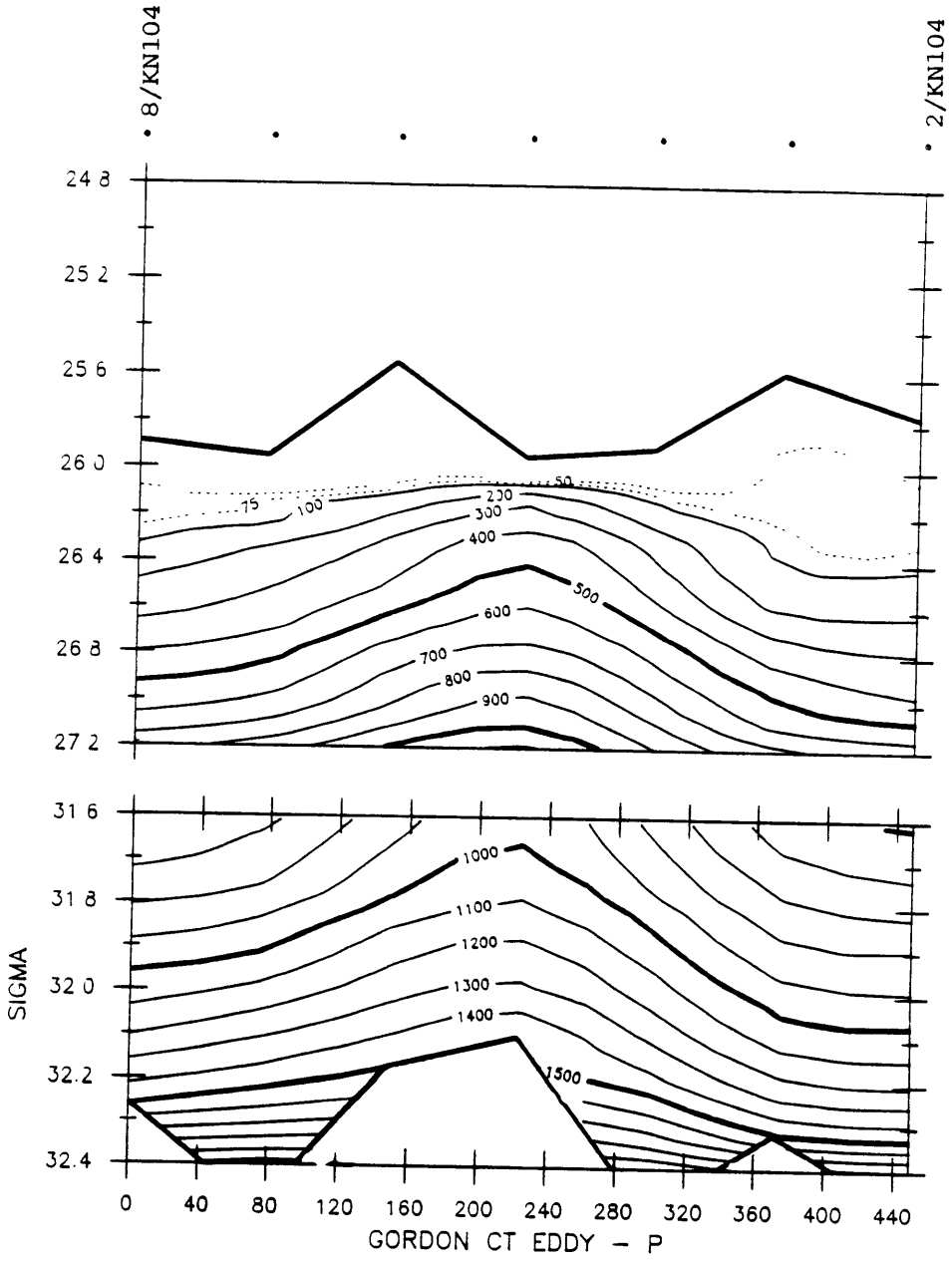
8/KN104
2/KN104
24 8
25 2
25 6
26 0
26 4
26 8
27 2
31 6
31 8
32 0
32.2
32.4
SIGMA
50
75
100
200
300
400
500
600
700
800
900
1000
1100
1200
1300
1400
1500
0
40
80
120
160
200
240
280
320
360
400
440
GORDON CT EDDY – P

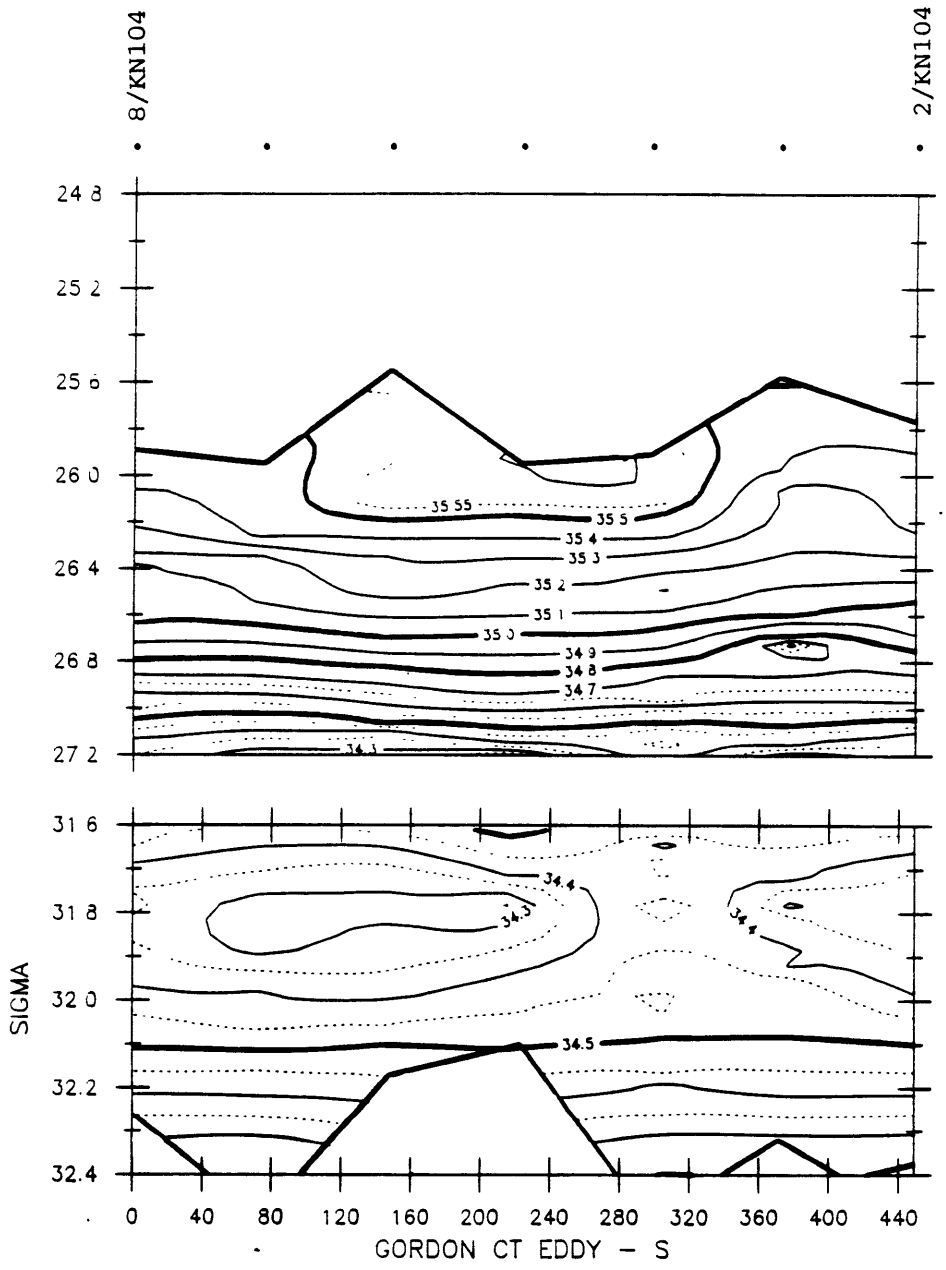
8/KN104
2/KN104
24 8
25 2
25 6
26 0
26 4
26 8
27 2
35 55
35 5
35 4
35 3
35 2
35 1
35 0
34 9
34 8
34 7
34.4
34.5
31 6
31 8
32 0
32.2
32.4
SIGMA
0
40
80
120
160
200
240
280
320
360
400
440
GORDON CT EDDY – S

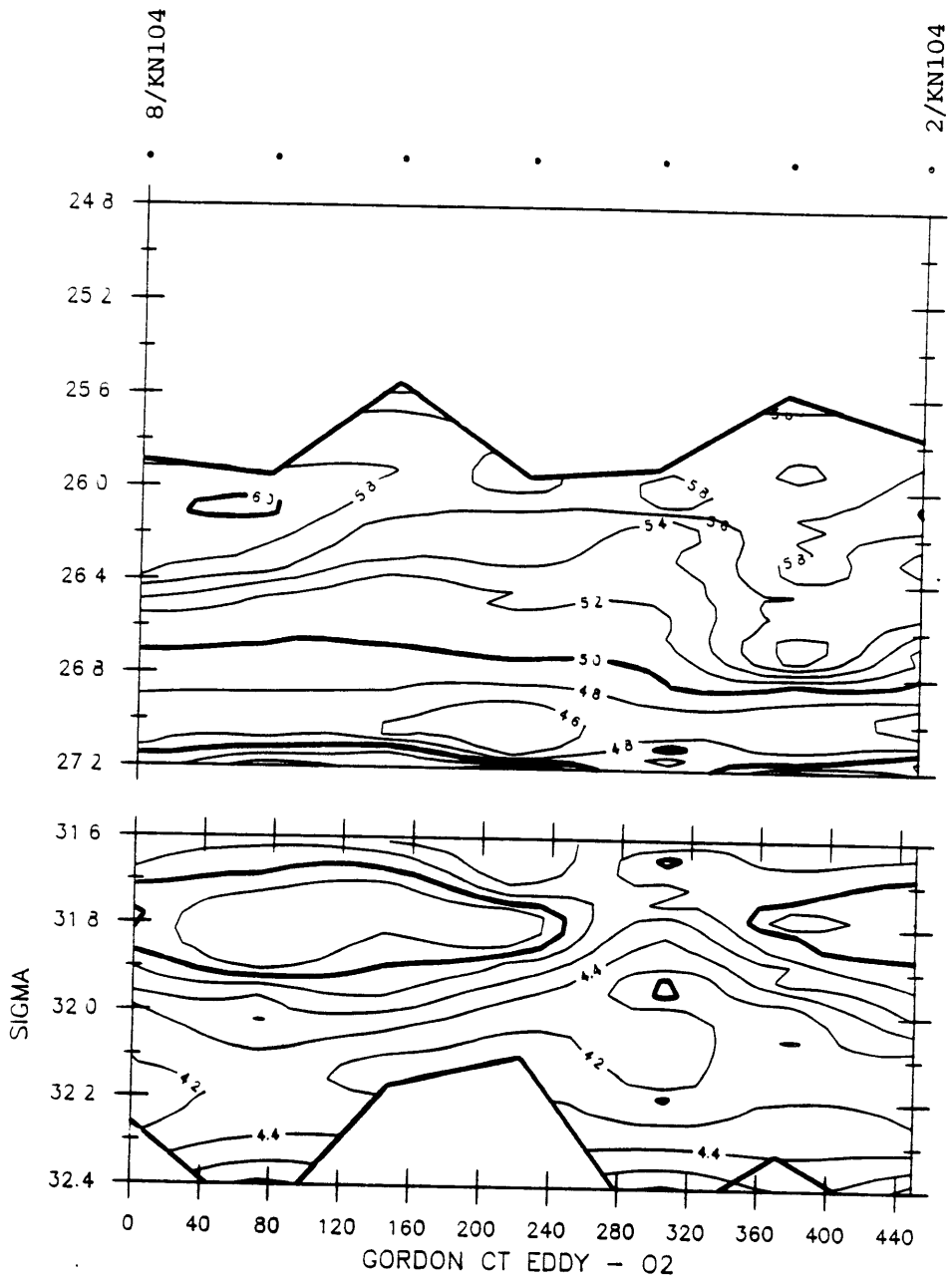
8/KN104
2/KN104
24.8
25.2
25.6
26.0
26.4
26.8
27.2
31.6
31.8
32.0
32.2
32.4
SIGMA
0
40
80
120
160
200
240
280
320
360
400
440
GORDON CT EDDY - 02

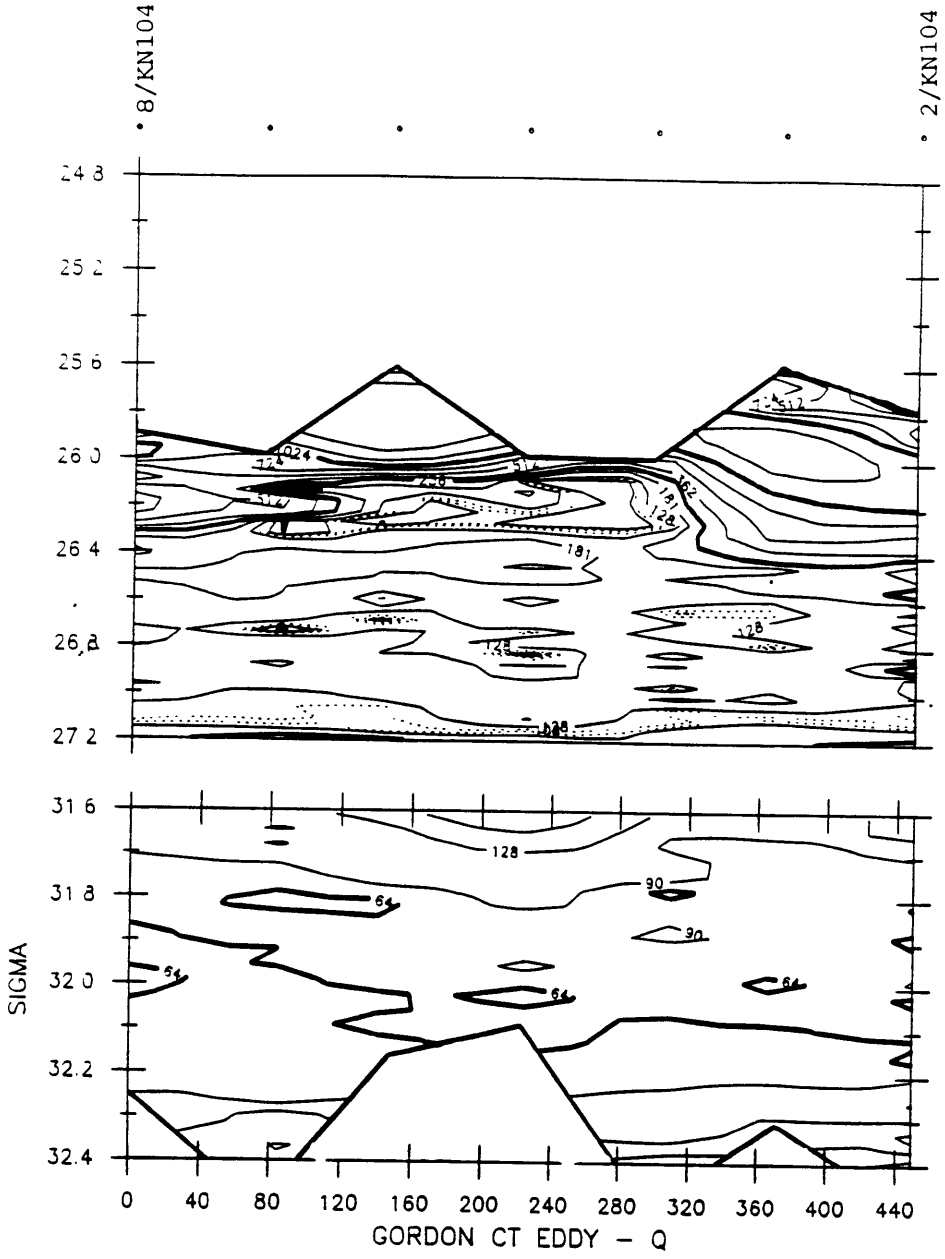
8/KN104
2/KN104
24.8
25.2
25.6
26.0
26.4
26.8
27.2
31.6
31.8
32.0
32.2
32.4
SIGMA
0
40
80
120
160
200
240
280
320
360
400
440
GORDON CT EDDY – Q

Appendix A: Potential vorticity in isopycnal natural coordinates

Definition of total potential vorticity. The definition of q is *(Ertel, 1942)*:

$$q = \frac{1}{\rho}(2\underset{\sim}{\Omega} + \underset{\sim}{\zeta}) \cdot \nabla\sigma \qquad \text{(A.1)}$$

with the potential density σ marking the separation of material surfaces, as in Eq. (A.2). Eq. (A.1) can be rewritten without approximation as

$$\rho q = \{ \underset{(a)}{2\Omega \sin(\theta + \phi)} + \underset{(b)}{\zeta_{(x)} \sin\varphi} + \underset{(c)}{\zeta_{(y)} \sin\phi} + \underset{(d)}{\zeta_{(z)} (\cos\phi \cos\varphi)} \} \, |\nabla\sigma| \qquad \text{(A.2)}$$

where $\underset{\sim}{\Omega}$ and Ω are the earth's rotation vector and rate, θ is the latitude, (φ, ϕ) are the (x, y) angles of tilt of isopycnals. $\underset{\sim}{\zeta}$ is the relative vorticity vector $\nabla \times \boldsymbol{u}$ and $\zeta_{(x,y,z)}$ its Cartesian components, and $|\nabla\sigma|$ is the magnitude of the potential density gradient vector.[1]

Simplification. Isopycnals tilt no more than 0.6° (0.01 rad) in the Agulhas, descending $\Delta h = 10^3$ m over a horizontal distance of $L = 10^5$ m. This allows the approximations:

$$\begin{aligned} &\sin(\varphi, \phi) \sim (\varphi, \phi) \\ &\cos(\varphi, \phi) \sim 1 \\ &|\nabla\sigma| = \frac{\partial\sigma}{\partial z} \sqrt{[\sin^2\varphi + \sin^2\phi + \cos^2\varphi \cos^2\phi]} \sim \frac{\partial\sigma}{\partial z} \end{aligned} \qquad \text{(A.3)}$$

Also, the variation of planetary vorticity with latitudinal isopycnal tilt ϕ, which appears in the term $2\Omega \sin(\theta + \phi)$, may be neglected since $\sin(\theta + \phi)$ and

[1]A discussion of the role of potential density reference pressure in potential vorticity calculations is given in Appendix B.

sin θ differ by only 0.01 *sin* θ, if isopycnals tilt $\phi = 0.01$ rad at a latitude of $\theta = 35°$.

The potential vorticity expression of Eq. (A.2) becomes, with these approximations:

$$\rho q \sim \underset{(a)}{\{ 2\Omega (\sin\theta)} + \underset{(b)}{\varphi \zeta_{(x)}} + \underset{(c)}{\phi \zeta_{(y)}} + \underset{(d)}{\zeta_{(z)}} \} \frac{\partial \sigma}{\partial z} \tag{A.4}$$

Horizontal vs. vertical components of relative vorticity. The potential vorticity terms due to the horizontal and vertical components of relative vorticity[2] have the scales:

$$\begin{aligned} \varphi\zeta_{(x)}, \phi\zeta_{(y)} \quad &\sim \quad \varphi \frac{\partial v}{\partial z}, \phi \frac{\partial u}{\partial z} \quad \sim \quad \frac{\varphi U}{H} \\ \zeta_{(z)} \quad &\sim \quad \frac{\partial v}{\partial x} - \frac{\partial u}{\partial y} \quad \sim \quad \frac{U}{L} \end{aligned} \tag{A.5}$$

where H and L are the vertical and horizontal length scales of velocity variation. It is assumed that the scales of (x, y) variation are similar over the course of the retroflecting path. Notice that the vertical component of the relative vorticity itself is much smaller than the horizontal component, since $\frac{U}{L} << \frac{U}{H}$. Relative vorticity terms due to the curl of the vertical velocity, $\nabla \times w$ have been neglected under the assumption that $\frac{\partial w}{\partial(x,y)} << \frac{\partial(u,v)}{\partial(x,y)}$.

---

[2]The horizontal component of the relative vorticity vector, $\zeta_{(x,y)}$, also called vertical shear vorticity, is due to vertical shear of velocity $\frac{\partial(u,v)}{\partial z}$. The vertical component of the relative vorticity vector, $\zeta_{(z)}$, also called horizontal shear vorticity, is due to horizontal shear of velocity, $\frac{\partial v}{\partial x} - \frac{\partial u}{\partial y}$.

The ratio of the potential vorticity terms due to horizontal and vertical relative vorticity is:

$$\frac{(\phi, \varphi)\zeta_{(x,y)}}{\zeta_{(z)}} \sim \frac{\phi L}{H} \sim \frac{\Delta h}{H} \qquad \text{(A.6)}$$

The value of this ratio for the Agulhas at the 1985 transects is roughly one, since depth variation on an isopycnal is at most Δh ~700 m, similar to the depth H over which velocity varies. Notice that the horizontal vorticity $|\hat{i}\,\frac{\partial v}{\partial z} - \hat{j}\,\frac{\partial u}{\partial z}|$ itself is much larger in magnitude than the vertical vorticity $|\frac{\partial v}{\partial x} - \frac{\partial u}{\partial y}|$.

Isopycnal vs. isotach slopes. The ratio of the potential vorticity terms due to horizontal and vertical relative vorticity can, in fact, be estimated by eye directly from velocity and potential density [*i.e.*, λ, see Eq. (A.2)] sections, since:

$$\frac{\Delta h}{H} = \frac{tan\,(\phi, \varphi)}{tan\,\gamma} \sim \frac{(\phi, \varphi)}{\gamma} \qquad \text{(A.7)}$$

where $\frac{\Delta h}{L} = tan\,(\phi, \varphi)$ and $\frac{H}{L} = tan\,\gamma$, with γ the off-horizontal angle of isotachs.[3] The approximations noted in Eq. (A.3) imply $tan\,\gamma \sim \gamma$. Maximum isopycnal tilt is only slightly less than maximum isotach tilt in the Agulhas, as can be seen in the Atlas contoured sections. Note that maximum isotach tilts are observed in the shoulders of the jet, particularly the cyclonic shoulder, offset from the maximum isopycnal tilts observed in the jet's velocity maximum core.

[3]Isopleths of velocity.

Scaling. The simplified potential vorticity expression, Eq. (A.4), can be scaled in the usual way. First, the relationship between the isopycnal tilts (ϕ, φ) and the scales U, N^2, f, L, and H is determined by the thermal wind balance:

$$[\phi, \varphi] \sim \frac{fU}{N^2 H} \sim \varepsilon S^{-1} \delta \tag{A.8}$$

where $\delta = \frac{H}{L}$.

Then the potential vorticity expression Eq. (A.4) scales as follows:

$$\rho q \sim \quad f \frac{\partial \sigma}{\partial z} \quad + \quad [\varphi \zeta_{(x)} + \phi \zeta_{(y)}] \frac{\partial \sigma}{\partial z} \quad + \quad \zeta_{(z)} \frac{\partial \sigma}{\partial z} \tag{A.9}$$

$$\downarrow \qquad\qquad \downarrow \qquad\qquad \downarrow$$

$$\frac{f\rho N^2}{g} \qquad \frac{f\rho U^2}{gH^2} \qquad \frac{U\rho N^2}{Lg}$$

$$\downarrow \qquad\qquad \downarrow \qquad\qquad \downarrow$$

$$\frac{f\rho N^2}{g} \left\{ \quad 1 \quad \right. \qquad \frac{U^2}{N^2 H^2} \qquad \frac{U}{fL} \quad \left. \right\}$$

$$\downarrow \qquad\qquad \downarrow \qquad\qquad \downarrow$$

$$\frac{f\rho N^2}{g} \left\{ \quad 1 \quad \right. \qquad \frac{\varepsilon^2}{S} \qquad \varepsilon \quad \left. \right\}$$

$$(a) \qquad\qquad (b, c) \qquad\qquad (d)$$

where S is the Burger number, $\frac{N^2 H^2}{f^2 L^2}$, ε is the Rossby number, $\frac{U}{fL}$, and N is the Brunt-Väisälä or buoyancy frequency $\sqrt{\frac{g \partial \rho}{\rho \partial z}}$.[4] The ratio of isopycnal and isotach slopes is just

$$\frac{\Delta h}{H} \sim \frac{(\phi, \varphi)}{\lambda} \sim \varepsilon S^{-1} \tag{A.10}$$

---

[4]The Richardson number is given by a combination of these scales, $Ri \sim \frac{N^2 H^2}{U^2} \sim S\varepsilon^{-2}$. The horizontal vorticity scale is thus Ri^{-1} as compared to the planetary vorticity *(J. Zemba, unpubl. man.; Garrett, 1982)*.

Transformation of simplified potential vorticity equation into natural coordinates. The potential vorticity may be transformed into terms that depend only on the physical state of the jet, not its *(x, y)* orientation, by transforming into along- and across-stream natural coordinates.

Let *(s, n)* represent the along- and across-stream coordinates and $(\hat{s}, \hat{n})$ the unit vectors. Then

$$
\begin{aligned}
u &= v'(x, y, z)\,\hat{s}(x, y, z) \\
\zeta &= v' \nabla \times \hat{s} + \nabla v' \times \hat{s} \qquad \text{(A.11)} \\
&= \hat{i}\left[v'\left(\frac{\partial s_{(z)}}{\partial y} - \frac{\partial s_{(y)}}{\partial z}\right) + s_{(z)}\frac{\partial v'}{\partial y} - s_{(y)}\frac{\partial v'}{\partial z}\right] + \\
&\quad \hat{j}\left[v'\left(\frac{\partial s_{(x)}}{\partial z} - \frac{\partial s_{(z)}}{\partial x}\right) + s_{(x)}\frac{\partial v'}{\partial z} - s_{(z)}\frac{\partial v'}{\partial x}\right] + \\
&\quad \hat{k}\left[K_s v' - \frac{\partial v'}{\partial n}\right]
\end{aligned}
$$

K_s is the horizontal path curvature, defined by $\frac{\partial \hat{s}_H}{\partial s} = K_s \hat{n}$. The radius of curvature is $R_s = K_s^{-1}$. The *(x, y, z)* components of $\hat{s}$ are $(s_{(x)}, s_{(y)}, s_{(z)})$. The horizontal cross-stream velocity gradient is defined by $\hat{n}\frac{\partial v'}{\partial n} = \nabla_H v'$.

Terms due to the curl of the vertical velocity may be neglected when

$$\frac{\partial v' s_{(z)}}{\partial(x,y)} = \frac{\partial w}{\partial(x,y)} << \frac{\partial(u,v)}{\partial(x,y)} \qquad \text{(A.12)}$$

Terms due to velocity veering may be neglected when

$$\left| v' \frac{\partial s_H}{\partial z} \right| << \frac{\partial v'}{\partial z} \qquad \text{(A.13)}$$

Dropping these terms leaves

$$\zeta \sim \underset{(b,\,c)}{\left(\hat{j}\, s_{(x)} - \hat{i}\, s_{(y)}\right)} \frac{\partial v'}{\partial z} + \underset{(d)}{\hat{k}\left[K_s v' - \frac{\partial v'}{\partial n}\right]} \qquad \text{(A.14)}$$

Cross-stream isopycnal tilt angle. The horizontal and vertical relative vorticity contributions can be combined in a single physically meaningful term, by introducing the cross-stream isopycnal tilt angle υ.

First we need the relationships:

$$\hat{\mathbf{n}} \cdot \nabla\sigma = \frac{\partial\sigma}{\partial n} = |\nabla\sigma| \sin\upsilon = \hat{\mathbf{n}} \cdot (\hat{\mathbf{s}} \times \nabla\sigma) \tag{A.15}$$

$$\sim (s_{(x)}\phi - s_{(y)}\varphi)\frac{\partial\sigma}{\partial z}$$

making use of $\hat{\mathbf{s}} \times \hat{\mathbf{n}} = \hat{\mathbf{k}}$ and the fact that the vertical component of $\nabla\sigma$ is opposite in sign from $\hat{\mathbf{k}}$. Define $\frac{\partial}{\partial n'} = \frac{\partial}{\partial n}\Big|_{\sigma = \text{const.}}$. Then the cross-stream isopycnal shear can be written as

$$\frac{\partial}{\partial n'} = \frac{\partial v'}{\partial n} - \frac{\partial\sigma}{\partial n}\frac{\partial v'}{\partial\sigma}\Big|_{n = \text{const.}} = \frac{\partial v'}{\partial n} - \frac{\partial\sigma}{\partial n}\frac{\partial v'}{\partial z}\left(\frac{\partial\sigma}{\partial z}\right)^{-1} \tag{A.16}$$

$$= \frac{\partial v'}{\partial n} - (s_{(x)}\phi - s_{(y)}\varphi)\frac{\partial v'}{\partial z}$$

which can be substituted into Eqs. (A.14) and (A.4), giving

$$q \sim \left[\underset{(a)}{f} + \underset{(d)}{K_s v'} - \underset{(b,\,c,\,d)}{\frac{\partial v'}{\partial n'}} \right] \frac{\partial\sigma}{\partial z} \tag{A.17}$$

This is the isopycnal natural-coordinate form of potential vorticity, appropriate for western boundary currents if veering vorticity is negligible.

The veering vorticity component of the relative vorticity vector, which was neglected from the natural coordinate formulation (Eq. A.13 above), is also neglected here, since it contributes only through the term $v\frac{\partial \hat{s}}{\partial z}\frac{\partial \sigma}{\partial n}$, whose ratio to term *(b, c, d)* of Eq. A.17 is $v'\frac{\partial \hat{s}}{\partial z}\frac{\partial h}{\partial n}\Big/\frac{\partial v'}{\partial n'}$, where $\frac{\partial h}{\partial n}$ represents the cross-stream slope of isopycnals. Thus veering contributes only order $\frac{\partial h}{\partial n}$ (<0.01 in the ocean) to <u>potential</u> vorticity when its contribution to <u>relative</u> vorticity is as large as that of vertical shear $\left(\frac{\partial v'}{\partial z}\right)$.

Summary. Total potential vorticity may be estimated using the expression given in Eq. (A.17) in strong jets. The only neglected terms are *(i)* potential vorticity due to velocity veering, *(ii)* terms due to the curl of the vertical velocity, and *(iii)* the product of the horizontal components of the planetary vorticity vector and the potential density gradient. Along- and across-stream directions is determined by the direction of flow itself and can vary with depth.

The relative importance of potential vorticity terms due to vertical shear vorticity and horizontal shear vorticity is given by the ratio of the isotach off-horizontal angle to the isopycnal off-horizontal angle, which can be estimated from contoured sections of velocity and potential density. This ratio is equivalent to εS^{-1} in terms of the usual non-dimensional numbers ε, the Rossby number, and S, the Burger number; and εS^{-1} is just $\Delta h/H$, where is Δh the depth variation on an isopycnal and H is the depth over which the velocity varies.

Appendix B
Buoyancy potential vorticity: conservation equation and relation to neutral surface potential vorticity

Abstract

The exact conservation equation is derived for potential vorticity constructed from the three-dimensional vector analog of buoyancy frequency. The effects of saline contraction and thermal expansion pressure-dependence appear in two distinct groups of source terms. One of these groups is related to changes in stability following the flow across pressure surfaces, and the other to the helicity of neutral trajectories. The groupings clarify the physical interpretation of neutral trajectories and surfaces, and neutral surface potential vorticity.

Buoyancy potential vorticity (BPV) varies with pressure, even when salt and potential temperature are conserved following the flow. When potential temperature decreases with pressure, BPV increases by a quarter of its value for warm water displaced from the surface to thermocline depth, and by a third for cold water displaced over the full water depth. These values are equivalent to a single contour interval on potential vorticity maps and sections appearing in the literature. Displacing neutrally stable water masses upward can cause convection, mixing salt and potential temperature vertically.

These BPV changes are proportional to the *non-zero* partial derivative of BPV with pressure alone and to changes in pressure following the flow. If absolute vorticity can be estimated, as is the case when relative vorticity is negligible, the derivative is a well-defined scalar function of the salinity, temperature, and pressure fields in the fluid.

BPV also varies along a trajectory by an amount proportional to the turning of isopycnals with pressure in salinity/potential temperature/pressure coordinates and the neutral part of potential temperature changes. It increases by 4×10^{-12} m^{-1} s^{-1} K^{-1} for cold water (1 C) where the isopycnal turning is greatest. This can be as large as changes from BVP pressure-dependence in weakly stratified water, but is an order of magnitude smaller than pressure-dependent changes in well-stratified water. The slight rectification (helicity) of neutral trajectories also results from the turning of isopycnals.

Gradients of changes following the flow in locally-referenced potential density also alter BPV, just as gradients of changes following the flow in a scalar λ alter Ertel's potential vorticity constructed from gradients of λ. Changes following the flow in locally-referenced potential density also alter BPV through the variation of isopycnal spacing with pressure in salinity/potential temperature/pressure coordinates.

A differential expression for neutral surface potential vorticity is derived from the BPV conservation equation.

B.1 Introduction

The non-linearities of the equation of state of seawater are a source of uncertainty for general circulation oceanographers. These non-linearities complicate the mapping of surfaces on which buoyancy restoring forces vanish and eddy stirring is presumably at a maximum. Constant potential density surfaces approximate these surfaces fairly well above the thermocline, where height variations on surfaces are relatively small [O(500 m)]; but in the global thermohaline circulation, where height variations approach the full water depth [O(5000 m)], potential density referenced to a single reference pressure is nearly useless. Several (often three) reference pressures are used in much of the later classical literature *(e.g., Lynn and Reid, 1971)* in an attempt to deal with this problem. Some recent investigations use many reference pressures separated by only hundreds of meters: the density field itself dictates the exact reference pressure for each isopycnal in *Armi and Stommel's (1983)* work, while descending isopycnals 'handshake' from one predetermined constant reference pressure to the next in *Rintoul's (1988)* inverse models. *Ivers (1975), Shepherd (1979), McDougall (1984)*, and *McDougall and Jackett (1988)* developed an even more sophisticated approach, finding 'neutral trajectories' between a parcel at one hydrographic station and its neutrally-buoyant height at the next.

The non-linearities of the equation of state also complicate potential vorticity formulation. Potential vorticity is conserved following the flow, except for friction and mixing source terms, when it is constructed such that vortex tube stretching can be accounted for independently of stretching due to thermodynamic effects. Various forms of potential vorticity that at least partially decouple the vortex and thermodynamic stretching appear in the literature: potential vorticity has been constructed from gradients of potential temperature, from gradients of potential density referenced to a constant pressure, from buoyancy frequency; and from neutral trajectories [by *Hall, 1985,*

McDowell et al., *1982*, *McCartney, 1982*, and *McDougall, 1987a, 1988*, respectively]. The physical differences between these forms received only passing mention, and quantitative differences were ignored, until *McDougall (1987a, 1988)* estimated that potential vorticity formed from buoyancy frequency can double or triple over a pressure change of 1500 dbar.

In this paper, the *exact* conservation equation is derived for potential vorticity constructed from the three-dimensional vector analog of buoyancy frequency. A familiar source appears, resulting from gradients of changes following the flow in the locally-referenced potential density. This potential vorticity source vanishes when salt and potential temperature *do not change* following the flow (adiabatic flow), or when the salt and potential temperature buoyancy fluxes *balance* (neutral flow).

In addition, two new and unfamiliar sources are found. Both depend upon the *variation in the speed of sound with salt and potential temperature* (or, equivalently, after interchanging derivatives, the pressure dependence of the thermal expansion and saline contraction coefficients). One new source is associated with changes in pressure following the flow (diabaric velocity), and the other with changes in salt and potential temperature following the flow. The Ertel's potential vorticity source term associated with baroclinic torques vanishes.

Both new sources can be decomposed into neutral and dianeutral parts in salinity/potential temperature coordinates. These parts correspond respectively to turning and crowding of isopycnals with increasing pressure. The turning and crowding effects are contained in the thermodynamic derivatives $\frac{\partial^2 \rho}{\partial s \partial p}$ and $\frac{\partial^2 \rho}{\partial \theta \partial p}$ (called thermobaricity by *McDougall, 1987)*. Variations in sound speed with *pressure*, and variations in saline contraction and potential temperature expansion with salt and potential temperature do not contribute explicitly.

(a) New source proportional to cross-isobar flow

The first new source can make a non-negligible contribution to buoyancy potential vorticity in the ocean. It is proportional to the change in pressure following the flow and thus can be non-zero even when salt and potential temperature do not change following the flow. Buoyancy potential vorticity can increase by a quarter of its value, for warm water displaced from the surface to thermocline depth, and by a third for cold water displaced over the full water depth. These values are equivalent to a single contour interval on potential vorticity maps and sections appearing in the literature.

The main mechanism for this buoyancy potential vorticity source can be understood as follows. *In situ* density surfaces squeeze together as pressure increases, governed by the speed of sound and changes with pressure in saline contraction and potential temperature expansion. Since the buoyancy vector is *defined* such that it differs from the *in situ* density gradient by an amount proportional to the speed of sound, the change in the buoyancy vector has only the parts due to the pressure dependence of saline contraction and potential temperature expansion. This thermodynamic alteration of the buoyancy vector with increasing pressure must appear as a source term for the buoyancy potential vorticity. Without it, pressure changes alone, in the presence of suitable salt and potential temperature gradients, would appear to induce relative vorticity or flow across planetary vorticity contours.

If the absolute vorticity can be estimated, as is the case when relative vorticity is negligible, this source is a mappable function of the salinity, temperature, and pressure fields in the fluid.

(b) New source proportional to salt and potential temperature changes following the flow

The neutral component of the second new source makes a contribution to buoyancy potential vorticity in the ocean that is as large as the pressure variation in weakly stratified seawater, but an order of magnitude smaller than pressure-dependent changes in well-stratified water. The neutral part of the second source arises from the turning of isopycnals with pressure in (s, θ, p) coordinates and is related to the slight non-closure of neutral trajectories. Plots are shown of the neutral part for representative neutral trajectories in the world ocean. (The dianeutral part is grouped with other dianeutral sources.)

(c) Neutral trajectories

Neutral trajectories are those along which salt and potential temperature changes, if any, compensate such that buoyancy restoring forces vanish. Such trajectories do not in general form exactly closed orbits when traced through a steady salinity/potential temperature/pressure field along a path whose horizontal component closes; a small difference in height between the beginning and end of the path usually remains. [*McDougall and Jackett (1988)* coined the word 'helicity' for this phenomenon. Here it is called 'rectification', to associate it with the non-closure of parcel trajectories in some kinds of waves.] The notation developed for the buoyancy potential vorticity conservation equation is used to show where rectification has the greatest magnitude.

(d) Neutral surface potential vorticity

A differential expression for neutral surface potential vorticity is derived from the buoyancy potential vorticity conservation equation. This equation shows that gradients of neutral surface potential vorticity are proportional to gradients of buoyancy

potential vorticity, plus terms proportional to the new buoyancy potential vorticity sources.

The physical insight afforded by this new differential equation parallels and clarifies points made by *McDougall (1988)* in his integral formulation of neutral surface potential vorticity.

(e) Overview of paper

Readers not interested in the mechanics of the derivation of the conservation equation may wish to skip the next three sections: basic definitions and discussion underlying the derivation of the are presented in Sec. B.2, the derivation itself is presented in Sec. B.3, and the conservation equation is refined further by dividing the salinity and potential temperature gradients and changes following the flow into neutral and dianeutral parts in Sec. B.4. The conservation equation before this step appears as Eq. (B.19); the decomposed source terms appear as Eq. (B.25) and (B.26). A glossary of symbols and guide to equations follows the body of the paper.

Pressure dependence of buoyancy potential vorticity is discussed and estimated in Sec. B.5. Dependence on neutral salinity and potential temperature changes and isopycnal turning is discussed and estimated in Sec. B.6. A brief mathematical explanation of neutral trajectory rectification based upon the buoyancy vector is given in Sec. B.7. The differential expression for neutral surface potential vorticity is derived from the conservation equation in Sec. B.8. The results are summarized in Sec. B.9.

B.2 Preliminaries: definitions and discussion

(a) *Ertel's potential vorticity*

Ertel's potential vorticity, q, is defined by:

$$q = \frac{\underset{\sim}{\omega_a}}{\rho} \cdot \nabla \lambda \tag{B.1}$$

where the ρ is the *in situ* density, the total vorticity is given by $\underset{\sim}{\omega_a} = 2\underset{\sim}{\Omega} + \underset{\sim}{\zeta}$ (planetary $2\underset{\sim}{\Omega}$ plus relative $\underset{\sim}{\zeta}$) and λ represents some scalar property of the fluid *(Pedlosky, 1979)*.

Changes in q following the flow are given by

$$\frac{Dq}{Dt} =$$

$$\underset{\text{(I)}}{\rho^{-1}\left(2\underset{\sim}{\Omega} + \underset{\sim}{\zeta}\right) \cdot \nabla \frac{D\lambda}{Dt}} + \underset{\text{(II)}}{\rho^{-3}(\nabla\lambda \times \nabla\rho) \cdot \nabla p} +$$

$$\underset{\text{(III)}}{\rho^{-1}\nabla\lambda \cdot \nabla \times \left(\frac{F}{\rho}\right)} \tag{B.2}$$

where p is the pressure. Both Eq. (B.1) and (B.2) are derived from the Navier-Stokes equations without approximation.

(b) *Sound speed*

The derivative $\left.\frac{\partial\rho}{\partial p}\right|_{(s,\theta)}$ is related to the sound speed c:

$$\frac{1}{c^2} = \left.\frac{\partial\rho}{\partial p}\right|_{(s,\theta)} \tag{B.3}$$

The salinity is represented by s, and the potential temperature by θ.

(c) Potential density

Potential density σ_r is defined by

$$\sigma_r(x_o, y_o, z_o) =$$

$$\rho(x_o, y_o, z_o) - 1000 + \int_{p(x_o,y_o,z_o)}^{r} dp' \left.\frac{\partial \rho}{\partial p'}\right|_{(s,\theta,p')} \qquad \text{(B.4)}$$

During the integration, (s, θ) are constant and equal to their values at (x_o, y_o, z_o). The integrand represents the change in density that the parcel would experience during a displacement from its *in situ* pressure p to the reference pressure r.

(d) Relationship between N^2 and potential density gradient

The buoyancy frequency is denoted by N. *Locally*, in the neighborhood of a pressure r, the usual definition of $\frac{-\rho}{g}N^2$ (g is gravitational acceleration):

$$\frac{-\rho}{g}N^2 = \frac{\partial \rho}{\partial z} - \left.\frac{\partial \rho}{\partial p}\frac{\partial p}{\partial z}\right|_{(s,\theta,p)} \qquad \text{(B.5)}$$

can be recovered from the definition of potential density (Eq. B.4) in two steps: *(i)* vertical differentiation, making use of Leibniz's rule

$$\frac{\partial \sigma_r}{\partial z} = \frac{\partial \rho}{\partial z} + \int_{p}^{r} dp \left.\frac{\partial^2 \rho}{\partial z \partial p}\right|_{(s,\theta,p)} - \left.\frac{\partial p}{\partial z}\frac{\partial \rho}{\partial p}\right|_{(s,\theta,p)} \qquad \text{(B.6)}$$

and *(ii)* letting $p \rightarrow r$ as the neighborhood becomes arbitrarily small; in this limit, the middle term of Eq. (B.6) vanishes.

(e) Neutral flow

The neutral flow condition is

$$\alpha' \frac{D\theta_n}{Dt} = \beta' \frac{Ds_n}{Dt} \tag{B.7}$$

where the thermal expansion coefficient is $\alpha' = -\rho^{-1} \frac{\partial \rho}{\partial \theta}\Big|_{(s,p)}$ and the saline contraction coefficient is $\beta' = \rho^{-1} \frac{\partial \rho}{\partial s}\Big|_{(\theta,p)}$ (see *Gill, 1982* for their relationships to the expansion coefficients in terms of *in situ* temperature).

Neutral tangent planes, defined by

$$\alpha' \nabla \theta_n = \beta' \nabla s_n \tag{B.8}$$

are tangent to potential density surfaces referenced to a pressure r in the neighborhood of r. Stirring processes such as eddies are thought to displace parcels laterally along these neutral tangent planes/local potential density surfaces, since buoyancy restoring forces vanish for such displacements. Other physical processes displace parcels across these planes *(McDougall, 1984)*.

The neutral flow condition will be used in this paper to decompose salinity and potential temperature gradients and changes following the flow into neutral (subscript n) and dianeutral (subscript d) parts.

(f) Potential temperature reference pressure

Potential temperature, like potential density, is referenced to some arbitrary pressure. Potential temperature reference pressure choice may influence potential temperature gradients on mapping surfaces slightly, through the salinity dependence of the adiabatic lapse rate.

The equations used in this paper follow from properties of the thermodynamic fields that do not depend on potential temperature reference pressure choice: the *in situ* density gradient, the speed of sound, and the pressure gradient. The quantities $\alpha' d\theta$ and $\beta' ds$, from which the θ reference pressure dependence has been removed, appear here, but $d\theta$ does not. Thus the reference pressure choice for θ need not worry us; any strictly constant pressure is acceptable.

3. Derivation of the conservation equation for buoyancy potential vorticity

(a) Three-dimensional vector analog of buoyancy frequency

The three-dimensional analog of $\frac{-\rho}{g} N^2 \hat{\mathbf{k}}$ is given by

$$\begin{aligned} \boldsymbol{L} &= \nabla\rho - \left.\frac{\partial\rho}{\partial p}\right|_{(s,\theta)} \nabla p \\ &= \left.\frac{\partial\rho}{\partial\theta}\right|_{(s,p)} \nabla\theta + \left.\frac{\partial\rho}{\partial s}\right|_{(\theta,p)} \nabla s \end{aligned} \tag{B.9}$$

(b) Buoyancy potential vorticity

The buoyancy potential vorticity is given by

$$Z = \frac{\underset{\sim}{\omega}_a}{\rho} \cdot \boldsymbol{L} \tag{B.10}$$

The buoyancy planetary vorticity is $\frac{-f}{g} N^2$.

(c) Search for λ

Ertel's potential vorticity (Eq. B.1) is constructed from gradients of a scalar quantity λ. Is there a scalar λ that corresponds to $\frac{\underset{\sim}{\omega}_a}{\rho} \cdot \nabla\lambda = Z$? Since $p \rightarrow r$ in the definition of N^2, we might (naively) try to define λ by taking the limit $r \rightarrow p$ in the

definition of potential density, Eq. (B.4). But we find that $\sigma_r \to \rho$, while $\frac{\tilde{\omega}_a}{\rho} \cdot \nabla \rho \not\to Z$.

We might also try to define λ by setting $\nabla\lambda$ equal to $\boldsymbol{L}$. However, it turns out that $\nabla\lambda$ *cannot* equal $\boldsymbol{L}$, since $\boldsymbol{L}$ is not in general irrotational, and gradient fields *always* are.[1]

Thus it appears that we must abandon the search for a globally-valid scalar λ that corresponds to Z.

(d) An alternative approach

Even without λ, we can still write a conservation equation for Z. First, we take the substantial derivative of $Z = \frac{\tilde{\omega}_a}{\rho} \cdot \left[\nabla\rho - \frac{\partial\rho}{\partial p}\Big|_{(s,\theta)} \nabla p\right]$:

$$\frac{DZ}{Dt} = \frac{D}{Dt}\left[\frac{\tilde{\omega}_a}{\rho} \cdot \nabla\rho\right] - \frac{D}{Dt}\left[\frac{\partial\rho}{\partial p}\Big|_{(s,\theta)} \frac{\tilde{\omega}_a}{\rho} \cdot \nabla p\right] \qquad \text{(B.11)}$$

---

[1]That is,

$$\nabla \times \boldsymbol{L} = -\nabla \frac{\partial p}{\partial s}\Big|_{(\theta,p)} \times \nabla p \neq 0 \text{ in general}$$

but for *any* scalar λ.

$$\nabla \times \nabla\lambda = 0.$$

[Recall that $\frac{\partial p}{\partial s}\Big|_{(\theta,p)}$ is related to the the sound speed c.]

Now, using the conservation equation for Ertel's potential vorticity (Eq. B.1) twice, once with $\lambda = \rho$, and once with $\lambda = p$, gives

$$\frac{DZ}{Dt} = \frac{Dq(\lambda=\rho)}{Dt} - \underset{\text{(a)}}{\frac{\omega_a}{\rho} \cdot \nabla p \; \frac{D}{Dt}\frac{\partial \rho}{\partial p}\Big|_{(s,\theta)}} - \frac{\partial \rho}{\partial p}\Big|_{(s,\theta)} \frac{Dq(\lambda=p)}{Dt} \tag{B.12}$$

The term labelled (a) does not have a parent term in Eq. (B.1). Substituting in the source terms for Ertel's potential vorticity from the *right-hand-side* of Eq. (B.2) gives

$$\frac{DZ}{Dt} = \frac{\omega_a}{\rho} \cdot \tag{B.13}$$

$$\{ \underset{\text{(I, }\lambda=\rho)}{\nabla \frac{D\rho}{Dt}} - \underset{\text{(I, }\lambda=p)}{\frac{\partial \rho}{\partial p}\Big|_{(s,\theta)} \nabla \frac{Dp}{Dt}} - \underset{\text{(a)}}{\nabla p \frac{D}{Dt}\left[\frac{\partial \rho}{\partial p}\Big|_{(s,\theta)}\right]} \}$$

$$+ \underset{\text{(III)}}{\rho^{-1} L \cdot \nabla \times \left(\frac{F}{\rho}\right)}$$

Labels beneath each term correspond to those under Eq. (B.2). Contributions from the baroclinic torques (term II) vanish for both $\lambda = p$ and $\lambda = \rho$.

The first term from this equation can be expanded in the thermodynamic derivatives:

$$\underset{\text{(I, }\lambda=\rho)}{\frac{\omega_a}{\rho} \cdot \nabla \frac{D\rho}{Dt}} = \frac{\omega_a}{\rho} \cdot \{$$

$$\nabla \left[\underset{\text{(b)}}{\frac{\partial \rho}{\partial s}\Big|_{(\theta,p)} \frac{Ds}{Dt}} + \underset{\text{(c)}}{\frac{\partial \rho}{\partial \theta}\Big|_{(s,p)} \frac{D\theta}{Dt}} + \underset{\text{(e)}}{\frac{\partial \rho}{\partial p}\Big|_{(s,\theta)} \frac{Dp}{Dt}} \right] \} \tag{B.14}$$

which follows from $\rho = \rho(s, \theta, p)$. The second term of Eq. (B.13) can be expanded using the product rule, which gives

$$\underset{\text{(I, } \lambda=p)}{\frac{\partial \rho}{\partial p}\Big|_{(s,\theta)} \frac{\tilde{\omega}_a}{\rho} \cdot \nabla \frac{Dp}{Dt}} = \frac{\tilde{\omega}_a}{\rho} \cdot \Big\{ \underset{\text{(e)}}{\nabla \Big[\frac{\partial \rho}{\partial p}\Big|_{(s,\theta)} \frac{Dp}{Dt}\Big]} - \underset{\text{(d)}}{\frac{Dp}{Dt} \nabla \frac{\partial \rho}{\partial p}\Big|_{(s,\theta)}} \Big\} \tag{B.15}$$

The terms marked (e) in Eq. (B.14) and (B.15) cancel in Eq. (B.13). Terms (b) and (c) combine to form $\frac{\tilde{\omega}_a}{\rho} \cdot \nabla \frac{D\sigma_r}{Dt}$, where σ_r is the locally-referenced potential density.

Terms (a) and (d) can be expanded in thermodynamic derivatives to yield:

$$\underset{\text{(a)}}{\frac{\tilde{\omega}_a}{\rho} \cdot \nabla p \frac{D}{Dt} \frac{\partial \rho}{\partial p}\Big|_{(s,\theta)}} = \frac{\tilde{\omega}_a}{\rho} \cdot \nabla p \Big\{ \tag{B.16}$$

$$\underset{\text{(a1)}}{\frac{Ds}{Dt} \frac{\partial}{\partial s}\Big|_{(p,\theta)}} + \underset{\text{(a2)}}{\frac{D\theta}{Dt} \frac{\partial}{\partial \theta}\Big|_{(s,p)}} + \underset{\text{(a3)}}{\frac{Dp}{Dt} \frac{\partial}{\partial p}\Big|_{(s,\theta)}} \Big\} \frac{\partial \rho}{\partial p}\Big|_{(s,\theta)}$$

and

$$\underset{\text{(d)}}{\frac{Dp}{Dt} \frac{\tilde{\omega}_a}{\rho} \cdot \nabla \frac{\partial \rho}{\partial p}\Big|_{(s,\theta)}} = \frac{Dp}{Dt} \frac{\tilde{\omega}_a}{\rho} \cdot \Big\{ \tag{B.17}$$

$$\underset{\text{(d1)}}{\nabla s \frac{\partial}{\partial s}\Big|_{(p,\theta)}} + \underset{\text{(d2)}}{\nabla \theta \frac{\partial}{\partial \theta}\Big|_{(s,p)}} + \underset{\text{(d3)}}{\nabla p \frac{\partial}{\partial p}\Big|_{(s,\theta)}} \Big\} \frac{\partial \rho}{\partial p}\Big|_{(s,\theta)}$$

With the cancellation of terms (a3) and (d3) and of the terms labelled (e) in Eq. (B.13) and (B.14), and the substitution

$$\boldsymbol{u} \cdot \boldsymbol{L} = \frac{\partial \rho}{\partial s}\Big|_{(\theta,p)} \boldsymbol{u} \cdot \nabla \theta + \frac{\partial \rho}{\partial \theta}\Big|_{(s,p)} \boldsymbol{u} \cdot \nabla s \tag{B.18}$$

we get the simplified conservation equation for Z from Eq. (B.13):

$$\frac{DZ}{Dt} = \frac{\underset{\sim}{\omega_a}}{\rho} \cdot \tag{B.19}$$

$$\{ \nabla \left[\frac{\partial \rho}{\partial s}\Big|_{(\theta,p)} \frac{\partial s}{\partial t} \right] + \nabla \left[\frac{\partial \rho}{\partial \theta}\Big|_{(S,p)} \frac{\partial \theta}{\partial t} \right] + \boldsymbol{u} \cdot \boldsymbol{L} -$$

(b1) (c1) (b2)+(c2)

$$\left[\left(\frac{Ds}{Dt} \frac{\partial c^{-2}}{\partial s}\Big|_{(\theta,p)} + \frac{D\theta}{Dt} \frac{\partial c^{-2}}{\partial \theta}\Big|_{(s,p)} \right) \right] \nabla p +$$

(a1) (a2)

$$\left[\left(\nabla s \frac{\partial c^{-2}}{\partial s}\Big|_{(\theta,p)} + \nabla \theta \frac{\partial c^{-2}}{\partial \theta}\Big|_{(s,p)} \right) \right] \frac{Dp}{Dt} \}$$

(d1) (d2)

$$+ \rho^{-1} \boldsymbol{L} \cdot \nabla \times \left(\frac{\boldsymbol{F}}{\rho} \right)$$

(III)

The terms are:

(b1), (c1) Time dependence.

(b2), (c2) Buoyancy advection. These vanish in neutral flow, which includes as a special case zero salt and potential temperature changes following the flow.

(a1), (a2) Proportional to isopycnal crowding and turning, and to salt and potential temperature changes following the flow. These terms vanish if salt and potential temperature do not change following the flow. They *do not* vanish in other types of neutral flow.

(d1), (d2) Pressure dependence of buoyancy potential vorticity. These vanish only if diabaric velocity $\frac{Dp}{Dt}$ is zero.

4. Decomposition into neutral and dianeutral parts

Isopleths of density rotate and crowd together with pressure on the salinity/potential temperature plane (Fig. B.1 and B.2). This plays a role in the buoyancy potential vorticity sources (a1) and (a2), and (d1) and (d2) in Eq. (B.19). The turning is also responsible for the slight non-closure of neutral trajectories.

(a) Isopycnal turning angle

The angle φ between constant density lines and the s-axis on an (s, θ) plot (Fig. B.1) is

$$\varphi = \arctan \frac{-\theta_o \partial\rho/\partial\theta}{s_o \partial\rho/\partial s} = \arctan \frac{\theta_o \alpha'}{s_o \beta'} \qquad \text{(B.20)}$$

where the thermal expansion coeffcient is $\alpha' = -\rho^{-1} \frac{\partial\rho}{\partial\theta}\Big|_{(s,p)}$ and the saline contraction coefficient is $\beta' = \rho^{-1} \frac{\partial\rho}{\partial s}\Big|_{(\theta,p)}$. The arbitrary scale of the (s, θ) diagram is specified by θ_o, the number of degrees of potential temperature per unit distance, and s_o, the number of practical salinity units per unit distance. The rate of rotation of isopleths of density with pressure is given by $\frac{\partial\varphi}{\partial p}$:

$$\frac{\partial\varphi}{\partial p} = \frac{s_o \theta_o}{\rho^2(\beta'^2 s_o^2 + \alpha'^2 \theta_o^2)} \left(\rho\beta' \frac{\partial\rho\alpha'}{\partial p} - \rho\alpha' \frac{\partial\rho\beta'}{\partial p} \right) \qquad \text{(B.21)}$$

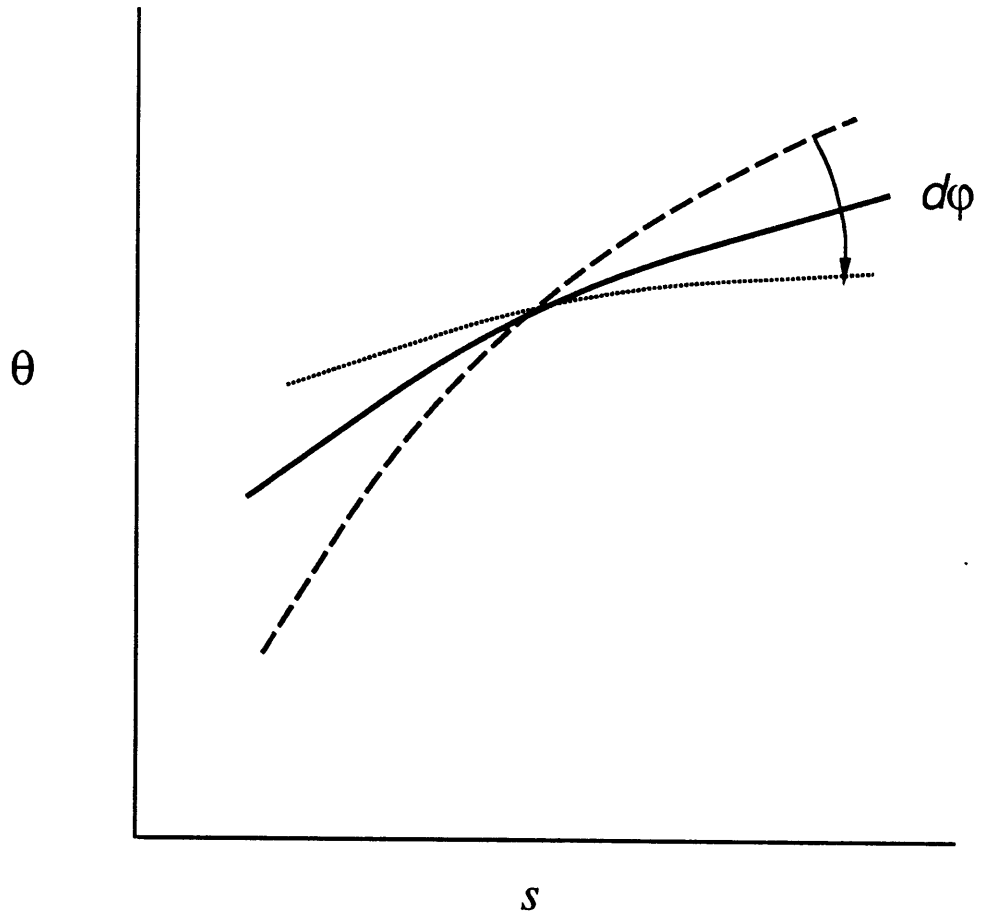

Fig. B.1 – Isopleths of density at different constant pressures in (s, θ) coordinates. The change in angle with pressure is marked $d\varphi$.

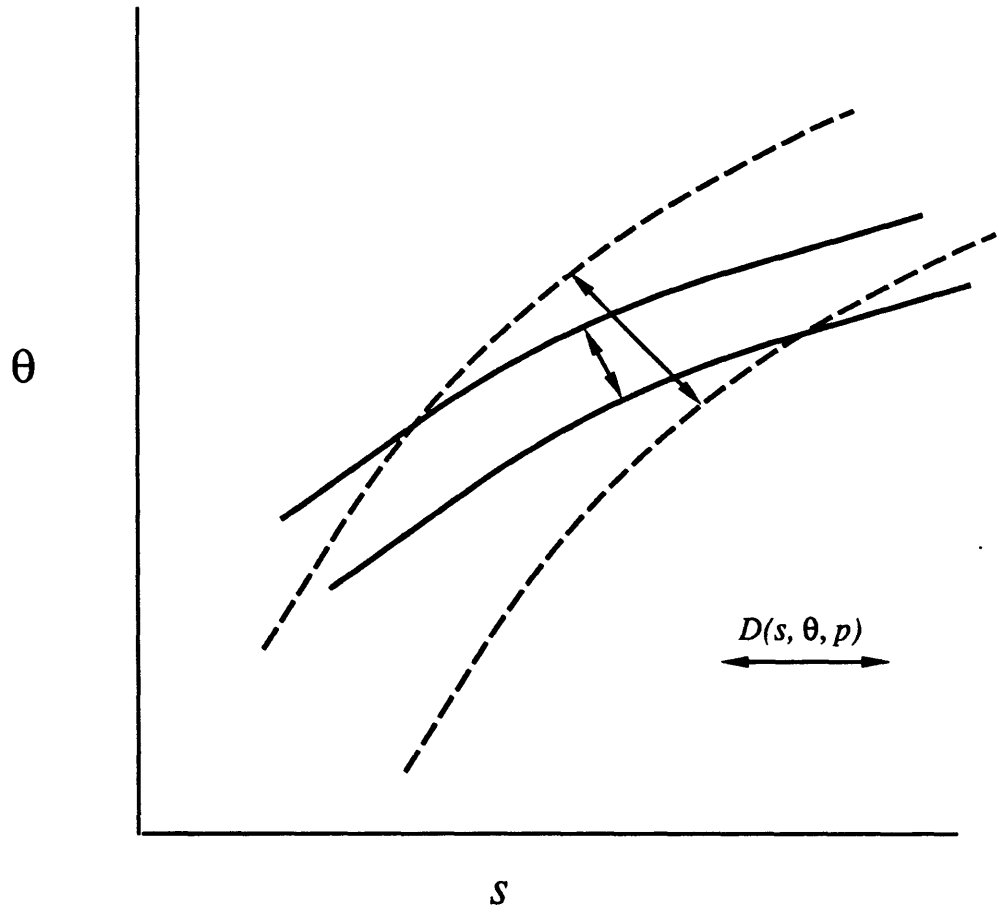

Fig. B.2 – Isopleths of density at different constant pressures in (s, θ) coordinates. Two pairs isopleths are shown, separated by an equal increment of density at the respective pressures. The separation D between isopleths decreases with pressure.

The quantity in the denominator of the fraction, which is given the symbol D^2, has units of density squared. It is the square of the density increment along the hypotenuse of a $(s_o \times \theta_o)$ square on the (s, θ) plot.

(b) *Neutral vs. dianeutral salt and potential temperature changes*

We divide salt and potential temperature gradients and changes following the flow into two parts: (i) neutral (subscript n) which is tangent to isopleths of density in the (s, θ) constant-pressure plane, and (ii) dianeutral (subscript d), perpendicular to the first:

$$\nabla\theta = \nabla\theta_n + \nabla\theta_d \,, \quad \nabla s = \nabla s_n + \nabla s_d \tag{B.22}$$

$$\frac{D\theta}{Dt} = \frac{D\theta_n}{Dt} + \frac{D\theta_d}{Dt} \,, \quad \frac{Ds}{Dt} = \frac{Ds_n}{Dt} + \frac{Ds_d}{Dt} \tag{B.23}$$

The decomposition is illustrated in Fig. (B.3). This segregates into separate terms salinity and potential temperature changes associated with different physical mechanisms. Neither part is necessarily small: local conditions such as the presence or absence of lateral (s, θ) fronts dictate the relative magnitudes neutral and dianeutral salinity and potential temperature changes.

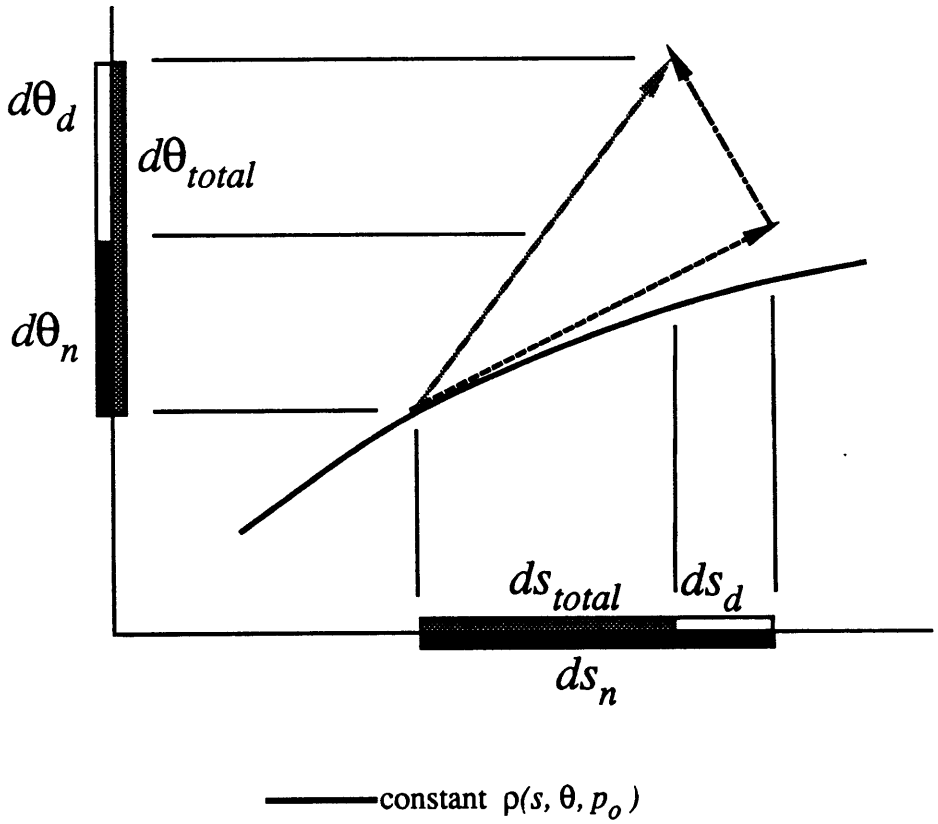

Fig. B.3 – Decomposition of salinity and potential temperature changes $(ds, d\theta)t_{otal}$ at p_o into neutral and dianeutral parts. Shaded arrow and boxes: total salinity and temperature change. Black box, dashed arrow, subscript *d*: dianeutral part of changes. Open box, dot-dashed arrow, subscript *n*: neutral part of changes.

(c) Decomposition of buoyancy potential vorticity sources

We use the neutral flow condition $\alpha' \frac{D\theta_n}{Dt} = \beta' \frac{Ds_n}{Dt}$ and the orthogonality of the neutral and dianeutral vectors on the *(s, θ)* plane to transform terms (a1) and (a2) of Eq. (B.19):

$$(a1)+(a2) = \frac{\underset{\sim}{\omega_a}}{\rho} \cdot \nabla p \quad \{ \underbrace{(\rho\beta')^{-1} \left(\rho\beta' \frac{\partial \rho\alpha'}{\partial p} - \rho\alpha' \frac{\partial \beta'}{\partial p}\right) \frac{D\theta_n}{Dt}}_{(a_n1)+(a_n2)} + \underbrace{(2\theta_o^2 \rho\alpha')^{-1} \frac{\partial D^2}{\partial p} \frac{D\theta_d}{Dt}}_{(a_d1)+(a_d2)} \} \tag{B.24}$$

(We could just as well have written this in terms of s_n and s_d.) Recall that D^2 is the square of the density increment along the hypotenuse of a $(s_o \times \theta_o)$ square on the *(s, θ)* plane. Buoyancy potential vorticity changes in proportion to the variation of this increment with pressure and dianeutral potential temperature changes.

Substituting the expression for $\frac{\partial \varphi}{\partial p}$ into Eq. (B.24) gives:

$$(a1) + (a2) = \frac{\underset{\sim}{\omega_a}}{\rho} \cdot \nabla p \quad \{ \underbrace{\left[\frac{D^2}{\rho\beta' s_o \theta_o} \frac{\partial \varphi}{\partial p} \right] \frac{D\theta_n}{Dt}}_{(a_n1)+(a_n2)} + \underbrace{(2\theta_o^2 \rho\alpha')^{-1} \frac{\partial D^2}{\partial p} \frac{D\theta_d}{Dt}}_{(a_d1)+(a_d2)} \} \tag{B.25}$$

This shows that changes in buoyancy potential vorticity result from the *neutral* component of potential temperature changes following the flow [source terms (a_n1) and (a_n2)].[2] Dianeutral potential temperature changes contribute through terms (a_d1) and (a_d2), as well as through the terms (b2), (c2) of Eq. (B.19).

Note that Eq. (B.25) is *subtracted* from the right-hand-side of the buoyancy potential vorticity equation.

The source terms (d1) and (d2) can be similarly decomposed, giving:

$$(d1) + (d2) \quad = \quad \frac{\omega_a}{\rho} \cdot \quad \Big\{ \quad \underbrace{\frac{D^2}{\rho\beta' s_o \theta_o} \frac{\partial \varphi}{\partial p} \nabla\theta_n}_{(d_n1)+(d_n2)} \; + \; \underbrace{(2\theta_o{}^2 \rho\alpha')^{-1} \frac{\partial D^2}{\partial p} \nabla\theta_d \Big\} \frac{Dp}{Dt}}_{(d_d1)+(d_d2)} \qquad \text{(B.26)}$$

This shows that both turning and crowding of isopycnals in (s, θ) coordinates with pressure play a role in the pressure dependence of Z.

B.5 Pressure dependence of buoyancy potential vorticity

The pressure dependence of buoyancy potential vorticity, $\frac{\partial Z}{\partial p}$, is given by terms (d1) and (d2) of Eq. (B. 19). Since Z is a function of $(s, \theta, p, \underset{\sim}{\omega_a}, \nabla s, \nabla\theta)$, in this partial derivative with pressure the other five variables are kept fixed.

---

[2] Term $(a_n1)+(a_n2)$, Eq. (26) is opposite in sign from $\frac{D\theta_n}{Dt}$, since $\frac{\partial\varphi}{\partial p}$ is always negative (again with the convention that planetary vorticity is always positive, *i.e.*, $\underset{\sim}{\omega_a} \sim -|f| \hat{k}$.

We may check the sign by noting that $\frac{\omega_a}{\rho} \cdot \nabla p \frac{Dc^{-2}}{Dt}$, the original term (a) in Eq. (12), is opposite in sign from potential temperature changes following a neutral trajectory, since as θ increases, c increases and $\frac{Dc^{-2}}{Dt} < 0$, using $f\frac{\partial p}{\partial z} > 0$ in both hemispheres.

What is the magnitude of $\partial Z/\partial p$ for ocean interior flow? The approximation $\underset{\sim}{\omega_a} \cdot \nabla \sim f \frac{\partial}{\partial z}$ is appropriate for interior flow, and we may neglect the salinity dependent part of $\partial Z/\partial p$ in favor of the potential temperature dependent part. Using these approximations, the scale of ΔZ for a pressure displacement Δp is:

$$\frac{-|f|}{\rho}(-2c^{-3}\frac{\partial c}{\partial \theta})\frac{\partial \theta}{dz}\Delta p \qquad \text{(B.27)}$$

Planetary potential vorticity constructed from density gradients and buoyancy frequency is reported with positive values in both hemispheres, so we use $-|f|$ in place of f.

Typical oceanic values are shown in Table B.1. Buoyancy potential vorticity *increases* by 40 x 10^{-12} $m^{-1}s^{-1}$ during a displacement of 10 C thermocline water from surface to the thermocline pressures (nominally 1 km or 10 MPa), and by 3 x 10^{-12} $m^{-1}s^{-1}$ during a displacement of 1 C deep water from surface to deep ocean pressures (nominally 4 km or 40 MPa). These changes are about a quarter (of 200 x 10^{-12} $m^{-1}s^{-1}$) and a third (of 10 x 10^{-12} $m^{-1}s^{-1}$) respectively of the buoyancy potential vorticity at depth. *McDougall (1988)* estimates that buoyancy potential vorticity doubles for $\theta = 6$ C and $\Delta p = 1.5$ MPa (1500 m).

Increasing pressure stabilizes the water column slightly when temperature decreases with depth and salinity effects are small, as is usually the case in the ocean. Conversely, decreasing pressure (upward motion) destabilizes the water column. Displacing neutrally stable water masses at depth upward can cause convection, mixing salt and potential temperature.

The magnitude of these buoyancy potential vorticity increases with pressure may be compared to (i) the buoyancy potential vorticity itself; to (ii) *gradients* of potential

Table B.1 – Scale values needed to estimate size of buoyancy potential vorticity changes associated with pressure change. Spatial estimates are from just south of Africa in the Agulhas Retroflection *(Bennett, 1988).*

f	1×10^{-4} s^{-1}	
ρ	1000 kg m^{-3}	
At 10 C:		
c	1490 m s^{-1}	at 0 dbar
	1506 m s^{-1}	at 1000 dbar
$\partial c/\partial\theta$	3.6 m s^{-1} K^{-1}	
$c^{-3}\partial c/\partial\theta$	1.1×10^{-9} m^{-2} s^{-2} K^{-1}	
$\partial\theta/\partial z$	1.7×10^{-2} K m^{-1}	
$\partial Z/\partial p$	3.8×10^{-18} m^{-1} s^{-1} Pa^{-1}	
Z	200×10^{-12} m^{-1} s^{-1}	
ΔZ	40×10^{-12} m^{-1} s^{-1}, 1 km displacement from surface to thermocline pressures	
At 1 C:		
c	1455 m s^{-1}	at 0 dbar
	1529 m s^{-1}	at 4000 dbar
$\partial c/\partial\theta$	4.5 m s^{-1} K^{-1}	
$c^{-3}\partial c/\partial\theta$	3.2×10^{-10} m^{-2} s^{-2} K^{-1}	
$\partial\theta/\partial z$	1.0×10^{-3} K m^{-1}	
$\partial Z/\partial p$	6.4×10^{-20} m^{-1} s^{-1}	
Z	10×10^{-12} m^{-1} s^{-1}	
ΔZ	3×10^{-12} m^{-1} s^{-1}, 4 km displacement from surface to bottom pressures	

vorticity on isopycnal or neutral surfaces; and to (iii) erosion of vertical extrema in potential vorticity across a basin:

(i) The increases are moderate compared to buoyancy potential vorticity values: a quarter to a third.

(ii) The increases are very small compared to the largest potential vorticity gradients on isopycnal/neutral surfaces. These are found across western boundary currents. Observed potential vorticity decreases from $>500 \times 10^{-12} m^{-1} s^{-1}$ near the surface to $<150 \times 10^{-12} m^{-1} s^{-1}$ at 700 m across the Gulf Stream *(Bower* et al., *1985)*, clearly greater than the change due to pressure dependence of buoyancy potential vorticity, and opposite in sign. Where observed potential vorticity gradients on surfaces are smaller and similar in magnitude to $\frac{\partial Z}{\partial p}$ – for example, near the edges of the uniform potential vorticity pools that play an important role in some thermocline theories *(Rhines and Young, 1982)* – the pressure dependence may influence the oceanographic interpretation.

(iii) The increases seem to be nearly comparable in magnitude and of the same sign as gradients of potential vorticity at the vertical minimum of the Labrador Sea Water (LSW) core. *Talley and McCartney, 1982,* using potential vorticity constructed from gradients of potential density referenced to 1500 m, found LSW potential vorticity minimum values increasing from the Labrador Sea value of 4 to $>16 \times 10^{-12} m^{-1} s^{-1}$ in the vicinity of the Mediterranean tongue, as the core descends from 200 to 1500 m. The vertical minimum of buoyancy potential vorticity would display the same increase, plus an additional $10 \times 10^{-12} m^{-1} s^{-1}$, approximately, due to pressure dependence.

B.6 Buoyancy potential vorticity source associated with neutral part of salinity and potential temperature changes and isopycnal turning with pressure

The effects of the buoyancy potential vorticity sources associated with the neutral part of potential temperature change and isopycnal turning with pressure may be visualized in the following manner (Fig. B.4). We consider a parcel centered at p_o pressure spanning a pressure interval *dp* in the direction of the absolute vorticity vector; part of the parcel's net salinity and potential temperature changes satisfies the neutral flow condition; any dianeutral changes are ignored for the moment, as they are governed by different source terms. The upper edge of the parcel follows an isopleth of density on the $(p_o - dp/2)$ constant pressure surface, while the lower edge follows an isopleth on the $(p_o + dp/2)$ surface. This induces a density increment across the parcel and an increase in buoyancy potential vorticity, as the upper edge becomes lighter and the lower edge heavier with potential temperature increasing.

The part of term $(a_n1)+(a_n2)$ of Eq. (B.25) that is enclosed in square braces is $\frac{-\partial Z}{\partial \theta_n}$. Again, since Z is a function of $(s_n, s_d, \theta_n, \theta_d, p, \underset{\sim}{\omega_a}, \nabla s, \nabla \theta)$, in this partial derivative with the neutral part of the potential temperature change, the other variables are kept fixed.

The scale of $\frac{\partial Z}{\partial \theta_n}$ in ocean interior flow is

$$-D^2 (\rho^2 \beta' s_o \theta_o)^{-1} \partial\varphi/\partial p \ (-|f|) (-g) \qquad \text{(B.28)}$$

where $\rho^{-1}\nabla p \sim -g$ has been used. The sign of $\frac{\partial Z}{\partial \theta_n}$ is always positive since $\frac{\partial \varphi}{\partial p}$ is always negative.

We can estimate values of the thermodynamic parameters from *Lynn and Reid's(1971)* plots of potential density referenced to 0, 2000, and 4000 dbar at low

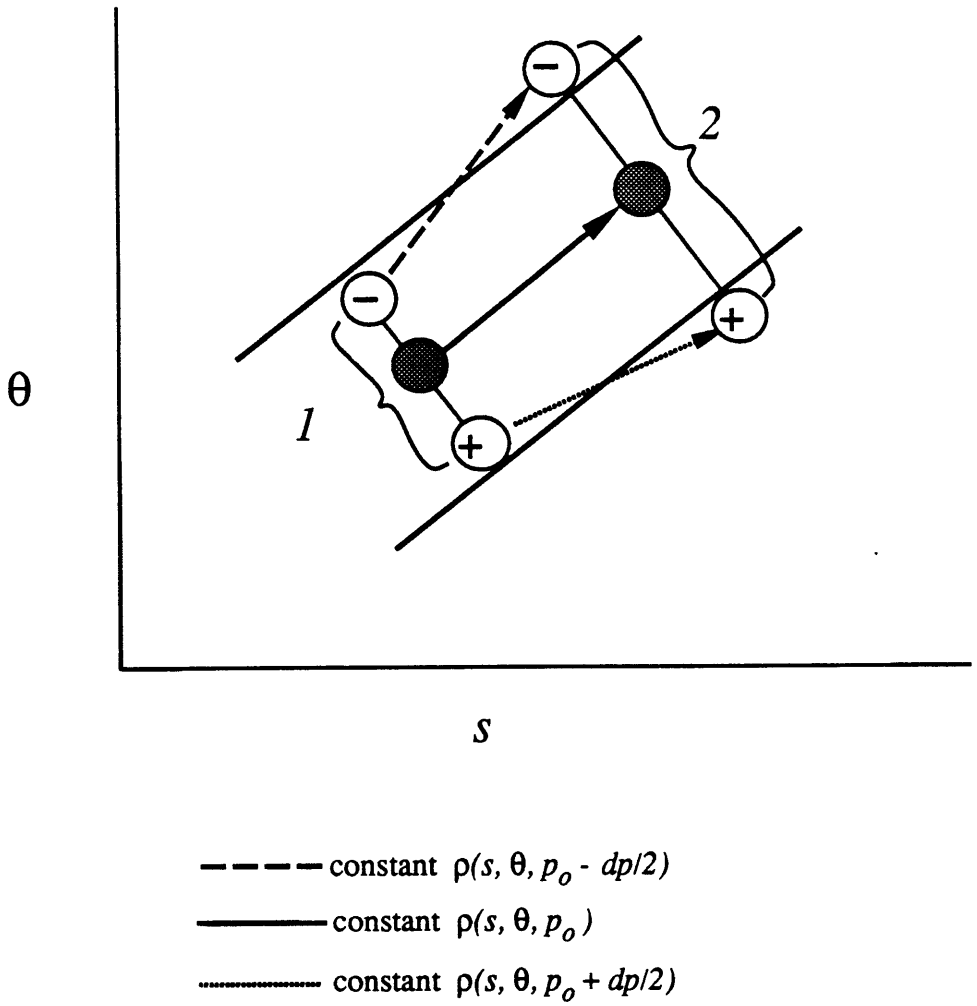

Fig. B.4 – Increase in density increment across parcel due to turning of isopycnals with pressure and neutral part of salinity and potential temperature increases. Shaded circles represent mean properties of parcel at p_O; circles marked with a minus (-) represent properties at $(p_O - dp/2)$; circles marked with a plus (+) represent properties at $(p_O + dp/2)$. Arrows indicate neutral direction for each level of parcel. Braces numbered *1* and *2* indicate density increment at p_O before and after neutral changes.

temperatures (-2 to 6 C); the greatest magnitudes of $\frac{\partial \varphi}{\partial p}$ occur at low temperatures and great depth; β' is relatively constant. The values are listed in Table (B.2).

Using these values, the scale expression (Eq. B.28) is approximately 4×10^{-12} m^{-1} s^{-1} K^{-1}. This is close to the maximum magnitude for the oceanic range of (s, θ, p) . It does not scale with the value of Z itself, so we may expect that it is *proportionally* most important in weakly stratified water.

The potential temperature changes from 0.8 to 1.6 C on the $\sigma_4 = 45.92$ contour, taking this as an approximation of a neutral surface, between Antarctica and Africa. The corresponding change in buoyancy potential vorticity is about 3.2×10^{-12} m^{-1} s^{-1}, or a third of the value south of Africa. The change in buoyancy potential vorticity due to *pressure* changes has the same sign and magnitude here, using the estimate of the previous section. (The pressure and potential temperature buoyancy potential vorticity sources have the same sign when potential temperature *increases* on a *descending* neutral trajectory.) The abyssal buoyancy potential vorticity itself is about 10×10^{-12} m^{-1}s^{-1} here.

B.7 Neutral trajectory rectification

Neutral trajectory rectification and the mathematical connection to buoyancy potential vorticity sources is briefly summarized here. Many of the equations parallel the work of *McDougall and Jackett (1988).*

McDougall and Jackett trace neutral trajectories around the N. Atlantic above the thermocline back to their starting point. These trajectories are found not to close by 1 – 5 m in the vertical. They estimate that this distance is an order of magnitude smaller than the vertical distance between an average neutral surface and the centrally-referenced potential density surface.

Table B.2 – Scale values needed to estimate maximum size of buoyancy potential vorticity changes associated with potential temperature change along a neutral trajectory. Estimates are from *Reid and Lynn (1971)*, Fig. 1.

$\Delta\varphi$	$-\pi/4$ between 0 and 4000 m at 0 C
Δp	40 MPa (4000 m)
$\partial\varphi/\partial p$	1.9×10^{-8} Pa^{-1} (kg^{-1} m^{-1} s^2)
s_o	0.1 psu per unit distance on (s, θ) plot
$\partial\rho/\partial s$	0.8 kg m^{-3} psu^{-1} (0.25 kg m^{-3} per 0.3 psu)
β'	8×10^{-4} psu^{-1}
θ_o	1 C per unit distance on (s, θ) plot
$\partial\rho/\partial\theta$	0.1 kg m^{-3} C^{-1} (0.25 kg m^{-3} per 2.6 C)
α'	1×10^{-4} C^{-1}
$\beta'^2 s_o^2 + \alpha'^2 \theta_o^2$	1.6×10^{-8}

These two distances are analogous, respectively, to the neutral potential temperature change/isopycnal turning contribution to buoyancy potential vorticity and the pressure-dependent contribution. As we have seen, in colder, weakly stratified water the ratio of buoyancy potential vorticity sources can be order one. This suggests that the ratio of rectification to neutral/potential density separation may be order one there also.

A neutral trajectory *cannot* exactly close around a non-zero plane area traced through (s, θ, p) space (Fig. B.5). This implies that a neutral trajectory cannot exactly close in (x, y, z) space either, unless the (x, y, z) trajectory maps onto a point or line curve in (s, θ, p) space. Such a mapping occurs only if:

(i) the (x, y, z) trajectory is traced through an ocean subvolume where there is a tight $\theta(s)$ relationship, or potential temperature or salinity are constant on pressure surfaces, *i.e.*, $\theta(p)$, $s(p)$; or

(ii) the trajectory is a point or line curve in (x, y, z) space.

Consider a closed contour C that is either neutral or consists of a neutral trajectory closed in the horizontal plus the vertical segment necessary to close it. The circulation of $\boldsymbol{L}$ around C is not in general zero:

$$\oint_C \boldsymbol{L} \cdot d\boldsymbol{r} = \iint_S (\nabla \times \boldsymbol{L}) \cdot d\boldsymbol{n}$$

$$= -\iint_S (\nabla c^{-2} \times \nabla p) \cdot d\boldsymbol{n} \qquad \text{(B.29)}$$

with S any surface bounded by C, $d\boldsymbol{r}$ everywhere tangent to C, and $d\boldsymbol{n}$ everywhere normal to S. This indicates that closed contours are not quite neutral trajectories except in certain special cases: S vanishing or $d\boldsymbol{n}$ everywhere parallel to ∇c^{-2} or ∇p.

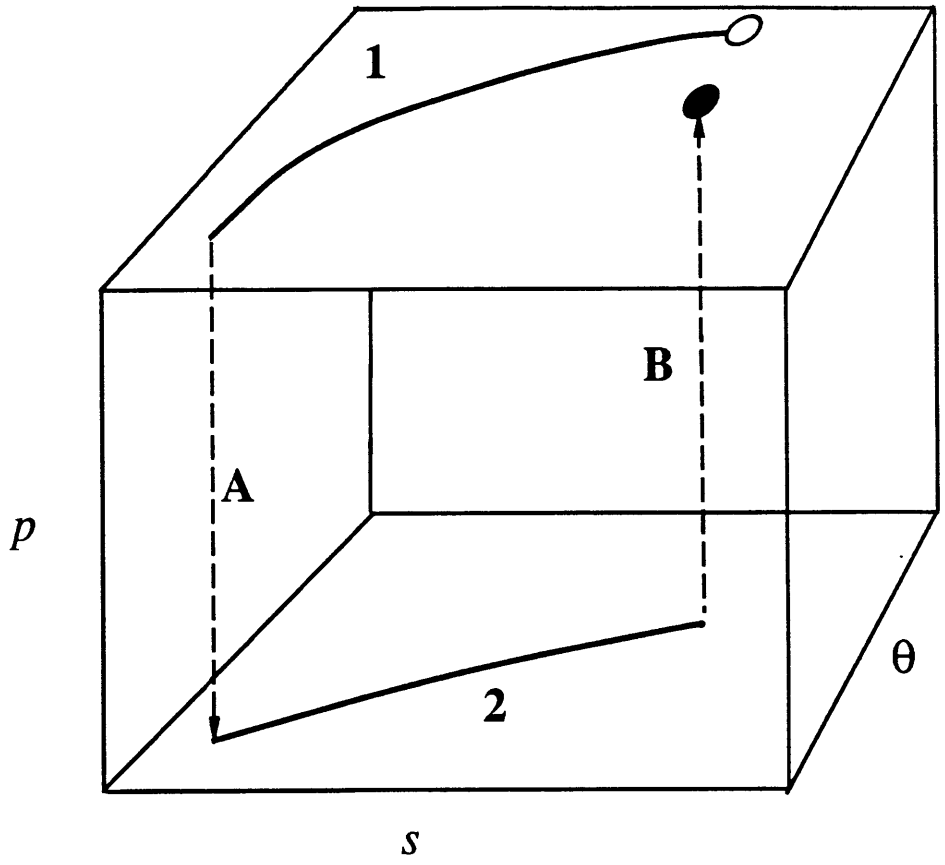

Fig. B.5 – Example of neutral trajectory rectification in (s, θ, p) coordinates. Open dot: parcel trajectory starts at the surfacewith warm salty characteristics. Curve 1: parcel cools and freshens along a surface neutral trajectory (isopleth of potential density referenced to the surface). Dashed line A: parcel descends without changing its potential temperature or salinity. Curve 2: parcel warms and gains salt along a neutral trajectory at depth (isopleth of potential density referenced to the new depth), until it regains its initial salinity. Dashed line B: parcel rises to the surface, again without changing potential temperature or salinity. Black dot: note slightly different potential temperature after completing neutral trajectory. Note that *any* neutral trajectory can be broken down into an alternating series of infinitesimal isobaric (like curves 1 and 2) and adiabatic (like dashed lines A and B) parts.

Mapping Eq. (B.26) into (s, θ, p) space, where the unit vectors are $\hat{s} = s_o^{-1}\nabla s$, $\underset{\sim}{\hat{\theta}} = \theta_0^{-1}\nabla\theta$ and $\hat{p} = p_o^{-1}\nabla p$; s_o, θ_o, and p_o are the salinity, potential temperature, and pressure increments per unit distance; and C maps onto C', S maps onto S'; and dn' is normal to S', gives

$$\oint_{S'} \left(\frac{\partial c^{-2}}{\partial s} s_o p_o \underset{\sim}{\hat{\theta}}\right) - \left(\frac{\partial c^{-2}}{\partial \theta} \theta_o p_o \hat{s}\right) \cdot dn' \qquad \text{(B.30)}$$

Evidently closed contours do not quite coincide with neutral trajectories unless S' vanishes, or dn' is everywhere parallel to $\hat{p}$, *i.e.*, the neutral trajectory is confined to a constant pressure surface. Since a neutral trajectory on a constant pressure surface must follow isopleths of constant density, S' vanishes for this case as well.

We may rewrite Eq. (B.30) very simply in terms of the unit vector in (s, θ, p) coordinates that is perpendicular to isopleths of density on a constant pressure surface:

$$\underset{\sim}{\hat{\rho}} = D^{-1}\left(\rho\beta s_o \hat{s} - \rho\alpha\theta_o \underset{\sim}{\hat{\theta}}\right) \qquad \text{(B.31)}$$

We will also use $\underset{\sim}{\hat{t}}$, which is tangent to isopleths of density; ($\underset{\sim}{\hat{\rho}}$, $\underset{\sim}{\hat{t}}$, $\hat{p}$) make a right-handed triple. The associated scalar τ *(Veronis, 1972)* is sometimes called spicyness. Eq. (B.30) becomes

$$p_o \oint_{S'} \left(\frac{\partial}{\partial p} D \underset{\sim}{\hat{\rho}}\right) \cdot dn' = p_o \oint_{S'} \left(\frac{\partial D}{\partial p}\frac{\partial \varphi}{\partial p} \underset{\sim}{\hat{t}}\right) \cdot dn' \qquad \text{(B.32)}$$

The partial derivatives are functions of the equation of state, mappable in (s, θ, p) coordinates; and $\underset{\sim}{\hat{t}} \cdot dn'$ is, roughly, the projected area on a constant-τ plane that is enclosed by the circuit C'.

Since the dependence of the speed of sound on salinity is small, from Eq. (B.32) we may say that the rectification of any particular trajectory is proportional

to (i) the variation of the speed of sound with potential temperature, and (ii) the projected area on the τ plane that is enclosed by the circuit C'. Rectification is largest per degree change in potential temperature following a neutral trajectory of cold (nominally 1 C) water that conserves (s, θ) as it sinks from the surface to great depth; warms/cools neutrally (isopycnally) at depth; conserves (s, θ) as it rises from great depth to the surface; and cools/warms neutrally at the surface back to its starting temperature. These are also the circumstances where neutral potential temperature changes produce the largest changes in buoyancy potential vorticity.

B.8 A differential equation for neutral surface potential vorticity

A differential equation for the separation between neutral surfaces in the direction of the absolute vorticity vector can be derived from the buoyancy potential vorticity conservation equation.

Neutral surface potential vorticity (*NSPV*) is defined by *(McDougall, 1988)*

$$NSPV = fN^2 \left(\frac{h_1 N_1^2}{h N^2}\right) \tag{B.33}$$

where the subscript (1) refers to the value at a reference cast. Here we use the three dimensional analog, $NSPV_3 = Z \frac{h_1 |\boldsymbol{L}|_1}{h . |\boldsymbol{L}|}$. The absolute vorticity vector makes the same angle with the neutral surface and with the plane perpendicular to $\boldsymbol{L}$. With this definition of $NSPV_3$,

$$dNSPV_3 = (h_1 |\boldsymbol{L}|_1)[(h\,|\boldsymbol{L}|)^{-1}\, dZ + Z\, d(h\,|\boldsymbol{L}|^{-1})\,] = S(\boldsymbol{F}) \quad + \quad S(e) \tag{B.34}$$

where $S(\boldsymbol{F})$ represents frictional and $S(e)$ dianeutral sources of $NSPV_3$.

We may rewrite this as

$$d\,(\ln h) = d\,(\ln |\boldsymbol{L}|^{-1}) + Z^{-1}\, dZ_{RHS} \; - \; (NSPV_3)^{-1}\; [S(\boldsymbol{F}) \; - \; S(e)\;] \tag{B.35}$$

where the subscript RHS indicates that the buoyancy potential vorticity source terms on the right-hand-side of Eq. (B.19) will be used here.

Since the location of the initial cast is arbitrary, we may deduce that in the last three terms of Eq. (B.35), the weighted frictional and dianeutral sources of Z and $NSPV_3$ cancel. This leaves a differential equation for the neutral surface separation in the direction of the absolute vorticity vector in terms of the $(s, \theta, p; Z)$ fields:

$$d \ln h = d|L|^{-1} + Z^{-1}\left(\frac{\partial Z}{\partial p} dp + \frac{\partial Z}{\partial \theta_n} d\theta_n\right) \qquad \text{(B.36)}$$

where we have used the partial derivatives defined by the square-bracketed part of terms (d1) and (d2) in Eq. (B.19), discussion in Sec. B.5, and the square-bracketed part of term $(a_n1)+(a_n2)$ in Eq. (B.25), discussed in Sec. B.6.

The differential equation for h shows that changes in h are proportional to changes in $|L|^{-1}$, plus the pressure and neutral potential temperature buoyancy potential vorticity source terms. *McDougall (1988)* gives an integral form of this equation that compares $NSPV$ to fN^2 in terms of gradients of properties along neutral surfaces and slopes of neutral surfaces, integrated along a parcel path (his equation 53).

B.9 Conclusions

The conservation equation for buoyancy potential vorticity allows buoyancy potential vorticity changes following the flow to be computed and related to changes in neutral surface potential vorticity. The conservation equation, with sources decomposed and grouped into neutral and dianeutral components, is:

$$\frac{DZ}{Dt} = \frac{\omega_a}{\rho}\cdot\Big\{ \underbrace{\nabla\frac{D\sigma_r}{Dt}}_{(A)} \underbrace{-(2\theta_o{}^2\rho\alpha')^{-1}\frac{\partial D^2}{\partial p}\frac{D\theta_d}{Dt}\nabla p}_{(B)} \underbrace{+\Big[\frac{D^2}{\rho\beta' s_o\theta_o}\frac{\partial\varphi}{\partial p}\nabla\theta_n + (2\theta_o{}^2\rho\alpha')^{-1}\frac{\partial D^2}{\partial p}\nabla\theta_d\Big]\frac{Dp}{Dt}}_{(C)} \Big\} \underbrace{-\frac{D^2}{\rho\beta' s_o\theta_o}\frac{D\theta_n}{Dt}}_{(D)} \underbrace{+\rho^{-1}L\cdot\nabla\mathbf{x}\left(\frac{F}{\rho}\right)}_{(E)} \tag{B.37}$$

A glossary of symbols and guide to equations follows the conclusions.

Source term (A) represents gradients, in the absolute vorticity vector direction, of locally-referenced potential density changes following the flow. This is analogous to the source term due to gradients of sources of a scalar λ in the equation for Ertel's potential vorticity equation constructed from gradients of λ.

Source term (B) arises from the crowding together in salinity/potential temperature coordinates of isopycnals with pressure, and the dianeutral part of potential temperature changes following the flow; this could, of course, have been written in terms of the dianeutral part of salinity changes instead. The dianeutral component of changes following the flow is perpendicular in salinity-potential temperature coordinates to the locally-referenced potential density isopleth; the neutral component is tangent to this isopleth.

Source term (C) arises from the turning in salinity/potential temperature coordinates of isopycnals with pressure, and the neutral part of potential temperature changes following the flow; again, this could have been written in terms of the neutral part of salinity changes. Buoyancy potential vorticity increases about 4×10^{-12} $m^{-1}s^{-1}$ K^{-1} with neutral potential temperature increases for cold water where the turning is greatest. Since the source term does not scale with the buoyancy potential vorticity itself, it is proportionally most important in weakly stratified water. It can be as large as the pressure dependent source (term D) in cold, weakly stratified ocean water. An integral equation for neutral trajectory rectification (helicity) shows that it scales with this source term.

Source term (D) arises from flow across isobars and the crowding and turning of isopycnals with pressure. Buoyancy potential vorticity increases by about a quarter of its value for warm water displaced from the surface to the thermocline, and by a third for cold water displaced from the surface to the bottom. These values are about equal to a single contour interval on potential vorticity plots appearing in the literature.

Source term (E) is due to frictional torques in the fluid.

Gradients of neutral surface potential vorticity are proportional to gradients of buoyancy potential vorticity, plus contributions due to the buoyancy potential vorticity source terms (C) and (D). A differential equation for neutral surface potential vorticity,

derived from the buoyancy potential vorticity conservation equation, appears as Eq. (B.36).

B.10 Glossary of symbols and guide to equations

c	sound speed (see Eq. B.3)
D	density increment on a (s, θ) plot (see Eq. B.21)
$\boldsymbol{F}$	frictional force vector
f	Coriolis parameter, $2\Omega sin\ \lambda$, where λ is latitude
g	gravitational acceleration
$\hat{\imath}, \hat{\jmath}, \hat{k}$	Cartesian unit vectors
$\boldsymbol{L}$	buoyancy gradient vector (see Eq. B.9)
N	Brunt-Väisälä or buoyancy frequency (see Eq. B.5)
q	potential vorticity (see Eq. B.1, B.2)
p	pressure
$\hat{\boldsymbol{p}}$	unit vector along salinity axis of (s, θ, p) coordinates
p_o	pressure per unit distance in (s, θ, p) coordinates
r	reference pressure
s	salinity
s_n, s_d	neutral and dianeutral parts of salinity gradients or changes following the flow (see Eq. B.22 and B.23).
s_o	salinity per unit distance in (s, θ, p) coordinates
$\hat{\boldsymbol{s}}$	unit vector along salinity axis of (s, θ, p) coordinates
t	time
u, v, w	Cartesian components of velocity vector
x, y, z	Cartesian coordinates
Z	buoyancy potential vorticity, constructed from $\boldsymbol{L}$ (see Eq. B.10)
α', β'	potential temperature expansion and salinity expansion coefficient in (s, θ, p) coordinates (see paragraph following Eq. B.7)
φ	angle between salinity axis and isopleth of density (see Eq. B.20)
ρ	density
σ	potential density (see Eq. B.4)

σ_m	potential density referenced to $(m \cdot 1000)$ dbar pressure, $n = 0, 1, 2, \ldots$
θ	potential temperature
θ_n, θ_d	neutral and dianeutral parts of potential temperature gradients or changes following the flow (see Eq. B.22 and B.23).
θ_o	potential temperature per unit distance in (s, θ, p) coordinates
$\underset{\sim}{\hat{\theta}}$	unit vector along potential temperature axis of (s, θ, p) coordinates
Ω	Earth's rotation rate
$\underset{\sim}{\Omega}$	planetary vorticity vector
$\underset{\sim}{\omega_a}$	absolute vorticity vector
ω	cross-isobar (diabaric) velocity $(\frac{Dp}{Dt})$
$\underset{\sim}{\zeta}$	relative vorticity vector

REFERENCES

Armi, L., and H. Stommel , 1983: Four views of a portion of the North Atlantic subtropical gyre. *J. Phys. Oceanogr.*, **13**, 828 - 857.

Bang, N. D. and F. C. Pearce, 1970: Hydrological data. Agulhas Current Project, March 1969. Institute of Oceanography, University of Cape Town. *Data Report No. 4*, 26 pp.

Boudra, D. B., and W. P. M. de Ruijter, 1986: The wind-driven circulation of the South Atlantic-Indian Ocean—II. Experiments using a multi-layer numerical model. *Deep-Sea Res.*, **33**, 447-482.

Bower, A. S., 1988: Isopycnal drifter studies in the Gulf Stream. Ph.D. dissertation, Univ. Rhode Island, 187 pp.

_____, 1988: Isopycnal drifter studies in the Gulf Stream. Ph.D. dissertation, University of Rhode Island. 187 pp.

Bryden, H., 1979: Poleward heat flux and conversion of available potential energy in Drake Passage. *J. Mar. Res.*, **37**, 1 - 22.

Bunker, A. F., 1980: Trends of variables and energy fluxes over the Atlantic Ocean from 1948 to 1972. *Mon. Wea. Rev.*, **108**, 720 - 732.

_____ 1987: Surface energy fluxes of the South Atlantic Ocean. *Mon. Wea. Rev.*, in press.

Chapman, P., and L. V. Shannon, 1985: The Benguela ecosystem, part II. Chemistry and related processes. *Oceanogr. Mar. Biol. Ann. Rev.*, **23**, 183-251.

Charney, J. G., 1955: The Gulf Stream as an inertial boundary layer. *Proc. Nat. Acad. Sci. U.S.A*, **41**, 477 - 498.

Cheney, R. E., J. G. Marsh, and B. D. Beckley, 1983: Global mesoscale variability from collinear tracks of SEASAT altimeter data. *J. Geophys. Res.*, **88**, 4343 – 4354.

Chew, F., 1974: The turning process in meandering currents: a case study. *J. Phys. Oceanogr.*, **4**, 27 - 57.

Cornillon, P., 1986: The effect of the New England Seamounts on Gulf Stream meandering as observed from satellite IR imagery. *J. Phys. Oceangr.*, **2**, 386 - 389.

Darbyshire, J., 1972: The effect of bottom topography on the Agulhas Current. *Pure Appl. Geophys.*, **101**, IX, 208 - 220.

de Ruijter, W. P. M., 1982: Asymptotic analysis of the Agulhas and Brazil Current systems. *J. Phys. Oceanogr.*, **12**, 361 - 373.

_____, and D. B. Boudra, 1985: The wind-driven circulation in the South Atlantic-Indian Ocean - I. Numerical experiments in a one-layer model. *Deep-Sea Res.*, **32**, 557 - 574.

_____, and D. B. Boudra, 1985: The wind-driven circulation in the South Atlantic-Indian Ocean—I. Numerical experiments in a one-layer model. *Deep-Sea Res.*, **32**, 557-574.

Deacon, G. E. R., 1937: The hydrology of the Southern Ocean. *Discovery Reports*, **15**,1-124.

Duncan, C. P., 1970: The Agulhas Current. Ph.D. thesis, University of Hawaii, 76 pp.

Ertel, H., 1942: *Ein neuer hydrodynamischer Wirbesatz. Meteorolol. Z.*, **59**, 277 - 281.

Fu, L., 1986: Mass, heat, and freshwater fluxes in the south Indian Ocean. *J. Phys. Oceanogr.*, **16**, 1683 – 1693.

Fuglister, F. C., and A. D. Voorhis, 1965: A new method of tracking the Gulf Stream. *Limnol. Oceanogr.*, **10** (Suppl.), 115 - 124.

Garrett, C., 1982: On spindown in the ocean interior. *J. Phys. Oceanogr.*, **12**, 989 - 983.

Gill, A. E., 1982: Atmosphere-Ocean Dynamics. International Geophysics Series, **30**, Academic Press, 662 pp.

_____, J. S. A. Green, and A. J. Simmons, 1974: Energy partition in the large scale ocean circulation and the production of mid-ocean eddies. *Deep-Sea Res.*, **21**, 499 - 528.

Gordon, A. L., 1985: Indian-Atlantic transfer of thermocline water at the Agulhas retroflection. *Science*, **227**, 1030 - 1033.

_____, 1986: Inter-ocean exchange of thermocline water. *J. Geophys. Res.*, **91**, 5037 - 5046.

_____, J. R. E. Lutjeharms, and M. L. Gründlingh, 1987: Stratification and circulation at the Agulhas Retroflection. *Deep-Sea Res.*, **34**, 565 - 599.

Gründlingh, M. L., 1977: Drift observations from *Nimbus VI* satellite-tracked buoys in the southwestern Indian Ocean. *Deep-Sea Res.*, **24**, 903-913.

_____, 1978: Drift of a satellite tracked buoy. *Deep-Sea Res.*, **25**, 1209-1224.

_____, 1980: On the volume transport of the Agulhas Current. *Deep-Sea Res.*, **27A**, 557-563.

_____, 1985: An intense cyclonic eddy east of the Mozambique Ridge. *J. Geophys. Res.*, **90**, 7163-7167.

_____, 1985: Occurrence of the Red Sea Water in the south western Indian Ocean, 1981. *J. Phys. Oceanogr.*, **15**, 207-212.

Hall, M. M., 1985: Horizontal and vertical structure of velocity, potential vorticity and energy in the Gulf Stream. Ph.D. dissertation, M.I.T./W.H.O.I. Joint Program in Oceanography, 165 pp.

Haney, R. L., 1971: Surface thermal boundary condition for ocean circulation models. *J. Phys. Oceanogr.*, **1**, 241 - 248.

Harris, T. F. W., 1972: Sources of the Agulhas Current in the spring of 1964. *Deep-Sea Res., 19*, 633 - 650.

_____, and N. D. Bang, 1974: Topographic Rossby waves in the Agulhas Current. *S. African J. Sci.*, **70**, 212-214.

_____, and D. van Foreest, 1978: The Agulhas current in March 1969. *Deep-Sea Res.*, **25**, 549-561.

Hastenrath, S., 1982: On meridional heat transports in the world ocean. *J. Phys. Oceanogr.*, **12**, 922-927.

Helland-Hansen, B., 1905: The Sognefjord section. *James Johnstone Memorial Volume*. Lancashire Sea-Fisheries Laboratory. University Press, Liverpool: 257–274.

Hellerman, S., 1967: An updated estimate of the wind stress in the World Ocean. *Mon. Wea. Rev., 95*, 607 - 626 (corrected tables in **96**, 62 - 626).

_____, and M. Rosenstein, 1983: Normal monthly wind stress over the world ocean with error estimates. *J. Phys. Oceangr.*, **32**, 1093–1104.

Holton, J. R., 1979: *An Introduction to Dynamic Meterorology, Int. Geophys. Ser.*, **23**, Academic Press, New York. 391 pp.

Ivers, W.D., 1975: The deep circulation in the northern North Atlantic, with especial reference to the Labrador Sea. Ph.D. thesis Univ. California, San Diego.

Jacobs, S. S., and D. T. Georgi, 1977: Observations on the Southwest Indian/Antarctic Ocean. In: *A Voyage of Discovery* , George Deacon 70th anniversary volume, M. Angel, ed., *Deep-Sea Res.*, **24**, (Suppl.), Pergamon Press, Oxford, 43-84.

Johns, W. E., 1988: One-dimensional baroclinically unstable waves on the Gulf Stream potential vorticity gradient near Cape Hatteras. *Dyn. Atmos. Oceans*, **11**, 323-350.

Kawai, H., 1957: On the natural coordinate system and its applications to the Kuroshio system. Bull. Tôhuku Reg. Reg. Fish. Lab., **10**.

Keffer, T., 1985: The ventilation of the world's oceans: maps of the potential vorticity field. *J. Phys. Oceanogr.*, **15**, 509–523.

Killworth, P. D., 1980: Barotropic and baroclinic instability in rotating stratified fluids. *Dyn. Atmos. Oceans*, **4**, 143 - 184.

Levitus, 1982: Climatological atlas of the World Ocean. NOAA professional paper 13, U.S. Department of Commerce. 173 pp.

Luetkemeyer, K., 1987: Satellite image processing for the Agulhas Retroflection Region. WHOI Technical Report 87-27. 76 pp.

Lutjeharms, J. R. E., and H. R. Valentine, 1984: Southern Ocean thermal fronts south of Africa. *Deep-Sea Res.*, **31**, 1461-1475.

_____, and R. C. van Ballegooyen, 1984: Topographic control in the Agulhas Current system. *Deep-Sea Res.*, **31**, 1321-1337.

_____, and R. C. van Ballegooyen, 1988: The retroflection of the Agulhas Current. *J. Phys. Oceanogr.*, submitted.

Lynn, R. J., and J. L. Reid, 1971: On the influence of the Norwegian-Greenland and Weddell seas upon the bottom waters of the Indian and Pacific oceans. *Deep-Sea Res.*, **18**, 1063 - 1088.

McCartney, M.S., 1976: The interaction of zonal currents with topography with applications to the Southern Ocean. *Deep-Sea Res.*, **23**, 413 - 427.

_____, 1977: Subantarctic Mode Water. In: *A Voyage of Discovery*. Pergamon Press, 103 - 119.

_____, 1982: Subtropical recirculation of Mode Waters. *J. Mar. Res.*, **40** *(Suppl.)*, 427 - 464.

_____, 1982: The subtropical recirculation of Mode Waters. *J. Mar. Res.*, **40** (Suppl.), 427 – 464.

McDougall, T. J., 1984: The relative roles of diapycnal and isopycnal mixing on subsurface water mass conversion. *J. Phys. Oceanogr.*, **14**, 1577 - 1589.

_____, 1987: Neutral surfaces in the ocean: implications for modelling. *Geophys. Res. Lett.*, paper no. 7L6552.

_____, 1987: Neutral surfaces. *J. Phys. Oceanogr.*, **17**, 1950 - 1964.

_____, 1987: Thermobaricity, cabbeling, and water-mass conversion. *J. Geophys. Res.*, **92**, 5448 - 5464.

_____, 1988: Neutral-surface potential vorticity. *Deep-Sea Res.*, submitted.

_____, and D. R. Jackett, 1988: On the helical nature of neutral trajectories in the ocean. *Deep-Sea Res.*, submitted.

McDowell, S., P. Rhines, and T. Keffer, 1982: North Atlantic potential vorticity and its relation to the general circulation. *J. Phys. Oceanogr.*, **12**, 1417 - 1436.

Munk, W. H., 1950: On the wind-driven ocean circulation. *J. Meteor.*, **7**, 79 - 93.

_____ and G. F. Carrier, 1950: The wind-driven circulation in ocean basins of various shapes. *Tellus*, **2**, 158 – 167.

Neumann, G., 1960: On the dynamical structure of the Gulf Stream as an equivalent-barotropic flow. *J. Geophys. Res.*, **65**, 239 - 247.

Olson, D.B., and R. H. Evans, 1986: Rings of the Agulhas Current. *Deep-Sea Res.*, **33**, 27-42.

Ou, H. W. and W. P. M. de Ruijter, 1986: Separation of an inertial boundary current from a curved coastline. *J. Phys. Oceanogr.*, **16**, 280-289.

Ou, H. W., W. P. M. de Ruijter, 1986: Separation of an inertial boundary current from a curved coastline, *J. Phys. Oceanogr.*, **16**, 280 - 289.

Pedlosky, J., 1979: Geophysical Fluid Dynamics. Springer-Verlag, 624 pp.

_____, 1985: The instability of continuous heton clouds. *J. Atmos. Sci..*, 1477 - 1486.

Press, W. H., B. P. Flannery, S. A. Teukolsky, W. T. Vetterling, 1988: *Numerical recipes in C: the art of scientific computing.* Cambridge University Press, 735 pp.

Rhines, P. B., 1983: Gyration. Unpubl. manuscript.

_____, and W. R. Young, 1982: A theory of wind-driven circulation - I. Mid-ocean gyres. *J. Mar. Res.*, **40** (Suppl.), 559 - 596.

Ring Group, 1981: Gulf Stream cold-core rings: their physics, chemistry, and biology. *Science*, **212**, 1091-1100.

Rintoul, S. R., 1988: Mass, heat, and nutrient fluxes in the Atlantic Ocean determined by inverse methods. Ph.D. dissertation, M.I.T./W.H.O.I. Joint Program. 287 pp.

Robinson, A. R., J. R. Luyten, and G. Flierl, 1975: On the theory of thin rotating jets: a quasi-geostrophic time dependent model. *Geophys. Fluid Dyn.*, **6**, 211 - 244.

Saetre, R., and A. Jorge da Silvia, 1984: The circulation of the Mozambique Channel. *Deep-Sea Res.*, **31**, 485 – 508.

Schmitt, R. W., 1981: Form of the temperature-salinity relationship in the Central Water: evidence for double-diffusive mixing. *J. Phys. Oceangr.*, **11**, 1015 - 1026.

Shepherd, J. G., 1979: On isopycnal movements, neutral surfaces, and vertical transport in the ocean. Unpublished manuscript.

Stommel, H., 1948: The western intensification of wind-driven ocean currents. *Trans. Amer. Geophys. Union,* **99**, 202 - 206.

Talley, L. D., 1982: Instabilities and radiation of thin, baroclinic jets. Ph.D. dissertation, M.I.T./W.H.O.I. Joint Program, 233 pp.

_____, and M. S. McCartney, 1982: Distribution and Circulation of Labrador Sea Water. *J. Phys. Oceanogr.*, **12**, 1189 - 1205.

Toole, J., and M. Raymer, 1985: Heat and fresh water budgets of the Indian Ocean - revisited. *Deep-Sea Res.*, **32**, 917-928.

Veronis, G. 1973: Model of world ocean circulation: I. Wind–driven, two layer. *J. Mar. Res.* **31**, 228-288.

_____, 1972: On properties of seawater defined by temperature, salinity, and pressure. *J. Mar. Res.*, **30**, 227 - 255.

Warren, B. A., 1963: Topographic influences on the path of the Gulf Stream. *Tellus*, **XV** (2), 167 - 183.

Warren, B. A., 1981: Transindian hydrographic section at lat. 18°S: property distributions and circulation in the South Indian Ocean. *Deep–Sea Res.*, **28A**, 259 – 788.

Watts, D. R., 1983: Gulf Stream variability. In: *Eddies in Marine Science,* 112 - 144. Springer-Verlag, 609 pp.

Worthington, L.V., and H. Kawai, 1972: Comparison between deep sections across the Kuroshio and the Florida Current and Gulf Stream. In: *Kuroshio, its physical aspects.* H. Stommel and K. Yoshida, ed., 371 - 386.

Wright, D. G., 1981: Baroclinic instability in Drake Passage. *J. Phys. Oceanogr.*, **11**, 231 - 246.

Wunsch, C., 1978: The North Atlantic circulation west of 50°W determined by inverse methods. *Rev. Geophys. Space Phys.*, **16**, 583 – 620.

Wyrtki, K., 1971: Oceanographic Atlas of the International Indian Ocean Expedition. National Science Foundation, Washington, D.C., 531 pp.

BIOGRAPHY AND LIST OF PUBLICATIONS

A native of a suburb of Cleveland, Ohio, the author attended Miami University in Oxford, Ohio, and worked and travelled in West Africa and Europe, eventually completing her undergraduate studies at Colorado State University, Fort Collins, at age 20. After university she worked as a writer, teacher, and research assistant for a variety of Colorado and Northern California companies engaged in solar, telecommunications, and software engineering. Her other interests include sports, history, music, and human rights.

PUBLICATIONS

Bennett, S.L, 1986: The relationship between vertical, diapycnal, and isopycnal velocity and mixing in the ocean general circulation. *J. Phys. Oceanogr.*, **16**, 167-174.

McCartney, M.S., S.L. Bennett, M.E. Woodgate-Jones, and M.L. Bremer: Eastward flow through the Mid-Atlantic Ridge at 11°N and its influence on the abyss of the eastern basin. *J. Phys. Oceanogr.*, submitted.

NON-REFEREED PUBLICATIONS

Bennett, S.L., M.S. McCartney, and M.L. Bremer, 1983: Some aspects of the deep circulation of the tropical North Atlantic. EOS, Transactions, American Geophysical Union, **65** (52), 1027 (abstract).

Bennett, Sara L., James R. Luyten, and John M. Toole, 1985: The Agulhas and Agulhas Return Currents: analysis of CTD/O_2 sections crossing the Currents and an XBT survey following the 15°C at 200 m contour. EOS, Transactions, American Geophysical Union, **66** (46), 930 (abstract).

IN PREPARATION

Bennett, S.L.: Buoyancy potential vorticity: conservation equation and relation to neutral surface potential vorticity.